Doctoral Course in Physics Cycle XXXVIII

Taking time to understand gamma-ray bursts: temporal variability as a probe of the inner engines and progenitors

Candidate: Romain Maccary
Supervisor: Prof. Cristiano Guidorzi

Università degli Studi di Ferrara
Dipartimento di Fisica e Scienze della Terra
October 2025 –

ABSTRACT

The aim of my thesis is the study of gamma-ray bursts (GRBs), powerful, short-lived events produced at cosmological distances by catastrophic phenomena, such as the collapse of a massive star or the coalescence of two compact objects. Since their discovery, GRBs and their following afterglow emission have been routinely scrutinised with observations across the whole electromagnetic spectrum, from radio to gamma-rays, up to TeV energies. Yet, many questions remain unanswered: what mechanism causes the prompt gamma-ray emission? What drives the extreme variability observed in GRB light curves? Can the nature of the GRB progenitor system be inferred from the temporal profile of the prompt emission?

In my PhD research, I studied the temporal properties of the GRB prompt emission. To this end, I used the Multiple Excess Pattern Search Algorithm (MEPSA) to identify and characterise the temporal variability of GRB light curves. The use of this algorithm led to several dedicated studies:

(i) investigation of the presence of self-organised criticality (SOC) in the GRB prompt emission;

(ii) identification of two variability components in GRB time profiles and the investigation of their origin in theoretical models and numerical simulations;

(iii) computation of the minimum variability timescale (MVT), a useful indicator of the GRB progenitor nature;

(iv) discovery of a unique set of temporal properties in a peculiar long GRB originating from compact object mergers (GRB 230307A), possibly shared by other similar events;

(v) use of stochastic differential equations (SDEs) to model GRB prompt emission as a stochastic process;

(vi) exploration of entropy metrics to characterise the dynamics of the prompt emission and assess its stochastic versus deterministic nature.

The first four points have led to scientific publications in peer-reviewed journals. The goal of the first study was to provide a precise description of the GRB dynamics and to constrain the way the central engine releases its energy over time. In the second study, we established that there are two different dynamics in GRB light curves, which could have strong implications on the possible interpretations. The last two works provide ways to identify events associated with compact object mergers, which are among the strongest sources of gravitational waves detected so far, directly from their early gamma-ray time profiles. The peculiar features identified in our last work, especially the observed pulse width increase, challenge the commonly accepted picture of the internal shocks model in which no variation of this timescale is expected. Along with the estimate of the MVT, they also offer new methods for identifying events from compact object mergers along with a constraining set of properties for the theoretical models, a development of particular relevance at the dawn of multi-messenger astronomy.

The last two points correspond to ongoing projects that require additional development. They aim to provide a more comprehensive characterisation of the complex dynamics governing the prompt emission and to assess whether its variability is stochastic or deterministic in nature.

RIASSUNTO

L'obiettivo della mia tesi è stato lo studio dei lampi di raggi gamma (GRB), eventi potenti e di breve durata prodotti a distanze cosmologiche da fenomeni catastrofici, come il collasso di una stella massiccia o la coalescenza di due oggetti compatti. Fin dalla loro scoperta, i GRB e la loro successiva emissione di afterglow sono stati sistematicamente osservati attraverso l'intero spettro elettromagnetico, dalle onde radio ai raggi gamma, fino alle energie del TeV. Tuttavia, molte domande rimangono ancora senza risposta: quale meccanismo genera l'emissione prompt in raggi gamma? Cosa determina l'estrema variabilità osservata nelle curve di luce dei GRB? È possibile identificare la natura del sistema progenitore di un GRB a partire dal profilo temporale della sua emissione prompt?

Nel mio lavoro di dottorato mi sono concentrato in particolare sullo studio delle proprietà temporali dell'emissione prompt dei GRB. A questo scopo, ho utilizzato l'algoritmo Multiple Excess Pattern Search Algorithm (MEPSA) per identificare e caratterizzare la variabilità temporale nelle curve di luce dei GRB. L'utilizzo di questo algoritmo ha portato a diversi studi specifici:

(i) l'indagine della presenza di criticità auto-organizzata, in inglese "self-organised criticality" (SOC), nell'emissione prompt dei GRB;

(ii) l'identificazione di due componenti di variabilità nei profili temporali dei GRB e lo studio della loro origine in modelli teorici e simulazioni numeriche;

(iii) il calcolo della variabilità temporale minima (MVT, dall'inglese "minimum variability timescale"), un indicatore utile per la natura del progenitore del GRB;

(iv) la scoperta di un insieme unico di proprietà temporali in un particolare GRB lungo, originato dalla coalescenza di due oggetti compatti (GRB 230307A), probabilmente condiviso anche da altri eventi simili;

(v) l'uso di equazioni differenziali stocastiche (SDE) per modellare l'emissione prompt dei GRB come un processo stocastico;

(vi) l'esplorazione di metriche entropiche per caratterizzare la dinamica dell'emissione prompt e valutarne la natura stocastica o deterministica.

I primi quattro punti hanno portato a pubblicazioni scientifiche su riviste con revisione tra pari. Lo scopo del primo studio è stato quello di fornire una descrizione precisa della dinamica dei GRB e vincolare il modo in cui il motore centrale rilascia energia nel tempo. Nel secondo studio abbiamo stabilito l'esistenza di due diverse dinamiche nelle curve di luce dei GRB, con importanti implicazioni per i modelli teorici. Gli ultimi due lavori propongono nuovi metodi per identificare gli eventi associati alle fusioni di oggetti compatti — tra le sorgenti più potenti di onde gravitazionali finora rilevate — direttamente dai loro profili temporali in raggi gamma. Le caratteristiche peculiari identificate nel nostro ultimo lavoro, mettono in discussione il modello comunemente accettato degli urti interni, secondo il quale non ci si aspetta alcuna variazione delle scale temporali osservate nella curva di luce. Insieme alla stima della MVT, essi offrono nuovi strumenti per riconoscere gli eventi prodotti da coalescenze di oggetti compatti e una serie di vincoli stringenti per i modelli teorici che cercano di spiegarli, un risultato di particolare rilevanza nell'alba dell'astronomia multi-messaggera.

Gli ultimi due punti sono progetti in corso che richiedono ancora ulteriore lavoro. Il loro obiettivo è migliorare la caratterizzazione della complessa dinamica alla base dell'emissione prompt e determinare se il suo comportamento sia di natura stocastica o deterministica.

PUBLICATIONS

As a first author,

Maccary, R. et al. (Aug. 2024a). "Distribution of the number of peaks within a long gamma-ray burst: The full Fermi/GBM catalogue." In: *A&A* 688, L8, p. L8. doi: `10.1051/0004-6361/202450666`. arXiv: `2407.06002 [astro-ph.HE]`.

Maccary, R. et al. (Apr. 2024b). "Distributions of Energy, Luminosity, Duration, and Waiting Times of Gamma-Ray Burst Pulses with Known Redshift Detected by Fermi/GBM." In: *ApJ* 965.1, 72, p. 72. doi: `10.3847/1538-4357/ad26f4`. arXiv: `2401.14063 [astro-ph.HE]`.

Maccary, R. et al. (Oct. 2025). "Gamma-ray burst minimum variability timescales with Fermi/GBM." In: *A&A* 702, A95, A95. doi: `10.1051/0004-6361/202555418`. arXiv: `2508.08995 [astro-ph.HE]`.

Maccary, R. et al. (Jan. 2026). "A set of distinctive properties ruling the prompt emission of GRB 230307A and other long γ-ray bursts from compact object mergers." In: *Journal of High Energy Astrophysics* 49, 100456, p. 100456. doi: `10.1016/j.jheap.2025.100456`. arXiv: `2509.05628 [astro-ph.HE]`.

As a co-author,

An, Zheng-Hua et al. (Mar. 2023). "Insight-HXMT and GECAM-C observations of the brightest-of-all-time GRB 221009A." In: *arXiv e-prints*, arXiv:2303.01203, arXiv:2303.01203. doi: `10.48550/arXiv.2303.01203`. arXiv: `2303.01203 [astro-ph.HE]`.

Bazzanini, L. et al. (Sept. 2024). "Long gamma-ray burst light curves as the result of a common stochastic pulse–avalanche process." In: *A&A* 689, A266, A266. doi: `10.1051/0004-6361/202450150`. arXiv: `2403.18754 [astro-ph.HE]`.

Camisasca, A. E. et al. (Mar. 2023). "GRB minimum variability timescale with Insight-HXMT and Swift. Implications for progenitor models, dissipation physics, and GRB classifications." In: *A&A* 671, A112, A112. doi: `10.1051/0004-6361/202245657`. arXiv: `2301.01176 [astro-ph.HE]`.

Guidorzi, C. et al. (May 2024a). "Distribution of the number of peaks within a long gamma-ray burst." In: *A&A* 685, A34, A34. doi: `10.1051/0004-6361/202449200`. arXiv: `2402.17282 [astro-ph.HE]`.

Guidorzi, C. et al. (Oct. 2024b). "New results on the gamma-ray burst variability–luminosity relation." In: *A&A* 690, A261, A261. doi: `10.1051/0004-6361/202451401`.

Guidorzi, C. et al. (May 2025a). "A search for periodic activity in multi-peaked long gamma-ray bursts." In: *A&A* 697, A228, A228. doi: `10.1051/0004-6361/202452326`. arXiv: `2504.07550 [astro-ph.HE]`.

Guidorzi, C. et al. (Sept. 2025b). "GRB X-ray plateaus as evidence that the afterglow begins before the prompt gamma-ray emission." In: *arXiv e-prints*, arXiv:2509.18996, arXiv:2509.18996. doi: `10.48550/arXiv.2509.18996`. arXiv: `2509.18996 [astro-ph.HE]`.

Maistrello, M., R. Maccary, and C. Guidorzi (2025). "FAST-MEPSA: An optimised and faster version of peak detection algorithm MEPSA." In: *Astronomy and Computing* 55, p. 101040. doi: `10.1016/j.ascom.2025.101040`. url: `https://doi.org/10.1016/j.ascom.2025.101040`.

Maistrello, M. et al. (Apr. 2024). “The dispersion of the $E_{p,i}$-L_{iso} correlation of long gamma-ray bursts is partially due to assembling different sources.” In: *A&A* 684, L10, p. L10. DOI: `10.1051/0004-6361/202449165`. arXiv: `2403.11923 [astro-ph.HE]`.

Maistrello, M. et al. (May 2025). “An advanced pulse-avalanche stochastic model of long gamma-ray burst light curves.” In: *A&A* 697, A76, A76. DOI: `10.1051/0004-6361/202553821`.

ACKNOWLEDGMENTS

Ringrazio Cristiano Guidorzi per la sua disponibilità e la sua costante dedizione durante il dottorato, che mi ha, tra l'altro, permesso di realizzare questa tesi. Ma soprattutto lo ringrazio per la sua perseveranza nel voler insegnarmi la musica classica francese, nonostante la mia totale ignoranza sull'argomento. Adesso conosco molto bene i nomi di Jean-Philippe Rameau, Georges Bizet, Erik Satie, Jean-Baptiste Lully, Claude Debussy e tutti gli altri nomi che mi avrà menzionato e che ho dimenticato. Questa cultura musicale che mi sarà certamente preziosa in quelle conversazioni colte che, molto probabilmente, non avrò mai, visto il mio costante stato di analfabetismo musicale. Ringrazio molto Sofia, che mi ha guidato sulla strada dell'astrofisica dei fenomeni transienti ad alte energie, in particolare i lampi di raggi gamma, quando stavo a Parigi e che mi ha fatto scoprire l'Italia e in particolare la città di Ferrara (certo che per un francese la doppia r non è facilissima da pronunciare ma fa lo stesso) e i suoi buonissimi cappellacci di zucca. Ringrazio tutti i compagni che sono passati nella C430 durante il mio dottorato: Bazz (la prima persona che ho conosciuto all'università), Giuseppe, Anna, Andrea, Martina, Manuele, Giorgia, Michele, Ridha (+ Valentina, anche se è un'intrusa cosmologa, e Pietro, anche se non c'è mai) e tutti i ragazzi del quarto piano, con cui mi sono divertito un sacco. Mi ricorderò i tornei di ping-pong e i dundies awards in cui vinsi il premio di "miglior francese" (essendo l'unico francese in lotta, sì mi piace vincere facile) soprattutto Andrea M. per la battuta della yellow pecora. Grazie a Viola per il suo sostegno, la sua simpatia e la pasta al pesto. Ringrazio Shahzeb e Mary, con cui ho condiviso casa per più di tre anni e con cui ho combinato molti disastri e grazie alle telecamere che mi hanno sempre protetto dagli intrusi. Grazie ai compagni Litz e Marta. Un grazie molto speciale alla mia carissima amica Silvia, che mi ha sempre sostenuto durante il dottorato. Merci à mes deux parents, Marie-Luce et Stéphane, qui m'ont toujours soutenu pendant ces longues années d'études. Je dédie cette thèse à la mémoire de ma tante bien-aimée Emmanuelle, malheureusement partie trop tôt, et à mes cousins Joaquim et Carla.

CONTENTS

1

GAMMA-RAY BURSTS: SO MUCH PHYSICS IN SUCH LITTLE TIME

More than half a century after their discovery, gamma-ray bursts (GRBs) remain at the forefront of high-energy astrophysics. Their extreme luminosities make them the most violent explosions since the Big Bang and exquisite laboratories for relativistic physics and particle acceleration.

Despite decades of study and increasingly sophisticated instrumentation, many aspects of GRB physics remain uncertain, including the plausible progenitors and central engines, energy dissipation mechanism(s), jet composition, high-energy radiative processes, etc.

Beyond their intrinsic astrophysical richness, GRBs have become indispensable pillars of multi-messenger astronomy. Long GRBs (LGRBs) trace the collapse of massive stars, linking high-energy transients to stellar evolution, core-collapse supernovae (SNe), and chemical enrichment. Short GRBs (SGRBs), in contrast, directly probe the population of compact binary mergers, which are the very same systems that also produce gravitational waves (GWs). The seminal association of GW170817 with a SGRB demonstrated that GRBs are unique electromagnetic beacons of the GW sky, providing arcsecond localisation, redshift measurement, and detailed insight into jet formation and structure.

The observation of GRBs at very high energies further complements neutrino and cosmic-ray observatories by probing Lorentz invariance, cosmic-ray acceleration, and leptonic/hadronic processes in regimes inaccessible on Earth.

As we enter the multi-messenger era, with third-generation GW detectors that will detect thousands of compact object merger (COM) up to $z = 10$, GRBs will become even more central as they will provide electromagnetic counterparts to these sources, enabling for instance precise cosmology with standard sirens. Their cosmological reach extends the multi-messenger frontier to redshifts $z > 8$, making them the primary tool to probe the first generation of stars (Pop III).

1.1 HISTORICAL BACKGROUND

Discovered by chance in the 1970s, no astrophysical sources somehow resembled GRBs. Their emission was remarkably different from the transient phenomena known at the time, such as SNe, flaring stars or periodic emission from pulsars, being both much shorter in duration and far more powerful. They thus formed a peculiar new class of transient events, with an unknown origin. Their compressed timescales implied a compact source and an irreversible evolution associated with a catastrophic phenomenon. However, their origin remained unknown until improved localisation capabilities finally allowed to measure their distance.

1.1.1 *Discovery of gamma-ray bursts*

GRBs were discovered by chance on July 2, 1967, by the American Vela satellites. These satellites were designed to detect gamma-ray radiation produced by nuclear tests in the atmosphere. A few years earlier, the principal nuclear powers—Great Britain, the United States, and the USSR—had signed the Partial Test Ban Treaty on October 10, 1963.

Following this agreement, the Vela [1] satellites were launched between October 1963 (Vela 1A & Vela 1B) and April 1970 (Vela 6A & Vela 6B) to monitor compliance with the agreement. On July 2, 1967, the satellites detected an unexpected gamma-ray signal that was clearly different from the signature of a nuclear explosion. Only seven years later, in 1973, the first paper on their discovery was published (Klebesadel, Strong, and Olson, 1973).

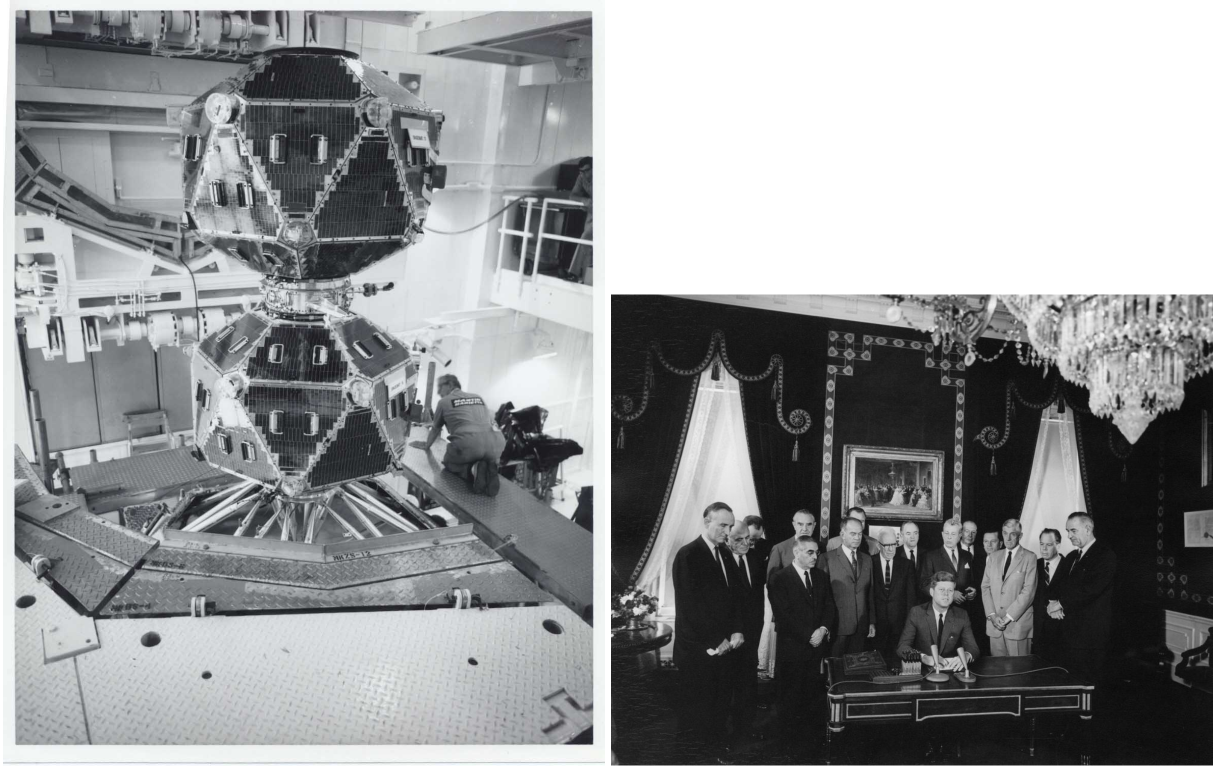

Figure 1: (Left) The Vela 5A/B pair in the clean room (Reproduced courtesy of NASA/Vela Project). (Right) President John F. Kennedy signing the Nuclear Test Ban Treaty on October 7, 1963.

Over time, the Vela satellites detected 16 additional bursts. By analysing the differences in arrival times across the various satellites, a rough estimate of the localisation (within a few degrees) was possible. This localisation was sufficient to establish that they did not originate from the Earth's atmosphere or the Sun, but from a cosmic source.

Between 1969 and 1979, the Vela satellites discovered a total of 73 GRBs. Remarkably, the very first detected burst, GRB 670702, already exhibited the main characteristics of the GRB population observed today: a duration of approximately 10 seconds, a temporal sub-structure composed of two emission episodes, and a peak energy around 1 MeV (Klebesadel, Strong, and Olson, 1973).

---

[1] The name Vela comes from the Spanish verb *velar*, which means *to watch*.

1.1.2 *The distance controversy*

As other GRBs were discovered, the question of their origin became crucial. However, without knowledge of the distance, the question remained unsolved for many years. Several satellites, including BATSE, obtained a distribution of burst positions that appeared isotropic. A very lively debate about the distance scale of gamma-ray bursters persisted until an optical counterpart was found by the BeppoSAX satellite (Sect. 1.1.3), tipping the balance towards an extragalactic origin. Two main hypotheses were proposed:

- (i) GRBs are produced at cosmological distances (e.g. Paczynski 1986; Paczynski 1991);
- (ii) GRBs are galactic, either located within a thick disc of the Milky Way (Colgate and Li, 1998), in a surrounding galactic halo (Mao and Paczynski, 1992), or possibly in an extended galactic "corona" (Lamb, 1995).

The leading advocates of these competing views were Bohdan Paczyński and Don Lamb. The cosmological model implied an isotropic sky distribution and required GRBs to be among the most luminous phenomena ever observed. In contrast, the galactic model struggled to explain the observed isotropy, though some argued that neutron stars (NSs) with high kick velocities could escape the Milky Way and populate a spherical galactic corona. Since the first soft gamma repeater (SGR) was detected in March 1979 (Mazets et al., 1979), it has been known that NSs could emit short bursts of gamma rays, resembling GRBs. We now understand that the 1979 event was in fact a magnetar giant flare, not a typical GRB.

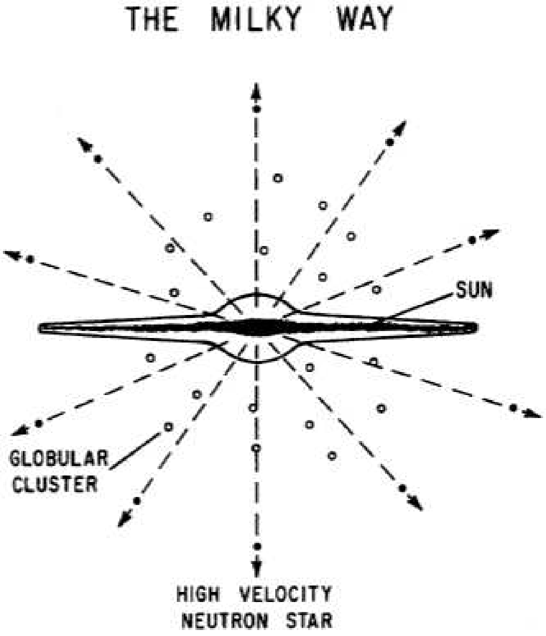

Figure 2: Sketch of one galactic GRB model supported by D. Lamb, in which rapidly orbiting NSs can escape the Milky way to reach a galactic corona. From Lamb (1995).

1.1.3 *The BATSE and BeppoSax era: resolving the distance debate*

BATSE (Burst and Transient Source Experiment, Fishman et al. 1994), on board the *Compton Gamma-ray Observatory* (CGRO, Gehrels et al. 1993), was launched on April 5, 1991. It consisted of eight completely open NaI(Tl) Large Area Detectors (LADs) at the corners of the spacecraft, each sensitive in the 30 keV–2 MeV energy range. For each LAD, there was a smaller spectroscopy detector (SD) with a large detection area, with a great energy resolution and a wide energy range (10 keV–11 MeV).

BATSE confirmed that GRBs were isotropically distributed all over the sky (Meegan et al. 1992, Fig. 3), discovered the bi-modality of the duration (T_{90}) distribution (Kouveliotou et al. 1993, Fig. 27), and identified the spectral distribution of the prompt emission (Band et al. 1993, Fig. 24) described by a smooth broken power law (the Band function; Sect. 1.6.1). In spite of these significant discoveries, the debate regarding the distance scale remained unsettled.

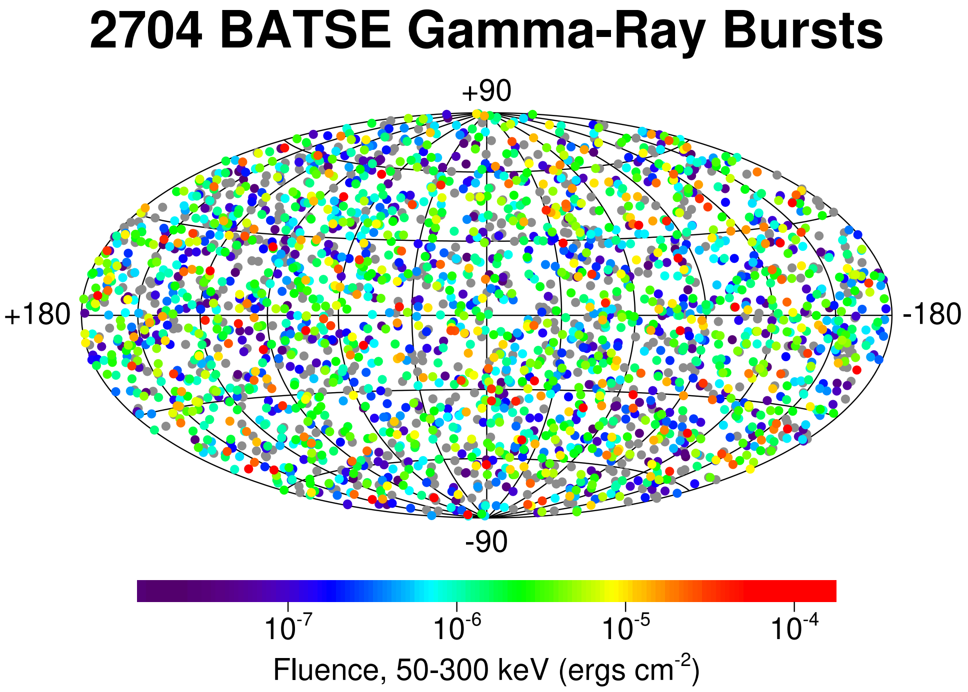

Figure 3: Open sky distribution in galactic coordinates of 2704 GRBs detected with the BATSE experiment aboard the Compton Gamma Ray Observatory satellite.

The resolution of the mystery of GRB distance came with the Italian-Dutch satellite SAX (Satellite per l'Astronomia X), renamed BeppoSAX (Boella et al., 1997a) after the successful launch on April 30, 1996, in honour of the Italian scientist Giuseppe Occhialini. The unique design of this satellite allowed for the discovery of the X-ray afterglow (Costa et al., 1997a) and enabled the first-ever detection of the optical counterpart of a GRB. BeppoSAX was equipped with a set of Narrow Field Instruments (NFIs) covering the energy range from 0.1 to 300 keV:

- LECs (Low Energy Concentration Spectrometer, Parmar et al. 1997), from 0.1 to 10 keV.
- MECs (Medium Energy Concentration Spectrometer, Boella et al. 1997b), from 1.3 to 10 keV.
- HPGSPC (collimated High Pressure Scintillation Proportional Counter, Manzo et al. 1997), from 4 to 120 keV.
- PDS (Collimated Phoswich Detection System, Frontera et al. 1997) 15-300 keV.

Perpendicular to the NFIs were two Wide Field Cameras (WFCs, Jager et al. 1997), each covering a large portion of the sky (20° × 20°) with an angular resolution of about 5 arcminutes. Additionally, the mission team repurposed the four anti-coincidence shields of the PDS as a Gamma-Ray Burst Monitor (GRBM, Frontera et al. 1997), sensitive from 40 to 700 keV. This add-on proved crucial, as two of the shields were aligned with the WFC axes, allowing simultaneous detection of GRBs in both X and gamma rays.

BeppoSAX enabled the first GRB afterglow discovery with GRB 970228 (Costa et al., 1997a). This event was identified by GRBM and localised by one of the WFCs within 5 arcmin. Eight hours later, the NFIs pointed to the burst localisation and were able to follow its fading evolution (Fig. 5).

The Dutch group led by Van Paradijs used the William Herschel and the Isaac Newton telescope to make two observations on 28 Feb 1997, and on 8 March and observed the fading source (van Paradijs et al., 1997).

The first measurement of a GRB distance came a few months later, with GRB 970508 (Costa et al., 1997b; Heise et al., 1997). On May 8, 1997, a GRB was detected by the GRBM and localised by one of the WFCs within 5 arcmin. Six hours later, the NFIs performed the X-ray follow up and saw a fading source. An optical source was detected by Keck-II telescope on 11 May. Several absorption lines were observed, from two locations, one situated at $z = 0.767$, and one at $z = 0.835$ (Metzger et al., 1997). Few weeks later, after the optical transient had faded, some absorption lines from a more extended region, containing the position of the point-like object, were detected: they were emitted by the galaxy that hosted the GRB. The problem of the distance was settled: at least one GRB came from a remote galaxy. This measurement further provided the first scale of the energy released by a GRB. With the observed flux, an energy of about 6×10^{51} erg was estimated.

1.1.4 *The Swift revolution: early afterglow follow-up*

Swift (Gehrels et al., 2004), launched in November 20, 2004, has been monitoring the X- and γ-ray sky for over 20 years. Thanks to its X-ray (XRT, Burrows et al. 2005) and optical (UVOT; Roming et al. 2005) instruments, *Swift* was able to perform rapid slewing and follow-up observations in both X and optical wavelengths, as fast as $1-2$ minutes right after the prompt trigger. This capability made it possible to promptly localise GRBs and monitor the X-ray afterglow of many events with unprecedented detail. This made *Swift*/XRT the ideal instrument to study the transition between prompt and afterglow emission. *Swift* discovered many features of the early afterglow. The canonical behaviour of the X-ray afterglow, as revealed by *Swift*, is shown in Fig. 6.

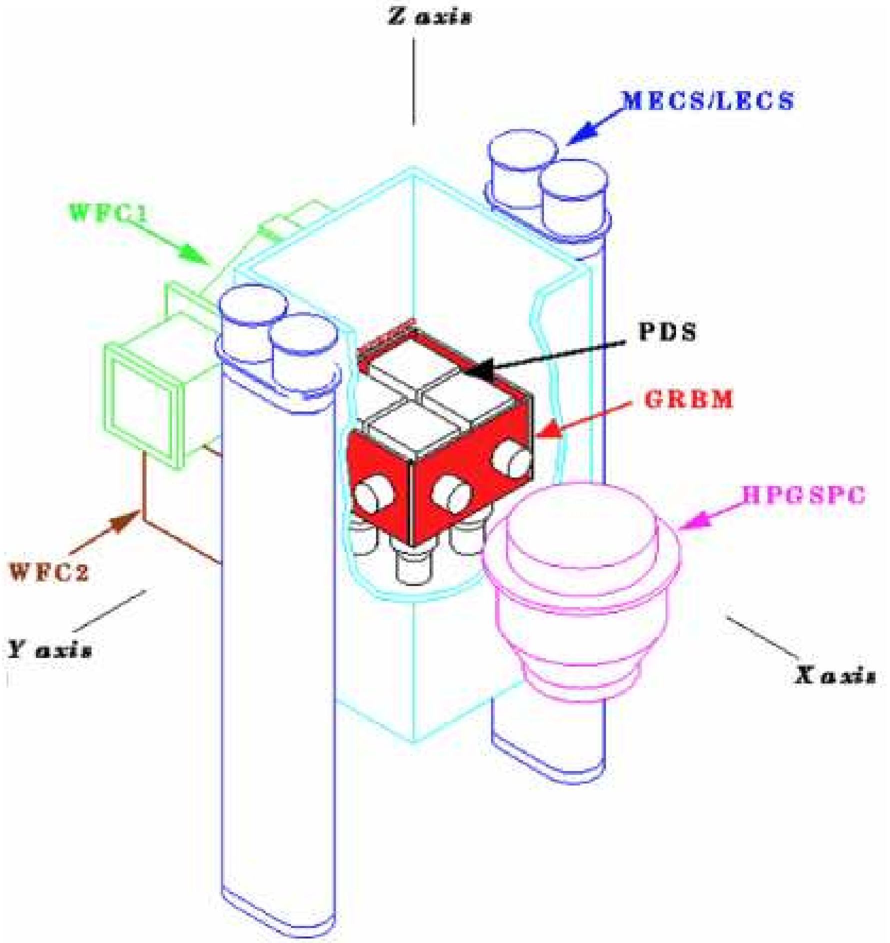

Figure 4: Final configuration of the BeppoSAX payload. The GRBM, shown in red as part of the PDS instrument, consists of four independent slabs of 1 cm thick CsI(Na) scintillators. These were originally designed as active anticoincidence shields for the four phoswich detection units. Notably, two of the GRBM slabs were aligned with the axes of the two Wide Field Cameras (WFCs). Reproduced from Frontera (2024).

In particular, an unexpected shallow phase (also called *plateau* phase), following the steep decay emission, was observed. Because of its slow decay implying a late activity of the central engine, this phase challenged the existing GRB emission picture. Several models tried to explain this phase:

- continuous energy injection (Fan and Piran, 2006; Ghisellini et al., 2007; Granot and Kumar, 2006; Stratta et al., 2018; Zhang et al., 2006);
- reverse-shock emission (Genet, Daigne, and Mochkovitch, 2007; Hascoët, Daigne, and Mochkovitch, 2014; Uhm and Beloborodov, 2007);
- re-brightening caused by inhomogeneities in the medium (Toma et al., 2006);
- high-latitude emission from structured jets (Ascenzi et al., 2020; Beniamini et al., 2020; Oganesyan et al., 2020);

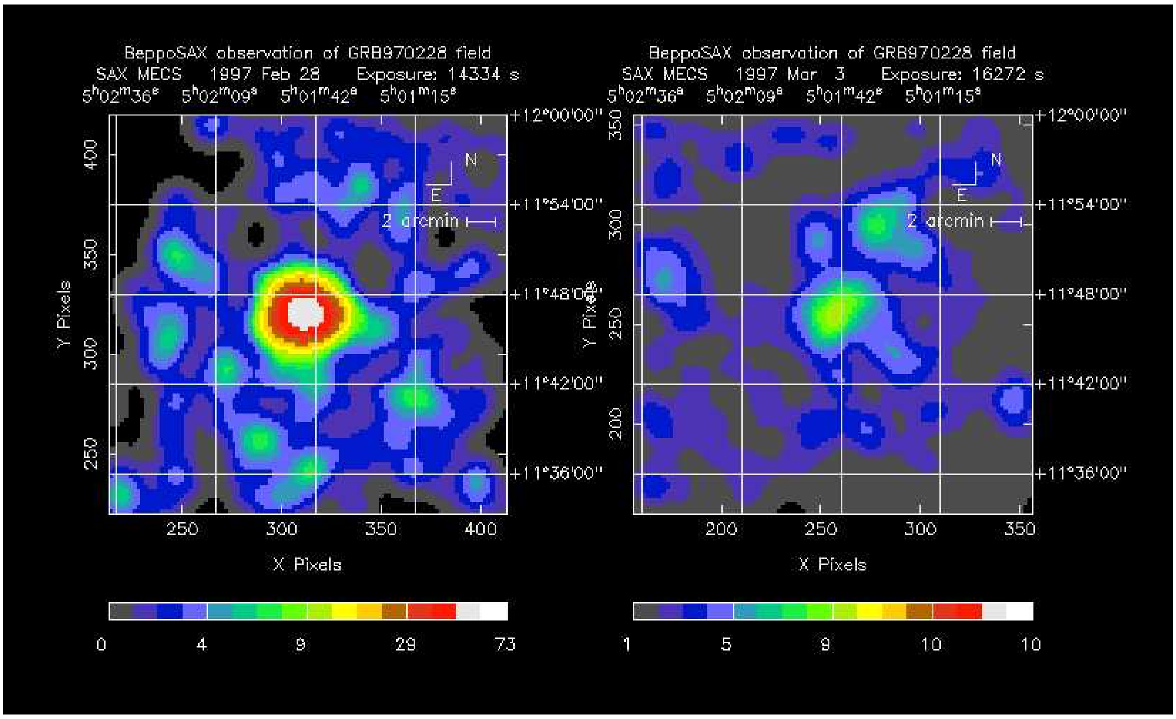

Figure 5: X-ray images of GRB 970228 captured by the MECS telescopes at two different times. The left image corresponds to the observation taken 8 to 16 hours after the burst; the right image shows the same region 3.5 days later. Between the two observations, the X-ray source faded by a factor of 20. Reprinted from Frontera (2024).

- echo from dust scattering of the X-ray prompt emission (Shao, Dai, and Mirabal, 2008);
- forward shock emission from relativistic ejecta in the coasting phase as they sweep up a wind-like medium (Dereli-Bégué et al., 2022; Shen and Matzner, 2012);
- prior activity models (Guidorzi et al., 2025; Ioka et al., 2006; Yamazaki, 2009).

The plateau phase raises an important issue for GRB emission models predicting very high efficiency, which is unaccounted for by these models (internal shocks can barely produce 10% efficiency (Sect. 1.5.2), and magnetic-reconnection based models do not exceed 50 %).

Short-timescale variability, known as X-ray flares, was observed during the afterglow (component V in Fig. 6) . The origin of the X-ray flares is strongly debated: on the one hand, X-ray flares show similar properties as GRB prompt emission pulses: as GRB pulses, the flares are asymmetric and their widths decrease with energy according to $w \propto \mathrm{E}^{-0.5}$ (Chincarini et al., 2010). Moreover, flares in LGRBs are consistent with the LGRB lag–luminosity relation (Margutti et al., 2010a) and share similar waiting time (WT) distributions, which could be the

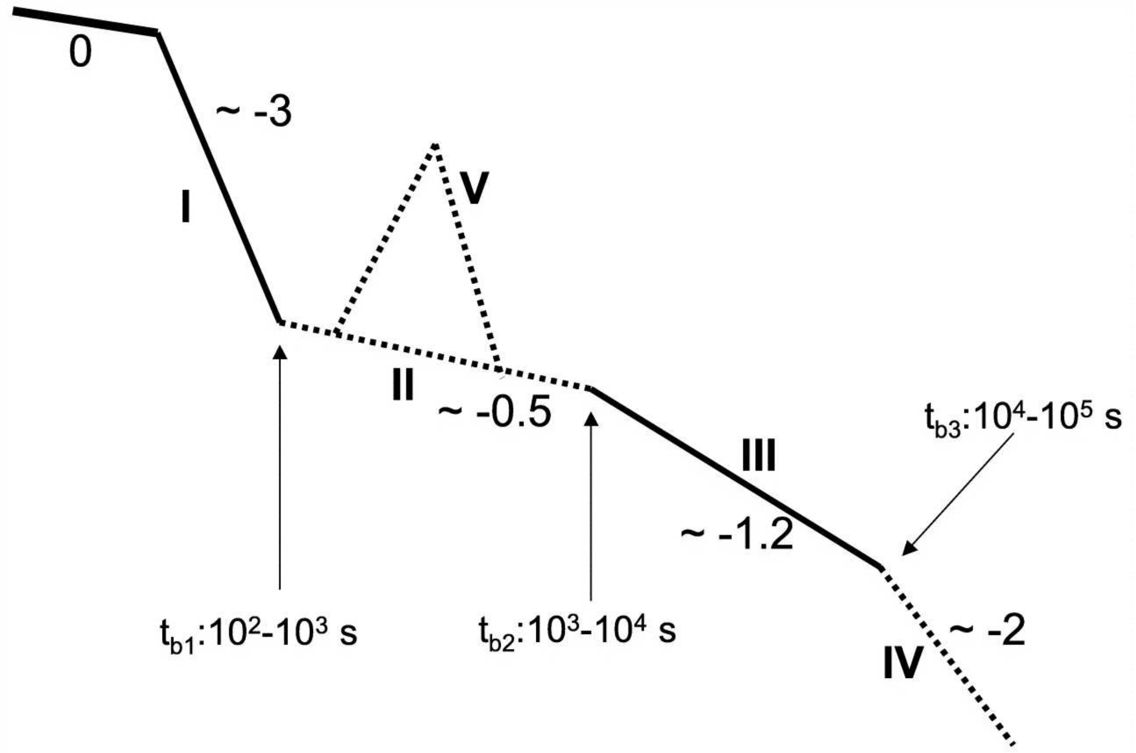

Figure 6: The early X-ray afterglow is featured by an early steep decay (phase I), sometimes followed by a shallow phase ($\alpha \sim -\frac{1}{2}$; called the plateau phase), followed by a normal decaying phase ($\alpha \sim -1$). This phase is sometimes followed by a jet break (phase IV). On top of this smooth decline, fast variability, in the form of X-ray flares (V), can be present during phase II.

result of a common stochastic process (see Guidorzi et al. 2015 and Sect 1.8.2). However, there is a fundamental difference in flares and prompt pulses properties: flare properties evolve with time, with flares getting broader and softer at late times (Chincarini et al., 2010). Lazzati and Perna (2007) however showed that flares produced by external shocks would evolve on much longer timescales than observed, arguing for late central engine activity.

1.1.5 *Fermi to monitor the high-energy sky*

The *Fermi* Gamma-ray Space Telescope is an international and multi-agency space mission that monitors the gamma-ray sky, from 10 keV up to 300 GeV[2]. The satellite, launched on 11 June 2008 and originally called Gamma-ray Large Area Space Telescope (GLAST), was soon renamed after Enrico Fermi. Its payload consists of two scientific instruments, a pair-production telescope known as the *Large Area Telescope* (LAT, Atwood et al. 2009) sensitive from 20 MeV up to 300 GeV and a scintillation-based detector known as *Gamma-Ray Burst Monitor* (GBM, Meegan et al. 2009), sensitive from 10 keV to 30 MeV. In this way, the combination of GBM and LAT provides burst spectra over seven decades in energy. The GBM consists of 12 thallium activated sodium iodide (NaI(Tl)) scintillation detectors sensitive from 10 keV to 1000 keV, and two bismuth germanate (BGO) scintillation detectors sensitive from 150 keV

---

[2] https://fermi.gsfc.nasa.gov/

to 30 MeV. *Fermi*/GBM provides a rich catalogue of GRBs containing spectral, temporal, and location data (von Kienlin et al., 2014, 2020).

Fermi/LAT extended GRB detection to high energies from ∼ 30 MeV to 100 MeV with LAT Low Energy (LLE; Pelassa et al. 2010) technique and from 100 MeV to 300 GeV with standard LAT technique. LAT observations allow the characterisation of the high-energy component of GRB prompt emission, revealing in particular that GRB emission above 100 MeV

- (i) requires an additional power law (PL) component to accurately model the GRB spectra;
- (ii) is delayed by a few seconds with respect to the lower energy emission;
- (iii) lasts significantly longer;
- (iv) has a flux that generally decays as a PL, with $F \propto t^{-\alpha}$ where $\alpha \sim 1$.

LAT observations at high energies impose constraints on the bulk Lorentz factor, which must be large for the fireball to be transparent to high-energy photons (e.g. Granot, Cohen-Tanugi, and Silva 2008; Hascoët et al. 2012), probe Lorentz invariance of the speed of light (Abdo et al., 2009a), and put constraints on the intergalactic magnetic field (notably through the observation of a 400 GeV photon from GRB 221009A, Xia et al. 2024). *Fermi*/LAT enabled the detection of several GRBs emitting at GeV energies such as GRBs 080916C (Abdo et al., 2009b), 090510 (Ackermann et al., 2010), 130427A (Ackermann et al., 2014), 221009A (Axelsson et al., 2025), with photons detected up to 95 GeV for GRB 130427A (Ackermann et al., 2014) and 400 GeV for GRB 221009A (Xia et al., 2024).

Additionally, LAT observations make it possible to probe the radiative processes involved in GRB emission. Synchrotron emission from relativistic electrons can hardly explain the observed high-energy photons. Synchrotron-self Compton (SSC), Inverse Compton (IC), and hadronic models, are promising candidates to explain the observations of photons at these energies. However, the delay of a few seconds between low and high energy components can hardly be accounted for by SSC, while hadronic models (proton synchrotron or cascades) require more energy stored in hadrons than in leptons, which is challenging for GRBs[3] (see discussion in Ajello et al. 2019). Conversely, IC scattering of the prompt MeV radiation streaming through the external blast wave could account for such delays (Beloborodov, Hascoët, and Vurm, 2014).

The combination of GBM and LAT enables joint time-resolved spectral analysis, combining GBM, LLE, and LAT data, using multi-mission frameworks such as the Multi Mission maximum likelihood framework (3ML; Vianello et al. 2015). A systematic joint analysis is under way (work in progress by A. Holzmann Airasca, D. Depalo, E. Bissaldi). When applied to GRBs with known redshift, the joint fit can provide better constrained spectral parameters, such as the peak energy, allowing for refined estimates of cosmological correlations (Aldowma et al., 2025). The joint use of GBM, LLE, and LAT data has also enabled the measurement of spectral lags, i.e. the time delay between photons of different energies (Castignani et al., 2014; Maraventano et al., 2025).

Fermi/LAT opened the way for GRB observations at high energies. At very high energies (VHE), including the TeV domain, this capability is extended by ground-based facilities such

---

[3] The fireball launched in GRBs must be clean, i.e. contain little baryonic mass and be primarily composed of photons and electron-positron pairs

as HESS (Pühlhofer, Leuschner, and Salzmann, 2023), MAGIC (Aleksić et al., 2016), VERITAS (Weekes et al., 2002), and LHAASO (di Sciascio and Lhaaso Collaboration, 2016). These facilities observed several GRBs at VHE, among them GRB 180720B (Abdalla et al., 2019), GRB 190829A (H. E. S. S. Collaboration et al., 2021), GRB 190114C (MAGIC Collaboration et al., 2019a,b), GRB 201216C (Abe et al., 2024), and GRB 221009A (Abe et al., 2025; LHAASO Collaboration et al., 2023). VHE observations paved the way for the upcoming CTA (Cherenkov Telescope Array Consortium et al., 2019) and its optimised sensitivity that will further probe the high-energy emission mechanisms at play in GRBs, also revealing in turn the GRB jet structure (Pellouin and Daigne, 2024).

1.1.6 *Other important facilities*

The Russian satellite Konus-Wind (Aptekar et al., 1995), launched on November 1, 1994, played a key role in GRB physics. In particular, its broad energy coverage (20 keV-20 MeV) and high energy resolution enabled accurate measurements of the spectral properties of GRBs, especially their peak energy E_p, allowing us to refine our knowledge about GRB empirical energy correlations, such as the $E_p - E_{iso}$ or the $E_p - L_{iso}$ correlations (Tsvetkova et al., 2017).

The Hard X-ray Modulation Telescope (HXMT, Zhang et al. 2020), named "Insight", was successfully launched as China's first X-ray astronomy satellite on June 15, 2017. Combined with the GECAM satellite, the observations by HXMT of the brightest-of-all-time burst GRB 221009A was key to study the temporal and spectral properties of this unique event (Zhang et al., 2025a).

1.1.7 *Recent and upcoming GRB missions*

The French-Chinese Space Variable Objects Monitor (SVOM, Götz et al. 2009) was recently launched on 22 June 2024. Its combination of γ (GRM, Dong et al. 2010), X-ray (ECLAIR, Godet et al. 2014 and MXT, Götz et al. 2023), and optical instruments (VT, Fan et al. 2020) provides a unique spectral range and enables an on-board automatic follow-up of GRBs (with optical afterglow obtained after 30 min-1h). SVOM is expected to measure the redshift on board for about 50% of the GRBs detected with ECLAIR (currently $\simeq 40\%$). SVOM has already enabled the discovery of many GRBs with redshifts, including one at $z = 7.3$, the fifth most distant GRB ever observed (Cordier et al., 2025).

The Chinese satellite *Einstein Probe* (EP, Yuan et al. 2022) was launched on 9 January 2024. With its two main instruments, the Wide-field X-ray Telescope (WXT, Zhang et al. 2022a, $0.5 - 4.0$ keV) and the Follow-up X-ray Telescope (FXT, Vernani et al. 2022, $0.5 - 8.0$ keV), EP is currently monitoring the variable X-ray sky. Owing to its detection energy range extending toward lower energies compared to typical GRB monitors, EP is expected to be sensitive to a distinct, softer GRB population, including those associated with shock breakouts (SBOs) and high-redshift GRBs.

The Transient High-Energy Sky and Early Universe Surveyor (THESEUS, Amati et al. 2021) is a space mission concept submitted to the European Space Agency (ESA) M7 call for future missions and was selected for a Phase A study that will end in mid-2026. THESEUS combines Swift's rapid slewing capability and wide field of view with Fermi's broad energy coverage and large effective area. Its key advantages include the high sensitivity of the Soft

X-ray Imager (SXI, O'Brien et al. 2021), the wide energy range and large effective area of the X–Gamma-ray Imaging Spectrometer (XGIS, Labanti et al. 2021), and the presence of an on-board Infrared Telescope (IRT, Götz et al. 2021). This unique suite of instruments will enable THESEUS to detect high-redshift GRBs and autonomously measure their redshifts on-board.

With these two (hopefully three with THESEUS) instruments, one can expect:

- to better understand the population of soft, X-ray rich GRBs and their origins;
- to substantially increase the number of GRBs at high redshift, enabling also a better understanding of the properties of their host galaxies, in particular in the reionisation period;
- to catch more events associated with COMs and their optical counterparts (kilonovae), which have become the focus of intense research at the dawn of multi-messenger astronomy.

Fig. 7 shows the energy coverage provided by the combination of the recent SVOM and EP missions when combined with established facilities such as *Swift*, *Fermi*, and GECAM.

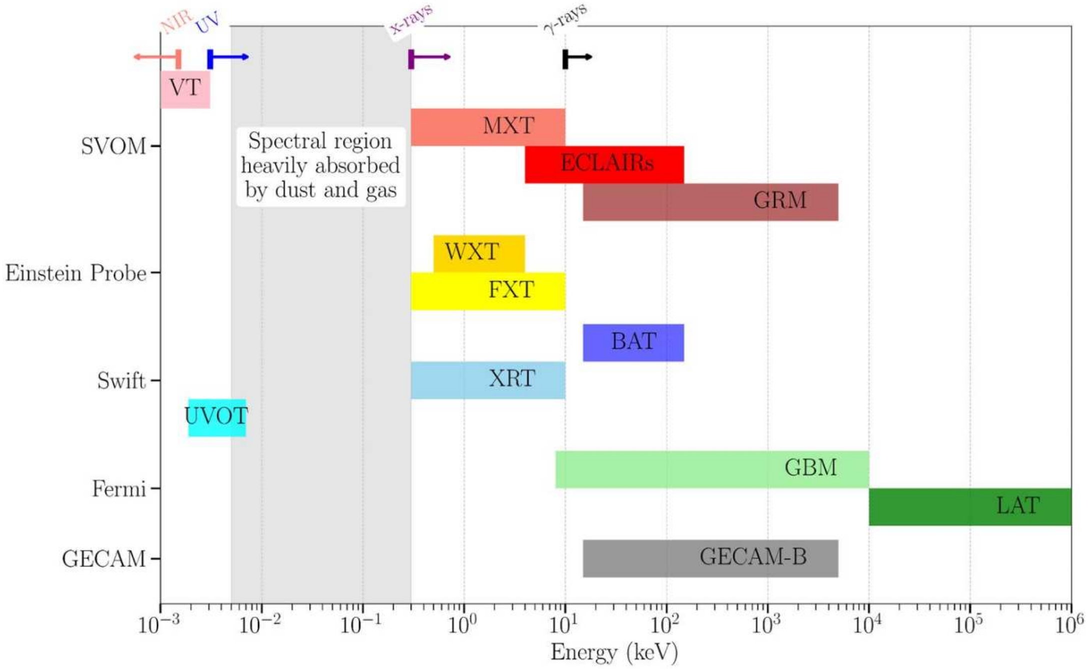

Figure 7: Energy range sensitivity from SVOM, Einstein Probe, *Swift*, *Fermi* and GECAM, covering optical, UV, X and γ-rays. Credit: Bertrand Cordier.

1.2 PROGENITORS AND THEIR ENVIRONMENTS

Long and short GRBs are produced in different environments. Tracing the properties of their respective host galaxies has historically helped to uncover the two distinct formation channels responsible for these bursts, associating the former class with the death of massive stars and the latter with compact objects mergers.

1.2.1 *Long GRBs and the death of massive stars*

GRBs are associated with core-collapse SNe (ccSNe). GRB 980425 was the first GRB to be associated with a SN, in particular a Type Ic-BL SN, named SN 1998bw (Galama et al., 1998). GRB 980425 was not a typical GRB, since its isotropic energy ($E_{\rm iso} \simeq 10^{48}$ erg) was several orders of magnitude lower than that of the bulk of GRBs. The second association involved a more typical GRB, GRB 030329, associated with SN 2003dh (Stanek et al., 2003). Further detections confirmed the link between GRBs and ccSNe, and showed that they are specifically associated with a particular subclass, namely Type Ic-BL SNe[4], as shown in Fig. 8.

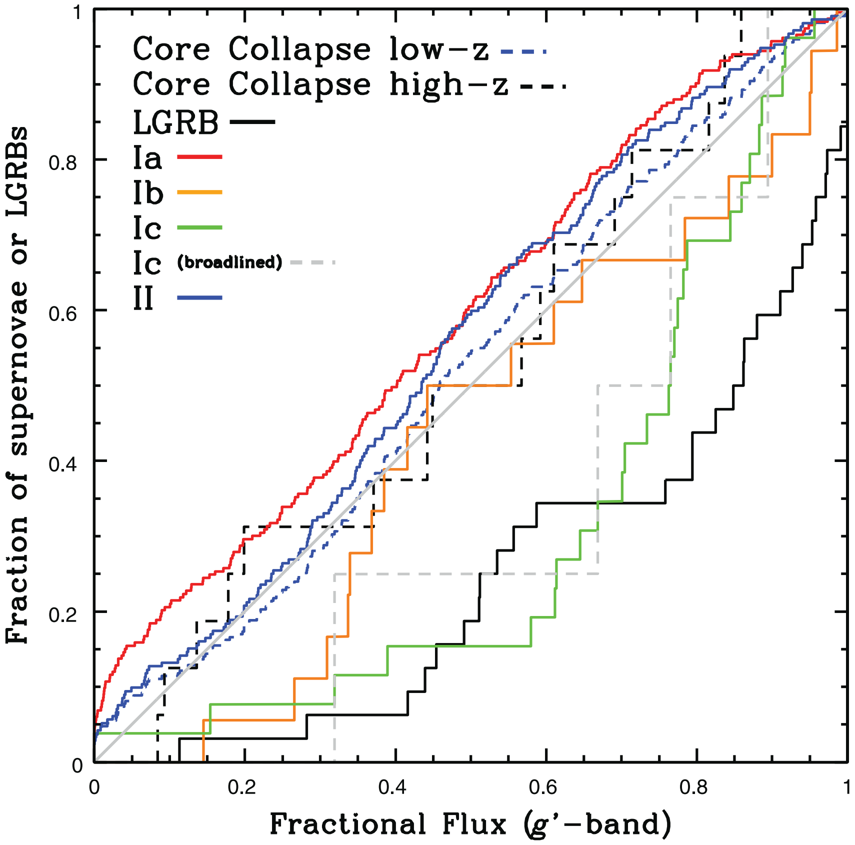

Figure 8: Fraction of SN or LGRBs against fractional flux in the g′ band (radio frequency). LGRBs (black line) and Type Ic BL (green line) are found at high fractional fluxes, corresponding to the brightest (hence most star-forming) regions of their host, while Type II SNe are found in fainter regions and track star formation rate. From Kelly, Kirshner, and Pahre (2008).

The link between LGRBs and ccSNe indicates that the former are associated with the end life of massive stars. Owing to the short-lived nature of massive stars, LGRBs are thus connected with recent star formation. GRB host galaxies studies over a statistically significant sample indeed confirmed that they are generally small, blue, young star-forming galaxies (e.g. Fynbo, Malesani, and Jakobsson 2012; Savaglio, Glazebrook, and Le Borgne 2009; Schnei-

---

[4] Type Ic is an extreme case of ccSN, where both hydrogen and helium have been expelled. A small fraction of Type Ic features broad lines (BL) in their spectra, which are due to a very fast ejecta with velocities of the order of $v \sim 2-3\times10^4$ km s^{-1}.

der et al. 2022). However, they also show a clear preference for low-metallicity environments (e.g. Palmerio et al. 2019; Perley et al. 2016; Vergani et al. 2015).

Generally, GRBs are produced close to the centre of their host, with a small associated offset, half of them lying at less than 1 kpc from their centre (Blanchard, Berger, and Fong, 2016; Bloom, Kulkarni, and Djorgovski, 2002). While one might expect to find ccSNe and LGRBs at similar locations within their galaxy, the latter are instead associated with the brightest locations of their host (Fruchter et al., 2006), as it is shown in Fig. 9.

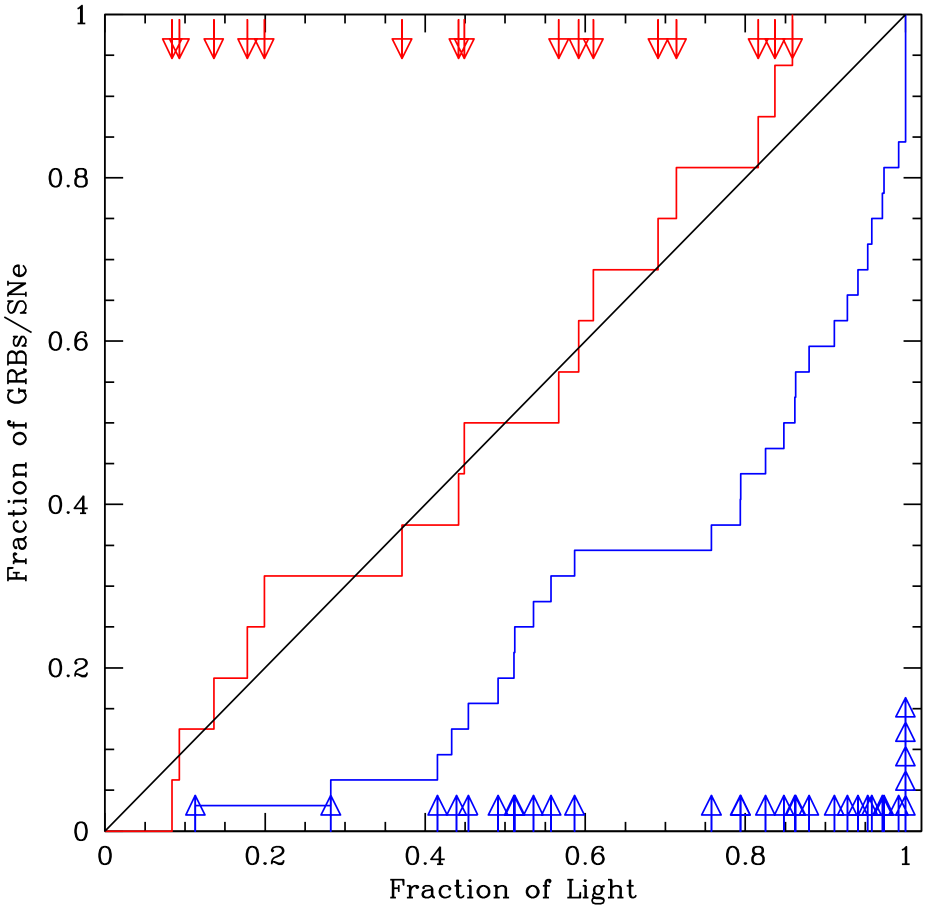

Figure 9: For each host galaxy, an arrow marks the fraction of total galaxy light contained in pixels fainter than or equal to the brightness at the transient's location. The cumulative distributions of GRBs and SNe over host light are shown as histograms: blue for GRBs and red for SNe. If both populations traced the host light identically, their histograms would follow the diagonal line. While SNe do follow the light distribution within statistical uncertainties, GRBs are significantly more concentrated in the brightest regions of their host galaxies. Taken from Fruchter et al. (2006).

However, not all Type Ic-BL SNe are associated with a GRB (e.g. SN2002ap, Berger, Kulkarni, and Chevalier 2002, SN2009bb, Soderberg et al. 2010, SN2012ap, Milisavljevic et al. 2015, etc.). While one possible reason for the absence of GRB accompanying these SNe could be the collimation of the jet, which makes it visible only when pointing towards the Earth, it is more likely that not every Type-Ic BL SN is associated with a relativistic jet. In some cases, the jet might fail to pierce the envelope of the progenitor (a so-called *choked jet*, e.g. Denton and Tamborra 2018; MacFadyen, Woosley, and Heger 2001; Pais, Piran, and Nakar 2022).

1.2.2 *Short GRBs and compact object mergers*

Unlike LGRBs, there is no evidence that SGRBs are associated with massive star collapse:

- Except for one special case[5], no SN has been detected in association with SGRBs. These non-detections put stringent constraints on the expected flux: if a SN is associated with a SGRB, it must be several orders of magnitude fainter than those typically observed with LGRBs.
- SGRBs are found in both early and late galaxy types, implying that SGRBs can also be found in low star-forming regions, while LGRBs are only found among young, star-forming regions.
- Offsets from their host galaxy centres are considerably larger than those of LGRBs (Fig. 10), and are compatible with objects being expelled from their birthplace by natal kicks to the suburbs of their host (Fong et al., 2013).

SGRBs, being associated with old stellar populations, are consistent with a compact binary merger origin: the binary system, owing to gravitational-wave losses, slowly merges into a more compact object with a delay between the birth and merger ranging from a few ten Myrs to several Gyrs (Beniamini and Piran, 2019).

The association with COMs was confirmed by the simultaneous detection of a SGRB with GW emissions in 2017, which marked the beginning of the multi-messenger astronomy (Sect. 1.2.3).

1.2.3 *Association of short GRBs with gravitational waves*

On August 17, 2017, a gravitational-wave (GW) signal from a binary NS (BNS) merger was detected for the first time. This detection occurred simultaneously with a SGRB observed by both *Fermi*/GBM and INTEGRAL, 1.7 seconds after the GW emission (Fig. 11), firmly establishing the connection between SGRBs and BNS mergers (Abbott et al., 2017).

This extraordinary event is also remarkable from the GRB standpoint. Observed at a very close distance ($D_L \simeq 40$ Mpc), its energy and luminosity are several orders of magnitude below typical SGRB values. This suggests either an intrinsically sub-energetic burst or a normal SGRB viewed off-axis. The broadband afterglow of this event disfavours the former interpretation and indicates that the jet was observed off-axis. It also implies the presence of a structured outflow, with energy and Lorentz factor distributed beyond the jet core, rather than a simple top-hat jet (see, e.g., Cheng et al. 2021; Geng et al. 2019; Gill and Granot 2018; Lamb and Kobayashi 2018; Li et al. 2019; Takahashi and Ioka 2021; Wei et al. 2022 and Salafia and Ghirlanda 2022 for a review)

---

[5] Namely GRB 200826A, which is a collapsar GRB with an unsually short duration (Ahumada et al., 2021; Rhodes et al., 2021; Rossi et al., 2022; Wang, Zhang, and Lei, 2022).

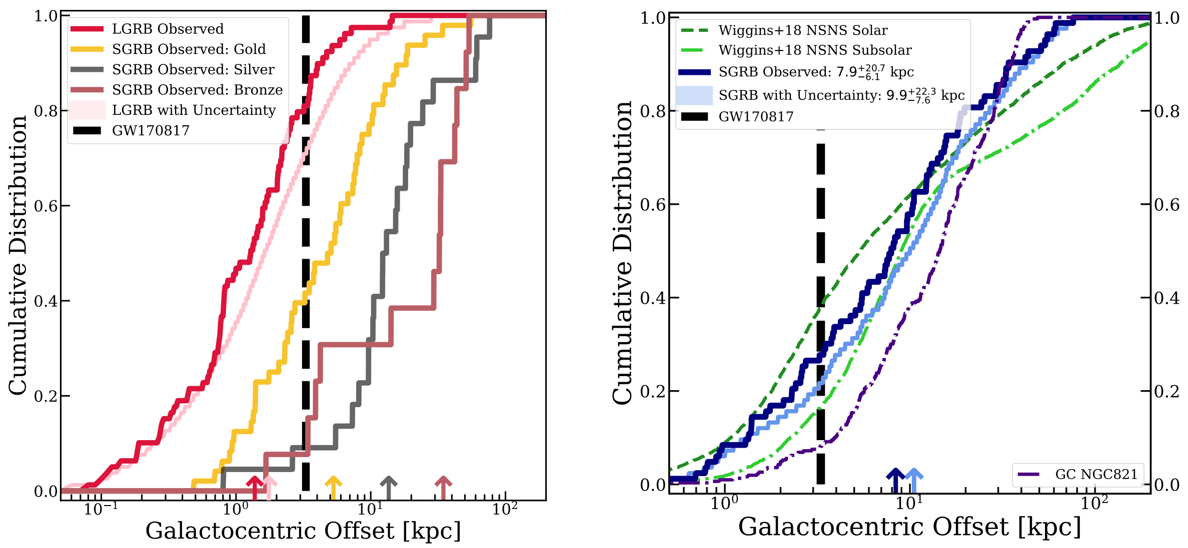

Figure 10: GRB host galaxy offset distribution from Fong et al. (2022). *Left panel:* gold, silver, and bronze sample are shown, with increasing chance alignment probability P_{cc} (increasing with increasing offset). Even for the SGRB sample with the smallest offsets (more reliable because lowest P_{cc}), SGRBs show considerably higher offsets than LGRBs ($\simeq 4.8$ kpc (Gold) against 1 kpc for LGRBs). *Right panel:* SGRB offsets compared with NS-NS model offset predictions.

1.2.4 *Kilonovae: the optical/IR counterpart of compact object mergers*

Kilonovae are day- to week-long thermal transients, which are powered by the radioactive decay of heavy, neutron-rich elements synthesised in the expanding ejecta of a COM (see Metzger 2020 for a review).

Heavy elements in the universe are mainly synthesised via the capture of neutrons onto lighter nuclei in a dense, neutron-rich environment in which the timescale for neutron capture is shorter than the β decay timescale. This rapid neutron capture (also called r-process) significantly destabilises the nuclei of these elements, that decay radioactively. This radioactive decay powers a thermal emission at ultraviolet, optical, and infrared wavelengths.

The merger ejecta is extremely hot immediately after being ejected from the merger. This thermal energy cannot, however, initially escape as radiation because of its high optical depth and long photon diffusion timescale at early times:

$$\tau = \rho \kappa R = \frac{3M\kappa}{4\pi R^2} \tag{1}$$

$$t_{\text{diff}} = \tau \frac{R}{c} = \frac{3M\kappa}{4\pi c R} = \frac{3M\kappa}{4\pi c v t} \tag{2}$$

As the ejecta expands, the diffusion time decreasing with time as t^{-1}, radiation can finally escape when reaching the expansion timescale, which is set by $t = t_{\text{diff}}$. This condition rules the characteristic timescale at which the peak of the light curve (LC) is observed:

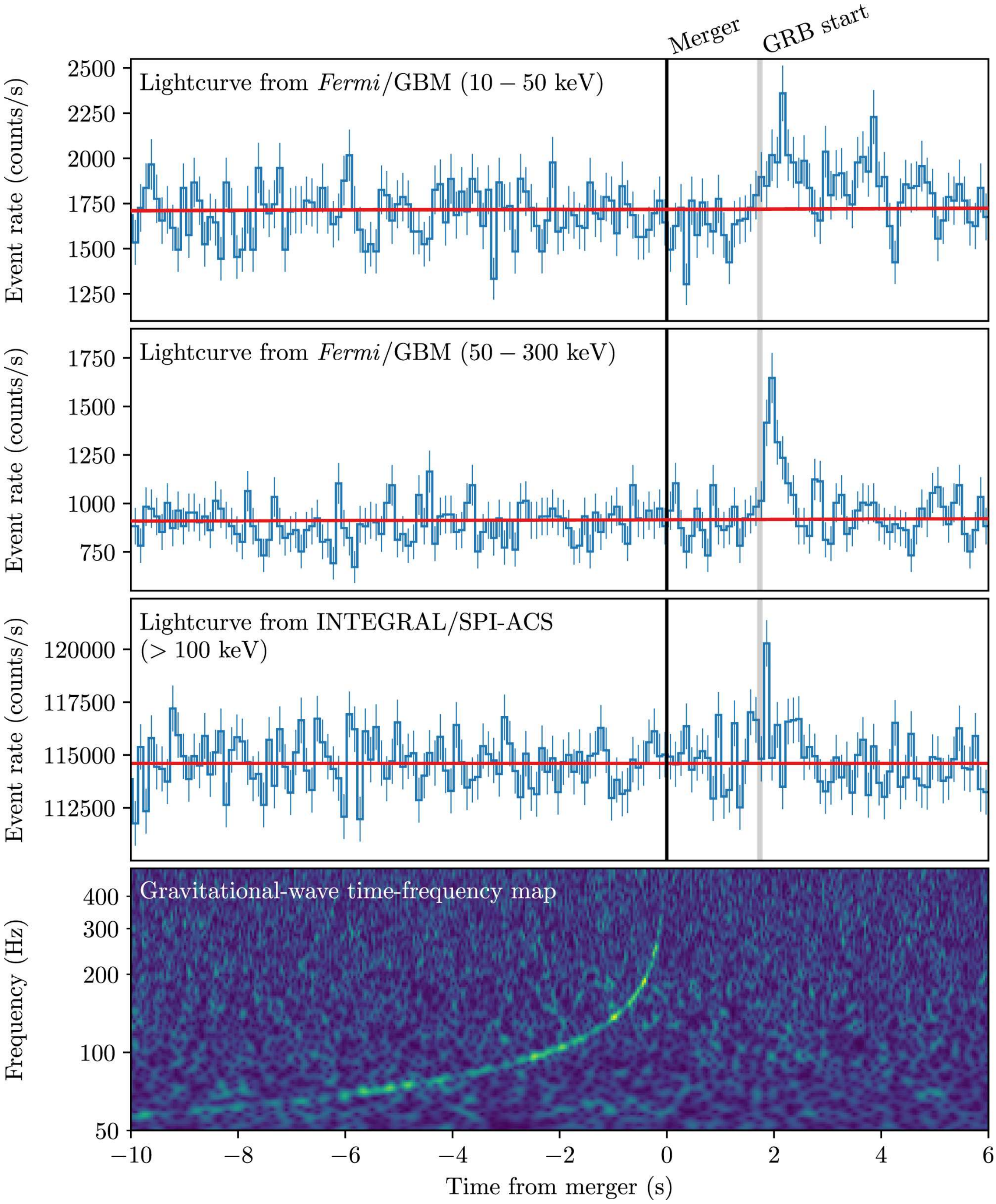

Figure 11: Joint, multi-messenger detection of GW170817 and GRB 170817A. The top two panels show GRB 170817A, a SGRB detected 1.7 seconds after GW170817, as detected by *Fermi*/GBM in two different energy ranges, while the third panel presents the detection by INTEGRAL. The bottom panel displays the frequency–time map of GW170817 obtained by coherently combining data from LIGO–Hanford and LIGO–Livingston. From Abbott et al. (2017).

$$t_{\text{peak}} = \sqrt{\frac{3M\kappa}{4\pi v c}} \simeq 2.7\ \text{days}\ \left(\frac{M}{10^{-2}\ M_{\odot}}\right)^{1/2} \left(\frac{v}{0.1\ c}\right)^{-1/2} \left(\frac{\kappa}{1\ \text{cm}^2\ \text{g}^{-1}}\right)^{1/2}, \tag{3}$$

where M is the ejected mass, v the ejecta velocity, and κ its opacity. The freshly ejected matter is extremely hot at early times ($T \sim 10^{9-10}$ K). Without a source of heating, the expanding ejecta would cool because of adiabatic expansion, losing almost all its initial thermal energy before reaching transparency. However, in a realistic situation, the ejecta is continuously heated by a combination of sources. These include at least the radioactive decay of r-process nuclei, and possibly the GRB central engine or the spindown of a magnetar remnant (magnetar-boosted kilonova).

The resulting kilonova properties are then ruled by the following key ingredients:

- mass and velocity of the ejecta and its different components;
- the opacity κ of the neutron-rich matter;
- the variety of sources that contributes to heat the merger ejecta.

In particular, increasing opacity, associated with heavier elements including lanthanides, shifts the kilonova flux towards near-infrared and delays the peak of the emission.

Different ejecta are produced by a BNS merger (Fig. 12):

- The dynamical ejecta is the first to be thrown out of the merging binary. This ejecta is ruled by gravitational forces and by the hydrodynamics of the collision between the two binary members. It is associated with a polar emission and a blue kilonova.
- Additional mass ejection may be driven by neutrino fluxes from the disc and from the central object, in the case the merger remnant does not collapse to a black hole (BH).
- Viscous heating is also expected to unbind a significant fraction of the disc mass. This ejecta is associated with a red kilonova, emitted along the merger plane.

The properties of the kilonova are also influenced by the nature of the merger remnant, which in turn depends on its total mass M_{tot} and the exact nature of the NS equation of state, setting M_{TOV}.

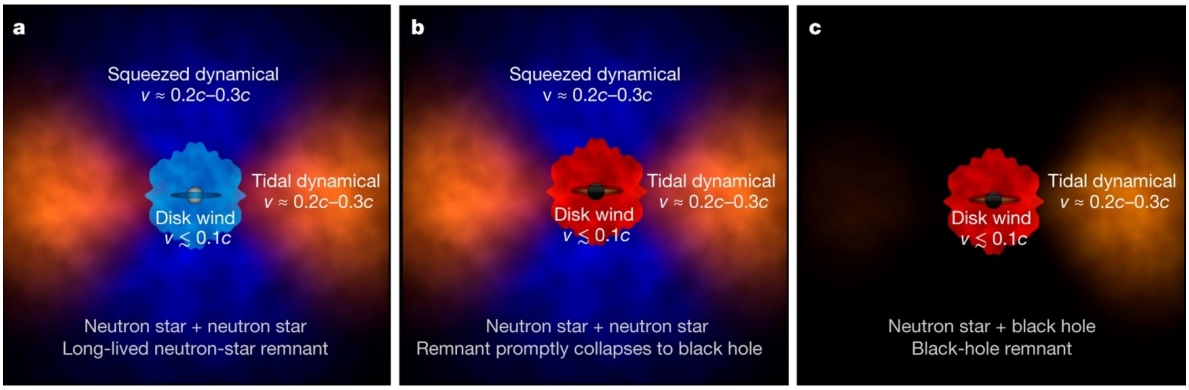

Figure 12: Different ejecta components depending on the merging components and on the nature of the merger remnant. Red colours indicate regions of heavy r-process elements, which radiate red/infrared light. Blue colours represent regions of light r-process elements which radiate blue/optical light. From Kasen et al. (2017).

Depending on the observation angle, the observer sees a bluer or redder kilonova, associated with a brighter or dimmer GRB and GW signals (Fig. 13).

Kilonova emission has been observed in association with a few SGRBs, such as GRB 070809 (Jin et al., 2020), GRB 130603B (Berger, Fong, and Chornock, 2013; Tanvir et al., 2013), GRB 160821B (Lamb et al., 2019) and with GRB 171017A (Arcavi et al., 2017; Smartt et al., 2017; Tanvir et al., 2017; Troja et al., 2017; Valenti et al., 2017), marking the beginning of the multi-messenger astronomy.

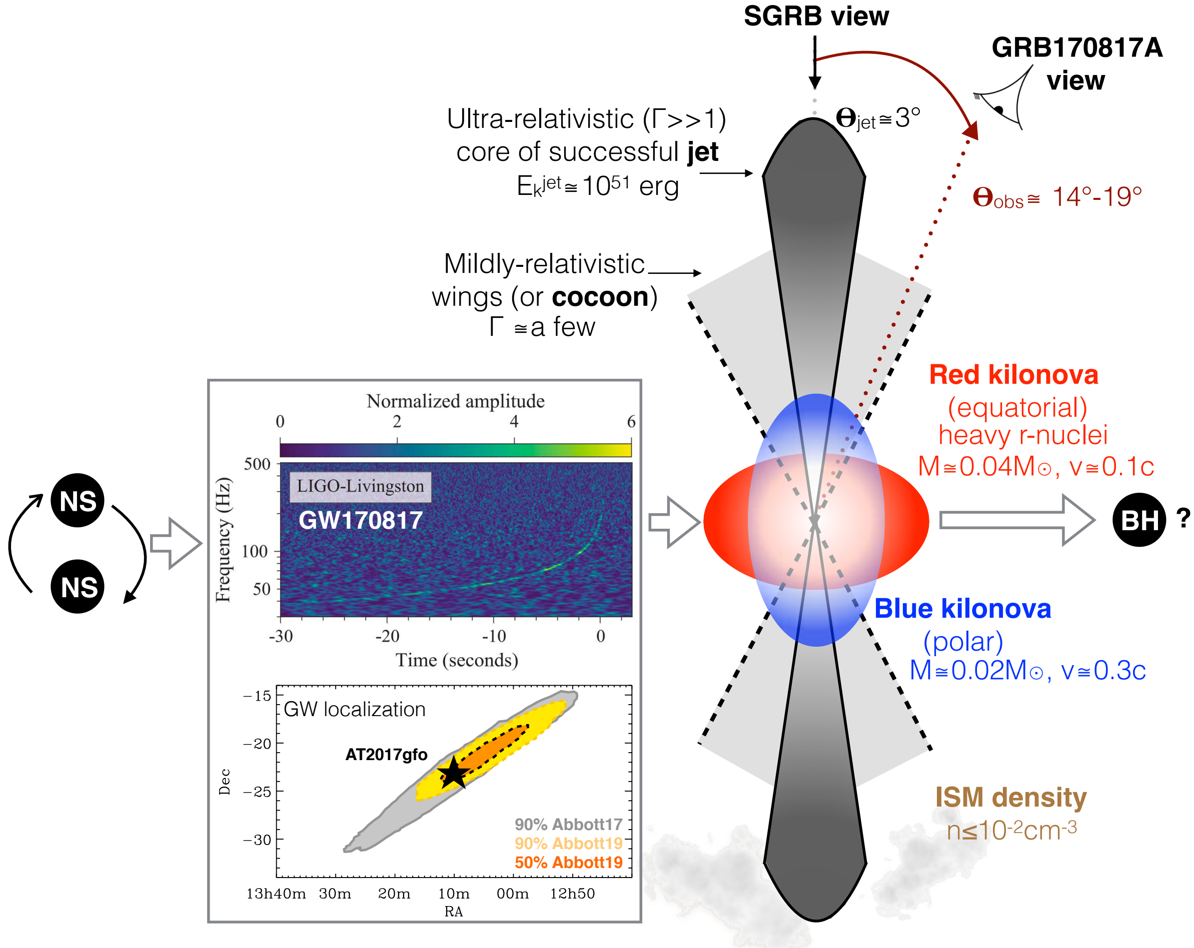

Figure 13: Scheme representing the detection and localisation of GW170817 and its optical counterpart. On the right panel are represented the different jet components produced by the BNS merger: a ultra-relativistic narrow jet corresponding to the SGRB, a mildly-relativistic jet (cocoon) developping at wider angles, a red kilonova (corresponding to a slow ejecta $v \sim 0.1c$), propagating on the equatorial plane and a blue kilonova (corresponding to a faster ejecta $v \sim 0.3c$) moving in the polar direction. All these components are observable at different times and frequency ranges. From Margutti and Chornock (2021).

Unexpectedly, kilonovae have also been observed in association with LGRBs, such as GRB 211211A (Rastinejad et al. 2022; Troja et al. 2022, Fig. 14) or GRB 230307A (Gillanders and Smartt, 2025; Levan et al., 2024), challenging our way to classify GRBs.

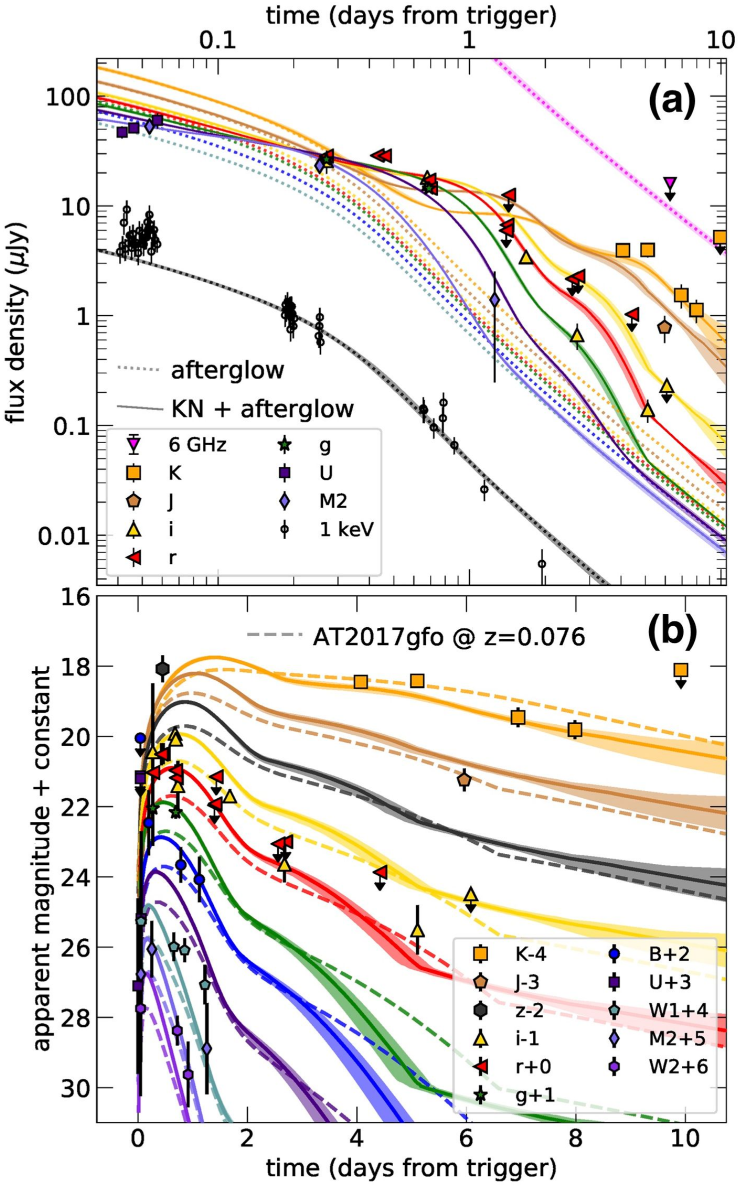

Figure 14: Observation and modelling of the kilonova associated with GRB 211211A. Points come from observations made at different wavelengths. The dotted lined indicate the predictions of the afterglow model while the plain ones show the superposition of the kilonova and afterglow models. Dashed lines show the kilonova model for AT2017gfo, the kilonova associated with GRB170817A, shifted to the redshift of GRB 211211A, for comparison. From Rastinejad et al. (2022).

1.3 CENTRAL ENGINES AND JET FORMATION

A GRB central engine can either be a hyper-accreting stellar mass BH (so-called *collapsar*, Sect. 1.3.1) or a rapidly spinning, highly magnetised NS (a.k.a *magnetar*, Sect. 1.3.3).

1.3.1 *Hyper-accreting black holes*

Massive stars in their late stages usually go through iron-core collapse, leading to the formation of a compact object, which can be a BH surrounded by an accretion disc. In the case of a GRB progenitor star, the accretion disc is fed at a very high accretion rate, between 0.01 and several solar masses per second.

The nature of the accretion disc in this case is totally different from the accretion disc surrounding active galactic nuclei (AGN). In this latter, the low accretion rate (inferior to Eddington limit) enables the disc to cool by releasing radiation. In the GRB case, a thick and opaque accretion disc is formed, meaning that photons are trapped inside the disc, which prevent it from cooling by emitting radiation.

The hydrodynamic evolution of the disc is dominated by neutrino cooling, and is described by the neutrino-dominated advection flow (NDAF, e.g. Popham, Woosley, and Fryer 1999) model. Neutrinos play a major role, ruling the energy transport and the disc structure. The disc structure is described in Fig. 15. In the inner regions of the accretion disc, cooling is dominated by neutrino emission. Neutrinos and anti-neutrinos escape from the disc. In the polar region located above the surface of the disc, close to the rotational axis, a small fraction of the emitted neutrinos can annihilate[6]. This region being poorly contaminated by baryons, neutrino annihilation powers a clean e^+e^- fireball expanding at ultra-relativistic speed, creating a funnel propagating along the rotational axis.

A small fraction of the energy stored by accretion is therefore deposited into a relativistic fireball expanding at high Lorentz factors ($\Gamma \sim 10^2 - 10^3$). Its power $L_\nu = \xi \dot{M}_\odot c^2$ depends on the neutrino efficiency ξ and and on the accretion rate $\dot{M}$. Efficiency being small ($\xi \sim 10^{-3}$), huge accretion rates ($\dot{M} \simeq 1\ M_\odot\ s^{-1}$) are required to power the GRB:

$$L_{\nu\bar{\nu}} = 1.8 \times 10^{51}\ \xi_{-3} \dot{M}_0 c^2 \text{ erg s}^{-1}. \tag{4}$$

1.3.2 *The Blandford-Znajek mechanism*

Another way to launch the jet, especially relevant for magnetised progenitors, is to tap the rotational energy of the BH via the Blandford-Znajek (BZ) mechanism (Blandford and Znajek, 1977).

This mechanism applies to a spinning BH surrounded by a magnetised accretion disc, orbiting around it. Magnetic field lines, anchored in the BH, are entrained by its spinning, and swirls outwards and downwards the BH. Electromagnetic forces then creates currents dragging the plasma outwards and downwards, producing a bipolar relativistic jet. This process converts the BH rotational energy into a magnetised outflow moving at relativistic speeds. The power extracted from a rotating BH L_{BZ} via the BZ mechanism depends on the BH spin angular velocity at the BH horizon Ω_H, the magnetic field strength B, and the BH mass M_{BH}.

The power extracted from BH rotation and converted into a relativistic outflow is generally described by:

$$L_{BZ} = kB^2 M_{BH}^2 \Omega_H^2, \tag{5}$$

---

[6] The energy released in neutrinos is expected to be several order of magnitude higher than the energy that serves to power the GRB jet.

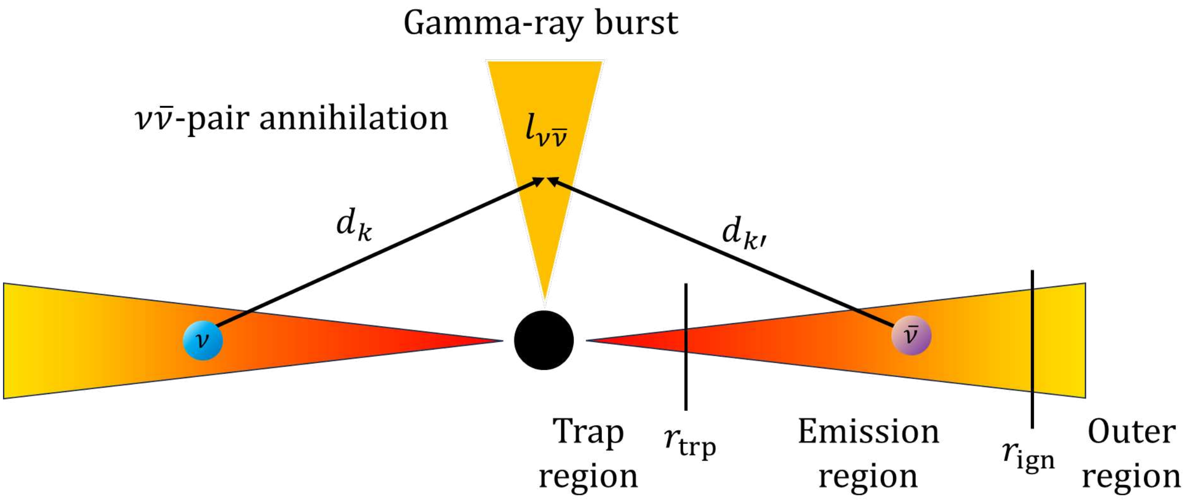

Figure 15: Sketch of the accretion disc around a stellar mass BH (not to scale). The disc is made of the trapping region where neutrinos are trapped ($r \leqslant r_{trp}$), the emission region where neutrinos can escape and cool the disc ($r_{trp} \leqslant r \leqslant r_{ign}$), and the outer region ($r \geqslant r_{ign}$). Neutrinos from the emission region can escape the disc and meet in the polar region situated above it. In the polar region, annihilation occurs and produces the relativistic fireball. Taken from Deesamer, Chainakun, and Sreethawong (2024).

where the proportionality constant k depends on the magnetic field geometry. Higher-order corrections can be obtained using perturbative methods (Camilloni et al., 2022). Higher terms ($L_{BZ} \propto \Omega_H^4$ or $\propto \Omega_H^6$) become relevant for rapidly spinning systems and thicker accretion discs (Tchekhovskoy, Narayan, and McKinney, 2010). For systems powering GRBs, the BZ mechanism typically powers a jet with $L_{BZ} \simeq 10^{49} - 10^{51}$ erg s^{-1}, which is in agreement with the required energy budget derived from the measurement of the energetics and opening angles (Sect. 1.4.2).

1.3.3 *Magnetars as central engines*

The GRB progenitor can also be a rapidly spinning ($P \sim 1$ ms), highly magnetised ($B \geqslant 10^{15}$ G) NS. In this case, the reservoir is the spinning energy of the NS. The available NS rotational energy is given by

$$K = \frac{1}{2}I\Omega^2 = 2 \times 10^{52} \left(\frac{M}{1.4\ M}\right)\left(\frac{R}{10\ \text{km}}\right)\left(\frac{P}{1\ \text{ms}}\right)^{-2} \text{erg}, \tag{6}$$

where $I = \frac{2}{5}MR^2$ is the NS moment of inertia, M the NS mass, R the NS radius, and P is the NS spin period such that $\Omega = \frac{2\pi}{P}$.

This provides a limit on the energy a magnetar can convert into a GRB. GRBs observed with higher energy cannot possibly have been produced by a magnetar. Although E_{iso} can easily exceed 10^{52} erg, the collimation-corrected energy $E_\gamma = (1 - \cos\theta_j)E_{iso}$ rarely exceeds 10^{52} erg (Sect. 1.4.2). The energy budget provided by the rotational energy of magnetars is, therefore, enough to power most GRBs. However, magnetars can hardly support the brightest

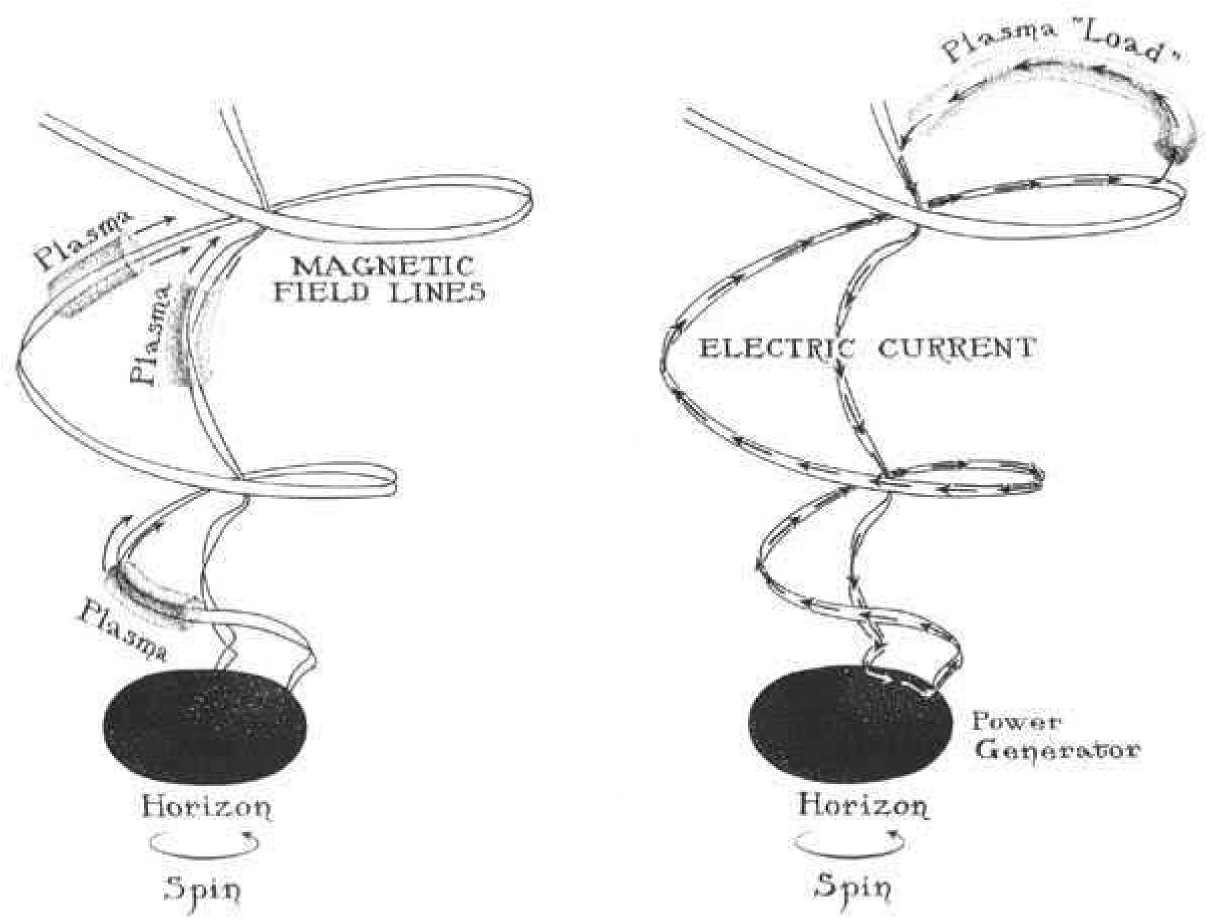

Figure 16: Scheme describing the BZ effect. Magnetic field lines are attached to a spinning BH. The BH spinning motion forces the lines to swirl around the BH spin axis, adopting a spiraling shape. Electromagnetic forces are generated, inducing a current that makes plasma slide along the lines. This launches a relativistic magnetised outflow which builds up upon the initial BH rotational energy. Taken from Kip Thorne's book, *Black holes and time warps: Einstein's outrageous legacy (Thorne, 1994).*

ones [7], for which a BH progenitor is favoured. The mechanism by which a magnetar can power a GRB can be described as follows (Metzger et al., 2011):

- **Stage I: SN shock** ($\sigma_0 \leqslant 10^{-3}$; $t \leqslant$ few 0.1 s). A successful SN shock is launched by neutrino heating;
- **Stage II: Non-relativistic wind** ($10^{-3} \leqslant \sigma_0 \leqslant 1$; a few 0.1 s $\leqslant t \leqslant$ a few 0.1 s). A wind powered by neutrinos is guided through a cavity originating from the SN shock. The wind is initially poorly magnetised and expanding at non relativistic speed;
- **Stage III: Relativistic wind and shock break out** ($1 \leqslant \sigma_0 \leqslant 10-100$; few s $\leqslant t \leqslant t_{bo}$). As the NS cools, the magnetisation increases and the winds become mildly relativistic. As Stage III is ending, the wind pierces and breaks out of the star;

---

[7] It would not have been able to power GRB 221009A ($E_{iso} \geqslant 10^{55}$erg).

- **Stage IV: GRB emission** ($10 - 100 \leqslant \sigma_0 \leqslant 10^4$; $t_{bo} \leqslant t \leqslant t_{end}$). A clean opening of the star is formed. The GRB is powered by direct magnetic dissipations near or above the photosphere or/and by internal shocks. GRB emission models would be discussed in Sect 1.5. During this phase, σ_0 steadily increases;
- **Stage V: Post GRB** ($\sigma_0 \geqslant 10^4$; $t \geqslant t_{end}$). As the NS become optically thin to neutrinos, σ_0 increases even more rapidly than in Stage IV and reach very large values. Jet acceleration and magnetic dissipations being inefficient at this stage, the GRB ends. The residual rotation energy can power late X-ray flares or the X-ray afterglow (e.g. shallow decay known as the plateau, Sect. 1.1.4).

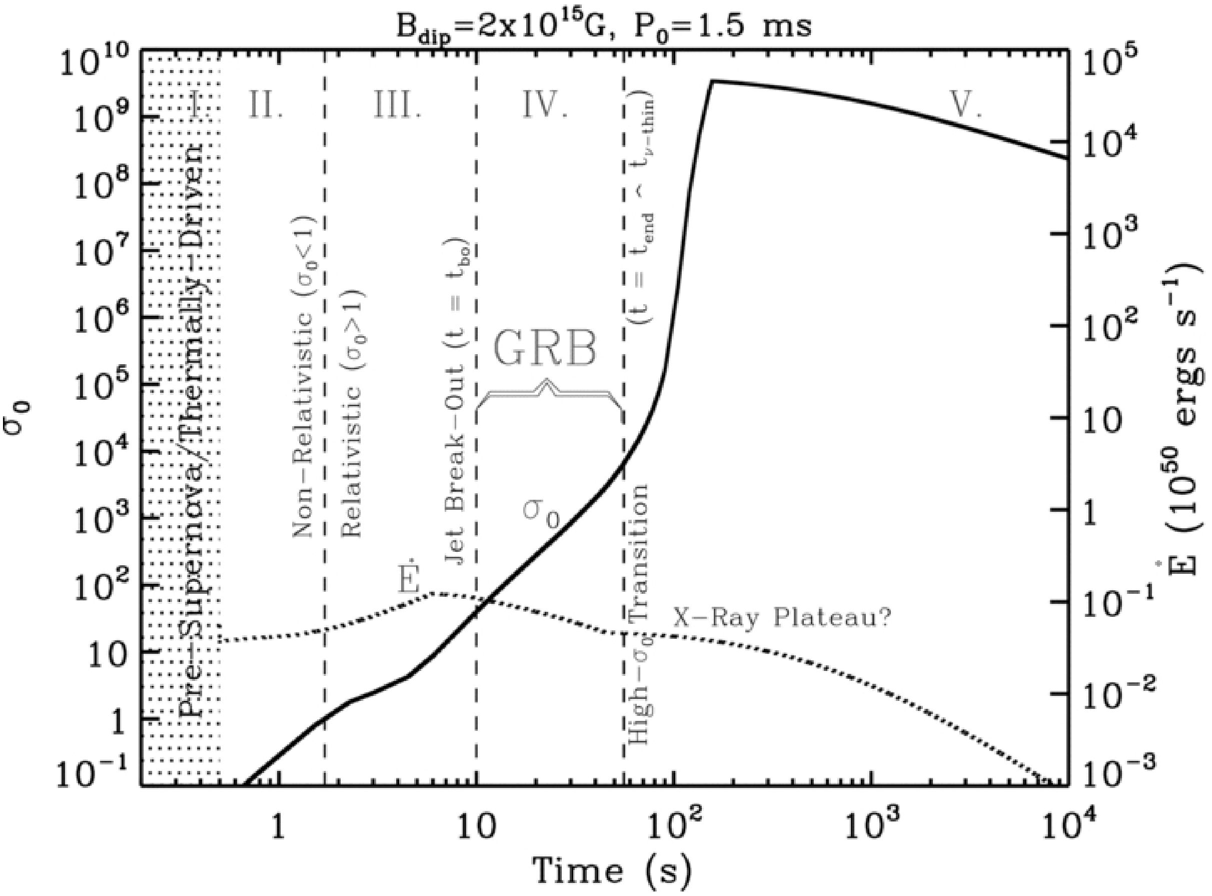

Figure 17: Different stages of the evolution of the wind launched by the SN shock. From Metzger et al. (2011).

The NS rotation decreases as angular momentum is lost through both electromagnetic (EM) and GW emission. The spin rotation evolution during the spin-down phase is described by (e.g. Zhang and Mészáros 2001):

$$-\frac{d}{dt}\left(\frac{1}{2}I\Omega^2\right) = -I\Omega\dot{\Omega} = \frac{B_p^2 R^6 \Omega^4}{6c^3} + \frac{32 G I^2 \epsilon \Omega^6}{5c^5}, \tag{7}$$

where B_p is the magnetic field strength at the poles, and ϵ the ellipticity of the NS (the other quantities have been defined where the first (second) right-hand side term of Eq. (7)) represents the EM (GW) losses. The spin-down luminosity is given by dipole radiation:

$$L_{sp} = \frac{B_p^2 R^6 \Omega^4}{6c^3}. \tag{8}$$

If EM dominates GW losses[8], the spin-down luminosity is given by:

$$L(t) = L_0 \left(1 + \frac{t}{\tau_{EM}}\right)^{-2} \simeq \begin{cases} L_0 & \text{if } t \ll \tau_{EM}, \\ L_0 \left(\frac{t}{\tau_{EM}}\right)^{-2} & \text{if } t \gg \tau_{EM} . \end{cases} \tag{9}$$

The typical dipole spin-down timescale is given by

$$\tau_{EM} \simeq 2 \times 10^3 \text{ s } I_{45} B_{p,15}^{-2} P_{0,-3}^2 R_6^{-6}. \tag{10}$$

Magnetar spin-down has been invoked to explain achromatic bumps in the optical afterglow (e.g GRB 000301C, Dai and Lu 2001; Zhang and Mészáros 2001), and also the shallow decay phases observed in X-ray afterglow (i.e. the phase II of Fig. 6 and its transition to III, e.g. Dall'Osso et al. 2011, see Bernardini 2015 for a review).

1.4 JET PROPAGATION

1.4.1 *Compactness and relativistic motion*

The short time variability ($\delta T \simeq 10$ ms) observed in GRBs implies that the emitting source must be very compact. The large amount of energy released by a GRB ($E_{iso} \simeq 10^{52}$ erg) in such a small volume implies a very high photon density, and hence a very high opacity for pair-production, preventing the escape of MeV–GeV photons and leading instead to a purely thermal spectrum. In fact, the pair-production opacity in the non-relativistic case can be approximated by (Sect. A.1 for a full proof):

$$\tau_{\gamma\gamma} = \frac{f_p \, \sigma_T \, \Phi \, D_L^2}{R_i^2 \, m_e \, c^2} = 10^{13} \, f_p \left(\frac{\Phi}{10^{-7} \text{ erg cm}^{-2}}\right) \left(\frac{D_L}{3 \text{ Gpc}}\right)^2 \left(\frac{\delta T}{10 \text{ ms}}\right)^{-2}, \tag{11}$$

where f_p is the fraction of photons that make pairs, σ_T the Compton cross-section, Φ the energy fluence, D_L the luminosity distance, R_i the emission radius, m_e the electron mass and c the speed of light. In the non-relativistic case, the size of the source is simply connected to the observed variability by $R_i = c\delta T$. This posed a serious theoretical conundrum at the time, the so-called *compactness problem*. This problem is resolved by considering that the fireball is moving ultra-relativistically, with a Lorentz factor $\Gamma > 100$.

Indeed, in the relativistic case, two relativistic effects must be taken into account in the calculation of $\tau_{\gamma\gamma}$:

- (i) the fraction of photons that can make pairs decreases by a factor of $\Gamma^{2(1+\beta)}$, where β is the high-energy PL index of the photon spectrum;

---

[8] GW spin-down is relevant only when an initial spin velocity $\Omega_0 \geqslant \Omega_* = 10^4$ rad s^{-1} is given to the NS. In such cases, the timescale for the GW-dominated regime is short, so that Ω rapidly falls below Ω_*.

- (ii) because of relativistic beaming, the relation between emission radius and variability becomes $R = \Gamma^2 c\Delta t$, reducing the opacity by an additional factor Γ^4 (since $\tau_{\gamma\gamma} \propto R_i^{-2}$).

Hence, in the relativistic case Eq. (11) has to be replaced by Eq. (12):

$$\tau_{\gamma\gamma} = 10^{13} \frac{f_p}{\Gamma^{2-2\beta}} \left(\frac{\Phi}{10^{-7}\ \text{erg cm}^{-2}}\right) \left(\frac{D_L}{3\ \text{Gpc}}\right)^2 \left(\frac{\delta T}{10\ \text{ms}}\right)^{-2}. \tag{12}$$

Therefore, a Lorentz factor of at least $100 - 1000$ is required to obtain $\tau_{\gamma\gamma} \sim 1$, corresponding to the optically thin regime.[9]

1.4.2 *Jet collimation and beaming*

GRB radiation is not emitted in all directions but rather within two narrow bipolar jets, with a half-opening angle θ_j of a few degrees. This has huge consequences for the energy budget, which is lowered by a factor of a few tens to a few thousand (Fig. 18). The true γ-ray energy explosion is given by the geometrically corrected energy E_γ, which can be derived from the isotropic energy $E_{\gamma,\text{iso}}$ and the jet half-opening angle θ_j using Eq. (13):

$$E_\gamma = (1 - \cos\theta_j) E_{\gamma,\text{iso}} \simeq \frac{\theta_j^2}{2} E_{\gamma,\text{iso}} = 10^{50} - 10^{52}\ \text{erg}. \tag{13}$$

The jet half-opening angle can be derived from the achromatic[10] steepening of the late afterglow (Fig. 19). This feature arises from the combined effects of relativistic beaming and jet deceleration: at early times, the jet moves with a Lorentz factor of several hundred, so the observer only sees the radiation in a cone of semi-angle $\Gamma^{-1} \ll \theta_j$. As the jet is slowed by its interaction with the medium, its Lorentz factor decreases, and the visible portion of the jet widens.

When the relativistic beaming cone size starts to be comparable to the jet opening angle θ_j, the edge of the jet becomes visible. Beyond this point, no additional emitting area comes into view, and lateral expansion causes the jet to spread and decelerate more rapidly. This results in a steepening of the afterglow decay to a PL index $\alpha \sim 2$, observed simultaneously in different spectral bands (so-called *achromatic* break).

The jet semi-opening angle θ_j can be obtained from the position of the jet break time t_j, using Eq. (14):

$$\theta_j \simeq 0.057\ \text{rad} \left(\frac{t_j}{1\ \text{day}}\right)^{3/8} \left(\frac{1+z}{2}\right)^{-3/8} \left(\frac{n}{0.1\ \text{cm}^{-3}}\right)^{1/8} \left(\frac{E_{\gamma,\text{iso}}}{10^{53}\ \text{erg}}\right)^{-1/8} \left(\frac{\eta_\gamma}{0.2}\right)^{1/8}, \tag{14}$$

where θ_j is the jet half-opening angle, t_j the jet break time in the observer frame, z the burst redshift, n the circumburst medium number density in cm^{-3}, $E_{\gamma,\text{iso}}$ the isotropic-equivalent energy in erg, and η_γ the radiative efficiency.

---

[9] For a typical value of $\beta \sim -2.5$ and $\Gamma = 100$, $\tau_{\gamma\gamma} \sim 0.1 f_p$.

[10] Achromatic means that it is observed in different wavelengths passbands, meaning that it cannot be attributed to the crossing of a critical spectral frequency.

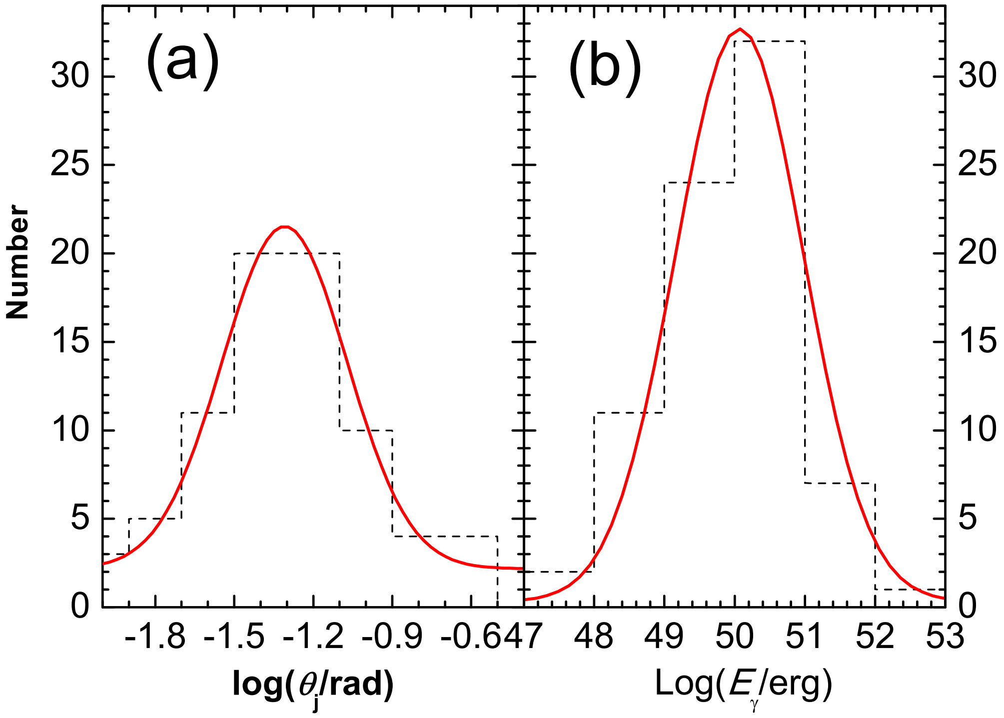

Figure 18: *Left panel:* Half-opening angle θ_j distribution from a sample of 77 GRBs. *Right panel:* Collimation-corrected energy released into γ-rays derived using the jet angle. From Lu et al. (2012).

1.4.3 *Jet propagation and breakout*

The jet is either launched by the BZ mechanism or by $\nu\bar{\nu}$ annihilation (Sections 1.3.1 and 1.3.2). As the jet propagates through the surrounding dense medium, either the stellar envelope of the progenitor star or the ejecta from a COM, it drives a forward shock into the ambient material and a reverse shock back into the jet. Material from both the jet and the environment is displaced sideways, forming an over-pressured cocoon that surrounds the jet and exerts pressure on it. The cocoon expands laterally at non-relativistic speeds. The jet is collimated by this cocoon and transfers part of its kinetic energy to it, giving rise to an angular structure, i.e. an energy profile $E_{\rm iso}(\theta)$, which differs from the simple top-hat jet configuration. When the jet head breaks out of the dense medium of the progenitor remnant, the jet and cocoon form a single structure, referred to as a *structured jet* (Fig. 20).

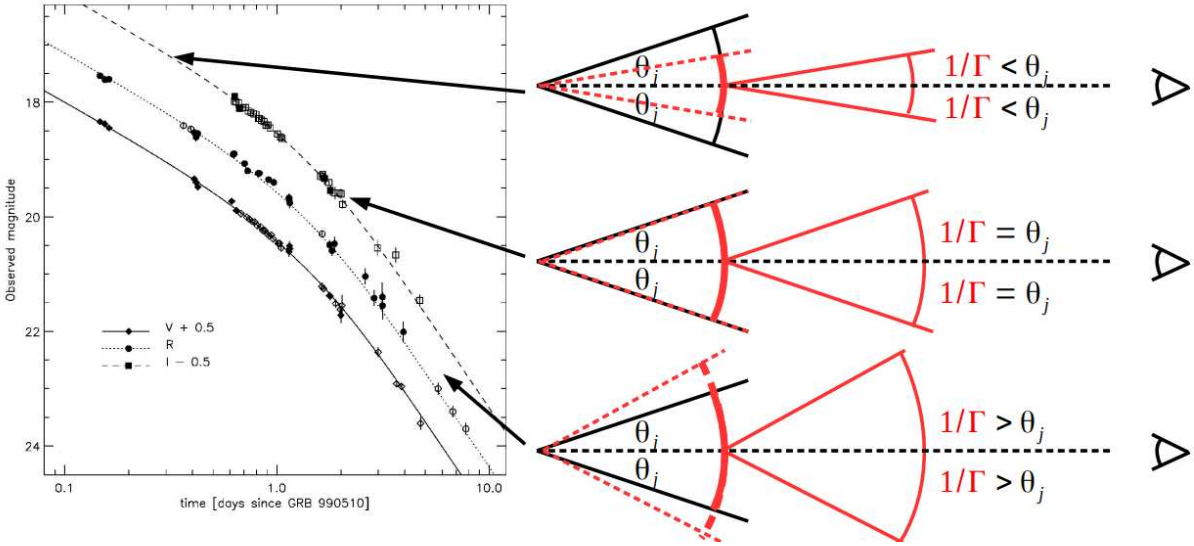

Figure 19: GRB 990510 multi-wavelength late afterglow. The afterglow features a break observed at different wavelengths. The sketch shows three different epochs: (a) before the jet break time where, because of relativistic beaming, only a tiny portion of the jet can be seen; (b) at the jet break time, the edge of the jet starts to be observed; (c) after the jet break time, the jet expands sideways into a bigger cone and no additional light comes from the jet. Credit: Cristiano Guidorzi.

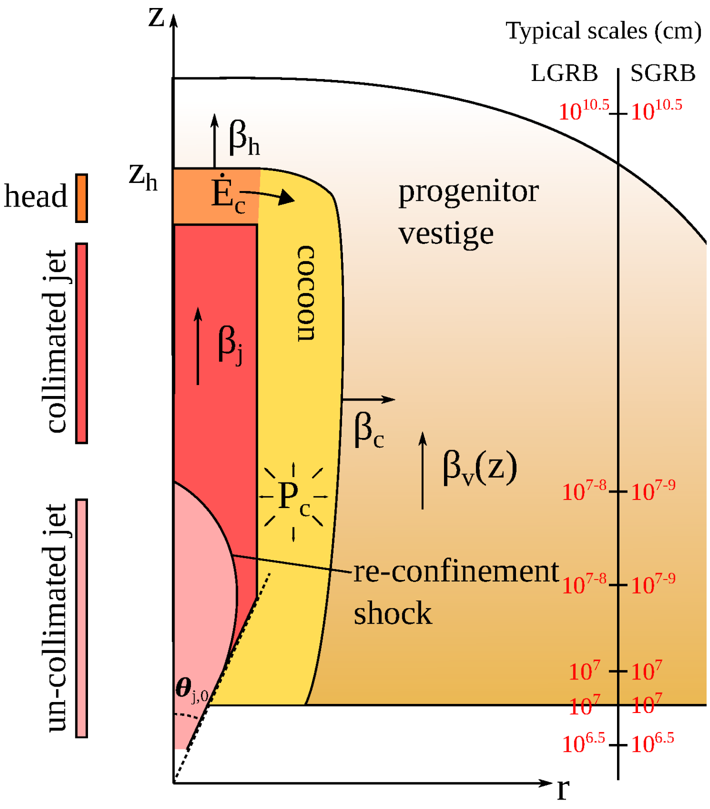

Figure 20: Sketch schematising the jet and cocoon formation. From Salafia and Ghirlanda (2022).

1.5 EMISSION MECHANISMS

1.5.1 *External shocks*

In the late 90's, an intense debate existed between an internal (associated with a central engine with variable activity) and external origin (associated with a single blast wave, sweeping up the medium) for GRB emission. While the latter currently well describes the afterglow radiation, it struggles to explain GRB prompt emission. In fact, if GRB radiation is produced by a single *expanding* shell, a temporal broadening of the pulses in the LC should be observed[11]. In the late 90's, most GRBs measured by BATSE did not show such evolution (e.g. Ramirez-Ruiz and Fenimore 1999). A notable case is GRB 990123, for which no pulse increase was noted despite the fireball started to decelerate before the end of the prompt emission (Fenimore, Ramirez-Ruiz, and Wu, 1999), ended the debate, tipping the balance towards a central engine based emission and *internal shocks*. Conversely, recent cases, such as GRB 230307A, for which there is a clear, systematic increase of the pulse width, could revive the debate (see Chapter 3.3.2).

1.5.2 *Internal shock model*

Internal shocks (IS) could occur within a variable ultra-relativistic wind produced by a highly variable source (Daigne and Mochkovitch, 1998; Kobayashi, Piran, and Sari, 1997; Rees and Meszaros, 1994).

Usually it is assumed that the Lorentz factors of the shells are highly dispersed, with a large spread $\delta\Gamma \sim \bar{\Gamma}$, where $\bar{\Gamma} \gg 1$ is the typical bulk Lorentz factor.

Consider two shells emitted by the central engine at times $t = t_e$ and $t = t_e + t_\nu$ with respective Lorentz factor Γ_1 and Γ_2, with $\Gamma_2 > \Gamma_1 \gg 1$. The timescale t_ν is the time elapsed between the emission of two consecutive shells and represents the intrinsic variability timescale of the central engine. The condition that the faster shell catches up with the slower one (see A.2 for the proof) defines the internal shock radius R_{IS} and the internal shock collision time t_{IS} (in the central engine rest frame):

$$R_{IS} = c\bar{\Gamma}^2 t_\nu = 3 \times 10^{14}\ \mathrm{cm} \left(\frac{\bar{\Gamma}}{100}\right)^2 \left(\frac{t_\nu}{1\ \mathrm{s}}\right), \tag{15}$$

and

$$t_{IS} = t_e + \frac{\beta_2}{\beta_2 - \beta_1} t_\nu\ . \tag{16}$$

A great strength of the IS resides in the fact that the observed GRB temporal variability faithfully mirrors the activity of the central engine. In fact, the pulse arrival times t_{obs} in the observer frame directly correspond to the emission times in the central engine rest frame:

$$t_{obs} = t_{IS} + \frac{D - R_{IS}}{c} \simeq \frac{D}{c} + t_e + t_\nu \tag{17}$$

---

[11] The duration of the pulse is given by $\Delta t_{ang} = \frac{R}{2\Gamma^2 c}$, where R is the radius of the expanding shell. If the shell is decelerating, the Blandford-McKee solution for the deceleration of a relativistic shell sweeping up a homogeneous medium providing $\Gamma \propto t^{-3/8}$ and $R \propto t^{1/4}$, the pulse duration $\Delta t_{ang} \propto t$ should increase linearly with time.

where D is the distance between the central engine and the observer (proof in Sect A.3). The sequence of pulses observed in the LC and the timescales separating them, therefore, reflect the activity of the central engine (Fig. 21).

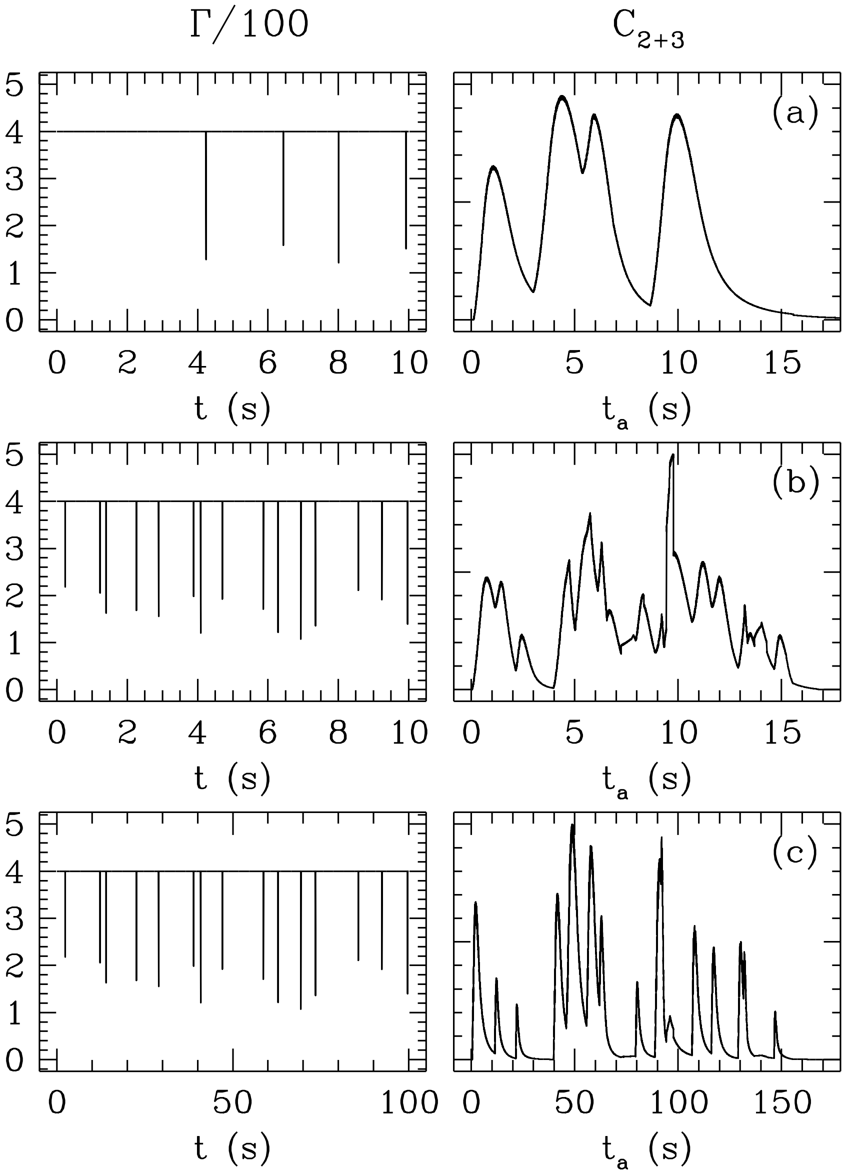

Figure 21: Initial Lorentz factor distribution (left panel) of the wind of shells and LCs (right panel) obtained with the internal shocks model of Daigne and Mochkovitch (1998). In all the three panels, the case of a fast layer with $\Gamma = 400$ slowed down by several slower layers is considered. The masses in the fast and in the slower layers are similar. Panel (a) shows a quite simple profile with four slow layers which produce exactly four pulses; Panels (b) and (c) present more intricate time profiles with 15 slow layers. The distributions of the Lorentz factor in (b) and (c) are homothetic, (c) being simply 10 times longer than (b).

The efficiency of converting kinetic energy to γ-ray radiation is given by (see proof at Sect. A.4):

$$\eta_\gamma = 1 - \frac{m_1 + m_2}{\sqrt{m_1^2 + m_2^2 + (\frac{\Gamma_1}{\Gamma_2} + \frac{\Gamma_2}{\Gamma_1})m_1 m_2}}, \tag{18}$$

where m_1 and m_2 are the masses of the two shells, and Γ_1 and Γ_2 their Lorentz factors. This leads to very low values, which implies that IS is not an efficient way to convert the kinetic energy of the fireball. Even in the case of equal masses ($m_1 \simeq m_2$), and a high contrast $\frac{\Gamma_2}{\Gamma_1} \gg 1$, η_γ hardly exceeds 20%, as also shown by Kobayashi, Piran, and Sari (1997) with a more realistic multiple-shell model.[12]

1.5.3 *Photospheric emission*

The relativistic wind, being initially opaque, should emit some thermal radiation when entering the optically thin regime. This transition happens when the optical depth of the relativistic wind reaches unity, which occurs at the photospheric radius r_{ph}, which is given by Eq. (19).

$$r_{ph} = \frac{\dot{E}\kappa_T}{8\pi c^3 \Gamma^3} = 6 \times 10^{12}\ \dot{E}_{52}\Gamma_2^{-3}\ \text{cm}, \tag{19}$$

where $\dot{E}$ is the energy rate injected by the central engine, κ_T the Compton opacity, c the speed of light, and Γ the Lorentz factor of the relativistic wind. To explain the non-thermal component produced during internal shocks, they must occur in an optically-thin regime. Therefore, the photospheric radius should lie below the internal shocks radius to account for the observed non-thermal spectra.

A bright thermal component dominating the non-thermal one was observed only in very few cases, such as GRB 090902B (Ryde et al., 2010), GRB 101219B (Larsson, Racusin, and Burgess, 2015), GRB 100507 (Ghirlanda, Pescalli, and Ghisellini, 2013). An additional thermal component, that significantly improves the spectral fit either on the whole GRB duration or only at the beginning of the burst, was found in a few cases (see e.g. Burgess et al. 2014; Guiriec et al. 2011, 2013). However, the thermal precursor appears only in a minority of GRBs. This difficulty in seeing the thermal component indicates that it is weaker than the non-thermal one for most GRBs. The absence of bright photospheric component in most GRBs could indicate that most of the energy carried by the wind is stored in magnetised form, the relative strength of these two components being regulated by the thermal/magnetic content of the jet (Hascoët, Daigne, and Mochkovitch 2013 but also Sect. 1.5.4).

1.5.4 *Magnetically dominated models*

The composition of the relativistic outflow produced by the central engine is still mysterious. In particular, the contribution of the magnetic field within the outflow is still uncertain. Generally, the outflow composition can be described by:

- an hydrodynamical outflow made of photons, $e^\pm$ pairs and baryons characterised by a baryonic flux F_b;

---

[12] A Lorentz factor distribution is considered with γ_{min} and γ_{max} as minimum and maximum values. For $\frac{\gamma_{min}}{\gamma_{max}} > 10^3$, η_γ can reach 40 %, while for more reasonable contrast $\frac{\gamma_{min}}{\gamma_{max}} = 10$, $\eta_\gamma = 20$ %.

- a Poynting-flux outflow which dynamics is dictated by the magnetic field, characterised by a Poynting (magnetic) flux F_p.

To measure the composition of the outflow, one can introduce the magnetisation parameter, which is defined by the ratio of the Poynting over the baryonic flux:

$$\sigma = \frac{F_p}{F_b} = \frac{B^2}{4\pi\Gamma\rho c^2}, \tag{20}$$

where B and ρ are the magnetic field strength and matter density in the rest frame of the central engine (lab frame). The jet is said to be Poynting-flux dominated when $\sigma \gg 1$, while it is photon dominated when $\sigma \ll 1$.

For an hydrodynamical outflow, the thermal energy of the fireball is converted into kinetic energy of the jet which is ultimately converted into non-thermal radiation, via internal shocks, as seen in Sec. 1.5.2. One expectation of this model is the presence of a photospheric emission, due to photons escaping the fireball when this one reaches the photospheric radius, at which the fireball becomes transparent (Sect. 1.5.3). However, the non-detection of a bright photosphere in bright GRBs, such as GRB 080916C, casts doubt on the composition of the relativistic jet. In fact, this bright GRB was observed simultaneously by *Fermi*/GBM and LAT which performed a joint spectral analysis over 5 energy decades (from ~ 10 keV to $10-100$ GeV; see Abdo et al. 2009b), which did not reveal any deviation from a Band function, suggesting a single non-thermal origin for the prompt emission of this event. This indicates that the majority of the energy contained in the outflow was not stored in a kinetically-dominated fireball but into a magnetised form ($\sigma = 15-20$ according to Zhang and Pe'er 2009), which is not released at the photospheric radius. The absence of a bright photosphere for the majority of the observed GRBs could imply that, in many cases, most of the energy is stored in the Poynting-flux component.

In the case of Poynting-flux dominated outflow ($\sigma \gg 1$), most of the energy of the outflow is stored into magnetic form. The magnetic energy can be either dissipated into thermal or kinetic energy of the outflow, but can also be dissipated directly into radiation via magnetic reconnections . More precisely, depending on the degree of magnetisation $\sigma_c = \Gamma^2 \sim 10^6\Gamma_3^2$, different regimes can be observed:

- **[1] Fireball model** [$\sigma \ll 1$]. Kinetic energy is dissipated via internal shocks.
- **[2] MHD models** [$1 \ll \sigma \ll \sigma_c$, **Drenkhahn and Spruit (2002)**]. Most energy is carried out by magnetic fields but may be first converted into bulk motion and then dissipated through internal shocks, although magnetic energy can be directly dissipated into radiation by magnetic dissipations.
- **[3] Electromagnetic model** [$\sigma > \sigma_c$, **Lyutikov (2006)]** Magnetic energy is converted to accelerated particles only through magnetic dissipations, not shocks.

The different possible energy transfers are summarised in Figure 22.

1.5.5 *The ICMART model*

The Internal-Collision-induced MAgnetic Reconnection and Turbulence model (ICMART, Zhang and Yan 2011) is a trade-off between internal shocks model where the fireball is purely hydrodynamic and magnetic-reconnection based models where the jet is Poynting-flux dominated.

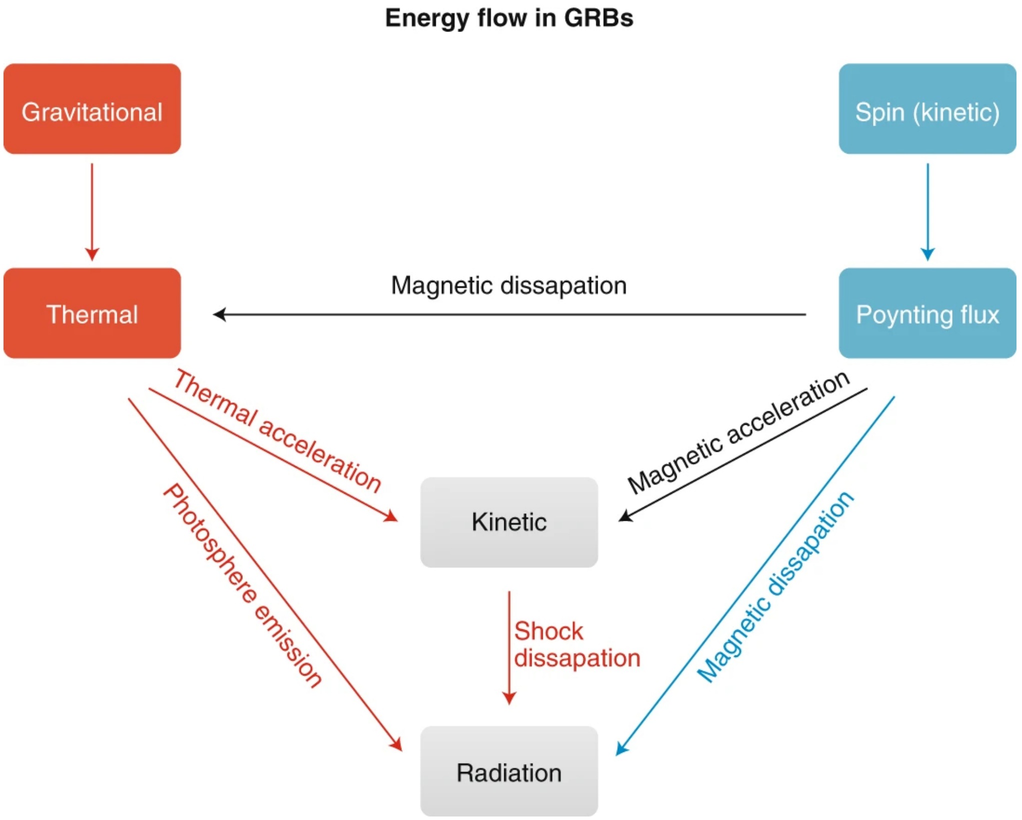

Figure 22: Energy transfer chart for different outflow compositions. From Zhang (2020)

In this model, the jet is only mildly magnetised, with $\sigma \sim 1 - 100$ when it reaches the emission region.

As in the standard IS model, the central engine launches a variable wind of shells that can interact and collide. However, most of the early collisions dissipate little energy and produce negligible radiation. In fact, initially the total released energy is at most $(1+\sigma)^{-1}$ of the total ejecta energy. This also explains the absence of a bright photosphere in most GRBs, as most of the energy is kept in magnetic form at this stage. Shocks progressively discharge the magnetisation that decreases as the jet expands. While the magnetic field lines entrained in the ejecta are initially globally ordered, the early collisions start to distort them, triggering in turn turbulence within the outflow.

Eventually, the magnetic field lines become sufficiently entangled to allow magnetic reconnection events. Once a reconnection seed event is triggered, the rapid energy release perturbs the surrounding material. The resulting turbulence further distorts the magnetic field lines, enabling additional reconnection events. This leads to a runaway release of magnetic energy, an ICMART event, which corresponds to a pulse in the GRB LC. The mechanism leading to an ICMART event is summarised in Fig. 23.

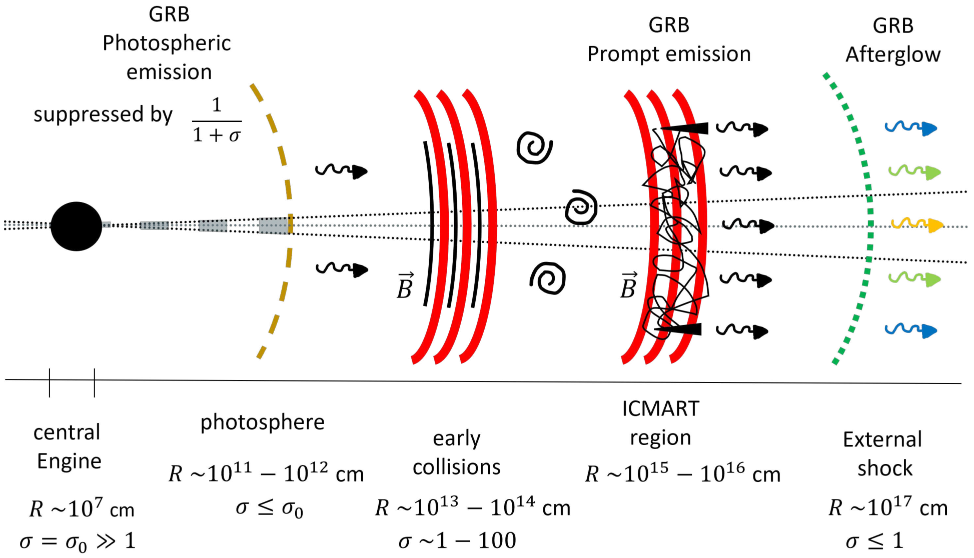

Figure 23: Scheme of the emission mechanism in the ICMART model. A Poynting-flux dominated jet is launched by the central engine. At the photosphere, the jet is magnetised therefore the photospheric emission is suppressed by a factor $\frac{1}{1+\sigma}$. Early collisions within the jet disrupt the initially order magnetic field lines, and trigger turbulence within the outflow. Turbulence grows as more shocks occur, until the magnetic lines get so entangled that fast magnetic reconnection events are made possible. At the emission site, a cascade of local magnetic reconnection events produces altogether an ICMART event, which can be seen as the superposition of the emission of all these local emitters. A GRB LC can be made of different ICMART events, occuring one after another, according to the central engine activity. Credit: Martina Sartori.

1.6 THE PROMPT EMISSION IN DETAIL

1.6.1 *Spectral properties of GRBs*

The prompt emission spectrum is usually well described by an empirical smoothly joined broken PL function, known as the Band function, discovered by D. Band on BATSE GRBs (Band et al., 1993).

$$N(E) = A \begin{cases} \left(\frac{E}{100\ \mathrm{keV}}\right)^{\alpha} e^{-(2+\alpha)\frac{E}{E_{\mathrm{peak}}}} & \text{if } E \leqslant (\alpha-\beta)\frac{E_{\mathrm{peak}}}{2+\alpha} \\ \left(\frac{(\alpha-\beta)E_{\mathrm{peak}}}{(2+\alpha)100\ \mathrm{keV}}\right)^{\alpha-\beta} \exp(\beta-\alpha)\left(\frac{E}{100\ \mathrm{keV}}\right)^{\beta} & \text{otherwise} \end{cases} \tag{21}$$

A is the amplitude in ph s^{-1} cm^{-2} keV^{-1}, E_{peak} is the νF_ν peak in keV, α is the low-energy PL index, and β is the high-energy PL index.

The Band function is a phenomenological function that accurately describes the spectrum of most GRBs. Its physical origin is still highly debated. The traditional way to explain GRB spectra is to invoke the synchrotron emission of non-thermal electrons in optically-thin regions (produced either by internal shocks, or by internal magnetic dissipation events), but a photospheric emission, reprocessed by some dissipation processes near the photosphere, could lead to a distorted black-body spectrum which could ultimately mimic a Band function.

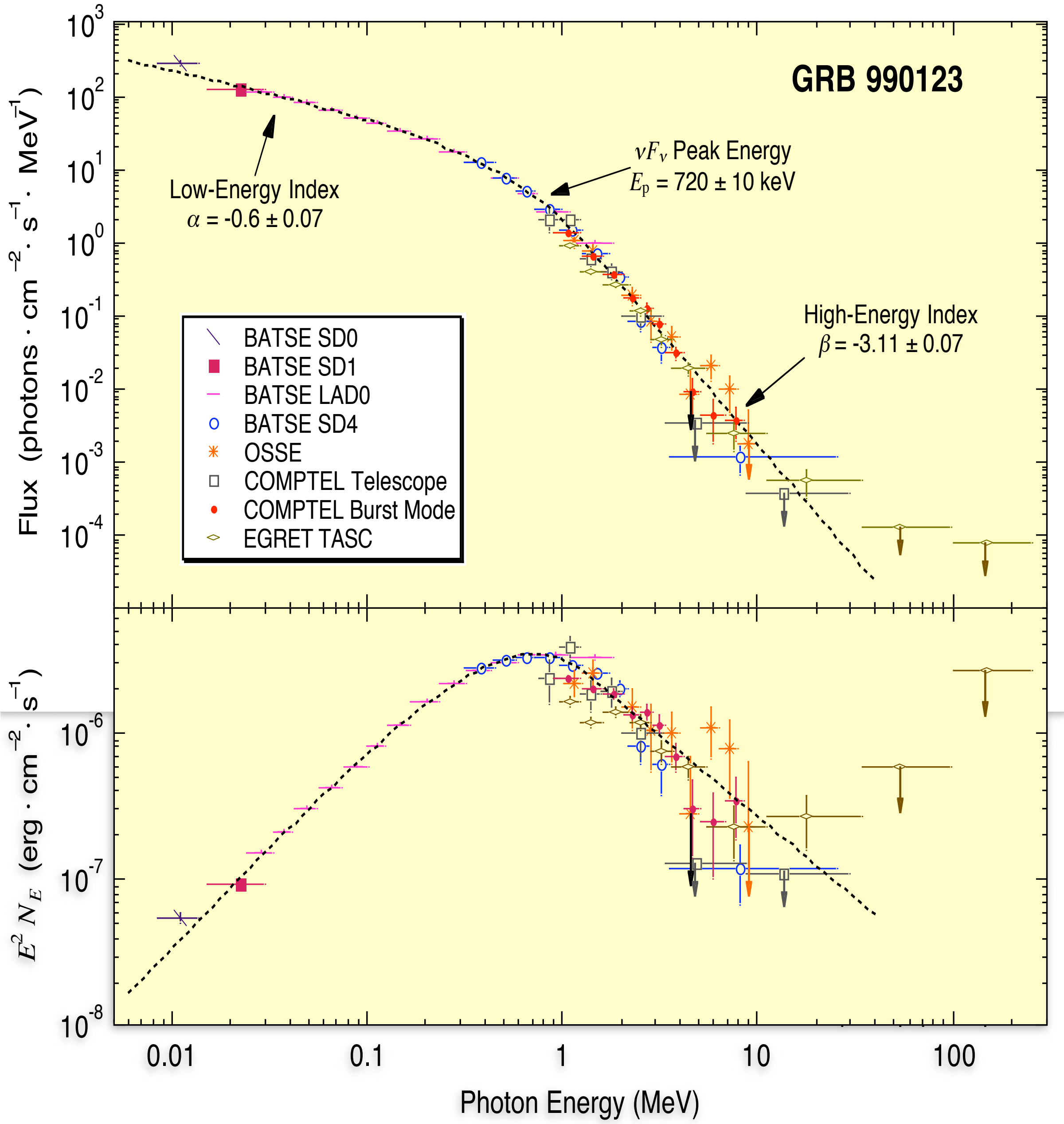

Figure 24: *Top panel:* Photon spectrum N(E) of GRB 990123 fitted by the Band function. *Bottom panel:* energy spectrum $E^2N(E)$. Credit: Rob Preece.

1.6.2 *Consequences of the relativistic motion*

The jet propagates at ultra-relativistic speeds, with a Lorentz factor of a few hundred. This implies that the radiation is beamed into a cone of semi-opening angle $1/\Gamma$. This causes a delay between photons emitted on the jet axis and those emitted on the edge of the jet, known as the angular spreading timescale Δt_{ang} (Fig. 25). The angular spreading timescale is given by Eq. (22):

$$\Delta t_{\mathrm{ang}} = \frac{R(1-\cos(\frac{1}{\Gamma}))}{c} \simeq \frac{R}{2\Gamma^2 c}, \tag{22}$$

where R is the emission radius.

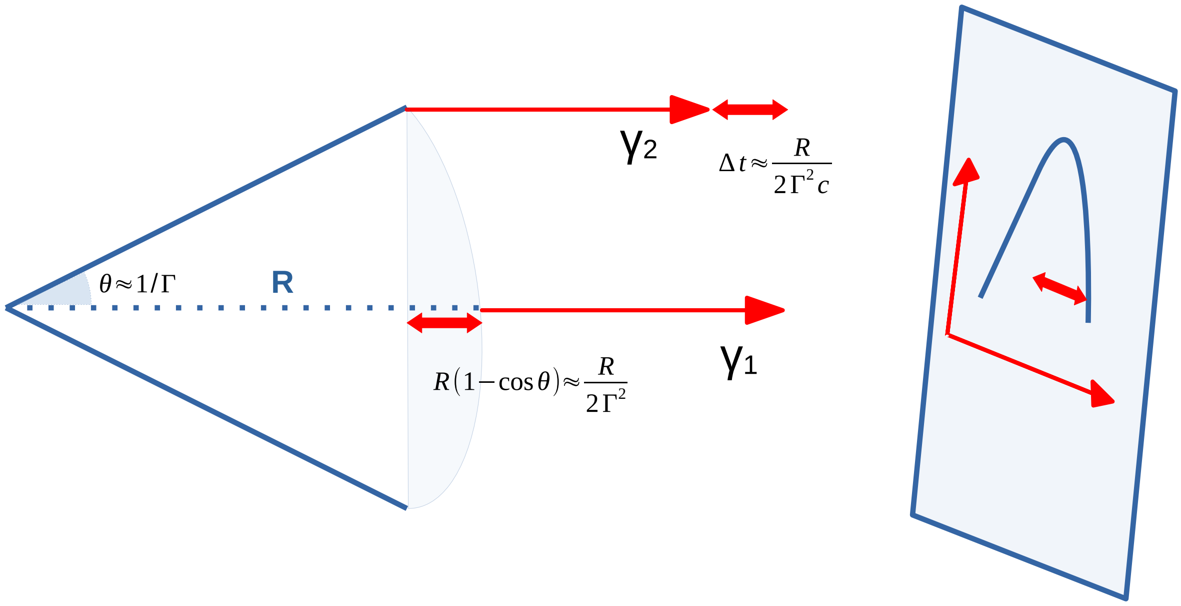

Figure 25: Sketch illustrating the angular spreading timescale. Photons emitted at the edge of the relativistic beaming cone are delayed with respect to those emitted on-axis. This delay is observed by the observer in the decaying part of the pulse.

1.6.3 *Empirical correlations*

After BeppoSAX made distance measurements possible, GRBs began to be examined in their rest frame, and a number of prompt-emission correlations emerged. Some correlations between the observables of the prompt emission were noted. Among them, the Amati relation linking the isotropic-energy E_{iso} and the intrinsic spectral peak energy $E_{\mathrm{p,i}} = (1+z)E_{\mathrm{p,obs}}$, where $E_{\mathrm{p,obs}}$ is the observed peak energy, has been consistently observed over many years of observation. The Amati relation reads:

$$\frac{E_{\mathrm{p,i}}}{\mathrm{keV}} = K\left(\frac{E_{\mathrm{iso}}}{10^{52}\ \mathrm{erg}}\right)^{m}, \tag{23}$$

with m close to 0.5 and $K \simeq 95$ (Amati et al., 2002). This relation was observed not only by grouping different bursts together but also within individual GRB time profiles using the corresponding time-resolved quantities (e.g. Maistrello et al. 2024). The correlation holds for both Type I and Type II GRBs (Fig. 26), with a similar slope but a different normalisation, the Type I GRBs lying above the Type II GRBs in the Amati plane (Minaev and Pozanenko, 2020; Tsvetkova et al., 2017; Zitouni, Guessoum, and Azzam, 2022). This difference can be used as a way to gain clues on the classification of ambiguous GRBs.

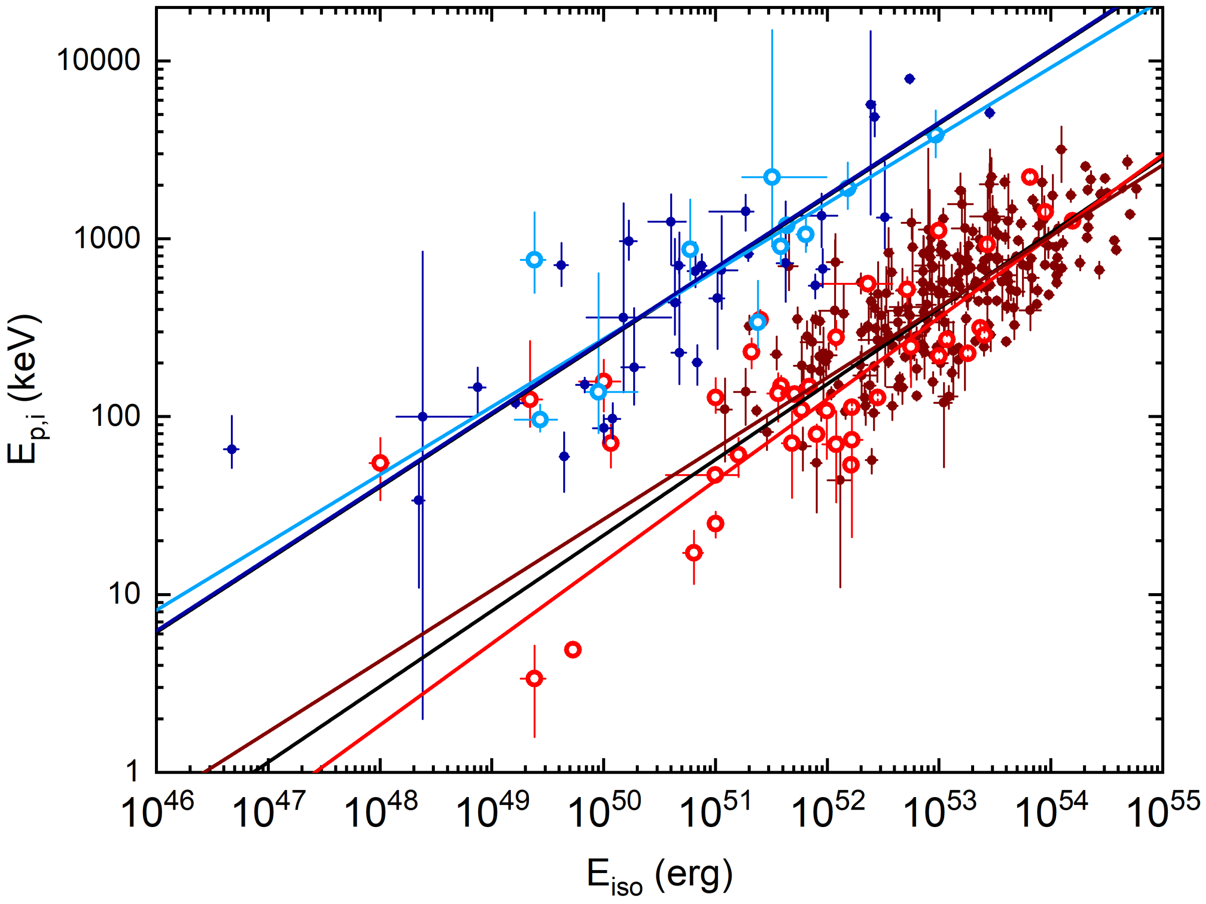

Figure 26: The $E_{p,i}$–E_{iso} correlation for subsamples of SGRBs (blue dots), SGRBs with an extended emission (cyan circles), LGRBs (dark red dots), and LGRBs with an associated SN (red circles). Corresponding fits are shown by the coloured lines (black lines represent fits of the whole type I and type II samples). From Minaev and Pozanenko (2020).

There exists the analogous time-resolved version of the Amati correlation, which therefore concerns $E_{p,i}$ and the peak luminosity L_p (Yonetoku et al., 2004).

In addition, these correlations can be exploited to use GRBs as probes of the cosmological parameters (see Moresco et al. 2022 for a review).

1.6.4 *Temporal properties of the GRB prompt emission*

GRB duration is characterised by the T_{90}[13], which is distributed according to a bimodal distribution, first discovered by the BATSE experiment (Kouveliotou et al. 1993, Fig. 27). This duration distribution, along with the hardness of the burst, was used to classify GRBs into two classes, short/hard and long/soft bursts. For a long time, these two classes were thought to be associated with two different formation channels, the former being associated with COMs, while the latter being linked to the collapse of a massive star. Several events, such as LGRBs associated with merger of compact objects, proved this classification wrong (Sect. 3.2.6).

---

[13] The T_{90} is the time interval covering from 5% to 95% of the total GRB fluence.

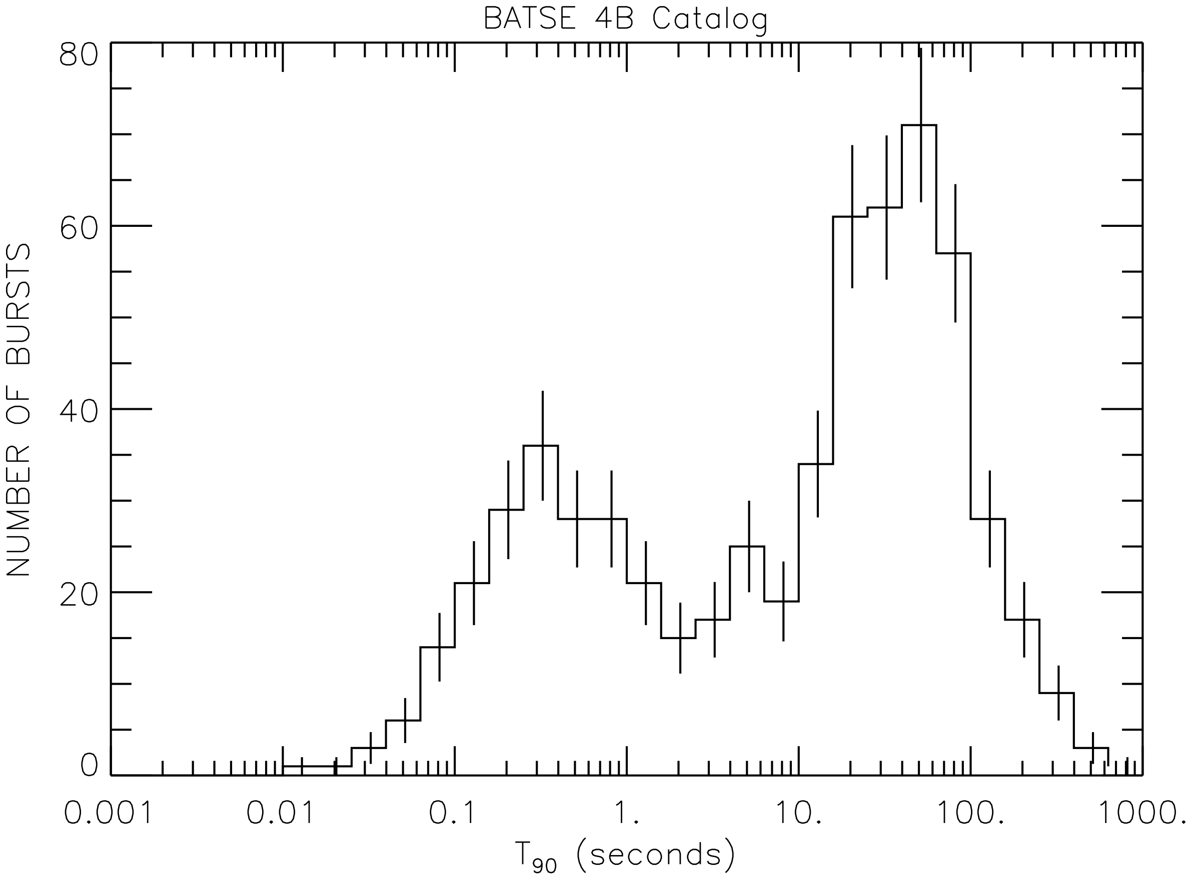

Figure 27: GRB T_{90} distribution for the bursts observed by BATSE. The two seconds dividing line was used to separate the short/hard bursts from the long/soft ones. From Meegan et al. (1998).

GRB LCs display a broad diversity, ranging from smooth profiles to highly complex and intricate structures. Sometimes GRB time profiles are characterised by a unique smooth pulse, which is often modelled as a FRED (fast rise exponential decay) template, whose expression is given by e.g. Norris et al. (1996):

$$f(t) = \begin{cases} A\ \exp\left[-\left(\dfrac{t_o - t}{\tau_r}\right)^{\nu}\right], & t < t_o \\ A\ \exp\left[-\left(\dfrac{t - t_o}{\tau_d}\right)^{\nu}\right], & t \geqslant t_o \end{cases} \tag{24}$$

with A the amplitude, t_0 the peak time, τ_r the rise time, τ_d the decay time[14]. The peakedness ν usually lies between 1 and 2, suggesting that the FRED pulse shape is between a simple exponential and a Gaussian. Other pulse templates have been proposed (Gowri et al., 2024; Hakkila and Preece, 2014; Kocevski, Ryde, and Liang, 2003; Norris et al., 2005) in the literature to account for the various GRB pulse shapes.

FRED-like pulses could constitute the building blocks of GRB LCs, as more complex LCs can be obtained as the superposition of multiple overlapping pulses, as it has been suggested

---

[14] Usually the decay time is larger than the rise time, so one can define $r = \tau_d/\tau_r > 1$, which can be more convenient to use when constraining the model.

by Stern and Svensson (1996). In this model, the LC is the result of a superposition of pulses generated recursively by a stochastic process operating in a nearly critical regime. This model well reproduces the temporal properties of GRB LCs, as also recently shown upon optimisation of this model through machine-learning techniques (Bazzanini et al., 2024; Maistrello et al., 2025).

FRED pulses show a different behaviour when studied at different energy ranges, in particular the width typically decreases for increasing energy, $w(E) \propto E_g^{-\alpha}$, with $\alpha \sim 0.4 - 0.6$ (Borgonovo et al., 2007; Fenimore et al., 1995). A time lag between different energy channels is also often observed, soft photons usually lagging behind harder ones (Bernardini, 2015; Cheng et al., 1995; Maraventano et al., 2025; Norris, Marani, and Bonnell, 2000; Shao et al., 2017; Ukwatta et al., 2010; Wu and Fenimore, 2000). LGRBs have positive lags and lag consistent with zero while SGRBs typically have lags consistent with zero (Bernardini et al., 2015). A correlation between time lag and peak luminosity was suggested in LGRBs prompt emission (e.g. Norris 2002; Norris, Marani, and Bonnell 2000; Schaefer and Collazzi 2007; Ukwatta et al. 2012), as well as in GRB X-ray flares (Margutti et al., 2010b). The relation has been claim to hold also for individual GRB pulses (Hakkila et al., 2008).

1.7 THE AFTERGLOW RADIATION

1.7.1 *Deceleration and interaction with the external medium*

The calculation of the deceleration of the GRB ejecta by the external medium is very similar to that of the braking of a SN envelope, but in a relativistic regime. A ultra-relativistic strong shock (matter moving at nearly the speed of light hitting the external medium at rest) propagates into the surrounding medium.

Energy conservation in the case of a strong relativistic shock can then be written as

$$\Gamma_0 M_0 c^2 + M_{\text{ext}} c^2 \simeq \Gamma M_0 c^2 + \Gamma^2 M_{\text{ext}} c^2, \tag{25}$$

where Γ_0 is the Lorentz factor of the ejecta before deceleration, and M_{ext} is the mass of the external medium swept up when the ejecta has reached a given radius R. The left-hand side of Eq. (172) consists of the initial energy of the ejecta and the rest-mass energy of the external medium at rest, and the right-hand side is the ejecta energy after braking plus the energy of the shocked external medium. One can rewrite it to obtain a second degree equation in the variable Γ: where $m = \frac{M_{\text{ext}}}{M_0/\Gamma_0}$. Three phases are observed, depending on m:

- phase 1: $\Gamma \simeq \Gamma_0$ if $m \ll 1$;
- phase 2: $\Gamma \simeq \Gamma_0 m^{-1/2}$ if $1 \ll m \ll \Gamma_0^2$;
- phase 3: $\Gamma \simeq 1$ if $m \gg \Gamma_0^2$.

Deceleration becomes important when $m = 1$, i.e. when M_{ext} is of the order of the initial ejecta mass reduced by the Lorentz factor, $M_{\text{ext}}(R_{\text{dec}}) \simeq \frac{M_0}{\Gamma_0}$. If the external medium has a constant mass density $\rho_{\text{ext}} = n m_p$, the swept-up mass at radius R is $M_{\text{ext}}(R) = \frac{4}{3}\pi R^3 \rho_{\text{ext}}$. This yields the deceleration radius:

$$R_{\text{dec}} \simeq \left(\frac{3 M_0}{4\pi \rho_{\text{ext}} \Gamma_0} \right)^{1/3}. \tag{26}$$

Since the isotropic equivalent kinetic energy of the ejecta is $E_{\mathrm{k,iso}} = \Gamma_0 M_0 c^2$, Eq. (26) can also be written as

$$R_{\mathrm{dec}} \simeq \left(\frac{3E_{\mathrm{k,iso}}}{4\pi\rho_{\mathrm{ext}}c^2\Gamma_0^2}\right)^{1/3} = 6.2\times10^{16}\ \mathrm{cm}\quad E_{\mathrm{iso},52}^{1/3}\,\Gamma_2^{-2/3}\,n^{-1/3}. \tag{27}$$

This defines the distance from the central engine at which the ejecta begins to efficiently transfer its energy to the shocked external medium, marking the onset of the afterglow emission.

During phase 2, for an homogeneous medium, then $\Gamma_*(R) \simeq \Gamma_0 \left(\frac{R}{R_{\mathrm{dec}}}\right)^{-3/2}$, which corresponds to the Blandford and McKee (1976) solution. At further radii, when $m \gg \Gamma_0^2$, the ejecta becomes non-relativistic and the Lorentz factor reaches unity[15].

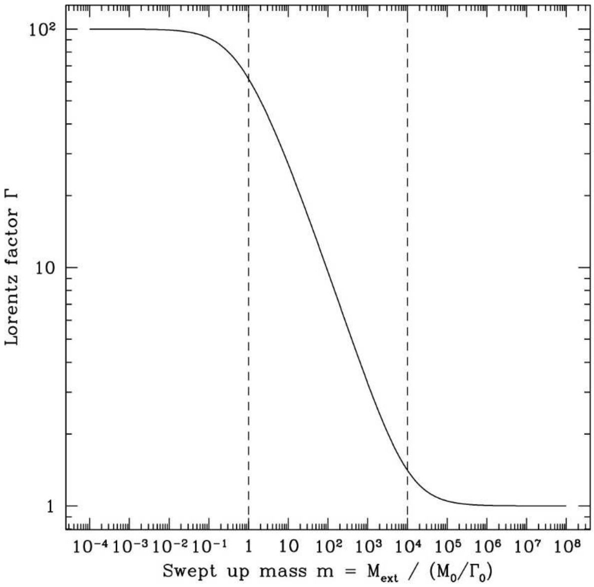

Figure 28: Deceleration of the GRB ejecta. The evolution of the Lorentz factor during the braking of the ejecta is shown as a function of the normalised mass $m = M_{\mathrm{ext}}/(M_0/\Gamma_0)$. The two vertical lines indicate $m = 1$ (start of deceleration) and $m = \Gamma_0^2$ (transition to the non-relativistic regime). The initial Lorentz factor is $\Gamma_0 = 100$. (Credits: F. Daigne).

The deceleration time is given by $t_{\mathrm{dec}} = \frac{R_{\mathrm{dec}}}{2\Gamma_0^2 c}$. It can be used to measure the initial Lorentz factor Γ_0 of the outflow before deceleration by measuring the afterglow peak (if the break effectively corresponds to the deceleration and not to different spectral regimes).

1.7.2 *Synchrotron emission and cooling regimes*

The afterglow radiation is a broad-band (from radio to X and γ-ray wavelengths, up to very high- energy), long-lived (lasting from hours to weeks) radiation following the prompt emission, which is caused by the shocks between the GRB ejecta and the interstellar medium.

---

[15] This occurs when $m = \Gamma_0^2$, at the transition radius $R_{\mathrm{Newton}} = \left(\frac{E_0}{\frac{4}{3}\pi n m_p c^2}\right)^{1/3}$, defining where the ejecta becomes non-relativistic.

Conversely to the prompt emission, in the case of the afterglow, the radiation mechanism is globally known: the shock accelerates electrons and propagates local magnetic fields, and electrons radiate through synchrotron radiation. It is composed of two components:

- the forward shock (FS), propagating into the shocked medium;
- the reverse shock (RS), propagating into the GRB ejecta.

The RS component is particularly important for a weakly magnetised jet (i.e. $\sigma \ll 1$). The exact shape of the afterglow spectrum depends on the electron cooling regimes: when all electrons cool efficiently (fast cooling, $\nu_m \gg \nu_c$) or when only high-energy electrons cool efficiently (slow cooling, $\nu_m \ll \nu_c$).

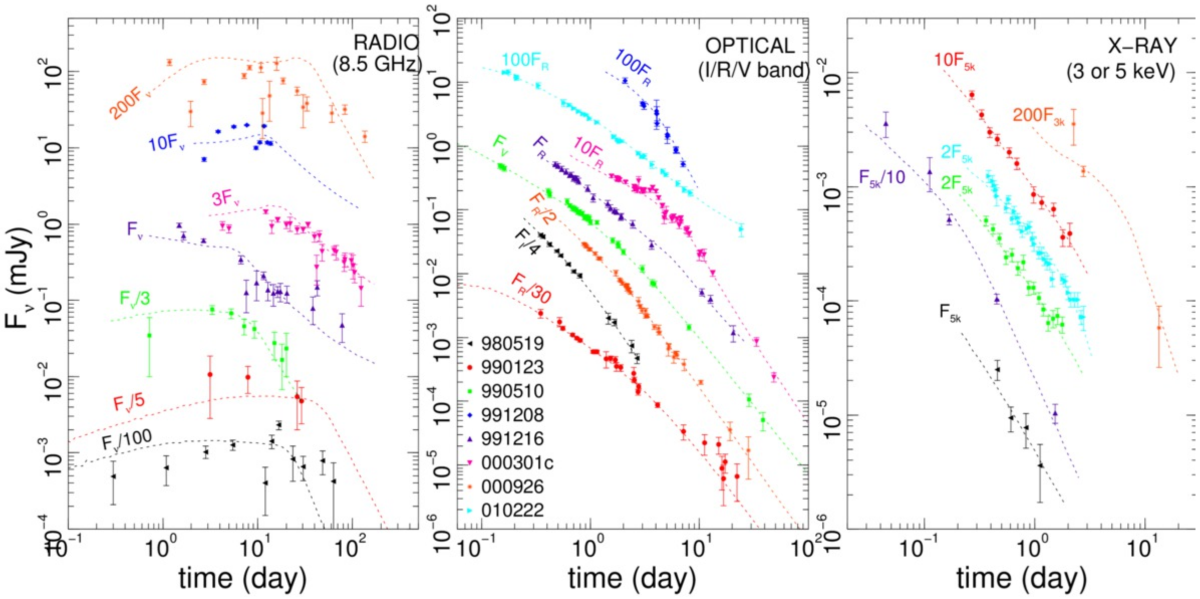

Figure 29: Radio, optical, and X-ray model LCs for eight GRB afterglows. From Kumar and Zhang (2015).

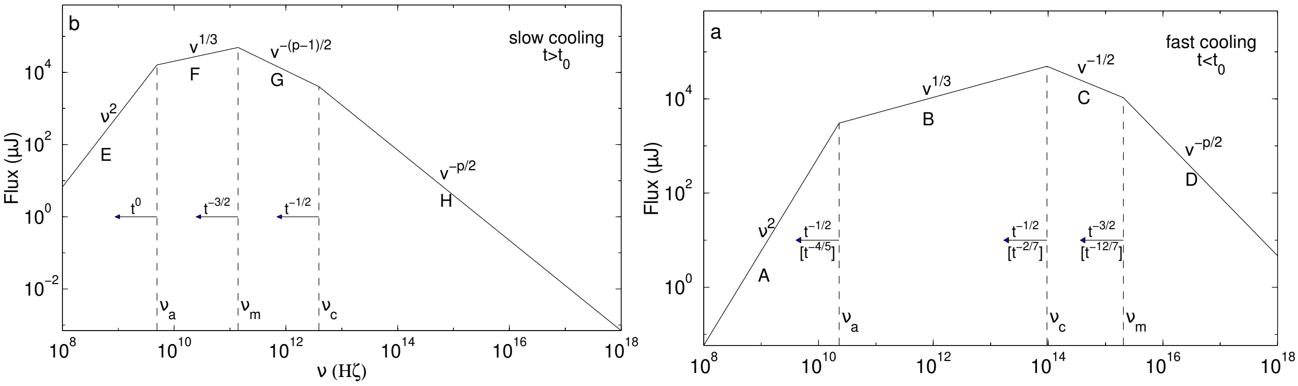

Figure 30: Expected GRB afterglow spectrum shapes in the cases of slow and fast cooling regimes. From Sari, Piran, and Narayan (1998).

1.8 WHY TIMING MATTERS

GRB LCs enclose a wealth of information, characterised by the duration, the temporal variability, the quiescent times between two strong emission episodes, the time lag between different energy channels, etc.

Studying the temporal behaviour of both LCs and energy spectra is fundamental to understanding how GRB central engines work (see Chapters 2 and 3) and can provide important clues on the nature of the GRB progenitor (see Sects. 3.2.10 and 3.3.2). It can help characterise the stochastic process that possibly rules GRB prompt emission. Even if the stochastic character of the central engine is unsettled (e.g. Greco et al. 2011 and Chapter 5), under this assumption it provides an accurate description of the temporal properties. The following sections illustrate how temporal variability can be used in this direction.

1.8.1 *Fourier analysis of individual GRBs*

Fourier power density spectra (PDS) provide a way to indirectly probe the GRB time variability by going into Fourier frequency space. In this space, low frequencies are associated with slow-varying time components, while high frequencies correspond to narrow time features. Usually, the GRB PDS is described by either a PL or a broken PL (BPL; Fig. 31), according to:

$$S_{PL}(f) = N f^{-\alpha} + B, \tag{28}$$

$$S_{BPL} = N\left[1 + \left(\frac{f}{f_b}\right)^{\alpha}\right]^{-1} + B, \tag{29}$$

The steepness of the PL decay at high frequency is associated with the strength of the fast variability components, as we will see in Sect. 3.1.1. The study of the PDS reveals a remarkable correlation between peak energy and PDS slope (Dichiara et al., 2016). This correlation has important consequences on the theoretical GRB emission models described in Sect. 1.5. In particular, it clashes with the $E_p \propto \Gamma^{-2}$ correlation expected in the IS framework (Ramirez-Ruiz and Lloyd-Ronning, 2002), unless the microphysics parameters depend on the Lorentz factor, while it is more naturally accounted for when the prompt emission is due to magnetic dissipations, as prescribed by the ICMART model.

1.8.2 *GRBs as a time-varying Poisson process*

The prompt emission and the early X-ray afterglow share many temporal properties, with periods of intense activity separated by long periods of inactivity (so-called *quiescent times*). While it is commonly thought that these two phenomena share a common origin, the physical mechanism(s) leading to this complex temporal behaviour are still uncertain (Section 1.5). Guidorzi et al. (2015) proved that the common WT distribution of pulses and flares shows a PL tail extending over four decades with a PL index close to $\alpha \sim 2$ (Fig. 33) and can be the manifestation of a common Poisson process with a time-varying rate. These results are consistent with a simple interpretation: a hyper-accreting disc breaks up into one or a few

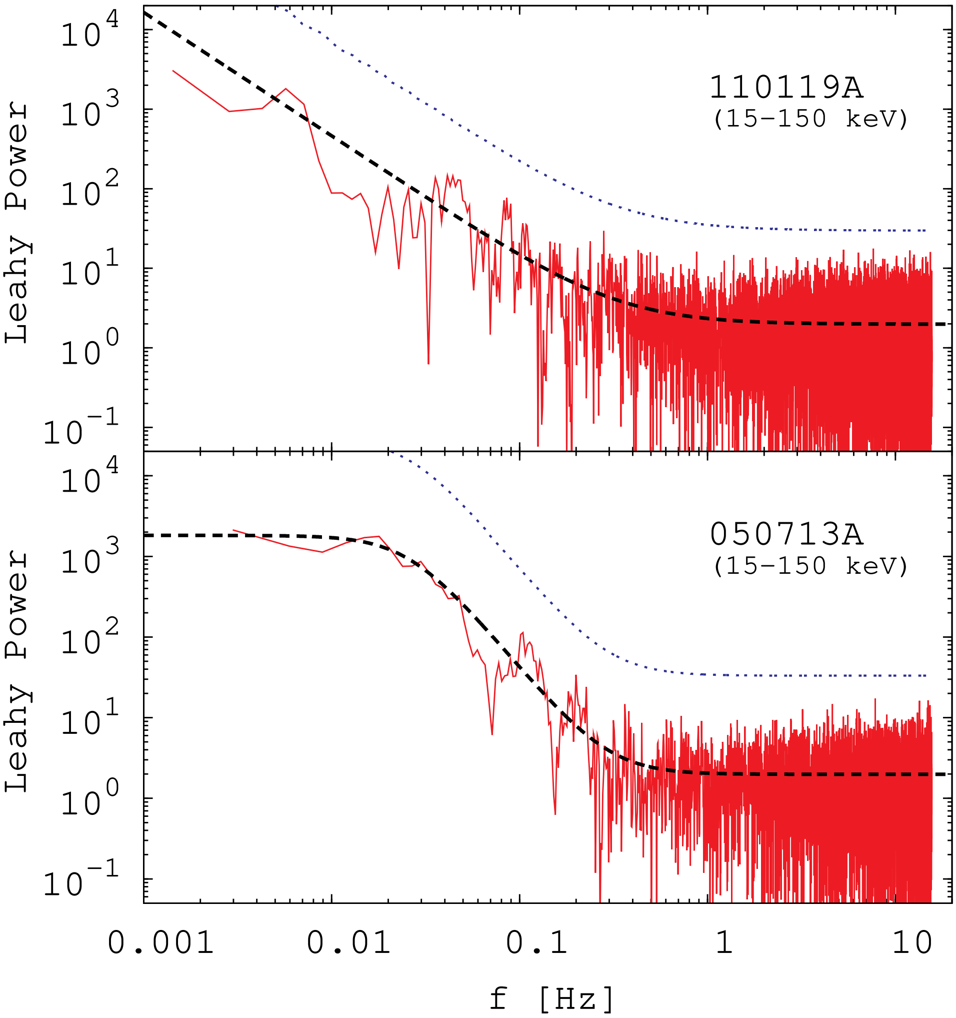

Figure 31: Power density spectra of GRB 110119A (top panel) and GRB 050713A (bottom panel), GRB 110119A is well modelled by the PL model described in Eq. (28) , while GRB 050713A is modelled by the BPL model described by Eq. (29).

groups of fragments, each of which is independently accreted with the same probability per unit time. In this picture, prompt γ-rays and late X-ray flares are due to different accretion episodes happening at the beginning and the end of the accretion process, following exactly the same stochastic process and likely the same mechanism.

1.8.3 *Different techniques to probe the temporal variability*

The temporal variability properties can be directly probed through PDS in the time domain (Li, 2001; Margutti et al., 2008), or in the frequency domain using Fourier transform (Beloborodov, Stern, and Svensson, 2000; Dichiara et al., 2013; Guidorzi, Dichiara, and Amati, 2016; Guidorzi et al., 2012; Ryde et al., 2003). The former studies show that different characteristic timescales in the range $0.1 - 10$ s were acting simultaneously in some GRB LCs, while the latter studies identify the presence of a dominant timescale in a fraction of GRBs.

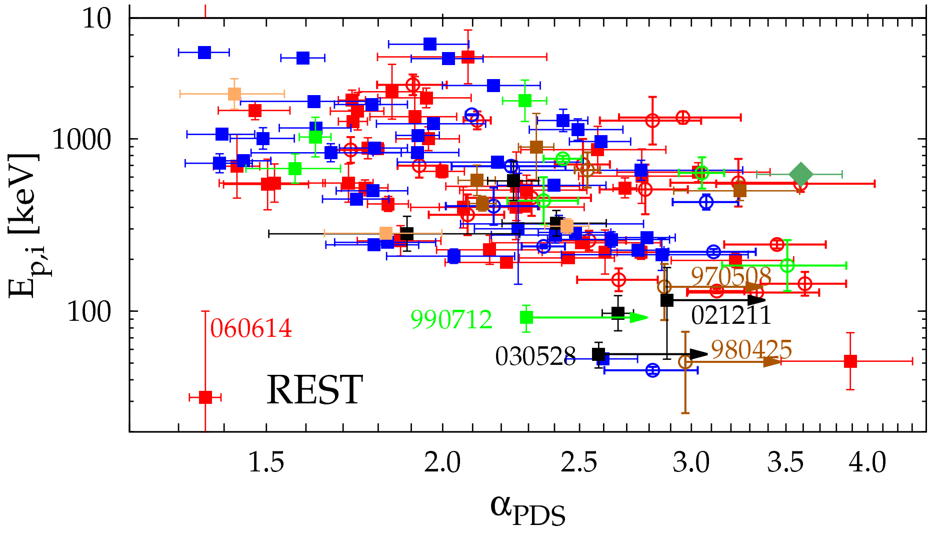

Figure 32: Peak energy vs. PDS slope in the source rest-frame. The different colours indicate values obtained with different experiments. The only SGRB available is also shown for comparison (diamond). Adapted from Dichiara et al. (2016).

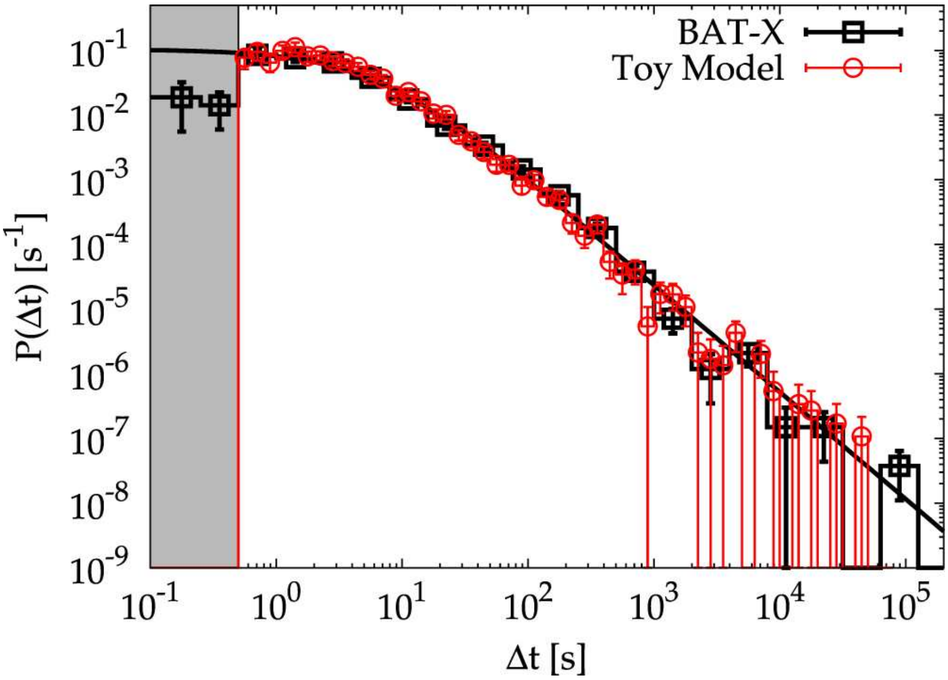

Figure 33: WT distribution of GRB prompt emission and X-ray flares. In black are shown the distribution derived using bursts from *Swift* data, while in red are shown the simulated distribution using the time-varying Poisson process based on the fragmented disc model described in Sect 1.8.2. Reproduced from Guidorzi et al. (2015).

The autocorrelation function (ACF) was used to measure the width of the time structures observed in GRB LCs (Borgonovo et al., 2007; Fenimore et al., 1995). It was used in particular to prove the lack of timescale evolution in GRB 990123, which at the time disfavoured the external shocks model (Fenimore, Ramirez-Ruiz, and Wu (1999) but also Sect. 1.5.1).

The structure function (see Eq. 50), combined with the use of Haar wavelets, was used to compute the minimum variability timescale (Sect. 3.2.8), which is the shortest timescale at which a GRB exhibits uncorrelated temporal variability (Camisasca et al., 2023b; Golkhou and Butler, 2014; Golkhou, Butler, and Littlejohns, 2015; MacLachlan et al., 2013; Maccary et al., 2025). The different methods used to compute the minimum variability timescale, as well as their application to gaining clues about GRB progenitors, are detailed in Chapter 3.

1.9 CONCLUSIONS

For nearly 30 years, the origin of GRBs remained unknown, owing to the poor localisation capabilities of early instruments. Two competing scenarios were proposed: a galactic origin and an extragalactic one, implying radically different energy budgets. The observation of the isotropic sky map of GRBs by BATSE tipped the balance towards an extragalactic origin, although the question remained unsettled until the first direct measure of the GRB distance.

With the launch of BeppoSAX and the first GRB redshift measurement with GRB 970508, the debate was finally settled: GRB sources are cosmological, requiring a energy budget of 10^{49-51} erg, achievable only by extraordinary events such as the collapse of a massive star, or the merger of two compact objects.

Starting in 2004 with the launch of *Swift*, the observation of the early X-ray afterglow revealed new features, such as a shallow decay phase and flaring episodes. The former feature was interpreted in various ways, some of which suggested an extended central engine activity. An event observed by *Swift* in 2006, namely GRB 060614, a SGRB with subsequent extended emission showing evidence of a collapsar origin, called into question the previously established classification scheme between short and long bursts.

In 2017, the first GW detection associated with a SGRB and its optical counterpart, AT2017gfo, marked a milestone. This discovery identified BNS mergers as the main sources of heavy elements production via the r-process and marked the birth of the multi-messenger astronomy.

In 2022, the brightest GRB ever recorded, GRB 221009A was detected. Its broad multi-wavelength emission, extended up to very high energies, provided clues on several aspects of the GRB physics, including jet structure and high-energy emission mechanisms. In 2021 and 2023, two LGRBs originating from COMs were observed, confirming the peculiar nature of the 2006 event. These bursts shared distinctive temporal properties, suggesting the existence of a subclass of LGRBs produced by mergers.

In 2024, the Sino-French mission SVOM was launched. Thanks to its capability for rapid X-ray and optical follow-up, SVOM is significantly increasing the number of well-localised bursts with measured redshifts. Einstein Probe is revealing that the event in X-rays can start before the γ-ray emission and last much longer.

If THESEUS is launched, it will likely unveil a new population of GRBs, including high-redshift and X-ray–rich events whose main emission is softer than that typically observed with current instruments. This would open a new observational window on the early Universe, enabling the detection of high-redshift galaxies otherwise beyond our reach.

What has the study of timing and temporal variability brought to this field? From the very beginning of their discovery, the temporal properties of GRBs were key to associating GRBs with extremely compact sources. They also posed a theoretical challenge with the compactness problem, whose resolution required the prediction of an ultra-relativistic jet. The study of the GRB temporal structures, and the absence of significant temporal evolution within them, favoured an internal origin for the prompt emission over external-shocks models. Later on, the analysis of temporal variability, including the measurement of the spectral time lag and minimum variability timescale, proved critical to distinguish LGRBs arising from COMs from the bulk of collapsar events, as demonstrated, for example, with the cases of GRB 211211A and GRB 230307A. As we will discuss later (see Sect. 3.3.2), the recent observation of peculiar temporal properties in GRB 230307A further highlights the importance of variability studies. These features not only challenge current GRB emission mechanisms but also offer a promising way to identify such events directly from their γ-ray time profile.

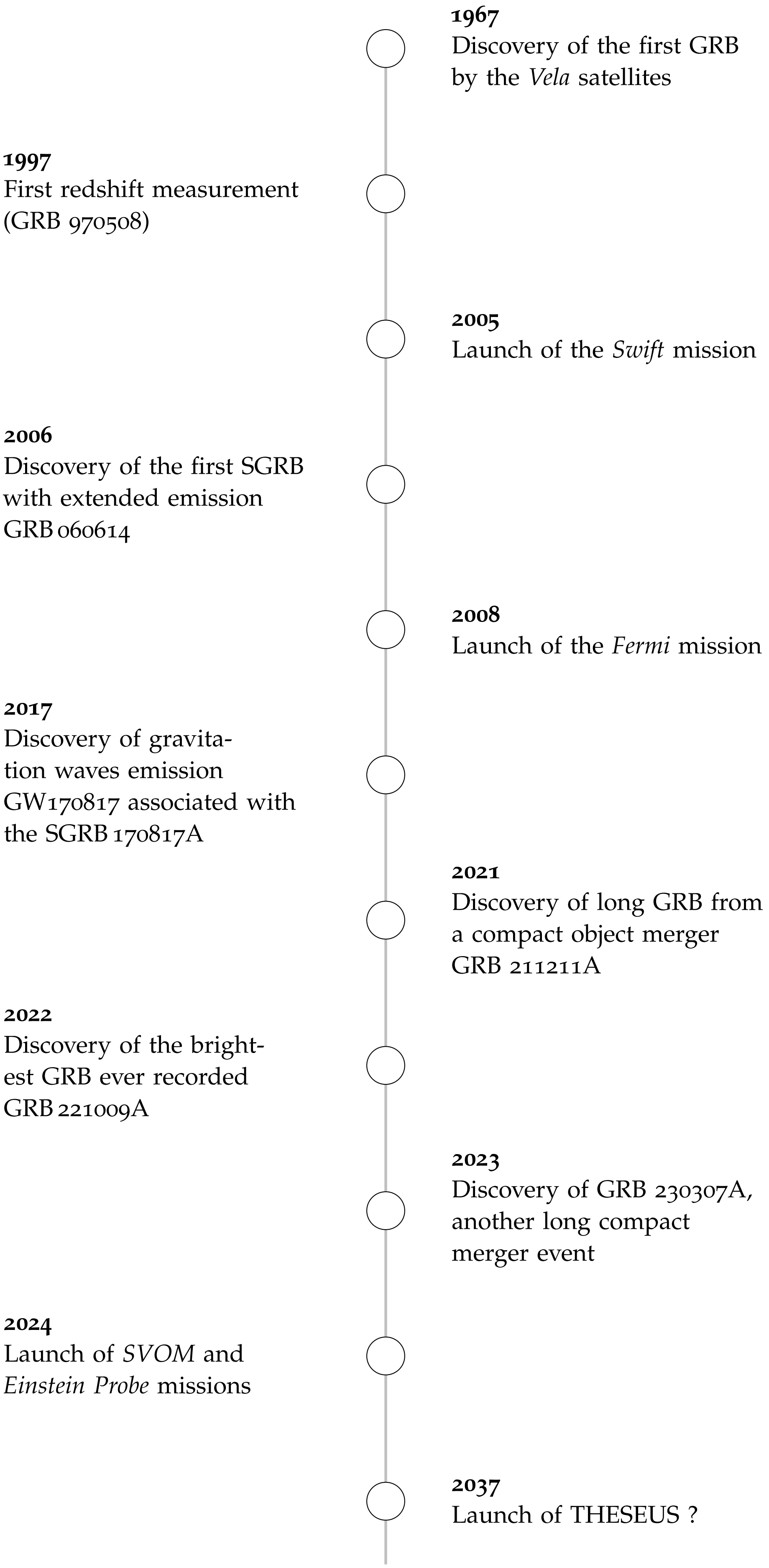

1967
Discovery of the first GRB by the *Vela* satellites

1997
First redshift measurement (GRB 970508)

2005
Launch of the *Swift* mission

2006
Discovery of the first SGRB with extended emission GRB 060614

2008
Launch of the *Fermi* mission

2017
Discovery of gravitation waves emission GW170817 associated with the SGRB 170817A

2021
Discovery of long GRB from a compact object merger GRB 211211A

2022
Discovery of the brightest GRB ever recorded GRB 221009A

2023
Discovery of GRB 230307A, another long compact merger event

2024
Launch of *SVOM* and *Einstein Probe* missions

2037
Launch of THESEUS ?

2

SELF-ORGANISED CRITICALITY AND GRBS

Although the origin of the GRB prompt emission is still an open issue, it is likely the result of a complex interaction between the different components of the jet that is launched by the central engine, either a hyper-accreting black hole or a magnetar. Lying at the edge of instability, the system would release its energy in a non-linear way, unstable episodes corresponding to intense emission periods and stable ones to quiescent times. The very peculiar shape and diversity of GRB LCs motivate their study in the dynamical system framework. Similar features, such as intermittency and non-linear energy release, can be found in other kinds of systems, such as the solar magnetosphere, or Earth's tectonic plates. These systems are usually ruled by self-organised criticality (SOC). Can a SOC dynamics describe GRBs and their irreversible evolution too? This is the object of this chapter.

2.1 WHAT IS SELF-ORGANISED CRITICALITY?

Self Organised Criticality (SOC) represents a peculiar type of dynamics that was proposed in the early 1980s to explain the occurrence of a PL distributed PDS (so-called coloured noise) in certain dynamical systems (Bak, Tang, and Wiesenfeld, 1987). These systems spontaneously reach a critical point at which energy is released in a non-linear and intermittent way, through avalanche episodes. SOC has been applied to various fields, including biology (e.g. Vidiella, Guillamon, and Sardanyès 2021), neurosciences (see Plenz et al. 2021 for a review), economics (Bouchaud, 2024), geology and Earth sciences (Sect 2.1.3), and astrophysics (Sect. 2.2).

2.1.1 *The origin of self-organised criticality: the sand-pile model*

SOC was first illustrated by the example of a sand pile onto which some sand grains are steadily added to the top (Fig. 34). As the sand pile slope grows, it eventually reaches a threshold above which the system cannot sustain mechanical equilibrium. Above this threshold, the system releases energy through avalanches to restore the lost equilibrium. As other sand grains are added, the process indefinitely repeats, the system releasing energy through avalanches whenever it exceeds the instability threshold.

2.1.2 *Cellular automata model*

This model is known as the Bak-Tang-Wiesenfeld (BTW) sand-pile model. Although real experimental setups of sand piles, and rice-pile avalanches were originally conceived, SOC was primarily observed in lattice-based simulations, known as cellular automata simulations (see Creutz 1996; Turcotte 1999 for a review). These are simple computer simulations that, using simple evolution rules based on the interaction between nearest neighbours, can mimic the behaviour of a complex non-linear system and recover its global properties. An example of such systems is the 2D BTW sand-pile model (Bak, Tang, and Wiesenfeld, 1987, 1988). This

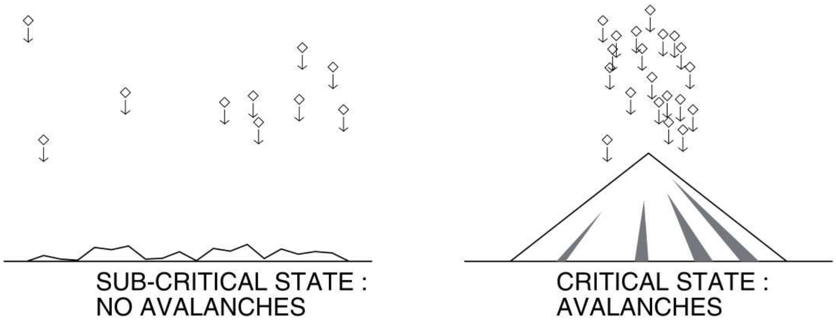

Figure 34: *Left panel:* the system is in a sub-critical state, and no avalanches are observed. *Right panel:* the system enters into the critical state, resulting in avalanches. From Aschwanden (2013).

system is represented by a 2D checkerboard, in which each cell at position (i, j) is characterised by a certain amount of sand $z_{i,j}$. This system evolves according to simple rules: (1) at each step one sand grain is added at a random position, (2) whenever the number of sand grains exceeds $z_c = 4$ at some position (i, j), the sand grains are redistributed to the four closest neighbours at positions $(i \pm 1, j \pm 1)$. When (2) occurs, it can cause the relaxation of other cells, triggering therefore an avalanche that stops when all the cells reach a sub-critical condition (here $z_{i,j} < 4$). The distribution of avalanche sizes then follows a PL. The evolution of the system is therefore given by this simple algorithm:

$$\begin{aligned} z_{i,j} &\to z_{i,j} + 1, && (30)\\ z_{i,j} &\to z_{i,j} - 4, \text{if } z_{i,j} \geqslant z_c = 4, && (31)\\ z_{i\pm1,j\pm1} &\to z_{i\pm1,j\pm1} + 1 \quad \text{for each nearest neighbour.} && (32) \end{aligned}$$

The evolution of the system is described in Fig. 35. Cellular automata numerical simulations with nearest-neighbour interactions were also used to address meaningful physical problems, such as the formation of earthquakes with the slider-block spring model (Sect. 2.1.3), solar flares (Sect. 2.2.1), and BH accretion-disc systems (Sect. 2.2.2).

2.1.3 *Self organised criticality and earthquakes*

Earth's outer layer is made of huge pieces called *tectonic plates*: these plates are always moving but sometimes get stuck (stick-slip motion) at their boundaries because of friction. When pressure builds up enough, the plates suddenly slip and release energy. The released energy propagates as shock waves, triggering a sudden shaking of the ground commonly known as *earthquakes*[1]. The number of earthquakes with magnitude M is given by the Gutenberg-Richter law (Gutenberg and Richter, 1944):

$$\log N = a - bM, \tag{33}$$

with b close to 1. The energy of an earthquake is linked to its magnitude by a similar relation (e.g. Båth 1955):

$$\log E = c + dM. \tag{34}$$

---

[1] `https://www.usgs.gov/programs/earthquake-hazards/science-earthquakes`

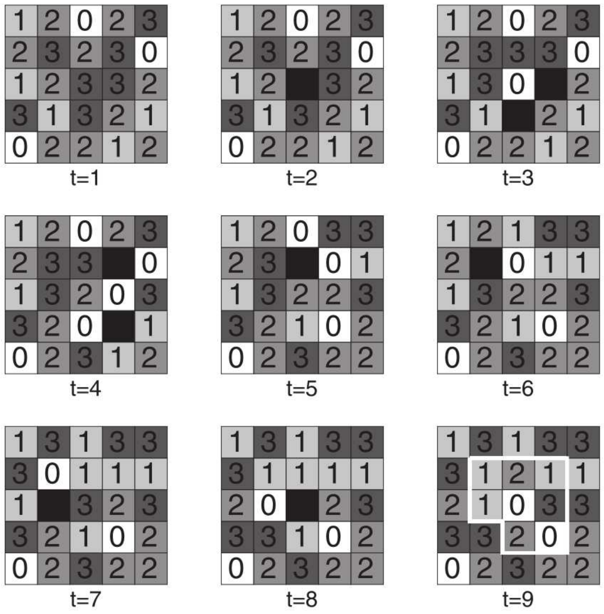

Figure 35: Example of an avalanche in a two dimensional BTW sand pile computer simulations. The initial state of the sand pile at time $t = 1$ is sub-critical, since none of the states $z_{i,j}$ overcomes the critical threshold $z_c = 4$. At time $t = 2$, a sand grain is dropped in the middle of the sand pile, triggering an avalanche of subsequent topplings. At times $t = 3$ and $t = 4$, two topplings occur in the same time step. At time $t = 9$, the sand pile regains its stability and the total avalanche size is shown a white polygon, encompassing 8 pixels (adapted from Bak 1996, p.53). From Aschwanden (2013).

The combination of the two previous equations leads to a PL scaling of the energy released by earthquakes:

$$N(E) \propto E^{-\tau}, \tag{35}$$

with $\tau = \frac{b}{d}$.

The slider-block spring model, first introduced by Burridge and Knopoff (1967), is a mechanical model used to mimic the tectonic of plates and model earthquakes. The model is made of two plates, with one being pulled with a constant force, and a set of masses connected to each other by springs of constant k_c and by springs of constant k_p to the upper plate (Fig. 36).

This system, owing to some pulling force, is going through a stick-slip motion: a given block is pulled by the spring connected with the upper plate and moves when the pulling force exceeds the friction force F_s. When moving, the dynamical friction F_d is slower than the static one. Being coupled to other blocks, when the block slips it triggers the slipping of a certain number of neighbouring blocks, provoking therefore an avalanche-like chain reaction of events through which the system releases the energy accumulated during the sticking phase.

Such kind of systems are governed by the ratio between static and dynamical force $\Phi = \frac{F_s}{F_d}$ and the ratio $\alpha = \frac{k_c}{k_p}$ ruling the stiffness of the system[2]. A certain number of numerical

---

[2] A system with a small α is "soft" and no large events occurred. A system with a large α is "stiff" and the entire grid of slider blocks are correlated: large slips including all blocks of the system occur regularly.

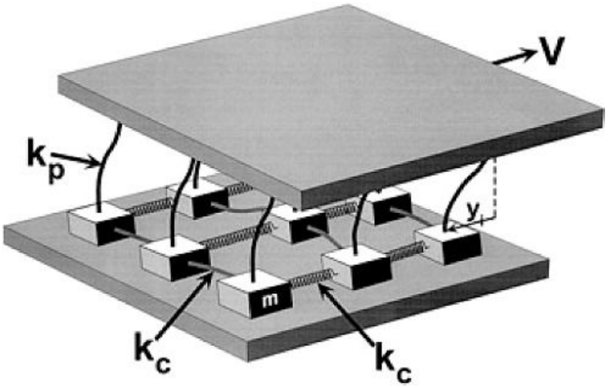

Figure 36: Sketch of the slider-block spring model of Burridge and Knopoff (1967). An upper plate, moving with a velocity V, is connected to a lower plate by a series of mass with a spring constant k_p. The masses are connected with each other by springs of spring constant k_c. From Turcotte (1999).

simulations were performed, in which the occurrence frequency distribution of events as a function of number of blocks that slip was studied (see e.g. Brown, Scholz, and Rundle 1991; Carlson and Langer 1989a,b; Huang, Narkounskaia, and Turcotte 1992; Nakanishi 1990, 1991; Otsuka 1972) and exhibit a PL form (Fig. 37).

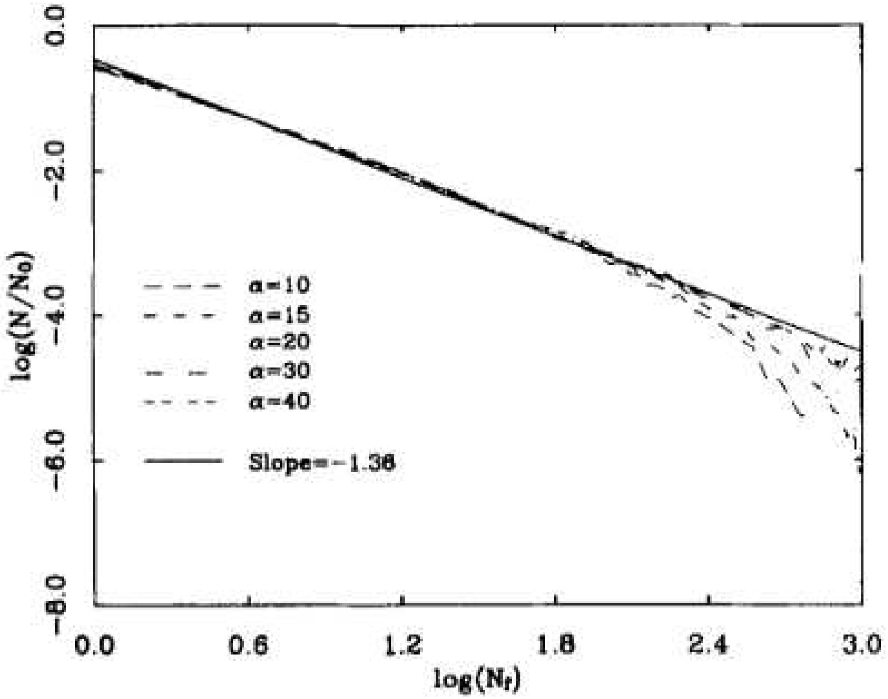

Figure 37: The ratio of the number of events N with size N_f, to the total number of events N_o is plotted against N_f. Results are shown for $\Phi = 1.5$ and $\alpha = 10$, 15, 20, 30, and 40. From Huang, Narkounskaia, and Turcotte (1992).

The mechanism building up earthquakes, in particular the sudden release of energy due to the stress build up at the border of the system, illustrated by the slider block spring model of Fig. 36, and the observation of both the Gutenberg-Richter law in real earthquakes and PL distributions in slider-block numerical simulations laid the foundation for associating earthquakes with SOC (see Turcotte 1999 for a review).

2.1.4 *The fractal-diffusive model of self-organised criticality*

Another way to approach SOC, done in particular by Aschwanden (2014), is to use simple probabilistic arguments to recover the PL indices describing the principal system properties. The primary assumption of this model, known as the *scale-free probability conjecture*, is that the avalanches occurring in a SOC system are PL distributed, i.e. following a relation of the type:

$$N(L) \propto L^{-d}, \tag{36}$$

where L is a characteristic length scale of the system and d is the Euclidean dimension. From this simple hypothesis, analytical scaling laws can be derived by making a simple change of variable in Eq. (36).

By measuring the radius of the circular area delimiting the propagating avalanche as a function of time for cellular automaton simulations (Aschwanden, 2012a) as well as for solar flare data (Aschwanden, 2012b)[3], one can establish that in SOC avalanches, the length and temporal scales T are linked by:

$$L \propto T^{\beta/2}, \tag{37}$$

where β is an exponent ruling the diffusion. A value of $\beta < 1$ corresponds to sub-diffusion, $\beta = 1$ to classical diffusion, $\beta > 1$ to hyper-diffusion or Lévy flight, and $\beta = 2$ to linear expansion (Fig. 38).

This yields the following scaling for the temporal scale:

$$N(T) = N(L)\left|\frac{dL}{dT}\right| \propto T^{-\alpha_T}, \tag{38}$$

where:

$$\alpha_T = 1 + \frac{(d-1)\beta}{2}. \tag{39}$$

Similar scalings can be obtained for the fluence (E) and the flux (P) distributions, leading to the values of the energy and peak luminosity distributions, given by Eq. (40) and Eq. (41) respectively:

$$\alpha_E = 1 + \frac{d-1}{D_d + 2/\beta}, \tag{40}$$

---

[3] The radial expansion of M- and X-class flares as a function of time phase has been measured by imaging instruments onboard of the Solar Dynamics Observatory. This consists of an exponentially growing phase, followed by a deceleration phase compatible with a sub-diffusive expansion ($\beta < 1$), slower than the diffusive one.

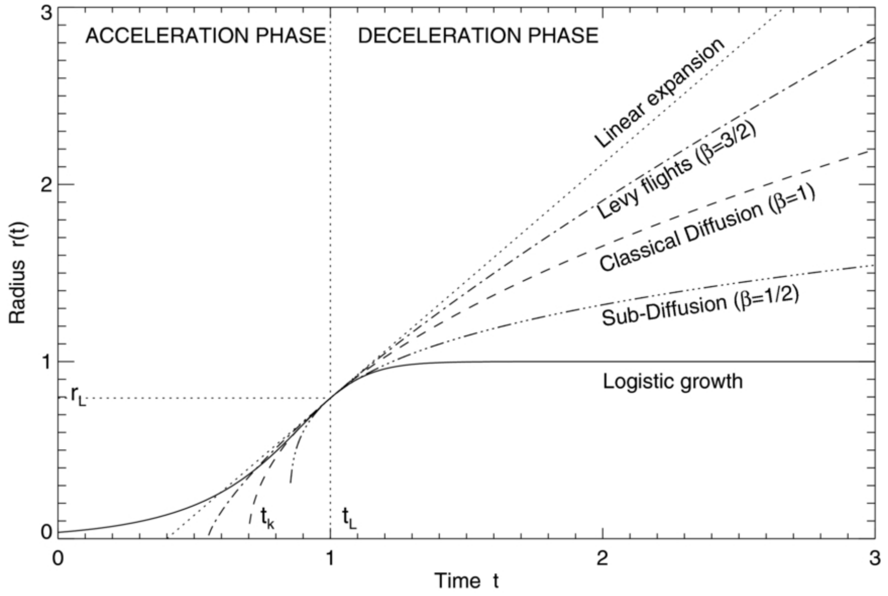

Figure 38: Different type of expansion, as a function of the parameter β. Linear expansion is obtained for $\beta = 2$ and classical diffusion for $\beta = 1$. Sub- and super-diffusion regimes are obtained for $\beta < 1$ and $\beta > 1$, respectively. Reproduced from Aschwanden (2012b).

where $D_d \simeq \frac{1+d}{2}$ is the so-called fractal dimension[4]. The peak flux (or equivalently the peak luminosity) distribution is ruled by:

$$\alpha_P = 1 + \frac{d-1}{d} \tag{41}$$

In the case of a 3-dimensional SOC region ($d = 3$) case with normal diffusion ($\beta = 1$), the set of values $\alpha_T = \alpha_{wt}$[5] $= 2$, $\alpha_E = 3/2$, $\alpha_P = 5/3$ is expected.

2.2 SELF-ORGANISED CRITICALITY IN ASTROPHYSICS

SOC models in astrophysics became popular because of their ability to account for wide PL distributions, such as those observed in solar flares energies and peak fluxes, which are observed over several decades (Fig. 39). Their use is now not limited to solar flares but is extended to a wide range of astrophysical systems (see Aschwanden et al. 2016 for a review).

2.2.1 *Self-organised criticality in solar flares*

Solar flares are very energetic phenomena happening in active regions of the Sun, characterised by an intense magnetic activity (see Fletcher et al. 2011 for a review). They release up to 10^{32} erg in a few minutes. Magnetic energy is dissipated via magnetic reconnection events

---

[4] Another important property of systems governed by SOC is the presence of *fractal geometry* (also linked to the notion of self-similarity and PL distributed quantities), characterised by structures repeating at arbitrary small scales.

[5] The indices of the waiting time and duration distributions, when there is no pile-up, are usually thought to be equal: $\alpha_{wt} = \alpha_T$.

into heating of thermal plasma and acceleration of particles. These accelerated particles radiate across the entire electromagnetic spectrum, from radio to gamma-rays. This high-energy emission was tracked during the period 1980-1989 by the *Solar Maximum Mission*, which detected solar flares in hard X and γ rays (Bohlin et al., 1980). The distribution of peak rates at these energies exhibits a perfect PL behaviour over four orders of magnitude (e.g. Crosby, Aschwanden, and Dennis 1993; Dennis 1985).

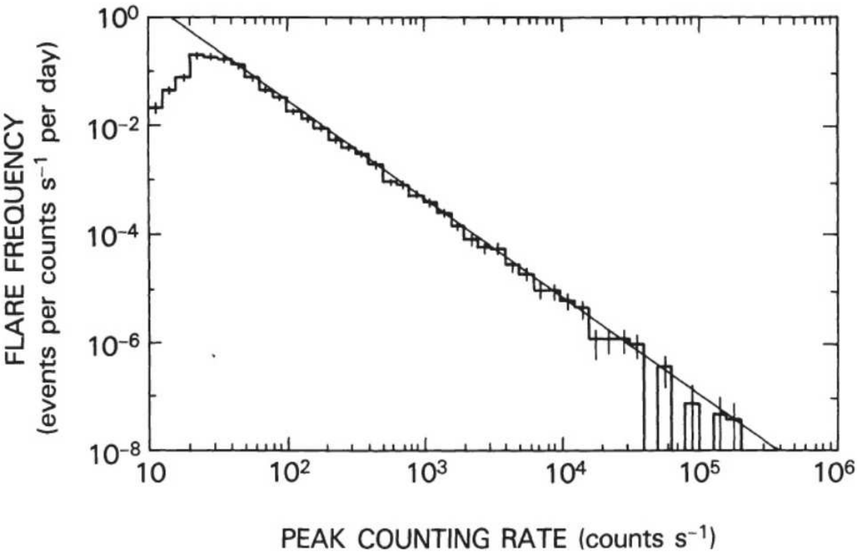

Figure 39: Peak count rate occurrence frequency distribution obtained over 6,000 hard X-ray flares with photon energies above 25 keV, recorded with the Hard X-Ray Burst Spectrometer (Orwig, Frost, and Dennis, 1980) onboard NASA's Solar Maximum Mission during 1980–1989. The distribution follows a PL with a slope of $\alpha \sim 1.8$ over 4 orders of magnitude. From Dennis (1985).

Flares of smaller sizes, so-called microflares (e.g. Christe et al. 2008; Lin, Feffer, and Schwartz 2001) and nanoflares (e.g. Aschwanden and Parnell 2002; Krucker and Benz 1998) , were detected afterwards at lower energies, in soft X-rays (SXRs) and extreme (EUVs), respectively. These detections extended the observed PL behaviour, which cover eight decades. Very recent results from Aschwanden and Schrijver (2025) show that stellar superflares from G-type stars can even further extend the PL behaviour up to 13 decades.

The omnipresence of PL distributions observed in several solar flares properties again led solar physicists to consider the SOC framework as a plausible explanation for solar flares (see Charbonneau et al. 2001 for a review).

Within this picture, the coronal magnetic field enters a SOC state. The photospheric convective motions disrupt the orientation of the coronal magnetic field lines, playing a role analogous to the random addition of sand grains in the SOC sand-pile model. According to Parker (1988), magnetic reconnection occurs when the angle between misaligned magnetic field lines reaches a critical value, in a similar way to avalanches that occur when the sand pile reaches a critical slope. Solar flares, equivalent to sand avalanches, are thus interpreted in this framework as the result of numerous small-scale reconnection events taking place within the highly stressed coronal magnetic field.

Lu and Hamilton (1991) proposed a cellular automata numerical model to reproduce the observed properties of solar flares. In this model, where a 3-D grid represents the solar corona, characterised by a magnetic field strength $\mathbf{B}_{ijk}$ in each volume element characterised by the coordinates i, j, k with a local magnetic field gradient $\boldsymbol{\delta}\mathbf{B}$ defined by the difference between the local magnetic field and the average of its six nearest neighbours $\mathbf{B}_{nn}$:

$$\boldsymbol{\Delta}\mathbf{B} = \mathbf{B}_{ijk} - \frac{1}{6}\sum_{nn}\mathbf{B}_{nn}. \tag{42}$$

A small magnetic field $\boldsymbol{\delta}\mathbf{B}$ is progressively added at random positions of the grid. The magnetic field becomes locally unstable to magnetic reconnection when the difference with its neighbour exceeds a critical threshold, $|\boldsymbol{\delta}\mathbf{B}| > B_c$, similar to the magnetic discontinuity angle suggested by Parker (1988). When the threshold is reached, the magnetic field is redistributed according to Eqs. (43) and (44):

$$\mathbf{B}'_{ijk} \to \mathbf{B}_{ijk} - \frac{1}{7}\boldsymbol{\Delta}\mathbf{B}, \tag{43}$$

$$\mathbf{B}'_{nn} \to \mathbf{B}_{nn} + \frac{1}{7}\boldsymbol{\Delta}\mathbf{B}, \tag{44}$$

so that the average gradient vanishes, $\boldsymbol{\delta}\mathbf{B} \to 0$. The redistribution of magnetic field can trigger other cells to become unstable, creating an avalanche of reconnection events. Each reconnection event dissipates the magnetic energy quantity given by Eq. (45)

$$\Delta E = \mathbf{B}'^2_{ijk} + \sum_{nn}\mathbf{B}'^2_{nn} - \left(\mathbf{B}^2_{ijk} + \sum_{nn}\mathbf{B}^2_{nn}\right) = \frac{6}{7}\boldsymbol{\Delta}\mathbf{B}^2. \tag{45}$$

The released energy E and peak fluxes P are PL distributed, according to $N(E) \propto E^{-1.4}$ and $N(P) \propto P^{-1.8}$, which is in agreement with the observed distribution of hard X-ray flares $N(P) \propto P^{-1.67\pm0.04}$ and $N(E) \propto P^{-1.53}$ (Crosby, Aschwanden, and Dennis, 1993; Dennis, 1985).

2.2.2 *SOC in BH accretion-disc systems*

Another class of astrophysical systems where evidence for SOC has been reported are accretion-driven sources, including AGN discs (Kunjaya et al., 2011; Lawrence and Papadakis, 1993; Leighly et al., 1997; Uttley and McHardy, 2005), X-ray binaries (Kennedy et al., 2018; Wang et al., 2017; Zhang et al., 2022b), and blazars (Ciprini et al., 2003; Li et al., 2015; Wang et al., 2015; Yuan et al., 2018). For instance, the X-ray emission of Sgr A* shows two distinct components: a steady quiescent state and a flaring activity whose fluence distribution follows a PL with index $dN/dF \propto F^{-1.65\pm0.17}$ (Li et al., 2015). In high-mass XRBs, the duration, waiting time, peak luminosity, isotropic energy, and mean luminosity of X-ray flares are also distributed as PLs with indices in the range 1.0–1.9 (Zhang et al., 2022b). Finally, in blazars, the optical variability of GC 0109+224 exhibits a PL power density spectrum $P(f) \propto f^{-\alpha}$, with $1.57 < \alpha < 2.05$, and the peak fluxes follow a PL distribution $N(P) \propto P^{-1.55}$ (Ciprini et al., 2003).

On a theoretical level, Mineshige, Ouchi, and Nishimori (1994) conceived a cellular-automaton model similar to the original BTW sandpile model, applied to the geometry of a BH-accretion disc system (Fig. 40). In this model, gas particles are randomly injected into the inner portions of the disc surrounding the BH. When mass density locally exceeds a critical value, matter is forced to drift inwards to adjacent cells via some instability, which can also occur by gradual diffusion. The gravitational energy lost by the inwards-drifting particles is released as X-ray luminosity[6]. After many iterations, the system evolves into a SOC state where each cell mass lies just below the critical mass, i.e. on the edge of instability. PL distributions of energy $D(\epsilon) \propto \epsilon^{-2.8}$ and duration $D(\tau) \propto \tau^{-1.4}$ are recovered, as well as a $1/f^{\beta}$ power density spectrum, capturing the principal SOC properties.

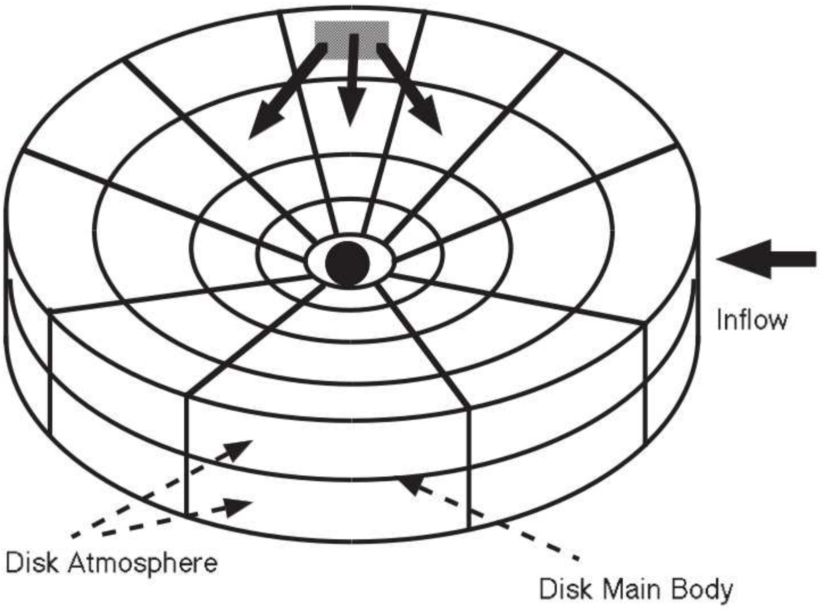

Figure 40: Mineshige's SOC model of BH-accretion disc system. Particles drift inwards to adjacent cells whenever the cell mass exceeds a critical mass. The difference of gravitational energy induced by the drift is released into X-ray radiation. From Aschwanden (2013).

2.2.3 *Self-organised criticality in gamma-ray bursts*

Evidence for a SOC behaviour has been claimed in GRB X-ray flares observed during GRB afterglow by Wang and Dai (2013). They used 83 X-ray flares observed by the *Swift* satellite, after 8 years of observations (Sect. 1.1.4), and measured their released energy, duration, and waiting time distributions. The PL indices of the X-ray flare duration and of the released energy distributions were compatible with the fractal-diffusive SOC model described in Sect. 2.1.4, provided that $d = 1$, whereas it is $d = 3$ for solar flares (Fig. 41). SOC and GRB X-ray flares were further investigated by Wei (2023), who also analysed the return distributions and modelled them with a q-Gaussian function. While SOC provides one possible explanation for the PL distributions observed in X-ray flares, these features can also be well reproduced by a

---

[6] The X-ray luminosity L_X resulting from such a mass transfer event is assumed to be approximately proportional to the change in gravitational energy ΔE_{grav}.

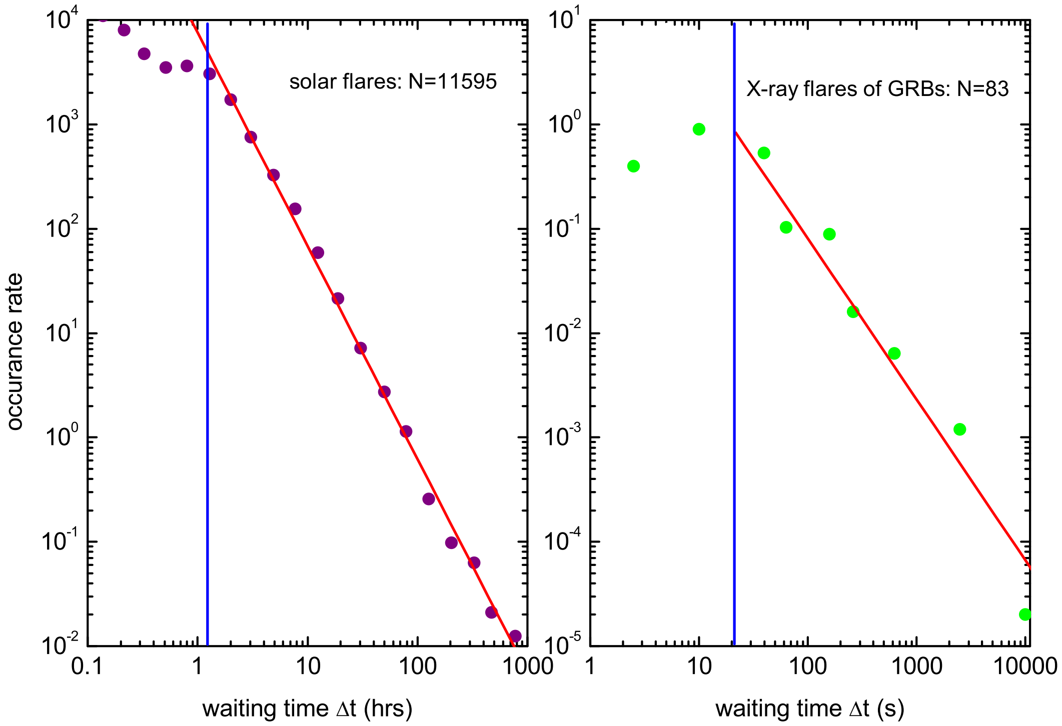

Figure 41: *Left panel:* waiting times frequency distributions for the 11,595 solar flares observed by the solar mission RHESSI (Lin et al., 2002) between 2002 and 2007. The best-fit PL index is -2.00 ± 0.05. *Right panel:* Same but for 83 GRB X-ray flares. The best-fit PL index is -1.10 ± 0.15. From Wang and Dai (2013)

variable Poisson process, in particular the waiting times distribution (Guidorzi et al., 2015). Evidence of SOC behaviour in GRB prompt emission was also investigated (Li and Yang, 2023; Li et al., 2023; Lyu et al., 2020), with similar conclusions. Lyu et al. (2020) used 454 pulses from 93 GRBs observed by *CGRO*/BATSE and measured their released energy, peak flux and duration distributions. They obtained that these distributions were compatible with SOC provided that $d = 3$, which contrasts with the results obtained for GRB X-ray flares. Li and Yang (2023) used a sample of GRB precursors from the third Swift/BAT catalogue (Li and Mao, 2022) and computed the distribution of peak flux and duration, and found a compatibility with a SOC model provided that $d = 3$. Li et al. (2023) analysed a sample of short GRBs from CGRO/BATSE, studying the peak flux and pulse FWHM distribution, finding a compatibility with SOC model, with $d = 3$ and $\beta = 1$.

Recently, the SOC hypothesis was investigated within two single exceptional GRBs, with GRB 221009A at Tev energy (Zhang et al., 2025b), and GRB 230307A (Zhang et al., submitted).

Cellular-automata simulation models as those performed for solar flares and BH accretion disc systems are still lacking in the GRB case. One interesting attempt was made by Dănilă, Harko, and Mocanu (2015), that implemented the magnetic induction equation in two dimension in the MHD approximation framework. They showed that two-dimensional magnetized plasma with a background flow system exhibits a SOC behaviour. This model was applied and compared to real GRB LCs. Overall, despite the absence of a SOC model expressly conceived for GRB engines, which would require some *ad hoc* relativistic MHD simulations, one may note that the SOC mechanism could be compatible with the turbulent avalanche-like reconnection events triggering GRB emission in the ICMART (Sect. 1.5.4) model of Zhang and Yan (2011).

2.2.4 *Our work: Distributions of energy, luminosity, duration, and waiting times of gamma-ray burst pulses with known redshift detected by Fermi/GBM*

Our work aimed to investigate the presence of SOC in the GRB prompt emission, computing the energy, peak luminosity, waiting times, and duration distributions of the individual pulses building up the GRB LC and modelling them with PL or broken PL functions.

In this work, we used a sample of 142 type-II GRBs with spectroscopically known redshift that were carefully selected by sifting through the GCN notices and dedicated studies, when available. Relying solely on robust spectroscopic redshift measurements was fundamental since photometric ones are more uncertain and can lead to widely incorrect estimates of the energetics of the burst. We then identified, using a dedicated peak-detection algorithm (MEPSA, Guidorzi 2015), the individual pulses building each GRB time profile and measured the energy and luminosity contained in each individual pulses, as well as their durations and temporal separations (waiting times). Each pulse was then modelled by the pulse template described in Norris et al. (1996). The peak luminosity and isotropic-energy were computed by converting the peak rates (resp. peak total counts, integrated over the pulse duration) of each pulse into a peak flux in erg cm^{-2} s^{-1} (resp. fluence in erg cm^{-2}), using a conversion factor obtained by computing the ratio between the GRB fluence and the corresponding counts.

Selection effects, also referred to as the Malmquist bias, tend to produce an overabundance of bright events (since they can be observed at larger distances) and a scarcity of faint events. In principle, unaccounted-for selection effects could bias this kind of analysis, as the observed low-energy tail is affected by the instrument sensitivity, thus creating an artificial rollover. To properly account for these effects, a non-trivial simulation of the detection process was required. In particular, one needs to compute the detection efficiency as a function of energy $\eta(E)$, which requires to divide the GRB sample in bins of redshift, to account for the different detection efficiency $\eta_z(E)$ in each redshift bin[7] (Fig. 42). Such careful study of the selection effects in this kind of analysis was performed for the first time in our work, Maccary et al. (2024b).

After having accounted for the selection effects, we were able to perform a fit of the observed distributions. To this end, we simulated PL and BPL distributions, and we simulated the selection effects, applying the method described above, and performed a χ^2 fit. We showed that, even after accounting for the selection effects, a BPL is required to correctly fit the observed data. The PL indices of the four distributions[8] studied in our work (E_{iso}, L_{iso}, duration, and WTs) are given by:

---

[7] For instance, a pulse with energy 10^{51} erg at a redshift $z = 0.1$ has a fluence of 4×10^{-5} erg cm^{-2} which is significantly larger than the instrumental limit, while the same pulse at $z = 1$ has a fluence of 4×10^{-7} erg cm^{-2}, very close to the instrumental limit (a few 10^{-7} erg cm^{-2}). Faint pulses with this energy are therefore not observed at larger distances, inducing an observational bias.

[8] Since we used a BPL model, these indices are actually given by the post-break PL index of the BPL distribution.

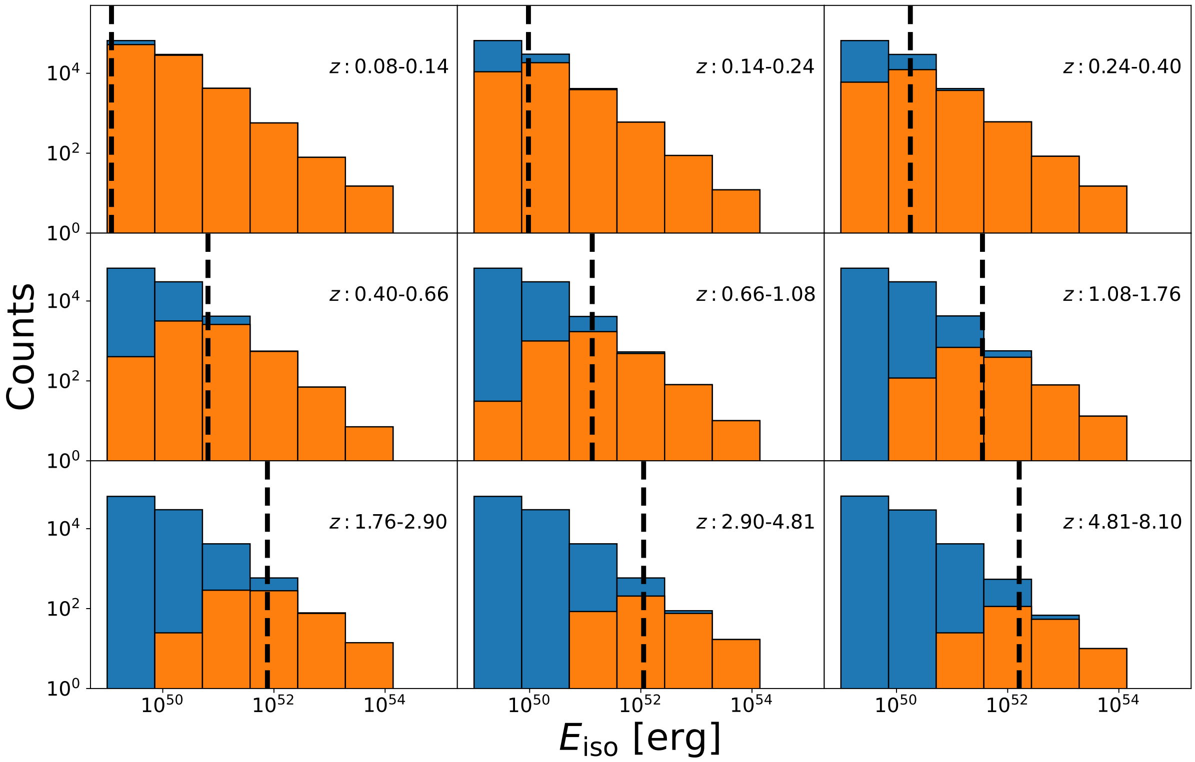

Figure 42: Simulated distributions of $E_{\rm iso}$, depending on whether selection effects due to detection efficiency are considered (orange) or not (blue). The nine panels refer to increasing redshift bins (left to right, top to bottom). The blue distribution was drawn assuming $dN/dE_{\rm iso} \propto E_{\rm iso}^{-2}$. Vertical dashed lines mark the 50% detection efficiency: pulses with lower values of $E_{\rm iso}$, highlighted by the gray area, are therefore hampered by a low detection efficiency. For the sake of clarity, 10^5 pulses were simulated in each redshift bin. Reproduced from Maccary et al. (2024b).

$$
\begin{aligned}
\alpha_E &= 1.67^{+0.23}_{-0.16}, \\
\alpha_P &= 1.47^{+0.60}_{-0.18}, \\
\alpha_T &= 2.08^{+0.19}_{-0.16}, \\
\alpha_{wt} &= 2.04^{+0.14}_{-0.12}.
\end{aligned}
$$

The four observed distributions and the corresponding simulated distributions are reported in Fig. 43. The conclusions of our work are that the PL indices of the four distributions considered are compatible with the predictions of SOC theory (given by Eqs. 39, 40, 41, Fig. 44) for $d = 3$, although we noted the presence of an energy/luminosity break that could not be entirely accounted by the selection effects. This work, published in the Astrophysical journal, is reported in Appendix A.7 of this thesis.

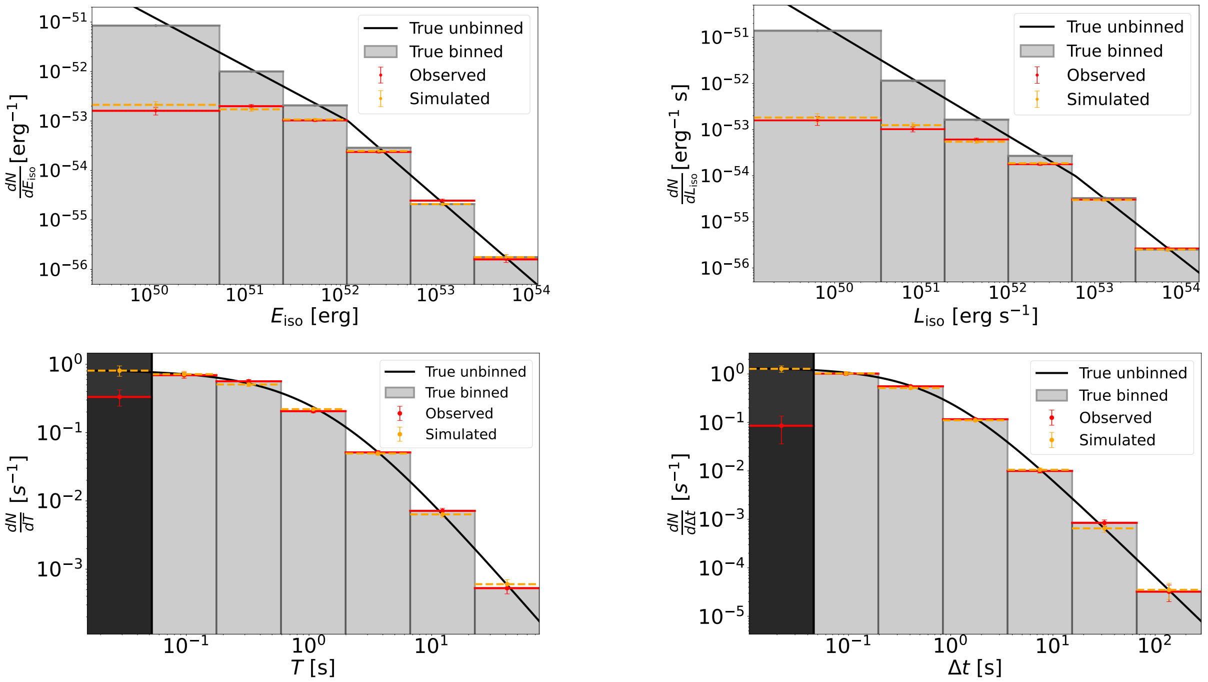

Figure 43: *From top to bottom, left to right.* E_{iso}, L_{iso}, duration, and waiting times distribution of individual pulses observed during prompt emission. The black line and the grey histograms represent the density function and predicted counts obtained by sampling a BPL probability density function. Red and orange points represent the observed and simulated (after having accounted for the selection effects through the process described in Fig. 42) counts. Adapted from Maccary et al. (2024b).

2.2.5 *Discussion of the compatibility of SOC with GRBs*

Magnetic reconnection events, triggered by some kind of magnetic instabilities, are often invoked to explain the PL character of GRB energy and waiting time distributions, similarly to what is seen in solar flares. While the dynamics could indeed share some similarities with the GRB case, the latter case is much more complex, being the result of an irreversible evolution: the progenitor is destroyed and the energy supply is rapidly exhausted. The question of whether SOC could manifest as well in such transient systems marked by an irreversible evolution remains still open.

Furthermore, SOC suffers from some controversies (see Watkins et al. 2016 for a review). In fact, while it is generally true that a system governed by SOC is marked by the appearance of PLs, observing PL distributed variables in a physical system is not a sufficient condition to prove that a system is governed by SOC, as other mechanisms could also lead to PL distributions, such as the case of waiting time distribution for a time-varying Poisson process (Guidorzi et al., 2015).

2.3 CONCLUSIONS

In our work, we tested the possibility that GRBs could be compatible with SOC dynamics. We proved that this is a plausible hypothesis, although we do not exclude alternative scenarios

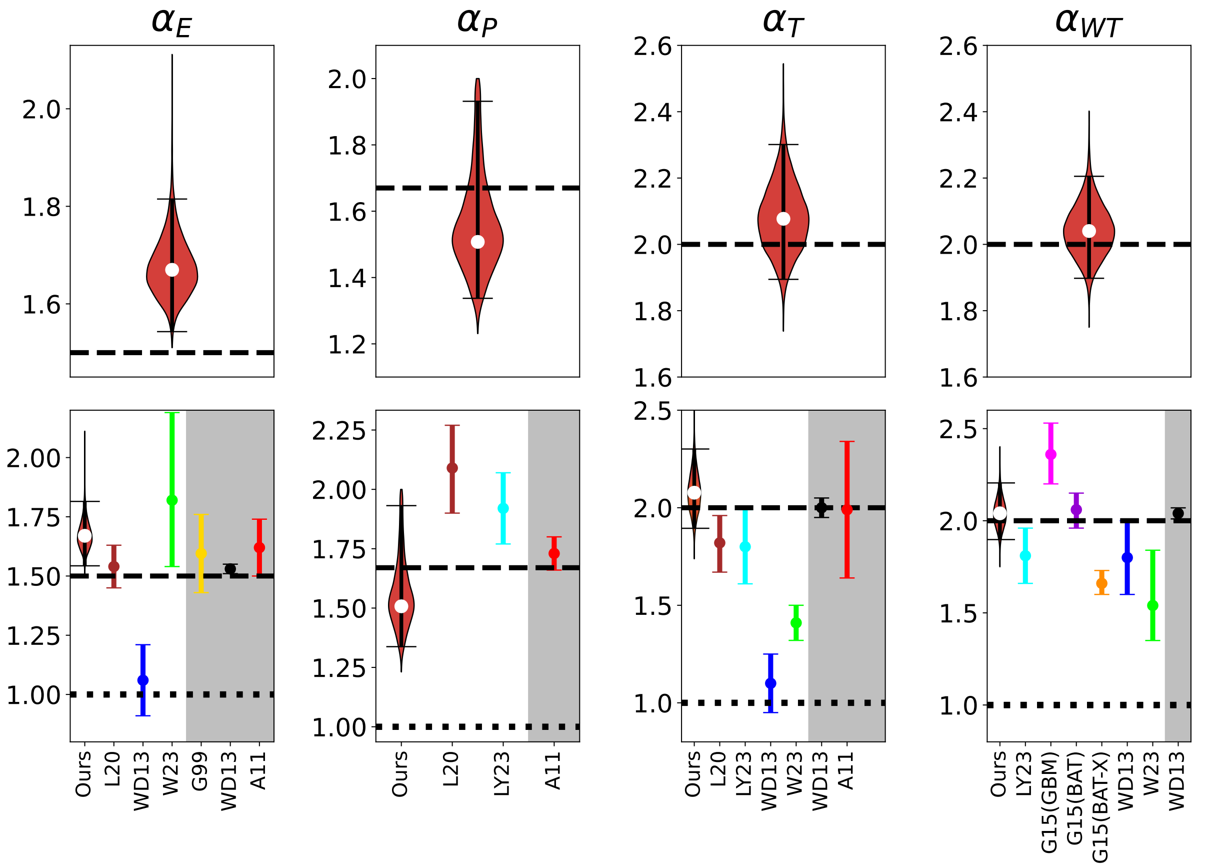

Figure 44: *Top panels*: violin plots showing the PL indices of energy, peak luminosity, duration, and waiting times distributions obtained in our work. *Bottom panels*: our results are compared with past studies from L20 (brown, Lyu et al. 2020), LY23 (cyan, Li et al. 2023), WD13 (blue, Wang and Dai 2013), W23 (green, Wei 2023), G15 (pink for GBM data, purple for BAT data, and orange for BAT-X data, Guidorzi et al. 2015), G99 (soft gamma-ray repeater from a magnetar, yellow, Göğüş et al. 1999), WD13 (solar flares, black, Wang and Dai 2013), A11 (solar flares, red, Aschwanden 2011). SOC predictions for $d = 3$ and $d = 1$ (Sect. 2.1.4) are shown with dashed and dotted lines, respectively. The grey region marks the boundary between GRB and non-GRB phenomena (soft gamma-ray repeaters, solar flares). From Maccary et al. (2024b).

that could account for the PL distributed properties observed in GRB prompt emission. If GRBs were indeed governed by SOC, this would constrain the physical mechanisms involved in the prompt emission and the way the central engine releases its energy over time. In particular, it would imply that the system powering the GRB emission operates close to a critical regime, which is an important constraint that theoretical models of GRB prompt emission must take into account in their formulation. The presence of SOC in GRBs would indeed provide a very precise picture of how the system releases its energy: that is, reaching *spontaneously* (this being precisely the meaning of "self" in self-organised criticality) a critical point. This represents a major constraint on the nature of the central engine capable of powering GRBs, as well as on the origin of the underlying instability, whether hydrodynamic, magnetic, or related to the accretion disc dynamics. Further progress on this hypothesis would require more detailed simulations, including full general-relativistic magnetohydrodynamic treatments. Nevertheless, this work laid the groundwork for such investigations by providing, for the first time, an analysis based on a GRB sample with reliable redshift measurements, analysing directly the intrinsic quantities (energy, luminosity, instead of simply fluence or peak flux), with a detailed and accurate treatment of the selection effects. This study led to the publication of an article published in the Astrophysical journal, which is reported in Appendix A.7 of this thesis.

3

A COMPREHENSIVE VIEW OF THE PROMPT EMISSION THROUGH TEMPORAL VARIABILITY

The prompt emission, from a time-series point of view, is highly complex and remarkably diverse. In particular, GRB LCs display a wide range of different timescales, each potentially revealing different aspects of the GRB phenomenon, from the activity of their central engines to the nature of their progenitors.

The most notable timescale is the duration of the burst, which was originally used to distinguish between two kinds of GRB progenitors, although several exceptions have shown the limitations of this classification. In many cases, the burst duration is not the only observable timescale. Indeed, GRB temporal profiles can feature multiple episodes of variability, possibly governed by distinct timescales, often without any apparent regularity. These episodes could either track directly the variability of the central engine in some models, or be influenced by other factors such as the interaction between the jet and the stellar environment, or the geometry and the jet structure, or be governed by local properties within the emission region.

Moving to the shortest timescales, very brief variability episodes lasting only a few milliseconds are sometimes observed. In this respect, the minimum variability timescale (MVT) represents a useful indicator of the nature of their progenitors. Extremely small MVT values, of the order of a few tens of milliseconds, are mostly associated with events produced by COMs rather than collapsars, even when their overall duration deceptively exceeds the conventional 2 s threshold.

Ultimately, the apparent absence of any deterministic evolution in the timescales governing the variability episodes has long been considered a pillar of current GRB emission models, such as the internal shocks scenario. If such an evolution were observed, its implications for the emission mechanisms would have to be considered, potentially opening the way to alternative scenarios.

3.1 TWO TEMPORAL VARIABILITY COMPONENTS OF GRB LIGHT CURVES

Two variability components have been identified in GRB time profiles. We investigate here how these components were identified and what they may reveal about the GRB central engine and the interaction between the jet and its stellar environment.

3.1.1 *Evidence for two variability components in GRB light curves*

During the era of GRBs observed by the WFCs onboard BeppoSAX (Sect. 1.1.3), two components, referred to as slow and fast, with different variability timescales were identified (Vetere et al., 2006). Some time profiles displayed narrow peaks superposed on a slowly evolving pedestal, and the slower components were generally found to be spectrally softer than the fast ones (Fig. 45).

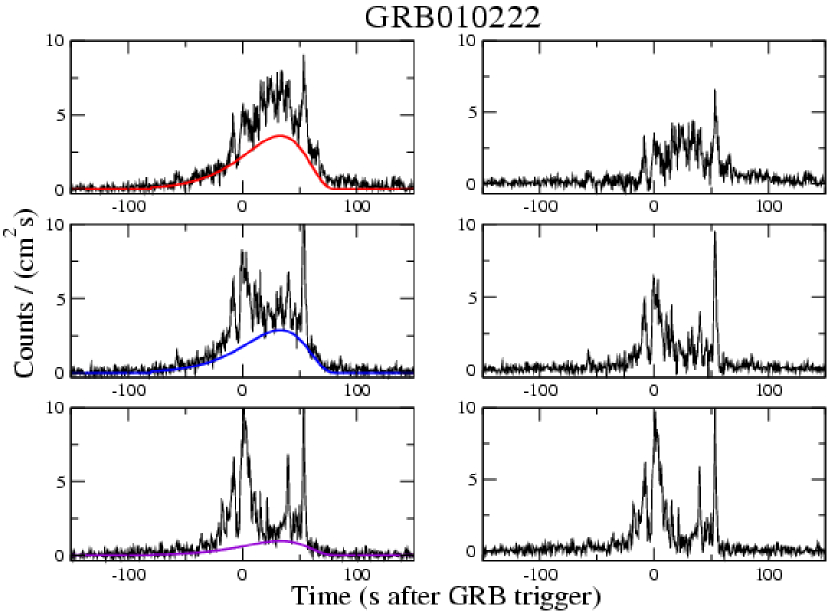

Figure 45: X-ray LCs of GRB 010222, as observed by the BeppoSAX/WFCs in three different energy ranges (2-5, 5-10, and 10-26 keV). The panels on the left show the total counts and the identified slow component. The panels on the right show the corresponding fast components, obtained by subtracting the slow component template. From Vetere et al. (2006).

The drawback of the technique employed in this study was the difficulty of separating the slow and fast components unambiguously. A bi-modality in the width of the autocorrelation function was also observed in WFC bursts (Borgonovo et al., 2007), with GRBs showing narrow and broad widths (Fig. 46).

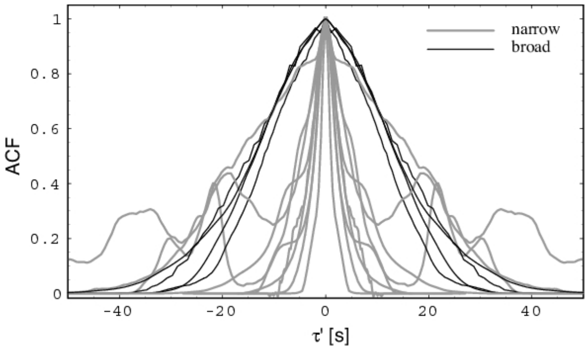

Figure 46: Autocorrelation functions calculated in the source rest-frame for a sample of 13 GRBs detected by the WFCs in the 2-28 keV energy band, as a function of the time lag corrected for cosmic dilation. The "narrow" and "broad" classes are shown in grey and black, respectively. From Borgonovo et al. (2007).

Other methods to study the slow and fast components were used, such as the so-called stepwise filter correlation method (Gao, Zhang, and Zhang, 2012). This method is based on the use of a low-frequency filter, in particular the Butterworth filter. This method consist in applying the filter, using a wide range of cut-off frequencies between f_{min} and f_{max}, to remove high-frequency fluctuations, generating a sequence of residual LCs (RLC). For each pair of successive filtered signals (RLC_i, RLC_{i+1}), the Pearson correlation coefficient between the two LCs is computed. For a given cut-off frequency, if no temporal power is present at this frequency, the Pearson correlation coefficient obtained for the couple (RLC_i, RLC_{i+1}) is high, whereas a significant drop in correlation (a "dip") indicates that a notable portion of the variability has been filtered out around that frequency. Plotting the correlation coefficient versus cut-off frequency therefore reveals characteristic timescales in the signal, allowing one to distinguish slow from fast components.

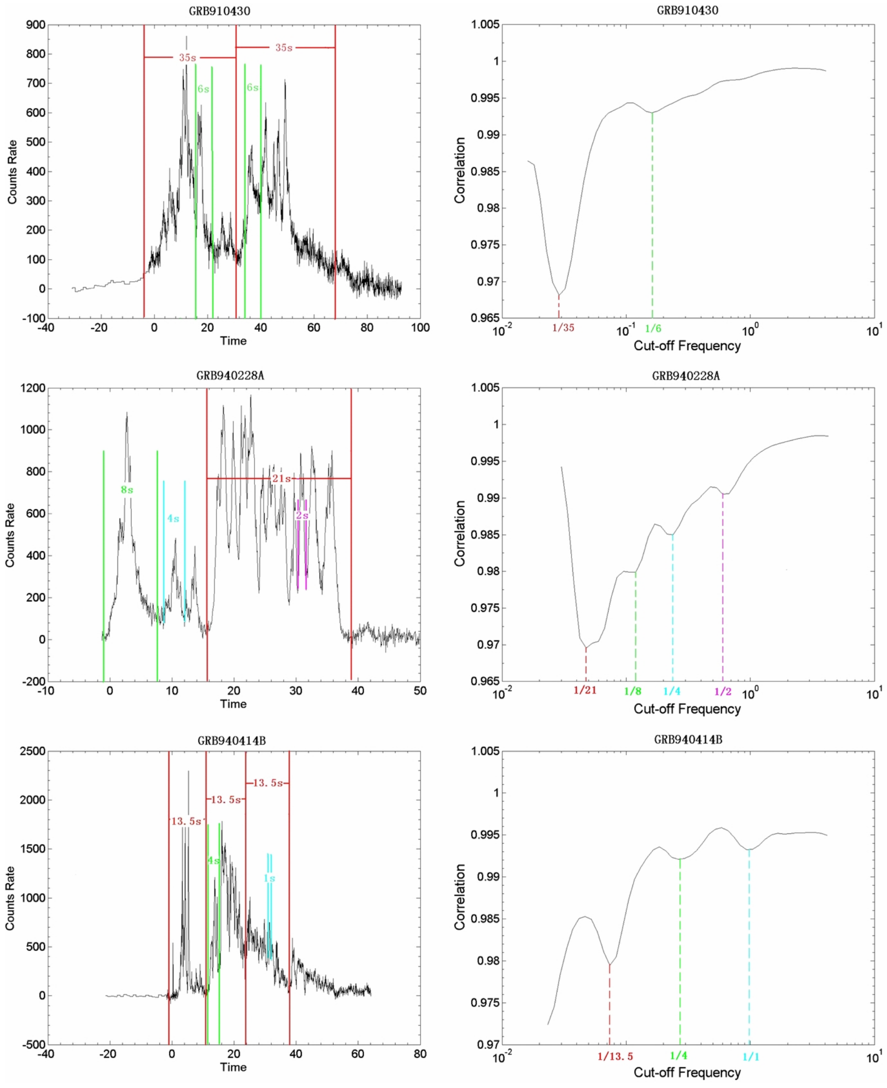

Figure 47: *Left panels*: BATSE LCs of GRB 910430, GRB 940228A, and GRB 940414B. *Right panels*: Pearson correlation coefficients between pairs of filtered LCs as a function of the cut-off frequency. A temporal structure of timescale Δt in the LC corresponds to a dip in the correlation curve at frequency $\frac{1}{\Delta t}$. From Gao, Zhang, and Zhang (2012).

The presence of two variability components in GRB prompt emission can also be studied in Fourier space, using the PDS, as described in Sect. 1.8.3. In particular, the PDS slope is connected to the relative strength of the fast component ($\tau < 1$ s) in the GRB time profile: when the fast component is dominant, the PDS is shallow ($\alpha < 2$) and does not show any break. On contrary, when the fast component either weak or missing, the PDS is steep ($\alpha > 2$), with or without a break in the range $0.01 - 1$ Hz (Fig. 48). Moreover, when a PL break is found in the PDS, the frequency break f_b is associated with a dominant timescale $\tau = \frac{1}{2\pi f_b}$, which defines the typical timescale observed in the LC.

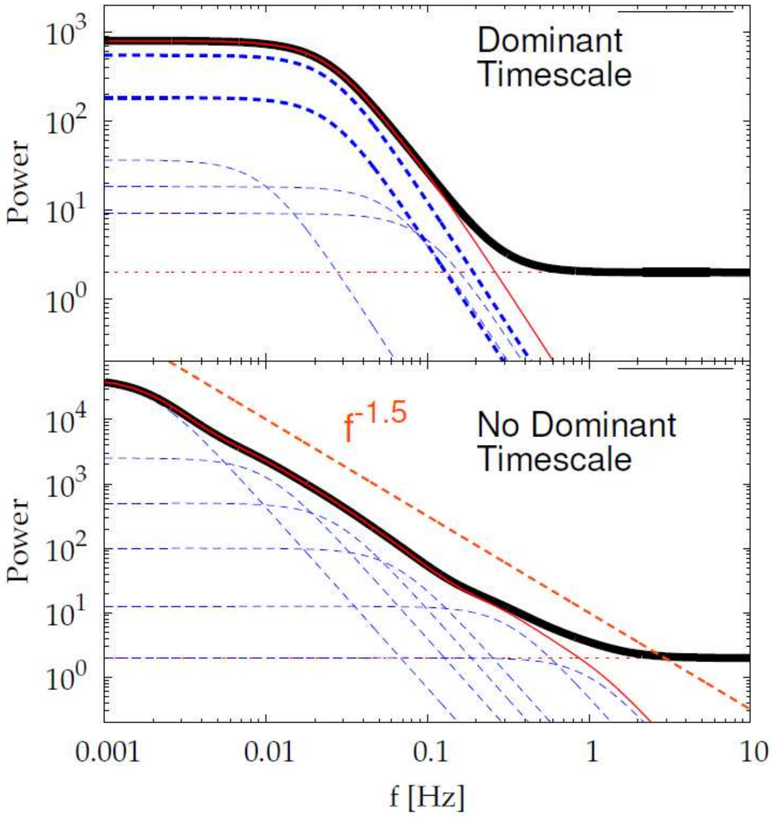

Figure 48: Typical PDS shape observed in GRBs. The top panel represents a steep PDS with a low-frequency break, characteristic of a dominant timescale. This kind of PDS is typically associated with GRBs without a fast variability component. In the bottom panel is shown a shallower PDS, without low frequency break, typical of GRBs exhibiting power on short timescales. From Dichiara et al. (2016).

In the following sections (Sect. 3.1.2 and Sect. 3.1.3), we will show that the presence of two variability components can be probed through the statistics of the number of peaks.

3.1.2 *Quantifying variability with the* MEPSA *algorithm*

MEPSA (Multiple Excess Pattern Search Algorithm; Guidorzi 2015) is an algorithm designed to detect peaks within a time series that is affected by uncorrelated Gaussian noise. This is typically the case of GRB LCs from *Swift*/BAT or *Fermi*/GBM[1]. The algorithm operates by scanning the LC at different time resolutions and applying a set of 39 patterns to each time bin. If a bin satisfies the criteria of one or more patterns, it is identified as a peak. It provides a set of parameters that characterise the peaks and, consequently, the variability of the LC. These include, for a given peak:

- the peak time t_p, i.e. the time bin at which the peak is detected, with its associated peak rate P_r and corresponding peak rate uncertainty ΔP_r;
- the detection timescale Δt_{det}, defined as the time scale at which the peak is identified, corresponding to an integer multiple of the original bin width, along with its associated rebin factor;
- the number of the pattern that detected the peak;
- the S/N ratio associated with the peak, which also provides its statistical significance;
- The number of adjacent bins N_{adiac} involved in the pattern that detected the peak.

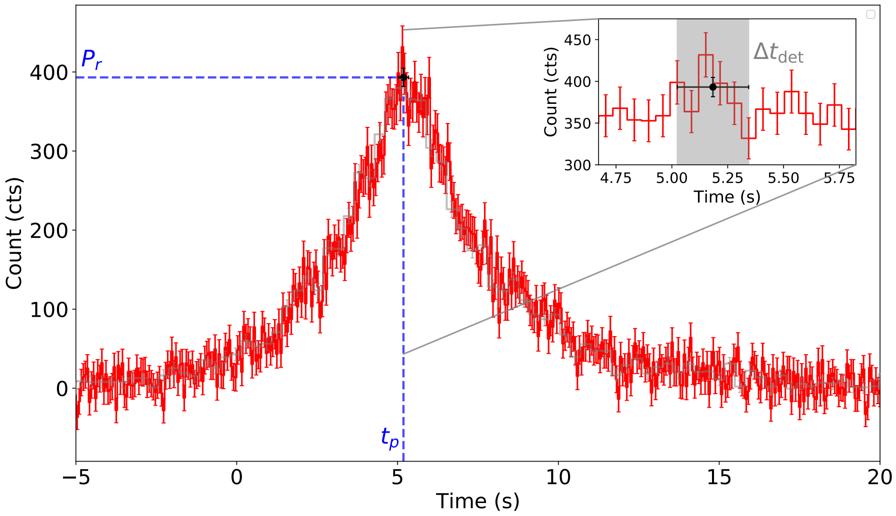

Figure 49: GRB 110117A LC (in red), as observed by *Fermi*/GBM, binned at 64 ms (8-1000 keV). The single peak detected by MEPSA in this case is shown by a black dot with its associated error bar. The peak time t_p and the peak rate R_p are indicated by the vertical and horizontal blue dashed lines, respectively. An inset is made around the peak time to show the detection timescale Δt_{det} (grey shaded region), which is 320 ms in this case (rebin factor of 5). Superimposed to the red 64 ms-LC curve is shown in shaded grey the LC rebinned at the detection timescale. $N_{adiac} = 7$ in this case, which corresponds to the number of bins involved in the pattern used to detect this peak (the 14th in this case). The statistical significance of this peak, given by the S/N, is around 34.

---

[1] In the case of Fermi/GBM, LCs are actually affected by Poisson noise. In the high count regime (count rate $\gg 1$ cts/bin), a Gaussian is a good approximation for the Poisson distribution, therefore MEPSA can be applied. When the count rate is close to $5-20$ cts/bin, MEPSA can still be used, providing that the minimum S/N ratio used to detect peaks is increased. However, in a very low count regime (count rate $\leqslant 1-2$ cts/bin) , MEPSA cannot be used and one must use techniques based on the Poisson statistics (e.g. see Guidorzi et al. 2020 and also Dilillo et al. 2024).

The number of peaks within a GRB also reflects its degree of variability: GRBs with little variability are characterised by only a few episodes of flux variation and thus by a few peaks, whereas highly variable GRBs exhibit numerous peaks in their LC (Fig. 50).

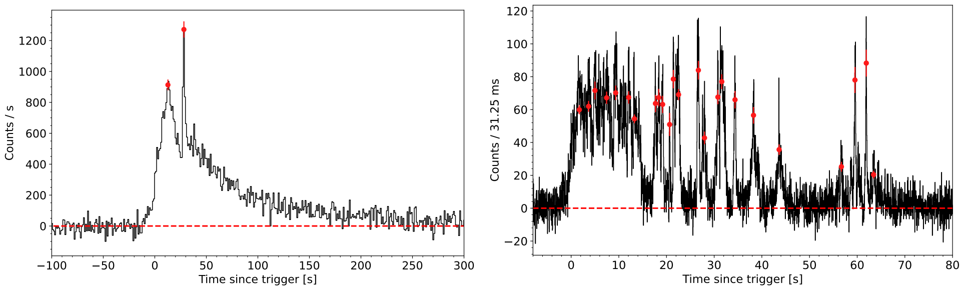

Figure 50: Examples of two GRBs displaying only 2 (left, GRB 981203A) and 24 peaks (right, GRB 010412), respectively, as observed in the 40–700 keV energy range with BeppoSAX/-GRBM. The red points mark the identified peaks, while the dashed lines indicate the interpolated background. Despite their very different temporal structures, these two GRBs have comparable fluence and peak flux. Reprinted from Guidorzi et al. (2024).

Counting the number of peaks within GRB time profiles therefore also provides a way to quantify their temporal variability, as we will see in the next section.

3.1.3 *The distribution of the number of peaks: new evidence for two variability components in GRB light curves*

The distribution of the number of peaks has been studied for the first time by Guidorzi et al. (2024). MEPSA was applied to GRB LCs from CGRO/BATSE, BeppoSAX/GRBM, *Swift*/BAT, and *Insight*-HXMT, and a distribution of the number of peaks within a GRB was built for each of these instruments (Fig. 51).

It was shown that only a mixture of two exponential functions could accurately fit the observed distribution, whereas a single exponential, a single or broken PL, or a stretched exponential provides unsatisfactory fits. The mixture of two exponentials model can be expressed as:

$$f(n) = k(e^{-\frac{n}{n_1}} + \xi e^{-\frac{n}{n_2}}), \tag{46}$$

where k is a normalisation constant, ξ is a relative normalisation parameter, and n_i $(i = 1, 2)$ are the characteristic number of peaks per GRB of the ith component. The expected number of peaks per GRB for the ith component is given by Eq. (47):

$$\langle n^{(i)} \rangle \;=\; \frac{\sum_{n=1}^{+\infty} n e^{-n/n_i}}{\sum_{n=1}^{+\infty} e^{-n/n_i}} \;=\; \frac{1}{1 - e^{-1/n_i}} \tag{47}$$

and the fraction of GRBs belonging to the peak-rich component, w_2, is given by Eq. (48):

$$w_2 = k\xi \sum_{n=1}^{\infty} e^{-\frac{n}{n_2}}. \tag{48}$$

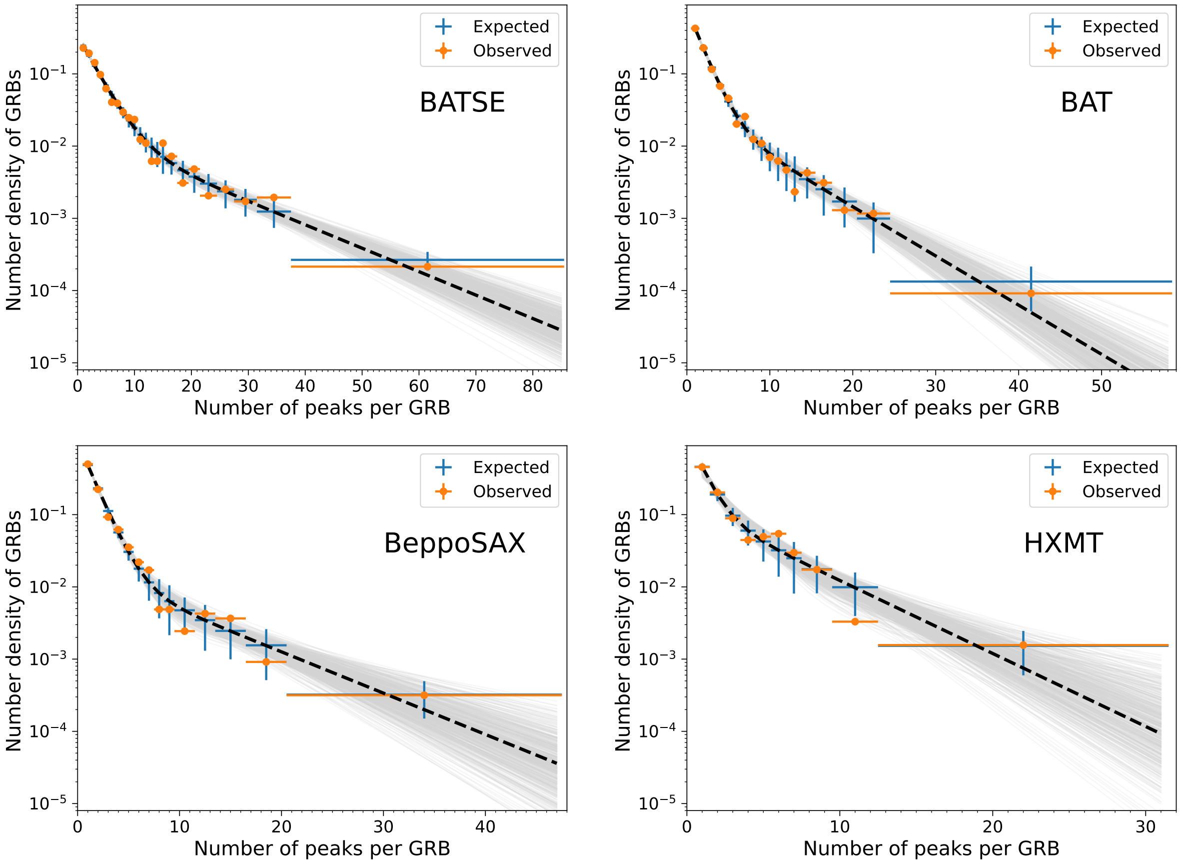

Figure 51: Distributions of number of GRBs per number of peaks for different catalogues: BATSE (top left), *Swift*/BAT (top right), *BeppoSAX*/GRBM, (bottom left), and *Insight*-HXMT (bottom right). Observed data and expected counts are shown in orange and blue, respectively. All histograms have been grouped so as to ensure a minimum number of counts per bin. Dashed lines show the best mixture model of two exponentials that fit each distribution. Grey models are the result of a random sampling of the posterior distribution of the parameters as determined via Markov Chain Monte Carlo. Reprinted from Guidorzi et al. (2024).

Guidorzi et al. (2024) found that w_2 is consistently found around 20%, across the different GRB data sets considered. This result holds despite their different energy passbands and effective areas, highlighting the robustness of the results.

This result implies that most GRBs only have a few peaks in their LC ($\langle n^{(1)} \rangle \simeq 2-3$), while a few GRBs exhibit many peaks ($\langle n^{(2)} \rangle \simeq 8-10$).

The number of peaks per GRB is also related to temporal variability. In fact, GRBs with many peaks tend to have shallower PDS (Guidorzi, Dichiara, and Amati, 2016) and shorter MVTs (Camisasca et al., 2023b). Therefore, the existence of two populations, peak-poor and peak-rich GRBs, can be interpreted as additional evidence for the simultaneous existence of GRBs with or without a fast variability component.

3.1.4 *Our work: Distribution of the number of peaks within a long gamma-ray burst: the full Fermi/GBM catalogue*

We confirmed the results obtained in Guidorzi et al. (2024), extending the analysis to the bursts detected by *Fermi*/GBM, one of the largest GRB catalogues available at the time of writing. In particular, in this study we obtained around 9,000 pulses across over 3,000 GRBs. The followed methodology was identical to that of Guidorzi et al. (2024). The distribution of the number of peaks obtained in this work is reported in Fig. 52.

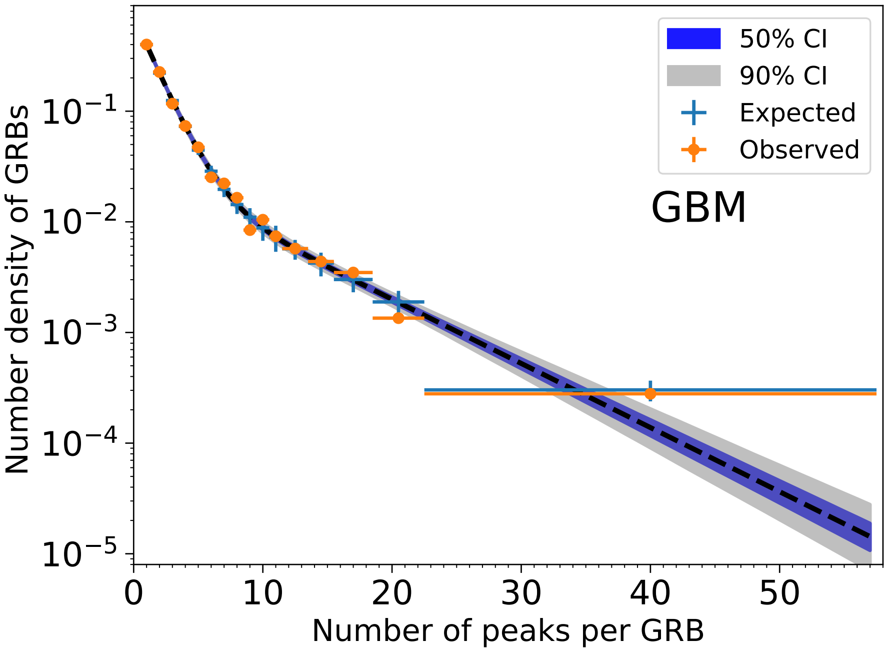

Figure 52: Distribution of the number of peaks per GRB for the *Fermi*/GBM catalogue. The observed and expected counts are displayed in orange and blue, respectively. The histogram bins were grouped to ensure a minimum number of 15 expected counts per bin. The dashed black line shows the best-fitting model of mixture of two exponentials. The blue and grey regions respectively show the 50% and 90% model confidence interval obtained from sampling the posterior distribution of the model parameters computed through Markov chain Monte Carlo simulations. Reproduced from Maccary et al. (2024a).

As for the other datasets, the observed distribution is described correctly only with a mixture of two exponential functions, as given by Eq. (46). The values derived for the parameters $\langle n^{(1,2)} \rangle$ (average number of peaks in the peak-poor and peak-rich families) and w_2 were consistent with those obtained from the other instruments considered in Guidorzi et al. (2024) (Fig. 54):

$$\begin{aligned} \langle n_1 \rangle &= 2.10^{+0.11}_{-0.11}, \\ \langle n_2 \rangle &= 7.61^{+0.97}_{-0.84}, \\ w_2 &= 0.21^{+0.04}_{-0.04}. \end{aligned}$$

This work therefore provides an independent confirmation of the results previously obtained. Given the excellent statistics of *Fermi*/GBM, it was of paramount importance to test this result on this data set. In this work, we also made a direct comparison with the results obtained on *Swift*/BAT, showing a global consistency between the results obtained with the two instruments.

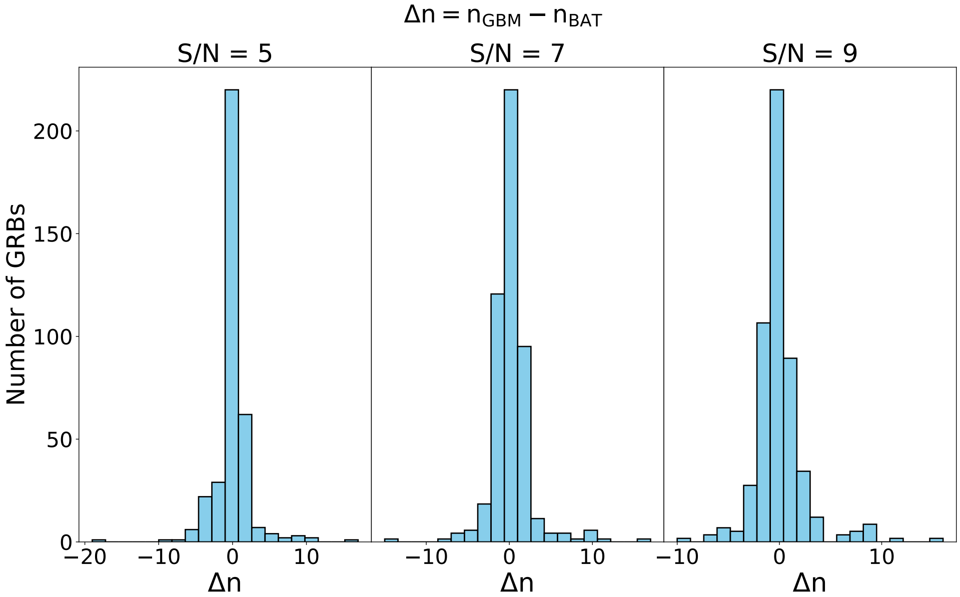

Figure 53: Distribution of $\Delta n = N_{p,GBM} - N_{p,BAT}$ for three different thresholds on S/N: 5, 7, and 9. Reproduced from Maccary et al. (2024a).

This work has therefore further demonstrated the robustness of the result obtained in Guidorzi et al. (2024). This work, published in Astronomy & Astrophysics (Maccary et al., 2024a), is reported in Appendix A.8 of this thesis.

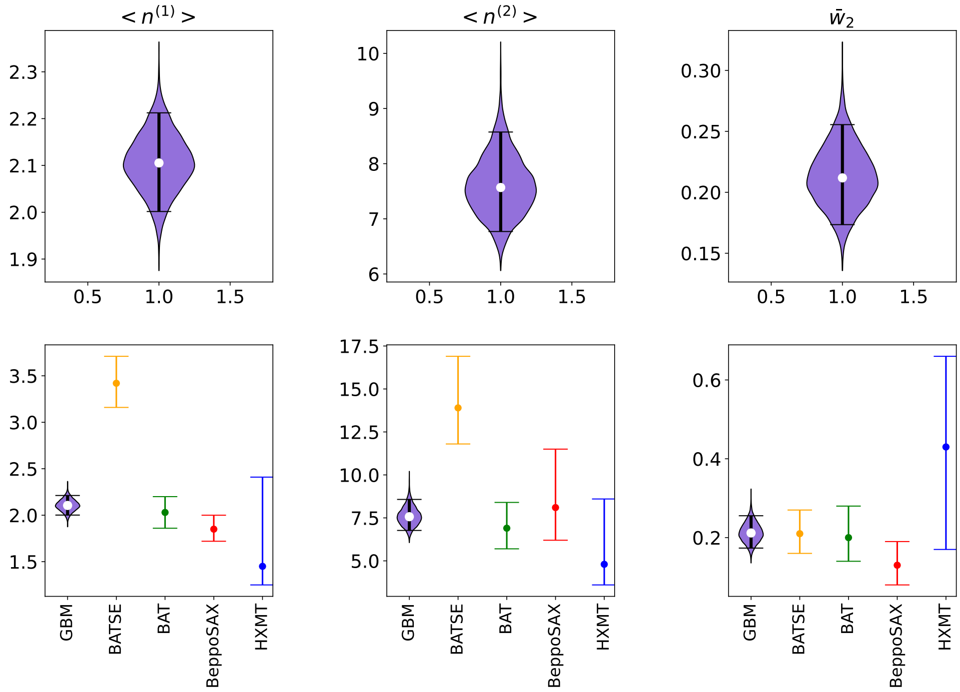

Figure 54: This figure describes our present results compared with those of Guidorzi et al. (2024). *Top panels, left to right:* violin plots of the posterior distributions of the three parameters $\langle n^{(1)} \rangle$, $\langle n^{(2)} \rangle$, and w_2, respectively representing the expected number of peaks per GRB of the peak-poor and the peak-rich classes, and the fraction of peak-rich GRBs obtained for the GBM sample. The horizontal bars span 5–95% quantiles. *Bottom panels, left to right:* comparison between the results obtained for the same parameters in this work, with those obtained by Guidorzi et al. (2024) from other catalogues. Taken from Maccary et al. (2024a).

3.2 THE ORIGIN OF VARIABILITY IN GRBS

The origin of these two variability components remains unclear. It has initially been argued by Vetere et al. (2006) that they could arise from two distinct mechanisms, with the slow variability being the result of photospheric emission while the fast one could be due to non-thermal emission resulting from IS. The variability could reflect the central engine activity, as it is the case in the IS model (Sect. 3.2.1.1). In this respect, the observed timescale could reflect the timescale associated with fluctuations in the accretion disc (Sect. 3.2.1.2) or with the magneto-rotational instability (Sect. 3.2.1.3). The interaction between the jet and the surrounding stellar material can also influence the observed variability, possibly erasing the initial variability imprinted by the central engine, depending also on the composition of the jet, especially its degree of magnetisation (Sect. 3.2.2). The fast component could be governed by local properties of the emission region, especially in models of GRB emission based on magnetic reconnections (Sect. 3.2.3).

3.2.1 *Variability imprinted by the central engine*

The observed variability may be a direct manifestation of the central-engine activity, as assumed in the IS model.

3.2.1.1 *Internal shocks*

In the IS model, the variability observed in the LC is a direct mirror of the activity of the central engine. The number of peaks observed in the LCs corresponds to the number of collisions within the relativistic wind and the time separations between them represent the periods of inactivity of the central engine. The widths of the pulses are governed by three[2] timescales: the cooling timescale, the hydrodynamical timescale and the angular spreading timescale. The cooling timescale is the time it takes for electrons to cool. The hydrodynamical timescale is the time that the reverse shock takes to cross the shocked shell. The angular spreading timescale is given by the light travel time between on and off-axis photons. The hydrodynamical and angular timescales correspond to the rise and decay times of the pulse (e.g., Kobayashi, Piran, and Sari 1997), the decay being typically twice or three times larger than the rise time.

Many uncertainties persist within the IS model, including variability. Bošnjak and Daigne (2014) show that if the parameters governing the microphysics of the shocked region (ϵ_e,ϵ_b, and ζ)[3] are evolving with the shock conditions (in particular if $\zeta(\epsilon_*) \sim \epsilon_*$, with ϵ_* the energy density of the shocked region[4]), then the IS model predictions are more in agreement with the observed temporal properties, such as the pulse width evolution with energy, time lags, and hardness/intensity and hardness/fluence correlations.

However, it remains unclear which IS model parameters rule the amount of temporal power at short timescales. This could depend on different factors, such as the shell widths, the ejection times t_{ej} and the corresponding Lorentz factor values $\Gamma(t_{ej})$. In particular, the contrast in Lorentz factors between the fastest and the slowest shells $\Gamma_{max}/\Gamma_{min}$ could play an important role, influencing in turn the radiative efficiency.

Some studies did investigate these aspects, especially by computing the PDS predicted by the IS model and investigating which parameters can produce the $f^{-5/3}$ feature observed in GRB PDS at the time (Beloborodov, Stern, and Svensson, 2000). Panaitescu, Spada, and Mészáros (1999) also argued that a modulated wind helps to reproduce the PDS shape, while it is not the case for a uniform Lorentz factor distribution. In Spada, Panaitescu, and Mészáros (2000), the wind optical thickness is suggested to be a relevant parameter that is influencing the shape of the PDS. Moreover, a low fraction of accelerated electrons $\zeta < 1$, and a large shell optical thickness to scattering on cold electrons are required to reproduce the observed PDS, while keeping a radiative efficiency of 1%. Despite these attempts, a quantitative agreement between the observed temporal properties and the LCs predicted by the IS model has not yet been achieved. Such agreement could be obtained by applying the techniques employed in Bazzanini et al. (2024) and Maistrello et al. (2025) to optimise the stochastic pulse avalanche model directly to the IS model (Maistrello et al., in preparation).

Rapid variability could result from fluctuations in the outflow velocity (Fig. 21 of Chapter 1). Indeed, the Lorentz factor itself may vary on millisecond timescales, which is plausible if the flow driving the wind is highly irregular and turbulent, since the millisecond corresponds to the typical dynamical timescale of a disc orbiting a stellar-mass BH (Sect. 3.2.1.2). Since in the

---

[2] In practice two because the cooling timescale is usually way smaller than the hydrodynamical timescale.

[3] They are the fraction of the dissipated energy transferred to magnetic field, to electrons (including both thermal and non-thermal electrons), and the fraction of accelerated non-thermal electrons, respectively.

[4] This condition means that the fraction of accelerated electrons increases for stronger, more energetic shocks.

IS model the variability is set by the activity of the central engine, in the next sections we are more directly investigating its physics to understand the origin of the variability.

3.2.1.2 *Variability from fluctuations in the viscous accretion disc*

If the central engine is an hyper-accreting BH, the variability may be driven by fluctuations in the disc, as is the case for BH binaries and active galactic nuclei (Lin et al., 2016). In this scenario, the propagating-fluctuations model links fluctuations of the viscosity parameter at different radii in the disc to variations in the mass accretion rate. These, in turn, are ultimately responsible for the variability of the emission: small viscosity fluctuations produce smooth GRB LCs, whereas large fluctuations generate complex, erratic time profiles, thereby reproducing the full range of observed morphologies (Fig. 55).

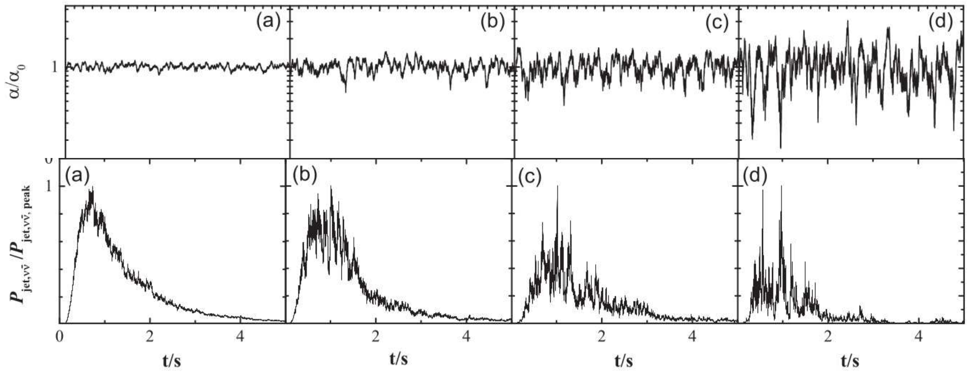

Figure 55: *Top panel:* viscosity parameter fluctuations in the model of propagating fluctuations from Lin et al. (2016). Panels (a), (b), (c), and (d) show increasing amplitudes of fluctuations. *Bottom panel*: LCs of jet power (in the case of $\nu\bar{\nu}$ annihilation) for the corresponding (a), (b), (c), and (d) cases. Small level of viscosity fluctuations lead to smooth time profiles while large fluctuations lead to more erratic and more variable LCs. Adapted from Lin et al. (2016).

3.2.1.3 *Variability and magneto-rotational instability*

While the previous scenario applied for both $\nu\bar{\nu}$ annihilation and BZ effect, Janiuk, James, and Palit (2021) considered a magnetised torus surrounding a spinning BH launching a Poynting-flux dominated jet powered mainly by BZ effect. In this case, the variability is set by the disc's magneto-rotational instability (MRI) timescale. In this framework, the variability and the Lorentz factor of the jet are anti-correlated, this anti-correlation being driven by the BH spin: highly-spinning BHs launch powerful jets with high Γ, related to short MVTs, whereas slowly-spinning BHs lead to powerful jets, with lower Γ, associated with longer MVTs (Fig. 56).

3.2.2 *Jet-stellar material interaction and its impact on variability*

Before dissipating its kinetic energy to γ-rays, the jet launched by the central engine must first cross the dense stellar material (DSM) of the progenitor star and ultimately break out of it. As the jet propagates through the DSM, two shocks propagating in two different directions are formed:

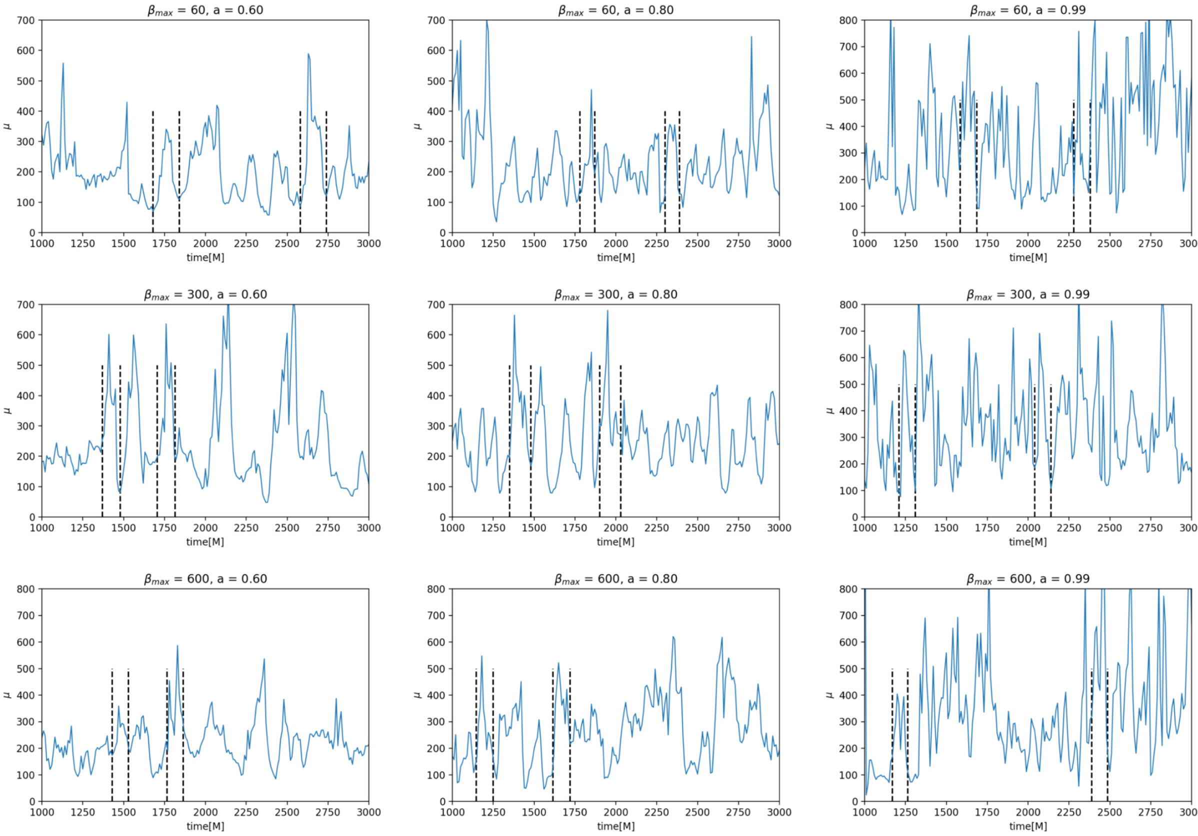

Figure 56: Variability of the jet μ parameter as a function of time, for various models with different ratio of gas to magnetic pressure (decreasing with increasing magnetisation σ) β_{max} (60, 300, and 600, from top to bottom) and three different values of the spin parameter ($a = 0.6$, 0.8, and 0.99, from left to right). The dashed lines represent the characteristic timescale of the MRI. From Janiuk, James, and Palit (2021).

- **a forward shock** propagating into the DSM, and
- **a reverse shock** propagating backward into the jet head.

These shocks inflate a cocoon of shocked stellar and jet material surrounding the jet. The cocoon applies pressure on the jet, favouring its collimation.

At the jet-cocoon boundary, hydrodynamical instabilities, such as the Rayleigh-Taylor instability (RTI)[5], can develop. As the jet propagates into the destroyed star, these instabilities grow, disrupting the jet's initial coherence and mixing its material with the DSM. This leads to the formation of an intermediate layer, called the jet-cocoon interface (JCI)[6]. The mixing between the jet and the DSM increases the jet baryon load and reduces the jet head velocity, thus increasing the breakout time. These effects are significant when a hydrodynamical jet is considered, where much of the energy carried by the jet is transferred to the interface layer with the cocoon.

---

[5] RTI takes place when a lighter fluid accelerates into a heavier one. RTI occurs in this case because of the lateral expansion of the jet into the cocoon.

[6] The JCI formation is associated with the structure of the jet. The jet structure (E_{iso}) is found to be a flat core (jet) + a decreasing power-law function at the JCI ($E_{iso} \propto \theta^{-\delta}$).

In contrast, if the jet is weakly magnetised ($\sigma \ll 1$), the magnetic field developing within the jet can stabilise it against hydrodynamical instabilities, and is not large enough to trigger global magnetic instabilities. In this case, the mixing is therefore greatly reduced, allowing the jet to maintain a coherent structure until breaking out from the star. A visualisation of jet propagation inside the progenitor star, in both hydrodynamical and weakly magnetised cases, can be found at this link: `https://www.oregottlieb.com/instabilities.html`.

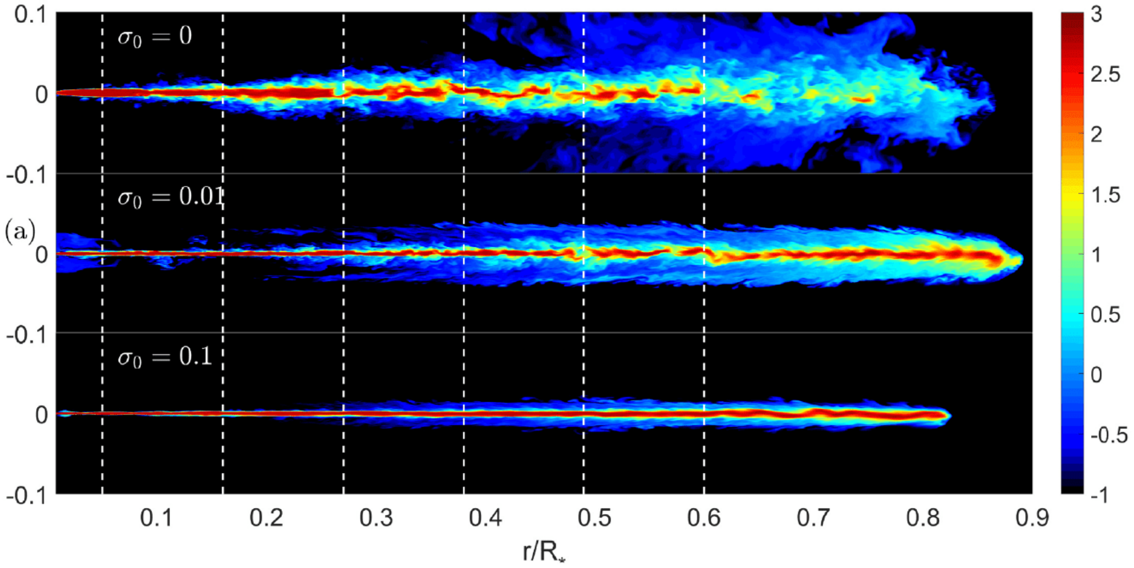

Figure 57: Simulation of the interaction between the jet and the stellar envelope for a jet with increasing degree of magnetisation, from top to bottom panels. In the top, middle and bottom panels are represented a purely hydrodynamical ($\sigma_0 = 0$), a poorly magnetised ($\sigma_0 = 0.01$) and a mildly magnetised ($\sigma_0 = 0.1$) jet, respectively. The x- and y-axis form a plane parallel to the the jet propagation axis, and are given in units of the radius of the exploded star $R_* = 10^{11}$ cm. The colour map represents $\log u_\infty$, where u_∞ stands for the terminal velocity of the jet (a lower u_∞ corresponding to a larger degree of mixing). From Gottlieb et al. (2020).

The interaction between the jet and the DSM also influences the GRB variability. The outcome depends on two main factors: (i) the variability pattern initially seeded by the central engine (continuous vs. intermittent), and (ii) the degree of magnetisation of the jet.

(a) **Continuous, purely hydrodynamical jet** (Gottlieb, Levinson, and Nakar, 2019; Gottlieb, Nakar, and Bromberg, 2021): variability is set by instabilities growing at the JCI, which mix the jet and the DSM, introducing different baryon loads.

(b) **Intermittent, purely hydrodynamical jet** (Gottlieb, Levinson, and Nakar, 2020): baryonic contamination becomes so severe that the jet fails to produce a GRB[7];

---

[7] Repeated shocks between the modulated jet-head elements and the DSM-entrained matter greatly increase the baryon load. The jet becomes weak, and the efficiency of photospheric emission or IS is too low to produce a GRB. In the magnetised case, this is avoided because the magnetic pressure inside the jet acts as a shield, preventing cocoon material from filling the region between two strong energy-injection cycles.

(c) **Continuous, weakly magnetised jet** (Gottlieb et al., 2020): the mixing is reduced because the magnetic field stabilises the jet against hydrodynamical instabilities, and GRBs are slowly variable.

(d) **Intermittent, weakly magnetised jet** (Gottlieb et al., 2021): such jets produce highly variable GRBs, the variability being set by the central engine's injection cycles rather than by hydrodynamical instabilities.

Note that in case (a), since mixing evolves with time (as the jet loses its coherence), one should see an evolution of the variability in the GRB LC which is not observed. Interestingly, case (b) that is often associated with IS fails to produce a GRB, while only in case (d) the variability does reflect the workings of the central engine, according to what is predicted by the IS model. This suggests that a modest degree of magnetisation may be necessary to successfully power a GRB.

3.2.3 *Emission-region-based variability*

Variability can also find its origin within the emission site, rather than being dictated by the central engine. This may occur in Poynting-flux dominated jets ($\sigma \gg 1$), in which the dissipation into γ-rays is due to magnetic dissipation mechanisms. In this vision, the fast variability arises from mini-emitters moving relativistically with respect to the bulk outflow. A similar picture is invoked in less extreme scenarios, such as the ICMART model, where the jet is only mildly relativistic (Sect. 1.5.5).

Zhang and Zhang (2014) performed Monte-Carlo simulations to compute the LCs and associated PDS predicted by the ICMART model. In this picture, a broad pulse in the LC is the direct outcome of an ICMART event, corresponding to the collective emission of all the mini-jets radiating altogether within the emission region. The simulation depends on a few key physical parameters of the emission region, such as the Lorentz factor of the mini-jets γ, the size of the reconnection regions L', the number of mini-jets N, the emission radius R, and the angle ϕ between the mini-jet direction and the bulk flow direction.

In that vision,

- bright, narrow pulses (fast variability) come from mini-jets beaming towards the observer.
- dimmer, broader pulses (slow variability) come from mini-jets beaming away from the line of sight.
- The rise of the pulses is governed by the turbulent reconnection cascade, whereas the decay is controlled by the high-latitude emission timescale.
- the number of ICMART events and their temporal spacing still reflect the erratic activity of the central engine (Fig. 58).

Key trends from the simulation include:

- **Larger** $\gamma \rightarrow$ more variable LCs (shallower PDS), due to an increased Doppler factor. Since magnetisation is linked to the mini-jet Lorentz factor via $\gamma \propto \sqrt{1+\sigma}$, this implies high magnetisation at the emission site (Fig. 59).

- **Larger** N → smoother LCs, as variability is averaged over mini-jets pointing away from the observer (Fig. 60).
- **Lower** L' → more erratic LCs, since the reconnection timescale is shorter (Fig. 61).
- **Larger** R → more asymmetric pulses, with decay dominated by high-latitude emission[8] (Fig. 61). Larger R also produces more erratic and realistic LCs, consistent with the ICMART requirement for fast turbulent reconnection cascades ($R > 5 \times 10^{15}$ cm).

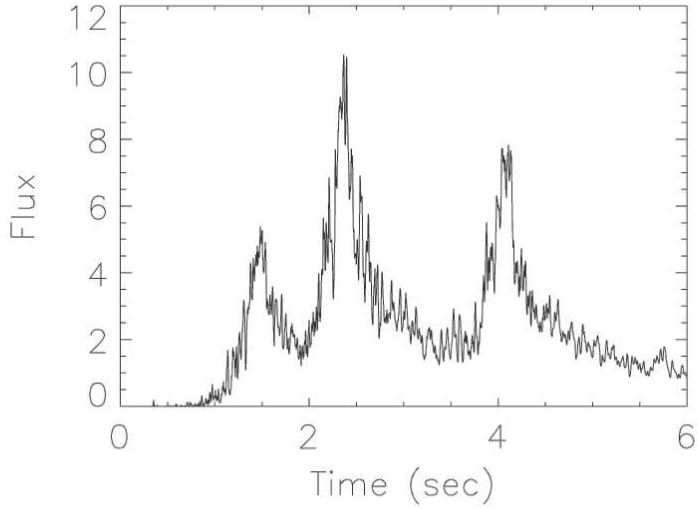

Figure 58: LC made of with three consecutive ICMART episodes. From Zhang and Zhang (2014).

---

[8] The delay between on-axis and off-axis photons at the limb of the jet cone (opening angle θ_j) is $R(1 - \cos\theta_j)/c$.

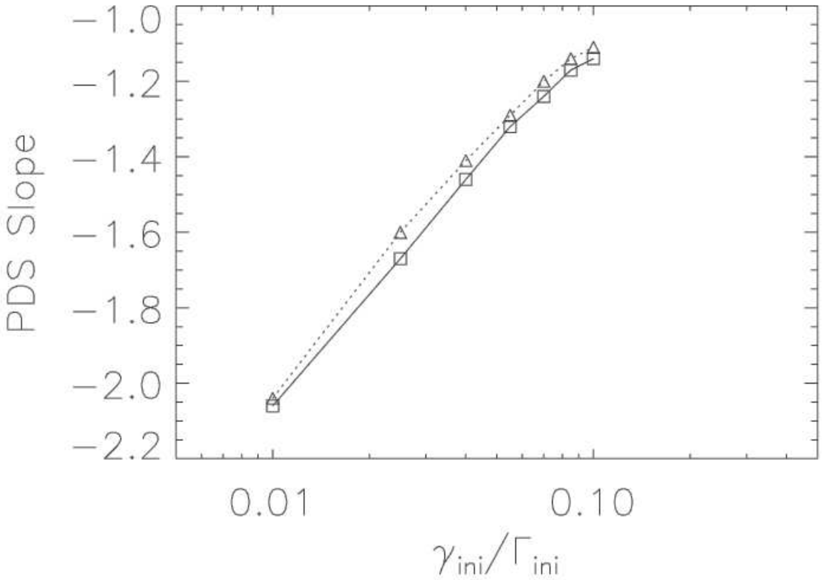

Figure 59: PDS slope for different Lorentz factor contrast with a fixed Γ_{ini}. The squares and the solid lines (triangles and dotted line) represent the PDS slopes as a function of Lorentz factor contrast when parameter evolution is (is not) taken into account. From Zhang and Zhang (2014).

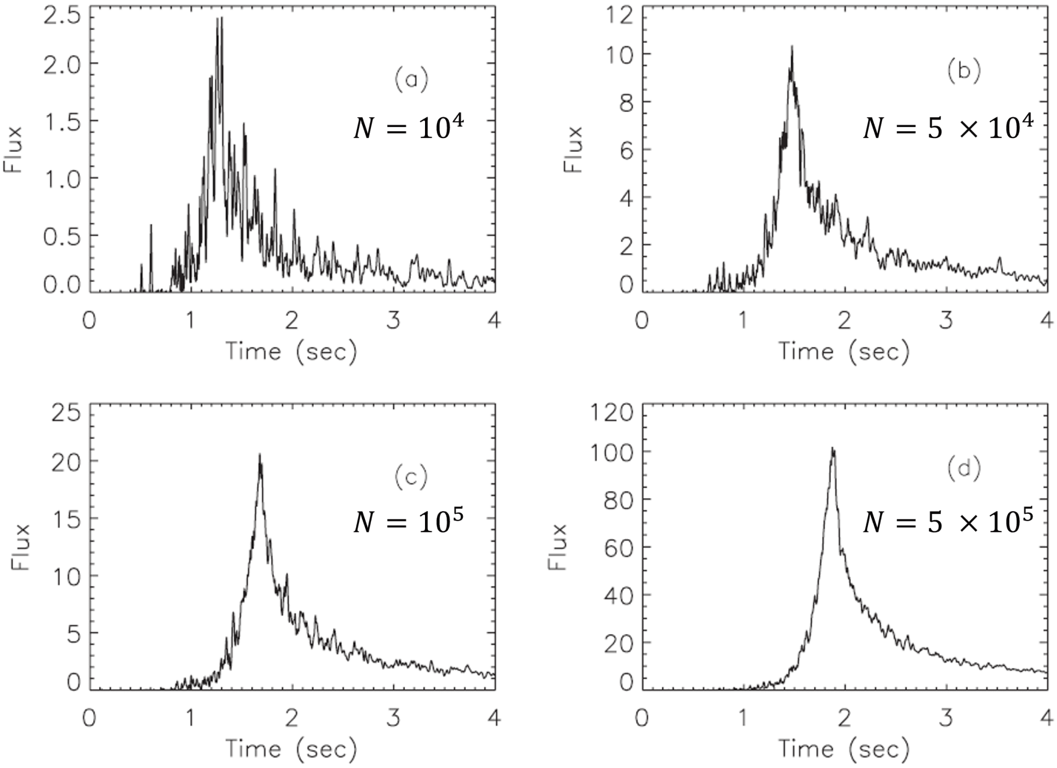

Figure 60: Simulated LCs with different (increasing from left to right, up to down) number of reconnection events N. Adapted from Zhang and Zhang (2014).

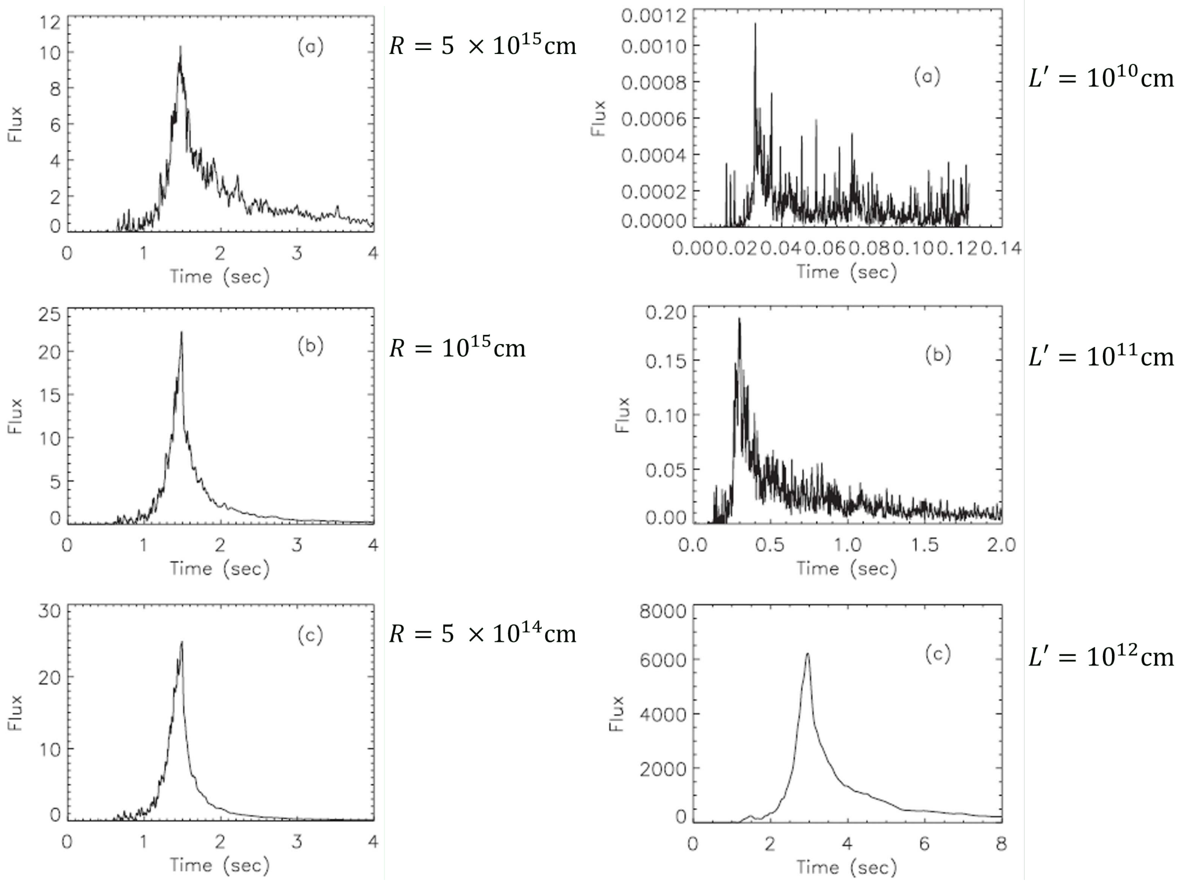

Figure 61: *Left panels*: LCs with decreasing emission radius R. *Right panels*: LCs with increasing reconnection region size L′. Adapted from Zhang and Zhang (2014).

3.2.4 *Using the distribution of the number of peaks as a test of prompt-emission models*

Theoretical models, such as those based on internal shocks or magnetic reconnections, could be tested using the observable identified in Sec. 3.1.3, i.e. the distribution of the number of peaks and its associated parameters, the average number of peaks in the peak-poor (resp. peak-rich) GRBs and the fraction of peak-rich GRBs. In fact, these models use parameter values that qualitatively reproduce GRB variability but not necessarily quantitatively. For instance, the GRB profiles shown in Fig. 21 clearly exhibit an excess of short narrow pulses with respect to real GRB LCs.

To obtain credible LCs, one could try to optimise their parameters through a comparison with a set of observed LCs. To this end, different metrics could be built to compare observed and simulated LCs, as done in Bazzanini et al. (2024) and Maistrello et al. (2025). In these works, the model parameters were optimised minimising the differences between the observed and simulated metrics[9]. Once the parameters are optimised, the observed distribution of the number of peaks can be used to compare the model with observations and validate it. At the time of writing, such a study is currently being pursued in Maistrello et al. (in prepa-

---

[9] See Sec. 4.2.2 of Chap. 4 where this technique is employed in the case of LCs generated using a stochastic model.

ration), where, using the IS model of Kobayashi, Piran, and Sari (1997), we aim to generate realistic LCs and, in turn, constrain the physical parameters of the IS model.

3.2.5 *Temporal variability as a key diagnostic of GRB progenitors*

Temporal variability can be used to probe the nature of the GRB progenitor, as we will see in the following sections.

3.2.6 *The need for a new classification*

GRBs were originally classified according to their duration and spectral hardness, with long/-soft GRBs associated with collapsars and short/hard GRBs with COMs (Sect. 1.6.4). In fact, they were traditionally divided in short and long GRBs according to $T_{90} < 2$ s, a classification originally introduced with BATSE. However, the first drawback of this classification is that it is detector dependent: the burst duration depends on the energy pass-band of the instrument, in particular longer durations are usually observed in lower energy bands. Therefore, the threshold separating the two GRB populations should vary from one instrument to another (e.g. Bromberg et al. 2013).

Moreover, peculiar events, known as short GRBs with extended emission such as GRB 060614–characterised by a short/hard pulse followed by a broader and softer emission episode–proved that the T_{90} classification can be misleading, as they are associated with COM events rather than collapsars, despite their overall long duration (Sect. 3.2.7). Other long duration events lasting a few tens of seconds, such as GRB 211211A and GRB 230307A, confirmed that classifying GRBs solely according to their duration could lead in some cases to misclassification. For these reasons, additional indicators are required to achieve a more reliable classification. In modern terminology, GRBs originating from COMs are referred to as type-I, while those from collapsars are referred to as type-II (Zhang, 2006).

3.2.7 *Short GRBs with extended emission*

A new class of GRBs emerged with GRB 060614 (Gehrels et al., 2006), the so-called short GRBs with extended emission (SEE-GRBs, see Norris and Bonnell 2006). This GRB, with a duration of $T_{90} = 102$ s observed at $z = 0.125$, did not show any evidence for a SN, with stringent limits 100 times lower than previously observed SN associated with long GRBs (Sect. 1.2.1).

On the contrary, this GRB shows several properties that are usually exhibited by short GRBs, such as a negligible spectral lag for the first spike and the subsequent extended emission. The early spike (first five seconds) is characterised by a peak energy $E_{\mathrm{peak}} = 302$ keV and $E_{\mathrm{iso}} = 1.8 \times 10^{50}$ erg, which falls off the Amati relation for type-II GRBs (Sect. 1.6.3). The LC of this event is shown in Fig. 62. The optical counterpart of GRB 060614, and in particular a significant flux excess with respect to the afterglow predictions, observed ~ 4 days after the burst trigger, was interpreted as a kilo/macronova emission powered by r-process (Jin et al., 2015; Yang et al., 2015).

This GRB demonstrated that classifying bursts based solely on the duration of the prompt emission alone can lead to false conclusions. After GRB 060614, other similar bursts, with negligible spectral lags and characterised by an initial short, hard pulse followed by softer and longer extended emission, were classified as SEE-GRBs (e.g. Kaneko et al. 2015; Lan et al. 2020; Lien et al. 2016; Norris and Bonnell 2006).

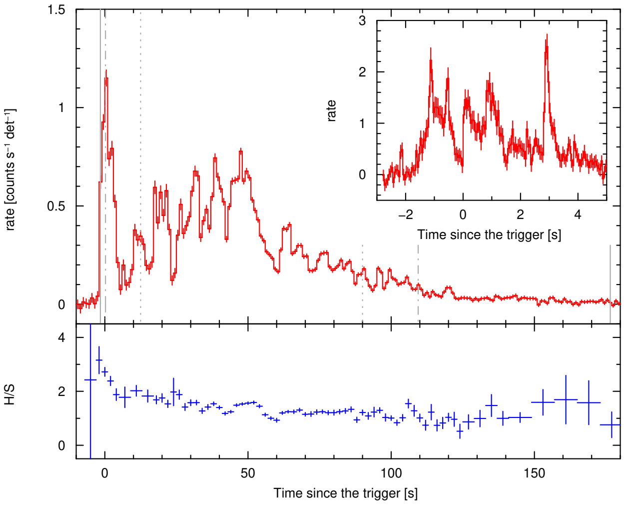

Figure 62: *Top panel:* GRB 060614 time profile, as observed by *Swift*/BAT, showing the peculiar temporal evolution of this GRB. *Bottom panel*: temporal evolution of the hardness ratio throughout the burst. From Mangano et al. (2007).

3.2.8 *Minimum variability timescale*

GRB variability can be studied in many ways, either directly in the temporal domain or in the frequency domain, as seen in Sect. 1.8.3. Numerous metrics for GRB variability have been proposed in the literature, aiming to quantify the net variance of the GRB time profile once the contribution of the statistical counting noise is removed. The MVT is the shortest timescale on which uncorrelated flux variations can be attributed to the GRB activity. In the IS model, it is related to the GRB emission region size (see also Sect. A.2):

$$R = 2\Gamma^2 c\Delta t \,. \tag{49}$$

Several analyses (Golkhou and Butler, 2014; Golkhou, Butler, and Littlejohns, 2015), including our recent works (Camisasca et al., 2023b; Maccary et al., 2025), also show that short GRBs tend to exhibit shorter MVT values than most long GRBs. The MVT can therefore serve as an indicator of the progenitor nature, type-I GRBs having statistically shorter MVTs than those of type-II GRBs (Fig. 64).

3.2.8.1 *Minimum variability timescale estimated with the structure function and Haar wavelets*

The MVT has been computed by estimating the structure function, defined as follows

$$SF(\tau) =< \left(X(t) - X(t+\tau)\right)^2 >, \tag{50}$$

where $X(t)$ is a time series, τ is the time lag, and $< . >$ stands for the temporal average. The structure function is computed using Haar wavelets[10]. With this method, the MVT is computed by estimating the lag value for which the structure function departs from the linear relation $SF(\tau) \propto \tau$ (Fig. 64 from Golkhou and Butler 2014).

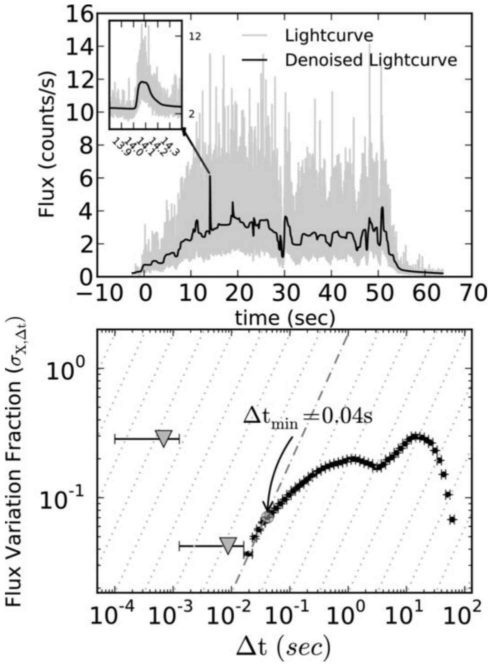

Figure 63: *Top panel: Swift*/BAT LC (15–350 keV band) of GRB 080319B (in grey). A filtered version of the LC is superimposed in black. *Bottom panel:* the structure function (here defined as $\sigma_{X,\Delta t}$) derived using Haar wavelets as a function of the timescale Δt for GRB 080319B. A MVT of 40 ± 10 ms is derived, which corresponds to the shortest timescale at which $\sigma_{X,\Delta t}$ departs from $\sigma_{X,\Delta t} \propto \Delta t$. From Golkhou, Butler, and Littlejohns (2015).

When applied to simulated GRB LCs composed of a smooth FRED pulse, the MVT typically recovers the rise time of the simulated pulse, provided that the S/N ratio is sufficiently high.

This technique was applied to the *Swift*/BAT and *Fermi*/GBM samples. These studies reveal that very few GRBs show evidence for variability on timescales below 2 ms. They also show that the median minimum timescale in the rest frame for short GRBs is larger than that of long GRBs (Fig. 64 and Sect. 3.2.8).

3.2.8.2 *Minimum variability timescale estimated using* MEPSA

We developed another way to compute the MVT using MEPSA, which consists of measuring the FWHM of the narrowest (statistically significant) pulse in the LC. Although MEPSA does not directly measure the FWHM of the pulses, it provides, for each detected pulse, a set of parameters closely related to it, as explained in Sect. 3.1.2. In particular, the algorithm identifies for each detected peak a *detection timescale* Δt_{det} (see Sect. 3.1.2), corresponding

---

[10] Haar wavelets are a particular family of wavelets functions. Wavelets functions are a set of functions forming an orthonormal basis. Wavelets are usually used to detect narrow features in time series.

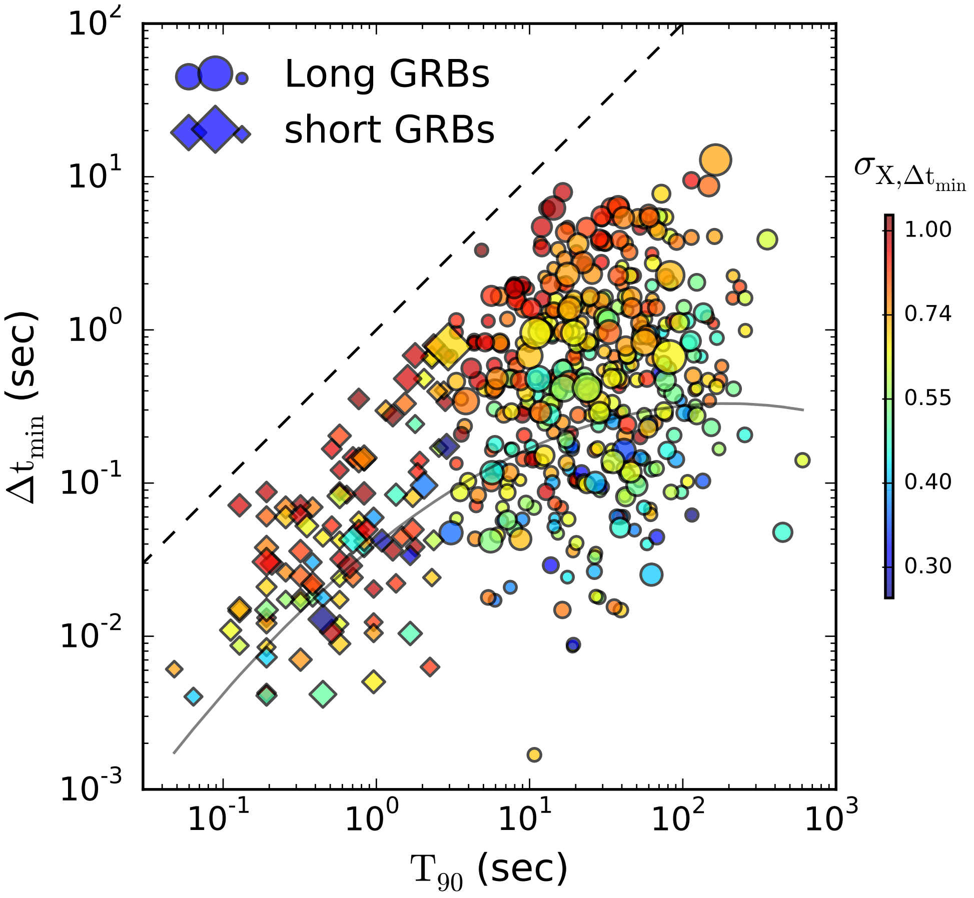

Figure 64: Minimum variability timescale of *Fermi*/GBM GRBs, computed with Haar wavelets and the structure function, against the T_{90} duration. Short GRBs (diamonds) tend to exhibit lower values, with a median value of 10 ms, than long GRBs (circles, median value 45 ms). The dashed line represents the equality line. The solid curve shows the typical minimum measurable timescale as a function of T_{90}. From Golkhou, Butler, and Littlejohns (2015).

to the timescale at which the peak is optimally detected. An approximate formula for the FHWM, involving these parameters was derived in Camisasca et al. (2023b):

$$\mathrm{FWHM} = 10^{-0.31}\,\Delta t_{\rm det}\left(\frac{S/N}{4.7} - 1\right)^{0.6} N_{\rm adiac}^{1.06}, \tag{51}$$

with S/N the S/N ratio and $N_{\rm adiac}$ the number of adjacent bins. The corresponding uncertainty is given by

$$\sigma_{\rm FWHM} = \mathrm{FWHM}(10^{\pm 0.13} - 1)\,. \tag{52}$$

The detailed procedure to compute the MVT with MEPSA is described in Fig. 65. MEPSA is first applied to 64 ms binned LCs. If a peak fulfils (i) $S/N > (S/N)^{(\Delta t)}_{\rm min}$[11] and (ii) $\Delta t_{\rm det} > 2\Delta t$, where Δt is the bin time, then it is promoted as a candidate for the MVT. If some peak satisfies (i) but not (ii), then MEPSA is applied recursively to LCs binned at lower time resolutions, 4 ms and 1 ms, until fulfilling both conditions. If no peak fulfilling (i) is found at 64 ms, MEPSA

---

[11] $(S/N)^{(\Delta t)}_{\rm min}$ depends on the bin time used and is fixed to 7, 6.8, 6.4, and 6 at 1, 4, 64, and 1024 ms, respectively.

is applied to the 1024 ms binned LC. The MVT then corresponds to the shortest FWHM (computed with Eq. (51)) observed in the peaks that satisfy both (i) and (ii). Our procedure is illustrated in Fig. 66.

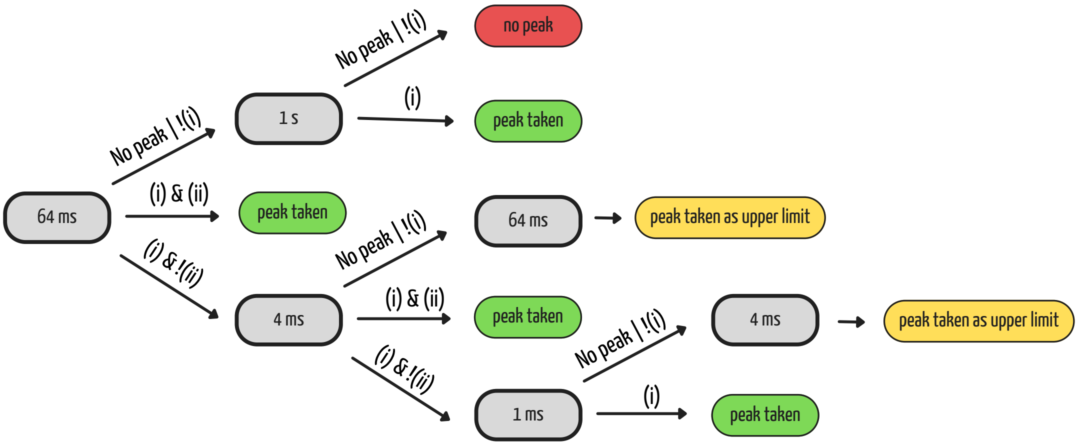

Figure 65: A schematic description of the procedure adopted to determine the MVT with MEPSA. From Camisasca et al. (2023b).

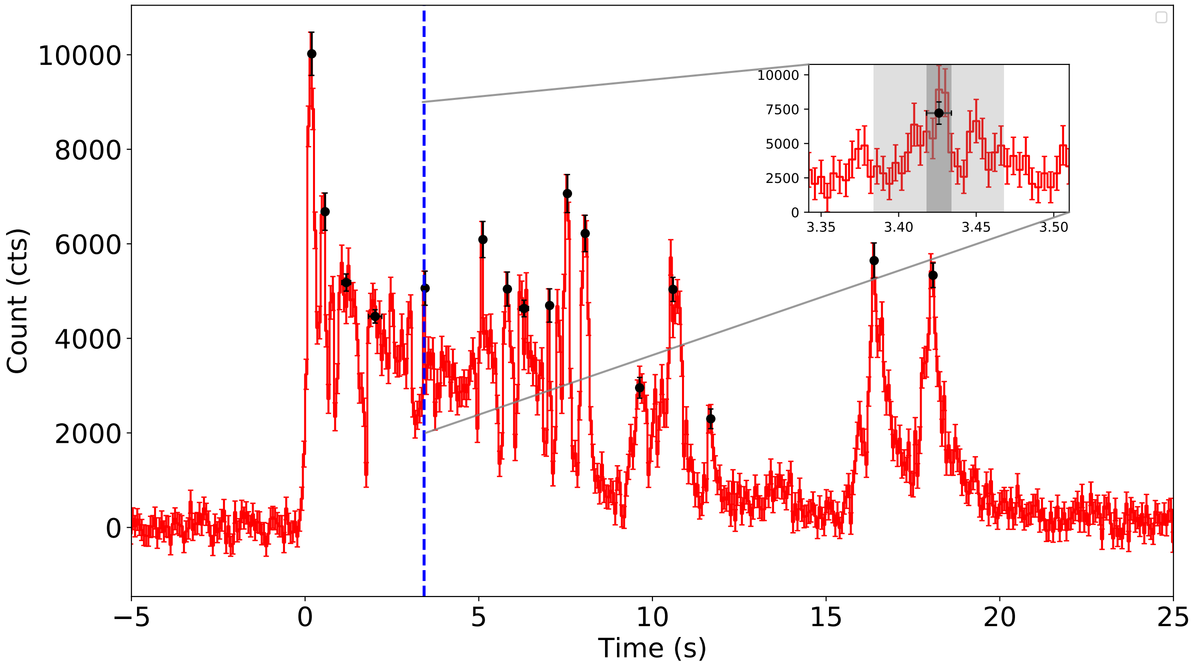

Figure 66: GRB 131109A LC observed by *Fermi*/GBM (8–1000 keV), shown as an example of how the MVT is derived with our method. Pulses detected by MEPSA are shown as black points. The vertical dashed line marks the shortest pulse identified by MEPSA. The inset zooms in on this pulse, and the light grey region indicates its FWHM (computed with Eq. (51)), i.e. the estimated MVT, while the darker grey region encloses the detection timescale.

Our MVT estimates are systematically larger than those obtained with the structure function and Haar wavelets, described in Section 3.2.8.1. This difference arises from the different definition of MVT. In our approach, MVT is the FWHM of the shortest pulse, whereas the other method provides values that are more closely linked to the rise time, typically smaller by a factor of three to four compared to the FWHM. Our choice of adopting the FWHM is also motivated by its physical connection with the variability imprinted by the central engine activity in the IS model. According to Kobayashi, Piran, and Sari (1997), the pulse rise time corresponds to the time required for the reverse shock to cross the shocked shell, while the decay time arises from the delay between off- and on-axis photons (the angular spreading timescale, see Eq. (22) of Sect. 1.6.2) and is linked to the emission radius R through $R/2\Gamma^2c$.

Despite this observed discrepancy between the two techniques, we also found a general consistency between the two approaches, as events such as GRB 230307A and GRB 211211A occupy extreme positions in both metrics.

3.2.9 *Correlations involving the minimum variability timescale*

- The MVT correlates with the peak luminosity $L_{\rm iso}$. Although this correlation is affected by selection effects, a detailed study through simulations revealed that this correlation is intrinsic, and not arising solely because of these selection effects (Camisasca et al., 2023b; Maccary et al., 2025). This correlation can be used to probe the jet launching mechanism, see also the next point.
- The MVT correlates with the Lorentz factor Γ. The shape of this correlation, along with the MVT-$L_{\rm iso}$ correlation, can be used to probe the mechanism launching the relativistic jet (for instance, to discriminate between Blandford-Znajek versus $\nu\bar{\nu}$ annihilation, Sect. 1.3.2 and 1.3.1).
- The MVT appears to correlate with the angle of the jet θ_j. This correlation could be exploited to probe the structure of the jet. In fact, when the afterglow is seen off-axis, the constrain obtained from the jet break time, actually provide an estimation of $\theta_{\rm obs} + \theta_j$, with $\theta_{\rm obs}$ the viewing angle, rather than θ_j alone. Hence, the differences in MVT in different GRBs could arise from GRBs seen with various viewing angles. For on-axis GRBs, with small $\theta_{\rm obs}$, the observer sees the core of the jet, and therefore narrow and hard pulses, while an observer looking at the jet with a larger viewing angle sees broader, fainter, and softer pulses, owing to the lower Doppler boosting in a region of the jet closer to the boundary with the stellar material (so-called cocoon, Sect. 1.4).

3.2.10 *Our work: Minimum variability timescales with Fermi/GBM*

In our work, we computed the MVT of the GRBs detected by *Fermi*/GBM from its launch up to June 2024, collecting more than 3,500 GRBs. We confirmed that short GRBs and SEE-GRBs tend to have shorter MVTs than long GRBs, making the MVT a robust diagnostic of the progenitor nature. To this picture, we added the recent cases of long GRBs coming from mergers, GRB 191019A, GRB 211211A, and GRB 230307A, which indeed present short MVT values, departing from the MVT distribution of long GRBs (Fig. 67).

This result is very promising, especially in a time in which facilities such as SVOM and Einstein Probe have already been incrementing the number of well localised bursts, host galaxy detections and redshift measurements. In this respect, the MVT represents a very

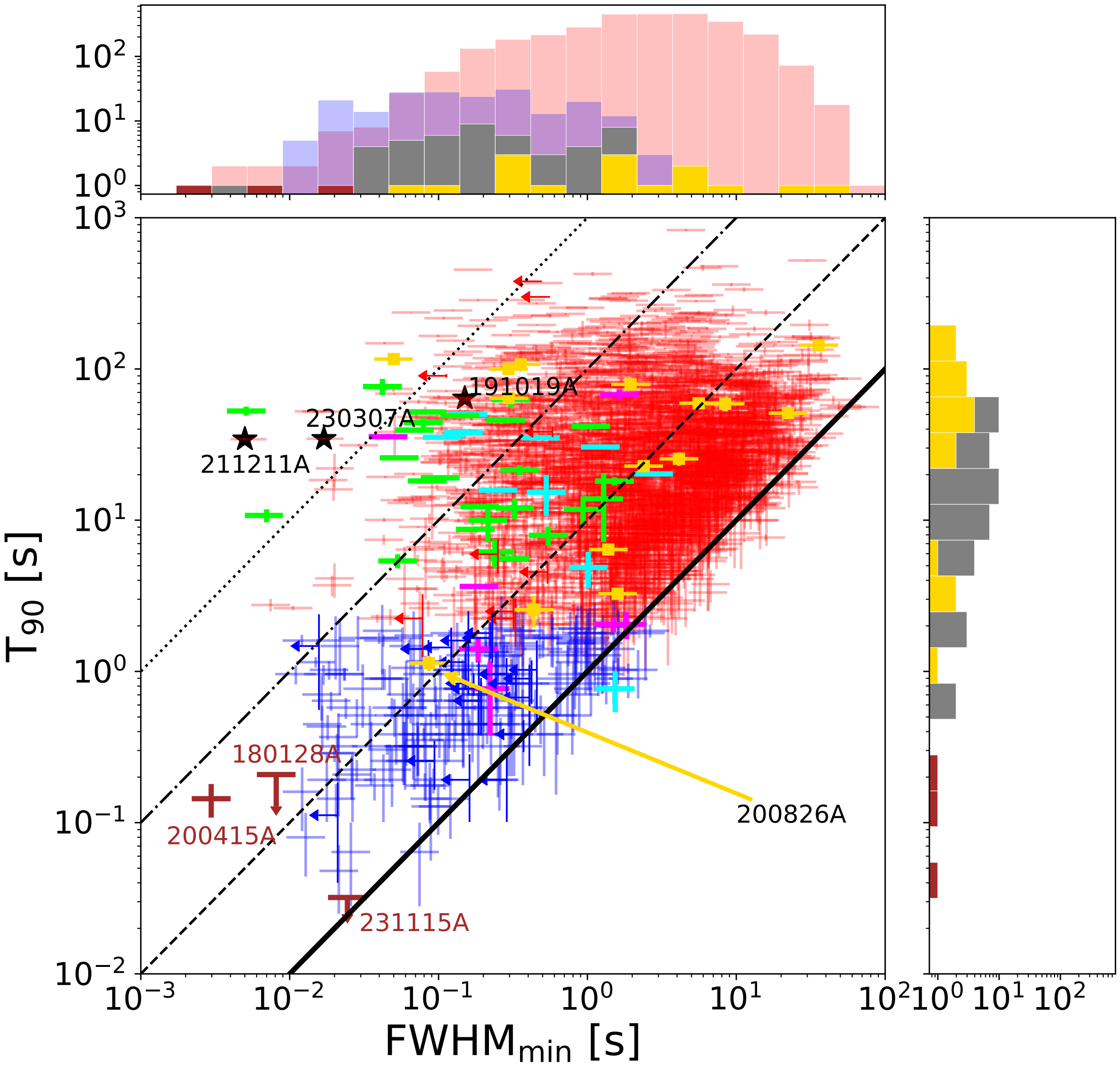

Figure 67: Scatter plot of $\mathrm{FWHM_{min}}$ and T_{90} for the *Fermi*/GBM sample, along with the corresponding marginal distributions. Blue (red) points represent short (long) GRBs. Gold points represent SN-associated GRBs. Magenta, lime, and cyan points represent SEE-GRBs from Kaneko et al. (2015), Lan et al. (2020), and Lien et al. (2016), respectively. Three extragalactic magnetar giant flares candidates, GRB 180128A, GRB 200415A, and GRB 231115A are shown in brown. SEE-GRBs from the three samples considered are shown altogether in grey in the top and right panel. We also showed with black stars the two peculiar LGRBs 211211A and 230307A associated with a KN event, and GRB 191019A which can be a short GRB that exploded in a dense environment. We also highlighted the peculiar short collapsar GRB 200826A associated with a SN. Reproduced from Maccary et al. (2025).

helpful hint to promptly spot GRBs with a merger origin directly from their γ-ray time profile, as was the case for GRB 230307A (see the GCN announcement of Camisasca et al. 2023a).

In this work, we also confirmed the existence of correlations between the MVT and different observables, including the peak luminosity and the Lorentz factor (Fig. 68).

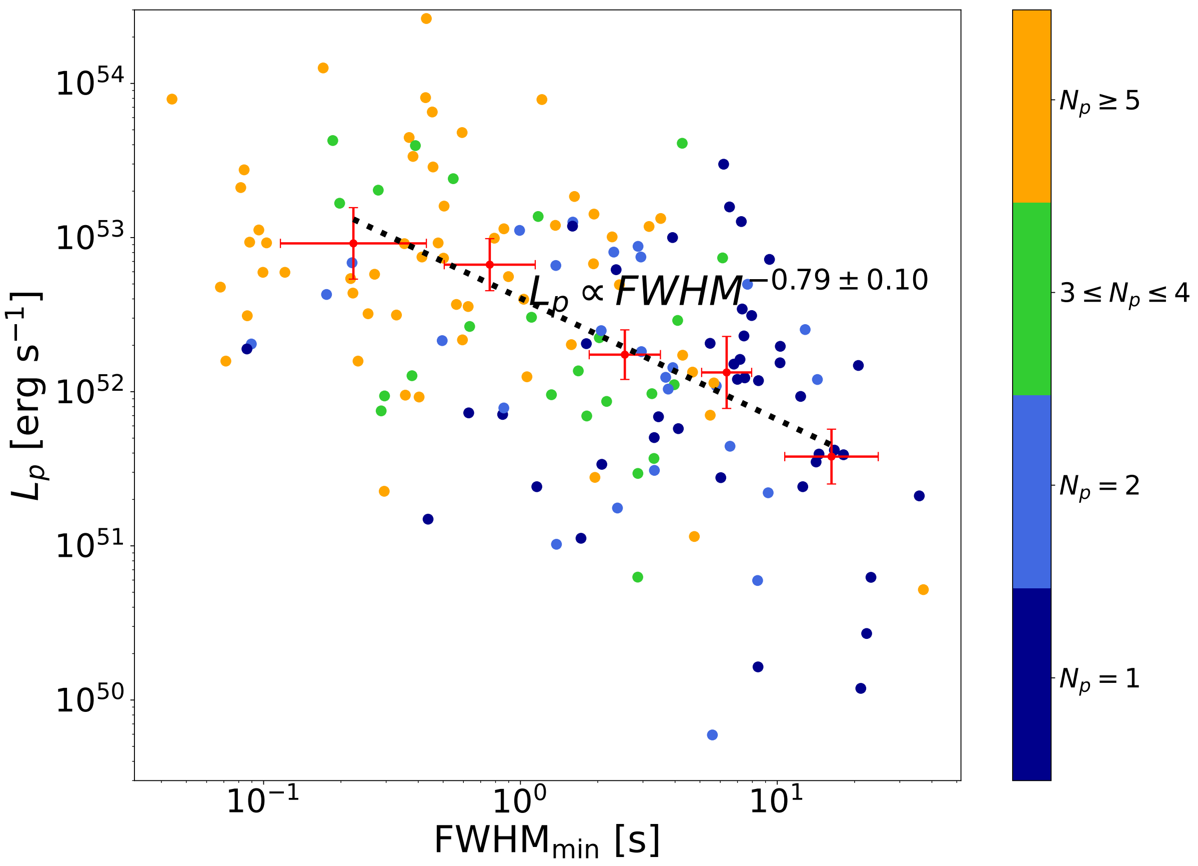

Figure 68: Peak luminosity versus FWHM$_{\min}$ for type-II GRBs. The red points represent the geometric means of GRB groups sorted by increasing FWHM$_{\min}$. The dashed line indicates the best fit. GRBs are also categorised by the number of peaks, with the more luminous ones having more peaks. From Maccary et al. (2025).

To assess the correlation between the MVT and the peak luminosity, we carefully accounted for the selection effects by performing a suite of simulations that aimed to reproduce the detection process inducing a selection bias (Fig. 69). For a full description of these simulations, the interested reader can consult the entire version of the paper in Appendix A.9.

We demonstrated that the observed correlation, although it is unavoidably affected by the selection effects, is stronger than any artificial correlation arising only from selection effects (Fig. 70). There is therefore a genuine correlation between these two observables, hence it is meaningful and could be used to provide constraints on theoretical models. We also confirmed the correlation between MVT and Lorentz factor, adding to this picture the few cases of short GRBs with measured Lorentz factor (Fig. 71). This work, published in Astronomy & Astrophysics, is reported in Appendix A.9 of this thesis.

3.3 DISCOVERY OF A PECULIAR SET OF PROPERTIES OF COMPACT OBJECT MERGER CANDIDATES

On March 2023, GRB 230307A, a long and very bright GRB event of compact merger origin was detected. With GRB 060614 and GRB 211211A, this is one of the few GRB events that are

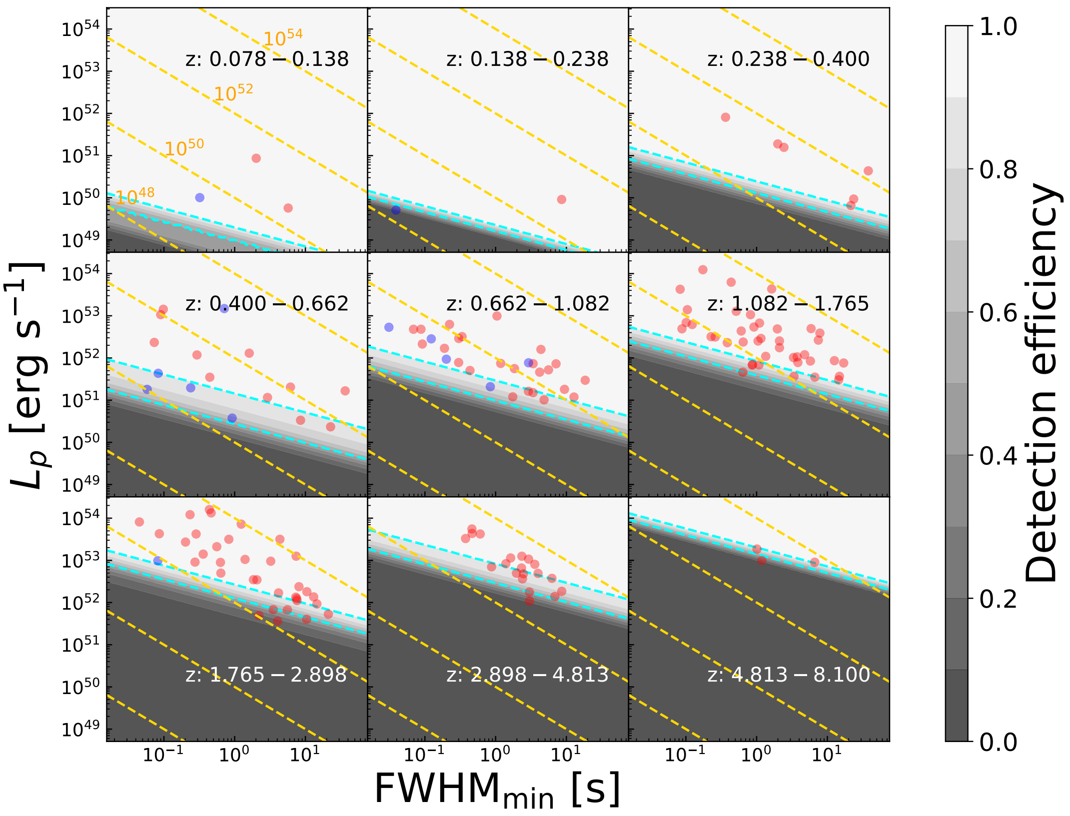

Figure 69: L_p versus FWHM$_{min}$ for the *Fermi*/GBM divided into nine redshift bins with equal logarithmic spacing in luminosity distance. Blue dots represent merger-candidates (or type-I GRBs), and red dots represent collapsar-candidates (or type-II GRBs). The dashed cyan lines show 90% and 50% detection efficiency (vertical bars). Gold dashed lines indicate regions of constant isotropic-equivalent released energy (in erg) for each peak, roughly calculated as $E_{iso} = L_p \times \text{FWHM}_{min}$.

associated with a kilonova emission. This very remarkable event was detected by GECAM, which recorded a signal with unprecedented S/N without any saturation effect. The quality of this LC revealed features so far not observed in other burst time profiles.

3.3.1 *GRB 230307A: an extraordinary event*

GRB 230307A is a very remarkable burst. It ranks second in brightness ever detected so far, after GRB 221009A, and is also among the closest ones. Despite its long duration, no accompanying supernova was observed, therefore ruling out a collapsar origin. Instead, both photometric and spectroscopic evidence for the presence of a KN was reported (Gillanders and Smartt, 2025; Levan et al., 2024), making a strong case for a merger of compact objects.

The extraordinary quality of the signal enables us to observe features in its LC that are very rarely observed in other GRBs. In particular, it exhibits a very distinctive temporal structure made up of three distinct episodes: a short initial soft spike, identified as a precursor (Dichiara et al., 2023), shortly followed by a long and hard main emission preceding a softer extended emission. The main and extended emissions are separated by a dip-like feature.

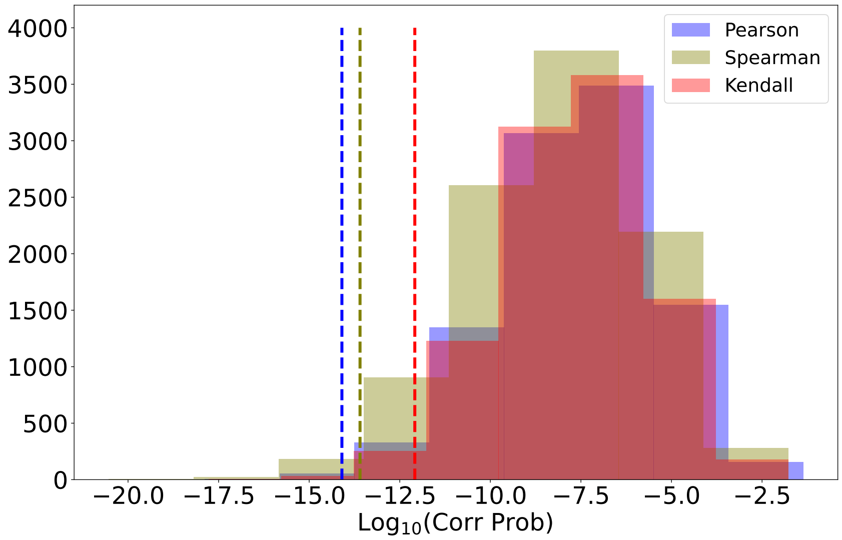

Figure 70: Pearson, Spearman, and Kendall correlation p-values (in logarithm units) computed on $N = 10^4$ simulated samples (blue, olive, and red histograms) compared to the ones computed on the real dataset (blue, olive, and red dashed lines, respectively). From Maccary et al. (2025).

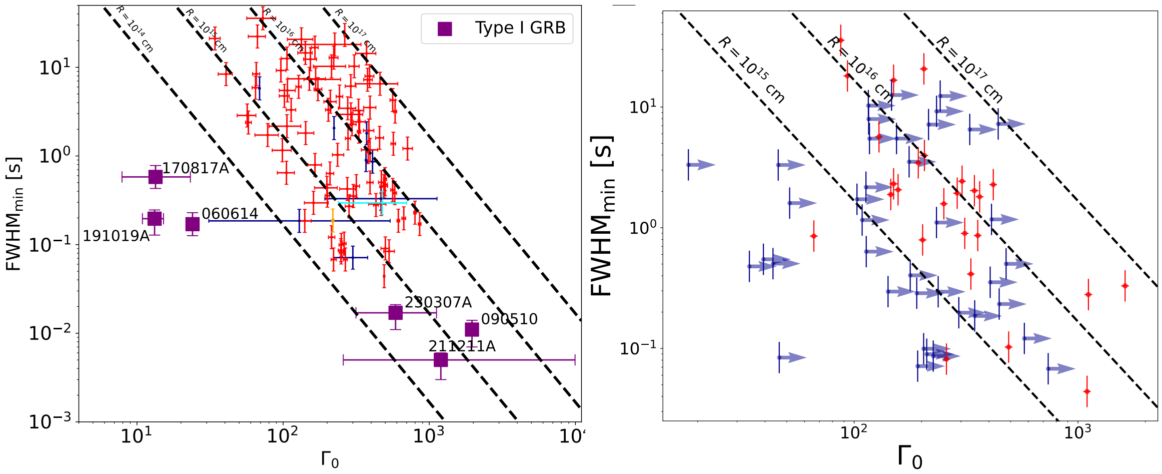

Figure 71: $\mathrm{FWHM}_{\mathrm{min}}$ versus the initial Lorentz factor Γ_0 for the type-II (red dots) and type-I GRBs (purple squares) present in our sample. *Left:* the Γ_0 values are taken from different datasets, colour-coded as follows: L12: Lü et al. (2012), X19: Xue, Zhang, and Zhu (2019), X16: Xin et al. (2016), and Gu21: Gupta et al. (2021). The dashed lines represent the typical distance $R = 2c\Gamma_0^2\mathrm{FWHM}_{\mathrm{min}}$ where the dissipation process responsible for the prompt emission could occur. *Right:* same as left, but Γ_0 is calculated using the dataset from Ghirlanda et al. (2018). Red points indicate GRBs from their golden and silver samples, while blue points represent lower limits on Γ_0. Reproduced from Maccary et al. (2025).

It has been proposed that such a three-fold time profile is characteristic of a sub-class of type-I GRBs, referred to as type-IL GRBs (e.g. Tan et al. 2025; Wang et al. 2025). In particular, GRB 230307A shares many similarities with GRB 211211A, another long GRB originating from COMs: both occurred in the local Universe ($z = 0.076$ for GRB 211211A and $z = 0.065$ for GRB 230307A), both display short MVTs of a few tens of milliseconds, both show a similar three-fold temporal structure, and both are robust outliers of the Amati relation for type-II GRBs (Peng, Chen, and Mao, 2024).

3.3.2 *Our work: discovery of a peculiar set of properties in the light curve of GRB 230307A*

In our work (Maccary et al., 2026), we exploited exceptional data from this event obtained by GECAM. Unlike other instruments, GECAM recorded this extraordinarily bright burst without suffering from electronics saturation, offering a unique opportunity to investigate in detail the temporal structure of a rare long GRB arising from a COM.

We identified four temporal properties that are evolving throughout the burst (Fig. 72), namely:

1. An exponential decrease of the peak rate.
2. An exponential increase of the waiting times.
3. An exponential increase of the pulse FWHMs.
4. An exponential decrease of the spectral peak energy.

These properties are particularly interesting for two reasons:

(i) if they are shared by other COM bursts, as we have shown in our study, they would provide a detailed characterisation of the temporal behaviour of long GRBs originating from COMs. Such characterisation could, in turn, be used to identify the nature of these events directly from their γ-ray time profiles;

(ii) they raise questions about the emission mechanism itself, as the supposed absence of timescale evolution throughout GRB time profiles was one of the main arguments historically used to disfavour external shocks models in favour of an internal origin. This argument, however, certainly does not hold for GRB 230307A, whose time profile clearly shows a marked increase in pulse width over time and, overall, a sort of deterministic evolution, in contrast with the higher degree of randomness which is thought to characterise most GRB LCs.

Regarding (i), we performed an analogous analysis for other long bursts from COMs, such as GRB 211211A and GRB 060614, and found that they exhibit a similar trend (Fig. 73).

This suggests that such temporal evolution could be a characteristic feature of this class of events. We also investigated the presence of these features in GRBs originating from collapsars. To this aim, we selected all GRBs for which there is evidence of association with a type Ic-BL SN and chose among them those verifying $N_p \geqslant 10$, where N_p is the number of statistically significant peaks detected by MEPSA ($S/N > 5$). We ended up with six candidates, which are GRB 111228A, 130427A, 190114C, 171010A, 211023A, and 221009A. However, none of these bursts showed similar properties to those of GRB 230307A (Fig. 74). Even GRB 221009A, the brightest GRB ever recorded, does not show such an evolution. In fact, since the LC observed by *Fermi*/GBM was affected by strong saturation effects due to its extreme brightness, to study this burst we used data from *Insight*-HXMT outside of the saturated time intervals, and from GECAM when entering the saturated region, since its time profile was free of any

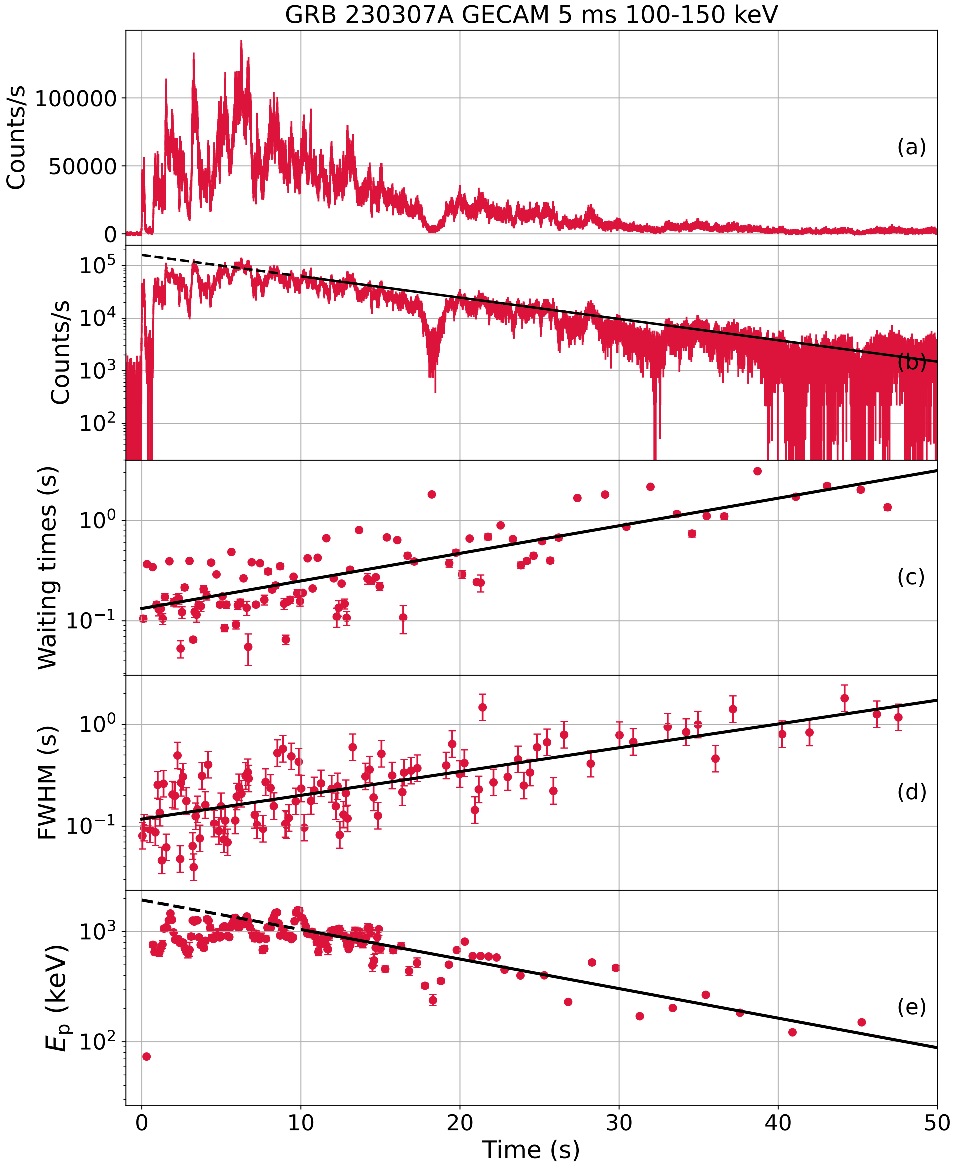

Figure 72: Properties of GRB 230307A. (a) LC in the 100-150 keV band with 5-ms bin time; (b) same as (a), but in semi-logarithmic scale; (c) WTs of the peaks detected with MEPSA as a function of time; (d) FWHMs of the same peaks of (c) as a function of time; (e) time-resolved evolution of spectral peak energy. In panel (b), the solid line represents the exponential fit of the peak rates of the pulses. In panels (c), (d), and (e), solid lines show the exponential models obtained within the corresponding temporal window, whereas the dashed line, if present, shows the extrapolated fit to the time interval that was ignored by the fitting procedure. Reproduced from Maccary et al. (2026).

saturation effects. Figure 75 shows the temporal evolution of GRB 221009A. This burst shows a complex time profile, marked by very intense periods separated by long quiescient times. In any case, the temporal evolution of the properties listed above is very different from those of GRB 230307A, highlighting the possibility that this peculiar evolution is only present in long type-I GRBs.

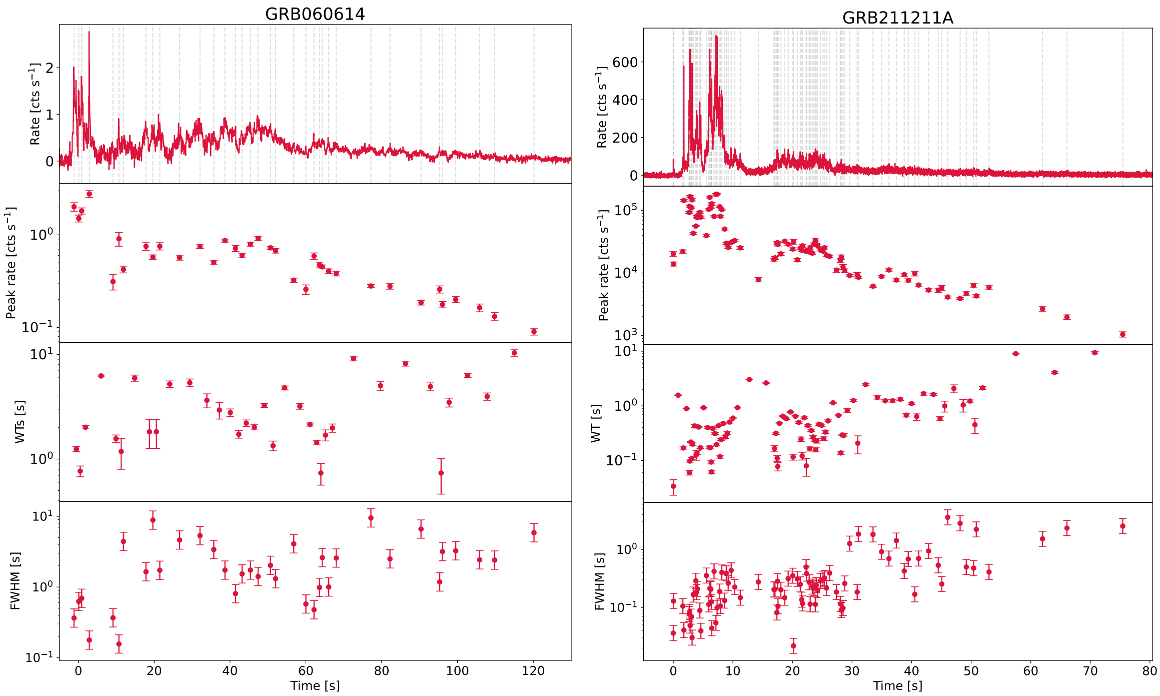

Figure 73: *From top to bottom panels, left to right*: *Fermi*/GBM LC of GRB 060614 (resp. GRB 211211A), peak rates, WTs, and FWHM evolution as a function of the peak occurrence times of the pulses observed during prompt emission. Reproduced from Maccary et al. (2026).

The absence of similar evolution in collapsar GRBs supports (or at least does not contradict) the idea that these features are distinctive of long GRBs originating from COMs.

Regarding (ii), we conceived a simple model based on the assumption of a massive, slowly expanding shell (referred to as the target shell) ejected prior to the subsequent, faster shells launched by the central engine. In this scenario, the later shells collide with the expanding target shell, and the shocks occur at progressively larger radii.

The LC of GRB 230307A shows pulses with increasing WTs (hence pulses getting progressively more separated) meaning that the central engine has a declining activity, emitting many shells at the beginning and a few at the end. To model this, we have generated the emission times (in lab frame) according to an exponential distribution:

$$f(t_{e,i}) \propto e^{-t_{e,i}/\tau}, \tag{53}$$

where $t_{e,i}$ be the emission time (in the lab frame) of the i-th shell. All shells are emitted with the same velocity $\beta = v/c$, whereas the target shell is moving with $\beta_s = v_s/c < \beta$. The target shell has been emitted prior to the start time of the activity of the central engine $t = 0$, and has reached at this time a radius R_0 when the first shell is emitted. We call $t_{c,i}$ the collision time (in the lab frame) of the i-th shell, which occurs at radius $R_{c,i}$. Since different collisions take place at different radii, the WTs seen by the observer will appear shorter than the corresponding WTs in the lab frame: to avoid confusion, the observed collision times are denoted as $t_{c,i}^{(\mathrm{obs})}$ and are measured by the observer since the arrival of the first pulse. Solving

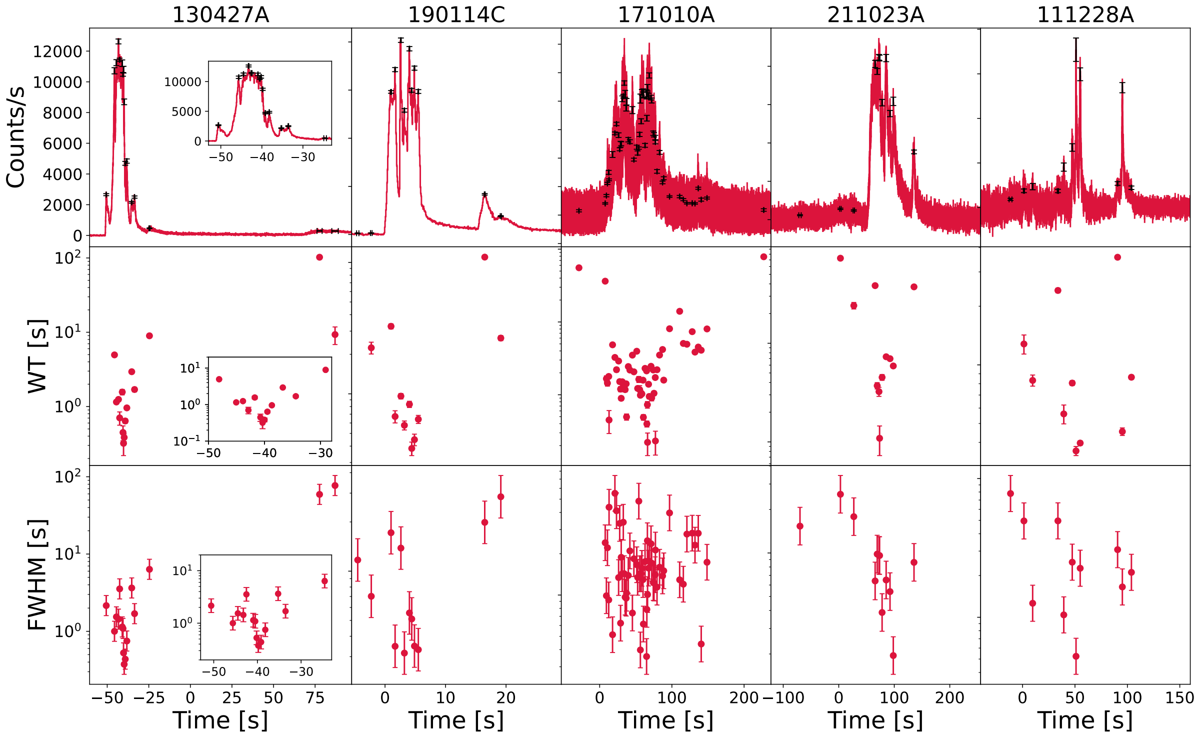

Figure 74: Five SN-GRBs having $N_p \geqslant 10$. Each top panel shows the γ-ray time profile (obtained with either *Fermi*/GBM or *Swift*/BAT). Black points represent the peaks detected by MEPSA. Middle and bottom panels respectively show the temporal evolution of WT and of FWHM throughout each burst. For GRB 130427A, two insets show a close-in view of the densely populated interval. Reproduced from Maccary et al. (2026).

the kinematics of the shocks between the target shell and the shells emitted by the central engine, we obtained the following expression for these quantities:

$$t_{c,i} = \frac{R_0/c}{\beta - \beta_s} + \left(\frac{\beta}{\beta - \beta_s}\right) t_{e,i} \,, \tag{54}$$

$$t^{(\mathrm{obs})}_{c,i} = \left(\frac{\beta}{\beta - \beta_s}\right) (1 - \beta_s)\, t_{e,i} \,, \tag{55}$$

$$R_{c,i} = \left(\frac{\beta}{\beta - \beta_s}\right) (R_0 + c\beta_s\, t_{e,i}) \,. \tag{56}$$

The pulse FWHM is then directly determined by the angular spreading timescale (Sec. 1.6.2), which increases as the radius grows, naturally reproducing the observed widening of pulses in GRB 230307A:

$$\mathrm{FWHM}_i = \frac{R_{c,i}}{2c\Gamma^2} = \frac{1}{2c\Gamma^2} \left(\frac{\beta}{\beta - \beta_s}\right) (R_0 + c\beta_s\, t_{e,i}) \,. \tag{57}$$

The total number of counts N_{cts} is kept constant for all pulses (implying that each pulse carries the same amount of energy). The peak rate of each pulse is then simply given by the

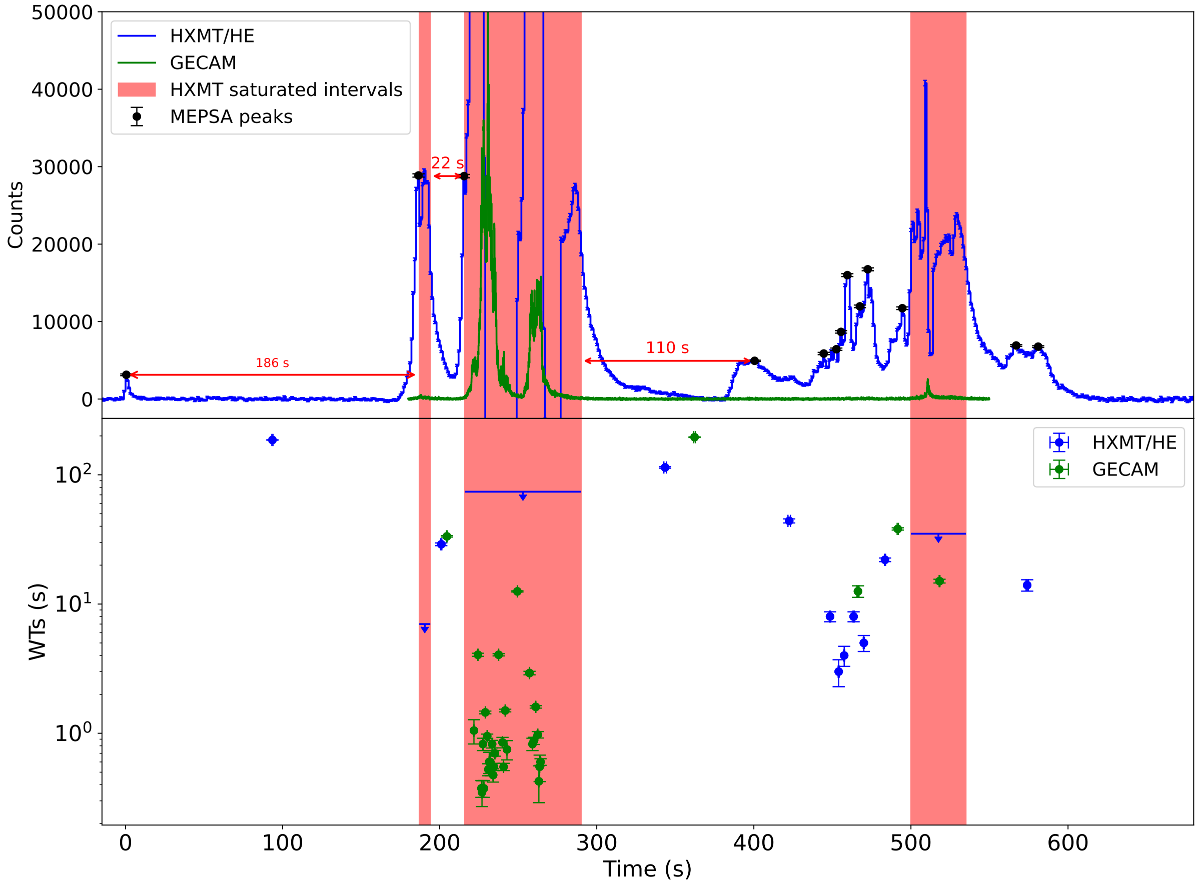

Figure 75: *Top panel*: Background-subtracted LCs of GRB 221009A from HXMT/HE (blue, 1 s binning) and GECAM (green, 50 ms binning). Red shaded areas mark intervals where HXMT/HE is affected by saturation. Peaks detected by MEPSA are shown as black markers. The two long quiescent intervals between the precursor and main emission (186 s) and between the main and late emission (110 s) are indicated. *Bottom panel:* WTs derived from MEPSA detections in HXMT/HE and GECAM data as a function of time. WTs inside HXMT/HE saturated intervals are computed from GECAM measurements. Reproduced from Maccary et al. (2026).

ratio of the total counts over the width of the pulse, given by FWHM_i, multiplied by an extra term accounting for the early rise of the GRB:

$$P_i = \frac{N_{cts}}{\mathrm{FWHM}_i} \times \Big(1 - \exp(-t/\tau_r)\Big), \tag{58}$$

where τ_{rise} is the timescale associated to the early rise of the LC. This extra term can be seen as an initial opacity, since the first shocks can occur in a region close to the central engine, where the optical depth for pair production can be moderately high.

Using the previous equations, we can compute the shape of each pulse, assuming the pulse template of Norris et al. (1996) with a common peakedness $\nu = 2$ and decay-to-rise time ratio $r = 3$. The synthetic LC is obtained as a superposition of all these pulses.

This model is illustrated in Fig. 76 and further described in Maccary et al. (2026). The (optimised)[12] parameters of this model are:

- $R_0 = 3.1^{+3.8}_{-1.5} \times 10^{10}$ cm the initial radius of the target shell at $t = 0$,
- $\Gamma = 94^{+8}_{-1}$ the Lorentz factor of the emitted by he central engine,
- $\Gamma_s = 8.6^{+0.1}_{-0.4}$ the Lorentz factor of the target shell,
- $\tau = 10.9^{+1.0}_{-2.3}$ s the e-folding timescale characterising the evolution of the waiting times,
- $N_0 = 1270^{+110}_{-90}$ the number of elementary energy bunches,
- $\tau_{\mathrm{rise}} = 2.9^{+0.3}_{-0.5}$ s the e-folding timescale characterising the early rise of the peak rates,
- $N_{\mathrm{cts}} = 920^{+30}_{-20}$ cts the number of counts in each pulse.

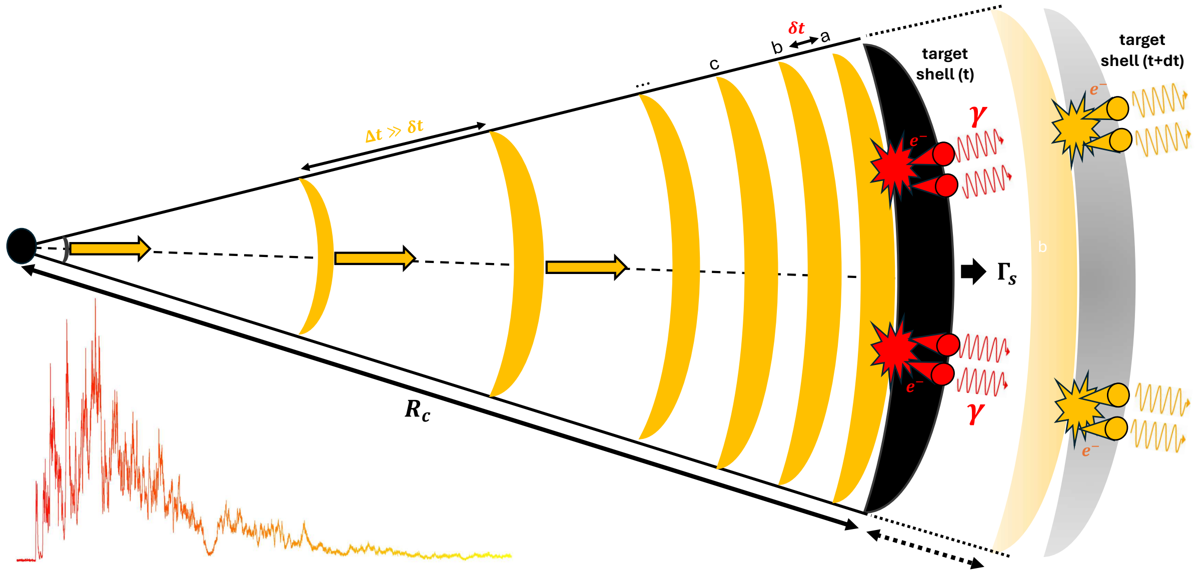

Figure 76: Sketch of the target-shell model explaining the time profile of GRB 230307A. Energy bunches emitted from the central engine collide with a slower target shell (shown in black) that was emitted earlier by the central engine. The first shocks that occur close to the central engine correspond to the intense and narrow peaks observed in the early prompt emission of GRB 230307A, while the later shocks happening at larger distances are associated with the dim and broad pulses seen in the extended emission phase.

We proved that our model was able to well reproduce the temporal properties of GRB 230307A listed above (Fig. 78). Moreover, we carried out a few tests to ensure that our model was physically consistent. In particular,

(a) We computed the optical depth to pair production and verified that the shocks are happening in an optically thin regime (except for the earliest ones, where the opacity reaches a few tens before dropping below unity).

---

[12] The parameters where optimised using a genetic algorithm, as described in Sec. 4.2.2.

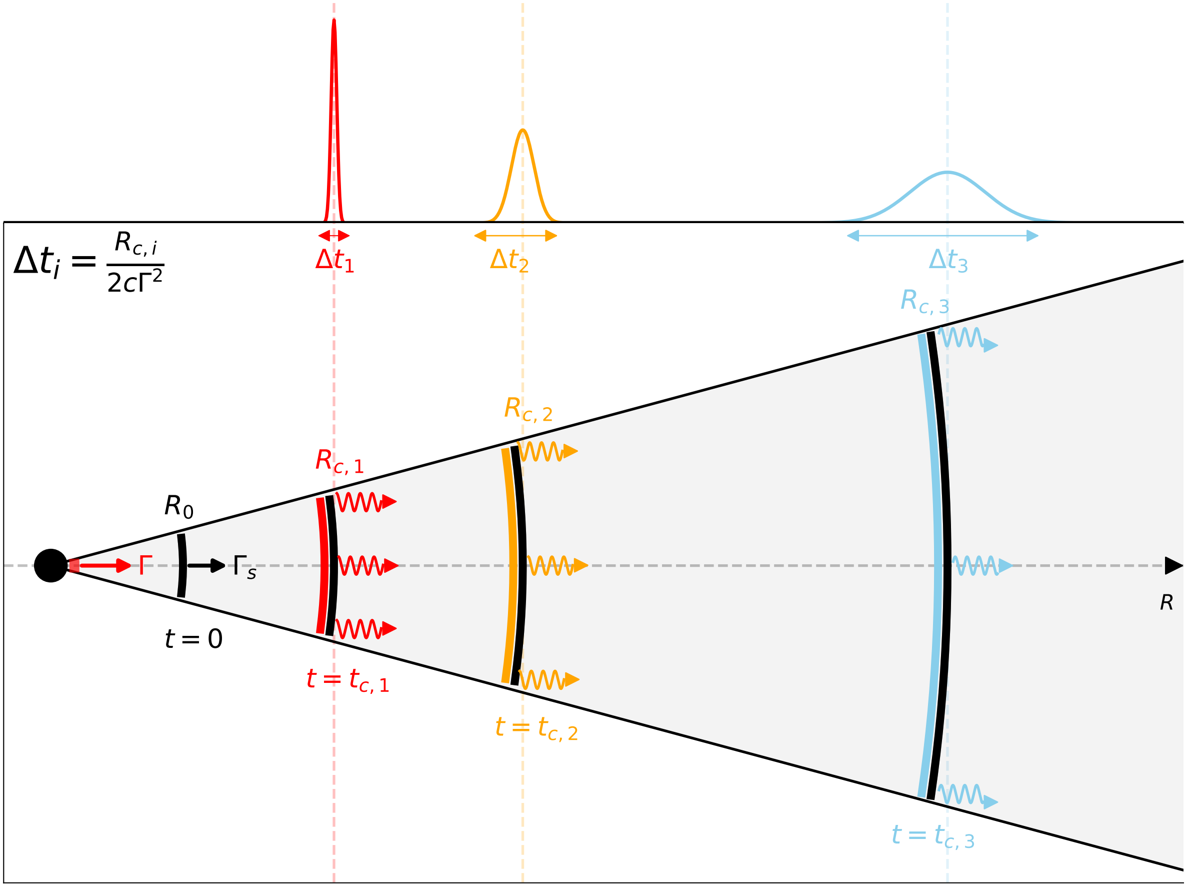

Figure 77: Sketch illustrating the temporal widening of the pulses observed during the prompt emission of GRB 230307A. This widening is due to the angular spreading timescale, i.e. the temporal delay between on-axis photons and photons emitted at the edge of the jet (Sec. 1.6.2). The first pulse (in red), resulting from a shock happening close to the central engine, is narrow and intense owing to the short radius and high Doppler boosting. The two subsequent pulses that occur at larger radii (in orange and blue), because of the larger delays and smaller Doppler boosting, are broader and fainter than the first one.

(b) We also checked that the shocks between the target shell and subsequent shells occur before any possible IS happening within the train of ejecta, i.e. at radii smaller than the IS emission radii given by Eq. (15). This condition is indeed satisfied in our model.

Some uncertainties remain in our model, in particular, regarding the origin of the target shell. There are two possibilities that we envisaged in our study: (i) the target shell corresponds to a shell that has begun to decelerate and will later collide with the ISM, producing the afterglow; (ii) the target shell consists of material expelled during merger, such as the dynamical ejecta.

The principal drawback of scenario (i) lies in the position of the deceleration radius, which for standard short GRB environments lies above the shock radii. Regarding scenario (ii), our model predicts a target shell with a Lorentz factor of a few units, implying a velocity very close to the speed of light ($v \simeq 0.99c$). Only a tiny fraction of the dynamical ejecta can reach such velocities during the merger.

A possible scenario is that some material is boosted by a prior activity of the central engine. In this picture, the newly formed central engine would launch some early shells that collide with the dynamical ejecta below the photosphere. Below the photosphere, the energy stored in these early shocks would not be dissipated to radiation but is instead reprocessed into kinetic energy, allowing the ejecta (which later forms the target shell) to reach the required velocity.

Other scenarios could be imagined, such as a central engine launching for some reason a first slow and massive shell followed by lighter, faster shells. We hope that this event will encourage the theoretical GRB community to reconsider existing emission models to account for the properties of such events.

This work, published in Journal of High Energy Astrophysics, is reported in Appendix A.10 of this thesis.

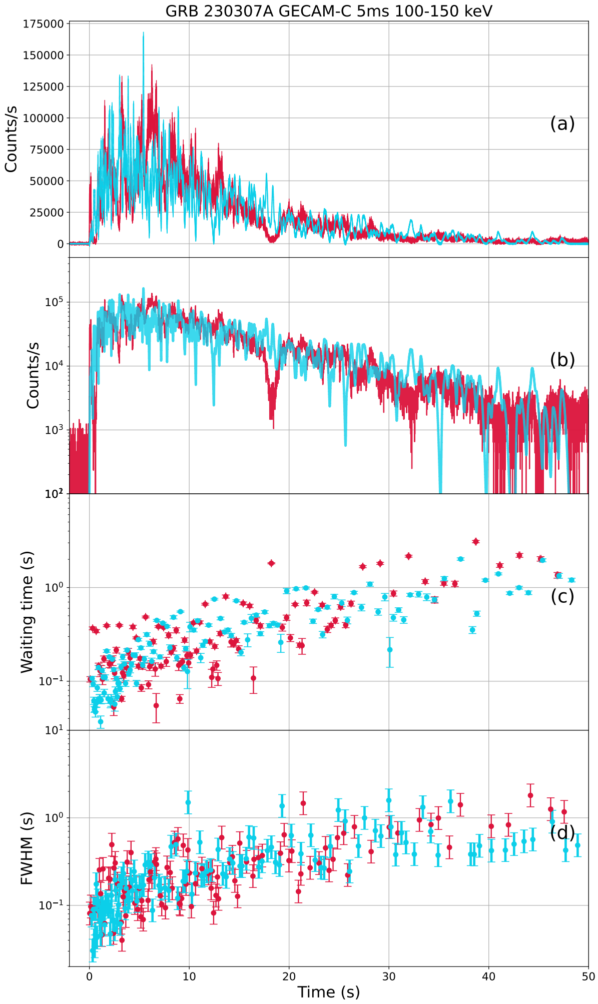

Figure 78: Comparison of the temporal properties of the synthetic LCs produced by the target shell model with GRB 230307A real data. Panels (a) and (b) illustrate the temporal evolution of count rates, (a) in linear and (b) in logarithmic scale. Panels (c) and (d) show the temporal evolution of the WTs and of the pulse FWHMs, respectively. Red points show real data, while blue points are simulated according to the target shell model. Reproduced from Maccary et al. (2026).

3.4 CONCLUSIONS

In this chapter, we saw that multiple aspects of the GRB prompt emission can be probed by studying its temporal variability. In particular,

- **The origin of variability in GRB theoretical models**. In Maccary et al. (2024a), we confirmed the existence of two GRB families, peak-poor and peak-rich GRBs, exhibiting a few (resp. many) peaks in their LCs. The existence of these two families is directly associated with the presence or the absence of variability at short timescales in GRB time profiles. The origin of this discrepancy is probably a combination of several factors: activity of the central engine, interaction with the stellar environment, influence of geometry and jet structure, and variability may arise also from relativistic turbulent magnetic reconnection events occurring within the emission region. In this sense, variability probes numerous facets of the GRB phenomenon.

- **Correlations involving variability.** In Maccary et al. (2025), we confirmed the existence of correlations between the MVT and observables such as peak luminosity, Lorentz factor, jet opening angle (actually more representative of the viewing angle), etc. These correlations can be directly used to probe the jet launching mechanism and the jet structure.

- **Clues about the GRB progenitor.** In particular, we showed in Maccary et al. (2025) that the MVT is a promising indicator of the nature of the GRB progenitor, as extremely short MVT values of a few milliseconds seem to be found only in short GRBs with or without extended emission and in the rare cases of long GRBs originating from COMs. We also found recently in Maccary et al. (2026) a peculiar set of temporal properties in the time profile of a GRB belonging to this latter class, namely GRB 230307A. This set of properties seems to be characteristic of the class, and therefore provides ways to identify its members directly from their γ-ray time profile, offering additional clues for their detection.

Overall, temporal variability thus emerges as a powerful diagnostic tool, offering unique insights into the inner workings of GRBs, ranging from their central engine activity to the nature of their progenitors, including also the emission mechanisms and jet dynamics. The study of the aforementioned aspects of prompt emission temporal variability led to the publication of three different articles, which are reported in Appendix A.8, A.9, and A.10 of this thesis.

4

GAMMA-RAY BURSTS AS STOCHASTIC PROCESSES

The temporal behaviour of GRB prompt emission is puzzling: the wide variety of observed morphologies makes it difficult for any deterministic model to account for all of them. A possible way to explain this remarkable diversity of temporal profiles is to interpret them as random realisations of a common underlying stochastic process.

Although evidence of deterministic behaviour have been suggested (Greco et al., 2011), the nature of the prompt emission remains elusive. The hypothesis that they are instead governed by a stochastic process has been put forward in the literature (Guidorzi et al., 2015), and has been successfully used to reproduce prompt emission temporal properties (Bazzanini et al., 2024; Maistrello et al., 2025).

In this chapter, assuming the latter hypothesis, we adopted here a new approach to model GRB LCs, fundamentally different from those presented in the previous chapters. In particular, we modelled the prompt emission using stochastic differential equations (SDEs), a concept widely applied across various disciplines, including astrophysics, finance and economics, biology, climate and Earth sciences. This approach, to our knowledge, was not considered so far in the GRB literature.

4.1 STOCHASTIC DIFFERENTIAL EQUATIONS

An SDE is a differential equation involving at least one stochastic term. The solution of such an equation is a stochastic process.

The general form of an SDE can be expressed as:

$$dX_t = \mu(X_t, t)dt + \sigma(X_t, t)dW_t, \tag{59}$$

where X_t is the unknown stochastic process, $\mu(X_t, t)$ and $\sigma(X_t, t)$ are called *drift* and *diffusion* terms, respectively, and W_t denotes a Wiener process. If $\sigma = 0$, Eq. (59) becomes an ordinary differential equation, with a deterministic solution. The stochastic character is therefore ruled by the diffusion term.

W_t is referred to as Wiener process, or equivalently called a Brownian motion, and satisfies the following temporal properties.

- $W_0 = 0$;
- $\forall\, 0 \leqslant t_1 \leqslant t_2$, $W_{t_2} - W_{t_1} \sim \mathcal{N}(0, t_2 - t_1)$[1];
- W_t has independent increments. That is, for all $0 \leqslant t_1 \leqslant t_2 \leqslant t_3 \leqslant \ldots \leqslant t_n$; $W_{t_n} - W_{t_{n-1}}$, $W_{t_{n-1}} - W_{t_{n-2}}$, ..., $W_{t_2} - W_{t_1}$ are jointly independent.
- W_t has continuous sample paths.

---

[1] We adopt the following standard notation for a random variable X that is normally distributed with expected value μ and standard deviation σ: $X \sim \mathcal{N}(0, \sigma^2)$.

In particular, $W_t - W_0 = W_t \sim \mathcal{N}(0, t)$, and so the expected values are $\mathbb{E}[W_t] = 0$ and $\mathbb{E}[W_t^2] = t = \mathbb{V}[W_t]$. Lastly, we can define a more general stochastic process built on Brownian motion, by simply rescaling it by a positive factor, i.e. $\tilde{W}_t = \sqrt{q}\, W_t$, with $q > 0$. In this case, $\mathbb{E}[\tilde{W}_t] = 0$ and $\mathbb{V}[\tilde{W}_t] = qt$. This process is illustrated in Fig. 79.

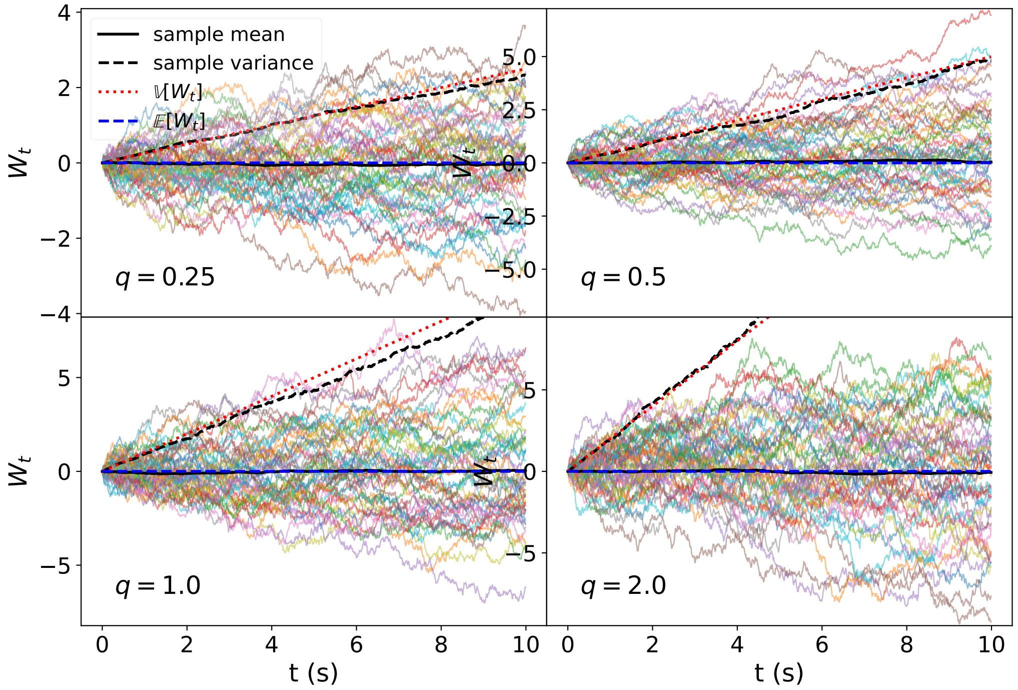

Figure 79: Realisations of the rescaled Brownian motion $\tilde{W}_t$. The coloured lines are different realisations of the stochastic process. The solid and dashed black lines represent the sample mean and the sample variance, respectively. The dashed blue line shows the expected value and the dotted red line indicates the expected variance. The four different panels indicate different values of the rescaling factor q.

4.1.1 *Itô's lemma*

The previous definition of the SDE is not entirely correct from a mathematical point of view. A more rigorous formulation requires the concept of the Itô integral, that we will not detail here. The SDE in its integral form can be written as:

$$X_t - X_0 = \int_0^t dX_t = \int_0^t \mu(X_t, t)\,dt + \int \sigma(X_t, t)\,dW_t, \tag{60}$$

where the last term is referred to as the *Itô's integral* and is a peculiar mathematical object. In particular, the rules of classical calculus do not apply to these objects, and one needs to use the so-called *Itô's calculus* to study them.

An example of the difference between classical and stochastic calculus is given by *Itô's lemma*, which extends the chain rule formula to the case of stochastic variables.

Suppose X_t is a solution of the SDE given by Eq. (59) and consider an arbitrary function $f : (\mathbb{R}, \mathbb{R}^+) \to \mathbb{R}$, twice differentiable in the first argument and once differentiable in the second. Then Itô's lemma provides the rule for differentiation in the case of stochastic variables:

$$df(X_t, t) = \frac{\partial f}{\partial t}(X_t, t)dt + \frac{\partial f}{\partial X_t}(X_t, t)dX_t + \frac{1}{2}\sigma(X_t, t)^2 \frac{\partial^2 f}{\partial X_t^2}(X_t, t)dt \,. \tag{61}$$

Note that the last term is not present in the classical chain rule, and is purely arising because X_t is a stochastic process verifying Eq. (59).

Intuitively, one can understand Ito's formula by applying the Taylor expansion *at second order* to the function f of the two variables (X_t, t):

$$df(X_t, t) = \frac{\partial f}{\partial t}dt + \frac{1}{2}\frac{\partial^2 f}{\partial t^2}dt^2 + \frac{\partial f}{\partial X_t}dX_t + \frac{1}{2}\frac{\partial^2 f}{\partial X_t^2}dX_t^2 + \frac{\partial^2 f}{\partial X_t \partial t}dX_t dt + ... \tag{62}$$

Using Eq. (59), we develop dX_t^2 as

$$dX_t^2 = (\mu^2 dt^2 + \sigma^2 (dW_t)^2 + 2\mu\sigma dX_t dW_t). \tag{63}$$

We now keep only first order terms in dX_t and dt. Since W_t verifies $(dW_t)^2 = dt$, the second-order term in dW_t is actually a first order term in dt that must be kept in the formula when approximating to first order. Instead $dW_t dt \propto dt^{3/2}$. Keeping only first order terms, we eliminate therefore dt^2 and $dW_t dt \sim dt^{3/2}$ terms. In particular, $dX_t dW_t$ contains one dt^2 and one $dW_t dt$ term and is therefore neglected when keeping only first order terms.

$$df(X_t, t) = \frac{\partial f}{\partial t}dt + \cancel{\frac{1}{2}\frac{\partial^2 f}{\partial t^2}dt^2} + \frac{\partial f}{\partial X_t}dX_t + \frac{1}{2}\frac{\partial^2 f}{\partial X_t^2}(\cancel{\mu^2 (dt)^2} + \cancel{2\mu\sigma dX_t dt} + \sigma^2 dt) + \cancel{\frac{\partial^2 f}{\partial X_t \partial t}dX_t dt}. \tag{64}$$

We therefore retrieve the formula previously enounced

$$df(X_t, t) = \frac{\partial f}{\partial t}dt + \frac{\partial f}{\partial X_t}dX_t + \frac{1}{2}\sigma^2 \frac{\partial^2 f}{\partial X_t^2}dt. \tag{65}$$

4.1.2 *Example: Langevin equation*

Many examples of SDEs can be found in physics. The most famous one is probably the Langevin equation, introduced by Paul Langevin in 1908 (Langevin, 1908)[2] as an alternative derivation of the properties of Brownian motion to that proposed by Albert Einstein in 1905 (Einstein, 1905). This equation describes the motion of a particle in a fluid subject to both deterministic and random forces, corresponding to the damping and the collisions with molecules of the fluid, respectively.

The Langevin equation reads:

$$m\frac{d\mathbf{v}}{dt} = -\lambda \mathbf{v} + \boldsymbol{\eta}(t), \tag{66}$$

---

[2] https://archive.org/details/rcin.org.pl.WA35_226705_8818_Art15_194893/mode/2up

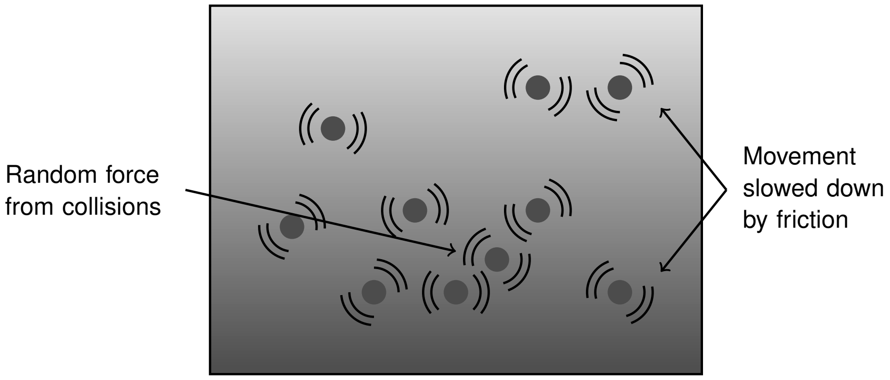

Figure 80: Illustration of the model used by Paul Langevin to describe Brownian motion. From Särkkä and Solin (2019).

where m is the mass of the particle, $\boldsymbol{v}$ its velocity, λ the damping coefficient[3], and $\boldsymbol{\eta}(\mathbf{t})$ a random force, due to the random collisions with the molecules of the fluid.

From now on, we restrict ourselves to the one–dimensional case in order to simplify the derivation. The one–dimensional Langevin equation then reads:

$$m\frac{d^2x}{dt^2} = -\lambda\frac{dx}{dt} + \eta(t), \tag{67}$$

where x is the position of the particle, satisfying $v = \frac{dx}{dt}$. If we multiply this equation by x, using the two following mathematical identities:

$$\frac{1}{2}\frac{d}{dt}(x^2) = x\frac{dx}{dt} \tag{68}$$

and

$$\frac{1}{2}\frac{d^2}{dt^2}(x^2) = \left(\frac{dx}{dt}\right)^2 + x\frac{d^2x}{dt^2}, \tag{69}$$

we obtain

$$m\left(\frac{1}{2}\frac{d^2}{dt^2}(x^2) - \left(\frac{dx}{dt}\right)^2\right) = -\frac{\lambda}{2}\frac{d}{dt}(x^2) + x\eta. \tag{70}$$

Calculating the expected value $\mathbb{E}[]$ of both sides, it is

$$m\left(\frac{1}{2}\frac{d^2}{dt^2}\mathbb{E}[x^2] - \mathbb{E}\left[\left(\frac{dx}{dt}\right)^2\right]\right) = -\frac{\lambda}{2}\frac{d}{dt}\mathbb{E}\left[(x^2)\right] + \mathbb{E}[x\eta]. \tag{71}$$

Assuming that the force is uncorrelated with the position yields $\mathbb{E}[x\eta] = 0$.

The equipartition theorem allows one to write

$$\mathbb{E}\left[\left(\frac{dx}{dt}\right)^2\right] = \frac{k_B T}{m}. \tag{72}$$

---

[3] When the damping force is given by Stokes' law, the damping coefficient λ is equal to $6\pi\eta r$, where η is the viscosity, and r is the diameter of the particle.

Letting $\mu(t) \coloneqq \frac{d}{dt}\mathbb{E}[x^2]$, we obtain the following ordinary differential equation

$$\frac{m}{2}\frac{d\mu}{dt} + \frac{\lambda}{2}\mu = k_B T, \tag{73}$$

which, assuming $\mu(0) = 0$, yields

$$\mu(t) = \frac{2k_B T}{\lambda}(1 - e^{-t/\tau}), \tag{74}$$

with $\tau = m/\lambda$.

Integrating again to obtain the mean square displacement and taking the limit as time goes to infinity, we retrieve the result found first by Einstein

$$\mu(t) = \mathbb{E}[x^2] = \frac{2k_B T}{\lambda}t. \tag{75}$$

If we assume that the stochastic force can be written as $\eta(t) = m\sigma W_t$, we can rewrite the Langevin equation in a form analogous to Eq. (59):

$$dV_t = -\theta V_t \, dt + \sigma \, dW_t, \tag{76}$$

where V_t replaces $\nu(t)$ and $\theta = \lambda/m$. This kind of SDE is also referred to as an *Ornstein–Uhlenbeck* (O-U) process.

To solve this equation, we first consider the deterministic case, i.e. when the stochastic term is neglected ($\sigma = 0$). In that case, Eq. (76) reduces to a simple exponential decay:

$$V_t = V_0 e^{-\theta t}. \tag{77}$$

Let us now return to the stochastic case and define a new process $Y_t = e^{\theta t} V_t$. Applying Itô's lemma (Eq. (61)) to $f(V_t, t) = e^{\theta t} V_t$, with

$$\frac{\partial f}{\partial t} = \theta e^{\theta t} V_t, \qquad \frac{\partial f}{\partial V_t} = e^{\theta t}, \qquad \frac{\partial^2 f}{\partial V_t^2} = 0,$$

we obtain

$$dY_t = \theta e^{\theta t} V_t \, dt + e^{\theta t} \, dV_t. \tag{78}$$

Substituting Eq. (76) into the expression above yields

$$dY_t = \theta e^{\theta t} V_t \, dt + e^{\theta t}(-\theta V_t \, dt + \sigma \, dW_t) = \sigma e^{\theta t} \, dW_t. \tag{79}$$

Integrating both sides from 0 to t, and reverting to $V_t = e^{-\theta t} Y_t$, we obtain the solution

$$V_t = V_0 e^{-\theta t} + \sigma \int_0^t e^{-\theta(t-s)} \, dW_s. \tag{80}$$

We thus see that the solution consists of a deterministic exponential decay term and an additional stochastic contribution arising from the Wiener process.

We can retrieve the result of Eq. (75) based on the following approach.

The displacement is linked with velocity according to $dX_t = V_t dt$, hence

$$X_t - X_0 = \int_0^t V_s \, ds \tag{81}$$

The mean square displacement is therefore given by

$$\mathbb{E}[(X_t - X_0)^2] = \int_0^t \int_0^t C(s, s') ds ds', \tag{82}$$

where $C(s, s') = \mathbb{E}[V_s V_s']$ is the autocorrelation function.

To compute $C(s, s')$, we need to compute the product $V_s V_s'$ and compute its mean. This computation will involve the product of four terms. The three first ones would vanish, the first one ($\propto V_0^2$) when s or s' goes to infinity (because proportional to $e^{-(s+s')}$), and the two cross products because $\mathbb{E}[dW_s] = \mathbb{E}[dW_s'] = 0$, leaving us with the last term which writes:

$$\mathbb{E}[V_s V_s'] = \sigma^2 \int_0^s \int_0^{s'} e^{-\theta(s+s'-u-v)} \mathbb{E}[dW_u dW_v] \tag{83}$$

since $\mathbb{E}[dW_u dW_v] = \delta(u - v) du$

$$\mathbb{E}[V_s V_s'] = \sigma^2 \int_0^s e^{-\theta(s+s'-2u)} du = \frac{\sigma^2}{2\theta} e^{-\theta(s'-s)}. \tag{84}$$

We implicitly assumed here $s' > s$ but the result should not depend on the ordering between s' and s as the autocorrelation function $C(s', s)$ should be a symmetric function. Therefore, in the general case,

$$C(s, s') = \frac{\sigma^2}{2\theta} e^{-\theta|s-s'|}, \tag{85}$$

which also provides the expected value of V_t^2 in the permanent regime $t \to \infty$,

$$\mathbb{E}[V_t^2] = \frac{\sigma^2}{2\theta}. \tag{86}$$

We can now compute the mean square displacement

$$\mathbb{E}[(X_t - X_0)^2] = \frac{\sigma^2}{2\theta} \int_0^t \int_0^t e^{-\theta|s'-s|} ds ds'. \tag{87}$$

This integral yields (see Sect. A.6 for a proof of this statement)

$$\int_0^t \int_0^t e^{-\theta|s'-s|} ds ds' = \frac{2}{\theta^2}[\theta t - 1 + e^{-\theta t}], \tag{88}$$

hence in a permanent regime $t \gg 1/\theta$,

$$\mathbb{E}[(X_t - X_0)^2] = \frac{\sigma^2}{\theta^2} t \, . \tag{89}$$

By using again the equipartition theorem, providing $\mathbb{E}[V_t^2] = \frac{k_B T}{m}$, we obtain[4]

$$\sigma^2 = \frac{2\theta k_B T}{m} . \tag{90}$$

We therefore retrieve

$$\mathbb{E}[(X_t - X_0)^2] = \frac{2k_B T}{\lambda} t . \tag{91}$$

This illustrates the analogies between Langevin equation, which describes Brownian motion, and the O-U process, which is a stochastic process whose temporal evolution is governed by an SDE.

4.1.3 *Example: Geometric Brownian motion*

A geometric Brownian motion is a stochastic process that verifies the following SDE:

$$dX_t = \mu X_t dt + \sigma X_t dW_t , \tag{92}$$

in which the stochastic term is also proportional to the process itself. We first solve this equation in the deterministic case ($\sigma = 0$), as in the previous section, to obtain an intuition about the solution in the general case. We then obtain

$$\frac{dX_t}{X_t} = d(\ln X_t) = \mu dt, \tag{93}$$

hence the solution in the deterministic case is simply given by

$$X_t = X_0 e^{\mu t}. \tag{94}$$

We now consider the general case: let $Y_t = \ln X_t = f(X_t, t)$ and apply Itô's lemma to compute dY_t:

$$d(\ln X_t) = 0 \times dt + [1/X_t] \times dX_t + \frac{1}{2}[-1/X_t^2] \times (\sigma X_t)^2 \times dt, \tag{95}$$

The terms between square brackets are the first time derivatives of $f(X_t, t)$ and the first and second derivatives with respect to X_t, respectively.

Hence, we obtain

$$d(\ln X_t) = \frac{dX_t}{X_t} - \frac{\sigma^2}{2} dt. \tag{96}$$

Using Eq. (92) into this equation, we obtain

$$d(\ln X_t) = (\mu - \frac{\sigma^2}{2}) dt + \sigma dW_t, \tag{97}$$

---

[4] This result, linking the noise intensity to the strength of the dissipative viscous force, is also known as the fluctuation-dissipation theorem.

which yields the solution of the SDE related to the geometric Brownian motion in the stochastic case

$$X_t = X_0 e^{(\mu - \frac{\sigma^2}{2})t} e^{\sigma W_t}. \tag{98}$$

For $\sigma = 0$, we effectively retrieve the solution of the deterministic case given in Eq. (94), and the general solution is the product of the deterministic term and the stochastic one, rather than the sum. The stochastic process associated with Eq. (92) is called a *geometric* Brownian motion is because its logarithm evolves similarly to Brownian motion. [5]

Knowing the solution, the mean and variance of this stochastic process can be easily computed. In fact, the expected value is given by:

$$\mathbb{E}[X_t] = X_0 e^{(\mu - \frac{\sigma^2}{2})t} \mathbb{E}[e^{\sigma W_t}]. \tag{99}$$

Using the Taylor expansion of the exponential function combined with the statistical properties of W_t, one can prove (see Sect. A.5 in Appendix for a full proof) that:

$$\mathbb{E}[e^{\sigma W_t}] = e^{\frac{\sigma^2 t}{2}}. \tag{100}$$

Hence,

$$\mathbb{E}[X_t] = X_0 e^{\mu t}. \tag{101}$$

The second moment $\mathbb{E}[X_t^2]$ is computed in a similar way, providing the variance:

$$\mathbb{V}[X_t] = \mathbb{E}[X_t^2] - (\mathbb{E}[X_t])^2 = X_0^2 e^{2\mu t}(e^{\sigma^2 t} - 1). \tag{102}$$

---

[5] However, it is not strictly a Brownian motion, because it does not satisfy all the properties defining the Brownian motion enounced in Sect. 4.1. In particular, because of the drift term, the expected value $\mathbb{E}[\ln X_t] = (\mu - \sigma^2/2)t$ is different from zero.

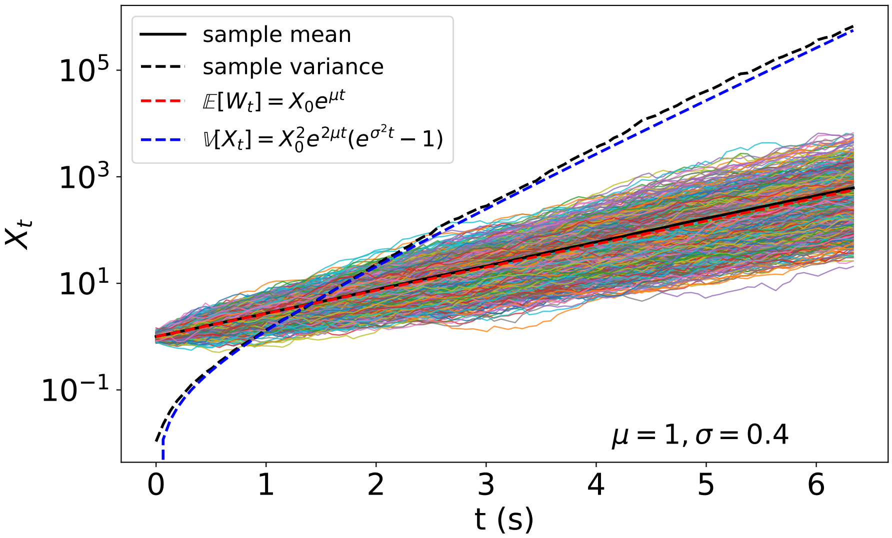

Figure 81: The geometric Brownian motion and its moments in log scale. The coloured lines represent different realisations of the stochastic process, for $\mu = 1$ and $\sigma = 0.4$. The black solid and dashed lines show the sample mean and variance, respectively. The red and blue dashed lines indicate the expected value and the variance of the stochastic process, respectively. The scale is logarithmic.

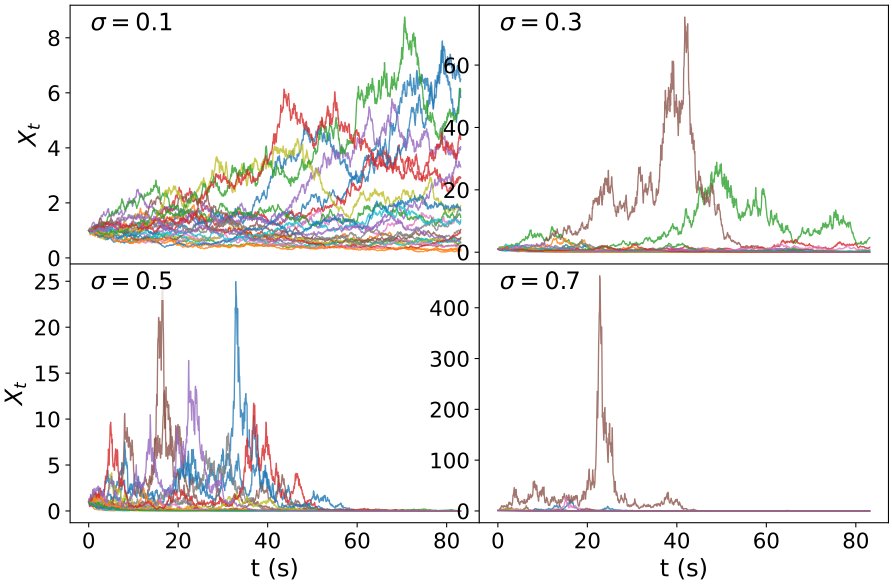

Figure 82: Different realisations of the geometric Brownian motion for different values of σ (μ is set to a fixed value of 0.01).

4.2 A STOCHASTIC DIFFERENTIAL EQUATION ADAPTED TO γ-RAY BURST LIGHT CURVES

Attempts to simulate GRB LCs within theoretical frameworks are usually carried out assuming internal shocks and/or instabilities developing within the accretion disc of a hyper-accreting BH, and/or full hydrodynamical/MHD simulations. However, owing to the persistent uncertainties on the energy dissipation mechanism(s) producing the prompt emission, these approaches are highly model-dependent, rely on some still poorly known aspects of GRB physics, and the predicted LCs often fail to reproduce some observed properties.

Here we adopted a more empirical and data-driven approach, based on the assumption that GRB LCs are different realisations of a common underlying stochastic process. Under this assumption, we tried to identify a stochastic process that accounts for the temporal properties of prompt emission. To this end, we explored the possible stochastic differential equations that can reproduce the temporal features of GRB LCs, in particular the average properties.

A similar strategy has been successfully applied to optical LCs of quasars (Kelly, Bechtold, and Siemiginowska, 2009). In this study, both long and short timescale variations were modelled with a continuous-time first-order autoregressive stochastic process CAR(1) (actually equivalent to an O-U process, also known as damped random walk). This framework allowed for a robust estimation of characteristic timescales and amplitudes of quasar flux variations characterising accretion onto super-massive BHs.

The crucial difference between AGNs and GRBs is that the former are persistent, stationary emitters whose variability can be meaningfully modelled as a stationary stochastic process. GRBs, in contrast, are short-lived, highly non-stationary, with statistical properties that evolve significantly over the duration of the burst. The non-stationary character of GRB LCs requires a specific modelling and another class of stochastic processes from those used to model quasar temporal variability.

In particular, contrary to the simple equations shown above, in the GRB case the drift term $\mu(X_t, t)$ must depend explicitly on time to describe their non-stationarity. The average post-peak aligned profile, obtained by aligning GRB time series at their peak, follows a stretched exponential of the kind $\exp\left(-(t/\tau_{se})^{1/3}\right)$ (Stern, 1996). Therefore, we built an SDE that accounts for this property.

An SDE that satisfies this property is

$$dX_t = \left[\frac{1}{2\tau_i} - \frac{1}{\tau_d} + \frac{\alpha}{t} - \frac{1}{3\tau_{se}}\left(\frac{t}{\tau_{se}}\right)^{-2/3}\right] X_t\,dt + X_t\,d\tilde{W}_t\,, \tag{103}$$

where $\tilde{W}_t = W_t/\sqrt{\tau_i}$ is a Wiener process and its variance is $E[\tilde{W}_t{}^2] = t/\tau_i$, where τ_i is the timescale over which a random instability leads to a substantial change in X_t, τ_d the timescale over which the exponential damping takes place, α an exponent modelling the early PL rise of the LC, and τ_{se} is the stretched-exponential timescale. Eq. (103) is similar to a geometric Brownian motion, however its drift term now explicitly depends on time.

A great advantage of this equation is that it can be solved analytically. Indeed, applying Itô's lemma to $Y_t = f(X_t, t) = \ln X_t$ as for the geometric Brownian motion yields:

$$dY_t = \frac{dX_t}{X_t} - \frac{dt}{2\tau_i}. \tag{104}$$

Now plugging Eq. (103) into the last equation gives:

$$d\ln X_t = \left[\cancel{\frac{1}{2\tau_i}} - \frac{1}{\tau_d} + \frac{\alpha}{t} - \frac{1}{3\tau_{se}}\left(\frac{t}{\tau_{se}}\right)^{-2/3}\right] dt - \cancel{\frac{dt}{2\tau_i}} + d\tilde{W}_t. \tag{105}$$

Integrating this equation between 0 and t and reverting from Y_t to $X_t = e^{Y_t}$ provides:

$$X_t = X_0 t^\alpha \exp\left[-\frac{t}{\tau_d} - \left(\frac{t}{\tau_{se}}\right)^{1/3} + \tilde{W}_t\right]. \tag{106}$$

The simulated GRB LCs are then simple realisations of this stochastic process, whose solution is given by Eq. (106). The stochastic character of these solutions is mainly driven by the timescale τ_i, which determines the timescale of the Brownian motion $\tilde{W}_t$.

Using Eq. (100), we obtain $\mathbb{E}[e^{\tilde{W}_t}] = \exp(t/2\tau_i)$ and therefore the expression of the expected value of the stochastic process associated with Eq. (103)

$$\mu(t) = \mathbb{E}[X_t] = X_0 t^\alpha \exp\left[-t\left(\frac{1}{\tau_d} - \frac{1}{2\tau_i}\right) - \left(\frac{t}{\tau_{se}}\right)^{1/3}\right]. \tag{107}$$

The condition $\tau_d = 2\tau_i$ corresponds to a pure stretched exponential in the average profile. We adopted the less constraining $\tau_d \lesssim 2\tau_i$, which prevents $\mu(t) \to +\infty$ as t goes to infinity. It is important to avoid this behaviour, as a GRB signal is a transient one that therefore stops after some time, unlike a persistent signal that could be modelled with $\tau_d > 2\tau_i$.

The variance of the stochastic process is computed similarly to the mean, and is given by

$$\mathbb{V}[X_t] = \mu(t)^2 \left(e^{t/\tau_i} - 1\right). \tag{108}$$

Figure 83 shows some realisations for different values of the ratio τ_d/τ_i.

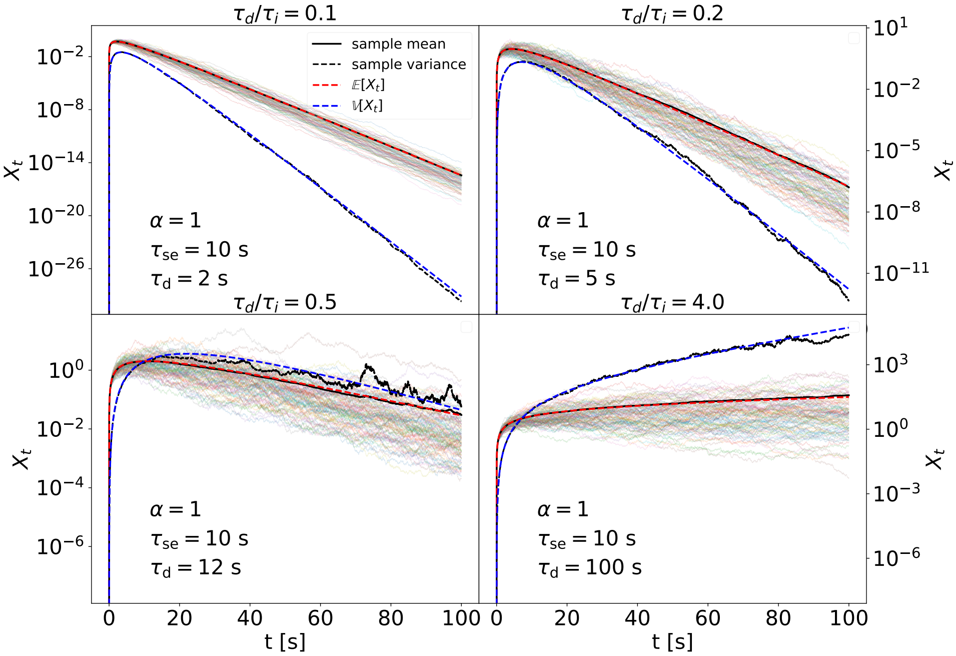

Figure 83: Different realisations of the stochastic process described by Eq. (103) for different values of τ_d/τ_i, in logarithmic scale. The four panels indicate realisations for fixed values of α, τ_{se}, and τ_i but increasing values of the ratio $\tau_d/\tau_i = 0.1, 0.2, 0.5$ and 4. The black solid and dashed lines indicate the sample mean and variance, while the red and blue dashed lines represent the expected value and variance of the stochastic process, respectively.

The normalisation value X_0 is sampled from a simple PL distribution, with parameters x_{min} and α_{pl}, the minimum value and the slope, respectively.

- τ_i is the timescale associated with the Brownian motion,
- τ_d is the timescale on which the exponential damping takes place,
- τ_{se} is the timescale associated with the stretched exponential,
- α is the PL index of the early rise of the averaged profile,
- α_{pl} is the PL index of the PL distribution from which the normalisation constant X_0 of each LC is drawn,
- x_{min} is the minimum value of this PL distribution.

The last two parameters are needed to model the S/N distribution: whereas the other parameters mainly control the variability properties, these two provide the scaling required to reproduce LCs with credible S/N ratios.

We tentatively considered alternative models, characterised by a different kind of rising part. Specifically, the initial PL behaviour t^α is replaced by an exponential rise $e^{-\tau_r/t}$, or alternatively $e^{-(t/\tau_r)^\delta}$. The 1/3 factor can be replaced by a parameter γ for a finer adjustment of the metrics.

4.2.1 *Metrics*

The values of the parameters of Eq. (103) should be such that the LCs produced by the stochastic process reproduce the temporal properties of the observed ones. To this aim, we adopted five temporal metrics that measure the similarity of the temporal properties of real vs. simulated LCs, building on the method used in Bazzanini et al. (2024) and Maistrello et al. (2025):

- the averaged normalised peak-aligned profile;
- the third moment of the averaged normalised peak-aligned profile;
- the autocorrelation function (ACF);
- the duration distribution, given by the T_{20};
- the S/N distribution.

The first metric is obtained by aligning and normalising the profiles at their peaks, and by computing the resulting averaged profile, using 150 s (that corresponds to 2343 bin time at 64 ms) before and after the peak. This metric is an extension of the average peak-aligned post-peak time profile (Stern, 1996) used in Bazzanini et al. (2024) and Maistrello et al. (2025). These functions were computed for *CGRO*/BATSE and *Swift*/BAT bursts and are shown in Fig. 84. We define a loss function which measures the overall difference between the properties of the simulated and of the observed LCs. Specifically, it is therefore the (weighted) average value of five individual losses, each of them accounting for one of the properties mentioned above.

$$\mathcal{L}_{tot} = \frac{w_{avgd}\mathcal{L}_{avgd} + w_{third}\mathcal{L}_{third} + w_{acf}\mathcal{L}_{acf} + w_{T_{20}}\mathcal{L}_{T_{20}} + w_{S/N}\mathcal{L}_{S/N}}{w_{avgd} + w_{third} + w_{acf} + w_{T_{20}} + w_{S/N}}, \qquad (109)$$

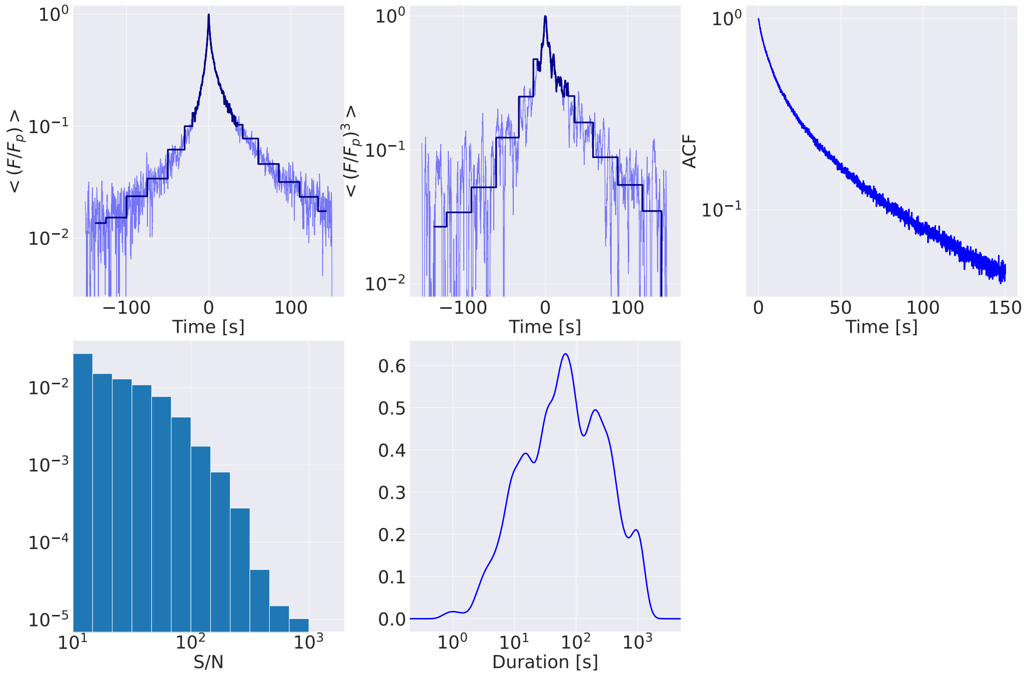

Figure 84: Five GRB properties serving as reference metrics to optimise the SDE parameters. Panel (a) represents the averaged peak-aligned profile, (b) its third moment, (c) the autocorrelation function, (d) the S/N distribution, (e) the T_{20} duration distribution.

where the w's represent the relative weight of each loss building up the total loss. The different losses are computed as follows.

- $\mathcal{L}_{\mathrm{avgd}}$ is computed on logarithmic quantities, by $\frac{1}{N}\sum_{i=1}^{N}\sqrt{|\log(\frac{y_{s,i}}{y_{r,i}})|}$, where N is the number of points, and where $y_{s,i}$ and $y_{r,i}$ are the binned versions of the simulated and real peak-aligned averaged profiles, respectively. These are obtained by binning the LC when the signal goes below a given threshold, to mitigate the effect of low statistics in the tail of the averaged profile.
- $\mathcal{L}_{\mathrm{third}}$ is computed similarly as $\mathcal{L}_{\mathrm{avgd}}$, except that cubic quantities are averaged.
- $\mathcal{L}_{\mathrm{acf}}$ as the L_2[6] distance between the simulated and observed ACFs.
- $\mathcal{L}_{T_{20}}$, as the L_2 distance between the observed and simulated T_{20} distributions, preliminary determined through a kernel density estimate applied to the logarithmic quantities.
- $\mathcal{L}_{S/N}$ is computed as $1-\log_{10}(p)$, where p is the p-value of a two-population Kolmogorov-Smirnov compatibility test between the simulated and observed S/N distributions. This formula is applied for $10^{-9} \leqslant p \leqslant 5\times10^{-2}$. When $p > 5\times10^{-2}$, $\mathcal{L}_{S/N}$ is set to 0 and to 10 when $p < 10^{-9}$.

---

[6] By L_2 distance, we intend $L_2(\{x_{s,i}\},\{x_{r,i}\}) = \sqrt{\sum_{i=1}^{N}(x_{s,i}-x_{r,i})^2}$, with $x_{s,i}$ and $x_{r,i}$ the points of a given metric either computed on the simulated on the real dataset, respectively.

4.2.2 *Genetic algorithm*

We optimised the parameters using a genetic algorithm that aims to minimise a loss function by mimicking the Darwinian natural evolution.

In this framework, an *individual* is characterised by a set of parameters that constitutes its *genome*. The *genes* are the values of the different parameters that compose the genome of the individual. A *population* of individuals is a collection of distinct genomes. The genetic algorithm evolves this initial population into a more adapted one, in which only the "fittest" individuals survive. The genetic algorithm proceeds as follows (Fig. 85).

- **Evaluation**. For each individual in the population, a set of LCs is produced, the five metrics defined in Sect. 4.2.1 are computed, and the loss function is evaluated.
- **Selection**. A given number of individuals with the best fitness (i.e. lowest loss) are selected to reproduce.
- **Reproduction**. The selected individuals mate, creating offspring that inherit part of the genes of their two parents.
- **Mutation**. In the case of mutation, gene values are randomly drawn from the parameter space, instead of being inherited from their parents.
- **New generation**. A new generation of individuals is obtained by combining reproduction and mutation, and the process is repeated iteratively.

Over successive generations, the fitness of the individuals progressively improves, ultimately converging towards a limit value. The best set of parameters is obtained by computing the median parameters among the population within the last generation[7].

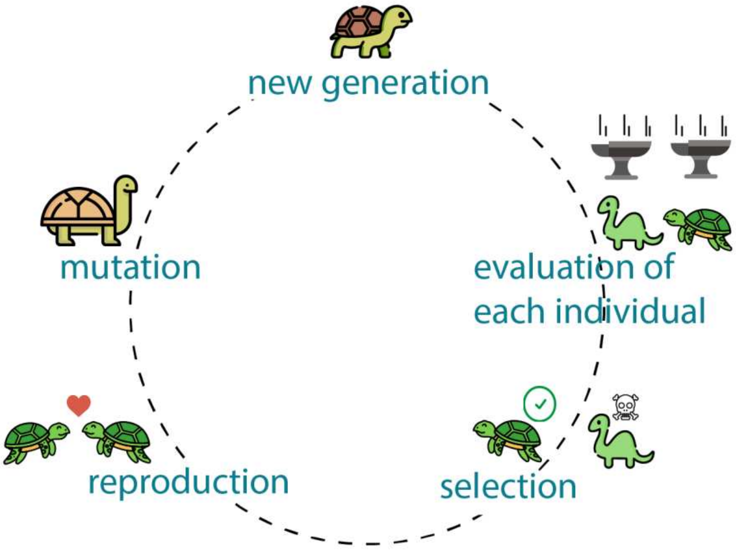

Figure 85: Scheme illustrating the different steps involved in the genetic algorithm.

---

[7] One could also use the best fitting individual, but this value is more prone to random fluctuations.

4.3 PRELIMINARY RESULTS

We obtained these optimised parameters, applied to the BATSE sample:

- $\tau_i = 3.08 \ ^{+0.07}_{-0.04}$,
- $\tau_d = 8.49 \ ^{+0.17}_{-0.42}$,
- $\alpha = 0.85 \ ^{+0.13}_{-0.14}$,
- $\tau_{se} = 2.23 \ ^{+1.50}_{-0.50}$,
- $X_0 = 0.91 \ ^{+1.74}_{-0.26}$.

In this preliminary version, we chose to assign the same normalisation X_0 for all the LCs, rather than drawing it for each realisation from a PL distribution, as we do now in a more recent version. In addition, γ was still fixed to the value of $\gamma_0 = 1/3$ and the constraint $\tau_d < 2 \times \tau_i$ was not implemented yet, although we used a weaker condition $\tau_d < 3 \times \tau_i$. At this stage of the work, the averaged profile and its third moment were computed only in the post-peak part, starting from the peak to 150 s after it.

The obtained values of the losses defined in Sect. 4.2.1 are shown in Fig. 86.

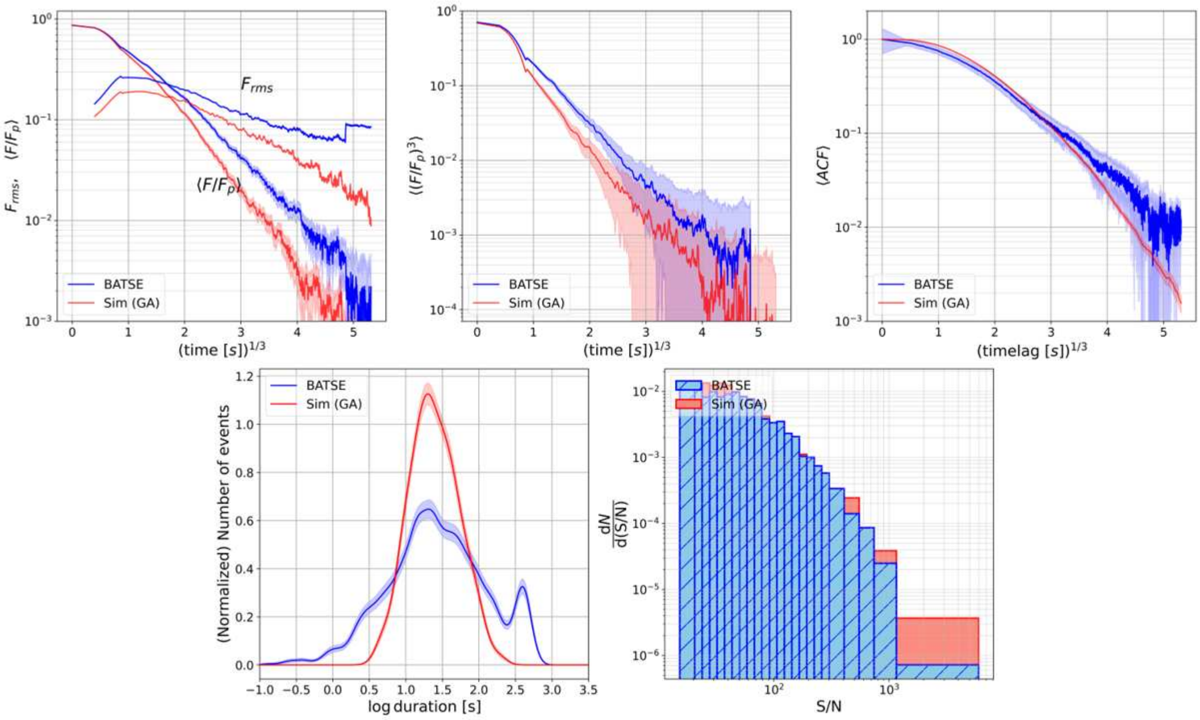

Figure 86: Results for the five losses. The five panels show the five different metrics of Sect. 4.2.1 computed either on the real (red) or simulated (blue) LCs. At this point of the work, the averaged profile and the third moment were computed only on the post-peak part of the LCs.

Some simulated LCs obtained within this model are shown in Fig. 87.

We are currently considering a modified version of the previous model in which the parameter α, originally describing the early-time power-law rise t^{α}, is replaced by an exponential rise of the form $\exp\left[-\left(\frac{\tau_r}{t}\right)^{\delta}\right]$, with τ_r and δ added to the set of free parameters of the SDE model. Instead of having X_0 as a free parameter, in this version we also sampled X_0 from a PL distribution with two parameters x_{min} (its minimum value) and α_{pl} (the slope), we replaced the $1/3$ exponent by a free parameter γ, and we enforced the condition $\tau_d < 2 \times \tau_i$. We also extended the computation of the averaged profile to the part before the peak.

A preliminary exploration yields very small values of $\tau_r \sim 10^{-2}$ s, resulting in LCs with an excessively steep initial rise. We are therefore attempting to optimise the model under the constraint $\tau_r > 1$ in order to avoid such unrealistically sharp onsets.

The optimised parameters are in this case

$$\begin{aligned}
\tau_i &= 20.03 \\
\tau_d &= 34.1 \\
\tau_r &= 1.04 \\
\tau_{se} &= 21.4 \\
\gamma &= 0.29 \\
\delta &= 5.6 \\
x_{min} &= 0.008 \\
\alpha_{pl} &= 8.1
\end{aligned}$$

The results of the losses are shown in Fig. 88.

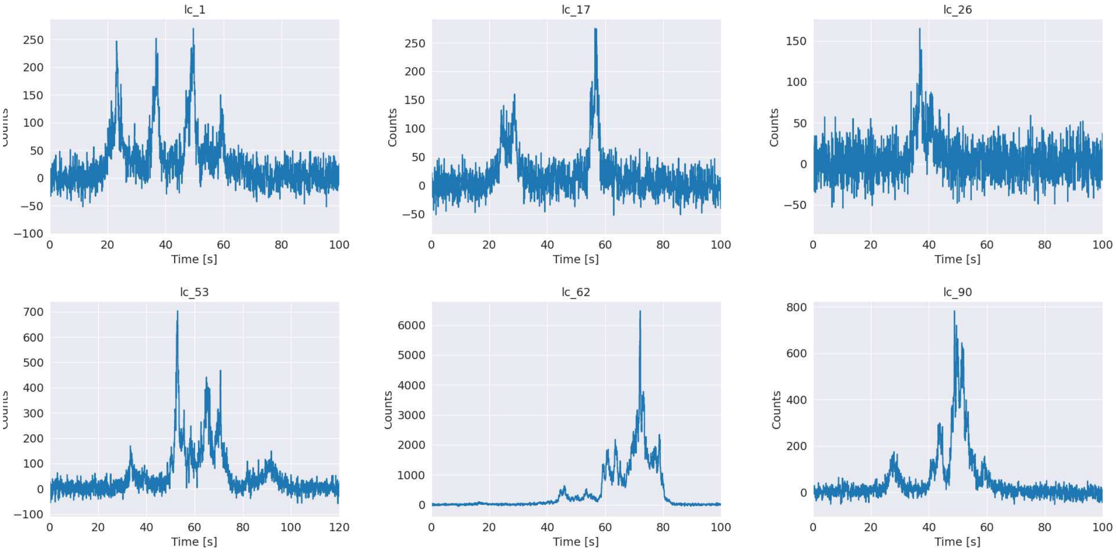

Figure 87: Realisation of the stochastic process associated with the SDE of Eq. (103), with the parameters shown above, that have been optimised using the metrics computed on the BATSE dataset.

The metrics resulting from this model are shown and compared with the observed metrics in Fig. 88 and some realisations of the stochastic process are represented in Fig. 89.

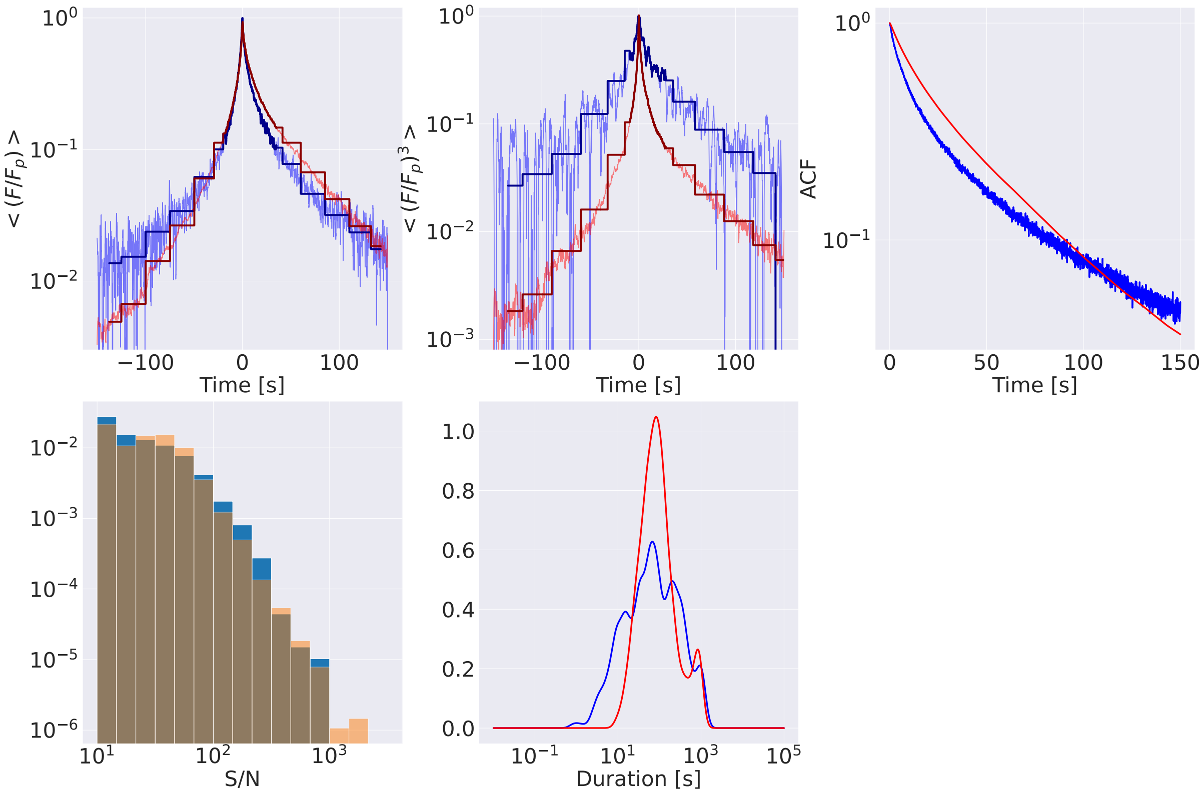

Figure 88: Same as Fig. 86, except we are now showing the results of the new model with τ_r and δ instead of α, and X_0 is now drawn from a PL distribution, with parameters α_{pl} and x_{min}. We are now showing the pre-peak part of the averaged profile along with the post-peak part. Binned simulated and real average profiles are shown in dark blue and brown, respectively. The reference metrics (in blue) used in this case are computed using the *Swift/BAT* data set

These results are still very preliminary and require further investigation. As in Sec. 3.2.4, the distribution of the number of peaks per GRB could be used to further validate the stochastic model developed above. We obtained, for this preliminary version of the model, the distribution of the number of peaks and compared it to the observed one (in the case of *Swift*/BAT). The comparison shows an excess of peak-rich GRBs in the simulated data (Fig. 90). In particular, the fraction of GRBs with more than 3 peaks is 56% in the simulated model while it is 31% in the observed distribution.

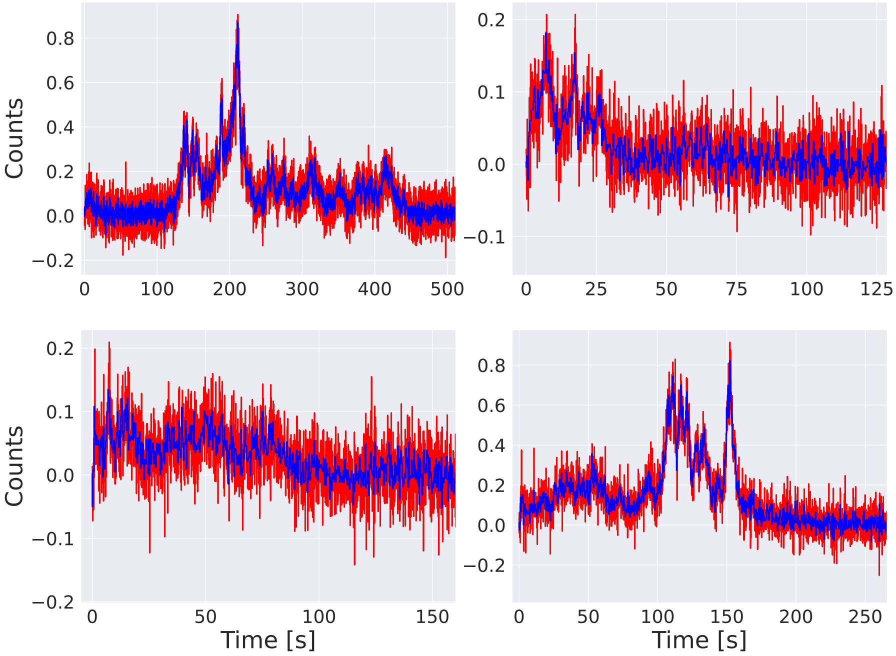

Figure 89: Realisation of the stochastic process associated with an alternative version of the SDE of Eq. (103), that have been optimised using the metrics computed on the *Swift*/BAT dataset. The red LCs are obtained with the original bin time of 64 ms, while the blue ones are rebinned versions of these LCs.

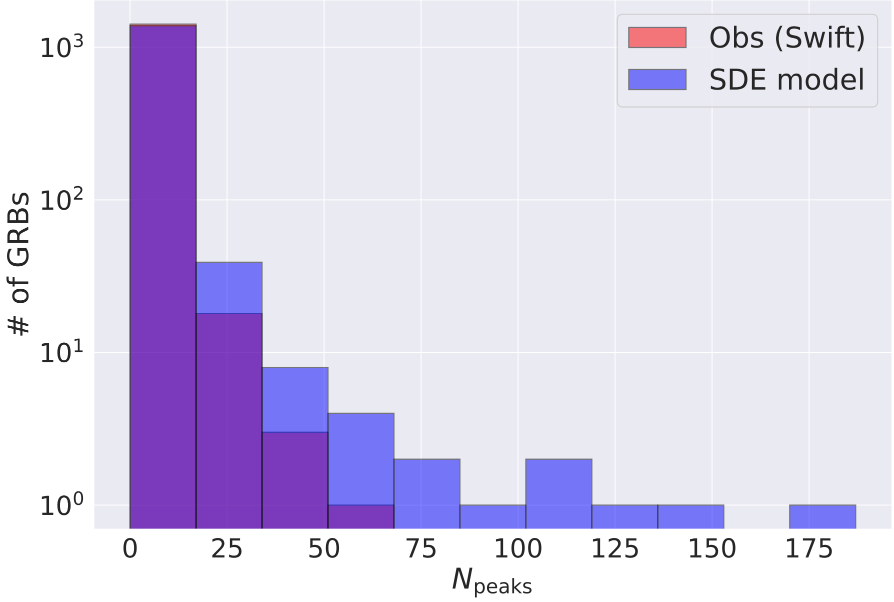

Figure 90: Distribution of the number of peaks for the simulated LCs obtained with the stochastic model of Sec. 4.2 (in blue), compared with the observed distribution in the case of *Swift*/BAT (in red).

4.4 CONCLUSION

In this chapter, we used stochastic differential equations (SDEs) to simulate credible GRB LCs. This was done by finding an SDE that reproduces the stretched exponential behaviour observed in the averaged peak-aligned profile of GRB LCs. In addition, the SDE parameters must follow a given condition to obtain a transient signal. To optimise the parameters of this SDE, we built a loss function that aims to reproduce five properties of GRB LCs: their average and third moment, the autocorrelation function, the duration and the S/N distributions. We employed a genetic algorithm to minimise this loss and find the optimised parameters. This analysis is still preliminary and the optimisation of the parameters is in progress, but the first results are encouraging.

5

ENTROPY METRICS APPLIED TO PROMPT EMISSION LIGHT CURVES

In this chapter we explored an interdisciplinary approach based on methods used in different fields of science. In principle, this setting can be highly rewarding, because problems from different fields may share a common basic logical structure and/or similar dynamics, as it is often the case whenever time series are involved. In particular, while there are specific treatments that depend on the field and on the nature of the associated signals, some methods used in time series analysis, such as Fourier transform, are shared across a wide range of scientific disciplines.

We examined various metrics that assess the degree of randomness of a signal. They are based on the concept of entropy from information theory. Entropy metrics are applied in various fields to quantify the amount of randomness in a time series or, on the contrary, to reveal deterministic features in a signal affected by noise. We calculated the entropy of GRB time series with two main purposes: (i) to investigate the stochastic versus deterministic nature of prompt emission, (ii) to define an algorithm able to identify weak GRBs with relatively low S/N.

What follows is the result of a three-month research visit at the Max Planck Institute for the Physics of Complex Systems (MPI-PKS),[1] in collaboration with the group of non-linear dynamics and time series analysis directed by Prof. Holger Kantz.

5.1 ENTROPY

Entropy, also referred to as information or Shannon entropy, is a measure of information, or a measure of the degree of uncertainty of a random variable. This concept was introduced by Claude Shannon in 1948 (Shannon, 1948). We consider a discrete random variable X that takes values within a finite alphabet χ. The alphabet, also referred to as the sample space Ω in probability theory, is the set of all possible outcomes. Let the probability mass function $p(x) = \mathbb{P}[X = x], x \in \chi$ associated with X. The entropy of the random variable X is defined as

$$H(X) = -\sum_{x\in\chi} p(x) \log_2 p(x), \tag{110}$$

where $\log_2$ is the logarithm in base 2. The entropy is measured in bits. In the particular case of a uniform distribution, where all outcomes have equal probability $p = 1/n$ to occur, with $n = |\chi|$, then

$$H(X) = -\sum_{x\in\chi} 1/n \log_2 1/n = \log_2(n) \ . \tag{111}$$

For instance, for two fair coin tosses, there are four equally probable outcomes (TT, HH, TH, HT) with probability $p = 1/4$. The entropy in this case is equal to $H = 2$ bits. On the

---

[1] https://www.pks.mpg.de/de/

contrary, for a certain event with probability $p(X = \{\chi_0\}) = 1$ of occurring, the entropy is zero. Between these two extreme cases, the entropy is different from 0. We can take a simple case to illustrate the behaviour of the entropy with the Bernoulli distribution, defined by $\chi = \{0, 1\}$, $p(X = 0) = p$ and $p(X = 1) = 1 - p$. In this case,

$$H(X) = -p \log_2 p - (1-p)\log_2(1-p) = H(p) \tag{112}$$

Figure 91 illustrates some of the basic properties of H: it peaks at $p = 1/2$, corresponding to the case of a uniform distribution and vanishes for $p = 0$ and $p = 1$, which represent the cases of a certain outcome.

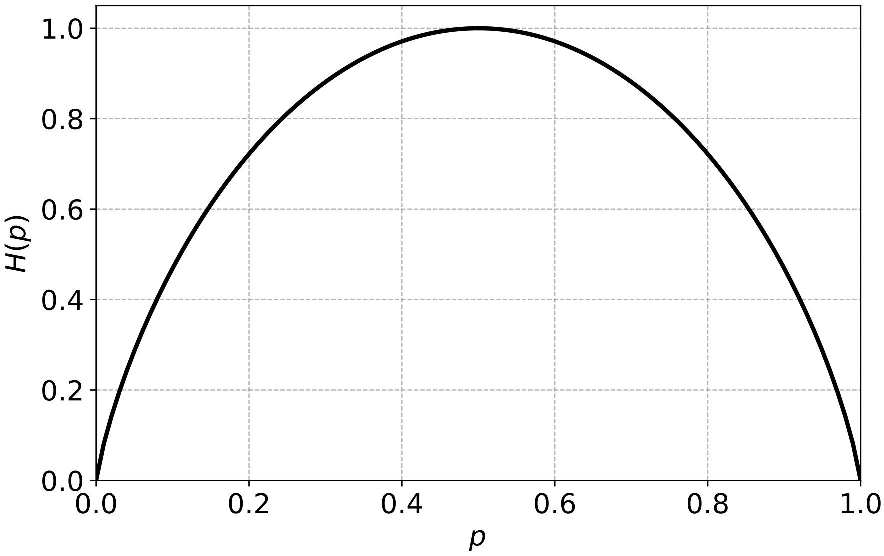

Figure 91: Entropy function for a Bernoulli-distributed random variable.

In this respect, H corresponds to the degree of uncertainty of X: if the outcome is certain, there is no room for uncertainty and H is therefore zero. Conversely, if all outcomes are equally probable, the uncertainty is the largest and the entropy is maximum.

There are generalisations of Shannon entropy, that depend on one parameter. One example is the so-called Rényi entropy, whose expression for a discrete random variable X with N possible outcomes with probabilities p_i is given by

$$R_\alpha = \frac{1}{1-\alpha} \log_2 (\sum_{i=1}^{N} p_i^\alpha) \tag{113}$$

The Rényi entropy generalises the Shannon entropy, the latter being the limit of Rényi entropy for $\alpha \to 1$. Indeed, as α goes to 1, if we let $\epsilon > 0$ such that $\alpha = 1 + \epsilon$

$$\sum_{i}^{N} p_i^\alpha = \sum_{i}^{N} p_i e^{\epsilon \log p_i} \simeq 1 + \epsilon \sum_{i} p_i \log p_i. \tag{114}$$

Therefore,

$$\log\left(\sum_i^N p_i^\alpha\right) = \log\left(1+\epsilon\sum_i^N p_i \log p_i\right) \simeq \epsilon\sum_i^N p_i \log p_i \;=(\alpha-1)\sum_i^N p_i \log(2)\times\log_2 p_i \tag{115}$$

Then, dividing the left-hand side of Eq. (115) by $\log(2)$ and $\alpha-1$, and using Eq. (113),

$$R_\alpha \simeq -\sum_i p_i \log_2 p_i, \tag{116}$$

and hence the limit of Rényi entropy when $\alpha \to 1$ is Shannon entropy.

If $\alpha > 1$, Rényi entropy is more influenced by the events of highest probability. In particular, as $\alpha \to +\infty$, Rényi entropy converges to the so called min-entropy $-\log_2 p_{\max}$.

In fact, one can easily get the following inequality

$$p_{\max}^\alpha \leqslant S(\alpha) \leqslant n p_{\max}^\alpha, \tag{117}$$

with $S(\alpha) = \sum_i^N p_i^\alpha$.

Applying logarithms on both sides of the inequality and dividing by $1-\alpha < 0$, one gets

$$\frac{\alpha\log_2 p_{\max} + \log_2 n}{1-\alpha} \leqslant R_\alpha \leqslant \frac{\alpha\log_2 p_{\max}}{1-\alpha}. \tag{118}$$

As both sides tend to $-\log_2 p_{\max}$, by the sandwich theorem we have as announced

$$\lim_{\alpha\to\infty} R_\alpha = -\log_2 p_{\max}. \tag{119}$$

In this limit, Rényi entropy is only influenced by the most probable event. Figure 92 shows Rényi entropy for Bernoulli distribution, for different values of $\alpha > 1$.

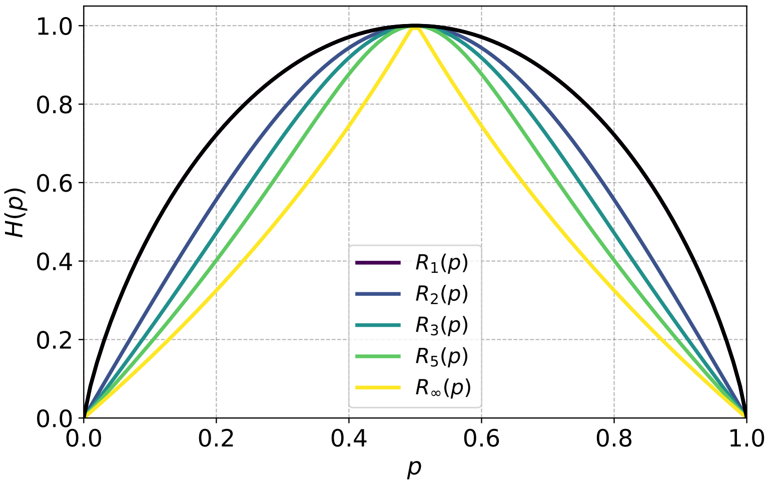

Figure 92: Rényi entropy R_α for Bernoulli distribution, for increasing values of α.

5.2 COMPLEXITY

Attempts have been made to define the complexity of a physical system. While entropy quantifies the amount of information contained in a system, it does not, by itself, measure complexity. Indeed, if we consider a perfect crystal and an isolated ideal gas, these are two extremes of the entropy scale. A perfect crystal is completely ordered. Knowing the configuration of a single elementary cell is enough to describe the entire structure, so the information content is minimal and the entropy is zero. On the other hand, the isolated ideal gas is totally disordered: all microscopic states are equally probable, and the information content is maximal since, in principle, one must specify all microstates to describe the system.

Yet both systems are "simple" in a certain sense, because they lack structure, patterns, or correlations. A perfect crystal is entirely predictable: its periodic structure repeats uniformly throughout space. Conversely, the ideal gas is so disordered that no particular configuration stands out from the rest. Neither system displays the mixture of order and unpredictability that we usually associate with complexity. Intuitively, complex systems should lie between these two extremes. They exhibit some degree of organisation and structure but also an element of unpredictability and disorder.

Therefore, any suitable measure of complexity should vanish for both extremal cases (perfect order and perfect disorder), and take positive values in between those two cases.

In the seminal paper of López-Ruiz, Mancini, and Calbet (1995), complexity relies on the concept of "disequilibrium". For a system defined by N microstates associated with probabilities $\{p_i\}$, the disequilibrium D is given by

$$D = \sum_{i=1}^{N} (p_i - \frac{1}{N})^2 \ . \tag{120}$$

The disequilibrium measures the deviation of the system from equipartition. In fact, for an isolated ideal gas with equally probable microstates, $p_i = \frac{1}{N}$, and hence $D = 0$. Conversely, for a perfect crystal, the system lies in a unique stable configuration, with probability $p_i \simeq 1$, the other states having $p_j \simeq 0$. The disequilibrium is therefore maximal in this case.

The complexity of the system C is then defined as

$$C = H \times D. \tag{121}$$

This definition of complexity is commonly known as LMC complexity, named after the three authors. It is easy to verify that it vanishes in the two extreme cases of a perfect crystal (since $H = 0$) and an isolated ideal gas (since $D = 0$).

Other more sophisticated definitions of complexity involve the Jensen-Shannon divergence, which still measures the distance from equipartition. By computing both entropy and complexity, one can draw the so-called complexity-entropy (CE) plane (Fig. 93).

5.3 ENTROPY METRICS

There are various entropy metrics used in very different fields. Several of them are shown in Fig. 94.

It is not clear which of them could be best suited for studying prompt emission time series. In this part, we studied the properties of a few bright long GRBs, and then applied them in

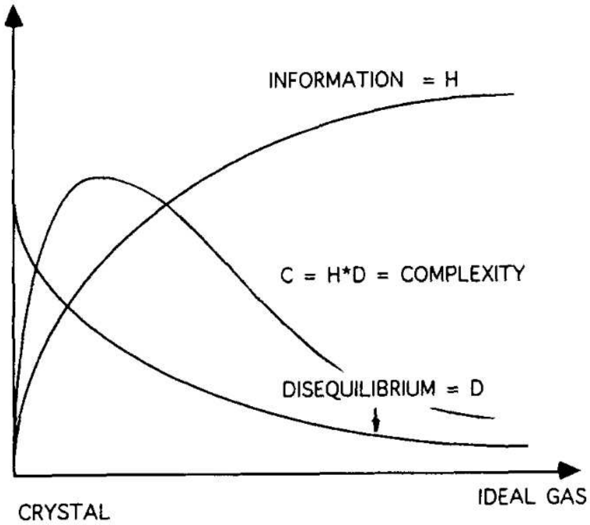

Figure 93: LMC complexity as a function of entropy. The perfect crystal case correspond to minimum information content and zero entropy while the ideal gas case is associated with maximum disorder and entropy. The LMC complexity is zero in both cases, which represent the simplest possible systems. From López-Ruiz, Mancini, and Calbet (1995).

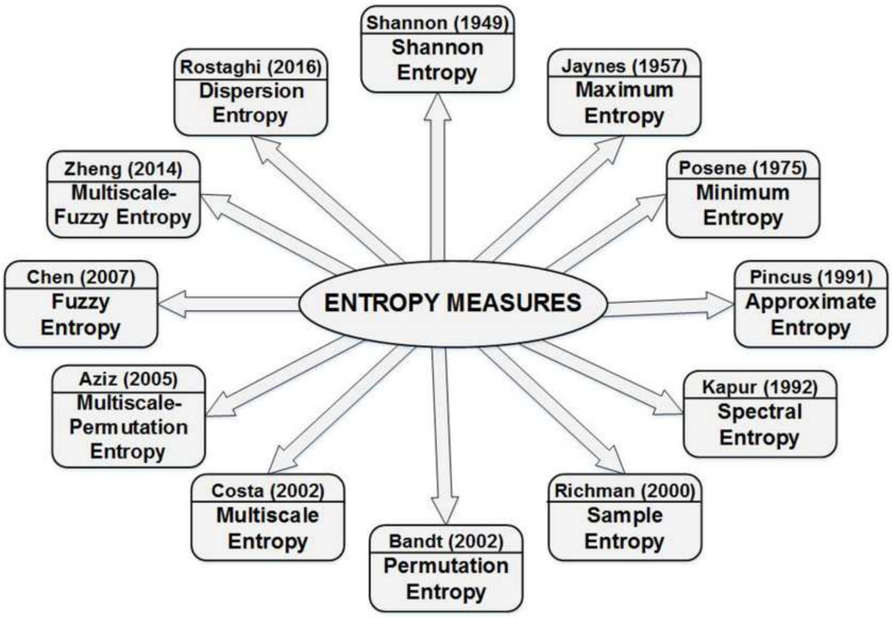

Figure 94: Different types of entropy measures, presented in chronological order. From Howedi, Lotfi, and Pourabdollah (2020).

Sect. 5.5 to the problem of detecting weak GRBs. To numerically compute these metrics, we used the publicly available Python package `antropy`[2].

---

[2] https://github.com/raphaelvallat/antropy

5.3.1 *Lempel-Ziv complexity*

Let s be a bi-infinite[3] string $s = \{s_i,\ i \in \mathbb{Z}\}$ with a finite alphabet χ with cardinal $|\chi|$. For instance,

- if $\chi = \{0, 1\}$, an example of such string is $s = ...001101101101...$,
- if $\chi = \{a, b, c, d, ..\}$, for instance $s = ...aabbccdeaaff....$

The amount of information carried by this sequence can be estimated by the entropy rate h, also called entropy density. This quantity is computed through the Shannon entropy of blocks $H(L)$. This approach consists in considering all $|\chi|^L$ possible sub-strings of length L, and computing their probability $p(s(L))$ of appearing in the sequence. Then the Shannon entropy of blocks is given by

$$H(L) = -\sum_{s(L)\in\chi^L} p(L)\log p(L), \tag{122}$$

where $s(L)$ is a sub-string of length L of s. The sum runs on every possible substring of length L. The entropy rate is then defined by

$$h = \lim_{L\to+\infty} \frac{H(L)}{L}\ . \tag{123}$$

The entropy rate is zero for a constant, a periodic, and a quasi-periodic string, while it reaches its maximum value $h_{\max} = \log|\chi|$ for a completely random sequence. Then, let $h(L) = H(L) - H(L-1)$. The excess entropy E is defined by

$$E = \sum_{L=1}^{+\infty} (h(L) - h). \tag{124}$$

To estimate the entropy rate for a finite sequence, one can use the Lempel-Ziv (LZ) factorisation of a sequence. This factorisation is obtained by separating the sequence into unique factors that have not appear previously in the sequence. We give in the following several examples

- For a binary alphabet $\chi = \{0, 1\}$, the sequence $s = 10010101110$ is factorised as 1.0.01.01011.10. The third factor is .01011. since 010 and 0101 already appeared in the sequence.
- For a standard alphabet $\chi = \{a, b, c, .., z\}$ to which the space character is added, the sequence "to sherlock holmes she is always the woman" factorises as t.o. .s.h.e.r.l.oc.k. h.ol.m.es. she .i.s a.lw.ay.s t.he w.om.an.

The Lempel-Ziv complexity $C_{LZ}(s)$ is then given by the number of factors (e.g. $C_{LZ}(s) = 5$ in this example). The utility of this quantity is that it can serve as an estimate of h. In fact, the Lempel-Ziv coding theorem (Lempel and Ziv, 1978) states, that, for a stationary and ergodic

---

[3] We intend by bi-infinite string a string without beginning and end.

process[4], the number of unique factors observed in a finite sequence $s(N)$ of length N, as it is given by the LZ complexity $C_{LZ}(s(N))$ verifies

$$\lim_{N\to+\infty} \frac{C_{LZ}\big(s(N)\big)\log_2 N}{N} = h, \tag{125}$$

where h is the entropy rate.

The excess entropy E can also be computed from a finite sequence as

$$E = \sum_{M=1}^{M_{max}} \Big(h\big(s(M)\big) - h\Big), \tag{126}$$

where $s(M)$ is a surrogate string obtained by partitioning the string s in non-overlapping blocks of length M and performing a random shuffling of the blocks, and M_{max} is the maximal length of the sequences. The shuffling for a given block of length M destroys all correlations between symbols for lengths larger than M while keeping the same symbol frequency. M_{max} is chosen appropriately given the sequence length to avoid fluctuations.

LZ complexity was applied to discrete sequences, such as written language (Estevez-Rams et al., 2019), and gene sequences (Mesa-Rodríguez et al., 2022). For written language, the (h, E) plane was obtained for writings of three different authors, namely Jacob Abbott, Arthur Conan Doyle, and William Shakespeare, in Fig. 95. This plane describes the trade-off between unpredictability and information production, expressed by h, and pattern recurrence and memory, expressed by E. Boring, repetitive texts containing redundant information yield high excess entropies E associated with low entropy values h, while highly unpredictable texts without repetitive structures, are associated with high entropy values and low excess entropy.

Applying this method to GRB time series presents two difficulties. First, since the GRB flux takes continuous values, we can not apply directly this method, but we have to discretize the data. This discretisation can be made simply by using the mean μ of the signal

$$Y(t) = \begin{cases} 1 & \text{if } y(t) > \mu, \\ 0 & \text{otherwise,} \end{cases} \tag{127}$$

where $y(t)$ and $Y(t)$ are the continuous and discrete versions of the signal. Data can also be divided into more levels (Fig. 96).

The second difficulty resides in the hypothesis underlying the Lempel-Ziv coding theorem. In fact, it can be applied in principle only to stationary and ergodic sources. GRB time series are non stationary, with their average properties clearly evolving over time. Since ergodicity requires stationarity, such signals cannot be ergodic either. In particular, ergodicity would imply that ensemble average could be inferred by computing the time average over a single GRB. This assumption is clearly not satisfied for GRB time series.

---

[4] For a stochastic process $x(t)$, stationarity implies that ensemble averages computed over various sample functions, such as $\mu_x(t_1) = \lim\limits_{N\to\infty} \frac{1}{N}\sum_{k=1}^{N} x_k(t_1)$, as well as higher-order moments, do not depend on the specific time t_1. Ergodicity further requires that these *ensemble averages* are equal to the corresponding *time averages* computed along a single sample function. For example, for the mean $\tilde{\mu}_x(k) = \lim\limits_{T\to\infty} \frac{1}{T}\int_0^T x_k(T)dt = \mu_x$, where the time average over one sample function equals the ensemble average μ_x. Hence, for an ergodic process, the average properties of the process can be determined using only a single, sufficiently long, realisation of this process.

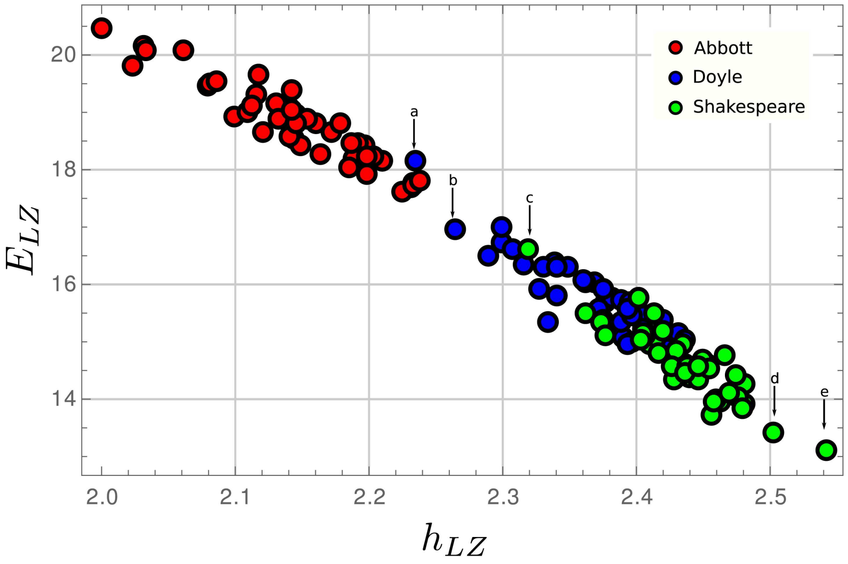

Figure 95: E-h plane for different books of Jacob Abbott, Arthur Conan Doyle, and William Shakespeare. Points located near the top left corner are associated with predictable, structured sequences, whereas random sequences without structure lie in the opposite corner, on the bottom-left part of the plot. Abbott wrote books dedicated for children, using simple vocabulary. Doyle is the father of Sherlock's Holmes, his writings were addressed mainly to newspapers, his style is therefore direct and not too complicated. Shakespeare, on the other hand, being considered as the master of English language, used more elaborated sentences in his writings. From Estevez-Rams et al. (2019).

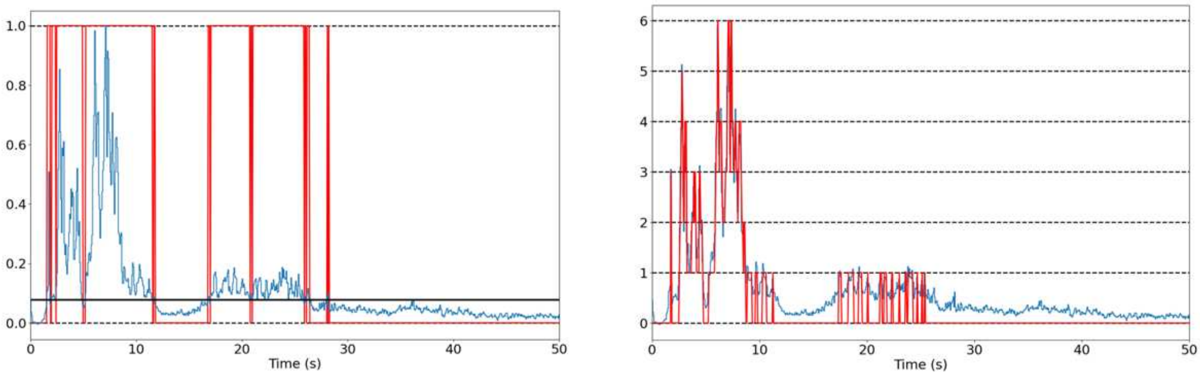

Figure 96: *Left panel:* GRB 230307A LC, discretised by the mean, with two levels ($\chi = \{0, 1\}$). *Right panel:* GRB 230307A LC, discretised by using six evenly spaced levels from the GRB peak to background level ($\chi = \{0, 1, \dots, 6\}$).

5.3.2 *Spectral entropy*

Spectral Entropy (SE) is a measure of the distribution of signal power in the frequency domain. Given a time series $x(t)$ and its associated Fourier transform $X(\omega)$, the normalised power density spectrum (PDS), $|X(\omega)|^2$, is used to build a probability distribution in the frequency domain as follows

$$p(\omega_i) = \frac{|X(\omega_i)|^2}{\sum_{i=1}^{N_b} |X(\omega_i)|^2}, \tag{128}$$

where N_b is the number of frequency bins. SE is then defined similarly to Shannon entropy.

$$SE(\{\omega_i\}) = -\sum_{i=1}^{N_b} p(\omega_i) \log_2 p(\omega_i). \tag{129}$$

It is also possible to define SE using alternative definitions of Shannon entropy, such as Rényi entropy.

The deterministic case here corresponds to a signal whose spectral power is concentrated in one frequency bin, i.e. a perfectly periodic one. In that case, $SE = 0$. On the contrary, if the power is equally distributed across all frequency bins, as is the case for uncorrelated white noise, then $P(\omega) = |X(\omega)|^2 \propto \omega^0 = \text{const.}$, and SE reaches its maximum value $SE_{\max} = \log_2 N_b$. If the signal is neither completely periodic nor totally random, SE takes values in between 0 and $SE_{\max}$. Figure 97 shows the behaviour of SE as a function of the noise intensity contained in a mixed signal composed of both deterministic and random components. A strength of this entropy metric is the absence of additional parameters, contrary to other metrics, such as the ones described in the following sections.

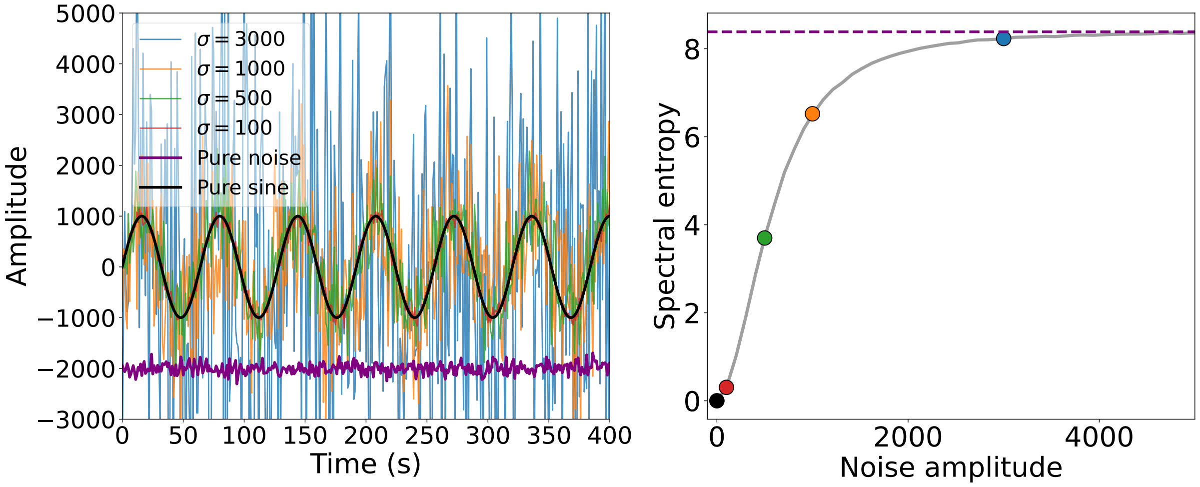

Figure 97: Effect of increasing noise amplitude on the spectral entropy of a sine wave. *Left panel:* a sine wave of amplitude $A = 1000$ (arbitrary units) and frequency $f = 16$ Hz (black) is progressively contaminated by the addition of Gaussian noise $\mathcal{N}(0, \sigma)$ with standard deviations $\sigma = 100, 500, 1000,$ and 3000. A purely random signal is shown for comparison (purple). *Right panel:* spectral entropy computed on noisy sine waves as a function of the noise level. The grey curve shows the spectral entropy as a function of the noise amplitude (averaged over 100 realisations for each value). Coloured points correspond to the entropy values of the four noisy signals displayed in the left panel, using matching colours. The dashed purple line denotes the spectral entropy of a purely noisy signal.

5.3.3 *Singular value decomposition entropy*

Similarly to Fourier decomposition, singular value decomposition (SVD) is another way to decompose a signal, this time on a basis of orthonormal singular vectors. This method can also be used to define an entropy measure. Consider N measurements of a time series $x(t) = \{x_1, x_2, x_3, ..., x_N\}$ represented by the vector

$$\mathbf{X}(t) = \begin{bmatrix} x_1 \\ x_2 \\ ... \\ x_N \end{bmatrix}, \tag{130}$$

where N is the number of points. The so-called *embedding matrix* is then defined as

$$M = \begin{bmatrix} x_1 & x_{1+\tau} & ... & x_D \\ x_2 & x_{2+\tau} & ... & x_{D+1} \\ ... & ... & .. & ... \\ x_{N-(D-1)\tau} & x_{N-D\tau} & ... & x_N \end{bmatrix}, \tag{131}$$

which is constructed by considering the τ-delayed measurements of $x(t)$, where τ is the lag, and D the so-called embedding dimension. The SVD provides a factorisation of this matrix according to

$$M = U\Sigma V^T, \tag{132}$$

where U is an orthogonal matrix, Σ is a diagonal matrix with non-negative real numbers on the diagonal and V is a orthogonal matrix. The diagonal entries $\sigma_j = \left[\Sigma\right]_{jj} \geqslant 0$ of the matrix Σ are the singular values of the matrix M. The column vectors of the matrices U and V are called left-singular vectors and right-singular vectors, respectively. They form two orthonormal bases $(\mathbf{U_1}, \mathbf{U_2}, ..., \mathbf{U_N})$ and $(\mathbf{V_1}, \mathbf{V_2}, ..., \mathbf{V_N})$, and the matrix M can be decomposed on these bases according to

$$M = \sum_{i=i}^{r} \sigma_i \mathbf{U_i} \mathbf{V_i^T}, \tag{133}$$

where r is the rank of the matrix M, i.e. the number of non null diagonal entries. One can use the normalised singular values to define a probability

$$\tilde{\sigma_i} = \frac{\sigma_i}{\sum_{j=1}^{r} \sigma_j}. \tag{134}$$

The SVD entropy could then be computed by using Shannon entropy (Eq. 110)

$$H_{SVD}(D, \tau) = -\sum_{i=1}^{r} \tilde{\sigma_i} \log_2(\tilde{\sigma_i}), \tag{135}$$

or alternatively Rényi entropy (Eq. 113)

$$H_{\mathrm{SVD}}(D,\tau,\alpha) = \frac{1}{1-\alpha}\sum_{i}^{r}\log_2(\tilde{\sigma_i}^{\alpha}). \tag{136}$$

SVD entropy depends directly on two parameters, the lag time τ, and the embedding dimension D, to which can be added α when it is defined via Rényi entropy.

5.3.4 *Permutation entropy*

Permutation entropy (PE) was introduced in the seminal paper of Bandt and Pompe (2002). PE uses the ordinal distribution of the data to construct probabilities of ordinal patterns. PE depends on two parameters, the embedding dimension D and the embedding time lag τ.

From a time series given by a collection of points $\{x_1, x_2, ..., x_N\}$, so-called *data vectors*

$$\mathbf{X_i} = \begin{bmatrix} x_i \\ x_{i+\tau} \\ ... \\ x_{i+(D-1)\tau} \end{bmatrix} \tag{137}$$

containing D data points delayed by τ are built. Ordinal patterns $\boldsymbol{\pi}_i$, corresponding to permutations obtained by sorting the components of $\mathbf{X_i}$ in ascending order, are then computed. A probability distribution $P(\boldsymbol{\pi}_i)$ is then obtained by measuring the relative frequency of these patterns in the dataset.

PE is then computed as the Shannon entropy, the sum running on the D! possible permutations of a collection of D elements. The construction of PE is illustrated in Fig. 98 and explained by the following example.

Let $S(t) = \{3, 5, 7, 9, 6, 110\}$ some time series, $D = 3$ and $\tau = 1$. The data vectors are given in this case by

$$\mathbf{X_1} = \begin{bmatrix} 3 \\ 5 \\ 7 \end{bmatrix}, \mathbf{X_2} = \begin{bmatrix} 5 \\ 7 \\ 9 \end{bmatrix}, \mathbf{X_3} = \begin{bmatrix} 7 \\ 9 \\ 6 \end{bmatrix}, \mathbf{X_4} = \begin{bmatrix} 9 \\ 6 \\ 110 \end{bmatrix}. \tag{138}$$

In our example, $3 < 5 < 7$, $5 < 7 < 9$, $6 < 7 < 9$, and $6 < 9 < 110$ hence the associated permutation vectors $\boldsymbol{\pi}_i$, obtained by sorting the vector components in increasing order, are given by

$$\boldsymbol{\pi}_1 = \begin{bmatrix} 0 \\ 1 \\ 2 \end{bmatrix}, \boldsymbol{\pi}_2 = \begin{bmatrix} 1 \\ 2 \\ 0 \end{bmatrix}, \boldsymbol{\pi}_3 = \begin{bmatrix} 1 \\ 0 \\ 2 \end{bmatrix}.$$

X_1 and X_2 are associated with π_1, while X_2 and X_3 are associated with π_2 and π_3, respectively. The probability $P(\boldsymbol{\pi_i})$ of a given permutation vector $\boldsymbol{\pi_i}$ is the observed frequency of this vector in the dataset. PE is then computed by using Eq. (110).

$$H_{PE} = -\sum_{i=1}^{D!=6} P(\boldsymbol{\pi_i}) \log_2 P(\boldsymbol{\pi_i}). \tag{139}$$

X_1 In our case, $P(\boldsymbol{\pi_1}) = \frac{2}{4} = \frac{1}{2}$, $P(\boldsymbol{\pi_2}) = P(\boldsymbol{\pi_3}) = \frac{1}{4}$, and $\forall j > 3$, $P(\boldsymbol{\pi_j}) = 0$. Hence,

$$H_{PE} = -\frac{1}{2}\log_2\frac{1}{2} - 2\frac{1}{4}\log_2\frac{1}{4} = \frac{3}{2}. \tag{140}$$

If the data are only increasing/decreasing (deterministic evolution), then all data vectors would be associated with a unique permutation pattern $\boldsymbol{\pi}$ ([0,1,2]/[2,1,0] for increasing/decreasing time series), and the PE in this case is zero. On the contrary, in the case of uncorrelated white noise, all ordinal patterns would be equally distributed, and PE would reach its maximum, given by $H_{PE} = \log D!$[5].

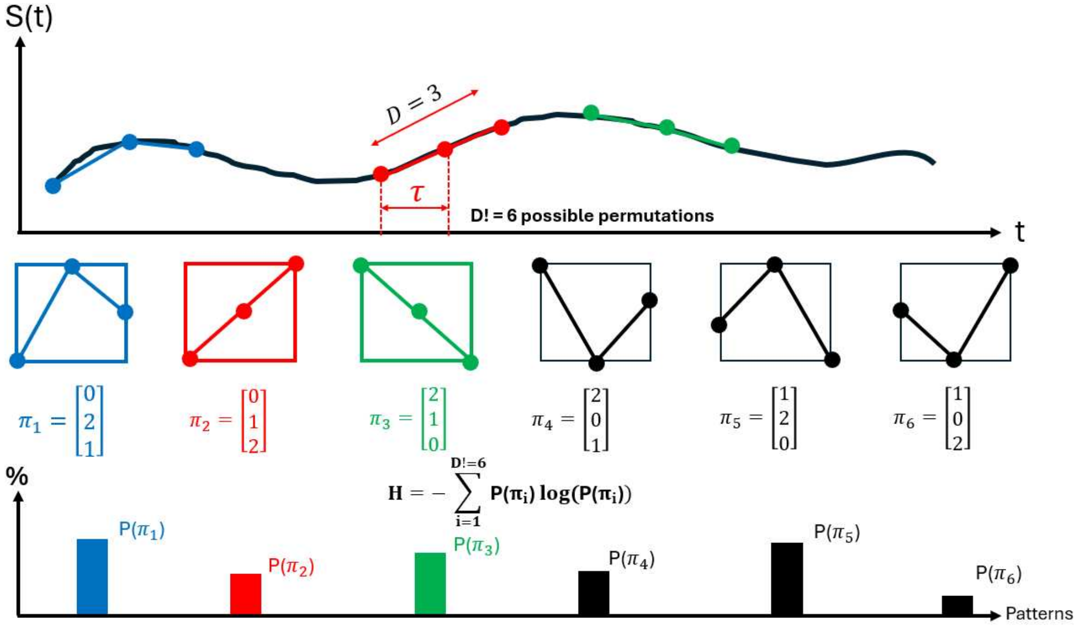

Figure 98: Sketch describing the computation of permutation entropy. *Top panel:* data vectors of dimension D are constructed by taking data evenly spaced by τ. *Middle panel:* Permutation vectors, obtained by sorting the vector components in increasing order, are computed. *Bottom panel:* The probability $P(\boldsymbol{\pi_i})$ of a given pattern $\boldsymbol{\pi_i}$ is given by the observed occurrence frequency of this pattern in the dataset.

A concept related to PE is that of *missing or forbidden permutation patterns*, i.e. patterns that never occur in a time series. The study of these patterns provides information about

---

[5] The number of permutations of a list of D elements being precisely D!.

the stochastic or deterministic nature of a time series (e.g. Amigó, Kocarev, and Szczepanski 2006).

In deterministic systems, such as chaotic maps, certain ordinal patterns are structurally impossible due to the map's functional constraints. Their absence is a sign of the underlying deterministic rules that govern the evolution of the system.

For instance, in the logistic map (defined in Sect. 5.4.2), the inequality $\forall x \in [0,1],\ f^2(x) < f(x) < x$ implies that the ordinal pattern $[2,1,0]$ (corresponding to three consecutive points in strictly decreasing order) can never occur. Moreover, the existence of one missing pattern generally implies the existence of other related missing patterns. For example, for the logistic map, any pattern of the form $[*, n+2, *, n+1, *, n, *]$, where $n \in \{0, .., 6\}$ and $*$ is any entry, is forbidden.

In contrast, stochastic time series should, in principle, generate all possible ordinal patterns, provided that the time series is long enough. However, some patterns can be missed in some random time series if its length is too small.

To ensure that all possible ordinal patterns of length D appear in a random series, the length of the time series should verify $L \gg D!$. A practical condition adopted by Amigó, Zambrano, and Sanjuán (2007) is $L \geqslant (D+1)!$. For shorter time series, a valid alternative is to analyse how the number of patterns decreases as a function of the time series length. This decay is typically much faster in deterministic systems than in stochastic ones, providing an alternative way to distinguish between them.

5.3.5 *Weighted permutation entropy*

PE is very sensitive to the presence of noise in the data. This is because PE only uses the ordinal distribution of the data, and puts on the same level small and high amplitude variations. This has several disadvantages, including (i) information about the time series are also contained in the amplitude, however this latter is lost by PE that extracts only the ordinal structure of the time series, (ii) ordinal pattern resulting from small fluctuations due to experimental noise are weighting equally as patterns arising from genuine flux variations. These issues make PE unable to detect strong spikes in noisy data for instance.

The so-called weighted permutation entropy (WPE, Fadlallah et al. 2013) was proposed to address these issues by assigning different weights to data vectors based on their variance, vectors associated with larger variance being weighted more than those associated with lower variance. Consider a data vector of a time series containing D data points such as the one defined in Eq. (137). The arithmetic mean of this data vector is given by:

$$\bar{X}_i = \frac{1}{D} \sum_{k=1}^{D} x_{i+(k-1)\tau}. \tag{141}$$

In the case of PE, each data vector yielding the same ordinal pattern weights equally, and the probability is given by the relative number of data vectors associated with this ordinal pattern. For WPE instead, to each data vector is associated a weight w_j, which is equal to the variance of the data vector $\mathbf{X}_i$, defined as follows:

$$w_i = \mathbb{V}[\mathbf{X}_i] = \frac{1}{D} \sum_{k=1}^{D} (x_{i+(k-1)\tau} - \bar{X}_i)^2. \tag{142}$$

The weight of a given permutation pattern w_{π_i} is then obtained as the sum of the variances of all data vectors associated with this pattern. The probability of a given ordinal pattern is computed as

$$p(\pi_i) = \frac{w_{\pi_i}}{\sum_{j=1}^{D!} w_{\pi_j}}, \tag{143}$$

and the entropy is computed using Eq. (110). If the weights are the same for all data vectors $\forall\, i,\ w_i = \beta$, WPE reduces to PE.

We now take the example used in the previous section to show how WPE is computed. The weights associated with the two first vectors are equal to $w_1 = w_2 = 2.667$, while the weight associated with the third and the fourth data vectors are given by $w_3 = 1.55$ and $w_4 = 2336$, respectively. The weight w_{π_1} associated with the permutation vector π_1 is obtained by summing the variances of the two first data vectors $w_{\pi_1} = w_1 + w_2$, while the weights for the other permutation vectors are $w_{\pi_2} = w_3$ and $w_{\pi_3} = w_4$. The entropy obtained in the WPE case is therefore $H_{WPE} = 0.03$, which is significantly smaller than the value obtained with PE for this time series ($H_{PE} = 1.5$). This is mainly due to the last data point which makes the last data vector associated with the permutation pattern π_3 weights more than the others, since it has an amplitude that is considerably larger than the others. This enhances the capacity of this entropy measure to detect spiky features among noisy data (Fig. 99).

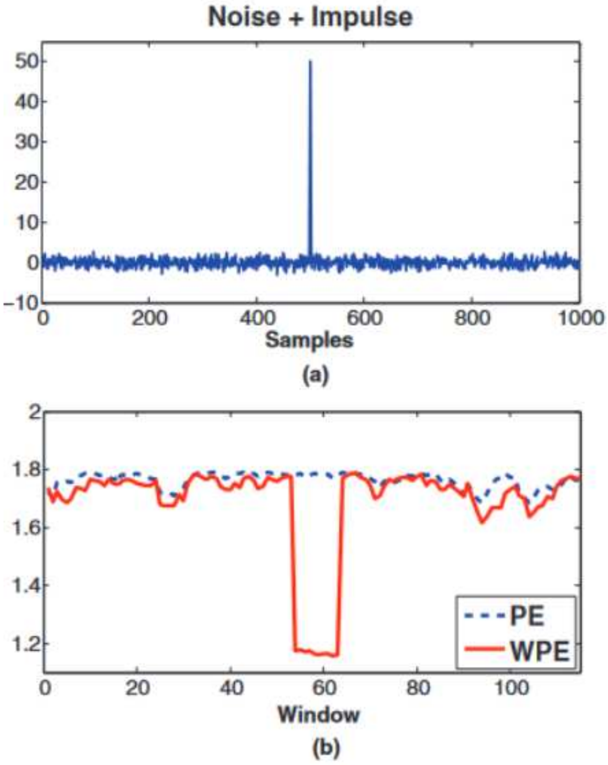

Figure 99: *Top panel:* Time series composed of uncorrelated noise with an impulsive input at some time. *Bottom panel:* Values of the entropy computed on different time windows, either using PE (dashed lines) or WPE (red lines). From Fadlallah et al. (2013).

5.4 CAN ENTROPY-BASED MEASURES DETERMINE WHETHER GRBS ARE DETERMINISTIC OR STOCHASTIC?

GRB time series present an extremely complex behaviour, with a wide variety of different time profiles. As we discussed in the previous chapter, the hypothesis that this diversity arises from different realisations of a common stochastic process is a promising way to model the temporal properties of the prompt emission.

Complex dynamical systems, composed of many interacting components can also exhibit a intricate temporal behaviour that can be mistaken for stochastic variability. Although these systems are governed by deterministic equations, the resulting dynamics can deceptively look random. Instead of settling into a steady state or displaying periodic evolution, they occasionally show irregular, aperiodic motions that could be wrongly interpreted as stochastic. These systems fall within the scope of *chaos theory*, and are commonly analysed using tools such as Lyapunov exponents or fractal dimensions.

An early attempt to apply such methods to GRB LCs was made by Greco et al. (2011), who found possible evidence of deterministic chaotic behaviour in the prompt emission. Nevertheless, more comprehensive investigations are required to assess and confirm this claim. In particular, quantities such as the Lyapunov exponent can rigorously be obtained only for infinitely long time series. Therefore, the use of such methods to short-lived signals such as those of GRBs, if valid, has to be established more firmly. In this section, we will see that the use of entropy-related concepts, in particular the complexity-entropy plane offers ways to distinguish chaotic from random time series.

5.4.1 *Different kinds of noises*

Uncorrelated white noise occupies one extreme of the entropy scale, corresponding to its maximum value. However, other kinds of noises are associated with lower values of the entropy measure. White noise ξ_t is associated with a flat PDS $P_\xi(f) \propto f^0 = \text{const.}$, with equal power at all frequencies. On the contrary, coloured noises are associated with a declining power-law PDS. For instance, stochastic processes with a PDS $P(f) \propto f^{-2}$ are referred to as red noise. An example of red noise is Brownian motion (as defined in Chapter 4). The time derivative of a Brownian motion dW_t/dt is white noise ξ_t, which has a flat PDS such that

$$\forall f, \left|\mathcal{F}\left[\xi\right]\right|^2(f) = \text{const.}, \tag{144}$$

where $\mathcal{F}$ is the Fourier transform operator[6].

However,

$$\mathcal{F}\left[\frac{dW_t}{dt}\right](f) \propto f \times \mathcal{F}\left[W_t\right](f), \tag{145}$$

---

[6] We define the Fourier transform of a time series $x(t)$ as

$$\mathcal{F}\left[x\right](f) = X(f) = \int_{-\infty}^{+\infty} x(t)\, e^{-2\pi i f t}\, dt.$$

because of the properties of the Fourier transform[7]. Hence, Brownian motion is associated with a PDS $P_{W_t}(f) \coloneqq |\mathcal{F}(W_t)(f)|^2$ such that

$$P_{W_t}(f) \propto \left| \frac{\mathcal{F}[dW_t/dt]}{f} \right|^2 \propto \left| \frac{\mathcal{F}[\xi_t]}{f} \right|^2 \propto f^{-2}, \tag{146}$$

and can therefore be considered as an example of red noise. Other examples of coloured noise include flicker noise, also known as pink noise, that follows $P(f) \propto 1/f$.

We also considered a generalisation of Brownian motion, called fractional Brownian motion (fBm), which is a continuous Gaussian stochastic process $B_H(t)$, defined by its mean $\forall t,\ \mathbb{E}[B_H(t)] = 0$, and covariance

$$\forall t, s,\ C(t,s) = \mathbb{E}\big[B_H(t) B_H(s)\big] = \frac{1}{2}(|t|^{2H} + |s|^{2H} - |t-s|^{2H}), \tag{147}$$

where H is the Hurst index, usually defined in the range $[0, 1]$. This stochastic process has stationary increments $X_H(t) = B_H(t+s) - B_H(s)$. However, these increments are not independent, unless $H = 1/2$, which corresponds to classical Brownian motion. Instead, they exhibit long-range correlations, with an autocorrelation function given by

$$C(\tau) \propto \tau^{2H-2}. \tag{148}$$

The process associated with the increments of fBm is called *fractional Gaussian noise* (fGn), which is a stationary stochastic process.

For $H > \frac{1}{2}$, fBm is said to be *persistent*, and corresponds to the physical regime of *super-diffusion*. The mean-squared displacement scales as

$$\mathbb{E}\left[\big(B_H(t) - B_H(0)\big)^2\right] \propto t^{2H}, \tag{149}$$

which follows directly from its two-point covariance function $C(s,t)$. Since $2H > 1$, the variance grows faster than linearly with time. For $H < \frac{1}{2}$, the process is *anti-persistent*, corresponding to *sub-diffusion*. In this regime, the mean-square displacement grows with an exponent $2H < 1$, and therefore increases more slowly than linearly in time. Figure 100 shows various realisations of the process for different values of H that correspond to sub- and super-diffusion.

---

[7] A short proof: integrating by parts,

$$\mathcal{F}\left[\frac{dx}{dt}\right](f) = \int_{-\infty}^{+\infty} \frac{dx}{dt}\, e^{-2\pi i f t}\, dt = -2\pi i f \int_{-\infty}^{+\infty} x(t)\, e^{-2\pi i f t}\, dt = -2\pi i f\, X(f),$$

assuming $x(t) \to 0$ as $t \to \pm\infty$.

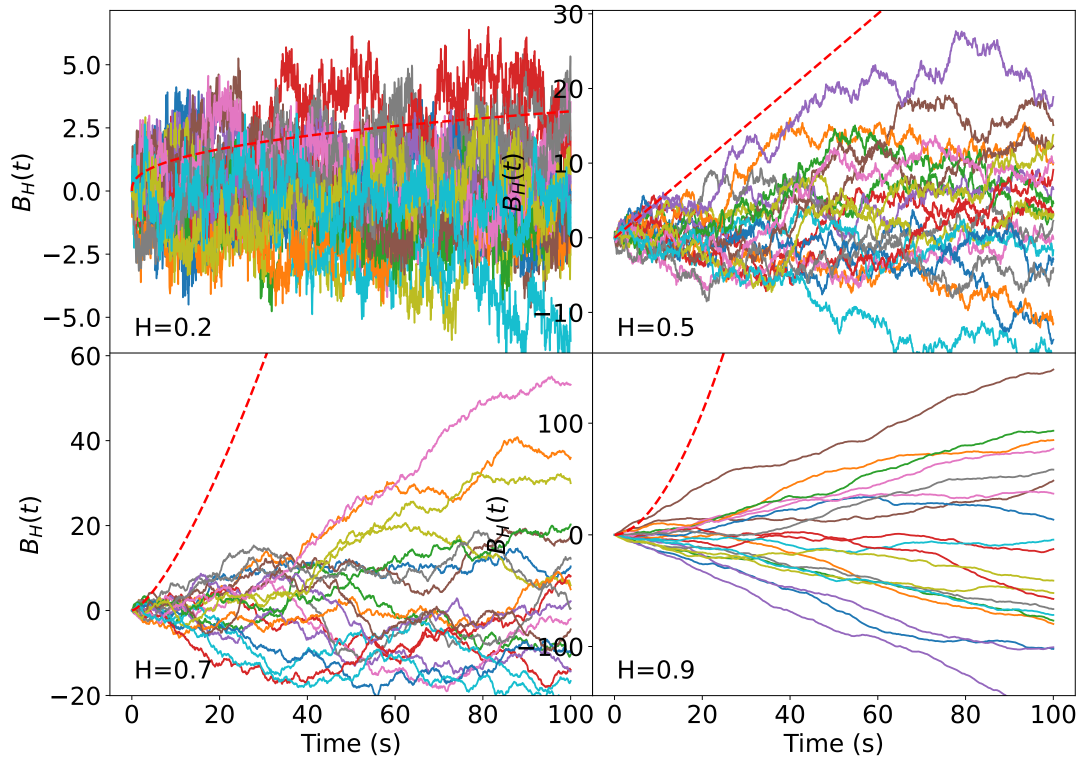

Figure 100: Realisations of the fBm process for different values of the Hurst exponent H. The four panels indicate increasing values of $H = 0.2, 0.5, 0.7, 0.9$, from top to bottom, left to right. The first panel corresponds to sub-diffusion, the second to Brownian motion, and the last two to super-diffusion processes. The red line shows the variance of the process, that scales as t^{2H}.

5.4.2 *Chaotic systems*

In contrast to the stochastic processes discussed previously, deterministic systems are governed by equations admitting a unique solution, once the initial conditions are fixed. These systems can nonetheless exhibit a highly complex behaviour, as shown in the following. Complex dynamics can arise even from simple one-dimensional maps such as the logistic map, a discrete sequence given by the equation

$$x_{n+1} = rx_n(1 - x_n) = f(x_n), \tag{150}$$

with $0 < r < 4$ so that f maps $[0, 1]$ into $[0, 1]$.

Analysing such systems consists in asking what is the long term behaviour of the sequence as $n \to \infty$, for a given initial condition x_0. The simplest behaviour is the appearance of *fixed points*, i.e. points satisfying $f(x^*) = x^*$. Once the map reaches such a value at some iteration n, so that $x^* = x_n$, all future iterations will remain at this value and the system will no longer evolve: $x_{n+1} = f(x_n) = f(x^*) = x^*$. In addition, if $|f'(x^*)| < 1$[8], then the fixed point x^* is

---

[8] This condition can be understood by expanding the function f close to the fixed point, introducing a small perturbation η_n such that $x_n = x^* + \eta_n$ and determining whether the perturbation grows or decays over successive

said to be stable: nearby trajectories eventually converge to it. If $|f'(x^*)| > 1$, the fixed point is unstable and nearby trajectories move away from it. In the case of the logistic map, a wide variety of behaviours are observed depending on the value of the parameter r:

- **Steady behaviour**. The logistic map admits two fixed points, 0 for all values of r and $1 - 1/r$ for $r > 1$. When $r < 1$, the unique stable fixed point is 0 and becomes unstable when $r > 1$, while $1 - 1/r$ is stable for $1 < r < 3$.
- **Periodic oscillations**. Above $r > 3$, we enter the phase of period doubling: there are no stable fixed points but there are two points that verify the following properties: $f(x_2) = x_1$ and $f(x_1) = x_2$. Therefore these satisfy $f^2(x_{1,2}) = x_{1,2}$, where $f^2 = f \circ f$ is the iterate of f. There is a stable 2-period cycle for $3 < r < 1 + \sqrt{6} \simeq 3.449$.
- **Cascades of period doubling**. As r goes beyond $1 + \sqrt{6}$, the 2-period cycle becomes unstable and we enter in a 4-period oscillations regime. As r further increases, the oscillation period keeps doubling. If we note (r_k) the sequence of r values at which a period doubling occurs, this sequence converges towards a limit value $r_\infty = 3.5699....$ The r_∞ value is referred to as *the onset of chaos*. The distance between two consecutive period doubling shrinks by a constant factor $\delta = \lim\limits_{n \to \infty} \frac{r_n - r_{n-1}}{r_{n+1} - r_n} = 4.696....$ This value, known as the *Feigenbaum constant*, is found in other doubling cascades that occur for different chaotic maps, not only the logistic one, and therefore bears a universal character.
- **Intermittency and chaos**. When $r > r_\infty$, periodic motion is no longer observed, apart from some periodic windows in which the system exhibits stable 3-period oscillations, and the system becomes very sensitive to initial conditions.

The long term behaviour of the logistic map as a function of r is shown in Fig. 101.

---

iterations. The expansion yields $x_{n+1} = x^* + \eta_{n+1} = f(x^* + \eta_n) = f(x^*) + \eta_n f'(x_n)$, leading to $\eta_n = \eta_0 \lambda^n$, with $\lambda = f'(x^*)$. If $\lambda < 1$, $\eta_n \to 0$ so the sequence (x_n) eventually converges to x^*. Therefore x^* is a stable fixed point in this case. Conversely, if $\lambda > 1$, η_n diverges and the fixed point is unstable.

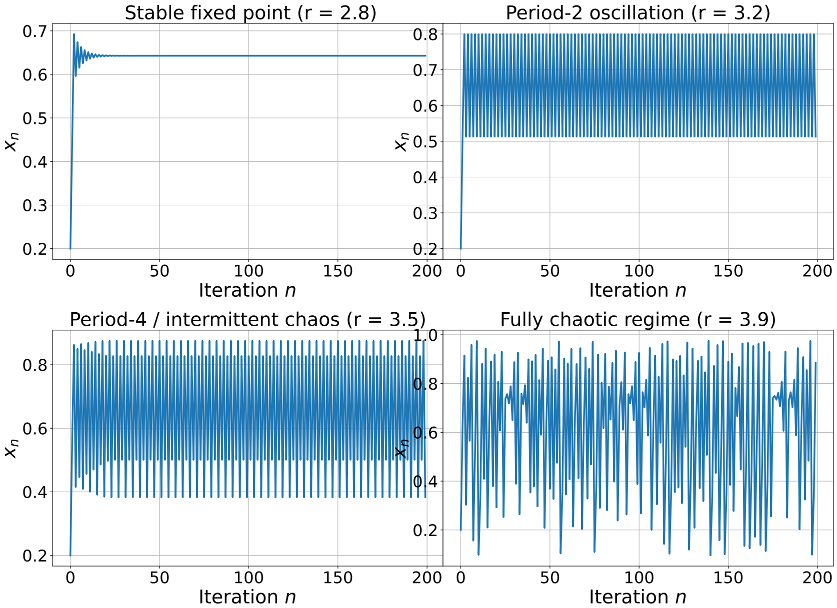

Figure 101: Dynamics of the logistic map $x_{n+1} = r x_n(1 - x_n)$ for different values of the control parameter r. Each panel shows the time evolution of the iterates x_n starting from the same initial condition $x_0 = 0.2$. Panel (a), $r = 2.8$: the trajectory converges to a stable fixed point. Panel (b), $r = 3.2$: the fixed point becomes unstable and the system enters a stable period-2 cycle. Panel (c), $r = 3.5$: further period-doubling leads to a period-4 orbit, signalling the onset of complex behaviour. Panel (d), $r = 3.9$: the map evolves into fully developed chaos, exhibiting aperiodic motion and strong sensitivity to initial conditions.

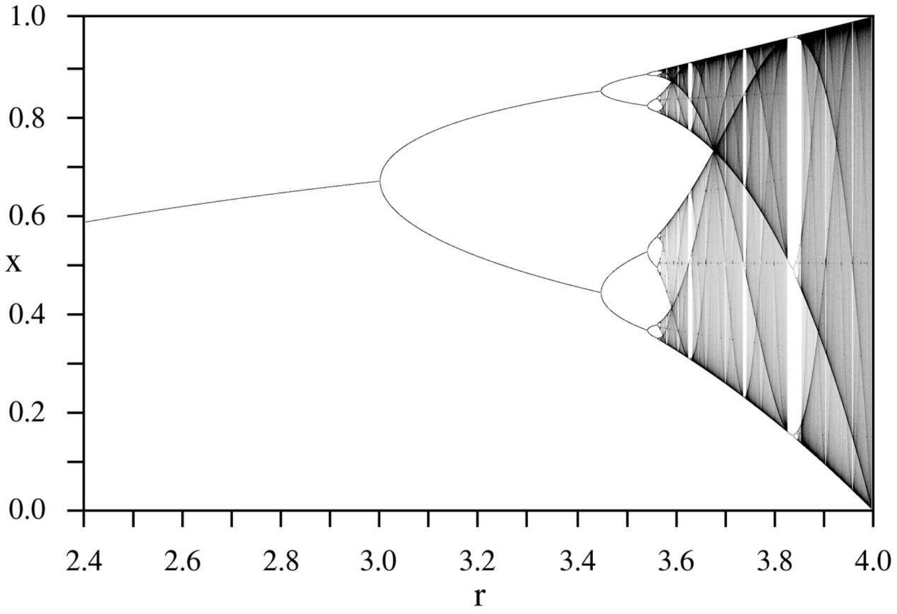

Figure 102: Bifurcation diagram of the logistic map showing the long-term behaviour of the system as a function of the control parameter r. The diagram illustrates the transition from a stable fixed point ($1 < r < 3$) to period-doubling oscillations and the onset of chaos at $r = r_\infty \simeq 3.5699$. Beyond this point, the system exhibits fully developed chaotic dynamics, interrupted by narrow periodic windows signalled by white regions.

The logistic map is just an example of chaotic maps, and many one or two dimensional maps exhibit similar behaviours. We mention here several other examples, that will be used later on in Sect. 5.4.3.

The *Hénon map* is a two-dimensional iterative dynamical system defined by

$$\begin{cases} x_{n+1} = 1 - a x_n^2 + y_n, \\ y_{n+1} = b x_n, \end{cases} \tag{151}$$

which exhibits chaotic behaviour for its canonical parameters $a = 1.4$ and $b = 0.3$.

The *skew tent map* is a one-dimensional piecewise-linear map given by

$$x_{n+1} = \begin{cases} \dfrac{x_n}{w}, & \text{if } x_n < w, \\ \dfrac{1 - x_n}{1 - w}, & \text{if } x_n \geqslant w, \end{cases} \tag{152}$$

where $0 < w < 1$ controls the asymmetry. For most values of w, the map is chaotic. In the following, we used $w = 0.1847$, as done by Pessa and Ribeiro (2021).

The *Schuster map* (or intermittent map) is defined by

$$x_{n+1} = x_n + x_n^z \pmod 1, \tag{153}$$

where $z > 1$. These values lead to intermittent dynamics characterised by intense outburst periods separated by quiescent times. Outbursts become rarer and the quiescient times periods longer as z increases (Fig. 103).

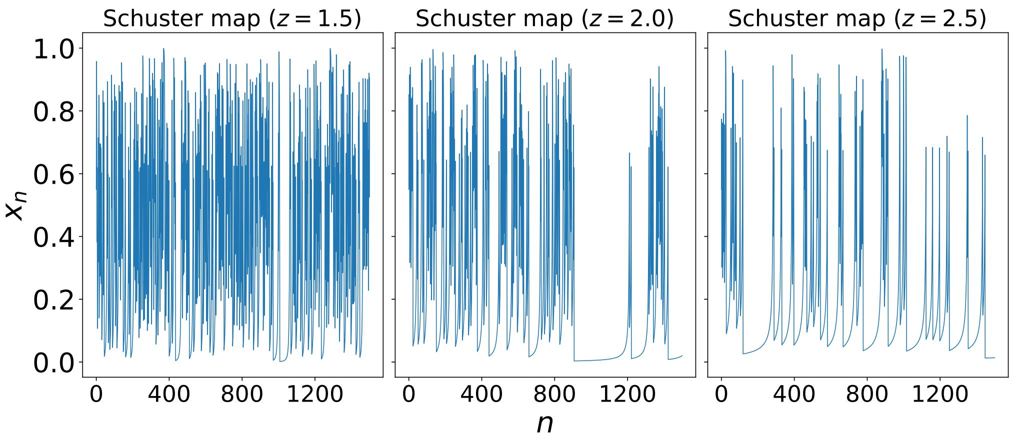

Figure 103: Three trajectories of the Schuster map, for $z = 1.5, 2$ and 3.5, from left to right panels.

5.4.3 *Complexity-entropy plane*

Stochastic and deterministic time series occupy different regions of the complexity–entropy (CE) plane. Purely uncorrelated Gaussian noise lies at the point $(H = 1, C = 0)$[9], while

---

[9] The entropy measure H is often normalised by its maximum value H_{max}, so that in the plane $(\tilde{H}, C)$ where $\tilde{H} = H/H_{max}$, uncorrelated white noise indeed lies at the point (1,0).

correlated stochastic processes, such as those described in Sect. 5.4.1, appear in regions of high entropy and low complexity. In contrast, deterministic time series typically exhibit higher complexity values for a similar level of entropy. For a given entropy level H, complexity values are bounded within the range $[C_{\min}(H), C_{\max}(H)]$. The bounded nature of the CE plane, as well as methods to compute its boundaries $C_{\min}(H)$ and $C_{\max}(H)$, is discussed in Martin, Plastino, and Rosso (2006).

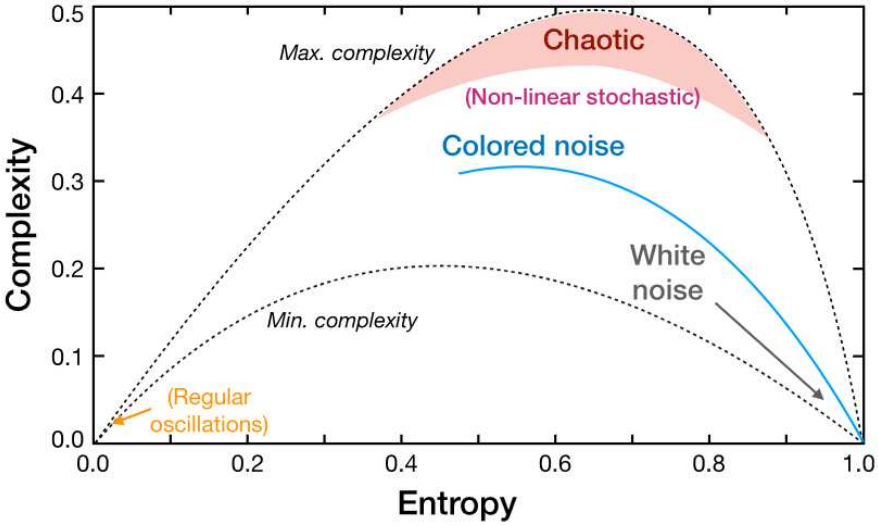

Figure 104: From Zanin and Olivares (2021). Approximate locations on the CE plane of time series from stochastic processes and chaotic maps. The two dotted lines show the minimum and maximum curves that delimit the range of possible complexity values a system can attain for a given entropy.

Pessa and Ribeiro (2021) considered different stochastic processes, such as coloured noise, and the fBm and fGn processes mentioned in Sect. 5.4.1. They compared their positions to those of chaotic maps, such as the logistic map, the Hénon map, the skew tent map, and the Schuster map mentioned in Sect. 5.4.2. Their results are shown in Fig. 105.

We attempted to reproduce their analysis, adding time series of different bright GRBs, and compared their relative positions with those of chaotic maps and stochastic processes. A caveat of this method in our case is the sensitivity to the length of the time series. In fact, as mentioned in Sect. 5.3.4, the method based on PE is rigorously applicable only if the length L verifies $L \geqslant (D+1)!$, where D is the embedding dimension, to avoid the problem of statistically missing patterns. In our case, we must therefore ensure that the number of points is sufficient to perform the analysis, e.g. by considering GRBs with a sufficient duration and low values of the embedding dimension D. For this reason, we restricted the analysis to $D \leqslant 5$, as larger embedding dimensions require time series of at least ~ 320 s (assuming a bin time of 64 ms), which exceeds the duration of most long GRBs. We considered GRBs of duration $T_{90} \simeq 30-50$s, therefore we restricted our analysis to $D = 5$, which requires $T > 46$ s for LCs binned at 64 ms. One could study shorter GRBs or use larger dimensions if using smaller bin sizes. However, the signal can be noisier at smaller timescales, which would hamper the possibility to distinguish GRBs from stochastic processes (Fig. 110). Note that the adopted time range is determined by the first and last time bins with signal exceeding the $S/N > 5$ threshold. With this definition of time interval, GRB 190114C has the shortest signal,

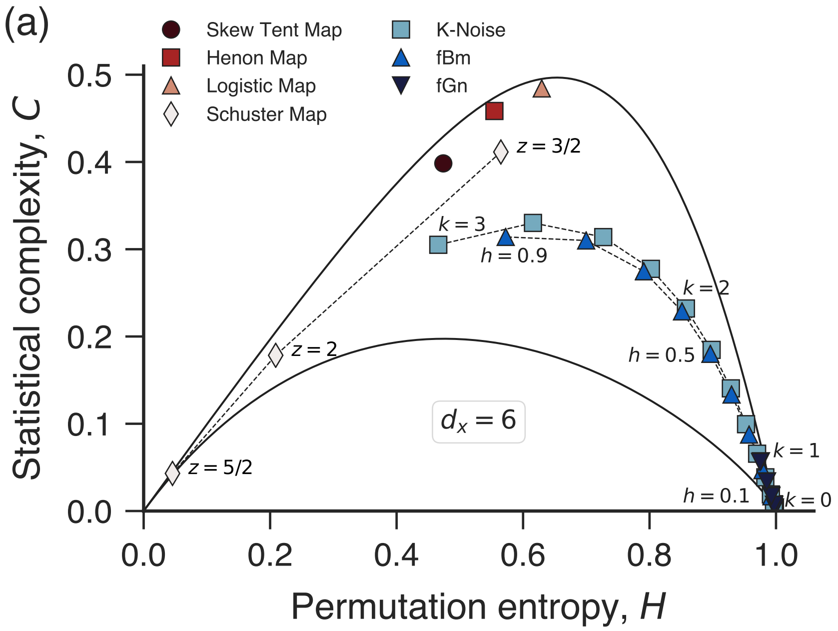

Figure 105: Complexity-PE plane. In this figure are shown time series from stochastic processes, such as coloured noise (blue squares), fBm and fGn (blue and black inverted triangles), chaotic maps such as the logistic map (orange triangle), the skew tent map (black dot), the Hénon map (red square), and the Schuster map (white diamond) for three different values of its parameter z. The embedding dimension is $d_x = 6$ (d_x corresponds here to the parameter D previously introduced). Deterministic chaotic systems lie above stochastic processes in this plane, exhibiting a lager degree of complexity for similar entropy values. From Pessa and Ribeiro (2021).

and marginally satisfies our criterion for $D = 5$ (715 bins for 720 required). However, it also lies above stochastic processes in the complexity-entropy plane for $D = 4$, where the constrain on the length of the time series is less severe (120 bins).

Another important issue is the strong sensitivity of PE to the counting noise that inevitably affects any real time series. In fact, as shown in Figure 106, PE fails to reveal the peculiar dynamics of GRB time series, as these lie very close to uncorrelated white noise and other stochastic processes in the CPE plane.

The inability of PE to distinguish GRB dynamics from purely stochastic behaviour is mainly due to the fact that standard PE relies solely on the ordinal relations between successive points to build the probability distribution and does not consider their relative amplitudes. As explained in Sect. 5.3.5, this limitation can be overcome by using WPE. We therefore performed a similar analysis in the CWPE plane. The results are shown in Fig. 107 for $D = 5$ and Fig. 108 for $D = 4$.

In the CWPE plane, GRBs occupy an intermediate region between chaotic maps and stochastic processes. Their complexity exceeds that of coloured noise and fBm processes for comparable entropy levels. This result suggests that, if GRBs can indeed be modelled as stochastic processes, the standard families of coloured noise and fBm processes do not possess a sufficient degree of complexity to reproduce them. At the same time, GRBs do not reach the high-complexity regime characteristic of purely chaotic systems. A possible reason is the presence of experimental Poisson noise in GRB time series, which tends to increase entropy and

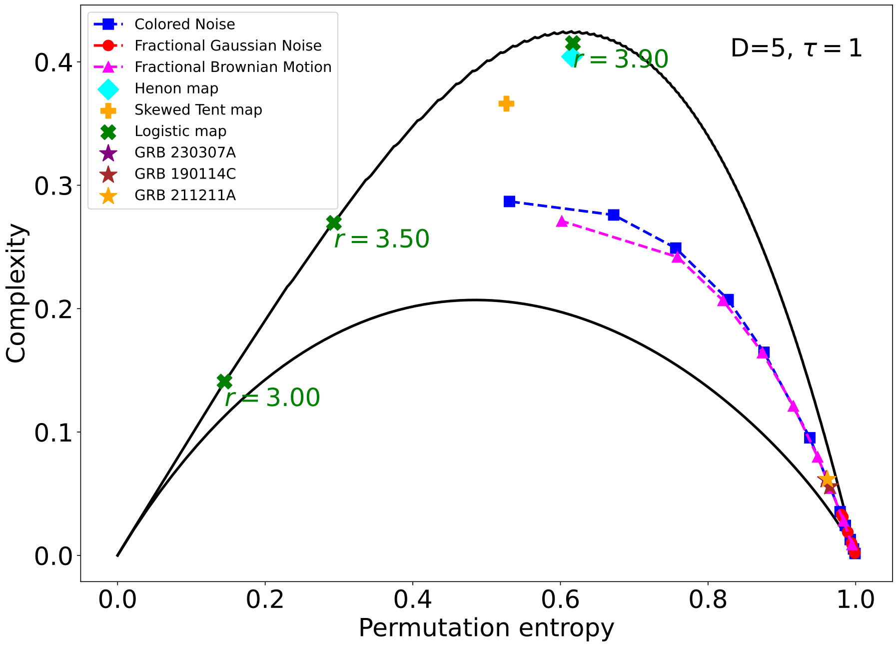

Figure 106: Relative positions of GRB 230307A, GRB 211211A, and GRB 190114C in the CPE plane. Green crosses show three different dynamics of the logistic map, corresponding to three different cases exposed in Sect. 5.4.2. The three GRBs considered here lie in the lower right corner of the CPE plane, making them indistinguishable from stochastic processes.

reduce complexity. To investigate this effect, we considered a noisy logistic map, constructed by adding uncorrelated noise to the standard logistic map, and showed that its position in the CWPE plane was shifted to higher entropy/lower complexity positions, moving it closer to the region occupied by some GRB time series. We also investigated the position of GRBs with different S/N ratios (Fig. 109). Nevertheless, the differences in the locations in the CE plane of GRB LCs with respect to chaotic maps may also reflect genuinely different underlying dynamics, and more tests should be performed to assess the chaotic nature of GRB time series.

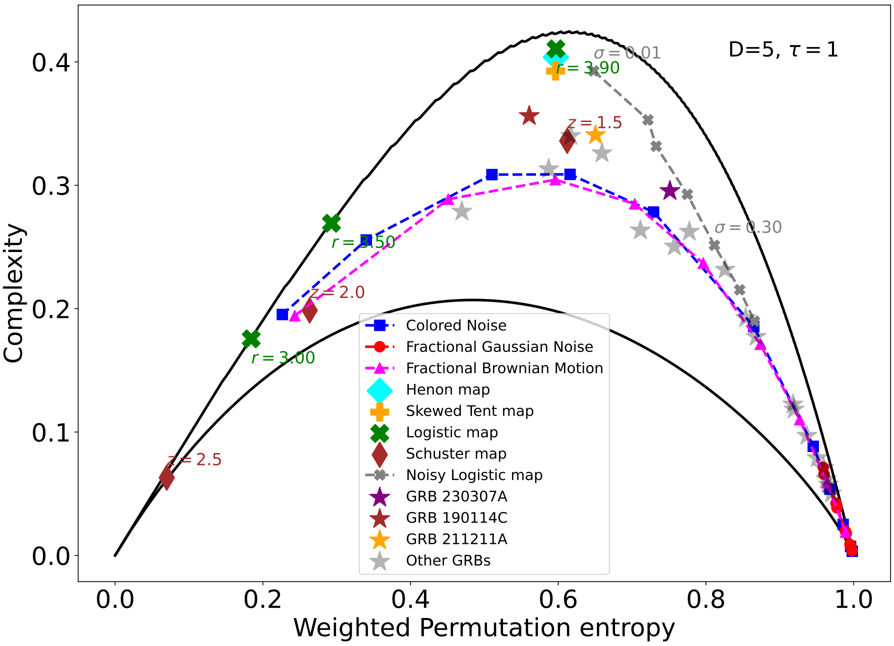

Figure 107: Complexity- entropy plane in the case of WPE. Grey crosses represent a noisy logistic map, obtained by adding a progressivey increasing amount of noise to the logistic map dynamics. As the noise level increases, these values are shifted towards lower entropy values. Stars of different colours represent the positions in the CWPE plane of GRB 230307A (purple), GRB 211211A (yellow), and GRB 190114C (brown). They lie in an intermediate position between stochastic processes and chaotic maps. Other GRBs are shown by grey stars. These were taken from the 200 brightest GRBs (with the larger fluence), and are long enough so that the number of bins in the time interval is larger than $(D+1)! = 720$ bins.

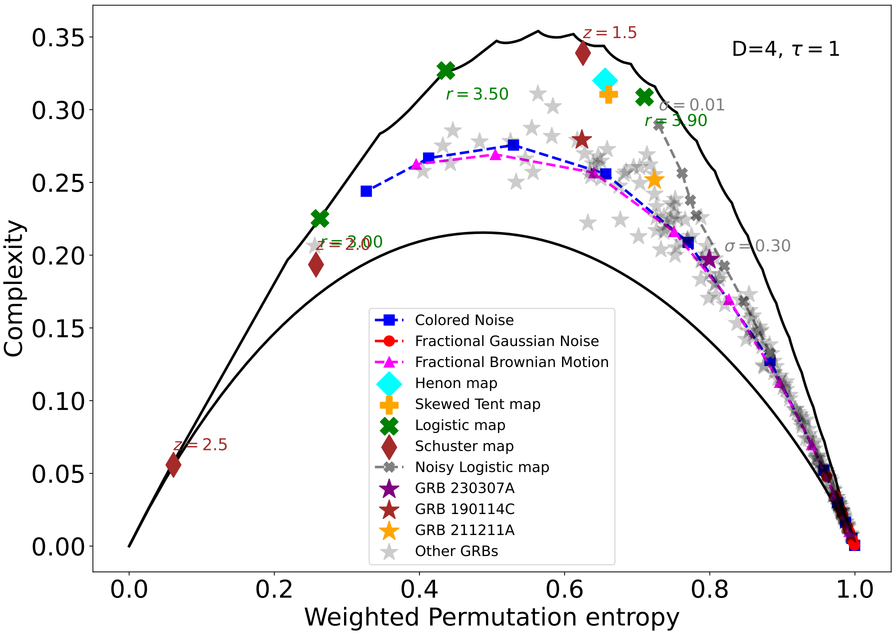

Figure 108: Same as Fig. 107, except that the embedding dimension in this case is $D=4$.

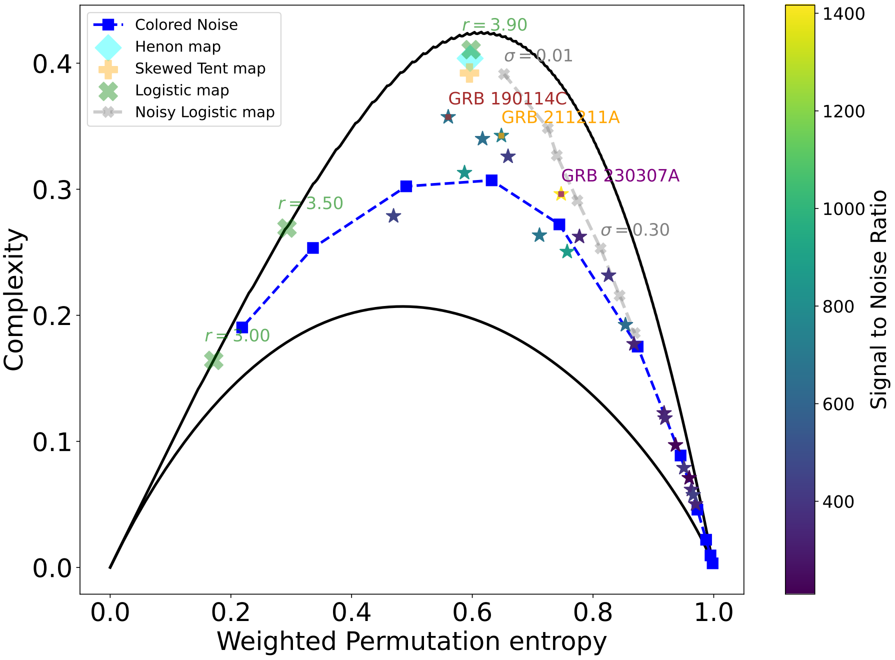

Figure 109: Same as Fig. 107, except that we are showing different GRBs with a colour bar showing the different S/N ratios.

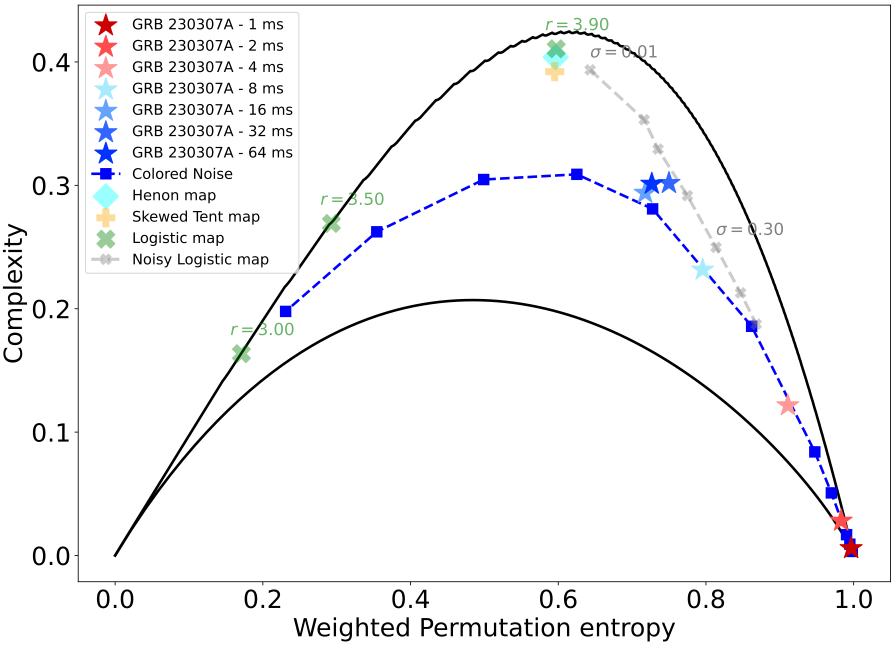

Figure 110: Same as Fig. 107, except that we are showing the position of GRB 230307A in this plane for different bin time sizes.

5.5 USING ENTROPY TO DETECT WEAK GRBS

The entropy metrics described in the previous sections can be used to detect GRBs with a relatively low S/N ratio. Indeed, since the value of entropy depends on the amount of randomness of the signal, it can be used to spot a sudden and dim change in the time series, such as the emergence of a transient signal.

This task is analogous to triggering a GRB. In fact, before and after the GRB onset, data are essentially background-dominated. The temporal evolution of entropy can reveal the burst occurrence through a sudden drop at the time of the burst. This method could be particularly useful to detect weak GRB precursors, given their important theoretical implications (e.g. Dichiara et al. 2023).

Consider a time series from t_0 to t_N, with $T = t_N - t_0$ its duration. We define a moving time window as a time interval of duration $\Delta t = T/M$, with M an integer, that is iteratively moving across the time series with a time step δt. We can define the segment $\Delta_i = x([t_i : t_i + \Delta t])$ of duration Δt, with $t_i = t_0 + i \times \delta t$ that can partially overlap with the previous one Δ_{i-1}, and compute some entropy measure H_i associated with Δ_i. The time step δt used for sliding the window over the time series is usually defined as a fraction of the total window width Δt. The method is illustrated in Figure 111.

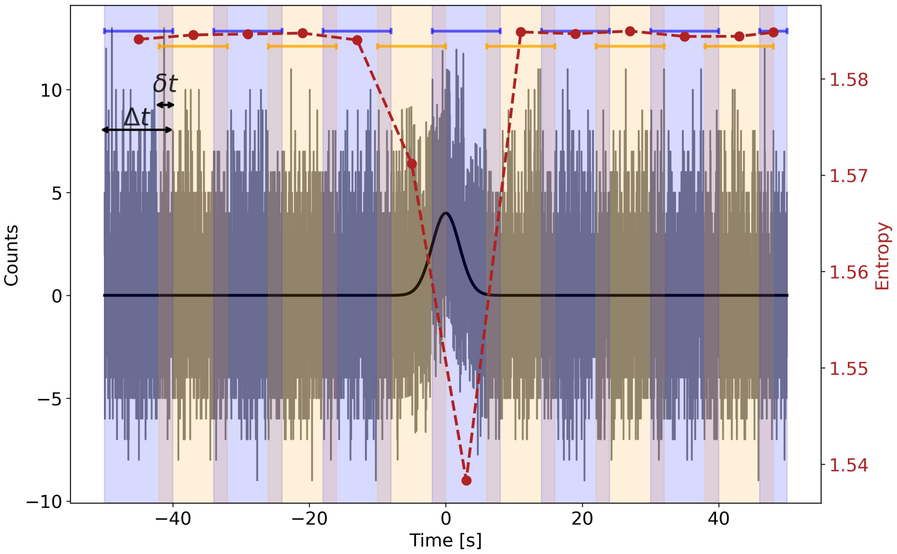

Figure 111: Illustration of the entropy-based detection method. A GRB is simulated with a FRED profile (black line), to which is added some Poisson noise. The grey curve represents the whole signal, defined as the sum of the pulse and the background noise. Entropy is computed on sliding windows (orange and blue intervals) of duration Δt with a time step δt, whose width is equal to 20% the total window width. When the window segment encompasses only background signal, the entropy is high, while when it reaches a segment containing the pulse, the entropy drops significantly and reaches a minimum value. By choosing a suitable threshold, a detection algorithm can be built on this principle.

Should a deterministic signal be present in Δ_{i_0}, then H_{i_0} would drop. Setting a threshold H_{thr}, one can detect this deterministic signal provided that $H_{i_0} < H_{thr}$. The principle of this detection is illustrated in Fig. 112.

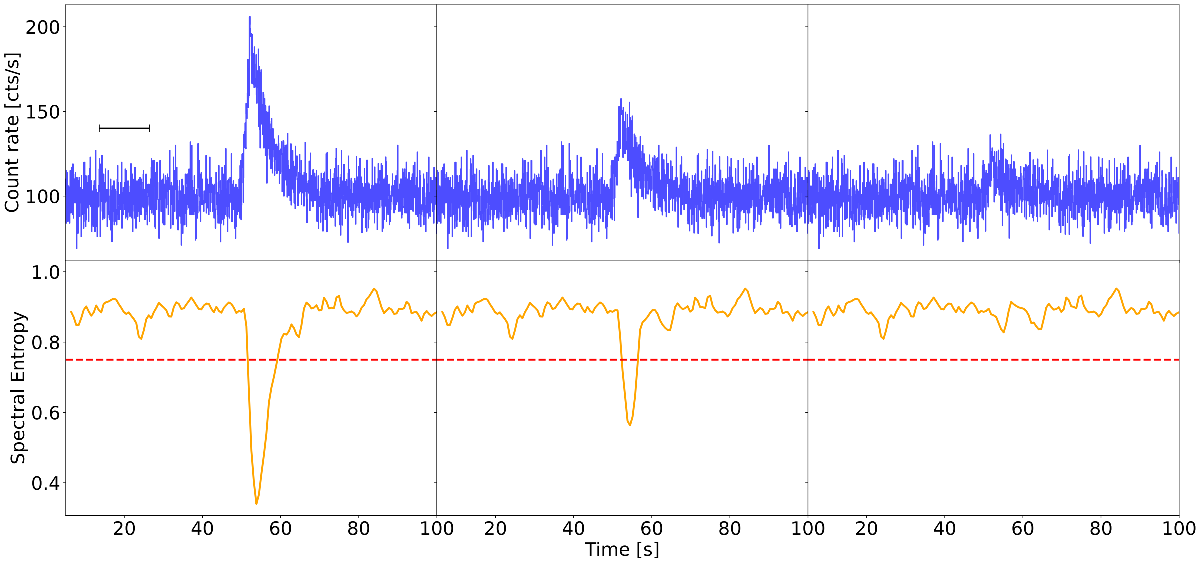

Figure 112: Illustration of the detection of a deterministic signal using entropy metrics. *Top panels:* a FRED-like signal (blue) with a rise time of 2 s and a decay time of 5 s with a decreasing intensity from left to right panels (100, 50, and 20 cts/s) plunged in a background Poisson noise of rate $\lambda = 100$ cts/s. The black segment indicates the width Δt of the window. *Bottom panels:* evolution of the spectral entropy as a function of the medium time of the sliding window. The red dashed line represents the value of the threshold $H_{thr} = 0.7$ chosen in this case. For the two leftmost panels, the deterministic signal is detected. In the rightmost bottom panel, the deterministic signal remains undetected.

There are two relevant quantities to assess the efficiency of a detection algorithm, that are both function of H_{thr}, namely the false positive (FP) and the true positive (TP) rates. The former corresponds to the fraction of time bins the algorithm takes a statistical fluke as a genuine signal, while the latter is the fraction of time bins the algorithm correctly identifies a true signal. Unfortunately, these two quantities are not independent, and generally a higher TP rate coincides with a higher FP rate (Fig. 113).

The threshold H_{thr} must be determined as the result of an optimal trade-off between a high TP rate and a low FP rate. To compare the performance of several algorithms, the FP rate must be preliminary fixed to a common value shared by all the algorithms. An alternative is to study these algorithms in the FP-TP rate plane. To determine the FP rate, we created a random signal by drawing 10^7 bins from a constant Poisson process and measured the entropy of each window segments of width Δt. We obtained a distribution of H_{thr}, whose length depends on the total number of bins and the sliding window step. The entropy threshold, for a given FP rate, is easily computed by sorting the entropy distribution and taking the value below which there are FP outliers, FP being the number of outliers for a given FP rate. This number is simply obtained by multiplying the desired FP rate by the length of the entropy distribution, which correspond to the number of tested windows (Fig. 114).

It is important to precise that, since this method does not test each time bin individually but instead evaluates the entropy on sliding windows separated by the window step (generally larger than one bin), we chose here to normalize it by the number of windows. Therefore, to compute the FP rate, we divided the number of FPs by the number of tested windows, rather

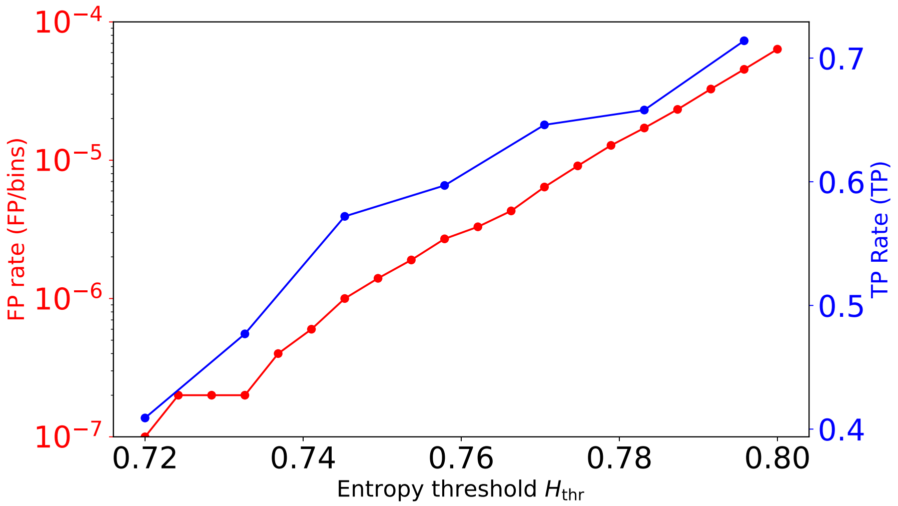

Figure 113: FP and TP rates as a function of the entropy threshold H_{thr}. The left y-axis (in log scale) represents the FP rate (red curve) while the right one shows the TP rate. As the entropy threshold H_{thr} gets closer to the noise level (high entropies), both the FP and TP rates increases, the algorithm becoming simultaneously more sensitive and more prone to false identifications.

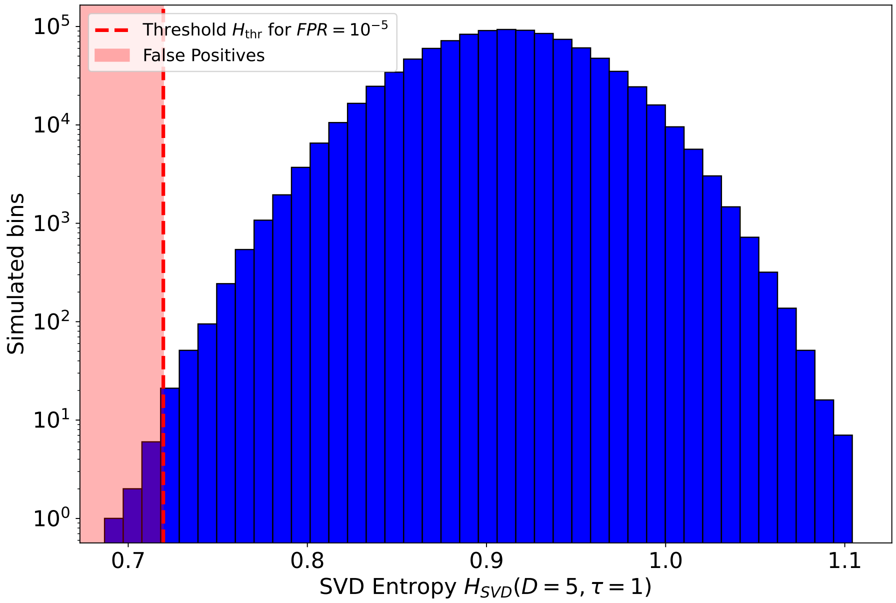

Figure 114: Distribution of entropy (in this case SVD entropy with $D = 5$ and $\tau = 1$) obtained by scanning 10^7 bins drawn from a Poisson distribution. The dashed vertical red line indicates the entropy threshold corresponding to a FP rate of 10^{-5} FP/window, while the shaded red region shows the FPs. In this simulated time series, 10^6 window segments are inspected (the step used for the sliding window being 10 bins), 10 FPs, lying on the red shaded region, are detected.

than by the total number of bins. This procedure allowed us to derive the FP rate as a function of the entropy threshold.

To determine the TP rate, we used a signal formed of both a random and deterministic part, the random one being given by Poisson noise with rate $\lambda = 100$ cts/s and the deterministic one by a Norris pulse with rise and decay times 2, and 5 s, respectively, and a peakedness of 1.5. For a great number N_{samples} of realisations of the random signal, we counted the fraction of time the entropy of a window that encompasses the deterministic signal was such that $H < H_{\text{thr}}$.

5.5.1 *Comparison of the efficiency of the algorithms*

We tested the efficiency of our algorithms for various configurations and parameter choices. In particular we compared the results obtained when varying

- the type of entropy measure used, among spectral entropy, SVD entropy, etc,
- the entropy definition used to compute it, including Shannon (110) and Rényi (113) entropies,
- the parameter values of these methods: the embedding dimension D, the lag time τ for SVD entropy, the α parameter of Rényi entropy, etc.

SVD entropy has two parameters, the embedding dimension D and the delay τ. We tested the various combinations to determine which is best suited to our case. This comparison is shown in Fig. 115. It seems that, for a lag time fixed to $\tau = 1$, $D = 10$ provides the most

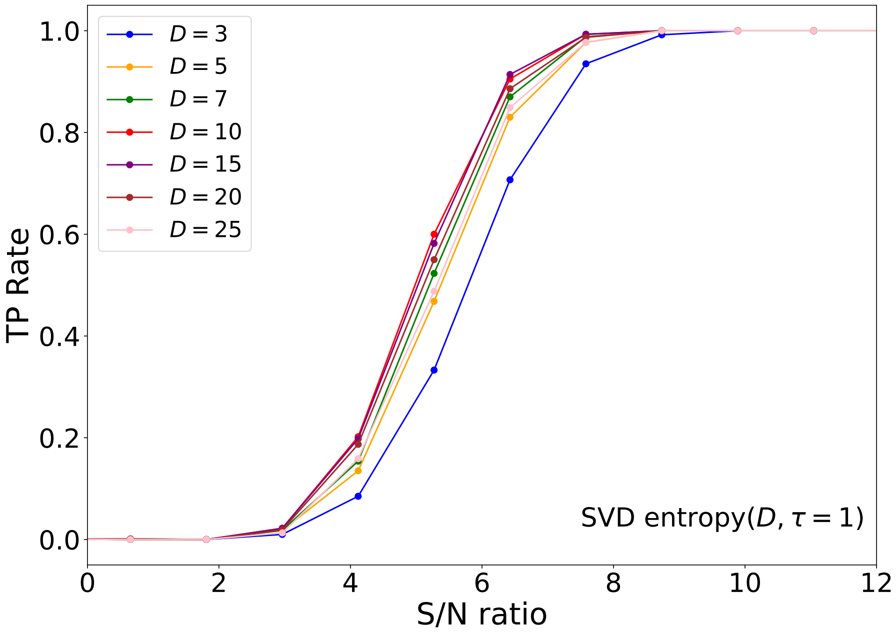

Figure 115: TP rate in the case of SVD entropy, for different values of the embedding dimension D. The x-axis represents the S/N ratio of a signal formed with of a deterministic time series (in this case, a Norris pulse) to which is added a background Poisson noise with a rate of 100 cts/s, while the y-axis represent the corresponding TP rate, for a FP rate of 10^{-5} FP/window. Coloured curves represent the TP rate values obtained for different values of D.

efficient algorithm. This is preliminary and more values of D should be tested.

We also tested the effect of τ on the efficiency of the algorithm, and the results are shown in Fig. 115.

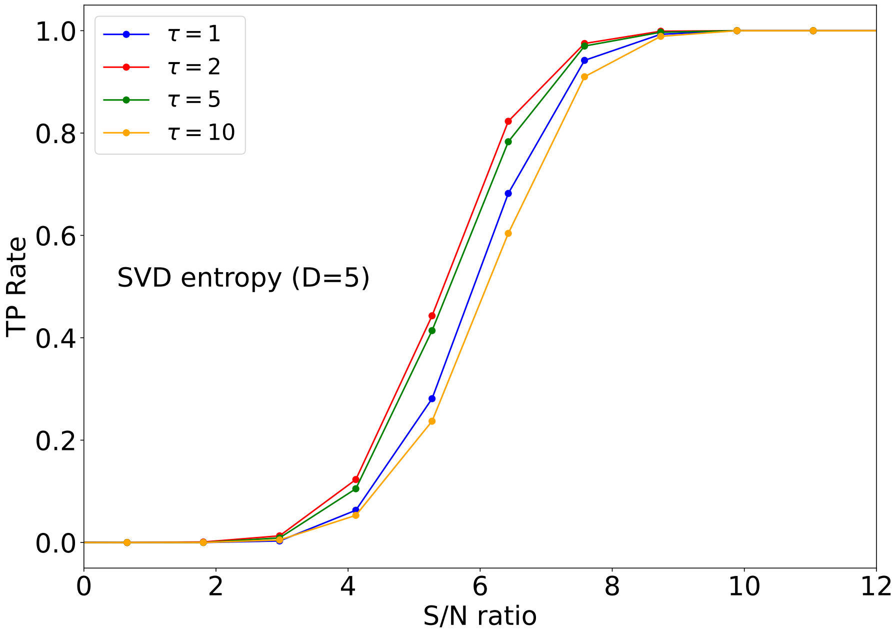

Figure 116: Same as Fig. 115, except that we tested different values of the lag time τ.

We tested, for a given entropy measure, whether Shannon (Eq. 110) or Rényi (Eq. 113) entropy yields the highest TP rate at a given FP rate. We found that Rényi entropy with $\alpha > 1$ systematically provides a higher TP rate for a fixed common FP rate. An example of this comparison, shown for SVD entropy, is presented in Fig. 117.

PE performed worse than both SVD and spectral entropy. As discussed in Sect. 5.3.4, its lack of sensitivity to the relative amplitudes of successive vector components makes it particularly vulnerable to noise. WPE mitigates this problem by adding weights to vectors with larger variance, as discussed in Sect. 5.3.5. However, even with this improvement, WPE still performs worse than SVD or spectral entropy for detecting the kind of deterministic signals considered here. Other entropy measures, such as those mentioned in Fig. 94, could be tested and compared to SVD entropy.

5.5.2 *Effect of the time window and the overlap*

The time step used between two consecutive sliding windows could also affect the TP rate. The step can range from a single time bin up to the full window size. In the former case, two adjacent windows almost fully overlap, whereas in the latter they do not overlap at all. The computational cost is larger for small window time steps, since the number of trials is increased. However, the smallest step size does not provide the highest TP rate, the maximum being reached for values around 5-20 % of the window length. The dependence of the TP rate on the chosen step size is illustrated in Fig. 118.

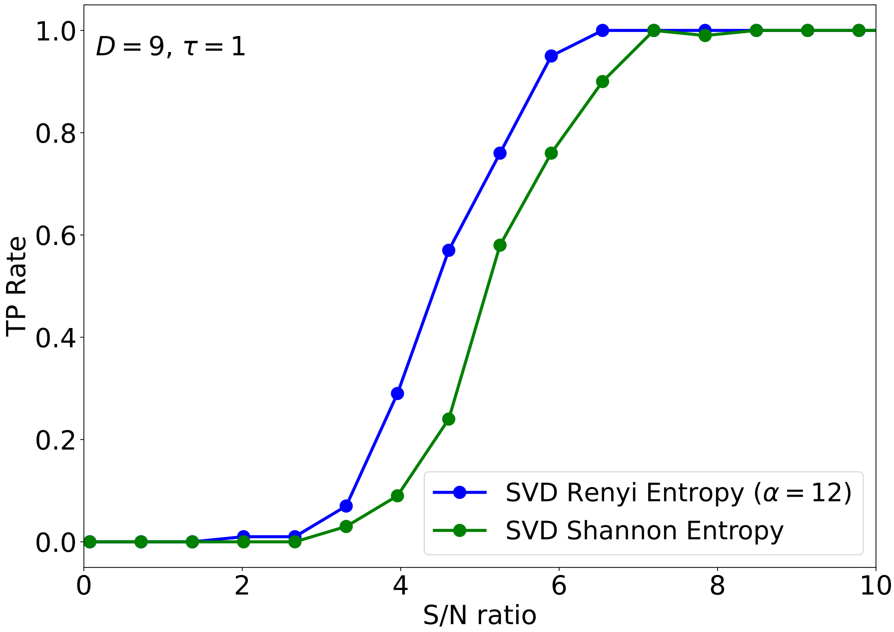

Figure 117: Comparison between Shannon and Rényi entropy. The green curve represents the TP rate as a function of the peak amplitude A, for a fixed FP rate of 1×10^{-5} FP/window, using Shannon entropy, while the blue one is obtaining using Rényi entropy. The entropy measure used in both cases is SVD entropy, with an embedding dimension $D = 9$ and a lag time $\tau = 1$.

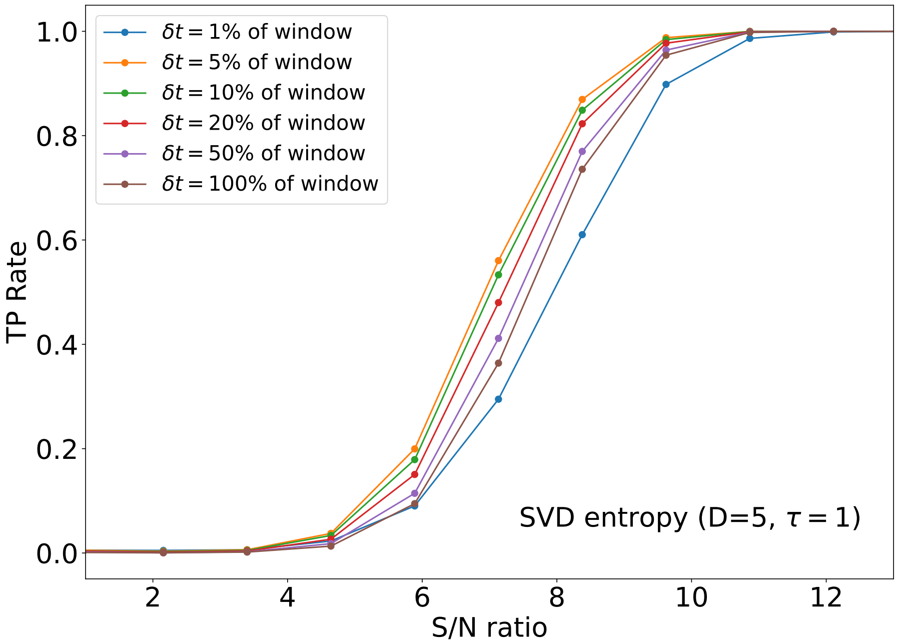

Figure 118: Same as Fig. 115, but we tested different values of the step δt between two consecutive sliding windows.

The length of the window also influences the TP rate. When the window is comparable to the intrinsic timescale of the signal (e.g. its FWHM), the TP rate reaches its highest values, whereas it decreases when the window length becomes significantly shorter or longer than the temporal extent of the signal. A comparison of this behaviour is shown in Fig. 119.

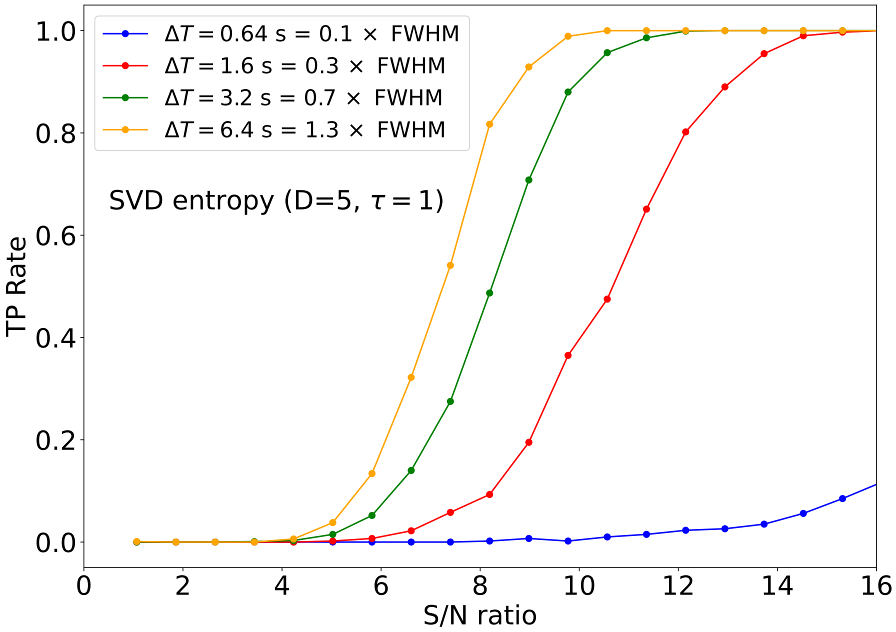

Figure 119: Same as Fig. 115, except that we tested different values of the window length, indicated as a fraction of the pulse FWHM.

This is actually a crucial aspect of GRB detection: in a typical detection scenario, the timescale of the signal is not known in advance. For this reason, standard trigger algorithms such as MEPSA or those implemented on-board of missions such as *CGRO*/BATSE, *Fermi*/GBM test multiple timescales. Therefore, the analysis we carried out so far using a fixed timescale is not sufficient to assess the true efficiency of the trigger algorithm. We should define a strategy that applies a series of time windows and test it on a set of simulated or/and real GRBs for which the timescale is not known a priori by the algorithm.

5.5.3 *Prospects*

This algorithm could be improved and further tested in several ways:

- by testing other entropy metrics;
- by applying the algorithm to pulses with different timescales and different shapes;
- by studying its performance on pulses affected by variable backgrounds;
- by running the algorithm on already detected GRBs and precursors;
- by applying it to new GRB detections, to spot weak GRBs with low S/N and/or weak GRB precursors.

Why is the last point important? Detecting GRB precursors can be extremely valuable. First, because it marks the true start of the activity of the central engine, allowing for the determination of its comprehensive duration. Second, for events originating from COMs, a precursor may result from resonant shattering flares occurring during the inspiral phase of a BNS or BHNS merger (Neill et al., 2022; Tsang et al., 2012), offering a rare insight into the pre-merger dynamics. For example, a precursor has been identified in the time profile of GRB 211211A and GRB 230307A, with properties compatible with the former interpretation (Dichiara et al., 2023). By studying the properties of GRB precursors, we can gain deeper clues into the physical properties of the binary system before the merger, including the strength of the magnetic field at the surface of the NS. This highlights the need for a robust algorithm capable of detecting these often very weak early signals.

5.6 CONCLUSION OF THIS CHAPTER

This chapter, more exploratory than the previous ones, introduced several techniques drawn from various areas of science that enable the characterisation of the type of dynamics underlying the time series arising from complex systems. These techniques originate from information theory, a discipline originally developed to quantify the amount of information contained in a signal and its associated structure. Although these techniques are usually applied to temporal signals very different from GRB LCs, and their applicability to GRBs is not immediately obvious, they can nonetheless provide powerful information about the underlying GRB dynamics. In particular, they could serve as tools to determine where GRB light curves lie with respect to deterministic and stochastic systems. Beyond this aspect, they may also prove useful for the detection of weak signals, a key challenge in GRB studies, by helping identify faint GRBs or precursor activity that might otherwise remain undetected.

6

CONCLUSIONS AND PROSPECTS

The temporal analysis of gamma-ray bursts (GRBs) carried out in this thesis sheds new light on the physical processes driving their prompt emission. By applying different definitions of variability to large samples of light curves (LCs), we have shown that the temporal behaviour of GRBs encodes key information about their central engines and progenitor systems.

- In Chapter 2, we showed that GRB prompt emission exhibits features typical of systems that are governed by self-organised criticality (SOC). This work, detailed in Maccary et al. (2024b), is the first that treated this problem in terms of rest-frame properties, accounting also for the selection effects. This suggests that the GRB central engine operates close to a critical regime, where magnetic reconnection or accretion instabilities could naturally give rise to avalanche-like energy releases.
- In Chapter 3, we identified the co-existence of two distinct variability components in GRB time profiles: a slow, long-timescale component, and a fast, sub-second one (Maccary et al., 2024a). This dual nature of variability provides a more complete picture of the mechanisms shaping GRB light curves.
- In Chapter 3, using the novel measurement of the minimum variability timescale (MVT) exposed in Camisasca et al. (2023b), we confirmed in Maccary et al. (2025) that this method was robust, comparing it with different more traditional measures, such as Bayesian blocks or pulse fitting. We confirmed already established correlations between MVT and peak luminosity, and between MVT and the Lorentz factor. The MVT then emerges as a valuable diagnostic tool to probe the dynamics of GRB outflows and to distinguish between collapsar- and merger-origin bursts.
- In Chapter 3, the detailed study of the exceptional event GRB 230307A, a long merger candidate that is also the second brightest GRB ever detected, revealed a very peculiar evolution of four properties (peak times, waiting times, full-width at half maximum, spectral peak energy) of the pulses that make up the time profile of this burst. This discovery calls into question the GRB emission mechanism itself, as it reveals that, for at least for some GRBs, the pulse width evolves throughout the burst, in contrast to what was previously concluded on a limited sample of LCs, at a time when most long multi-peaked GRBs had not yet been observed. This evolution is reviving older scenarios, such as external or refreshed shocks models, that naturally predict a similar kind of evolution. We further show that these features are shared by other long compact object merger candidates, such as GRB 211211A and GRB 060614. This discovery (i) opens promising prospects for identifying merger-driven GRBs directly from their γ-ray time profiles, a particularly relevant step with the recent launch of SVOM and the increasing number of well-localised bursts with a peculiar profile, as demonstrated by a few recent GCN notices; (ii) impose strong constraints on the physics of the prompt emission of these candidates: in **Maccary25b** we proposed a few simple models that try to account for the observed properties.

- In Chapter 4, we attempted to model GRB time series as a stochastic process using stochastic differential equations (SDEs). Based on the observed average properties of prompt emission, we proposed a SDE that is able to model non-stationary short lived signals and reproduce the distributions of a number of properties that are observed in real events. At the time of writing, we are still in the process of optimising the parameters of this model through a genetic algorithm, a method that turned out to be successful in modelling GRB light curves in a couple of previous works to which I contributed. This innovative approach could open a field yet totally unexplored: specifically, it may help understand to which extent GRBs are stochastic processes and, in this case, what kind of dynamics drives their energy release.
- In Chapter 5, we examined entropy-based measures as a tool to characterise the dynamical behaviour of prompt emission time series. We have in particular used the complexity-entropy plane to investigate the position of prompt emission time series on this plane compared to time series from stochastic processes and chaotic maps. We have preliminarily explored the potential of this technique as a triggering algorithm and, although further work is required to characterise its strengths and weaknesses, it might represent a valid alternative to more traditional algorithms that are currently adopted.

Our work laid the basis for the following developments:

- **Search for additional long merger candidates and test their compatibility with the Amati relation for Type-II GRBs**. We identified several long merger candidates that exhibit the same distinctive set of properties found in GRB 230307A and other long mergers. We inspected their trajectories in the Amati plane for GRBs without redshift and found significant outliers of the Type-II Amati relation. Based on these results, we built a statistical test assessing the hypothesis that these long merger candidates are randomly drawn from the Type-II GRB population under the assumption that the latter satisfy the relation. We found that we can confidently reject (> 3 Gaussian σ) this hypothesis, implying that at least one of these candidates is incompatible with the Type-II Amati relation. A paper reporting these results is under way.
- **Search for long merger candidates in the BATSE sample**. BATSE provides a large dataset of GRBs with great signal-to-noise ratio, making it particularly suitable for identifying the properties observed in GRB 230307A and for testing pulse width evolution. The previously suggested absence of pulse width increase with time was based on a limited sample. A systematic investigation of the BATSE dataset could reveal additional events with analogous properties, thus contributing to better constrain the fraction of merger candidates among long GRBs.
- **Simulate GRBs via stochastic differential equations**. We will keep working on the approach described in Chapter 4 to simulate LCs via a stochastic process generated through a SDE and apply this method to reproduce prompt emission time series, as they are observed by *CGRO*/BATSE, *Swift*/BAT, and *Fermi*/GBM.
- **Assess the stochastic or deterministic character of GRB light curves using the complexity-entropy plane**. We will continue the approach of Chapter 5 to determine the relative position of some bright GRB LCs with respect to time series from various stochastic processes and chaotic maps.

- **Detection of weak GRB signals and precursors using entropy-based metrics.** After having robustly tested the algorithm, we aim to apply it to real time series to (i) test its performance on previously identified weak triggers and reported precursor episodes, and (ii) search for new and/or previously unreported precursor activity. Combined with our existing tools we previously developed, this would constitute an additional piece in the set of tools we developed that allow for the identification of long merger candidates.

In summary, this thesis contributes to a deeper understanding of GRB temporal variability, connecting observational signatures to their underlying physical origins. The methodologies and results presented here pave the way for future studies with recently launched missions such as SVOM, Einstein Probe, and proposed missions like THESEUS, which will vastly expand the accessible GRB population.

A
APPENDIX

A.1 COMPACTNESS PROBLEM

We begin by expressing the isotropic-equivalent energy of the burst. For a measured fluence Φ and luminosity distance D_L, the isotropic energy release is

$$E_{\gamma,\mathrm{iso}} = 4\pi D_L^2 \Phi = 10^{50}\ \mathrm{erg} \left(\frac{D_L}{3\ \mathrm{Gpc}}\right)^2 \left(\frac{\Phi}{10^{-7}\ \mathrm{erg\ cm^{-2}}}\right). \tag{154}$$

The emitting region cannot be larger than the causality radius associated with the observed variability timescale δT:

$$R_i = c\,\delta T. \tag{155}$$

High–energy photons propagating through this region may annihilate into electron–positron pairs. Pair production requires that $\sqrt{E_1 E_2} > m_e c^2$. The corresponding optical depth is approximately

$$\tau_{\gamma\gamma} \sim n \sigma_T R_i, \tag{156}$$

where n is the photon number density. To relate n to observable quantities, we note that the flux can be written as $\Phi = (n E_i) c = L_{\gamma,\mathrm{iso}}/(4\pi R_i^2)$, which gives

$$n = \frac{L_{\gamma,\mathrm{iso}}}{4\pi R_i^2 c E_i}, \tag{157}$$

where $L_{\gamma,\mathrm{iso}}$ is the isotropic-equivalent luminosity, and E_i the mean photon energy.
The luminosity is related to the isotropic-equivalent energy through

$$L_{\gamma,\mathrm{iso}} = \frac{E_{\gamma,\mathrm{iso}}}{\delta T} = \frac{E_{\gamma,\mathrm{iso}} c}{R_i} \tag{158}$$

The characteristic photon energy relevant for pair production is of order the electron rest mass energy $E_i \sim m_e c^2$. Substituting these relations into the expression for $\tau_{\gamma\gamma}$, and retaining only the fraction f_p of photons energetic enough to participate in pair creation, we obtain

$$\tau_{\gamma\gamma} = f_p \Phi \left(\frac{D_L}{R_i}\right)^2 \frac{\sigma_T}{m_e c^2}. \tag{159}$$

Finally, writing $R_i = c\,\delta T$ and inserting fiducial values gives

$$\tau_{\gamma\gamma} = 10^{13} f_p \left(\frac{\Phi}{10^{-7}\ \mathrm{erg\ cm^{-2}}}\right) \left(\frac{D_L}{3\ \mathrm{Gpc}}\right)^2 \left(\frac{\delta T}{10\ \mathrm{ms}}\right)^{-2}. \tag{160}$$

This equation provide the expression of the optical depth in the classical non-relativistic case. The excessively large value obtained in this case enter in contradiction with the observed non-thermal emission. The resolution of this issue is provided by the existence of a relativistic outflow, as explained in Sect. A.1.

A.2 INTERNAL SHOCKS: RADIUS OF THE SHOCKS

The first shell is emitted at $t = t_e$, with velocity $\beta_1 \simeq 1$ and $\Gamma_1 \gg 1$. It expands as

$$R_1 = \beta_1 c(t - t_e). \tag{161}$$

The second shell is emitted at $t = t_e + t_{var}$, with Lorentz factor $\Gamma_2 > \Gamma_1$ and velocity β_2. Its radial evolution is given by

$$R_2 = \beta_2 c(t - t_e - t_{var}). \tag{162}$$

The internal shock occurs when the faster shell catches up with the slower one, i.e. when $R_1 = R_2$. This happens at time $t = t_{IS}$, such that

$$t_{IS} = t_e + \frac{\beta_2}{\beta_2 - \beta_1} t_{var}. \tag{163}$$

The corresponding internal shock radius is

$$R_{IS} = \frac{\beta_1 \beta_2}{\beta_2 - \beta_1} c\, t_{var}. \tag{164}$$

In the ultra-relativistic limit (UR; $\Gamma >\!\!> 1$), $\beta \simeq 1 - \frac{1}{2\Gamma^2}$, so Eq. (164) can be expressed as

$$R_{IS} = \frac{2\Gamma_1^2 \Gamma_2^2}{\Gamma_2^2 - \Gamma_1^2} c\, t_{var}, \tag{165}$$

and for $\delta\Gamma \sim \Gamma$,

$$R_{IS} \simeq \Gamma^2 c\, t_{var}. \tag{166}$$

A.3 INTERNAL SHOCKS: VARIABILITY IN THE OBSERVER FRAME

The collision between shells 1 and 2 in the rest frame of the central engine occurs at $t = t_{IS}$. Correspondingly, a pulse is observed by the observer located at a distance D from the central engine (see Fig. 120) at the arrival time t_{obs}, given by:

$$t_{obs} = t_{IS} + \frac{D - R_{IS}}{c}. \tag{167}$$

Using Eq. (161) to express R_{IS} in function of t_{IS}:

$$t_{obs} = \frac{D}{c} + \beta_1 t_e + (1 - \beta_1) t_{IS}. \tag{168}$$

Using Eq. (163):

$$t_{obs} = \frac{D}{c} + t_e + \frac{(1 - \beta_1)\beta_2\, t_{var}}{\beta_2 - \beta_1}. \tag{169}$$

In the ultra-relativistic regime, it becomes:

$$t_{obs} \simeq \frac{D}{c} + t_e + \frac{1}{2} \frac{\Gamma_2^2 + \Gamma_1^2}{\Gamma_2^2 - \Gamma_1^2} t_{var}. \tag{170}$$

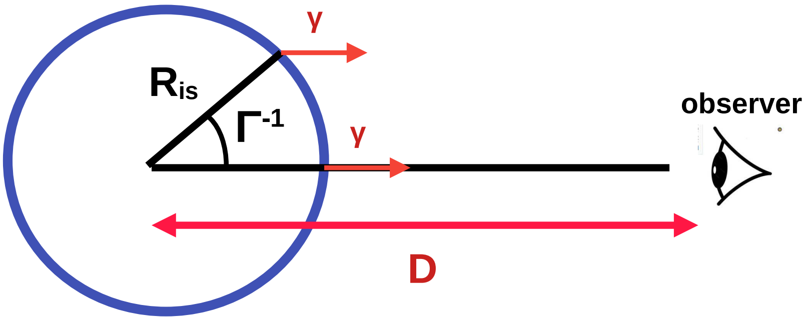

Figure 120: A pulse emitted at radius $R = R_{IS}$ at time t_{IS} is seen by the observer at distance D at time t_{obs}.

Using $\Gamma_2 \gg \Gamma_1$, we finally obtain:

$$t_{obs} \simeq \frac{D}{c} + t_e + t_{var}. \tag{171}$$

Hence the variability observed in the light curve is reflecting the initial variability imprinted by the central engine.

A.4 INTERNAL SHOCKS: CONVERSION EFFICIENCY INTO γ-RAYS

The two shells moving with $\Gamma_1 > \Gamma_2$ collide and merge into a final shell with a Lorentz factor Γ_f. Some internal energy $\mathcal{E}$ is produced by the collision, in the co-moving frame of the merged shell. The conservation of energy and momentum can be expressed as follows:

$$\Gamma_1 m_1 c^2 + \Gamma_2 m_2 c^2 = \Gamma_f \left(m_1 + m_2 + \frac{\mathcal{E}}{c^2} \right) c^2, \tag{172}$$

$$m_1 \Gamma_1 c \sqrt{1 - \frac{1}{\Gamma_1^2}} + m_2 \Gamma_2 c \sqrt{1 - \frac{1}{\Gamma_2^2}} = \left(m_1 + m_2 + \frac{\mathcal{E}}{c^2} \right) \Gamma_f c \sqrt{1 - \frac{1}{\Gamma_f^2}} \tag{173}$$

or equivalently,

$$\Gamma_1 m_1 + \Gamma_2 m_2 = \Gamma_f \left(m_1 + m_2 + \frac{\mathcal{E}}{c^2} \right), \tag{174}$$

$$m_1 \sqrt{\Gamma_1^2 - 1} + m_2 \sqrt{\Gamma_2^2 - 1} = \left(m_1 + m_2 + \frac{\mathcal{E}}{c^2} \right) \sqrt{\Gamma_f^2 - 1}, \tag{175}$$

Assuming $\Gamma_1, \Gamma_2 \gg 1$:

$$\Gamma_f \simeq \sqrt{\frac{m_1 \Gamma_1 + m_2 \Gamma_2}{m_1/\Gamma_1 + m_2/\Gamma_2}} \tag{176}$$

The conversion efficiency of kinetic into internal energy is defined as ($\Gamma_f \mathcal{E}$ being the internal energy in the observer frame):

$$\eta_{\text{eff}} \equiv \frac{\Gamma_f \mathcal{E}}{(m_1\Gamma_1 + m_2\Gamma_2)c^2} = 1 - \frac{(m_1+m_2)\Gamma_f}{m_1\Gamma_1 + m_2\Gamma_2} \simeq 1 - \frac{m_1+m_2}{\sqrt{m_1^2+m_2^2+(\Gamma_1/\Gamma_2+\Gamma_2/\Gamma_1)m_1m_2}} \tag{177}$$

For equal masses and putting $x = \frac{\Gamma_2}{\Gamma_1}$, we obtain:

$$\eta_\gamma(x) = 1 - \frac{2}{\sqrt{2+x+1/x}}. \tag{178}$$

The conversion efficiency as a function of x is drawn in Fig. 121, showing that a high contrast in Lorentz factors is needed to obtain the high conversion efficiency values required by observations.

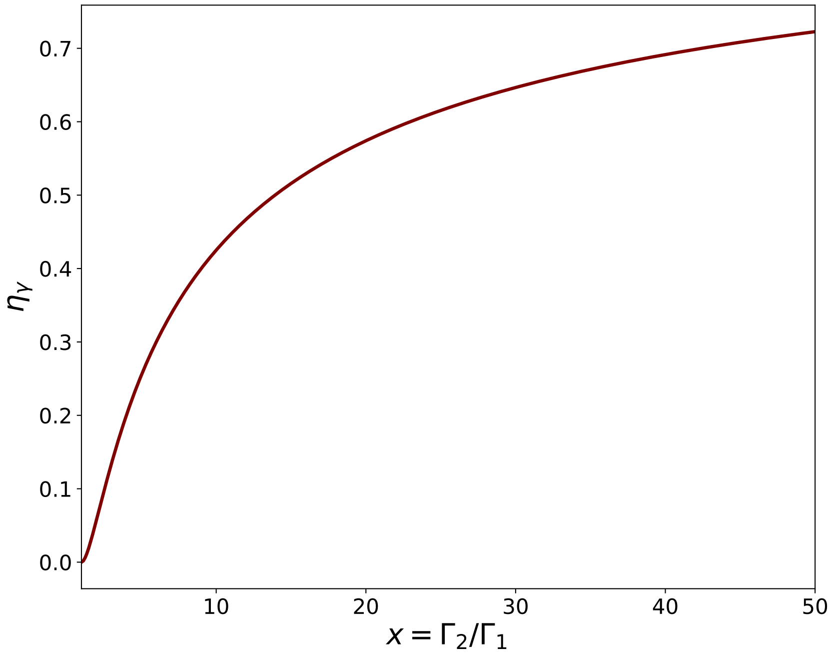

Figure 121: Conversion efficiency factor as a function of the Lorentz factor ratio of the two shells.

A.5 SDE: COMPUTATION OF THE MEAN OF THE GEOMETRIC BROWNIAN MOTION

To obtain the mean of the geometric Brownian motion, we essentially need to compute $\mathbb{E}[e^{\sigma W_t}]$. For that, since $W_t \sim \mathcal{N}(0,t)$, the moments of W_t are given by:

$$\begin{cases} \mathbb{E}[W_t^n] = 0 \text{ if } n \text{ is odd} \\ \mathbb{E}[W_t^n] = t^{n/2}(n-1)!!, \text{ if } n \text{ is even,} \end{cases} \tag{179}$$

with $(n-1)!! = (n-1) \times (n-3) \times ....$

Using the Taylor expansion of the exponential function and the linearity of the $\mathbb{E}$ operator:

$$\mathbb{E}[e^{\sigma X_t}] = \sum_{n=0}^{+\infty} \sigma^n \frac{\mathbb{E}(W_t^n)}{n!} = \sum_{n \text{ even}} \frac{\sigma^n t^{n/2}(n-1)!!}{n!} \tag{180}$$

By letting $n = 2k$ in the sum,

$$\mathbb{E}[e^{\sigma X_t}] = \sum_{k=0}^{+\infty} \frac{\sigma^{2k} t^k (2k-1)!!}{(2k)!} = \sum_{k=0}^{+\infty} \frac{\sigma^{2k} t^k \cancel{(2k-1)} \times \cancel{(2k-3)} \times \ldots}{(2k) \times \cancel{(2k-1)} \times (2k-2) \times \cancel{(2k-3)} \times \ldots} = \sum_{k=0}^{+\infty} \frac{\sigma^{2k} t^k}{2^k k!} = e^{\sigma^2 t/2}. \tag{181}$$

A.6 SDE:COMPUTATION OF THE MEAN SQUARE DISPLACEMENT À LA ORNSTEIN-UHLENBECK

When computing the mean square displacement, we admit the computation of $\int_0^t \int_0^t e^{-\theta|s-s'|} ds ds'$. We now give a proof of it. To integrate the absolute value, we split the integration square $[0,t] \times [0,t]$ into two triangles delimited by the equality line $s = s'$. The lower triangle is defined as $s \in [0,t]$ and $s' \in [0,s]$. Since there is a clear symmetry between s and s', we can therefore integrate only on the lower triangle and multiply the result by 2:

$$\int_0^t \int_0^t e^{-\theta|s-s'|} ds ds' = 2 \int_0^t \Big(\int_0^s e^{-\theta(s-s')} ds' \Big) ds \tag{182}$$

Then, we easily get

$$\frac{2}{\theta} \int_0^t (1 - e^{-\theta s}) ds = \frac{2}{\theta}(t - \frac{1}{\theta}(1 - e^{-\theta t})), \tag{183}$$

proving therefore that

$$\int_0^t \int_0^t e^{-\theta|s-s'|} ds ds' = \frac{2}{\theta^2}(\theta t - 1 + e^{-\theta t}). \tag{184}$$

A.7 PAPER I: DISTRIBUTIONS OF ENERGY, LUMINOSITY, DURATION, AND WAITING TIMES OF GAMMA-RAY BURST PULSES WITH KNOWN REDSHIFT DETECTED BY FERMI/GBM

The Astrophysical Journal, 965:72 (17pp), 2024 April 10 https://doi.org/10.3847/1538-4357/ad26f4

Distributions of Energy, Luminosity, Duration, and Waiting Times of Gamma-Ray Burst Pulses with Known Redshift Detected by Fermi/GBM

R. Maccary[1], C. Guidorzi[1,2,3], L. Amati[3], L. Bazzanini[1,3], M. Bulla[1,2,4], A. E. Camisasca[1], L. Ferro[1,3], F. Frontera[1,3], and A. Tsvetkova[3,5]
[1] Department of Physics and Earth Science, University of Ferrara, Via Saragat 1, I-44122 Ferrara, Italy
[2] INFN—Sezione di Ferrara, Via Saragat 1, 44122 Ferrara, Italy
[3] INAF—Osservatorio di Astrofisica e Scienza dello Spazio di Bologna, Via Piero Gobetti 101, 40129 Bologna, Italy
[4] INAF—Osservatorio Astronomico d'Abruzzo, Via Mentore Maggini snc, 64100 Teramo, Italy
[5] Department of Physics, University of Cagliari, SP Monserrato-Sestu, km 0.7, 09042 Monserrato, Italy

Received 2023 October 14; revised 2023 December 22; accepted 2024 January 24; published 2024 April 8

Abstract

Discovered more than 50 years ago, gamma-ray burst (GRB) prompt emission remains the most puzzling aspect of GRB physics. Its complex and irregular nature should reveal how newborn GRB engines release their energy. In this respect, the possibility that GRB engines could operate as self-organized critical (SOC) systems has been put forward. Here, we present the energy, luminosity, waiting time, and duration distributions of individual pulses of GRBs with known redshift detected by the Fermi Gamma-ray Burst Monitor. This is the first study of this kind in which selection effects are accounted for. The compatibility of our results with the framework of SOC theory is discussed. We found evidence for an intrinsic break in the power-law models that describe the energy and the luminosity distributions.

Unified Astronomy Thesaurus concepts: Gamma-ray bursts (629); High energy astrophysics (739); Gamma-ray transient sources (1853); Relativistic jets (1390)

Supporting material: machine-readable table

1. Introduction

Gamma-ray prompt emission is the first electromagnetic radiation observed from a gamma-ray burst (GRB) source. It is caused by at least two different types of catastrophic events: (i) the merger of a binary system of compact objects (Eichler et al. 1989; Paczynski 1991; Narayan et al. 1992; Abbott et al. 2017); (ii) the core collapse of fast-rotating, hydrogen-stripped massive stars (dubbed as "collapsars"; Woosley 1993; Paczyński 1998; MacFadyen & Woosley 1999; Yoon & Langer 2005). Most events of the first (second) class are associated with short (long) GRBs (SGRBs/LGRBs), with some notable exceptions: short with extended emission GRBs (Gehrels et al. 2006; Norris & Bonnell 2006), short GRBs coming from collapsars (Ahumada et al. 2021; Rossi et al. 2022), and long GRBs coming from mergers (Rastinejad et al. 2022; Troja et al. 2022; Gompertz et al. 2023; Yang et al. 2024). In light of the emerging complexity, classes (i) and (ii) are often now referred to as merger and collapsar GRBs, or, equivalently, as type I and type II GRBs, respectively (Zhang 2006).

The nature of the central engine that powers a GRB is still debated, as either a hyper-accreting stellar-mass black hole (BH; Lei et al. 2013; Janiuk et al. 2017; Sado 2019) surrounded by a thick accretion disk, or a fast-rotating, highly magnetized neutron star (NS, known as a "millisecond magnetar"; Usov 1992; Wheeler et al. 2000; Thompson et al. 2004; Metzger et al. 2011). In the case of a hyper-accreting BH, the jet can be produced either by a neutrino-dominated accretion flow (NDAF; Liu et al. 2017) in which neutrinos tap the thermal energy of the accretion disk via neutrino–antineutrino annihilation, launching a thermally dominated fireball (Popham et al. 1999; Di Matteo et al. 2002), or through the Blandford–Znajek (BZ) effect (Blandford & Znajek 1977), which converts the BH spinning energy into a Poynting-flux-dominated outflow. Also, in the case of a millisecond magnetar, the rotational energy could be the source of energy (Duncan & Thompson 1992; Metzger et al. 2011). Magneto-hydrodynamic instabilities can also be considered to launch the jet, possibly for both engines (Bromberg & Tchekhovskoy 2016).

GRB temporal profiles exhibit a remarkable variety in intensity, duration, number of pulses, and variability in general. Most profiles can be seen as a superposition of fast-rise exponential decay pulses (FRED; Fishman & Meegan 1995). Prompt emission is often characterized by phases of intense activity separated by periods of prolonged inactivity (quiescent times).

The study of the waiting times (WTs) indicates that a GRB central engine could emit pulses according to a nonstationary Poisson process (Guidorzi et al. 2015). The diversity of all observed bursts could be understood as different realizations of a common stochastic process. Should this be the case, an open question is whether this process can be characterized in a more detailed way, so as to reveal the dynamics that rule the energy release. If positive, this would strongly constrain the way GRB engines work and, ultimately, help identify their nature and the powering mechanism(s).

Complex systems with many interacting elements, presenting erratic on–off intermittency (such as earthquakes, neuronal activity, the stock market, the evolution of species) can be interpreted in the framework of self-organized criticality (SOC; Sornette & Sornette 1989; Bak & Sneppen 1993; Bartolozzi et al. 2005; de Arcangelis 2012). Invoked to explain the ubiquitousness of $1/f$ noise spectra, SOC was originally applied to describe sandpile avalanches (Bak et al. 1987, 1988). A SOC system can be seen as an out-of-equilibrium nonlinear dynamical system in which energy steadily brought by an external source drives the system toward a critical point, at which the energy is liberated through scale-free avalanches (Aschwanden 2014).

One of the signatures of SOC lies in its scale invariance: the released energy, luminosity (or peak flux, depending on the context), duration, and WT of individual avalanches are power-law (PL) distributed, with a set of relations between the different PL indices (see Section 4).

SOC has been utilized to explain a wide range of astrophysical phenomena, such as solar flares, lunar craters, Saturn rings, auroral emission from Earth's magnetosphere, pulsar glitches, blazars, and stellar flares (see Aschwanden et al. 2018 for a review; Aschwanden & Güdel 2021). One of the main accomplishments of SOC theory is the successful and exhaustive description of solar flares (Lu & Hamilton 1991; Charbonneau et al. 2001; Aschwanden & Aschwanden 2008a, 2008b; Aschwanden & McTiernan 2010; Wang & Dai 2013). A body of evidence for SOC behavior was also found in the case of soft gamma-ray repeaters (SGRs) or magnetars (Nakazato 2014), which are also GRB engine candidates. It is worth noting that SOC behavior in the case of a BH surrounded by an accretion disk was also investigated as well as for the X-ray flaring activity of the Galactic center, Sgr A* (Li et al. 2015; Yuan et al. 2018).

Do GRB engines work as SOC systems? Cellular automata (CA) simulations of 1D and 2D magnetized outflow demonstrated that such systems could reach a SOC state (Dănilă et al. 2015; Harko et al. 2015). This is consistent with the picture of prompt emission being the result of fast magnetic reconnection events occurring in a Poynting outflow powered by a highly magnetized NS. Such CA simulations were also performed in the case of a hyper-accreting BH (Mineshige et al. 1994), another leading candidate as a GRB progenitor. Thus, the SOC interpretation could actually be consistent with radically different theoretical pictures of prompt emission. In the case of a hyper-accreting BH, SOC avalanches could be triggered either by the thermal instability of the accretion disk (Janiuk et al. 2007; Janiuk & Yuan 2010; Taylor et al. 2011) or by magnetic instabilities, such as a kink-mode instability (Giannios & Spruit 2006; Bromberg et al. 2019) or a tearing-mode instability (Del Zanna et al. 2016; Yang 2019), while only magnetic instabilities are expected in the millisecond-magnetar scenario.

Evidence for SOC in GRB X-ray flares was suggested by Wang & Dai (2013), whose results could be understood as a 1D SOC system with normal diffusion. Multipulsed LGRBs (Lyu et al. 2020), SGRBs (Li et al. 2023), and LGRB precursors (Li & Yang 2023) seem roughly compatible with a 3D one. In these works, the GRB properties are PL distributed, even if the agreement with SOC theory is not always compelling. Moreover, observables such as the fluence or peak flux of pulses are often considered, which might not necessarily reflect an intrinsic property of GRB engines, but strongly depend, among other things, on redshift. In this paper, we used a sample of type II GRBs detected by the Fermi Gamma-ray Burst Monitor (GBM; Meegan et al. 2009) with known (spectroscopic) redshift to compute the distributions of the isotropic-equivalent released energy, of the luminosity, of the duration, and of the WT of the individual pulses that compose GRB light curves. We performed a thorough estimation of the selection effects, splitting our sample into redshift bins and estimating the detection efficiency separately for each redshift bin. The redshifts of our data sample were determined through spectroscopic observations of either the optical afterglow or the host galaxy.

Section 2 describes the GRB samples and the data analysis, and the results are reported in Section 3 and discussed in Section 4, with conclusions in Section 5. In Appendix, the impact of performing a time-averaged analysis instead of a time-resolved one is discussed. Hereafter, we used a flat Lambda cold dark matter (ΛCDM) cosmology model with the latest cosmological parameter values $H_0 = 67.66$ km Mpc^{-1} s^{-1} and $\Omega_0 = 0.31$ (Planck Collaboration et al. 2020).

2. Data Analysis

2.1. Sample Selection

The GBM consists of 12 Na I scintillators sensitive in the 8–1000 keV energy range and two BGO scintillators, sensitive to higher energies (150 keV–30 MeV), overlapping at low energies with Na I detectors.

We first selected all the GRBs detected by the GBM from 2008 August to 2022 July, with redshift measured spectroscopically, except for a few constraining photometric estimates.[6] We excluded 130427A and 221009A from our analysis since the main burst saturates all Na I detectors of the GBM (Ackermann et al. 2014; Lesage et al. 2023).

To ensure that the population of GRB progenitors is as homogeneous as possible, we selected only type II GRBs. To this aim, we first considered events with $T_{90} \geqslant 2$ s (Kouveliotou et al. 1993). We used T_{90}, after excluding the LGRBs that have been reported as credible type I candidates. The boundary value of $T_{90} = 2$ s was originally derived from the catalog of the Burst And Transient Source Experiment (BATSE; Paciesas et al. 1999); this threshold depends on the energy passband of the instrument and, as such, is consequently different for the BATSE ($\sim$2.4 s), the Neil Gehrels Swift Observatory BAT (0.8 s, see Gehrels et al. 2004; Bromberg et al. 2013) and the GBM ($\sim$4.2 s; see von Kienlin et al. 2020). We therefore assumed the more conservative threshold of $T_{90} > 4.2$ s, as it is more suitable for the GBM. T_{90} values were taken from the GBM catalog (von Kienlin et al. 2020).

Despite its $T_{90} = 2.6 \pm 0.6$ s, we included 141004A because two independent telescopes (the Gran Telescopio Canarias and the Reionization and Transients Infrared Camera) detected a possible brightening in the optical counterpart that was interpreted as an emerging supernova (Schulze et al. 2014b; Littlejohns et al. 2014). The same applies for 200826A, with $T_{90} = 1.14 \pm 0.13$ s, for which robust evidence for a collapsar origin was found (Ahumada et al. 2021; Zhang et al. 2021; Rossi et al. 2022). Among the long-lasting GRBs we excluded 211211A, for which compelling evidence for a type I burst was reported despite its T_{90} of 34 s and a multipeaked light curve that deceptively looks like that of a typical type II GRB (Rastinejad et al. 2022; Troja et al. 2022; Yang et al. 2022; Gompertz et al. 2023). We also excluded two GRBs (090510 and 161129A) among the so-called short with extended emission GRBs (Norris & Bonnell 2006), which are likely

---

[6] They are 120922A, 151111A, and 200829A with, respectively, $z = 3.1 \pm 0.2$, $z = 3.5 \pm 0.3$, and $z = 1.25 \pm 0.2$.

Table 1
The First Five GRBs of the Final Sample

GRB	Trigger Name	Trigger Time (UT)	T_{90} (s)	$T_{90,\mathrm{err}}$ (s)	z	z_{ref}[a]
080804	bn080804972	23:20:14.879	24.704	1.46	2.2045	(1)
080810	bn080810549	13:10:12.581	75.201	3.638	3.35	(2)
080905B	bn080905705	16:55:46.843	105.984	6.802	2.374	(3)
080916A	bn080916406	09:45:18.938	46.337	7.173	0.689	(4)
080928	bn080928628	15:04:56.048	14.336	4.007	1.692	(5)

Notes.

[a] (1) Thoene et al. (2008), (2) Prochaska et al. (2008), (3)Rowlinson et al. (2010), (4) Fynbo et al. (2008), (5) Vreeswijk et al. (2008), (6) D'Avanzo et al. (2008), (7) Krühler et al. (2015), (8) Berger & Rauch (2008), (9) Krühler et al. (2015), (10) Cucchiara et al. (2008), (11) de Ugarte Postigo et al. (2009b), (12) Krühler et al. (2015), (13) Chornock et al. (2009), (14) Cenko et al. (2009), (15) Salvaterra et al. (2009), (16) Wiersema et al. (2009a), (17) de Ugarte Postigo et al. (2009a), (18) Thoene et al. (2009a), (19) Cano et al. (2011), (20) Cucchiara et al. (2009c), (21) Fynbo et al. (2009), (22) D'Elia et al. (2010), (23) Cucchiara et al. (2009b), (24) Xu et al. (2009), (25) Cucchiara et al. (2009a), (26) Thoene et al. (2009b), (27) Wiersema et al. (2009b), (28) Cucchiara & Fox (2010), (29) Kruehler et al. (2013b), (30) Thoene et al. (2010), (31) Kruehler et al. (2013a), (32) Flores et al. (2010), (33) O'Meara et al. (2010), (34) Tanvir et al. (2010), (35) Chornock & Berger (2011), (36) de Ugarte Postigo et al. (2011), (37) Chornock et al. (2011b), (38) Sparre et al. (2011), (39) Milne & Cenko (2011), (40) Tanvir et al. (2011), (41) D'Avanzo et al. (2011), (42) Chornock et al. (2011a), (43) Klose et al. (2019), (44) Malesani et al. (2013), (45) Cucchiara & Prochaska (2012), (46) Tello et al. (2012), (47) de Ugarte Postigo et al. (2013b), (48) Tanvir et al. (2012b), (49) Xu et al. (2012), (50) Tanvir & Ball (2012), (51) Thoene et al. (2012), (52) Sanchez-Ramirez et al. (2012), (53) Hartoog et al. (2012), (54) Knust et al. (2012), (55) Tanvir et al. (2012a), (56) Perley et al. (2012), (57) Cucchiara & Fumagalli (2013), (58) de Ugarte Postigo et al. (2013a), (59) Levan et al. (2013), (60) Jeong et al. (2014b), (61) Smette et al. (2013), (62) Tanvir et al. (2013), (63) Singer et al. (2013), (64) Sudilovsky et al. (2013), (65) Selsing et al. (2019), (66) Xu et al. (2013), (67) de Ugarte Postigo et al. (2013b), (68) Malesani et al. (2014), (69) Schulze et al. (2014a), (70) Jeong et al. (2014a), (71) Tanvir et al. (2014), (72) Fynbo et al. (2014), (73) Wiersema et al. (2014), (74) de Ugarte Postigo et al. (2014c), (75) Singer et al. (2015), (76) Kasliwal et al. (2014), (77) Bhalerao et al. (2014), (78) Castro-Tirado et al. (2014b), (79) de Ugarte Postigo et al. (2014a), (80) Gorosabel et al. (2014a), (81) Castro-Tirado et al. (2014a), (82) Xu et al. (2014), (83) de Ugarte Postigo et al. (2014b), (84) Gorosabel et al. (2014b), (85) de Ugarte Postigo et al. (2015a), (86) de Ugarte Postigo et al. (2015c), (87) Pugliese et al. (2015), (88) de Ugarte Postigo et al. (2015b), (89) Tanvir et al. (2015), (90) D'Elia et al. (2015), (91) Perley et al. (2015), (92) Bolmer et al. (2015), (93) Tanvir et al. (2016), (94) Castro-Tirado et al. (2016a), (95) Xu et al. (2016b), (96) Castro-Tirado et al. (2016b), (97) Xu et al. (2016a), (98) Selsing et al. (2019), (99) Castro-Tirado et al. (2016c), (100) Malesani et al. (2016), (101) Cano et al. (2016), (102) Xu et al. (2017), (103) Kruehler et al. (2017), (104) de Ugarte Postigo et al. (2017e), (105) de Ugarte Postigo et al. (2017b), (106) de Ugarte Postigo et al. (2017d), (107) de Ugarte Postigo et al. (2017c), (108) Melandri et al. (2019), (109) de Ugarte Postigo et al. (2017a), (110) Tanvir et al. (2018), (111) Sbarufatti et al. (2018), (112) Izzo et al. (2018), (113) Izzo et al. (2019), (114) Vreeswijk et al. (2018), (115) Rossi et al. (2018), (116) Vielfaure et al. (2018), (117) Fynbo et al. (2018), (118) Castro-Tirado et al. (2019), (119) Perley et al. (2019), (120) Rossi et al. (2019), (121) Valeev et al. (2019), (122) Malesani et al. (2019), (123) Yao et al. (2021), (124) de Ugarte Postigo et al. (2021a), (125) Rossi et al. (2022), (126) Oates et al. (2020), (127) Kann et al. (2020a), (128) Kann et al. (2020b), (129) Vielfaure et al. (2020a), (130) Vielfaure et al. (2020b), (131) Xu et al. (2021), (132) de Ugarte Postigo et al. (2021a), (133) Zhu et al. (2021), (134) de Ugarte Postigo et al. (2021b), (135) Thoene et al. (2021), (136) Kann et al. (2021), (137) Pozanenko et al. (2021), (138) Fynbo et al. (2022a), (139) Castro-Tirado et al. (2022), (140) Fynbo et al. (2022b), (141) Saccardi et al. (2022), (142) Izzo et al. (2022).

(This table is available in its entirety in machine-readable form.)

type I GRBs in spite of their long duration due to a spectrally soft, long-lasting tail. As a result, we were finally left with a sample of 142 type II GRBs. The sample is described in Table 1.

2.2. Light-curve Extraction and Background Interpolation

The GBM has 12 Na I detectors oriented so as to provide a nearly uniform coverage of the sky. Only a fraction of the 12 detectors have a good view of any given GRB, typically the ones with a small angle between the normal of the detector and the direction of the GRB. To increase the signal-to-noise ratio (S/N), one conveniently sums up the most illuminated detectors' light curves. Summing too many detectors would mainly add noise and end up with a worse S/N. To find the optimal combination, we applied the following strategy: (i) we preliminarily selected the detectors with a viewing angle $\theta < 60°$, as recommended by the GBM team (Bhat et al. 2016), unless no detector fulfilled the previous condition or when these detectors had been used by the GBM team to compute the T_{90} (von Kienlin et al. 2020); (ii) we generated all combinations of detectors and their corresponding light curves (e.g., if we selected detectors n1, n2, n3 at step 2, then we considered the different combinations n1+n2, n2+n3, n1+n3 and n1+n2+n3); (iii) we took the combination with most pulse candidates (with $S/N > 6$). In case of equality, we opted for the combination of detectors that maximizes the total S/N of all identified pulse candidates. For each GRB, we extracted the Time-Tagged Event (TTE) light curves for the selected Na I detectors in three different energy channels: 8–1000, 30–1000, and 40–1000 keV. TTE data typically cover from −30 to 300 s with respect to the trigger time. For some extended triggers, TTE data coverage extend from −100 to 450 s. For very long GRBs ($T_{90} \gtrsim 600$ s), TTE data do not cover the full extent of the events, as in the case of the ultra-long 091024 (Virgili et al. 2009; Gruber et al. 2011a), so we used instead the CSPEC data.[7] For the ultra-long 160625B (e.g., Zhang et al. 2018) we used TTE data for the first part of the event ($t < 400$ s) and CSPEC data for the second part ($t > 400$ s).

The light curves were extracted using the publicly available GBM tools (Goldstein et al. 2022).[8] We binned these light curves with a time resolution from 16 to 1024 ms. Some GRBs had particularly short timescales that required the higher resolution of 4 ms [9] (see Section 2.3 for more details on the identification of the optimal bin time for each GRB).

---

[7] CSPEC data are continuous high-spectral-resolution data with 1.024 s time resolution during bursts.

[8] https://fermi.gsfc.nasa.gov/ssc/data/analysis/gbm/gbm_data_tools/gdt-docs/

[9] This was the case for 090424, 090902B, 090926, 130427A, 180720B, and 190114C.

In order to interpolate the background in the "on-source" time interval (where the burst is present), we chose two "off-source" windows and modeled the background with a polynomial function with order up to three. To check the quality of the interpolation, we computed the normalized residuals ϵ_i in the off-source windows, defined as

$$\epsilon_i = \frac{r_i - b_i}{\sigma_{r_i}}, \tag{1}$$

where r_i is the count rate in the ith bin, b_i is the interpolated background count rate, and σ_{r_i} is the count-rate uncertainty in the ith bin, given by

$$\sigma_{r_i} = \sqrt{\frac{r_i}{\Delta t}}, \tag{2}$$

obtained assuming a Gaussian regime in counts per bin time Δt. An optimal background modeling is characterized by normally distributed residuals with null mean value and unity standard deviation $\mathcal{N}(0, 1)$ (standardized normal distribution).

The background-subtracted light curve was considered for the next steps in the analysis, provided that the following conditions on the mean value μ_ϵ and standard deviation σ_ϵ were fulfilled: $|\mu_\epsilon| < 0.2$ and $|\sigma_\epsilon - 1| < 0.2$. Otherwise, the corresponding detector was ignored.

We obtained a background-subtracted light curve independently for each detector and energy passband, and then we added them through all the combinations mentioned above to obtain as many background-subtracted light curves. We selected for the following study the light curve associated with the best combination of detectors.

2.3. Pulse Identification

Pulses were identified using MEPSA (Guidorzi 2015), a peak-search algorithm designed and calibrated to find statistically significant local maxima in GRB light curves.[10] Each pulse candidate is characterized in terms of the pulse peak time t_0, the pulse peak rate A, the S/N, and the detection timescale at which the pulse was detected with the highest S/N, hereafter denoted Δt_{det}. For the goal of the present analysis, we rejected all the pulse candidates with S/N < 6 to ensure a high purity.

Since MEPSA applies to uniformly binned light curves, we preliminarily had to determine the optimal bin time for any given GRB. On the one hand, using an unnecessarily short bin may lead to relatively numerous statistical fluxes. On the other hand, a too coarse resolution would wash out genuine temporal structures with a consequent loss of information. We opted for the longest bin time Δt for which all the pulses detected by MEPSA are resolved. This condition was implemented by requiring $\Delta t \leqslant \Delta t_{\mathrm{det},i}/2$ for any generic ith pulse candidate. As for the choice of the combination of detectors, we took the one with the most pulse candidates, as explained in Section 2.2.

We applied MEPSA to the light curves in the three energy passbands mentioned in Section 2.1 and with a bin time in the range 16–1024 ms, with a maximum rebin factor of 100 (see Guidorzi 2015 for details), except for the few GRBs which required a 4 ms resolution (see Section 2.2). In harder channels, pulses tend to be narrower (Fenimore et al. 1995): We exploited this property to improve our ability in identifying and separating partially overlapped pulses.

Since most photons are relatively soft due to GRB spectral shapes, neglecting the softer energy channels turns into a statistically poorer S/N. We therefore chose to merge the results obtained with MEPSA on the three different energy ranges, whenever visual inspection suggested the presence of blended pulses that were missed by MEPSA in the analysis of individual energy channels. We made sure to count just once the pulses that were identified in more than one energy band. To this aim, we adopted the following strategy: let t_{0i} and $\Delta t_{\mathrm{det},i}$ be, respectively, the pulse peak time and the detection timescale of the ith pulse candidate detected by MEPSA in the 8–1000 keV band. Let t'_{0j} and $\Delta t'_{\mathrm{det},j}$ be the analogous quantities of the jth pulse candidate from one of the harder channels. The two pulse candidates are tagged as distinct ones if their intervals do not overlap:

$$\left[t_{0i} - \frac{\Delta t_{\mathrm{det},i}}{2};\, t_{0i} + \frac{\Delta t_{\mathrm{det,i}}}{2}\right] \bigcap \left[t'_{0j} - \frac{\Delta t'_{\mathrm{det},j}}{2};\, t'_{0j} + \frac{\Delta t'_{\mathrm{det},j}}{2}\right] = \varnothing \tag{3}$$

The condition of Equation (3) eliminates most multiple detections of the same pulse, except for a few cases, which were corrected after visual inspection.

2.4. Light-curve Modeling

We modeled each identified pulse candidate with a FRED profile, which was found to describe most GRB pulses (Norris et al. 1996):

$$N(t|t_0, A, \tau_r, \xi, \nu) = A \begin{cases} \exp\left[-\left(\dfrac{|t - t_0|}{\tau_r}\right)^{\nu}\right] & (t \leqslant t_0) \\ \exp\left[-\left(\dfrac{|t - t_0|}{\xi\tau_r}\right)^{\nu}\right] & (t > t_0), \end{cases} \tag{4}$$

where A is the pulse peak rate, t_0 the pulse peak time, τ_r the pulse rise time, ξ the decay-to-rise ratio (note that the pulse decay time is $\tau_d = \xi\tau_r$), and ν the so-called peakedness, which determines the pulse sharpness. As first noted by Norris et al. (1996) in the analysis of BATSE bursts, ξ mostly ranges between 2 and 3, whereas ν lies between 1 (pure exponential) and 2 (Gaussian). Finally, we investigated the impact of the choice of the pulse model by alternatively adopting the one proposed in Norris et al. (2005). In this model, two parameters (two timescales) instead of three are needed to define the shape of a pulse.

We used a nonlinear least-squares algorithm to fit the light curves with a superposition of Norris pulses,[11] as in Equation (5):

$$f(t) = \sum_{i=1}^{N_{\mathrm{p}}} N(t|t_{0i}, A_i, \tau_{ri}, \xi_i, \nu_i). \tag{5}$$

The number of pulses N_p was given by the results of MEPSA. We used the pulse peak times and the pulse peak rates given by MEPSA as starting values for the fit. We set some boundaries on the $5N_p$ parameters (five for each pulse). The pulse peak time of a generic ith pulse was constrained to be in the interval

---

[10] This code is registered at the ASCL with the code entry ASCL 1410.002 and is also available at https://www.fe.infn.it/u/guidorzi/new_guidorzi_files/code.html.

[11] The fit was done using `scipy.optimize.curve_fit` from the `scipy` library (Virtanen et al. 2020).

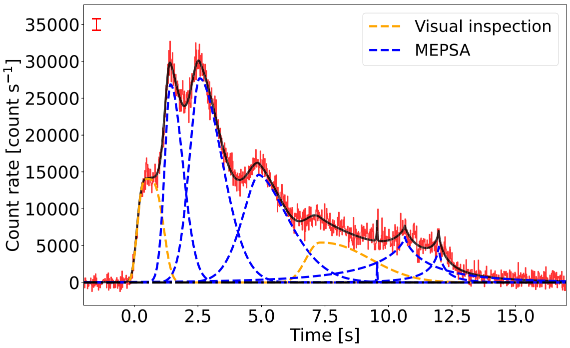

Figure 1. 150314A background-subtracted light curve (red) along with the best-fit model (black). The typical error size is shown in the top left. The black horizontal line represents the interpolated background. Blue dashed curves represent the individual pulses detected by MEPSA while orange ones represent pulses added by visual inspection to improve the fit of this complex GRB time profile.

$[t_{0i} - \Delta t_{\mathrm{det},i}/2;\, t_{0i} + \Delta t_{\mathrm{det},i}/2]$. The pulse peak rate was allowed to vary within the interval $[A_i - n_2\sigma_{A_i};\, A_i + n_2\sigma_{A_i}]$, where σ_{A_i} is the pulse peak rate error given by MEPSA, whereas n_2 can be adjusted by the user. For well-separated pulses, we used $n_2 = 1$. Instead, for partially overlapped pulses, we allowed larger values for n_2. For the GRB light curves consisting of a forest of overlapped pulses, we left the pulse peak rate unconstrained. To avoid unrealistic modeling of pulses, we constrained ξ and ν in the following ranges: $0.1 < \xi < 10$ and $0.4 < \nu < 4$, as suggested by the results by Norris et al. (1996) in their systematic analysis of BATSE GRBs, which shared energy passband with the GBM Na I detectors.

Similarly to the validation of the background modeling (Section 2.2), we here verified the quality of the fit by computing the corresponding normalized residuals, defined as

$$\epsilon_i = \frac{r_i - f(t_i)}{\sigma_{r_i}} \tag{6}$$

where r_i is the ith count rate, σ_{r_i} its associated uncertainty, and $f(t_i)$ the count rate predicted by the model of Equation (5) at time t_i.

We computed the mean, median, and standard deviation of $\{\epsilon_i\}$ over the same time interval that was used for the background interpolation plus the one that includes the GRB profile. Ideally, ϵ_i should be distributed as a standardized Gaussian $\mathcal{N}(0, 1)$. A nonzero mean would reveal unaccounted trends in the modeling, whereas a value of $\sigma > 1$ ($\sigma < 1$) would indicate under- or overfitting. A poor modeling often turned out to be due to the presence of weak and/or blended unaccounted pulses; in such cases, we applied the strategy described in Section 2.3 to add pulses to the signal until we reached an acceptable solution. In some cases, we had to add pulses by visual inspection, until the quality of the fit improved sufficiently. Figure 1 shows an example. For a few challenging GRBs, we could only come up with a relatively poor fit. More details are reported in Section 3.

For each GRB, we obtained a set of $5N_{\mathrm{p}}$ best-fit parameters μ_{fit} with an associated covariance matrix Σ_{fit}, which was used to estimate the uncertainties on the best-fit parameters. The uncertainties on the best-fit parameters are given by the square root of the diagonal of the covariance matrix. For each GRB, we randomly generated a sample of 10^3 sets of parameters around the best-fit solution according to a multivariate Gaussian distribution $\mathcal{N}(\mu_{\mathrm{fit}}, \Sigma_{\mathrm{fit}})$ truncated along the positive-definite parameters. Once the best-fit profile of Equation (4) was known for every pulse, we computed the integral counts of the ith pulse:

$$C_i = \int_{-\infty}^{+\infty} N(t|t_{0i}, A_i, \tau_{r,i}, \xi_i, \nu_i)\, dt. \tag{7}$$

The uncertainty on C_i was estimated as the standard deviation of the corresponding distribution of values generated by random realizations of the set of parameters using $\mathcal{N}(\mu_{\mathrm{fit}}, \Sigma_{\mathrm{fit}})$.

2.5. Isotropic-equivalent Energy and Luminosity

In the following, energy flux (erg per square centimeter second) and fluence (erg per square centimeter) are denoted with F and Φ, respectively.

We estimated the fluence of the ith pulse as $\Phi_i = C_i f_{\mathrm{tot}}$, where $f_{\mathrm{tot}} = \Phi_{\mathrm{tot}}/C_{\mathrm{tot}}$ is the conversion factor obtained from the corresponding time-integrated quantities. Φ_{tot} is the fluence of the whole GRB and C_{tot} is the corresponding counts calculated on the same time interval.

Φ_{tot} was estimated by taking the best-fit model and its associated spectral parameters provided by the GBM GRB catalog.[12] For 091024, we used instead fluence values on the whole event provided by Gruber et al. (2011b). K-corrections, needed to estimate the fluence in the common rest-frame energy passband 1–10^4 keV, were computed in the following way:

$$k_c = \frac{\int_{\frac{1}{1+z}}^{\frac{10^4}{1+z}} EN(E)\, dE}{\int_8^{1000} EN(E)\, dE}. \tag{8}$$

This choice complies with what is usually adopted in the GRB literature (e.g., Amati et al. 2002). Therefore, we computed Φ_{tot} as $\Phi_{\mathrm{tot}} = k_c\, \Phi_{8-1000}$. This procedure assumes a negligible impact of the spectral evolution throughout the GRB; in Appendix, we show that the impact of our approximation on the resulting pulse energy distribution does not affect our conclusions significantly.

The corresponding released isotropic-equivalent energy is calculated as

$$E_{\mathrm{iso},i} = \frac{4\pi d_L^2}{1+z}\, \Phi_i, \tag{9}$$

where d_L is the luminosity distance.[13] The corresponding isotropic-equivalent luminosity is computed as

$$L_{\mathrm{iso},i} = 4\pi d_L^2\, F_i, \tag{10}$$

where $F_i = A_i f_{\mathrm{tot}}$.

---

[12] The considered spectral models are power law, band, Comptonized, and smooth broken power law. Their descriptions are available at https://fermi.gsfc.nasa.gov/ssc/data/analysis/gbm/gbm_data_tools/gdt-docs/api/api-spectra.html#spectral-functions.

[13] The luminosity distance was computed with cosmological parameters mentioned in Section 1 using the package `Planck18` of the `astropy.cosmology` library.

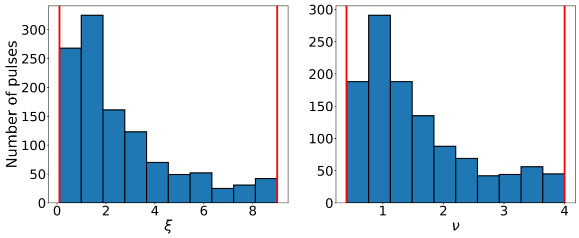

Figure 2. ξ and ν distributions for the whole sample. Red vertical lines indicate the chosen parameter boundaries ($0.1 < \xi < 9$ and $0.4 < \nu < 4$).

3. Results

MEPSA detected 974 pulses in the 8–1000 keV band, while 13 additional pulses were detected in the harder channels. We had to add at least one pulse by visual inspection for 45 GRBs. Overall, we added 159 undetected pulses to the 987 detected by MEPSA, so that the final sample consisted of 1146 pulses, of which 14% had to be identified through visual inspection.

We split the GRB sample in two groups, depending on the quality of the modeling and on the presence of pulses with extreme values of the parameters which define the pulse shape (ξ and ν). The Silver Sample[14] (hereafter, SS) includes both (i) GRBs with a standard deviation of the normalized residuals deviating from 1 by at least 0.1, $|\sigma_\epsilon - 1| > 0.1$, and (ii) GRBs for which the best-fit model contains at least one pulse with an extreme shape in terms of parameters ξ and ν (either $\xi < 0.11$ or $\xi > 8.99$ and $\nu < 0.41$ or $\nu > 3.99$, respectively). The Golden Sample (hereafter, GS) includes all the remaining GRBs.

The GS (SS) consists of 119 (23) GRBs. In terms of pulses, the GS (SS) includes 696 (450) pulses. On average, SS GRBs have more pulses per GRB, with a median of 15 against three of the GS. They are also brighter and more energetic, with a median fluence ~4.5 times higher (4.4×10^{-5} versus 9×10^{-6} erg cm^{-2}). The isotropic-equivalent energy of SS GRBs is on average ~7 times bigger (4.3×10^{53} versus 6.2×10^{52} erg). The fact that, on average, the GRBs having the best signal are also the most problematic ones to model reveals the degree of complexity of GRB time profiles as well as the limits of our approach.

Our mean values of $\langle\xi\rangle$ and $\langle\nu\rangle$ for the whole sample (GS +SS) are, respectively, 2.6 and 1.6, which is broadly compatible with the corresponding distribution obtained by Norris et al. (1996) for BATSE GRBs (Figure 2).

3.1. Detection Efficiency

To account for the completeness limit of the energy and of the luminosity distributions, we estimated the detection efficiency as a function of the pulse peak rate A. In the case of energy, the detection efficiency is a function of the pulse counts I.

In either case, we estimated MEPSA efficiency to detect features on samples of simulated pulses with different shapes for given pulse peak rates/pulse counts. We carried out two complementary kinds of simulations: (i) single- and (ii) multipulse.

For (i), for every GRB we took its interpolated background profile and added a randomly generated FRED pulse. We finally added Poisson noise.

For (ii), for every GRB we randomly generated and added a FRED pulse to the best-fit model of the real GRB light curve plus the modeled background curve. Hence, we ended up with as many replicates of the original GRB light curves, each of which included one additional synthetic pulse. This was done in order to mimic the more realistic situation in which a given pulse might have occurred in conjunction with other ones that were already identified. We finally added Poisson noise.

Each simulated pulse was generated assuming for t_r, ξ, and ν the corresponding log-normal distributions that best fit the observed distributions of the same parameters in the real samples. These best-fit log-normal distributions were validated through a two-population Kolmogorov–Smirnov (KS) test.[15] A random variable X is log-normally distributed if $\ln(X) \sim \mathcal{N}(\mu, \sigma^2)$. The best-fit log-normal distribution parameters (μ, σ) are (-0.69, 1.5), (0.66, 0.97), and (0.35, 0.62) for t_r (expressed in seconds), ξ, and ν distributions, respectively.

In the case of energy, the simulated pulse peak rate A was computed as a function of a given I, which is the total counts assigned to a given pulse. The rationale behind this choice is to describe the detection efficiency for pulses with a given I, which is the most important parameter for a pulse to be detected (against a given background rate). Since I scales linearly with A (see Equation (7)), this is easily done:

$$I_1 = \int_{-\infty}^{+\infty} N(t;\, A_1,\, t_0,\, t_r,\, \xi,\, \nu)\, dt, \tag{11}$$

where we set $A_1 = 1$. A is then calculated as follows:

$$A = A_1 \frac{I}{I_1}. \tag{12}$$

In the case of luminosity, as pulses of different shapes are grouped by count rates, we simply assigned a given pulse peak rate to a given group of simulated pulses.

For (i), the pulse peak time was set to $t_0 = 0$ s by convention, as its position is not relevant in the single-pulse case. For (ii), the pulse peak time was drawn from a uniform distribution with the constraint to obtain pulses with separability (defined as the distance between the simulated pulse and its nearest neighbor divided by its FWHM) between 1 and 10.

For each GRB, we generated a sample of 100 simulated FRED-like pulses with parameters [t_0, t_r, ξ, ν] randomly chosen from the corresponding best-fit log-normal distributions.

We repeated the process for evenly spaced logarithmic values of I (A), in the range 10^2–10^4 counts (10^2–10^4 counts s^{-1}). We used the same sample of FRED parameters for each value of I or A. This procedure allowed us to model the detection efficiency as a function of the pulse counts and of the pulse peak rate of a generic pulse. We finally obtained the detection efficiency as a function of either $E_{\rm iso}$ or $L_{\rm iso}$, using Equations (9) and (10) separately for nine bins in redshift;[16] these were obtained through an evenly spaced logarithmic sampling of the luminosity distance range.

The detection efficiency $\eta_z(E_{\rm iso})$ ($\eta'_z(L_{\rm iso})$) was estimated as the fraction of simulated pulses with $E_{\rm iso}$ ($L_{\rm iso}$) (taken from the grid of simulated values) that had been identified by our

---

[14] They are 080810, 090328, 090927, 091003, 091024, 100414A, 100728A, 120711A, 130528A, 131108A, 140304A, 141220A, 150403A, 160629A, 161117A, 170214A, 171010A, 180205A, 180720B, 180728A, 181020A, 220101A, and 220627A.

[15] The KS test was done using `scipy.stats.ks_2samp`.

[16] The bin edges are given by [0.078 , 0.139, 0.238, 0.400, 0.662, 1.082, 1.76, 2.898, 4.813, 8.100]

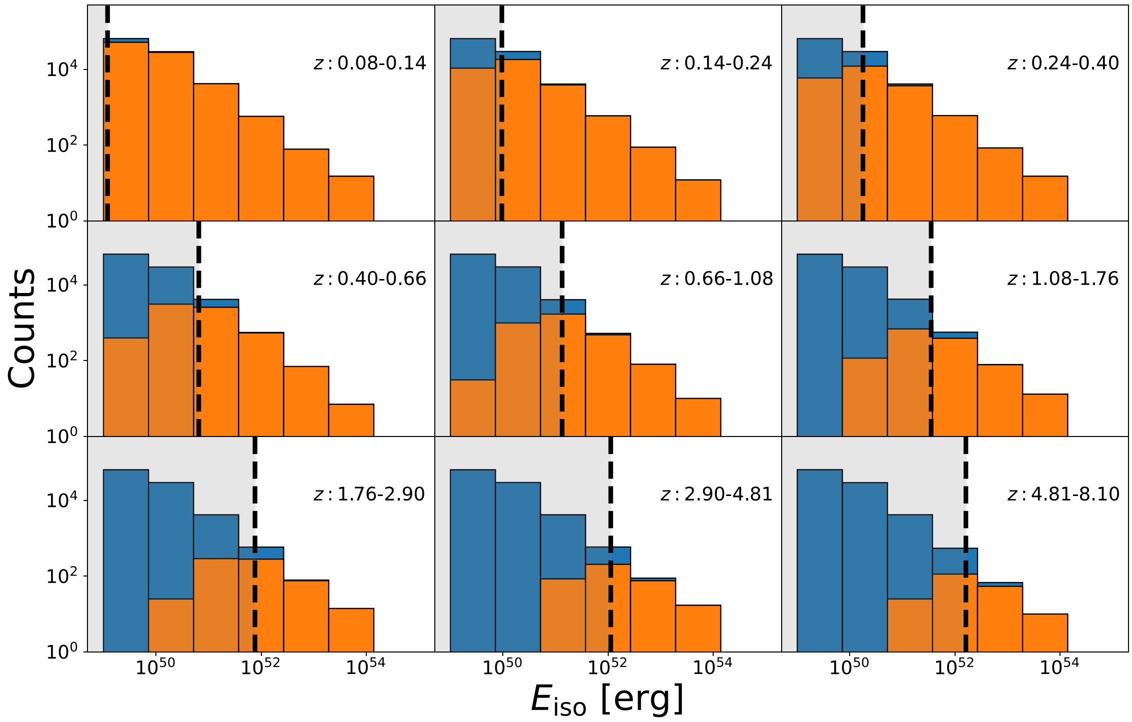

Figure 3. Simulated distributions of $E_{\rm iso}$, depending on whether selection effects due to detection efficiency are considered (orange) or not (blue). The nine panels refer to increasing redshift bins (left to right, top to bottom). The blue distribution was drawn assuming $dN/dE_{\rm iso} \propto E_{\rm iso}^{-2}$. Vertical dashed lines mark the 50% detection efficiency; pulses with lower values of $E_{\rm iso}$, highlighted by the gray areas, are therefore hampered by a low detection efficiency. For the sake of clarity, 10^5 pulses were simulated in each redshift bin.

procedure at the given redshift bin. Finally, $\eta_z(E_{\rm iso})$ ($\eta'_z(L_{\rm iso})$) was obtained for any value of $E_{\rm iso}$ ($L_{\rm iso}$) through interpolation.[17]

3.2. Modeling of Energy and Luminosity Distributions

Having modeled the redshift-dependent selection effects that are present in the observed $E_{\rm iso}$ and $L_{\rm iso}$ distributions, we now aim to test if/which given conjectural intrinsic differential distribution $f(E_{\rm iso}) = dN/dE_{\rm iso}$ ($f'(L_{\rm iso}) = dN/dL_{\rm iso}$) may explain the results, once the selection effects are properly simulated. To this aim, we started with the simplest distribution, that is, a PL: $f(E_{\rm iso}) \propto E_{\rm iso}^{-s}$ ($f'(L_{\rm iso}) \propto L_{\rm iso}^{-\kappa}$), with s and κ being the energy and luminosity PL indices. As an alternative, we considered a broken power law (BPL): $f(E_{\rm iso}) \propto E_{\rm iso}^{-s_1}$ for $E_{\rm iso} < E_b$ and $f(E_{\rm iso}) \propto E_{\rm iso}^{-s_2}$ for $E_{\rm iso} \geqslant E_b$, where s_1 and s_2 are the low- and high-energy indices, respectively, and E_b the break energy. We first tried to fix the low-energy index to zero, $s_1 = 0$, such that the resulting BPL is similar to a thresholded PL (Aschwanden 2015), although not mathematically equivalent to it. Similarly, we considered a BPL distribution for the luminosity distribution: $f'(L_{\rm iso}) \propto L_{\rm iso}^{-\kappa_1}$ for $L_{\rm iso} < L_b$ and $f'(L_{\rm iso}) \propto L_{\rm iso}^{-\kappa_2}$ for $L_{\rm iso} \geqslant L_b$, where κ_1 and κ_2 are the low- and high-luminosity indices, respectively, and L_b the break luminosity.

For each redshift bin, we assigned a detection probability $p = \eta_z(E_{\rm iso})$ ($p' = \eta'_z(L_{\rm iso})$) to any given value of $E_{\rm iso}$ ($L_{\rm iso}$), that was randomly generated from $f(E_{\rm iso})$ ($f'(L_{\rm iso})$). Each simulated value of $E_{\rm iso}$ ($L_{\rm iso}$) was kept, provided that a Bernoulli trial with the probability of success given by $\eta_z(E_{\rm iso})$ ($\eta'_z(L_{\rm iso})$) turned out to be 1.[18] This process was iterated until we ended up with as many pulses as in the observed distribution for that redshift bin. Consequently, the resulting simulated distribution has the same number of events and the same redshift distribution as the observed distribution. To appreciate the impact of the selection effects, Figure 3 displays the simulated energy distribution for each of the nine different redshift bins, along with the one predicted assuming $dN/dE_{\rm iso} \propto E_{\rm iso}^{-2}$ and the same number of GRBs per each redshift bin.

3.2.1. Validation of a Putative Intrinsic Differential Distribution

To assess the probability that the observed $E_{\rm iso}$ ($L_{\rm iso}$) distribution is the result of an assumed intrinsic differential distribution $f(E_{\rm iso})$ ($f'(L_{\rm iso})$) net of selection effects, we carried out a few tests: a likelihood ratio test (LRT), χ^2, two-population KS, and Anderson–Darling (AD) tests.[19]

We divided the range of $E_{\rm iso}$ ($L_{\rm iso}$) values into $M = 6$ (6) logarithmic evenly spaced bins, ensuring that each bin contained $\geqslant$20 pulses. Let $C_{o,i}$ ($C_{s,i}$) be the number of pulses in bin i of the observed (simulated) distribution, either in the case of $E_{\rm iso}$ or $L_{\rm iso}$. Let $N_{\rm o} = \sum_{i=1}^{M} C_{o,i}$ and $N_{\rm s} = \sum_{i=1}^{M} C_{s,i}$ be the total number of pulses in the observed and simulated distributions, respectively. For any simulated distribution s the χ_s^2 and the LRT$_s$ are

---

[17] We applied a kernel density estimate with a Gaussian kernel as implemented in python class `scipy.stats.Gaussian_kde`.

[18] In other words, if we let S be a random variable that equals 1 if a given pulse with energy $E_{\rm iso}$ is detected and 0 otherwise, $S \sim \mathcal{B}(p)$ with $p = P(S = 1) = \eta_z(E_{\rm iso})$.

[19] The two-sample AD test was done using `scipy.stats.anderson_ksamp`.

Table 2
Results of the Modeling of the $dN/dE_{\rm iso}$ Distribution, Once Selection Effects Are Accounted for

Model	Data Set	s_1	s_2	E_b (10^{51}erg)	KS Test p-value	AD Test p-value	(χ^2/dof ; p-value)
PL	All	$\sim$1.4	⋯	⋯	10^{-5}	$<10^{-3}$	$(60/5\ ;\ 10^{-11})$
PL	All (second model)	$\sim$1.4	⋯	⋯	7×10^{-5}	$<10^{-3}$	$(75/5\ ;\ 10^{-14})$
BPL	All	[0]	$\sim$1.5	$\sim$2	0.096	0.015	$(26.8/5\ ;\ 6 \times 10^{-5})$
BPL	All	$\sim$1	[1.5]	$\sim$6	0.17	0.08	(11.3/5 ; 0.046)
BPL	All	$0.96^{+0.23}_{-0.15}$	$1.67^{+0.23}_{-0.16}$	$12^{+29}_{-11.4}$	0.11	0.14	(5.25/5 ; 0.39)
BPL	All (second model)	$1.02^{+0.10}_{-0.10}$	$1.79^{+0.08}_{-0.10}$	21^{+21}_{-6}	0.23	0.22	(13/5 ; 0.025)
PL	GS	$\sim$1.4	⋯	⋯	0.02	0.002	$(27/5; 6 \times 10^{-5})$
BPL	GS	[0]	$\sim$1.4	$\sim$1	0.07	0.025	(14.8/5; 0.01)
BPL	GS	$1.03^{+0.21}_{-0.27}$	[1.5]	$11^{+27}_{-10.6}$	0.23	0.21	(9.3/5; 0.097)
BPL	GS	$1.07^{+0.16}_{-0.03}$	$1.68^{+0.38}_{-0.11}$	24^{+59}_{-7}	0.2	0.25	(5.6/5; 0.34)
PL	$z < 1.76$	$\sim$1.4	⋯	⋯	10^{-3}	$<10^{-3}$	$(47.5/5; 4 \times 10^{-9})$
BPL	$z < 1.76$	[0]	$1.48^{+0.14}_{-0.02}$	$0.93^{+0.86}_{-0.16}$	0.3	0.25	(11/5; 0.05)
BPL	$z < 1.76$	$0.82^{+0.10}_{-0.19}$	[1.5]	$2.85^{+1.28}_{-1.79}$	0.28	0.25	(9.87/5; 0.08)
BPL	$z < 1.76$	$0.77^{+0.41}_{-0.39}$	$1.65^{+0.35}_{-0.15}$	$4.9^{+24}_{-3.2}$	0.6	0.53	(3.6/5; 0.6)
PL	$N_p \leqslant 6$	$\sim$1.4	⋯	⋯	0.10	0.02	$(17/5; 4 \times 10^{-3})$
PL	$N_p > 6$	$\sim$1.5	⋯	⋯	5×10^{-3}	$<10^{-3}$	$(50/5; 10^{-9})$
BPL	$N_p > 6$	[0]	$\sim$1	$\sim$1.5	0.38	0.17	(14/5; 0.01)
BPL	$N_p > 6$	$\sim$0.7	[1.5]	$\sim$1.5	0.35	0.17	(11.5/5; 0.04)
BPL	$N_p > 6$	$0.73^{+0.23}_{-0.15}$	$1.54^{+0.08}_{-0.03}$	$2.7^{+1.7}_{-0.5}$	0.5	>0.25	(9.2/5; 0.1)

Note. Values of frozen parameters are reported in square brackets.

obtained by computing the following quantities:

$$\chi^2_s = \sum_{i=1}^{M} \frac{(C_{o,i} - C_{s,i})^2}{C_{o,i} + C_{s,i}}, \qquad (13)$$

$$\mathrm{LRT}_s = 2 \log \prod_{i=1}^{M} \frac{\left(\frac{C_{o,i}}{N_o}\right)^{C_{o,i}} \left(\frac{C_{s,i}}{N_s}\right)^{C_{s,i}}}{\left(\frac{C_{o,i} + C_{s,i}}{N_o + N_s}\right)^{C_{o,i}+C_{s,i}}}. \qquad (14)$$

Both metrics were calculated for a sample of 100 simulated distributions. We then took the median values of both. In Equation (14), the numerator represents the maximum likelihood under the assumption that the two sets are independently distributed, whereas the denominator is the maximum likelihood under the alternative assumption that both sets share the parent distribution. Under the assumption that the two sets have a common distribution, LRT is χ^2_{M-1} distributed: We therefore carried out a one-tail test, calculating the p-value as $P(\chi^2_{M-1} \geqslant \mathrm{LRT})$.[20]

In the case of the $E_{\rm iso}$ distribution, we were not able to find a satisfactory solution for the PL model according to all of the four tests. In particular, the best PL model yielded a value of $\sim$60 for both χ^2 and LRT (Equations (13) and (14)). Consequently, a simple PL model is confidently rejected.

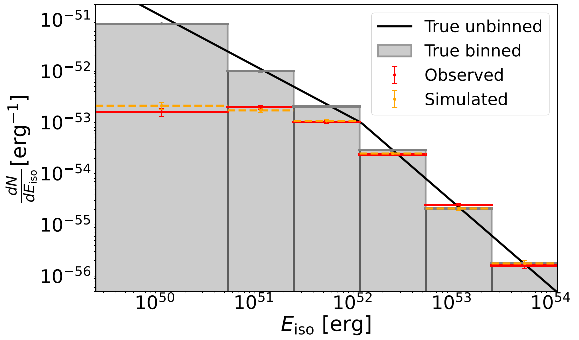

Figure 4. The black solid line represents the best-fit BPL intrinsic differential energy distribution $dN/dE_{\rm iso}$ obtained for the full sample. The gray shaded histogram is a binned version of the same distribution. The orange distribution was simulated from the intrinsic one after accounting for the selection effects, to be compared with the red distribution, which is the observed one.

Moving to the BPL model, given that two additional parameters come into play, we initially considered two alternative approaches: (i) we fixed $s_2 = 1.5$ and let both s_1 and E_b free to vary; (ii) we fixed $s_1 = 0$ and let both s_2 and E_b free. This was done to make a preliminary exploration of the parameter space. Then we allowed all parameters to vary and performed Markov Chain Monte Carlo (MCMC) simulations with EMCEE (Foreman-Mackey et al. 2013) to sample the LRT around its minimum value. We took a Gaussian ball around the minimum LRT value of model (i) and performed a MCMC run with 1000 samples and 64 walkers. Then we computed the LRT on a cube of parameters around the minimum LRT value given by the MCMC run to find the minimum LRT value and the confidence intervals. We found that the BPL that minimized the χ^2 and the LRT was around $s_1 \sim 1$, $s_2 \sim 1.67$, and $E_b \sim 1 \times 10^{52}$ erg, with $\chi^2_5/5 = 5.25/5$.

Confidence intervals were found by considering regions of the parameter space that satisfy $p_\alpha > 1 - \alpha$, where α is the confidence level and p_α is the p-value of the statistical test (either KS, AD, or χ^2 test). We took $\alpha = 0.95$. Fit goodnesses (estimated with the p-values) and confidence intervals for the different models, either for the full sample or for the GS sample, are reported in Table 2. Analogous conclusions were obtained for the GS, that is, a PL distribution cannot account for the data, whereas a BPL with similar shape as the one obtained for the whole sample does. Hence, the need for a break in the intrinsic distribution does not depend on the quality of the modeling of the GRB light curves, at least as long as $dN/dE_{\rm iso}$ is concerned. Figure 4

---

[20] This is the reason why we incorporated a factor of 2 in Equation (14).

Table 3

Results of the Modeling of the $dN/dL_{\rm iso}$ Distribution, once Selection Effects Are Accounted for

Model	Data Set	κ_1	κ_2	L_b (10^{52} erg s^{-1})	KS Test p-value	AD Test p-value	(χ^2/dof ; p-value)
PL	All	$\sim$1.3	…	…	0.04	0.003	(20/5 ; 10^{-3})
PL	All (second model)	$\sim$1.4	…	…	0.01	0.001	(37/5 ; 5×10^{-7})
BPL	All	$1.10^{+0.07}_{-0.34}$	$1.47^{+0.60}_{-0.18}$	$6^{+14}_{-5.8}$	0.33	0.17	(3.4/5 ; 0.63)
BPL	All (second model)	$1.03^{+0.05}_{-0.06}$	$1.51^{+0.05}_{-0.07}$	$1.1^{+0.9}_{-0.6}$	0.12	0.03	(17/7 ; 0.02)
PL	GS	$1.32^{+0.06}_{-0.05}$	…	…	0.23	0.09	(9/5 ; 0.1)
BPL	GS	$1.17^{+0.13}_{-0.10}$	$1.47^{+0.33}_{-0.06}$	3^{+25}_{-1}	0.74	>0.25	(2.8/5 ; 0.73)
PL	$z < 1.76$	$\sim$1.3	…	…	10^{-3}	10^{-3}	(46/5 ; 10^{-8})
BPL	$z < 1.76$	$0.93^{+0.20}_{-0.21}$	$1.73^{+0.64}_{-0.26}$	$2.3^{+5.1}_{-1.2}$	0.7	>0.25	(2.5/5; 0.77)
PL	$N_p \leqslant 6$	$1.65^{+0.16}_{-0.16}$	…	…	0.5	>0.25	(6.9/5; 0.23)
PL	$N_p > 6$	$\sim$1.2	…	…	0.025	$<10^{-3}$	(32/5; 6×10^{-6})
BPL	$N_p > 6$	$1.03^{+0.05}_{-0.11}$	$1.73^{+0.64}_{-0.26}$	$15^{15}_{-14.3}$	0.5	>0.25	(5.3/5; 0.38)

shows the best-fit model for $dN/dE_{\rm iso}$ obtained for the full sample.

We obtained similar results for $dN/dL_{\rm iso}$ for the full sample, i.e., a simple PL distribution is unable to describe the observed distribution (the best fit is obtained around $\kappa \sim 1.3$ with $\chi^2_5/5 \sim 20/5$), while a BPL works better (the best fit is obtained around $\kappa_1 \sim 1.1$, $\kappa_2 \sim 1.5$, $L_b \sim 6 \times 10^{52}$ erg s^{-1} with $\chi^2_5/5 \sim 3.4/5$). For the GS sample, the observed distribution is compatible with a PL distribution, the BPL distribution leading only to a marginal improvement. Results regarding $L_{\rm iso}$ distribution, either for the full sample or for the GS sample, can be found in Table 3. Figure 5 shows the BPL that best fits the $dN/dL_{\rm iso}$ of the full sample.

The need for a break in the $E_{\rm iso}$ distribution could be either real or due to our possible inability to model very accurately the selection effects. To verify the latter possibility, we carried out the same analysis after excluding the three redshift bins with the highest redshift, which are most severely affected by the selection effects. As a result, we limited to pulses from GRBs with $z_{\rm max} < 1.76$, which make up ~60% of the entire sample. Our conclusions remained essentially unchanged: The PL model is rejected (p-values from KS, AD, and χ^2 tests were 8×10^{-3}, $<10^{-3}$, and 10^{-11}, respectively), whereas the BPL model was acceptable, with best-fit values fully compatible with those obtained for the full sample. Figure 6 shows the BPL that best fits the $dN/dE_{\rm iso}$ of the sample of pulses with $z < 1.76$.

It is worth noting that we did not add pulses missed by MEPSA in the simulated light curves, as we did in Section 2.4 in the case of the real ones. Consequently, the estimated detection efficiency in the low tail of the distribution is somewhat lower than the effective one acting on real data. This further supports the evidence for a break a fortiori.

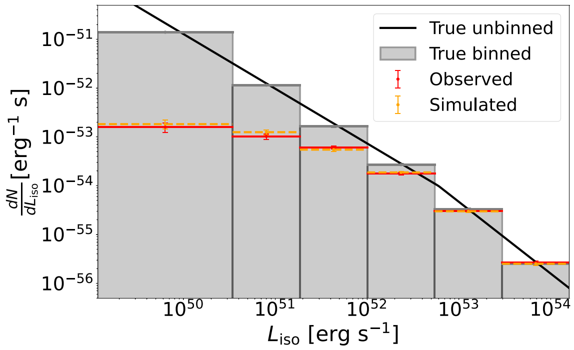

Figure 5. Same as Figure 4, except that here it is the differential luminosity distribution $dN/dL_{\rm iso}$.

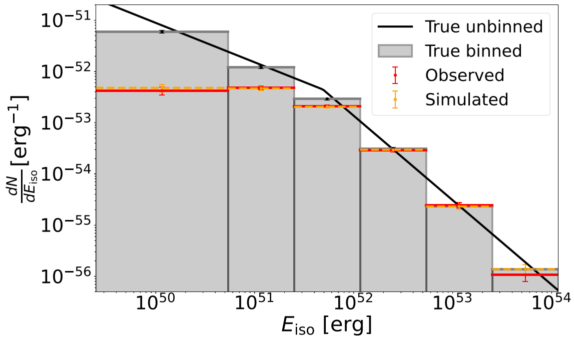

Figure 6. Same as Figure 4, except that here we are considering only pulses with redshift $z < 1.76$.

3.2.2. Comparison between Pulse-rich and Pulse-poor GRBs

We studied separately pulse-rich ($N_p > 6$) and pulse-poor ($N_p \leqslant 6$) GRBs. The separation value was chosen so that the number of pulses belonging to pulse-poor GRBs is large enough to enable a statistical analysis. To this aim, we chose six pulses as the boundary, which corresponds to ~20% of the whole sample, that is, 220 pulses, belonging to the pulse-poor GRBs. In the case of $dN/dE_{\rm iso}$, a two-population KS (AD) test between the two subsamples yielded a p-value of 0.3 (>0.25), thus providing no evidence for a different parent population. On the contrary, for $dN/dL_{\rm iso}$, the same tests yielded a p-value of 10^{-15} (<0.001), thus rejecting a common parent distribution for the two groups. As shown in Figure 7, least luminous pulses in pulse-poor GRBs are relatively more abundant than in pulse-rich GRBs, although being comparably energetic, suggesting that they are on average less luminous and longer. As was noted in Section 3.2.1, the SS is predominantly populated by pulse-rich GRBs; thus, the difference in the luminosity distribution that was pointed out in the comparison between GS and SS is due to the pulse richness here considered.

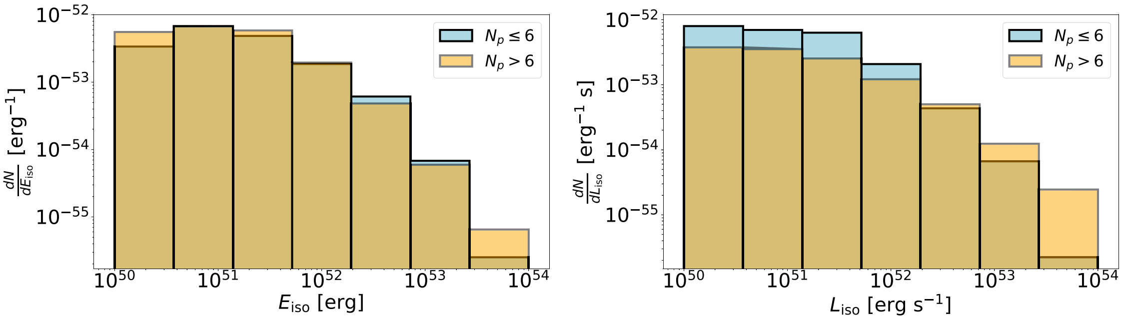

Figure 7. Left (right) $dN/dE_{\rm iso}$ ($dN/dL_{\rm iso}$) distributions for pulses belonging to pulse-poor GRBs (cyan) and to pulse-rich GRBs (orange).

3.2.3. Populations of Pulses within Individual GRBs

Thus far, we have studied the population of pulses as a whole, regardless of which GRB a given pulse may belong to. We explore this aspect in more detail by testing whether pulses distribute among different GRBs completely randomly, starting from the overall sample. To this aim, we considered the distribution of the peak luminosity of GRBs (that is, the luminosity of the most prominent pulse within each GRB) and focused on individual redshift bins, to limit the impact of selection effects.

For the $1.08 < z < 1.76$ redshift bin, which includes most GRBs ($N_{\rm grb} = 41$, collecting $N_p = 287$ pulses), we computed the GRB peak luminosity distribution. We then compared it with a distribution obtained by mixing together all the pulses belonging to the GRBs in the same redshift bin in the following way: For each GRB ($i = 1,\ldots,N_{\rm grb}$), we drew a random set of $N_{p,i}$ pulses, where $N_{p,i}$ is the real number of pulses of GRB i, and took the peak luminosity of simulated GRB i. Repeating this for all of the $N_{\rm grb}$ GRBs, we obtained a fake peak luminosity distribution, which appears to be significantly different from the real one (AD test p-value $<10^{-3}$ that both sets share a common parent population); in particular, the fake distribution has a more populated hard tail (see Figure 8). This indicates that pulses belonging to a given GRB are not completely independent of one another, or, at least, that they are not the result of randomly assembling from the whole population of observed pulses. High-luminosity pulses, in particular, tend to cluster within a few GRBs, rather than being randomly distributed among all the GRBs.

To further test this possibility, we performed a multinomial test. First, we counted $N_{\rm grb,lum} = 4$ GRBs that contain the top 10% most luminous pulses ($n = 28$ out of 287 pulses). We then compared this number with the one that would be obtained by randomly distributing the pulses among all the GRBs, keeping the same distribution of number of pulses per each GRB. This problem is similar to simulating the outcomes of n throws of a dice with m faces and can be addressed by sampling from the multinomial distribution, described by its probability mass function:[21]

$$\mathrm{PMF}(\boldsymbol{n} \mid \boldsymbol{p}, m, n) = n! \prod_{i=1}^{m} \frac{p_i^{n_i}}{n_i!}, \tag{15}$$

where $\boldsymbol{n} = (n_1, n_2,\ldots,n_m)$ is an array of the number of luminous pulses in each GRB ($\sum_{i=1}^{m} n_i = n = 28$), $m = N_{\rm grb} = 41$, and $\boldsymbol{p} = (p_1, p_2,\ldots,p_m)$, with $p_i = N_{p,i}/N_p$ being the probability for a pulse to belong to GRB i, calculated from all $N_p = 287$ pulses in the chosen redshift bin. We performed 10^7 simulations and in all cases the number of GRBs that contained the luminous pulses was higher (4 times in average) than the real one, $N_{\rm grb,lum} = 4$. The p-value that luminous pulses randomly distribute among GRBs within this redshift bin is $<5 \times 10^{-5}$.

We replicated the same analysis on the next redshift bin, $1.76 < z < 2.90$, which contains $N_{\rm grb} = 25$ and $N_p = 253$ pulses. The top 10% most luminous pulses ($n = 25$) belong to five GRBs. The same test yielded a p-value of 0.9×10^{-4} that luminous pulses are distributed over $\leqslant 5$ GRBs. We can therefore conclude that the most luminous pulses are more likely to belong to fewer GRBs than what is expected from a pure random distribution.

3.3. Waiting Time and Duration Distributions

We obtained the distribution of the rest-frame WT, calculated as $\Delta t_i = (t_{0,i+1} - t_{0,i})/(1 + z)$, where $t_{0,i}$ is the pulse peak time of the ith pulse. We also calculated the pulse duration distribution, where duration was defined as the FWHM of the modeled pulse, $T_i = \tau_{ri}(1 + \xi_i)\log(2)^{1/\nu_i}$. Durations were not corrected for cosmological dilation because of the combination of different effects that mostly cancel each other (see Camisasca et al. 2023 and references therein for a detailed explanation).

To ease the comparison with previous results, we modeled the distributions as in Guidorzi et al. (2015), using the following model:

$$\frac{dN}{d\Delta t} = (2 - \gamma)\delta^{2-\gamma}(\delta + \Delta t)^{-(3-\gamma)}, \tag{16}$$

consisting of a PL hard tail with a PL index $3 - \gamma$, plus a characteristic break time δ below which the distribution flattens (γ and δ correspond to α and β in Equation (8) of Guidorzi et al. 2015). The first bin of the two distributions was not considered ($\Delta t \geqslant 0.05$ s) since the efficiency of MEPSA drops at low WTs/durations. We sampled the posterior distribution by running a MCMC simulation with 10^4 steps and 32 walkers. We discarded the 10^3 first steps of the posterior distribution and we used only every 15 steps from the chain. For the duration and the WTs distribution, we obtained a PL index $3 - \gamma_T = 2.08^{+0.19}_{-0.16}$ and $3 - \gamma_{WT} = 2.04^{+0.14}_{-0.12}$, respectively.

---

[21] We made use of `scipy.stats.multinomial.rvs` to draw samples from the multinomial distribution.

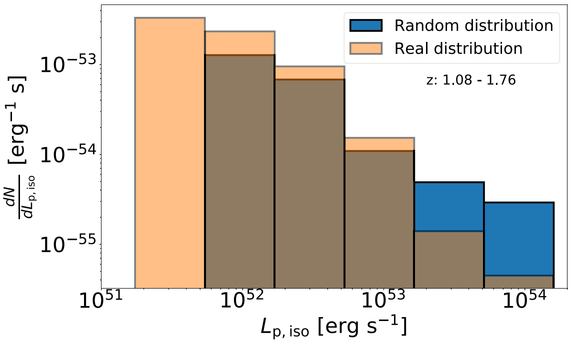

Figure 8. GRB peak luminosity distributions in the redshift bin $1.08 < z < 1.76$: real (orange) vs. randomly simulated (blue). The latter was obtained assuming that all pulses distribute randomly among the different GRBs. The harder tail of the simulated distribution suggests that luminous pulses belong to relatively few GRBs. See Section 3.2.3.

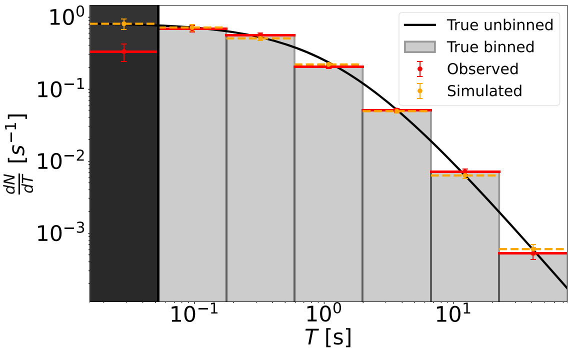

Figure 9. Same as Figure 4, except that here it is the differential duration distribution dN/dT. The black area represents the first bin, which is not considered in the computation of the posterior distribution.

Table 4
Results of the Modeling of the Differential Distributions $dN/d\Delta t$ and dN/dT

	$3-\gamma$	δ (s)
WT	$2.04^{+0.14}_{-0.12}$	$0.78^{+0.18}_{-0.15}$
Pulse FWHM	$2.08^{+0.19}_{-0.16}$	$1.30^{+0.37}_{-0.28}$

Note. Uncertainties are given with a 90% confidence level.

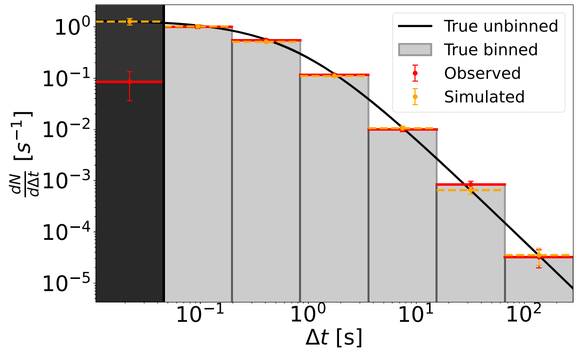

Figure 10. Same as Figure 4, except that here it is the differential duration distribution $dN/d\Delta t$. The black area represents the first bin, which is not considered in the computation of the posterior distribution.

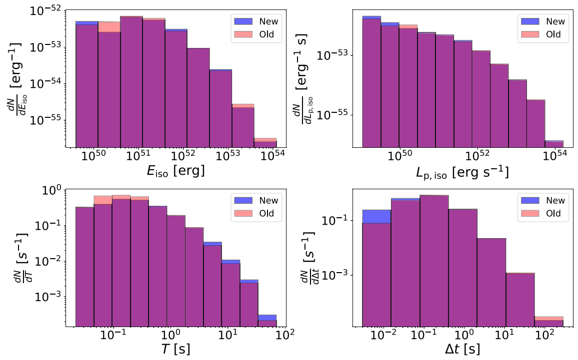

Figure 11. $E_{\rm iso}$ (upper left), $L_{\rm iso}$ (upper right), duration (lower left), and WT (lower right) distributions computed either with the first pulse model (in red; Section 2.4) or the second (in blue; Norris et al. 2005).

Best-fit parameters are reported in Table 4, while the distributions along with the best-fit models are shown in Figures 9 and 10.

3.4. Effects of the Pulse Model

We repeated the analysis by adopting the alternative pulse model of Norris et al. (2005), to explore to which extent our results are sensitive to the choice of the model described in Section 2.4. Overall, the fit quality is worse than the one obtained with the former pulse model, since the number of GRB light curves that do not fulfill the condition $|\sigma_\epsilon - 1| > 0.1$ (see Section 3) is 57 versus former 15. This was to be expected because of the smaller number of model parameters. We then computed the four different distributions considered in this paper and compared them with the ones obtained with the former pulse model (Figure 11).

We also performed two-population KS and AD tests. All but one test yielded p-values above 5%, except for the 0.3% obtained for the time duration distribution. This is due to the fact that the FWHM computed with the second model is on average longer (by a factor $\lesssim 2$) than the one computed with the first model. The distributions were modeled following the same procedure adopted for the first pulse model. Overall, the PL indices do not differ significantly from the previous corresponding ones: $\alpha_E^{(2)} = 1.79^{+0.08}_{-0.010}$, $\alpha_P^{(2)} = 1.51^{+0.05}_{-0.07}$, $\alpha_T^{(2)} = 2.13^{+0.21}_{-0.08}$, and $\alpha_{WT}^{(2)} = 2.14^{+0.16}_{-0.14}$. Compared with previous values reported in Table 5, they are all consistent. While the need for a break in energy/luminosity distributions is confirmed for both pulse models, in the luminosity case the value of the break point depends on the pulse model; for the second one, we found $L_{\rm break}^{(2)} \sim 1 \times 10^{52}$ erg s^{-1}, which deviates by 2.5σ from the previous $L_{\rm break}^{(1)} \sim 6 \times 10^{52}$ erg s^{-1}. As a result, we proved that our results do not depend significantly on the pulse shape model, except for the value of the break luminosity, which we conservatively estimate in the range $L_b \sim 10^{52-53}$ erg s^{-1}.

Table 5
Energy, Luminosity, Duration, and Waiting Times PL Indices Obtained in Our Study and in the Literature in the Case of GRB Prompt Emission, X-Ray Flares, Precursors, Solar Flares, and SGRs

	α_E	α_P	α_T	$\alpha_{\rm WT}$	SOC $d = 3$	SOC $d = 1$
GRB Prompt Emission						
Our study	$1.67^{+0.23}_{-0.16}$	$1.47^{+0.60}_{-0.18}$	$2.08^{+0.19}_{-0.16}$	$2.04^{+0.14}_{-0.12}$	Roughly	No
Guidorzi et al. (2015) (GBM)	…	…	…	$2.36^{+0.17}_{-0.16}$	…	…
Guidorzi et al. (2015) (BAT)	…	…	…	$2.06^{+0.10}_{-0.09}$	…	…
Lyu et al. (2020)	$1.54^{+0.09}_{-0.09}$	$2.09^{+0.18}_{-0.19}$	$1.82^{+0.14}_{-0.15}$	…	Roughly	No
Li & Yang (2023)	…	$1.92^{+0.15}_{-0.15}$	$1.80^{+0.19}_{-0.19}$	…	Roughly	No
GRB X-Ray Flares						
Wang & Dai (2013)	$1.06^{+0.15}_{-0.15}$		$1.10^{+0.15}_{-0.15}$	$1.80^{+0.20}_{-0.20}$	No	Very roughly
Wei (2023)	$1.82^{+0.37}_{-0.28}$		$1.41^{+0.09}_{-0.08}$	$1.54^{+0.30}_{-0.19}$	No	No
GRB Prompt Emission and X-Ray Flares						
Guidorzi et al. (2015) (BAT-X)	…	…	…	$1.66^{+0.07}_{-0.06}$	No	No
GRB Precursors						
Li & Yang (2023)	…	$2.22^{+0.20}_{-0.20}$	$1.82^{+0.19}_{-0.19}$	$1.81^{+0.15}_{-0.15}$	No	No
SGRs						
Göğüş et al. (1999, 2000)	1.43-1.76	…	…	…	Roughly	No
Solar Flares						
Wang & Dai (2013)	$1.53^{+0.02}_{-0.02}$	…	$2.00^{+0.05}_{-0.05}$	$2.04^{+0.03}_{-0.03}$	Yes	No
Aschwanden (2011)	$1.62^{+0.12}_{-0.12}$	$1.73^{+0.07}_{-0.07}$	$1.99^{+0.35}_{-0.35}$	…	Yes	No
SOC predictions ($\beta = 1$)	$3\frac{d+1}{d+5}$	$2 - \frac{1}{d}$	$\frac{d+1}{2}$	$\frac{d+1}{2}$	…	…
$d = 3$	$\frac{3}{2}$	$\frac{5}{3}$	2	2	…	…
$d = 1$	1	1	1	1	…	…

Notes. Values predicted by SOC theory are also indicated, in the case where $\beta = 1$. Special cases of $d = 1$ or $d = 3$ are also reported. The last two columns indicate whether the obtained values are in agreement with the values predicted by SOC theory in the two special cases.

4. Discussion

For the distributions of energy, peak flux (or the corresponding intrinsic quantity, which is luminosity), and duration, the corresponding PL indices predicted by SOC models are given by the following (Aschwanden 2014):

$$\alpha_E = 1 + \frac{d - 1}{D_d + \frac{2}{\beta}}, \tag{17}$$

$$\alpha_P = 1 + \frac{d - 1}{d}, \tag{18}$$

$$\alpha_T = 1 + \beta\frac{(d - 1)}{2}, \tag{19}$$

where β is the spreading exponent ($\beta = 1/2$ for sub-diffusion, $\beta = 1$ for normal diffusion, $\beta = 2$ for linear expansion), d is the Euclidean space dimension, and D_d is the fractal dimension of SOC avalanches, which is usually approximated by $D_d \simeq \frac{1+d}{2}$. SOC theory also predicts $\alpha_{\rm WT} = \alpha_T$, where $\alpha_{\rm WT}$ is the PL index of the WT distribution (this holds for short WTs: for WTs longer than the longest pulse duration, the WT distribution should break exponentially; see Aschwanden 2014). In the case of 3D avalanches ($d = 3$) and normal diffusion ($\beta = 1$), it is $\alpha_E = 1.5$, $\alpha_P = 5/3$, and $\alpha_T = \alpha_{\rm WT} = 2$. Our estimates of the duration and of the WT duration distribution PL indices agree with SOC predictions: $\alpha_{\rm T} = 3 - \gamma_T = 2.08^{+0.19}_{-0.16}$ and $\alpha_{\rm WT} = 3 - \gamma_{WT} = 2.04^{+0.14}_{-0.12}$.

The PL indices of the high-value tails of the energy and luminosity distributions, respectively, $s_2 = 1.67^{+0.23}_{-0.16}$ and $\kappa_2 = 1.47^{+0.60}_{-0.18}$, are also roughly in agreement with SOC predictions (see Figure 12).

However, our results show evidence for a break in both distributions, which is not predicted by SOC theory. Given the accuracy with which the detection efficiency was modeled, the evidence for a break seems to be hardly entirely ascribable to unaccounted selection effects. In our study, we have selected all type II GRB candidates. Our study implicitly assumes that all type II GRB engines are behaving in the same way. However, one cannot reject the possibility that the observed population is actually the mixture of different kinds of engines, or at least different behaviors. Even for a given type of central engine, say a hyper-accreting BH, two or more jet formation scenarios ($\nu\bar{\nu}$ annihilation or the BZ effect) producing different energy/luminosity distributions can be at play and contribute to the observed population of GRBs. In principle, the observed deviations from the SOC predictions could also be ascribed to the physics and geometry of the prompt emission, i.e., the properties of the jet and its interactions with the stellar envelope. Finally, a PL behavior does not unavoidably imply SOC; it is just a necessary condition, not a sufficient one, given that hard-tailed distributions modeled as PL or BPL can result from a number of different processes.

Table 5 summarizes and compares our findings with analogous studies. Interestingly, the energy index obtained is consistent with what was found for the burst activity observed in Galactic magnetars, $\alpha_E = 1.43$–1.76 (Göğüş et al. 1999,

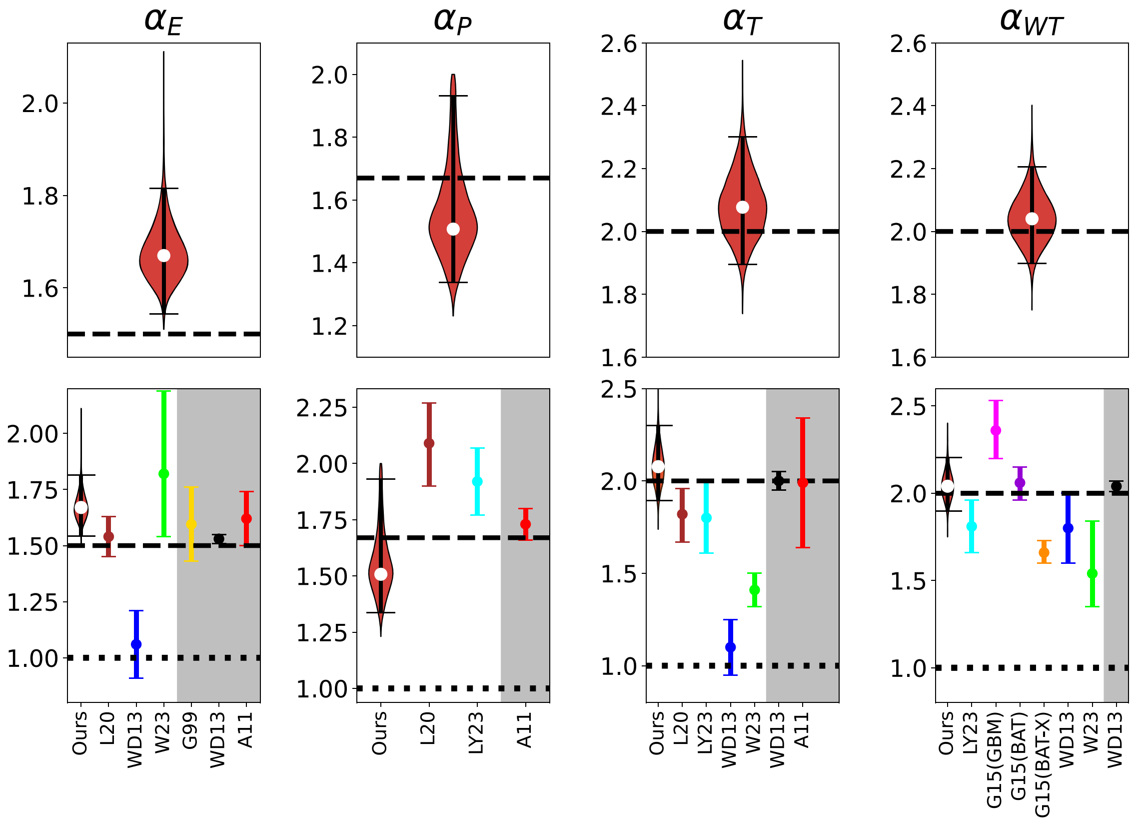

Figure 12. Top panels, left to right: violin plots of the posterior distributions for the PL indices of the energy, luminosity, duration, and WT distributions, respectively, obtained in this work on GRB prompt emission (for the energy and luminosity distributions, the postbreak values were considered); the horizontal bars span 5%–95% quantiles. Dashed lines show the SOC predictions for $d = 3$. Bottom panels, left to right: the same corresponding violin plots as in the top, including values reported from the literature. For GRB prompt emission, values from Lyu et al. (2020, L20; brown), Li & Yang (2023, LY23; cyan), and Guidorzi et al. (2015, G15(GBM) and G15(BAT); in pink and purple). For GRB X-ray flares, values from Wang & Dai (2013, WD13; blue), and Wei (2023, W23; green). The orange point refers to a study where prompt emission pulses and X-ray flares were considered as a unique process (Guidorzi et al. 2015, G15(BAT-X)). The shaded areas show the results reported in the literature from analogous investigations about different classes of astrophysical sources: for solar flares, values from Wang & Dai (2013, WD13; black) and Aschwanden (2011, A11; red). For magnetars, values reported in Göğüş et al. (1999, 2000) are displayed (G99; yellow). Dashed (dotted) lines show SOC predictions for $d = 3$ ($d = 1$) and $\beta = 1$.

2000), and in solar flares, $\alpha_E = 1.62^{+0.12}_{-0.12}$ (Aschwanden 2011). We obtained substantially lower values for α_P than Lyu et al. (2020) and Li & Yang (2023). In these studies, α_P is determined by analyzing the distribution of pulse count rates given by the instrument, as it was also done for solar flares. While the latter case is justified, as all flares come from the same source at a fixed distance from the detector, for GRBs the range of distances is so large that one should either consider a group of GRBs with similar redshift or better use luminosities and model the selection effects that inevitably affect the observed sample.

We compared $dN/dL_{\rm iso}$ with the GRB (peak) luminosity function, as modeled for example in Ghirlanda & Salvaterra (2022). Even though the latter is in principle different from $dN/dL_{\rm iso}$, the two distributions are not completely independent of one another. Ghirlanda & Salvaterra (2022) modeled the distribution with a BPL with low-/high-luminosity indices $a_1 \sim 1$ and $a_2 \sim 2.2$ and a break luminosity $L_b \sim 10^{52}(1+z)^{0.64}$ erg s^{-1} slightly dependent on redshift. Our values are consistent with the low-luminosity index and with the break luminosity of the luminosity function. We find a flatter high-luminosity index that can be understood since our distribution contains all pulses of all GRBs, while the GRB peak luminosity function is determined by the most luminous pulse within each GRB. As we already pointed out, high-luminosity pulses tend to cluster in relatively few luminous GRBs; consequently, the distribution resulting from the selection of the most luminous pulse of each GRB turns into a depletion of luminous pulses and hence into a smaller fraction of high-luminosity events in the GRB distribution compared with the pulse distribution.

Finally, our results do not seem to crucially depend on redshift, given that they did not change in essence when we ignored GRBs with redshift $z > 1.76$. Specifically, the evidence for a break in both distributions holds true in both cases, suggesting that the break is not likely to be entirely due to selection effects, but is an intrinsic feature.

5. Conclusions

We determined the energy, luminosity, duration, and WT distributions of individual pulses identified with a well-calibrated algorithm from 142 type II GRBs with known redshift detected by the GBM. We then carried out a careful analysis of the selection effects through a suite of simulations, dividing our sample into nine redshift bins, and modeled for each of them the detection efficiency as a function of energy (luminosity), $\eta_z(E_{\rm iso})$ ($\eta'_z(L_{\rm iso})$). For each redshift bin, we then generated energy/luminosity samples of pulses accounting for the detection efficiency, under the assumption of some putative distribution models like simple PL or BPL. The plausibility of each assumed distribution was finally tested by comparing the resulting distribution with the observed one.

We found that a simple PL can reproduce neither $E_{\rm iso}$ nor $L_{\rm iso}$ distributions (especially in the case of $E_{\rm iso}$). Rather, for the first time, we found evidence for a break in $E_{\rm iso}$ and $L_{\rm iso}$ distributions ($E_b \sim 10^{52}$ erg and $L_b \sim 10^{52-53}$ erg s^{-1}), which appears to be hardly ascribable to unaccounted selection effects. A possible interpretation for this break is that the underlying assumption of a unique stochastic process ruling the GRB dynamics is not valid, but instead different kinds of dynamics, possibly connected with different progenitors or different regimes, contribute to the observed population of GRBs.

Interpreting our results in the SOC framework with $\beta = 1$, our results are compatible with prompt emission being the result of 3D ($d = 3$) avalanches produced by a nonlinear dynamical system driven slowly to a SOC state. The SOC interpretation of GRB prompt emission could be compatible with utterly different theoretical models. Indeed, this scenario could be consistent either with the picture of a NDAF surrounding a hyper-accreting stellar-mass BH becoming thermally unstable and cooled by neutrino emission, with rotational energy being extracted by the BZ effect and converted into a Poynting-flux-dominated outflow, or with cascades of magnetic reconnection events produced within a magnetically dominated relativistic outflow at the GRB emission site, as foreseen in the ICMART model (Zhang & Yan 2011).

Acknowledgments

We acknowledge the anonymous reviewer for a constructive report which improved the manuscript. R.M. and C.G. acknowledge the Dept. of Physics and Earth Science of the University of Ferrara for the financial support through the "FIRD 2022" grant. R.M. acknowledges the University of Ferrara for the financial support of his PhD scholarship. R.M. acknowledges the Fermi team for covering the flight costs needed to attend the Fermi summer school 2023. A.T. acknowledges financial support from "ASI-INAF Accordo Attuativo HERMES Pathinder operazioni n. 2022-25-HH.0."

Appendix
Time-resolved Spectral Analysis

We computed the isotropic-equivalent released energy using Equation (9), thus assuming a negligible impact of a possible spectral evolution.

GRB spectra are known to be temporally evolving. This is usually described in terms of two alternative behaviors: (i) a monotonic hard-to-soft evolution, and (ii) pulse tracking (see Lu et al. 2012 and references therein). Therefore, the isotropic-equivalent energy should be computed using the time-resolved fluence Φ'_k instead of the time-averaged fluence Φ_k used in Equation (9), where Φ'_k is calculated from modeling the spectrum extracted within the time interval that includes only the kth pulse (or, at least, centered on it, given that pulses occasionally overlap and therefore their spectra cannot completely be separated).

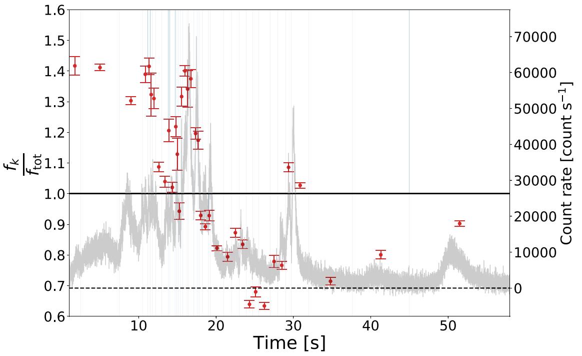

Figure 13. Evolution of the ratio of the time-resolved over time-averaged counts-to-fluence conversion factor, $f/f_{\rm tot}$ (shown by the red points), as a function of time for 180720B (the horizontal solid line shows the $f = f_{\rm tot}$ case). Blue vertical lines mark the boundaries of adjacent temporal intervals. The light curve is displayed in gray (right-hand y-axis).

We conveniently defined the time-resolved conversion factor $f_k = \Phi'_k / C'_k$, where C'_k are the counts integrated over the same time interval used to compute Φ'_k. In this way, the degree of approximation introduced in Equation (9) by assuming time-averaged instead of time-resolved fluences can be studied through the ratio $f_k/f_{\rm tot}$.

To this aim, we considered a few cases of bright GRBs with numerous pulses, some of them being already known to show spectral evolution.

We modeled time-resolved spectra of these GRBs and we studied the impact of spectral evolution on the $E_{\rm iso}$ distribution. For this study, we considered five GRBs among our sample having, respectively, 57, 34, 21, 20, and 13 pulses; thus totaling 145, that is, enough to build a statistically sound distribution.[22] These GRBs are among the brightest of the GBM catalog, with three of them ranking in the 12 top fluences of the whole catalog.[23]

Figure 13 illustrates the case of 180720B. For the time-averaged spectrum, we took the fluence from the GRB catalog $\Phi_{\rm tot} = (2.9853 \pm 0.0008) \times 10^{-4}$ erg cm^{-2}, integrated from -60.416 to 137.220 s. Our results are consistent with those by Chen et al. (2021). Our analysis shows a hard-to-soft evolution, modulated by $f/f_{\rm tot}$ tracking the light-curve peaks (Figure 13). As a consequence, the fluence of the brightest peaks is underestimated by up to 40%, whereas the fluence of the weakest ones is overestimated by a comparable amount. Among the examined GRBs, 180720B, 190114C, and 171010A exhibited the larger deviations of $f/f_{\rm tot}$ from 1, reaching 60%–70%, indicating that the effect is probably stronger for brightest GRBs. We can therefore safely assume that neglecting the spectral evolution for the bulk of GRBs considered in this work has a milder effect than what we assessed for the brightest cases.

We finally explored to what extent the $E_{\rm iso}$ distribution was affected by ignoring the spectral evolution: We compared $E_{\rm iso}$ calculated with both time-resolved and time-averaged analysis

---

[22] They are 171010A, 180720B, 190114C, 170405A, and 090424.

[23] 171010A, with 6.3×10^{-4} erg cm^{-2}; 190114C, with 4.4×10^{-4} erg cm^{-2}, and 180720B, with 3.0×10^{-4} erg cm^{-2}.

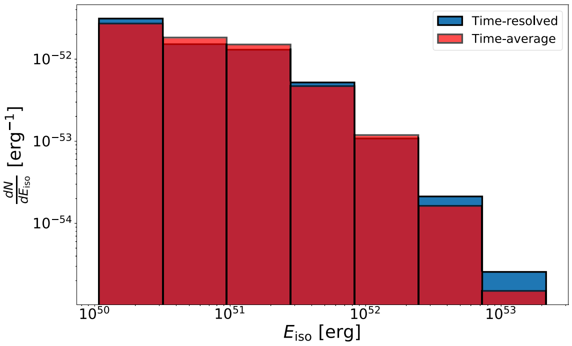

Figure 14. $E_{\rm iso}$ distributions obtained with either time-resolved (blue) or time-averaged (red) spectral analysis.

and derived the corresponding distributions (Figure 14). We ran statistical tests to assess the null hypothesis that the two $E_{\rm iso}$ distributions are drawn from the same population. A KS test yielded a p-value of 0.87, while an AD test gave a lower limit on the p-value of >0.25. We concluded that we cannot reject the hypothesis that the two distributions are drawn from the parent population, so we can safely ignore the bias introduced by neglecting the spectral evolution.

Additionally, we compared the best-fit values for the PL index α that models the tail of each distribution: We obtained $\alpha_{\rm tr} = 1.62^{+0.20}_{-0.18}$ and $\alpha_{\rm ta} = 1.63^{+0.19}_{-0.19}$ for the time-resolved and for the time-averaged distribution, respectively. The two values are indistinguishable within uncertainties, which confirms that neglecting the no-spectral-evolution assumption is safe.

ORCID iDs

R. Maccary https://orcid.org/0000-0002-8799-2510
C. Guidorzi https://orcid.org/0000-0001-6869-0835
L. Amati https://orcid.org/0000-0001-5355-7388
L. Bazzanini https://orcid.org/0000-0003-0727-0137
M. Bulla https://orcid.org/0000-0002-8255-5127
A. E. Camisasca https://orcid.org/0000-0002-4200-1947
L. Ferro https://orcid.org/0009-0006-1140-6913
F. Frontera https://orcid.org/0000-0003-2284-571X
A. Tsvetkova https://orcid.org/0000-0003-0292-6221

References

Abbott, B. P., Abbott, R., Abbott, T. D., et al. 2017, ApJL, 848, L13
Ackermann, M., Ajello, M., Asano, K., et al. 2014, Sci, 343, 42
Ahumada, T., Singer, L. P., Anand, S., et al. 2021, NatAs, 5, 917
Amati, L., Frontera, F., Tavani, M., et al. 2002, A&A, 390, 81
Aschwanden, M. J. 2011, SoPh, 274, 99
Aschwanden, M. J. 2014, ApJ, 782, 54
Aschwanden, M. J. 2015, ApJ, 814, 19
Aschwanden, M. J., & Aschwanden, P. D. 2008a, ApJ, 674, 530
Aschwanden, M. J., & Aschwanden, P. D. 2008b, ApJ, 674, 544
Aschwanden, M. J., & Güdel, M. 2021, ApJ, 910, 41
Aschwanden, M. J., & McTiernan, J. M. 2010, ApJ, 717, 683
Aschwanden, M. J., Scholkmann, F., Béthune, W., et al. 2018, SSRv, 214, 55
Bak, P., & Sneppen, K. 1993, PhRvL, 71, 4083
Bak, P., Tang, C., & Wiesenfeld, K. 1987, PhRvL, 59, 381
Bak, P., Tang, C., & Wiesenfeld, K. 1988, PhRvA, 38, 364
Bartolozzi, M., Leinweber, D. B., & Thomas, A. W. 2005, PhyA, 350, 451
Berger, E., & Rauch, M. 2008, GCN, 8542 https://gcn.nasa.gov/circulars/8542.txt
Bhalerao, V. B., Singer, L. P., Kasliwal, M. M., et al. 2014, GCN, 16442, https://gcn.nasa.gov/circulars/16442.txt
Bhat, P., Meegan, C. A., von Kienlin, A., et al. 2016, ApJS, 223, 28
Blandford, R. D., & Znajek, R. L. 1977, MNRAS, 179, 433
Bolmer, J., Graham, J., Knust, F., & Greiner, J. 2015, GCN, 18598, https://gcn.nasa.gov/circulars/18598.txt
Bromberg, O., Nakar, E., Piran, T., & Sari, R. 2013, ApJ, 764, 179
Bromberg, O., Singh, C. B., Davelaar, J., & Philippov, A. A. 2019, ApJ, 884, 39
Bromberg, O., & Tchekhovskoy, A. 2016, MNRAS, 456, 1739
Camisasca, A. E., Guidorzi, C., Amati, L., et al. 2023, A&A, 671, A112
Cano, Z., Bersier, D., Guidorzi, C., et al. 2011, MNRAS, 413, 669
Cano, Z., Malesani, D., de Ugarte Postigo, A., et al. 2016, GCN, 20245, https://gcn.nasa.gov/circulars/20245.txt
Castro-Tirado, A. J., Cunniffe, R., Sanchez-Ramirez, R., et al. 2014b, GCN, 16505, https://gcn.nasa.gov/circulars/16505.txt
Castro-Tirado, A. J., Fatkhullin, T. A., Moskvitin, A. S., et al. 2016b, GCN, 19632, https://gcn.nasa.gov/circulars/19632.txt
Castro-Tirado, A. J., Gorosabel, J., & Garcia-Rodriguez, A. 2014a, GCN, 16797, https://gcn.nasa.gov/circulars/16797.txt
Castro-Tirado, A. J., Hu, Y., Fernandez-Garcia, E., et al. 2019, GCN, 23708, https://gcn.nasa.gov/circulars/23708.txt
Castro-Tirado, A. J., Valeev, A. F., Jeong, S., et al. 2016a, GCN, 19710, https://gcn.nasa.gov/circulars/19710.txt
Castro-Tirado, A. J., Valeev, A. F., Sokolov, V. V., et al. 2016c, GCN, 20077, https://gcn.nasa.gov/circulars/20077.txt
Castro-Tirado, A. J., Valeev, A. F., Vinokurov, A., et al. 2022, GCN, 31423, https://gcn.nasa.gov/circulars/31423.txt
Cenko, S. B., Bloom, J. S., Morgan, A. N., & Perley, D. A. 2009, GCN, 9053, https://gcn.nasa.gov/circulars/9053.txt
Charbonneau, P., McIntosh, S. W., Liu, H.-L., & Bogdan, T. J. 2001, SoPh, 203, 321
Chen, J.-M., Peng, Z.-Y., Du, T.-T., Yin, Y., & Wu, H. 2021, ApJ, 920, 53
Chornock, R., & Berger, E. 2011, GCN, 11544, https://gcn.nasa.gov/circulars/11544.txt
Chornock, R., Berger, E., & Fox, D. 2011a, GCN, 12537, https://gcn.nasa.gov/circulars/12537.txt
Chornock, R., Berger, E., & Fox, D. B. 2011b, GCN, 11538, https://gcn.nasa.gov/circulars/11538.txt
Chornock, R., Perley, D. A., Cenko, S. B., & Bloom, J. S. 2009, GCN, 9028, https://gcn.nasa.gov/circulars/9028.txt
Cucchiara, A., Fox, D., & Tanvir, N. 2009a, GCN, 10065, https://gcn.nasa.gov/circulars/10065.txt
Cucchiara, A., & Fox, D. B. 2010, GCN, 10606, https://gcn.nasa.gov/circulars/10606.txt
Cucchiara, A., Fox, D. B., Cenko, S. B., & Berger, E. 2008, GCN, 8713, https://gcn.nasa.gov/circulars/8713.txt
Cucchiara, A., Fox, D. B., Cenko, S. B., Tanvir, N., & Berger, E. 2009b, GCN, 10031, https://gcn.nasa.gov/circulars/10031.txt
Cucchiara, A., Fox, D. B., Tanvir, N., & Berger, E. 2009c, GCN, 9873, https://gcn.nasa.gov/circulars/9873.txt
Cucchiara, A., & Fumagalli, M. 2013, GCN, 14207, https://gcn.nasa.gov/circulars/14207.txt
Cucchiara, A., & Prochaska, J. X. 2012, GCN, 12865, https://gcn.nasa.gov/circulars/12865.txt
D'Avanzo, P., D'Elia, V., & Covino, S. 2008, GCN, 8350, https://gcn.nasa.gov/circulars/8350.txt
D'Avanzo, P., Sparre, M., Watson, D., et al. 2011, GCN, 12284, https://gcn.nasa.gov/circulars/12284.txt
de Arcangelis, L. 2012, EPJST, 205, 243
de Ugarte Postigo, A., Campana, S., Thöne, C. C., et al. 2013b, A&A, 557, L18
de Ugarte Postigo, A., Fynbo, J. P. U., Thoene, C., et al. 2015c, GCN, 17583, https://gcn.nasa.gov/circulars/17583.txt
de Ugarte Postigo, A., Goldoni, P., Milvang-Jensen, B., et al. 2011, GCN, 11579, https://gcn.nasa.gov/circulars/11579.txt
de Ugarte Postigo, A., Gorosabel, J., Malesani, D., Fynbo, J. P. U., & Levan, A. J. 2009a, GCN, 9383, https://gcn.nasa.gov/circulars/9383.txt
de Ugarte Postigo, A., Gorosabel, J., Thoene, C. C., et al. 2014a, GCN, 16657, https://gcn.nasa.gov/circulars/16657.txt
de Ugarte Postigo, A., Gorosabel, J., Xu, D., et al. 2014c, GCN, 16310, https://gcn.nasa.gov/circulars/16310.txt
de Ugarte Postigo, A., Izzo, L., Kann, D. A., et al. 2017a, GCN, 22272, https://gcn.gsfc.nasa.gov/gcn3/22272.gcn3
de Ugarte Postigo, A., Izzo, L., Thoene, C. C., et al. 2017b, GCN, 21240, https://gcn.gsfc.nasa.gov/gcn3/21240.gcn3
de Ugarte Postigo, A., Izzo, L., Thoene, C. C., et al. 2017c, GCN, 21799, https://gcn.gsfc.nasa.gov/gcn3/21799.gcn3
de Ugarte Postigo, A., Jakobsson, P., Malesani, D., et al. 2009b, GCN, 8766, https://gcn.nasa.gov/circulars/8766.txt
de Ugarte Postigo, A., Kann, D. A., Izzo, L., & Thoene, C. C. 2017d, GCN, 21298, https://gcn.gsfc.nasa.gov/gcn3/21298.gcn3

de Ugarte Postigo, A., Kann, D. A., Thoene, C., et al. 2021b, GCN, 30272, https://gcn.nasa.gov/circulars/30272.txt

de Ugarte Postigo, A., Kann, D. A., Thoene, C. C., et al. 2017e, GCN, 20990, https://gcn.nasa.gov/circulars/20990.txt

de Ugarte Postigo, A., Kruehler, T., Flores, H., & Fynbo, J. P. U. 2015a, GCN, 17523, https://gcn.gsfc.nasa.gov/gcn3/17523.gcn3

de Ugarte Postigo, A., Tanvir, N., Sanchez-Ramirez, R., et al. 2013a, GCN, 14437, https://gcn.nasa.gov/circulars/14437.txt

de Ugarte Postigo, A., Thoene, C., Agui Fernandez, J. F., et al. 2021a, GCN, 30194, https://gcn.gsfc.nasa.gov/gcn3/30194.gcn3

de Ugarte Postigo, A., Thoene, C. C., Gorosabel, J., et al. 2014b, GCN, 17198, https://gcn.gsfc.nasa.gov/gcn3/17198.gcn3

de Ugarte Postigo, A., Xu, D., Malesani, D., & Tanvir, N. R. 2015b, GCN, 17822, https://gcn.gsfc.nasa.gov/gcn3/17822.gcn3

Del Zanna, L., Papini, E., Landi, S., Bugli, M., & Bucciantini, N. 2016, MNRAS, 460, 3753

D'Elia, V., Fynbo, J. P. U., Covino, S., et al. 2010, A&A, 523, A36

D'Elia, V., Kruehler, T., Wiersema, K., et al. 2015, GCN, 18187, https://gcn.nasa.gov/circulars/18187.txt

Di Matteo, T., Perna, R., & Narayan, R. 2002, ApJ, 579, 706

Dănilă, B., Harko, T., & Mocanu, G. 2015, MNRAS, 453, 2982

Duncan, R. C., & Thompson, C. 1992, ApJL, 392, L9

Eichler, D., Livio, M., Piran, T., & Schramm, D. N. 1989, Natur, 340, 126

Fenimore, E. E., in 't Zand, J. J. M., Norris, J. P., Bonnell, J. T., & Nemiroff, R. J. 1995, ApJL, 448, L101

Fishman, G. J., & Meegan, C. A. 1995, ARA&A, 33, 415

Flores, H., Fynbo, J. P. U., de Ugarte Postigo, A., et al. 2010, GCN, 11317, https://gcn.gsfc.nasa.gov/gcn3/11317.gcn3

Foreman-Mackey, D., Hogg, D. W., Lang, D., & Goodman, J. 2013, PASP, 125, 306

Fynbo, J. P. U., de Ugarte Postigo, A., D'Elia, V., et al. 2018, GCN, 23356, https://gcn.gsfc.nasa.gov/gcn3/23356.gcn3

Fynbo, J. P. U., de Ugarte Postigo, A., Xu, D., et al. 2022a, GCN, 31359, https://gcn.gsfc.nasa.gov/gcn3/31359.gcn3

Fynbo, J. P. U., Malesani, D., Hjorth, J., Sollerman, J., & Thoene, C. C. 2008, GCN, 8254, https://gcn.gsfc.nasa.gov/gcn3/8254.gcn3

Fynbo, J. P. U., Malesani, D., Jakobsson, P., & D'Elia, V. 2009, GCN, 9947, https://gcn.gsfc.nasa.gov/gcn3/9947.gcn3

Fynbo, J. P. U., Tanvir, N. R., Jakobsson, P., et al. 2014, GCN, 16217, https://gcn.gsfc.nasa.gov/gcn3/16217.gcn3

Fynbo, J. P. U., Zhu, Z., Xu, D., et al. 2022b, GCN, 32079, https://gcn.gsfc.nasa.gov/gcn3/32079.gcn3

Gehrels, N., Chincarini, G., Giommi, P., et al. 2004, ApJ, 611, 1005

Gehrels, N., Norris, J. P., Barthelmy, S. D., et al. 2006, Natur, 444, 1044

Ghirlanda, G., & Salvaterra, R. 2022, ApJ, 932, 10

Giannios, D., & Spruit, H. C. 2006, A&A, 450, 887

Goldstein, A., Cleveland, W. H., & Kocevski, D. 2022, Fermi GBM Data Tools: v1.1.1, https://fermi.gsfc.nasa.gov/ssc/data/analysis/gbm

Gompertz, B. P., Ravasio, M. E., Nicholl, M., et al. 2023, NatAs, 7, 67

Gorosabel, J., de Ugarte Postigo, A., Thoene, C., Perley, D., & Garcia Rodriguez, A. 2014a, GCN, 16671, https://gcn.gsfc.nasa.gov/gcn3/16671.gcn3

Gorosabel, J., de Ugarte Postigo, A., Thoene, C. C., et al. 2014b, GCN, 17234, https://gcn.gsfc.nasa.gov/gcn3/17234.gcn3

Göğüş, E., Woods, P. M., Kouveliotou, C., et al. 1999, ApJL, 526, L93

Göğüş, E., Woods, P. M., Kouveliotou, C., et al. 2000, ApJL, 532, L121

Gruber, D., Krühler, T., Foley, S., et al. 2011a, A&A, 528, A15

Gruber, D., Lachowicz, P., Bissaldi, E., et al. 2011b, A&A, 533, A61

Guidorzi, C. 2015, A&C, 10, 54

Guidorzi, C., Dichiara, S., Frontera, F., et al. 2015, ApJ, 801, 57

Harko, T., Mocanu, G., & Stroia, N. 2015, Ap&SS, 357, 84

Hartoog, O. E., Malesani, D., Wiersema, K., et al. 2012, GCN, 13730, https://gcn.gsfc.nasa.gov/gcn3/13730.gcn3

Izzo, L., Arabsalmani, M., Malesani, D. B., et al. 2018, GCN, 22823, https://gcn.gsfc.nasa.gov/gcn3/22823.gcn3

Izzo, L., D'Elia, V., de Ugarte Postigo, A., et al. 2022, GCN, 32291, https://gcn.gsfc.nasa.gov/gcn3/32291.gcn3

Izzo, L., Noschese, A., D'Avino, L., & Mollica, M. 2019, GCN, 23699, https://gcn.gsfc.nasa.gov/gcn3/23699.gcn3

Janiuk, A., Bejger, M., Sukova, P., & Charzynski, S. 2017, Galax, 5, 15

Janiuk, A., Yuan, Y., Perna, R., & Di Matteo, T. 2007, ApJ, 664, 1011

Janiuk, A., & Yuan, Y. F. 2010, A&A, 509, A55

Jeong, S., Castro-Tirado, A. J., Bremer, M., et al. 2014b, A&A, 569, A93

Jeong, S., Sanchez-Ramirez, R., Gorosabel, J., & Castro-Tirado, A. J. 2014a, GCN, 15936, https://gcn.gsfc.nasa.gov/gcn3/15936.gcn3

Kann, D. A., de Ugarte Postigo, A., Blazek, M., et al. 2020a, GCN, 28765, https://gcn.gsfc.nasa.gov/gcn3/28765.gcn3

Kann, D. A., de Ugarte Postigo, A., Blazek, M., et al. 2020b, GCN, 28717, https://gcn.gsfc.nasa.gov/gcn3/28717.gcn3

Kann, D. A., Izzo, L., Levan, A. J., et al. 2021, GCN, 30583, https://gcn.gsfc.nasa.gov/gcn3/30583.gcn3

Kasliwal, M. M., Cenko, S. B., & Singer, L. P. 2014, GCN, 16425, https://gcn.nasa.gov/circulars/16425.txt

Klose, S., Schmidl, S., Kann, D. A., et al. 2019, A&A, 622, A138

Knust, F., Kruehler, T., Klose, S., & Greiner, J. 2012, GCN, 13810, https://gcn.gsfc.nasa.gov/gcn3/13810.gcn3

Kouveliotou, C., Meegan, C. A., Fishman, G. J., et al. 1993, ApJL, 413, L101

Kruehler, T., Greiner, J., & Kann, D. A. 2013a, GCN, 14500, https://gcn.gsfc.nasa.gov/gcn3/14500.gcn3

Kruehler, T., Malesani, D., Xu, D., et al. 2013b, GCN, 14264, https://gcn.nasa.gov/circulars/14264.txt

Kruehler, T., Schady, P., Greiner, J., & Tanvir, N. R. 2017, GCN, 20686, https://gcn.gsfc.nasa.gov/gcn3/20686.gcn3

Krühler, T., Malesani, D., Fynbo, J. P. U., et al. 2015, A&A, 581, A125

Lei, W.-H., Zhang, B., & Liang, E.-W. 2013, ApJ, 765, 125

Lesage, S., Veres, P., Briggs, M. S., et al. 2023, ApJL, 952, L42

Levan, A. J., Cenko, S. B., Perley, D. A., & Tanvir, N. R. 2013, GCN, 14455, https://gcn.gsfc.nasa.gov/gcn3/14455.gcn3

Li, X.-J., & Yang, Y.-P. 2023, ApJL, 955, L34

Li, X.-J., Zhang, W.-L., Yi, S.-X., Yang, Y.-P., & Li, J.-L. 2023, ApJS, 265, 56

Li, Y.-P., Yuan, F., Yuan, Q., et al. 2015, ApJ, 810, 19

Littlejohns, O., Butler, N., Watson, A. M., et al. 2014, GCN, 17003, https://gcn.gsfc.nasa.gov/gcn3/17003.gcn3

Liu, T., Gu, W.-M., & Zhang, B. 2017, NewAR, 79, 1

Lu, E. T., & Hamilton, R. J. 1991, ApJL, 380, L89

Lu, R.-J., Wei, J.-J., Liang, E.-W., et al. 2012, ApJ, 756, 112

Lyu, F., Li, Y.-P., Hou, S.-J., et al. 2020, FrPhy, 16, 14501

MacFadyen, A. I., & Woosley, S. E. 1999, ApJ, 524, 262

Malesani, D., Kruehler, T., Heintz, K. E., & Fynbo, J. P. U. 2016, GCN, 20180, https://gcn.gsfc.nasa.gov/gcn3/14225.gcn3

Malesani, D., Kruehler, T., Perley, D., et al. 2013, GCN, 14225, https://gcn.gsfc.nasa.gov/gcn3/14225.gcn3

Malesani, D., Xu, D., Fynbo, J. P. U., et al. 2014, GCN, 15800, https://gcn.gsfc.nasa.gov/gcn3/25991.gcn3

Malesani, D. B., de Ugarte Postigo, A., Kann, D. A., et al. 2019, GCN, 25991, https://gcn.gsfc.nasa.gov/gcn3/25991.gcn3

Meegan, C., Lichti, G., Bhat, P. N., et al. 2009, ApJ, 702, 791

Melandri, A., Malesani, D. B., Izzo, L., et al. 2019, MNRAS, 490, 5366

Metzger, B. D., Giannios, D., Thompson, T. A., Bucciantini, N., & Quataert, E. 2011, MNRAS, 413, 2031

Milne, P. A., & Cenko, S. B. 2011, GCN, 11708, https://gcn.gsfc.nasa.gov/gcn3/11708.gcn3

Mineshige, S., Ouchi, N. B., & Nishimori, H. 1994, PASJ, 46, 97

Nakazato, K. 2014, PhRvD, 90, 043010

Narayan, R., Paczynski, B., & Piran, T. 1992, ApJL, 395, L83

Norris, J. P., & Bonnell, J. T. 2006, ApJ, 643, 266

Norris, J. P., Bonnell, J. T., Kazanas, D., et al. 2005, ApJ, 627, 324

Norris, J. P., Nemiroff, R. J., Bonnell, J. T., et al. 1996, ApJ, 459, 393

Oates, S. R., Kuin, N. P. M., De Pasquale, M., et al. 2020, GCN, 28338, https://gcn.gsfc.nasa.gov/gcn3/28338.gcn3

O'Meara, J., Chen, H. W., & Prochaska, J. X. 2010, GCN, 11089, https://gcn.gsfc.nasa.gov/gcn3/11089.gcn3

Paciesas, W. S., Meegan, C. A., Pendleton, G. N., et al. 1999, ApJS, 122, 465

Paczynski, B. 1991, AcA, 41, 257

Paczyński, B. 1998, ApJL, 494, L45

Perley, D. A., Hillenbrand, L., & Prochaska, J. X. 2015, GCN, 18487, https://gcn.gsfc.nasa.gov/gcn3/18487.gcn3

Perley, D. A., Izzo, L., Kann, D. A., & Malesani, D. B. 2019, GCN, 23999, https://gcn.gsfc.nasa.gov/gcn3/23999.gcn3

Perley, D. A., Prochaska, J. X., & Morgan, A. N. 2012, GCN, 14059, https://gcn.gsfc.nasa.gov/gcn3/14059.gcn3

Planck Collaboration, Aghanim, N., Akrami, Y., et al. 2020, A&A, 641, A6

Popham, R., Woosley, S. E., & Fryer, C. 1999, ApJ, 518, 356

Pozanenko, A., Moiseev, A., Moskvitin, A., et al. 2021, GCN, 31053, https://gcn.nasa.gov/circulars/31053.txt

Prochaska, J. X., Perley, D., Howard, A., et al. 2008, GCN, 8083, https://gcn.gsfc.nasa.gov/gcn3/8083.gcn3

Pugliese, V., Xu, D., Tanvir, N. R., et al. 2015, GCN, 17672, https://gcn.gsfc.nasa.gov/gcn3/17672.gcn3

Rastinejad, J. C., Gompertz, B. P., Levan, A. J., et al. 2022, Natur, 612, 223

Rossi, A., Heintz, K. E., Fynbo, J. P. U., et al. 2019, GCN, 25252, https://gcn.gsfc.nasa.gov/gcn3/25252.gcn3

Rossi, A., Izzo, L., Milvang-Jensen, B., et al. 2018, GCN, 23055, https://gcn.gsfc.nasa.gov/gcn3/23055.gcn3

Rossi, A., Rothberg, B., Palazzi, E., et al. 2022, ApJ, 932, 1

Rowlinson, A., Wiersema, K., Levan, A. J., et al. 2010, MNRAS, 408, 383

Saccardi, A., Izzo, L., Xu, D. & the Stargate Collaboration 2022, GCN, 32144, https://gcn.nasa.gov/circulars/32144.txt

Sado, F. 2019, IJAA, 9, 247

Salvaterra, R., Della Valle, M., Campana, S., et al. 2009, Natur, 461, 1258

Sanchez-Ramirez, R., Gorosabel, J., de Ugarte Postigo, A., & Gonzalez Perez, J. M. 2012, GCN, 13723, https://gcn.gsfc.nasa.gov/gcn3/13723.gcn3

Sbarufatti, B., Bolmer, J., de Ugarte Postigo, A., et al. 2018, GCN, 22484, https://gcn.gsfc.nasa.gov/gcn3/22484.gcn3

Schulze, S., de Ugarte Postigo, A., Wiersema, K., et al. 2014b, GCN, 16936, https://gcn.gsfc.nasa.gov/gcn3/15831.gcn3

Schulze, S., Wiersema, K., Xu, D., & Fynbo, J. P. U. 2014a, GCN, 15831, https://gcn.gsfc.nasa.gov/gcn3/15831.gcn3

Selsing, J., Malesani, D., Goldoni, P., et al. 2019, A&A, 623, A92

Singer, L. P., Cenko, S. B., Kasliwal, M. M., et al. 2013, ApJL, 776, L34

Singer, L. P., Kasliwal, M. M., Cenko, S. B., et al. 2015, ApJ, 806, 52

Smette, A., Ledoux, C., Vreeswijk, P., et al. 2013, GCN, 14848, https://gcn.gsfc.nasa.gov/gcn3/14848.gcn3

Sornette, A., & Sornette, D. 1989, EL, 9, 197

Sparre, M., de Ugarte Postigo, A., Fynbo, J. P. U., et al. 2011, GCN, 11607, https://gcn.gsfc.nasa.gov/gcn3/11607.gcn3

Sudilovsky, V., Kann, D. A., Schady, P., et al. 2013, GCN, 15250, https://gcn.gsfc.nasa.gov/gcn3/15250.gcn3

Tanvir, N. R., & Ball, J. 2012, GCN, 13532, https://gcn.gsfc.nasa.gov/gcn3/13532.gcn3

Tanvir, N. R., Heintz, K. E., Selsing, J., et al. 2018, GCN, 22384, https://gcn.gsfc.nasa.gov/gcn3/22384.gcn3

Tanvir, N. R., Levan, A. J., Cenko, S. B., et al. 2016, GCN, 19419, https://gcn.gsfc.nasa.gov/gcn3/19419.gcn3

Tanvir, N. R., Levan, A. J., & Matulonis, T. 2012a, GCN, 14009, https://gcn.gsfc.nasa.gov/gcn3/14009.gcn3

Tanvir, N. R., Levan, A. J., Wiersema, K., et al. 2014, GCN, 16150, https://gcn.gsfc.nasa.gov/gcn3/16150.gcn3

Tanvir, N. R., Wiersema, K., Levan, A. J., Cenko, S. B., & Geballe, T. 2011, GCN, 12225, https://gcn.nasa.gov/circulars/12225.txt

Tanvir, N. R., Wiersema, K., & Levan, A. J. 2010, GCN, 11230, https://gcn.gsfc.nasa.gov/gcn3/11230.gcn3

Tanvir, N. R., Wiersema, K., Levan, A. J., et al. 2012b, GCN, 13441, https://gcn.gsfc.nasa.gov/gcn3/13441.gcn3

Tanvir, N. R., Wiersema, K., Xu, D., & Fynbo, J. P. U. 2013, GCN, 14882, https://gcn.nasa.gov/circulars/14882.txt

Tanvir, N. R., Xu, D., Zafar, T., Covino, S., & Schulze, S. 2015, GCN, 18080, https://gcn.gsfc.nasa.gov/gcn3/18080.gcn3

Taylor, P. A., Miller, J. C., & Podsiadlowski, P. 2011, MNRAS, 410, 2385

Tello, J. C., Sanchez-Ramirez, R., Gorosabel, J., et al. 2012, GCN, 13118, https://gcn.nasa.gov/circulars/13118.txt

Thoene, C. C., de Ugarte Postigo, A., Gorosabel, J., et al. 2012, GCN, 13628, https://gcn.nasa.gov/circulars/13628.txt

Thoene, C. C., de Ugarte Postigo, A., Kann, D. A., et al. 2021, GCN, 30487, https://gcn.gsfc.nasa.gov/gcn3/30487.gcn3

Thoene, C. C., de Ugarte Postigo, A., Vreeswijk, P., et al. 2010, GCN, 10971, https://gcn.gsfc.nasa.gov/gcn3/10971.gcn3

Thoene, C. C., de Ugarte Postigo, A., Vreeswijk, P. M., Malesani, D., & Jakobsson, P. 2008, GCN, 8058, https://gcn.gsfc.nasa.gov/gcn3/8058.gcn3

Thoene, C. C., Goldoni, P., Covino, S., et al. 2009b, GCN, 10233, https://gcn.nasa.gov/circulars/10233.txt

Thoene, C. C., Jakobsson, P., De Cia, A., et al. 2009a, GCN, 9409, https://gcn.gsfc.nasa.gov/gcn3/9409.gcn3

Thompson, T. A., Chang, P., & Quataert, E. 2004, ApJ, 611, 380

Troja, E., Fryer, C. L., O'Connor, B., et al. 2022, Natur, 612, 228

Usov, V. V. 1992, Natur, 357, 472

Valeev, A. F., Castro-Tirado, A. J., Hu, Y. D., et al. 2019, GCN, 25565, https://gcn.gsfc.nasa.gov/gcn3/25565.gcn3

Vielfaure, J. B., Izzo, L., Xu, D., et al. 2020b, GCN, 29077, https://gcn.gsfc.nasa.gov/gcn3/29077.gcn3

Vielfaure, J. B., Japelj, J., Malesani, D. B., et al. 2018, GCN, 23315, https://gcn.gsfc.nasa.gov/gcn3/23315.gcn3

Vielfaure, J. B., Xu, D., Palmerio, J., et al. 2020a, GCN, 28739, https://gcn.gsfc.nasa.gov/gcn3/28739.gcn3

Virgili, F. J., Liang, E.-W., & Zhang, B. 2009, MNRAS, 392, 91

Virtanen, P., Gommers, R., Oliphant, T. E., et al. 2020, NatMe, 17, 261

von Kienlin, A., Meegan, C. A., Paciesas, W. S., et al. 2020, ApJ, 893, 46

Vreeswijk, P., Malesani, D., Fynbo, J., et al. 2008, GCN, 8301, https://gcn.gsfc.nasa.gov/gcn3/8301.gcn3

Vreeswijk, P. M., Kann, D. A., Heintz, K. E., et al. 2018, GCN, 22996, https://gcn.gsfc.nasa.gov/gcn3/22996.gcn3

Wang, F. Y., & Dai, Z. G. 2013, NatPh, 9, 465

Wei, J.-J. 2023, PhRvR, 5, 013019

Wheeler, J. C., Yi, I., Höflich, P., & Wang, L. 2000, ApJ, 537, 810

Wiersema, K., de Ugarte Postigo, A., & Levan, A. 2009a, GCN, 9250, https://gcn.gsfc.nasa.gov/gcn3/9250.gcn3

Wiersema, K., Tanvir, N., Levan, A., & Karjalainen, R. 2014, GCN, 16231, https://gcn.nasa.gov/circulars/16231.txt

Wiersema, K., Tanvir, N. R., Cucchiara, A., Levan, A. J., & Fox, D. 2009b, GCN, 10263, https://gcn.nasa.gov/circulars/10263.txt

Woosley, S. E. 1993, ApJ, 405, 273

Xu, D., Fynbo, J. P. U., D'Elia, V., & Tanvir, N. R. 2012, GCN, 13460, https://gcn.gsfc.nasa.gov/gcn3/13460.gcn3

Xu, D., Fynbo, J. P. U., Tanvir, N. R., et al. 2009, GCN, 10053, https://gcn.gsfc.nasa.gov/gcn3/10053.gcn3

Xu, D., Heintz, K. E., Malesani, D., Wiersema, K., & Fynbo, J. P. U. 2016a, GCN, 19773, https://gcn.nasa.gov/circulars/19773.txt

Xu, D., Heintz, K. E., Malesani, D., & Fynbo, J. P. U. 2017, GCN, 20458, https://gcn.gsfc.nasa.gov/gcn3/20458.gcn3

Xu, D., Izzo, L., Fynbo, J. P. U., et al. 2021, GCN, 29432, https://gcn.nasa.gov/circulars/29432.txt

Xu, D., Levan, A. J., Fynbo, J. P. U., et al. 2014, GCN, 16983, https://gcn.gsfc.nasa.gov/gcn3/16983.gcn3

Xu, D., Malesani, D., Fynbo, J. P. U., et al. 2016b, GCN, 19600, https://gcn.gsfc.nasa.gov/gcn3/19600.gcn3

Xu, D., Malesani, D., Tanvir, N., Kruehler, T., & Fynbo, J. 2013, GCN, 15450, https://gcn.gsfc.nasa.gov/gcn3/15450.gcn3

Yang, J., Ai, S., Zhang, B. B., et al. 2022, Natur, 612, 232

Yang, S. D. 2019, ApJ, 880, 44

Yang, Y.-H., Troja, E., O'Connor, B., et al. 2024, Natur, 626, 742

Yao, Y., Miller, A., Ho, A., & Perley, D. 2021, GCN, 29673, https://gcn.gsfc.nasa.gov/gcn3/29673.gcn3

Yoon, S. C., & Langer, N. 2005, A&A, 443, 643

Yuan, Q., Wang, Q. D., Liu, S., & Wu, K. 2018, MNRAS, 473, 306

Zhang, B. 2006, Natur, 444, 1010

Zhang, B., & Yan, H. 2011, ApJ, 726, 90

Zhang, B. B., Liu, Z. K., Peng, Z. K., et al. 2021, NatAs, 5, 911

Zhang, B. B., Zhang, B., Castro-Tirado, A. J., et al. 2018, NatAs, 2, 69

Zhu, Z. P., Xu, D., Fu, S. Y., & Liu, X. 2021, GCN, 30164, https://gcn.nasa.gov/circulars/30164.txt

A.8 PAPER II: DISTRIBUTION OF THE NUMBER OF PEAKS WITHIN A LONG GAMMA-RAY BURST: THE FULL FERMI/GBM CATALOGUE

A&A, 688, L8 (2024)
https://doi.org/10.1051/0004-6361/202450666

Astronomy & Astrophysics

LETTER TO THE EDITOR

Distribution of the number of peaks within a long gamma-ray burst: The full *Fermi*/GBM catalogue

R. Maccary[1,2], M. Maistrello[1,2], C. Guidorzi[1,2,3], M. Sartori[1], L. Amati[2], L. Bazzanini[1,2], M. Bulla[1,3,4], A. E. Camisasca[7], L. Ferro[1,2], F. Frontera[1,2], and A. Tsvetkova[5,2,6]

[1] Department of Physics and Earth Science, University of Ferrara, via Saragat 1, 44122 Ferrara, Italy
e-mail: `mccrnl@unife.it`
[2] INAF – Osservatorio di Astrofisica e Scienza dello Spazio di Bologna, Via Piero Gobetti 101, 40129 Bologna, Italy
[3] INFN – Sezione di Ferrara, via Saragat 1, 44122 Ferrara, Italy
[4] INAF, Osservatorio Astronomico d'Abruzzo, via Mentore Maggini snc, 64100 Teramo, Italy
[5] Department of Physics, University of Cagliari, SP Monserrato-Sestu, km 0.7, 09042 Monserrato, Italy
[6] Ioffe Institute, Politekhnicheskaya 26, 194021 St. Petersburg, Russia
[7] Astronomical Observatory of the Autonomous Region of the Aosta Valley (OAVdA), Loc. Lignan 39, 11020 Nus (Aosta Valley), Italy

Received 9 May 2024 / Accepted 3 July 2024

ABSTRACT

Context. The dissipation process responsible for the long gamma-ray burst (GRB) prompt emission and the kind of dynamics that drives the release of energy as a function of time are still key open issues. We recently found that the distribution of the number of peaks per GRB is described by a mixture of two exponentials, suggesting the existence of two behaviours that turn up as peak-rich and peak-poor time profiles.

Aims. Our aims are to study the distribution of the number of peaks per GRB of the entire catalogue of about 3000 GRBs observed by the *Fermi* Gamma-ray Burst Monitor (GBM) and to make a comparison with previous results obtained from other catalogues.

Methods. We identified GRB peaks using the MEPSA code and modelled the resulting distribution following the same procedure that was adopted in the previous analogous investigation.

Results. We confirm that only a mixture of two exponentials can model the distribution satisfactorily, with model parameters that fully agree with those found from previous analyses. In particular, we confirm that (21 ± 4)% of the observed GRBs are peak-rich (8 ± 1 peaks per GRB on average), while the remaining 80% are peak-poor (2.12 ± 0.10 peaks per GRB on average).

Conclusions. We confirm the existence of two different components, peak-poor and peak-rich GRBs, that make up the observed GRB populations. Together with previous analogous results from other GRB catalogues, these results provide compelling evidence that GRB prompt emission is governed by two distinct regimes.

Key words. methods: statistical – gamma-ray burst: general

1. Introduction

Long-lasting gamma-ray bursts (GRBs) are thought to be produced by the collapse of the core of some hydrogen-stripped massive stars, in which a relativistic jet is launched by the newborn compact object, either a neutron star (NS) or a black hole (BH), and makes it to the stellar photosphere (Woosley 1993; Paczyński 1998; MacFadyen & Woosley 1999; Yoon & Langer 2005). Today, almost 30 years since the first discoveries of the long-lasting multiwavelength counterpart (from gamma rays, X-rays, and optical light to radio waves) following the initial gamma-ray emission (so-called afterglow), the wealth of knowledge of the GRB phenomenon, such as the energetics, the jet structure, its Lorentz factor, the density of surrounding environment, and the properties of the progenitor stars has grown remarkably (see e.g. van Eerten 2018; Salafia & Ghirlanda 2022; Levan et al. 2016 for reviews). However, the kind of mechanism and energy reservoir powering the GRB prompt emission, the nature of the dissipation process into gamma-rays, and the distance from the progenitor star at which it takes place, remain highly debated and hot topics (see Pe'er 2015; Zhang 2018 for reviews).

Even inexperienced eyes are caught by the variety of prompt emission light curves (LCs), which range from simple and smooth single pulses all the way up to very complex spiky profiles including many peaks and occasionally quiescent times in between, during which the signal can temporarily drop below instrumental sensitivity. Ever since, attempts to interpret the variability and apparent lack of systematic temporal evolution of the most variable LCs have resulted in mechanisms based on internal dissipation of some kind of energy (either kinetic or magnetic) into gamma-rays through shocks within a wind of relativistic shells (see e.g. Kumar & Zhang 2015 for a review). However, the rich wealth of information hidden in the observed complexity of GRB LCs remains mostly unintelligible. In particular, an open question is whether this variety could be the result of a common stochastic process. If positive, a precise characterisation of this process would reveal how GRB inner engines work, shedding light on the nature of the powering mechanism and on the nature of the engines themselves. Under this assumption, a way to gain clues is by studying the distributions of a number of properties, such as the duration, energy, and luminosity of individual peaks that make up GRB LCs, as well as their waiting times. Possible evidence for self-organised criticality was found and discussed in analogy with other astrophysical transient sources, such as solar flares or magnetar bursts, which might also be ruled by similar kinds of instabilities (Wang & Dai 2013; Lyu et al. 2020; Li et al. 2023; Li & Yang 2023; Maccary et al. 2024).

The distribution of the number of peaks within long GRB LCs has been studied and modelled in detail for the first time only recently (Guidorzi et al. 2024, hereafter G24). This distribution was studied in four different experiments: the Burst And Transient Source Experiment (BATSE; Paciesas et al. 1999), on board the Compton Gamma-Ray Observatory; the Burst Alert Telescope (BAT; Barthelmy et al. 2005) on board the *Neil Gehrels Swift* Observatory; the *Beppo*SAX Gamma-Ray Burst Monitor (GRBM; Frontera et al. 1997); and the Insight-HXMT High Energy instrument (HE; Liu et al. 2020). The result, which emerged from the analysis of these four independent catalogues, is that the distribution of the number of peaks is modelled by a mixture of two exponentials (M2E). The two components are characterised by two different average numbers of peaks per GRB: 2.1 ± 0.1 and 8.3 ± 1.0, nicknamed 'peak-poor' and 'peak-rich', respectively. The result was unexpected, given also the diversity of the four experiments in terms of energy passbands and effective areas. The existence of two distinct components was interpreted as evidence of two correspondingly different dynamical regimes, through which long GRB inner engines work.

In their work, G24 could not extend the same analysis to the entire GRB catalogue of the *Fermi* Gamma-ray Burst Monitor (GBM; Meegan et al. 2009), but reported an analogous preliminary result obtained over a sample of nearly 400 GRBs. In the present work we report the same kind of analysis applied to the full GRB catalogue of GBM currently available. The importance of this additional investigation cannot be overstated: not only does it represent a further test on independent data, but it is also statistically very sensitive, given that the GBM data set outnumbers the data sets previously analysed by G24. In addition, since GBM and BAT share the largest number of GRBs, it is possible to further explore to what extent the number of peaks of any given GRB depends on the detector.

The paper is organised as follows. Section 2 describes the data sample and reduction. Section 3 presents the results of the statistical analysis, whose discussion and conclusions are reported in Sect. 4.

2. Data analysis

2.1. Data set

The GBM is composed of 12 NaI scintillators sensitive in the 8–1000 keV energy range and of two BGO scintillators, sensitive to the high energy tail of a typical GRB spectrum (150 keV–30 MeV), overlapping with NaI detectors at low energies. We started from 3091 long GRBs detected by GBM from 14 July 2008 to 4 February 2024. We excluded short GRBs by discarding those with $T_{90} < 2$ s, where T_{90} is the time interval encompassing from 5% to 95% of the total fluence, as well as those with clear evidence of a compact merger origin, such as 211121A and 230307A[1] (Levan et al. 2023; Troja et al. 2022; Gompertz et al. 2023; Levan et al. 2024). Very bright GRBs that saturated the GBM detectors, such as 130427A and 221009A (Preece et al. 2014; Burns et al. 2023), were also left out. From the remaining GRBs, 154 have a known (spectroscopic) redshift, and 410 are in common with BAT.

Gamma-ray bursts affected by the simultaneous occurrence of a solar flare were discarded. Solar flares were identified by observing the relative intensity between the flare and the GRB on different units and on different energy ranges, taking into account the direction of the Sun. Being spectrally softer than GRBs, most solar flares are barely visible above 40 keV.

We finally rejected all the GRBs whose LC was lacking data points within the T_{90} interval. Eventually, we ended up with 2971 GRBs, which is hereafter referred to as the GRB sample used for the analysis.

2.2. Background subtraction

Gamma-ray burst LCs were extracted in the full NaI energy range (8−1000 keV), using a 64 ms bin time. We subtracted the background using the GBM data tools[2] (Goldstein et al. 2022) following standard prescriptions: we selected one time window preceding the burst and another one following, both having comparable or longer duration than that of the interval containing the burst[3], and interpolated the background with a polynomial function of order up to 3. For each GRB we looked into the 'scat detector mask' entry on the HEASARC catalogue[4] to identify the detectors used by the GBM team. We used the TTE (Time Tagged Event) data whenever they covered the whole GRB, from the start of its T_{90} interval to the end.

We removed the spikes caused by charged particles hitting the detectors as follows: all the bins whose counts exceeded the neighbouring counts by $\geq 9\sigma$ were tagged as spike candidates. Once visual inspection of different GBM units confirmed the particle, and thus the spurious nature of a given spike candidate, its counts were replaced with the mean of the neighbouring bins.

The quality of the background subtraction was assessed by computing mean and standard deviation of the normalised residuals[5] of the time windows used for background interpolation. In particular, we made sure that the background-subtracted counts satisfied the uncorrelated Gaussian noise assumption required by MEPSA (Guidorzi 2015; see Sect. 2.3) first by carrying out a normality test on the normalised residuals (Kolmogorov-Smirnov), to ensure that the noise was Gaussian, and then by examining the autocorrelation function (ACF) of the normalised residuals and by carrying out a runs test, to ensure they were uncorrelated.

---

[1] 191019A should also appear in this list, but it was not seen by the GBM.

[2] https://fermi.gsfc.nasa.gov/ssc/data/analysis/gbm/gbm_data_tools/gdt-docs/

[3] This requirement ensures that all the harmonics that significantly contribute to the background in the burst interval can be adequately modelled in the selected adjacent windows.

[4] https://heasarc.gsfc.nasa.gov/db-perl/W3Browse/w3table.pl?tablehead=name%3Dfermigbrst&Action=More+Options

[5] They are defined as the difference between counts and model, divided by the corresponding uncertainty (see Maccary et al. 2024).

2.3. Identification of peaks

In line with G24, all the 64 ms background-subtracted LCs were sifted with MEPSA, a well-calibrated code tailored to identify statistically significant GRB peaks in uniformly sampled time series affected by Gaussian uncorrelated noise. We discarded peaks with signal-to-noise ratio $S/N < 5$. We ended up with 9625 peaks from 2954 GRBs having at least one significant peak. In parallel, we repeated the same selection by imposing two further thresholds on S/N: 8822 peaks from 2790 GRBs for $S/N > 7$; 7371 from 2388 GRBs for $S/N > 9$.

3. Results

3.1. Fermi-GBM sample

We computed the distribution of the number of peaks per GRB, following the procedure by G24, and tested the various models considered therein (simple exponential, simple and broken power law, and stretched exponential). As did G24, we found that the data can only be satisfactorily fitted by a M2E model given by

$$f(n) = k\,(e^{-n/n_1} + \xi\, e^{-n/n_2})\,, \tag{1}$$

where k is a normalisation constant, n_i is the characteristic number of peaks per GRB of the ith component ($i = 1, 2$), and ξ is a relative normalisation parameter. The expected number of peaks per GRB of the ith component is given by

$$\langle n^{(i)}\rangle = \frac{\sum_{n=1}^{+\infty} n e^{-n/n_i}}{\sum_{n=1}^{+\infty} e^{-n/n_i}} = \frac{1}{1 - e^{-1/n_i}}\,, \tag{2}$$

and the fraction of GRBs contributing to the second component is given by

$$\bar{w}_2 = k\,\xi \sum_{n=1}^{+\infty} e^{-n/n_2}\,. \tag{3}$$

The observed distribution along with the best fit model are shown in Fig. 1, while Table 1 reports the best fit values of the model parameters and the corresponding p-value of the χ^2 test.

The M2E model fits the data very well (e.g. p-value of the two-tail χ^2 test of 0.80), while other models were unable to describe it (e.g. a fit with a stretched exponential yielded a p-value of 0.0026), thus confirming the previous results. The mean number of peaks for the peak-poor and for the peak-rich component is $\langle n^{(1)}\rangle = 2.10^{+0.10}_{-0.10}$ and $\langle n^{(2)}\rangle = 7.61^{+0.97}_{-0.84}$, respectively. The fraction of peak-rich GRBs is $\bar{w}_2 = 0.21^{+0.04}_{-0.04}$.

3.2. Swift-BAT/Fermi-GBM common sample

Fermi/GBM shares 410 GRBs with *Swift*/BAT, 361 of which were covered by BAT in burst mode. As G24 did for the common sample between CGRO/BATSE and *Beppo*SAX/GRBM, here we used the BAT-GBM common sample to study how the number of peaks of any given GRB depends on the detector; the ultimate goal was to test the robustness of our result.

Following G24, we considered the difference $\Delta n = n_{\rm GBM} - n_{\rm BAT}$ between the number of peaks detected by GBM and that of BAT for each common GRB. We replicated the same analysis assuming the three different thresholds on S/N: $S/N > 5$; $S/N > 7$; and $S/N > 9$. Figure 2 shows the distributions of Δn for the three different thresholds on S/N. The median value of Δn is zero for all S/N thresholds. The interval $|\Delta n| \leq 2$ collects from 85 to 88% of the complete common samples, whereas from 92 to 94% common GRBs have $|\Delta n| \leq 3$. These values prove that both experiments are equivalently sensitive to the number of peaks, in spite of their different energy passbands. As noted by G24, Δn for most GRBs is significantly smaller than the difference between the mean values of peak-rich and peak-poor GRBs, $\langle n^{(2)}\rangle - \langle n^{(1)}\rangle = 5.5^{+0.9}_{-0.7}$ (90% confidence), which makes the identification of the two families of long GRBs robust and essentially detector-independent.

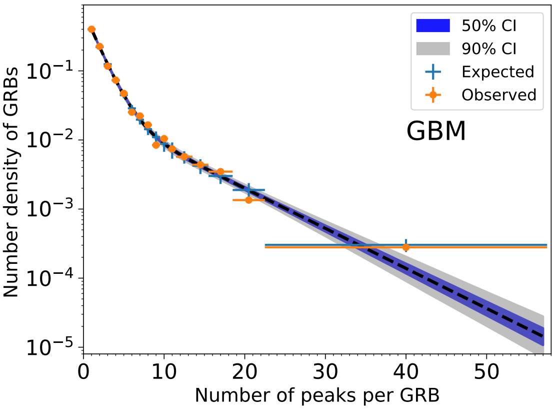

Fig. 1. Distribution of the number of peaks per GRB for the *Fermi*/GBM catalogue. The observed and expected counts are displayed in orange and blue, respectively. The histogram bins were grouped to ensure a minimum number of 15 expected counts per bin. The dashed black line shows the best-fitting model of mixture of two exponentials. The blue and grey regions respectively show the 50% and 90% model confidence interval obtained from sampling the posterior distribution of the model parameters computed through Markov chain Monte Carlo simulations.

3.3. Combined sample

We merged the results of the five catalogues and treated them as if they were a single result. The GBM result reported in the present work, is clearly dominant as its 2954 GRBs outnumber those from the other catalogues (which included 1457, 1277, 820, and 202 GRBs). We obtained an acceptable fit (p-value of 0.06) with the same but more accurate value for the fraction of peak-rich GRBs: $\bar{w}_2$ (all) $= 0.20^{+0.02}_{-0.02}$, and similar values for the mean number of peaks for the peak-poor and peak-rich component $\langle n^{(1)}\rangle = 2.25^{+0.08}_{-0.07}$ and $\langle n^{(2)}\rangle = 9.08^{+0.72}_{-0.66}$, respectively.

3.4. Impact of selection effects and the Malmquist bias

The number of peaks per GRB clearly depends on the S/N of each peak. As such, the selection of GRBs with suitable peaks as well as their classification of peak-poor versus peak-rich depends on S/N, too. Any given GRB that would have been observed at higher-than-actual redshift, could have been either tagged with fewer peaks or missed altogether. Consequently, our results are potentially affected by a significant Malmquist bias. As we also did in G24, repeating the analysis for a range of different S/N thresholds, and thus mimicking the effect of moving given GRBs further away, our aim was to explore the robustness of our results against any distance-related bias. Two interesting facts emerge from this analysis:

1. The fraction $\bar{w}_2$ of peak-rich GRBs essentially remains constant for all catalogues and for the different S/N thresholds,

Table 1. Results obtained from our analysis of the *Fermi*/GBM sample.

S/N Threshold	N	N_p	k	n_1	$\langle n^{(1)} \rangle$	n_2	$\langle n^{(2)} \rangle$	ξ	$\bar{w}_2$	χ^2 test p-value
5	2954	9625	$0.71^{+0.05}_{-0.05}$	$1.55^{+0.11}_{-0.11}$	$2.10^{+0.11}_{-0.11}$	$7.07^{+0.99}_{-0.82}$	$7.61^{+0.97}_{-0.84}$	$0.04^{+0.01}_{-0.01}$	$0.21^{+0.04}_{-0.04}$	0.80
7	2790	8822	$0.82^{+0.06}_{-0.06}$	$1.39^{+0.11}_{-0.10}$	$1.95^{+0.10}_{-0.10}$	$6.78^{+0.93}_{-0.77}$	$7.53^{+0.90}_{-0.77}$	$0.04^{+0.01}_{-0.01}$	$0.23^{+0.04}_{-0.04}$	0.78
9	2388	7371	$0.93^{+0.08}_{-0.08}$	$1.26^{+0.10}_{-0.10}$	$1.83^{+0.10}_{-0.10}$	$6.70^{+0.93}_{-0.75}$	$7.23^{+0.90}_{-0.77}$	$0.039^{+0.012}_{-0.010}$	$0.23^{+0.04}_{-0.04}$	0.43

Notes. Best-fit values and 90% confidence intervals of the parameters of the model of the mixture of two exponentials applied to the *Fermi*/GBM data set. All these parameters are defined in Sect. 3.

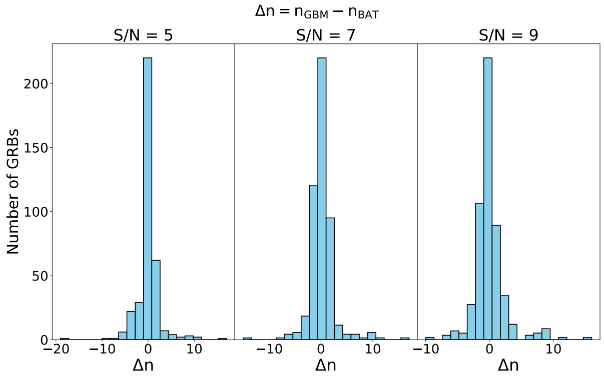

Fig. 2. Distribution of Δn for three different thresholds on S/N: 5, 7, and 9.

and therefore appears to be a robust property that is least affected by anything that depends on peak brightness. In the following, we delve further into this aspect, which seems to clash with the Malmquist bias;

2. The average number of peaks per GRB changes only slightly for different thresholds on S/N: from 2.1 ($S/N > 5$) to 1.8 ($S/N > 9$) for the peak-poor class, and, correspondingly, from 7.6 to 7.2 for the peak-rich class (Table 1). This is understood by the following argument: not only does the number of peaks decrease by increasing the threshold on S/N of any given GRB (mimicking the consequence of moving it to higher redshifts), but the number of GRBs featuring at least one significant peak also decreases. As a result, the average number of peaks per surviving GRB decreases less abruptly than the overall number of peaks.

In principle, a direct way to understand the impact of the Malmquist bias is by focusing on a sample of GRBs with measured redshift. Unfortunately, this sample is currently too small to make a statistically sound analysis feasible. Nonetheless, we explored in more detail the reasons for the first consideration above as follows. We addressed two questions: By moving a peak-rich GRB to progressively higher redshifts, we wanted to know (a) at what relative distance it becomes peak-poor, thus contributing to altering the true distribution, and (b) at what relative distance the GRB disappears, an event coinciding with the brightest peak sinking below threshold?

The answer to (b) depends on the intensity of the brightest peak, while we assume that the answer to (a) depends on the intensities of the third or fourth brightest peaks, once we take three or four as a reasonable proxy of the number of peaks for discriminating between peak-poor and peak-rich GRBs.

For each of the peak-rich GRBs with at least 6 $S/N > 5$ peaks, we took the four brightest ones. We ended up with 399 GRBs. For each GRB we calculated the three following ratios: $r_{21} \geq r_{31} \geq r_{41}$, respectively corresponding to the ratio of the intensities of the second, of the third, and of the fourth brightest peaks to the intensity of the brightest peak.

As a result, on average it is $r_{41} \sim 2/3$, with 0.56–0.77 as interquartile, so the range of intensities of the four brightest peaks is relatively narrow. Specifically, from the disappearing of the fourth peak to the disappearing of the brightest peak, the threshold on S/N increases only by ~50% on average. Translating the relative change of the S/N threshold in terms of the relative change in the maximum volume within which a given peak can be detected, the volume increases by a factor of $(2/3)^{-3/2} \approx 1.8$, so 80% (we used the scaling $V \propto p^{-3/2}$ of volume V on peak flux p). This is a relatively short range compared with the range of redshifts spanned by the GRB populations that make up the observed catalogues and the GBM catalogue in particular. Replacing the fourth with the third brightest peak, the relative volume change shrinks to 60%, so the previous conclusion holds true a fortiori. This property of most peak-rich GRBs may explain why the Malmquist bias does not strongly affect the result of a constant peak-rich fraction throughout the different catalogues and GRB populations.

4. Discussion and conclusions

Guidorzi et al. (2024) modelled for the first time the distribution of the number of peaks in long GRB LCs through the analysis of four independent catalogues (CGRO/BATSE, *Swift*/BAT, *Beppo*SAX/GRBM, and Insight-HXMT/HE), which differ from each other in terms of energy passbands and effective areas. Only a mixture of two exponentials was found to model all four distributions, supporting the existence of two families, called peak-poor and peak-rich, characterised by an average number of peaks per GRB of around 2.1 ± 0.1 and 8.3 ± 1.0, respectively. It was also found that peak-poor GRBs make up about 80% of the GRB populations observed by past and present experiments.

In the present work we carried out the analogous investigation over the *Fermi*/GBM GRB catalogue, which currently includes about 3000 GRBs and therefore offers a further opportunity to test the previous results with a high degree of statistical accuracy. Remarkably, not only did we confirm that the distribution can only be modelled by a mixture of two exponentials, but we also found that the best-fitting parameter values are fully consistent with what was found by G24 from different and independent data sets. Specifically, the expected numbers of peaks for the two families of peak-poor and of peak-rich GRBs are remarkably similar to the G24 results. Analogously, the fraction of peak-rich GRBs is found to be 0.21 ± 0.04, fully consistent with what was found by G24. Although they were ignored in the present analysis, long-merger candidates would belong to the hard tail of the peak-rich family: 211211A has 48 peaks and

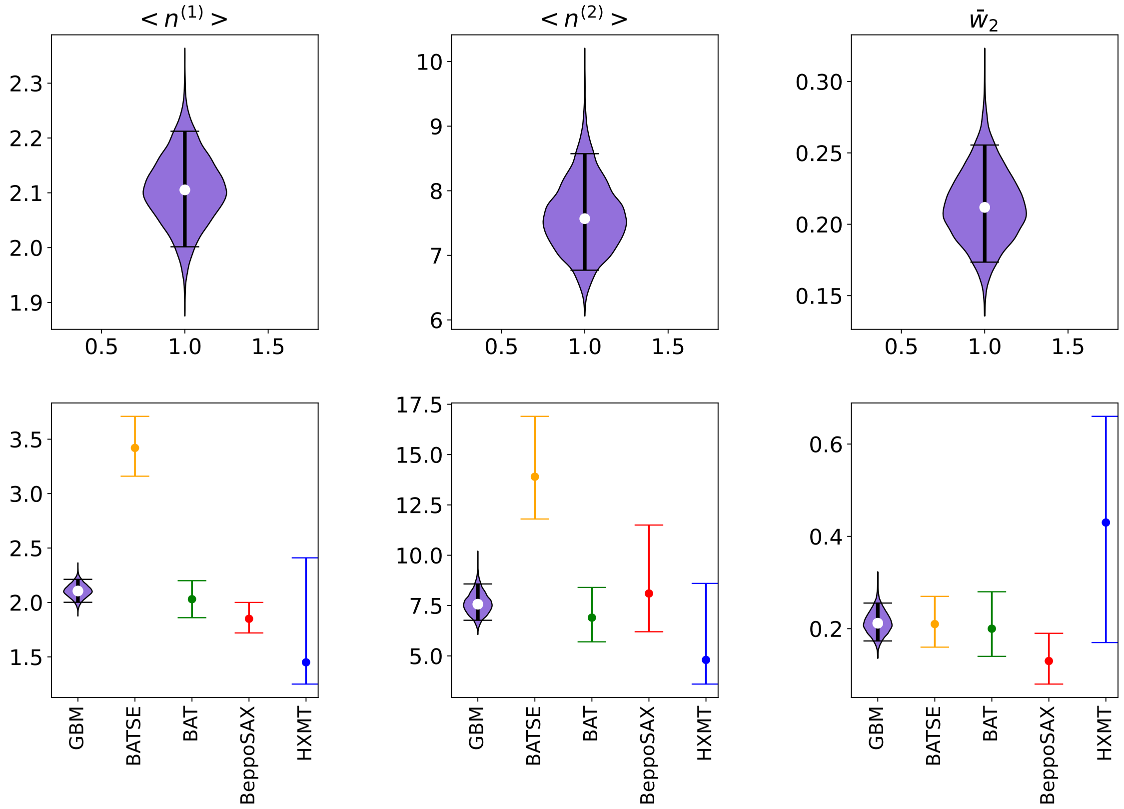

Fig. 3. This figure describes our present results compared with those of G24. *Top panels, left to right*: violin plots of the posterior distributions of the three parameters $\langle n^{(1)}\rangle$, $\langle n^{(2)}\rangle$, and $\bar{w}_2$, respectively representing the expected number of peaks per GRB of the peak-poor and the peak-rich classes, and the fraction of peak-rich GRBs obtained for the GBM sample. The horizontal bars span 5–95% quantiles. *Bottom panels, left to right:* comparison between the results obtained for the same parameters in this work, with those obtained by G24 from other catalogues.

230307A has 53 peaks. Should peak richness be confirmed in future analogous events, it would provide a clue to the way the inner engines of these mergers work.

Figure 3 shows a visual comparison between the GBM results reported here and the results obtained by G24. Interestingly, while the fraction of peak-poor GRBs is basically the same for all the five catalogues, the average numbers of peaks per each GRB for both families of the only BATSE is somewhat higher. As discussed in G24, this is ascribed to the larger effective area of BATSE compared with the other instruments, including GBM.

In conclusion, we confirmed that the existence of these two families is a robust result that is not sensitive to the experiments and their energy passbands. As discussed by G24, these two different dynamics ruling long GRB prompt emission might point to either two different families of engines left over by the collapse of the core, either a NS or a BH, or two different regimes in which GRB engines release their energy. As noted in G24, the distinctive property of peak-rich GRBs is the presence of sub-second variability that adds to the slow-varying component, which is instead observed in both kinds of GRBs.

The existence of two distinct dynamics in the observed population of GRBs can be interpreted within different models of how dissipation into gamma-rays takes place (see G24 for a detailed discussion). Consequently, it does not directly help to discriminate between different interpretations. Nevertheless, it provides a solid clue to how GRB engines work, with the possibility that they could operate close to a critical regime. In this way, a completely different dynamical behaviour can result from a small difference in some key properties, such as the degree of magnetisation of the relativistic ejecta, as discussed in G24. Should the peak richness of GRBs be found preferentially associated with other key properties in future investigations, the implications would help to narrow down the identity of GRB engines and the nature of the dissipation process that governs the prompt emission.

Acknowledgements. We thank the anonymous reviewer for providing insightful comments that improved the manuscript. R.M. and M.M. acknowledge the University of Ferrara for the financial support of their PhD scholarships. R.M. acknowledges the *Fermi* team for covering flight costs for attending the *Fermi* summer school 2023. A.T. acknowledges financial support from ASI-INAF Accordo Attuativo HERMES Pathfinder operazioni n. 2022-25-HH.0 and the basic funding program of the Ioffe Institute FFUG-2024-0002. L.A. acknowledges support from INAF Mini-grant programme 2022. A.C. is partially supported by the 2023/24 "Research and Education" grant from Fondazione CRT. The OAVdA is managed by the Fondazione Clément Fillietroz-ONLUS, which is supported by the Regional Governement of the Aosta Valley, the Town Municipality of Nus and the "Unité des Communes valdotaines Mont-Emilius". L.F. acknowledges support from the AHEAD-2020 Project grant agreement 871158 of the European Union's Horizon 2020 Program.

References

Barthelmy, S. D., Barbier, L. M., Cummings, J. R., et al. 2005, Space Sci. Rev., 120, 143
Burns, E., Svinkin, D., Fenimore, E., et al. 2023, ApJ, 946, L31
Frontera, F., Costa, E., dal Fiume, D., et al. 1997, A&AS, 122, 357

Goldstein, A., Cleveland, W. H., & Kocevski, D. 2022, Fermi GBM Data Tools: v1.1.1

Gompertz, B. P., Ravasio, M. E., Nicholl, M., et al. 2023, Nat. Astron., 7, 67

Guidorzi, C. 2015, Astron. Comput., 10, 54

Guidorzi, C., Sartori, M., Maccary, R., et al. 2024, A&A, 685, A34

Kumar, P., & Zhang, B. 2015, Phys. Rep., 561, 1

Levan, A., Crowther, P., de Grijs, R., et al. 2016, Space Sci. Rev., 202, 33

Levan, A. J., Malesani, D. B., Gompertz, B. P., et al. 2023, Nat. Astron., 7, 976

Levan, A. J., Gompertz, B. P., Salafia, O. S., et al. 2024, Nature, 626, 737

Li, X.-J., & Yang, Y.-P. 2023, ApJ, 955, L34

Li, X.-J., Zhang, W.-L., Yi, S.-X., Yang, Y.-P., & Li, J.-L. 2023, ApJS, 265, 56

Liu, C. Z., Zhang, Y. F., Li, X. F., et al. 2020, Sci. China-Phys. Mech. Astron., 63, 249503

Lyu, F., Li, Y.-P., Hou, S.-J., et al. 2020, Front. Phys., 16, 14501

Maccary, R., Guidorzi, C., Amati, L., et al. 2024, ApJ, 965, 72

MacFadyen, A. I., & Woosley, S. E. 1999, ApJ, 524, 262

Meegan, C., Lichti, G., Bhat, P. N., et al. 2009, ApJ, 702, 791

Paciesas, W. S., Meegan, C. A., Pendleton, G. N., et al. 1999, ApJS, 122, 465

Paczyński, B. 1998, ApJ, 494, L45

Pe'er, A. 2015, Adv. Astron., 2015, 22

Preece, R., Burgess, J. M., von Kienlin, A., et al. 2014, Science, 343, 51

Salafia, O. S., & Ghirlanda, G. 2022, Galaxies, 10

Troja, E., Fryer, C. L., O'Connor, B., et al. 2022, Nature, 612, 228

van Eerten, H. 2018, Int. J. Mod. Phys. D, 27, 1842002

Wang, F. Y., & Dai, Z. G. 2013, Nat. Phys., 9, 465

Woosley, S. E. 1993, ApJ, 405, 273

Yoon, S. C., & Langer, N. 2005, A&A, 443, 643

Zhang, B. 2018, The Physics of Gamma-Ray Bursts (Cambridge Univeristy Press)

A.9 PAPER III: GAMMA-RAY BURST MINIMUM VARIABILITY TIMESCALES WITH FERMI/GBM

A&A, 702, A95 (2025)
https://doi.org/10.1051/0004-6361/202555418

Astronomy & Astrophysics

Gamma-ray burst minimum variability timescales with *Fermi*/GBM

R. Maccary[1,2,⋆], C. Guidorzi[1,2,3], A. E. Camisasca[8,1], M. Maistrello[1,2], S.Kobayashi[7], L. Amati[2], L. Bazzanini[1,2], M. Bulla[1,3,4], L. Ferro [1,2], F. Frontera[1,2], and A. Tsvetkova[5,6]

[1] Department of Physics and Earth Science, University of Ferrara, Via Saragat 1, I–44122, Ferrara, Italy
[2] INAF – Osservatorio di Astrofisica e Scienza dello Spazio di Bologna, Via Piero Gobetti 101, I-40129 Bologna, Italy
[3] INFN – Sezione di Ferrara, Via Saragat 1, I–44122, Ferrara, Italy
[4] INAF, Osservatorio Astronomico d'Abruzzo, Via Mentore Maggini snc, 64100 Teramo, Italy
[5] Department of Physics, University of Cagliari, SP Monserrato-Sestu, km 0.7, 09042 Monserrato, Italy
[6] Ioffe Institute, Politekhnicheskaya 26, 194021 St. Petersburg, Russia
[7] Astrophysics Research Institute, Liverpool John Moores University, Liverpool Science Park IC2, 146 Brownlow Hill, Liverpool L3 5RF, UK
[8] Alma Mater Studiorum, Università di Bologna, Dipartimento di Fisica e Astronomia (DIFA), Via Gobetti 93/2, 40129 Bologna, Italy

Received 7 May 2025 / Accepted 10 August 2025

ABSTRACT

Context. Gamma-ray bursts (GRBs) have traditionally been classified by duration as long (LGRBs) or short (SGRBs), with the former believed to originate from massive star collapses and the latter from compact binary mergers. However, events such as the SGRB 200826A (coming from a collapsar) and the LGRBs 211211A and 230307A (associated with a merger) suggest that duration-based classification could sometimes be misleading. Recently, the minimum variability timescale (MVT) has emerged as a key metric for classifying GRBs.

Aims. We calculated the MVT, defined as the full width at half maximum (FWHM) of the narrowest pulse in the light curve, using an independent dataset from *Fermi*/GBM, and we compared our results with other MVT definitions. We updated the MVT-T_{90} plane and analysed peculiar events such as long-duration merger candidates 211211A, 230307A, and other short GRBs with extended emission (SEE-GRBs). We also examined extragalactic magnetar giant flares (MGFs) and explored possible new correlations with peak energy.

Methods. We used the MEPSA algorithm to identify the shortest pulse in each GRB light curve and measured its FWHM. We calculated the MVT for around 3700 GRBs, 177 of which have spectroscopically known redshift.

Results. The SEE-GRBs and SGRBs share similar MVTs (from a few tens of to a few hundred milliseconds, indicating a common progenitor, while extragalactic MGFs exhibit even shorter values (from a few milliseconds to a few tens of milliseconds). Our MVT estimation method consistently yields higher values than another existing technique, the latter aligning with the pulse rise time. For LGRBs, we confirm the correlations of MVT with peak luminosity and Lorentz factor.

Conclusions. We confirm that although MVT alone cannot determine the GRB progenitor, it is a valuable tool when combined with other indicators, as it helps flag long-duration mergers and distinguish MGFs from typical SGRBs.

Key words. methods: statistical – gamma-ray burst: general

1. Introduction

Gamma-ray bursts (GRBs) are brief yet extremely intense flashes of gamma rays produced at cosmological distances. They are thought to arise from at least two types of catastrophic events: (i) the core-collapse of certain types of massive star, known as collapsars (Woosley 1993; Paczyński 1998; MacFadyen & Woosley 1999; Yoon & Langer 2005) – typically occurring at the centre of star-forming galaxies (Fruchter et al. 2006) and associated with Type Ic-BL supernovae (Galama et al. 1998; Hjorth et al. 2003), and (ii) binary compact object mergers (Blinnikov et al. 1984; Paczynski 1986; Eichler et al. 1989; Paczynski 1991; Narayan et al. 1992; Abbott et al. 2017). The central engine, which powers an ultra-relativistic jet, could be either a stellar-mass black hole surrounded by a hyper-accreting thick accretion disc (Popham et al. 1999; Di Matteo et al. 2002; Janiuk et al. 2007; Lei et al. 2013) or a strongly magnetised, rapidly spinning neutron star, also known as a magnetar (Usov 1992; Wheeler et al. 2000; Thompson et al. 2004; Metzger et al. 2011). Despite much progress, the exact nature of the central engine(s), the mechanism(s) by which the relativistic jet is launched, the jet composition, and the radiation process(es) responsible for the gamma-ray emission remain unresolved questions.

Initially, GRBs were classified by their duration, with long GRBs (LGRBs) typically linked to collapsars and short GRBs (SGRBs) to mergers. However, a class of events known as SGRBs with extended emission (SEE-GRBs) and presenting a short, hard spike followed by a longer softer emission (sometimes lasting tens of seconds) challenged this simple classification (Norris & Bonnell 2006). For instance, events such as 060614 (Gehrels et al. 2006; Della Valle et al. 2006; Fynbo et al. 2006; Jin et al. 2015; Yang et al. 2015), which exhibited zero spectral lag and no evidence of a supernova despite occurring at low redshift, raised doubts about the reliability of using duration alone to infer the kind of progenitor. In many cases, the

---

[⋆] Corresponding author: `mccrnl@unife.it` host galaxy remains undetected, and redshift measurements are unavailable, making it difficult to determine the progenitor type. Recent cases, such as 211211A ($T_{90} \simeq 34$ s; Rastinejad et al. 2022; Gompertz et al. 2023; Yang et al. 2022; Troja et al. 2022; Xiao et al. 2022) and 230307A ($T_{90} \simeq 35$ s; Dalessi et al. 2023; Xiong et al. 2023; Du et al. 2024; Dai et al. 2024; Levan et al. 2024; Yang et al. 2024) were followed by a kilonova (KN), which provided compelling evidence that even mergers can produce long-duration GRBs, further emphasising the need for a new classification system. Given the growing complexity, families (i) and (ii) are now frequently described as merger GRBs and collapsar GRBs or, alternatively, as Type-I and Type-II GRBs, respectively (Zhang 2006).

Among fast, high-energy transient events, there is another category known as magnetar giant flares (MGFs), which is sometimes mistaken for typical SGRBs. These events, produced by galactic or extragalactic magnetars, are characterised by a shorter rise time and duration, a harder peak energy, and a lower equivalent-isotropic energy, $E_{\rm iso} \approx 10^{44-46}$ erg, compared to cosmological SGRBs. When occurring within the Milky Way, they exhibit a long decaying tail modulated by the neutron star rotation period (Mazets et al. 1979; Feroci et al. 1999; Hurley et al. 1999, 2005), which is below instrumental sensitivity when they happen in nearby galaxies (Ofek et al. 2006; Mazets et al. 2008; Burns et al. 2021; Svinkin et al. 2021; Roberts et al. 2021; Fermi-Lat Collaboration 2021; Mereghetti et al. 2024; Trigg et al. 2024; Rodi et al. 2025).

Numerous attempts to classify GRBs using different prompt emission properties have been made (Goldstein et al. 2010; Lü et al. 2010, 2014; Tsvetkova et al. 2025). Many efforts have also been made to develop machine-learning (ML) based GRB classification methods (Jespersen et al. 2020; Salmon et al. 2022; Steinhardt et al. 2023; Dimple et al. 2023; Garcia-Cifuentes et al. 2023; Chen et al. 2024; Zhu et al. 2024; Dimple et al. 2024). These methods generally recover the usual properties of the two GRB classes. ML-identified Type I GRBs tend to be shorter and spectrally harder than ML-identified Type II GRBs. However, complex cases – such as GRB 211211A and GRB 230307A – continue to challenge even the most advanced classification algorithms (see e.g. Zhu et al. 2024). This highlights the persistent challenges in GRB classification and the importance of identifying the most relevant parameters for distinguishing GRB progenitors. A promising approach involves the minimum variability timescale (MVT), defined as the shortest timescale over which the signal shows uncorrelated temporal variability. Several methods have been proposed to calculate the MVT, such as temporal deconvolution into pulses (Norris et al. 1996, 2005; Bhat et al. 2012) and wavelet decomposition (MacLachlan et al. 2013; Golkhou & Butler 2014; Golkhou et al. 2015; Vianello et al. 2018).

The MVT could be directly linked to the activity of the central engine, as is the case for the internal shock (IS) model (Rees & Meszaros 1994; Kobayashi et al. 1997; Daigne & Mochkovitch 1998), or it may originate locally in the emission region. In the latter case, either relativistic turbulence (Kumar & Narayan 2009) or the emission of Doppler-boosted local emitters (Lyutikov et al. 2003) could determine the MVT. These two pictures are being unified by the Internal Collision-Induced Magnetic Reconnection and Turbulence model (ICMART; Zhang & Yan 2011), according to which longer timescales are linked to the central engine activity, while the shorter ones are attributed to relativistic magnetic turbulence within the emission region.

Camisasca et al. (2023a, hereafter C23) defined the MVT as the full width half maximum (FWHM) of the shortest pulse that is detected with statistical confidence within a GRB light curve (LC). This method builds on the MEPSA algorithm (Guidorzi 2015), which was designed to identify statistically significant peaks in a given GRB LC. This method has the advantage of having a straightforward interpretation. In their study, they explored various possible correlations between the MVT, Lorentz factor, jet opening angle, and peak luminosity.

This method was also applied to the case of 230307A, where an MVT of 28 ms was reported by Camisasca et al. (2023b), suggesting a merger origin, in agreement with the discovery of a KN (Bulla et al. 2023; Levan et al. 2024). This confirms the usefulness of the MVT in identifying long-duration merger candidates. The MVT can also be useful in distinguishing extragalactic MGFs from regular SGRBs.

The combination of MVT and other metrics may help further identify interesting merger candidates. In fact, Guidorzi et al. (2024a) showed that the combination of high variability ($V > 0.1$), relatively low luminosity $L_{\rm iso} < 10^{51}$ erg s^{-1}, and short MVT ($\lesssim 0.1$ s) may be indicative of a compact binary merger origin, in spite of the long duration and misleading temporal profile.

Our goal is to verify the results obtained by C23 using the complementary dataset of the *Fermi* Gamma-ray Burst Monitor (GBM; Meegan et al. 2009). This is an all-sky monitor, and it is sensitive to soft gamma-rays, with 12 sodium iodide (NaI) scintillators working in the range from 8 to 1000 keV and two additional bismuth germanate (BGO) detectors operating from 150 keV to 30 MeV.

On the one hand, it is important to test the results obtained by C23 through an independent dataset. On the other hand, the GBM data in particular allow us to update and extend the analysis to interesting candidates that were detected exclusively with GBM. With over 3000 recorded GRBs, excellent time resolution (<10 µs), and its large energy passband, *Fermi*/GBM is ideally suited to a statistical analysis of GRB MVTs.

We have organized this work as follows: Section 2 describes the GRB sample and the data analysis. Results are reported in Section 3. We discuss the implications and conclude in Section 4. Hereafter, we use the flat-ΛCDM cosmology model with the latest cosmological parameters values $H_0 = 67.66$ km Mpc^{-1} s^{-1} and $\Omega_0 = 0.31$ (Planck Collaboration VI 2020).

2. Data analysis

2.1. Dataset

We started with 3792 GRBs triggered by *Fermi*/GBM from 14 July 2008 to 11 June 2024. We kept 3720 of them, as the others were not entirely covered by time tagged events (TTE) data. Some very bright GRBs, such as 221009A and 130427A, were also removed due to their brightness, which saturated the NaI detectors (Ackermann et al. 2014; Lesage et al. 2023). Among the remaining GRBs, 177 have a measured redshift, with 152 classified as collapsar candidates (or Type-II), 20 as merger candidates (or Type-I), and 5 as SEE-GRBs. Seventeen GRBs of the former class are associated with a supernova (SN). We also have 44 SEE-GRBs, either identified by Kaneko et al. (2015), Lien et al. (2016), Lan et al. (2020) or reported as such by the Gamma-ray Coordinate Network. Additionally, two long-duration merger candidates, 211211A and 230307A, appear in our sample. They are LGRBs, having $T_{90} > 2$ s, and do not necessarily follow the morphology of SEE-GRBs. Table 1 reports the data.

Table 1. First five GRBs of our sample. This table is available in its entirety in machine-readable form (see Section 5).

GRB	Fermi Id	FWHM$_{\rm min}$ [s]	T$_{90}$ [s]	z	N$_{\rm p}$	Type
080714B	bn080714086	$2.429^{+0.848}_{-0.628}$	5.376	–	2	II
080714C	bn080714425	$5.387^{1.880}_{-1.393}$	40.192	–	2	II
080714A	bn080714745	$3.825^{1.335}_{-0.990}$	59.649	–	1	II
080715	bn080715950	$0.172^{0.060}_{-0.045}$	7.872	–	2	II
080717	bn080717543	$7.252^{2.532}_{-1.876}$	36.608	–	1	II

Table 2. Three MGFs in our sample.

GRB	Fermi Id	FWHM$_{\rm min}$ [ms]	T$_{90}$ [s]	d [Mpc]
180128A	bn180128215	$8.12^{+2.80}_{-2.1}$	0.208	3.7
200415A	bn200415367	$2.97^{+1.04}_{-0.77}$	0.144	3.5
231115A	bn231115650	$24.41^{+8.52}_{-6.31}$	0.032	3.5

We also considered three extragalactic MGFs: 200415A (Yang et al. 2020; Roberts et al. 2021; Svinkin et al. 2021; Fermi-Lat Collaboration 2021), 231115A (Mereghetti et al. 2024; Minaev et al. 2024), and 180128A (Trigg et al. 2024). Their data are reported in Table 2.

2.2. Data reduction

We used the TTE data in the 8–1000 keV energy range, with an integration time of 64 ms. Whenever it was required by the procedure described in C23, we also used 1024, 4, and 1 ms. For each burst, we selected the GBM detectors based on the 'bcat detector mask' entry in the HEASARC catalogue[1]. We discarded the GRBs affected by solar flares and those with profiles not entirely contained in the TTE mode of GBM. The background was interpolated and subtracted using the GBM data tools[2] (Goldstein et al. 2022) and following the standard procedures also applied in Maccary et al. (2024).

2.3. Minimum variability timescale computation

We adopted the MVT calculation defined in C23 as the FWHM of the narrowest, statistically significant peak in the LC (denoted hereafter as FWHM$_{\rm min}$). We measured FWHM$_{\rm min}$ following the prescriptions of C23, which build upon MEPSA:

- The MVT is tentatively computed on the 64 ms LC, and the binning scheme is refined down to 4 ms or even 1 ms when needed.
- MEPSA is applied to the corresponding LCs, using a maximum rebin factor of 256.
- Peaks are filtered using S/N thresholds following a scheme ensuring the same false alarm probability through different bin times[3] (see Figure 1 of C23).
- The FWHM of each peak is computed using the calibrated formula established in C23, which depends on MEPSA parameters. Then, the FWHM of the shortest significant peak is defined as FWHM$_{\rm min}$.

We compared the results of this method with a more direct computation of the FWHM of the shortest significant pulse obtained by fitting its time profile with a fast rise exponential decay (FRED) model (see Appendix A for more details). In Appendix B, we present a comparison of the results obtained using *Swift*/BAT and *Fermi*/GBM data. Also, in Appendix C we compare the results of our method with those obtained with the Bayesian blocks (Scargle et al. 2013) algorithm.

Out of 3720 GRBs, we obtained 3350 GRBs with a reliable measure of FWHM$_{\rm min}$. Of these, 2992 of them are LGRBs ($T_{90} > 2$ s), while 358 are SGRBs ($T_{90} < 2$ s). For 29 GRBs, we could only determine an upper limit of FWHM$_{\rm min}$. For 339 GRBs, the S/N was not high enough to enable a reliable measure of FWHM$_{\rm min}$.

3. Results

In the following, we present the results of the MVT measurements for the 3350 GRBs for which FWHM$_{\rm min}$ was successfully determined. We analyse the distribution of MVT of different GRB classes, examine correlations with other burst properties, and compare these findings with models and former studies.

3.1. Comparison between our MVT estimation with other techniques

We compared three possible ways to measure the MVT: (i) the FWHM of the narrowest pulse, denoted as FWHM$_{\rm min}$; (ii) the MVT as computed by Golkhou et al. (2015, hereafter G15) and Veres et al. (2023, hereafter V23) using wavelet decomposition, denoted as $\Delta t_{\rm min}$; and (iii) the detection timescale of the narrowest pulse identified by MEPSA, denoted as $\Delta t_{\rm det}$, which is the time interval over which the detection significance is maximised (see Guidorzi 2015 for details). The FWHM$_{\rm min}$ can be computed either by directly fitting the LC or by using MEPSA along with the procedure described in Sect. 2.3. As demonstrated in Appendix A, the two methods give similar results, with most estimates compatible within uncertainties. Therefore, for the purpose of (i), we only consider the latter approach, as it gives a reliable estimate of the narrowest pulse FWHM.

Figure 1 compares FWHM$_{\rm min}$ and $\Delta t_{\rm min}$. We observed a significant discrepancy between the two, with FWHM$_{\rm min}$ being significantly longer. Interestingly, the $\Delta t_{\rm min}$ values are consistent with the detection timescale values $\Delta t_{\rm det}$ calculated by MEPSA (Figure 2).

According to simulations carried out in Guidorzi (2015) and C23, the brighter the pulse, the smaller the ratio of $\Delta t_{\rm det}$/FWHM. Specifically, C23 came up with a calibrated relation between FWHM$_{\rm min}$ and $\Delta t_{\rm det}$, which they used to estimate the former from the latter while also using other ancillary information yielded by MEPSA and modelling the corresponding uncertainty (see Equation A3 therein).

Our analysis confirms that $\Delta t_{\rm min}$ is more closely related with the detection timescale (Figure 2) and the rise time, t_r (Figure 3), than the FWHM (Figure 1) of the pulse, as also mentioned by G15. Indeed, $\Delta t_{\rm det} \sim \Delta t_{\rm min} \sim t_r$, with median values of 0.6 and 1.1 for $\Delta t_{\rm det}/\Delta t_{\rm min}$ and $\Delta t_{\rm min}/t_r$, respectively. The GRB pulses are typically asymmetric, with a decay-to-rise time ratio of 3–4. As a consequence, the FWHM is comparably longer than the rise time alone and explains why FWHM$_{\rm min}$ is longer than $\Delta t_{\rm min}$ by a comparable factor. This difference between FWHM$_{\rm min}$ and

---

[1] `https://heasarc.gsfc.nasa.gov/db-perl/W3Browse/w3table.pl?tablehead=name%3Dfermigbrst&Action=More+Options`

[2] `https://fermi.gsfc.nasa.gov/ssc/data/analysis/gbm/gbm_data_tools/gdt-docs/`.

[3] S/N ≥ 7, 6.8, 6.4, 6 at 1, 4, 64, 1024 ms.

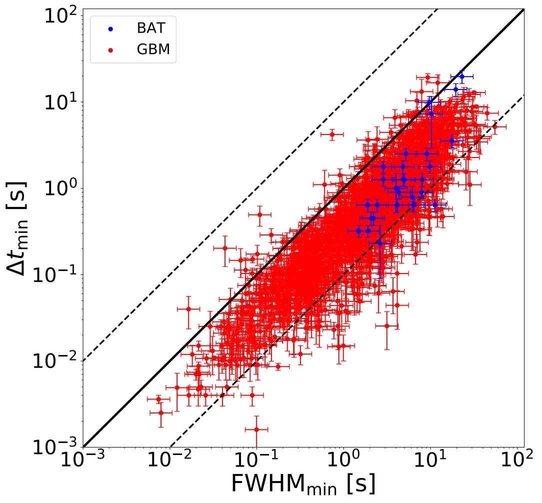

Fig. 1. Plot representing $\Delta t_{\min}$ versus $\mathrm{FWHM}_{\min}$ for the GRBs in common. Red points show GBM data, where $\Delta t_{\min}$ was taken from G15 and V23, while blue points are BAT data, with $\Delta t_{\min}$ being taken from Golkhou & Butler (2014). Equality is shown with a solid line, while dashed lines show ±1 dex.

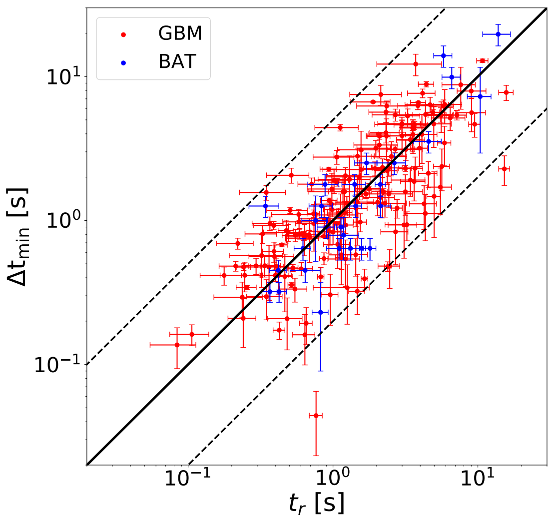

Fig. 3. Plot showing $\Delta t_{\min}$ versus the rise time t_r of the fitted pulse for the samples of GRBs defined in Appendix A. Red points show GBM data, where $\Delta t_{\min}$ was taken from G15 and V23, while blue points are BAT data, with $\Delta t_{\min}$ taken from Golkhou & Butler (2014). The solid and dashed lines have the same meaning as in Figure 1.

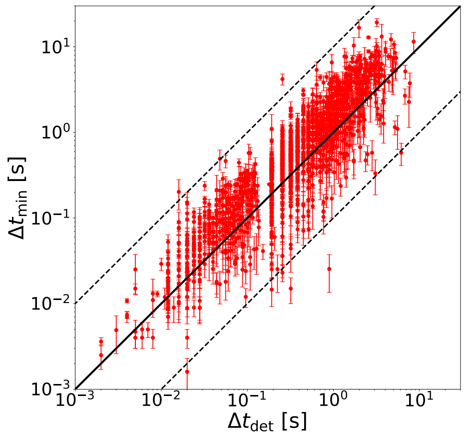

Fig. 2. Plot representing $\Delta t_{\min}$ versus $\Delta t_{\det}$ for the GRBs in common. $\Delta t_{\min}$ is the MVT estimate from G15 and V23 obtained with GBM, while $\Delta t_{\det}$ is the detection timescale found with MEPSA. Solid and dashed lines have the same meaning as in Figure 1.

$\Delta t_{\min}$ is important to bear in mind, especially when it is to be interpreted within a theoretical context.

3.2. $\mathrm{FWHM}_{\min}$–T_{90} plane

Following C23, in Figure 4 we plot $\mathrm{FWHM}_{\min}$ versus T_{90} for the bursts of our sample. We also computed the median value of $\mathrm{FWHM}_{\min}$ for the various GRB classes and applied two-population Kolmogorov-Smirnov (KS) tests to investigate their mutual compatibility. Results are reported in Table 3. Clearly, LGRBs show greater $\mathrm{FWHM}_{\min}$ values, with a median value of 2.4 s, while it is about 0.2 s for the SGRBs. The GRBs with an ascertained SN association have typical $\mathrm{FWHM}_{\min}$ values similar to the bulk of LGRBs, with a median value of about 1.6 s, thus pointing towards a common collapsar origin for the bulk of LGRBs.

Conversely, SEE-GRBs $\mathrm{FWHM}_{\min}$ values (about 0.15 s) are closer to those of SGRBs than LGRBs, supporting a common origin. Our results are consistent with those of Kaneko et al. (2015) and Lan et al. (2020). Among them, 161129A was also noted by Guidorzi et al. (2024a) to have a combination of high variability $V \sim 0.6$, relatively low luminosity ($L_p \sim 2 \times 10^{51}$ erg s^{-1}), and short MVT, which is potentially characteristic of long-duration merger candidates. The initial spike has an MVT of about 20 ms, although it is slightly below the threshold detection of our technique, having $\mathrm{SNR}_{4\mathrm{ms}} = 6.6 < \mathrm{SNR}^{\mathrm{thr}}_{4\mathrm{ms}} = 6.8$ for the 4 ms binned LC.

Long-duration merger candidates, such as 211211A and 230307A, are definite outliers in the LGRB $\mathrm{FWHM}_{\min}$ distribution, with an MVT of 5 and 17 ms, respectively. These two cases show that duration alone could be misleading and showcase the potential of MVT to unveil these baffling merger candidates, as already pointed out in C23 and V23. Notably, 2% of LGRBs have $\mathrm{FWHM}_{\min} \leq 0.1$ s, indicating that LGRBs could include unidentified merger candidates. A few of these events, which also look similar to canonical SEE-GRBs, are displayed in Figure 5. Additionally, we considered 191019A, a long GRB ($T_{90} = 64$ s) at redshift $z = 0.248$ and with no associated SN, which might also be a merger candidate (Levan et al. 2023; Stratta et al. 2025). We note that 191019A was not detected by GBM; however, using *Swift*/BAT data, Camisasca et al. (2023a) reported an MVT of 0.196 s. Assuming the scaling of $\mathrm{FWHM}_{\min}$ with photon energy (see Appendix D), we estimated that we would have found 0.14 – 0.15 s with the GBM, placing 191019A in the outskirts of the LGRB $\mathrm{FWHM}_{\min}$ distribution. 221009A is not included in this analysis, owing to the strong saturation issues in *Fermi*/GBM. A MVT of 0.1 s, obtained with HXMT/HE data, was reported by Zhang et al. (2025), compatible with both Type I and II $\mathrm{FWHM}_{\min}$ distributions.

The MGFs have a mean $\mathrm{FWHM}_{\min}$ of 12 ms, hence exhibiting even shorter values than typical SGRBs. Table 3 shows the

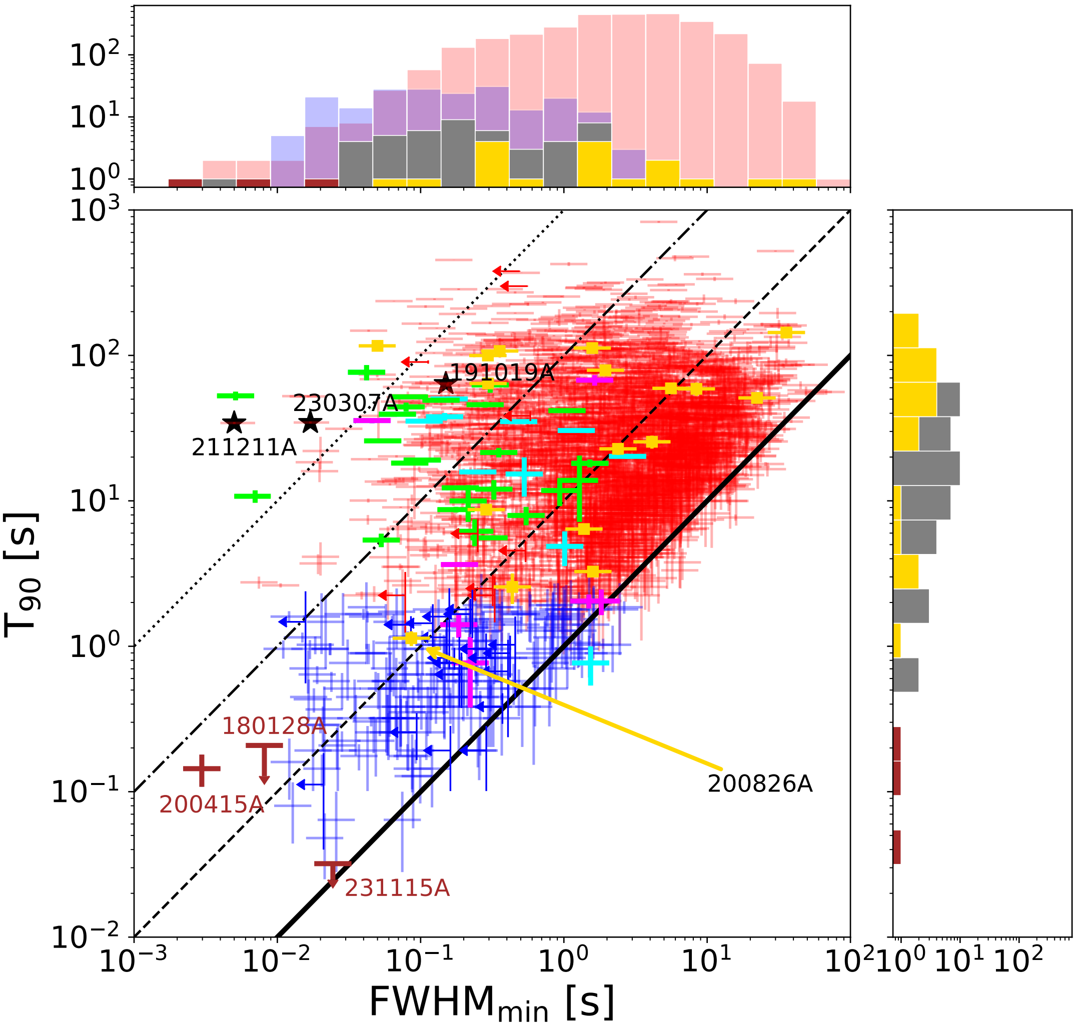

Fig. 4. Scatter plot of $\mathrm{FWHM_{min}}$ and $\mathrm{T_{90}}$ for the *Fermi*/GBM sample along with the corresponding marginal distributions. Blue (red) points represent short (long) GRBs. Gold points represent SN-associated GRBs. Magenta, lime, and cyan points represent SEE-GRBs from Lien et al. (2016), Lan et al. (2020), Kaneko et al. (2015), respectively. Three extragalactic MGFs candidates, 180128A, 200415A, and 231115A, are shown in brown. The SEE-GRBs from the three samples considered are shown altogether in grey in the top and right panel. We also show with a black star the two peculiar LGRBs, 211211A and 230307A, associated with a kilonova event and 191019A, which may be a short GRB that exploded in a dense environment. We also highlight the peculiar short collapsar GRB 200826A associated with an SN.

median $\mathrm{FWHM_{min}}$ value for the different populations as well as the result of the KS tests.

3.3. Peak rate versus $\mathrm{FWHM_{min}}$

In line with the procedure of C23, we characterised the detection efficiency of MEPSA applied to GBM data as a function of both $\mathrm{FWHM_{min}}$ and $\mathrm{PR_{max}}$, the latter being the maximum peak rate of any given pulse. To this aim, we generated synthetic pulses assuming the Norris function (Norris et al. 1996) and added a constant background with a count rate selected from a sample of real background rates observed with GBM. For each GRB, the background rate is the sum of the individual rates across all the NaI detectors involved. Poisson noise was finally simulated for the total expected counts per bin. We simulated GRBs with $\mathrm{PR_{max}}$ ranging from 10^2 to 10^5 cts s^{-1} and with $\mathrm{FWHM_{min}}$ going from 10^{-2} to 10^2 s. For each point of this grid, we simulated 100 pulses and estimated the detection efficiency by counting how many times MEPSA detected the peak with a $S/N > 5$. The detection efficiency, ϵ_{det}, is approximately described by a linear function of the logarithm of both quantities:

$$\epsilon_{\mathrm{det}} = a\log_{10}\left(\frac{\mathrm{FWHM_{min}}}{\mathrm{s}}\right) + b\log_{10}\left(\frac{\mathrm{PR_{max}}}{\mathrm{cts\ s^{-1}}}\right) + c. \quad (1)$$

The optimal coefficients were found to be $a = 1.27$, $b = 2.83$, and $c = -7.33$. Eq. (1) is the GBM analogous of Eq. (2) of C23:

$$\mathrm{PR_{max}} \geq 877\ \mathrm{cts\ s^{-1}}\left(\frac{\mathrm{FWHM_{min}}}{\mathrm{s}}\right)^{-0.45} 10^{0.35(\epsilon-1)}. \quad (2)$$

The meaning of Eq. (2) is illustrated by the following example: For a pulse with MVT of 10 ms to be correctly identified with

Table 3. Median $\mathrm{FWHM_{min}}$ values for different GRB groups along with the p-values of the two-population KS test between the $\mathrm{FWHM_{min}}$ values of each corresponding pair of groups.

Sample	$\mathrm{FWHM_{min}^{(a)}}$ (s)	LGRBs	SGRBs
LGRBs (2994)	2.4	–	10^{-69} (×)
SN GRBs (17)	1.6	0.17 (✓)	7.1 10^{-5} (×)
SGRBs (358)	0.15	10^{-69} (×)	–
SEE-GRBs$^{(b)}$ (6)	0.11	0.0004 (×)	0.73 (✓)
SEE-GRBs$^{(c)}$ (16)	0.16	7.5 10^{-5} (×)	0.75 (✓)
SEE-GRBs$^{(d)}$ (22)	0.2	1.3 10^{-12} (×)	0.73 (✓)
MGFs $^{(e)}$ (3)	0.008	2.3 10^{-7} (×)	0.003 (×)

Notes. $^{(a)}$Median value. $^{(b)}$Identified by Lien et al. (2016). $^{(c)}$Identified by Kaneko et al. (2015). $^{(d)}$Identified by from Lan et al. (2020). $^{(e)}$From extragalactic magnetars.

90% confidence, its peak rate has to be $\gtrsim$6430 cts s^{-1} (a condition that is fulfilled by just 13% of the bursts in our sample). Figure 6 illustrates ϵ_{det} in the $\mathrm{PR_{max}}$–$\mathrm{FWHM_{min}}$ plane.

3.4. *Peak luminosity versus* $\mathrm{FWHM_{min}}$

We computed the isotropic-equivalent peak luminosities, L_{p}, as done in Maccary et al. (2024) for 152 collapsar-candidate GRBs with known redshift. We studied the $L_p - \mathrm{FWHM_{min}}$ correlation, which was observed in other catalogues (C23). The result is shown in Figure 7.

The selection effects significantly influence the distribution in the L_p–$\mathrm{FWHM_{min}}$ plane. Specifically, narrower pulses require a higher peak rate to be detected. This selection bias could hide possible weak and short bursts that could contribute to demote the correlation. To account for this bias, we carried out a suite of simulations following the procedure set up in C23. We divided our sample into nine bins of redshift and simulated points within the $L_p - \mathrm{FWHM_{min}}$ plane for each bin. For each bin, we randomly generated as many points as in the corresponding observed sub-sample, where L_p was drawn from the distribution of the observed luminosities in that bin and $\mathrm{FWHM_{min}}$ was sampled from a probability density function derived from Gaussian kernel density estimation of the Type-II LGRBs with known redshift. Each point was accepted or rejected based on two conditions: (1) a Bernoulli trial with probability $p = \epsilon_{\mathrm{det}}$ calculated using Eq. (1) for that specific point was successful, and (2) the isotropic energy of this synthetic pulse did not exceed the maximum observed energy in that bin, given by $L_p \mathrm{FWHM_{min}} \leq \mathrm{E_{iso,max}^{(pulse)}}$.

We carried out $N = 10^4$ simulations. In this way, we did not assume any correlation between L_p and $\mathrm{FWHM_{min}}$, whereas the resulting apparent correlation is entirely due to the selection effects (Figure 8).

We then applied Pearson, Spearman, and Kendall correlation tests to the real data using logarithmic values for the analysis. For Type-II GRBs, we obtained p-values of 8×10^{-15}, 2.5×10^{-14}, and 8×10^{-13}, respectively. In contrast, we found no evidence of such a correlation for Type-I GRBs, with p-values of 0.96, 0.83, and 0.86, respectively. We then applied the same correlation test to the $N = 10^4$ simulated datasets to build the corresponding reference distributions for the p-values that account for the selection effects discussed above. The results are shown in Figure 9 and reveal that the simulated datasets were more correlated than the real ones only in 0.5%, 2.1%, and 2.3% of cases, respectively, which represent the probabilities that the observed correlation could arise purely from selection effects.

3.5. *Number of peaks versus* $\mathrm{FWHM_{min}}$

Figure 10 shows $\mathrm{FWHM_{min}}$ versus the number of peaks within a GRB. GRBs with numerous peaks (peak-rich GRBs) tend to have shorter MVTs compared with those with fewer peaks (peak-poor GRBs), as was also observed in *Swift*/BAT GRBs (Guidorzi et al. 2016). The same authors also found that peak-richness correlates with a shallower power density spectrum, which means that shorter timescales have relatively more temporal power than in peak-poor GRBs (Guidorzi et al. 2024b).

3.6. *Lorentz factor versus* $\mathrm{FWHM_{min}}$

We took the Lorentz factors (LFs, hereafter noted as Γ_0) from the same references as in C23, that is Lü et al. (2012), Xue et al. (2019), and Xin et al. (2016). We found 95 GRBs both detected by *Fermi*/GBM and reported in these studies. For 87 of them, Xue et al. (2019) made use of the $L_{\mathrm{iso}} - E_p - \Gamma_0$ correlation to get pseudo values of Γ_0, while for the remaining nine, we used the early afterglow peak to compute Γ_0. We then considered additional references for individual GRBs: 140102A, whose Γ_0 was reported by Gupta et al. (2021) (who also modelled the forward and reverse shock), as well as 211211A and 230307A. The value of the LF of 211211A (approximately $\Gamma_0 \sim 1000$) has been obtained by modelling the forward shock (Mei et al. 2022) and by measuring the deceleration peak (Veres et al. 2023). According to Zhong et al. (2024), 230307A has $\log(\Gamma_0) \sim 2.77$. Our sample also includes one SGRB, 090510, which is a rare case of SGRB detected by Fermi/LAT. In this case, Γ_0 was estimated from the peak of the high-energy afterglow (Ghirlanda et al. 2010). The other SGRB in our sample is 170817A, for which a considerably less reliable measure of Γ_0 was obtained using $E_{\mathrm{p,i}} - E_{\mathrm{iso}}$ and $\Gamma_0 - E_{\mathrm{iso}}$ correlations (Zou et al. 2018). We also considered the sample of GRBs from Ghirlanda et al. (2018) separately. We collected 65 Type-II GRBs in common with our sample, with 26 of them being part of their golden or silver sample and 39 taken as upper limits. We also report the six cases of Type-I GRBs for which a measure of Γ_0 is possible. The results are shown in Figure 11. The left panel shows $\mathrm{FWHM_{min}}$ versus Γ_0, while the right panel displays $\mathrm{FWHM_{min}}$ versus Γ_0 as measured by Ghirlanda et al. (2018).

We computed the radius, R, at which the gamma-ray emission is produced using

$$R \;=\; 2\,c\,\Gamma_0^2\,\mathrm{FWHM_{min}} \;= 6\times10^{14}\ \mathrm{cm}\left[\frac{\Gamma_0}{100}\right]^2\left[\frac{\mathrm{FWHM_{min}}}{1\ \mathrm{s}}\right]. \quad (3)$$

Eq. (3) is derived from the IS model (Rees & Meszaros 1994; Daigne & Mochkovitch 1998). We used $\mathrm{FWHM_{min}}$ as a proxy of the MVT in the emission radius calculation rather than Δt_{min} because the former can be considered as the sum of the rise and the decay time, while the latter gives only the rise time. This choice was motivated by the fact that the emission radius in the IS framework is linked to the angular spreading timescale, $R/c\Gamma^2$, which also governs the decay time of the pulse (Kobayashi et al. 2002). Since the decay of GRB pulses is three to four times slower than the rise, it is more accurate to consider $\mathrm{FWHM_{min}}$ than Δt_{min} when computing the emission radius. Figure 12 shows the R distribution for the Type-II GRBs in our sample. The emission radii, R, for all of our GRBs range from

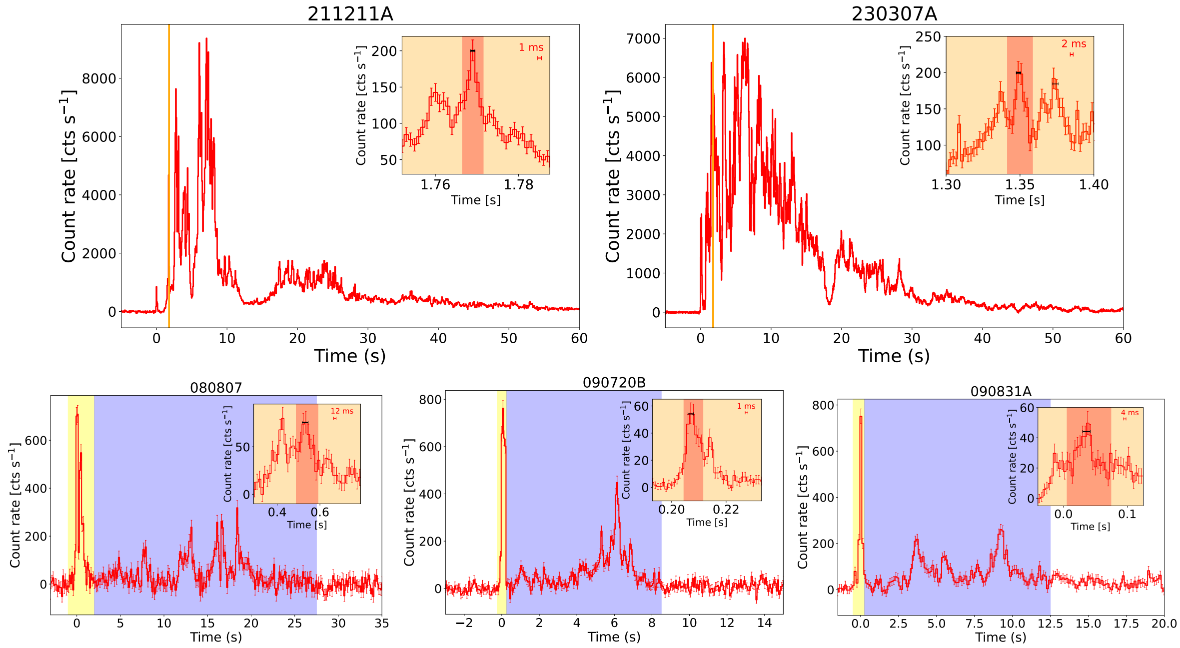

Fig. 5. *Top panels:* LC of 211211A (left) and of 230307A (right) when using the 8–1000 keV range. *Bottom panels, left to right:* LC of 080807, 090720B, and 090832A, respectively (in the same energy range as top panels). The yellow window includes the initial short spike, while the blue one includes the extended emission. The inset in each panel shows a zoom-in on the narrowest pulse. The black point indicates the detection timescale, $\Delta t_{\rm det}$, of the narrowest pulse, while the orange region shows the window encompassing $\rm FWHM_{min}$.

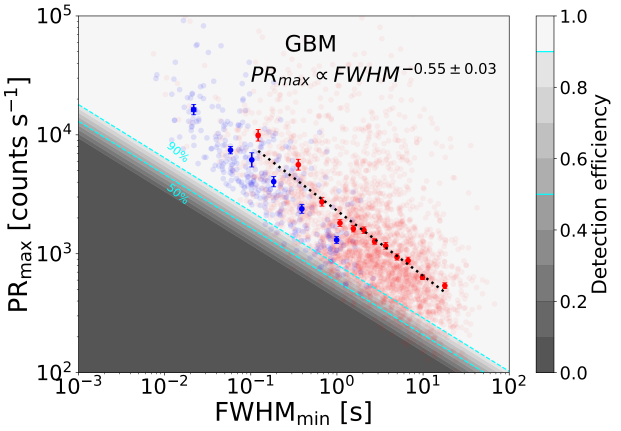

Fig. 6. For the GBM sample, $\rm PR_{max}$ versus $\rm FWHM_{min}$. Blue dots represent Type-I GRBs (i.e. SGRBs and SEE-GRBs), while red dots represent Type-II GRBs. Lighter dots correspond to individual GRB data, and darker dots indicate the geometric mean of data from GRB groups sorted by increasing $\rm FWHM_{min}$. Each Type-I group consists of 50 GRBs; each Type-II group consists of 270 GRBs. Dotted lines show the best fit for Type-II GRBs. Shaded areas illustrate ten regions with a detection efficiency ranging from 0 to 1. Cyan dashed lines indicate the 50% and 90% detection efficiency contours.

10^{14} to 10^{17} cm. Notably, 80% of the bursts have R values greater than 10^{15} cm, with a mean value of $\sim 6 \times 10^{15}$ cm. As a further test, we computed the deceleration radius, $R_{\rm dec}$, and we checked that $R < R_{\rm dec}$ using

$$R_{\rm dec} = 6.2 \times 10^{16}\ {\rm cm}\quad E_{\rm iso,52}^{1/3}\, \Gamma_2^{-2/3}\, n^{-1/3}, \tag{4}$$

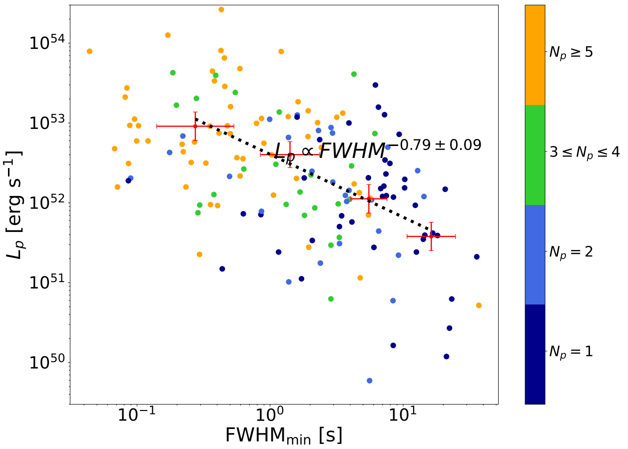

Fig. 7. Peak luminosity versus $\rm FWHM_{min}$ for collapsar-candidate (or Type-II) GRBs. The red points represent the geometric means of GRB groups sorted by increasing $\rm FWHM_{min}$. The dashed line indicates the best fit. GRBs are also categorised by the number of peaks, with the more luminous ones having more peaks.

where $E_{\rm iso,52} = E_{\rm iso}/10^{52}$ erg and $\Gamma_2 = \Gamma/100$, with $E_{\rm iso}$ being the explosion energy ($E_{\rm iso} = E_{\gamma,{\rm iso}}/\eta$, with efficiency η) and n the medium density. This was derived from Sari & Piran (1999), Molinari et al. (2007) and corresponds to the thin shell case. We assumed a constant density medium of $n = 1$ cm^{-3} and an efficiency of $\eta = 0.2$. We found only two cases where $R > R_{\rm dec}$, namely 090423 and 171222A, with $R/R_{\rm dec}$ ratios of 1.1 and 1.3, respectively. Unfortunately, there is no broadband modelling of the afterglow for these GRBs, so we are

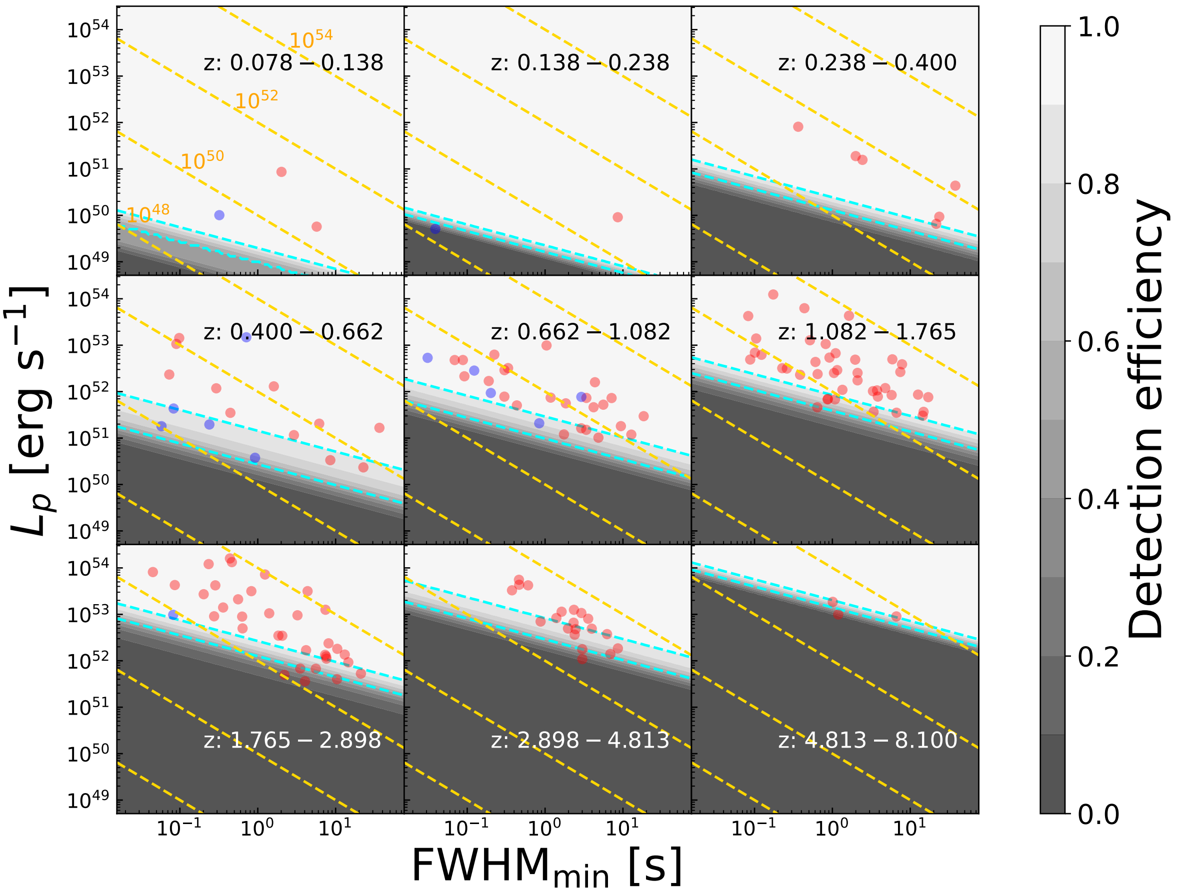

Fig. 8. Diagram showing L_p versus FWHM$_{\mathrm{min}}$ for the *Fermi*/GBM divided into nine redshift bins with equal logarithmic spacing in luminosity distance. The blue dots represent merger-candidates (or Type-I GRBs), and red dots represent collapsar-candidates (or Type-II GRBs). The dashed cyan lines show 90% and 50% detection efficiency (vertical bars). Gold dashed lines indicate regions of constant isotropic-equivalent released energy (in erg) for each peak, roughly calculated as $E_{\mathrm{iso}} = L_p \times \mathrm{FWHM}_{\mathrm{min}}$.

unable to verify whether our fiducial values are accurate estimates of the explosion energy and medium density in these cases.

3.7. *Peak energy versus* FWHM$_{\mathrm{min}}$

We explored the relationship between the MVT and the peak energy, E_p. We took the E_p information from the GBM catalogue (Goldstein et al. 2012). For 1921 bursts, measures of both E_p and FWHM$_{\mathrm{min}}$ are available. For a subsample of 107 with measured redshift, we could also compute the rest-frame peak energy $E_{p,i} = (1+z)\,E_p$. We calculated the Pearson, Spearman, and Kendall correlation coefficients using the logarithmic values, which turned out to be −0.29, −0.30, and −0.21, with associated p-values of $(5, 2.4, \text{and } 2)\times 10^{-4}$, respectively. This suggests that the two quantities are somehow correlated, despite the large dispersion, as shown in Figure 13.

We fitted the data with a power law, $\log(E_p/\mathrm{keV}) = m \log(\mathrm{FWHM}_{\mathrm{min}}/\mathrm{s}) + q$, and modelled the dispersion as a further parameter, minimising the D'Agostini likelihood (D'Agostini 2005). This likelihood is suitable to model correlations affected by a significant scatter, which is treated as a model parameter and is referred to as intrinsic dispersion of the correlation, denoted with σ. The resulting parameters are $m = -0.19^{+0.10}_{-0.09}$, $q = 2.66 \pm 0.07$, and $\sigma = 0.43^{0.06}_{-0.05}$.

4. Discussion and conclusions

As previously investigated in C23, we confirm that FWHM$_{\mathrm{min}}$ is a robust estimate of the MVT, although it carries a slightly different meaning compared to G15, which is more tightly connected to the rise time of the pulse. The MEPSA detection timescale, however, also proves to be a good indicator of the rise time of the narrowest pulse, thus providing a very simple and practical method to compute it. These differences are important to keep in mind, especially when the MVT values are interpreted within a theoretical context.

In the IS model, the hydrodynamic timescale and the angular spreading timescale govern the rise and the decay time of a GRB pulse, respectively (e.g. Kobayashi et al. 2002). The hydrodynamic timescale, which dictates the rise time, is the shock-crossing time, approximately $\sim l/c$, where l represents the characteristic irregularity scale or shell width in the outflow. The angular spreading timescale, which determines the decay time, results from the time delay or spread due to the angular extent of the emission region. This timescale is roughly $R/c\Gamma^2$, where

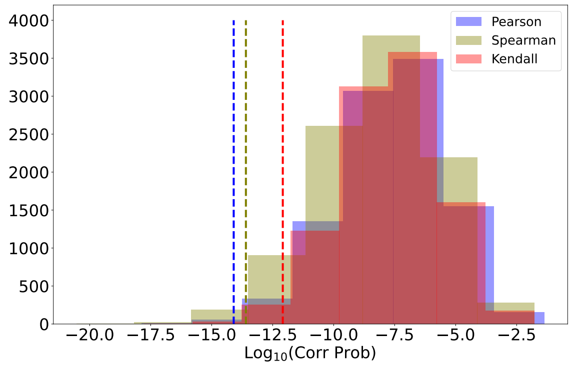

Fig. 9. Pearson, Spearman, and Kendall correlation p-values (in logarithm units) computed on $N = 10^4$ simulated samples (blue, olive, and red histograms) compared to the ones computed on the real dataset (blue, olive, and red dashed lines, respectively).

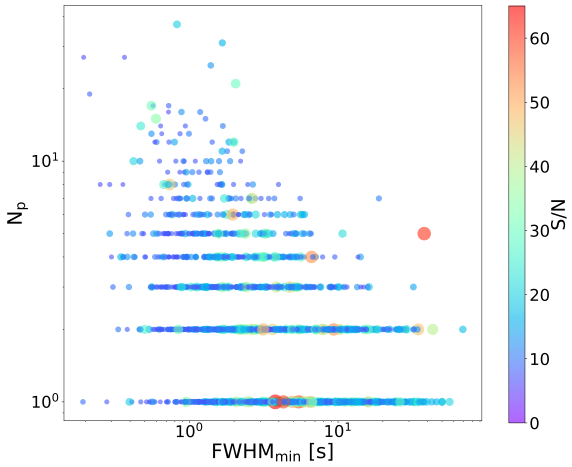

Fig. 10. Number of pulses within a GRB as a function of $\mathrm{FWHM}_{\mathrm{min}}$ colour-coded by S/N. The GRBs that are composed of a large number of pulses are more likely to have a shorter $\mathrm{FWHM}_{\mathrm{min}}$.

R is the emission radius and Γ is the Lorentz factor of the emission region. Since most observed pulses exhibit a faster rise than decay, the pulse width is primarily set by the angular spreading time.

We confirm that millisecond-long pulses are very rare in GRBs. While partly affected by detection thresholds, their scarcity appears to be a genuine feature. Having investigated three independent studies, we confirm that SEE-GRBs have shorter MVTs than LGRBs, compatible with the bulk of SGRBs. Additionally, the three well-known long-duration merger candidates 211211A, 230307A, and 191019A to a lesser extent have very short MVTs (5, 17, and 150 ms) , providing further evidence that short MVTs are characteristic of Type-I GRBs, regardless of the total duration. Our MVT results align with the conventional interpretation that SEE-GRBs are essentially SGRBs with an additional emission component. The exact physical mechanism behind the extended emission remains unclear. Several models have been proposed, including long-lasting activity from the central engine, such as a magnetar formed during the merger (Metzger et al. 2008; Jordana-Mitjans et al. 2022) or energy release from a late fallback accretion disc (Rosswog 2007; Musolino et al. 2024), both of which can continue powering the emission after the main burst. These results emphasise the importance of multi-wavelength follow-up observations, particularly for LGRBs with low MVTs, as these could reveal other merger events that might otherwise be misclassified as collapsar candidates.

The differences in MVT between Type-I and Type-II GRBs may indicate distinct progenitors or disparities in jet propagation. The irregularity in GRB jets arises from a combination of internal factors, such as variability in the central engine, and external factors such as interaction with the surrounding medium and jet instabilities. The conventional central engines are magnetars or black hole accretion disc systems. Even if both types of GRBs are powered by black hole accretion discs, the black holes in Type I events (SGRBs) likely have smaller masses, resulting in shorter dynamical timescales. The GRB jets must also penetrate a dense medium surrounding the central engines: a stellar envelope in the case of LGRBs (Type II) or neutron star merger ejecta in the case of SGRBs (Type I). This interaction fosters the growth of hydrodynamic instabilities along the jet boundary (e.g. Gottlieb et al. 2020). Type II jets are likely more unstable due to the higher density of the surrounding stellar envelope. Additionally, pulses emitted within the photospheric radius are obscured, adding further complexity. Extragalactic MGFs have an even shorter MVT than every GRB population, thus offering an additional tool to distinguish them from traditional GRB events.

We have confirmed, using an independent dataset, that in the case of Type-II GRBs, peak luminosity does correlate with $\mathrm{FWHM}_{\mathrm{min}}$, while the same does not hold true for Type-I GRBs. The question as to whether this is a result of a much poorer sample or due to the intrinsic absence of correlation will be addressed through future richer datasets. We confirmed that GRBs with many pulses (pulse-rich GRBs, as defined in Guidorzi et al. 2024b) tend to have shorter MVTs, supporting the presence of two temporal behaviours: rapid variability atop a slower FRED-like envelope and purely slow, FRED-like evolution. This distinction may reflect differences in central engine activity, circumburst interactions, or progenitor type. We computed the LF and source emission radius, R. The R values we found generally do not align with the IS model, where R typically ranges from 10^{13} to 10^{14} cm. However, they are consistent with the ICMART model, which predicts gamma-ray emission at larger radii, $R > 10^{15-16}$ cm (Zhang & Yan 2011), through magnetic reconnection cascades.

We have investigated the plausible correlation between MVT and peak energy. Given the established anti-correlation between MVT and peak luminosity (see also C23, Wu et al. 2016) and the known correlation between peak energy and peak luminosity (Yonetoku et al. 2004; Ghirlanda et al. 2005), in principle, we expected an anti-correlation between the MVT and $E_{p,i}$. Moreover, several GRBs with a small MVT have also been detected at higher energies by *Fermi*/LAT, such as 080916C (0.3 s, Tajima et al. 2008); 090510 (0.011 s, Ohno & Pelassa 2009); 090720B (0.014 s, Rubtsov et al. 2012); and 210410A (0.07 s, Arimoto et al. 2021). Although we do find a correlation, it is very dispersed. Smaller MVTs may imply shorter angular spreading times and smaller emission radii, resulting in higher shock energy density in the emission region. In the standard synchrotron shock model, a constant fraction of the shock energy is transferred to magnetic fields, with radiation from smaller radii generally expected to be harder. However, since both the shock energy generated through internal dissipation and the blue-shift of emission frequencies depend on the Lorentz factor, velocity

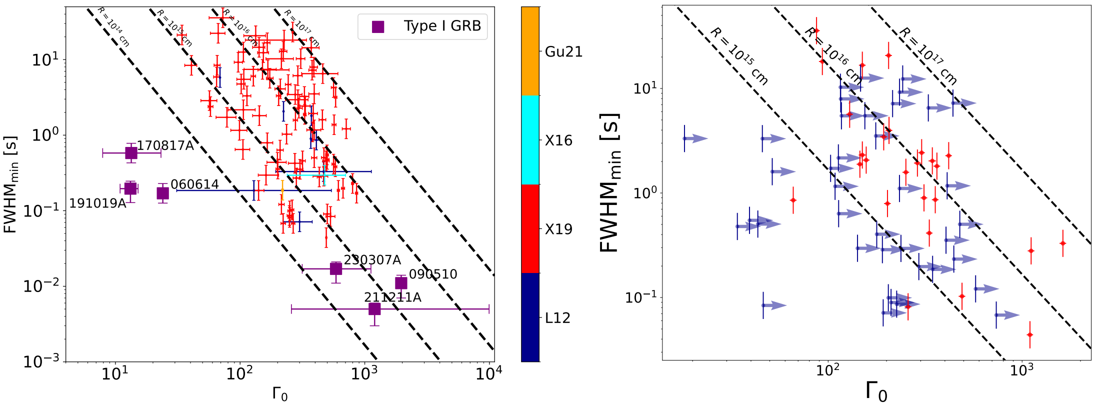

Fig. 11. For the Type-II (red dots) and Type-I GRBs (purple squares) present in our sample, FWHM$_{\rm min}$ versus the initial Lorentz factor Γ_0. In the left panel, the Γ_0 values are from different datasets and colour-coded as follows: L12 Lü et al. (2012), X19 Xue et al. (2019), X16 Xin et al. (2016), and Gu21 Gupta et al. (2021). The dashed lines represent the typical distance $R = 2c\Gamma_0^2\mathrm{FWHM}_{\rm min}$ where the dissipation process responsible for the prompt emission could occur. The right panel is the same as the left, but Γ_0 has been calculated using the dataset from Ghirlanda et al. (2018). Red points indicate GRBs from their golden and silver samples, while blue points represent lower limits on Γ_0.

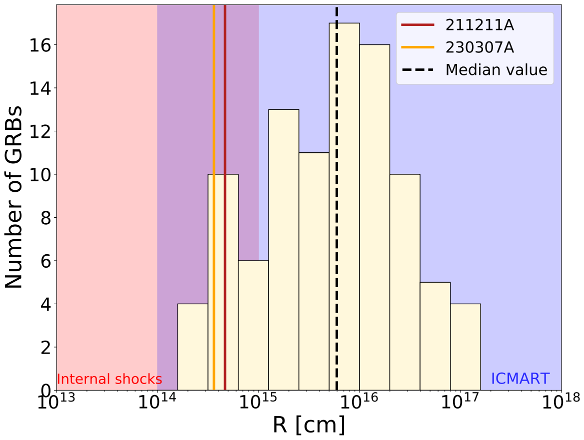

Fig. 12. Source emission region radii for the GBM sample. The red and orange vertical lines represent the value of this radius for 211211A and 230307A, while the dashed vertical line represents the median value of the distribution. The red shaded regions indicate the values expected by the IS model (10^{13} cm $\lesssim$ R $\lesssim$ 10^{15} cm; Rees & Meszaros 1994; Daigne & Mochkovitch 1998), while the blue one indicates the expectations for the ICMART model ($R \gtrsim 10^{14-15}$ cm; Zhang & Yan (2011)). In the decade 10^{14-15} cm (purple), the two regions overlap, and the emission radii in this region are marginally compatible with both models.

irregularities in the outflow–an essential assumption of the IS model–can introduce significant dispersion in this relationship.

5. Data availability

Table 1 is available at the CDS via `https://cdsarc.cds.unistra.fr/viz-bin/cat/J/A+A/702/A95`.

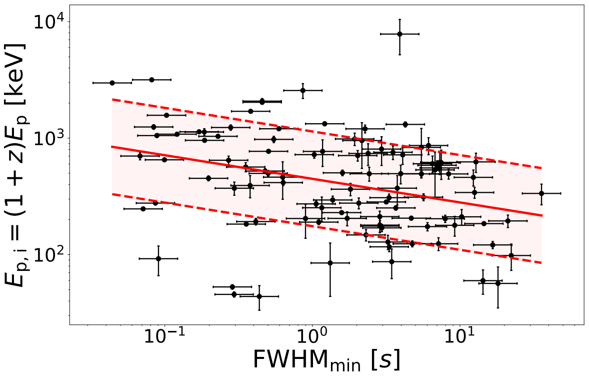

Fig. 13. For all Type-II GRBs with known redshift, $E_{p,i}$ versus FWHM$_{\rm min}$. The solid red line shows the best fit, while the two dashed red lines show the dispersion of the correlation.

Acknowledgements. We are grateful to the anonymous reviewer for their precious report which helped us to cross-check our results and to overall improve the quality of this work. R.M. and M.M. acknowledge the University of Ferrara for the financial support of their PhD scholarships. L.F. acknowledges support from the AHEAD-2020 Project grant agreement 871158 of the European Union's Horizon 2020 Program. A.T. acknowledges financial support from ASI-INAF Accordo Attuativo HERMES Pathfinder operazioni n. 2022-25-HH.0 and the basic funding program of the Ioffe Institute FFUG-2024-0002. L.A. acknowledges support from INAF Mini-grant programme 2022. A.E.C received support from the European Research Council (ERC) via the ERC Synergy Grant ECOGAL (grant 855130). Views and opinions expressed by ERC-funded scientists are however those of the author(s) only and do not necessarily reflect those of the European Union or the European Research Council. Neither the European Union nor the granting authority can be held responsible for them. M. B. acknowledges the Department of Physics and Earth Science of the University of Ferrara for the financial support through the FIRD 2024 grant.

References

Abbott, B. P., Abbott, R., Abbott, T. D., et al. 2017, ApJ, 848, L13
Ackermann, M., Ajello, M., Asano, K., et al. 2014, Science, 343, 42
Arimoto, M., Ohno, M., Longo, F., Axelsson, M., & Fermi-LAT Team 2021, GRB Coordinates Network, 29781, 1
Bhat, P. N., Briggs, M. S., Connaughton, V., et al. 2012, ApJ, 744, 141
Blinnikov, S. I., Novikov, I. D., Perevodchikova, T. V., & Polnarev, A. G. 1984, Sov. Astron. Lett., 10, 177
Bulla, M., Camisasca, A. E., Guidorzi, C., et al. 2023, GRB Coordinates Network, 33578, 1
Burns, E., Svinkin, D., Hurley, K., et al. 2021, ApJ, 907, L28
Camisasca, A. E., Guidorzi, C., Amati, L., et al. 2023a, A&A, 671, A112

Camisasca, A. E., Guidorzi, C., Bulla, M., et al. 2023b, GRB Coordinates Network, 33577, 1

Chen, J.-M., Zhu, K.-R., Peng, Z.-Y., & Zhang, L. 2024, MNRAS, 527, 4272

D'Agostini, G. 2005, ArXiv e-prints [arXiv: `physics/0511182`]

Dai, C.-Y., Guo, C.-L., Zhang, H.-M., Liu, R.-Y., & Wang, X.-Y. 2024, ApJ, 962, L37

Daigne, F., & Mochkovitch, R. 1998, MNRAS, 296, 275

Della Valle, M., Chincarini, G., Panagia, N., et al. 2006, Nature, 444, 1050

Di Matteo, T., Perna, R., & Narayan, R. 2002, ApJ, 579, 706

Dimple, Misra, K., & Arun, K. G. 2023, ApJ, 949, L22

Dimple, Misra, K., & Arun, K. G. 2024, ApJ, 974, 55

Du, Z., Lü, H., Yuan, Y., Yang, X., & Liang, E. 2024, ApJ, 962, L27

Eichler, D., Livio, M., Piran, T., & Schramm, D. N. 1989, Nature, 340, 126

Fenimore, E. E., in 't Zand, J. J. M., Norris, J. P., Bonnell, J. T., & Nemiroff, R. 1989, ApJ, 448, L101

Dalessi, S., Roberts, O. J., Meegan, C., & Fermi GBM Team 2023, GRB Coordinates Network, 33411, 1

Fermi-Lat Collaboration 2021, Nat. Astron., 5, 385

Feroci, M., Frontera, F., Costa, E., et al. 1999, ApJ, 515, L9

Fruchter, A. S., Levan, A. J., Strolger, L., et al. 2006, Nature, 441, 463

Fynbo, J. P. U., Watson, D., Thöne, C. C., et al. 2006, Nature, 444, 1047

Galama, T. J., Vreeswijk, P. M., van Paradijs, J., et al. 1998, Nature, 395, 670

Garcia-Cifuentes, K., Becerra, R. L., De Colle, F., Cabrera, J. I., & Del Burgo, C. 2023, ApJ, 951, 4

Gehrels, N., Norris, J. P., Barthelmy, S. D., et al. 2006, Nature, 444, 1044

Ghirlanda, G., Ghisellini, G., & Firmani, C. 2005, MNRAS, 361, L10

Ghirlanda, G., Ghisellini, G., & Nava, L. 2010, A&A, 510, L7

Ghirlanda, G., Nappo, F., Ghisellini, G., et al. 2018, A&A, 609, A112

Goldstein, A., Preece, R. D., & Briggs, M. S. 2010, ApJ, 721, 1329

Goldstein, A., Burgess, J. M., Preece, R. D., et al. 2012, ApJS, 199, 19

Goldstein, A., Cleveland, W. H., & Kocevski, D. 2022, Fermi GBM Data Tools: v1.1.1

Golkhou, V. Z., & Butler, N. R. 2014, ApJ, 787, 90

Golkhou, V. Z., Butler, N. R., & Littlejohns, O. M. 2015, ApJ, 811, 93

Gompertz, B. P., Ravasio, M. E., Nicholl, M., et al. 2023, Nat. Astron., 7, 67

Gottlieb, O., Bromberg, O., Singh, C. B., & Nakar, E. 2020, MNRAS, 498, 3320

Guidorzi, C. 2015, Astron. Comput., 10, 54

Guidorzi, C., Dichiara, S., & Amati, L. 2016, A&A, 589, A98

Guidorzi, C., Maccary, R., Tsvetkova, A., et al. 2024a, A&A, 690, A261

Guidorzi, C., Sartori, M., Maccary, R., et al. 2024b, A&A, 685, A34

Gupta, R., Oates, S. R., Pandey, S. B., et al. 2021, MNRAS, 505, 4086

Hjorth, J., Sollerman, J., Møller, P., et al. 2003, Nature, 423, 847

Hurley, K., Cline, T., Mazets, E., et al. 1999, Nature, 397, 41

Hurley, K., Boggs, S. E., Smith, D. M., et al. 2005, Nature, 434, 1098

Janiuk, A., Yuan, Y., Perna, R., & Di Matteo, T. 2007, ApJ, 664, 1011

Jespersen, C. K., Severin, J. B., Steinhardt, C. L., et al. 2020, ApJ, 896, L20

Jin, Z.-P., Li, X., Cano, Z., et al. 2015, ApJ, 811, L22

Jordana-Mitjans, N., Mundell, C. G., Guidorzi, C., et al. 2022, ApJ, 939, 106

Kaneko, Y., Bostancı, Z. F., Göğüş, E., & Lin, L. 2015, MNRAS, 452, 824

Kobayashi, S., Piran, T., & Sari, R. 1997, ApJ, 490, 92

Kobayashi, S., Ryde, F., & MacFadyen, A. 2002, ApJ, 577, 302

Kumar, P., & Narayan, R. 2009, MNRAS, 395, 472

Lan, L., Lu, R.-J., Lü, H.-J., et al. 2020, MNRAS, 492, 3622

Lei, W.-H., Zhang, B., & Liang, E.-W. 2013, ApJ, 765, 125

Lesage, S., Veres, P., Briggs, M. S., et al. 2023, ApJ, 952, L42

Levan, A. J., Malesani, D. B., Gompertz, B. P., et al. 2023, Nat. Astron., 7, 976

Levan, A. J., Gompertz, B. P., Salafia, O. S., et al. 2024, Nature, 626, 737

Lien, A., Sakamoto, T., Barthelmy, S. D., et al. 2016, ApJ, 829, 7

Lü, H.-J., Liang, E.-W., Zhang, B.-B., & Zhang, B. 2010, ApJ, 725, 1965

Lü, J., Zou, Y.-C., Lei, W.-H., et al. 2012, ApJ, 751, 49

Lü, H.-J., Zhang, B., Liang, E.-W., Zhang, B.-B., & Sakamoto, T. 2014, MNRAS, 442, 1922

Lyutikov, M., Pariev, V. I., & Blandford, R. D. 2003, ApJ, 597, 998

Maccary, R., Guidorzi, C., Amati, L., et al. 2024, ApJ, 965, 72

MacFadyen, A. I., & Woosley, S. E. 1999, ApJ, 524, 262

MacLachlan, G. A., Shenoy, A., Sonbas, E., et al. 2013, MNRAS, 432, 857

Mazets, E. P., Golentskii, S. V., Ilinskii, V. N., Aptekar, R. L., & Guryan, I. A. 1979, Nature, 282, 587

Mazets, E. P., Aptekar, R. L., Cline, T. L., et al. 2008, ApJ, 680, 545

Meegan, C., Lichti, G., Bhat, P. N., et al. 2009, ApJ, 702, 791

Mei, A., Banerjee, B., Oganesyan, G., et al. 2022, Nature, 612, 236

Mereghetti, S., Rigoselli, M., Salvaterra, R., et al. 2024, Nature, 629, 58

Metzger, B. D., Quataert, E., & Thompson, T. A. 2008, MNRAS, 385, 1455

Metzger, B. D., Giannios, D., Thompson, T. A., Bucciantini, N., & Quataert, E. 2011, MNRAS, 413, 2031

Minaev, P. Y., Pozanenko, A. S., Grebenev, S. A., et al. 2024, Astron. Lett., 50, 1

Molinari, E., Vergani, S. D., Malesani, D., et al. 2007, A&A, 469, L13

Musolino, C., Duqué, R., & Rezzolla, L. 2024, ApJ, 966, L31

Narayan, R., Paczynski, B., & Piran, T. 1992, ApJ, 395, L83

Norris, J. P., & Bonnell, J. T. 2006, ApJ, 643, 266

Norris, J. P., Nemiroff, R. J., Bonnell, J. T., et al. 1996, ApJ, 459, 393

Norris, J. P., Bonnell, J. T., Kazanas, D., et al. 2005, ApJ, 627, 324

Ofek, E. O., Kulkarni, S. R., Nakar, E., et al. 2006, ApJ, 652, 507

Ohno, M., & Pelassa, V. 2009, GRB Coordinates Network, 9334, 1

Paczynski, B. 1986, ApJ, 308, L43

Paczynski, B. 1991, Acta Astron., 41, 257

Paczyński, B. 1998, ApJ, 494, L45

Planck Collaboration VI. 2020, A&A, 641, A6

Popham, R., Woosley, S. E., & Fryer, C. 1999, ApJ, 518, 356

Rastinejad, J. C., Gompertz, B. P., Levan, A. J., et al. 2022, Nature, 612, 223

Rees, M. J., & Meszaros, P. 1994, ApJ, 430, L93

Roberts, O. J., Veres, P., Baring, M. G., et al. 2021, Nature, 589, 207

Rodi, J. C., Pacholski, D. P., Mereghetti, S., et al. 2025, ApJ, 979, L25

Rosswog, S. 2007, MNRAS, 376, L48

Rubtsov, G. I., Pshirkov, M. S., & Tinyakov, P. G. 2012, MNRAS, 421, L14

Salmon, L., Hanlon, L., & Martin-Carrillo, A. 2022, Galaxies, 10, 78

Sari, R., & Piran, T. 1999, ApJ, 520, 641

Scargle, J. D., Norris, J. P., Jackson, B., & Chiang, J. 2013, ApJ, 764, 167

Steinhardt, C. L., Mann, W. J., Rusakov, V., & Jespersen, C. K. 2023, ApJ, 945, 67

Stratta, G., Nicuesa Guelbenzu, A. M., Klose, S., et al. 2025, ApJ, 979, 159

Svinkin, D., Frederiks, D., Hurley, K., et al. 2021, Nature, 589, 211

Tajima, H., Bregeon, J., Chiang, J., & Thayer, G. 2008, GRB Coordinates Network, 8246, 1

Thompson, T. A., Chang, P., & Quataert, E. 2004, ApJ, 611, 380

Trigg, A. C., Burns, E., Roberts, O. J., et al. 2024, A&A, 687, A173

Troja, E., Fryer, C. L., O'Connor, B., et al. 2022, Nature, 612, 228

Tsvetkova, A., Amati, L., Bulla, M., et al. 2025, A&A, 698, A169

Usov, V. V. 1992, Nature, 357, 472

Veres, P., Bhat, P. N., Burns, E., et al. 2023, ApJ, 954, L5

Vianello, G., Gill, R., Granot, J., et al. 2018, ApJ, 864, 163

Wheeler, J. C., Yi, I., Höflich, P., & Wang, L. 2000, ApJ, 537, 810

Woosley, S. E. 1993, ApJ, 405, 273

Wu, Q., Zhang, B., Lei, W.-H., et al. 2016, MNRAS, 455, L1

Xiao, S., Peng, W.-X., Zhang, S.-N., et al. 2022, ApJ, 941, 166

Xin, L.-P., Wang, Y.-Z., Lin, T.-T., et al. 2016, ApJ, 817, 152

Xiong, S., Wang, C., & Huang, Y. Gecam Team 2023, GRB Coordinates Network, 33406, 1

Xue, L., Zhang, F.-W., & Zhu, S.-Y. 2019, ApJ, 876, 77

Yang, B., Jin, Z.-P., Li, X., et al. 2015, Nat. Commun., 6, 7323

Yang, J., Chand, V., Zhang, B.-B., et al. 2020, ApJ, 899, 106

Yang, J., Ai, S., Zhang, B. B., et al. 2022, Nature, 612, 232

Yang, Y.-H., Troja, E., O'Connor, B., et al. 2024, Nature, 626, 742

Yonetoku, D., Murakami, T., Nakamura, T., et al. 2004, ApJ, 609, 935

Yoon, S. C., & Langer, N. 2005, A&A, 443, 643

Zhang, B. 2006, Nature, 444, 1010

Zhang, B., & Yan, H. 2011, ApJ, 726, 90

Zhang, W.-L., Xue, W.-C., Li, C.-K., et al. 2025, ApJ, 986, 170

Zhong, S.-Q., Li, L., Xiao, D., et al. 2024, ApJ, 963, L26

Zhu, S.-Y., Sun, W.-P., Ma, D.-L., & Zhang, F.-W. 2024, MNRAS, 532, 1434

Zou, Y.-C., Wang, F.-F., Moharana, R., et al. 2018, ApJ, 852, L1

Appendix A: FWHM$_{\mathrm{min}}$ compared to a direct fit of the narrowest pulse

We compared FWHM$_{\mathrm{min}}$ measurements obtained using MEPSA calibration and the procedure described in C23 with the results derived from fitting the LC with FRED shaped pulses (denoted as FWHM$_{\mathrm{fit}}$; see Maccary et al. (2024) for a detailed description of the technique). To do so, we analysed a sub-sample of GRBs with either one or a few peaks, for which a direct and accurate modelling of the pulses' shapes and FWHMs was feasible. We initially selected 639 single-peaked GRBs with S/N > 10. We excluded the GRBs that displayed a more complex temporal structure than a single well-shaped pulse, ending up with 544 GRBs. Their pulses were then fitted with a FRED template and discarded the cases, whose best-fit parameters were too close to the boundaries (chosen to avoid unrealistic parameter values), or with relative errors on the rise time greater than 50%, reducing the sample to 410 GRBs. We used *Swift*/BAT data as well, taking a sub-sample of GRBs with less than 8 peaks in their LC. After intersecting these data with the G15 and V23 results, we retained 244 GRBs in the GBM sample and 28 in the BAT sample for a comparative analysis. In Fig. A.1 we illustrated the comparison between FWHM$_{\mathrm{min}}$ and FWHM$_{\mathrm{fit}}$, showing how closely the two methods agree across different GRBs. As we can see, for most peaks, $\frac{\mathrm{FWHM_{fit}}}{2} \leq \mathrm{FWHM_{min}} \leq 2 \cdot \mathrm{FWHM_{fit}}$; more precisely, 90% of events are in the range $0.66 \cdot \mathrm{FWHM_{fit}} \leq \mathrm{FWHM_{min}} \leq 1.92 \cdot \mathrm{FWHM_{fit}}$.

We furthermore performed a linear fit of the form $y = mx+q$, applied to the logarithmic values, modelling the intrinsic dispersion σ_{int} as a further parameter, adopting the D'Agostini likelihood (D'Agostini 2005). Optimising the parameters using MCMC, we found $m = 0.990^{+0.011}_{-0.004}$, $q = 0.051^{+0.016}_{-0.017}$, and $\sigma_{\mathrm{int}} = 0.071^{+0.023}_{-0.028}$. The uncertainty on log FWHM$_{\mathrm{min}}$, previously estimated as $\sigma_{\mathrm{min}} = 0.13$ (i.e a 35% relative error on FWHM$_{\mathrm{min}}$), leads to a total uncertainty, accounting for the intrinsic dispersion σ_{int}, of $\sigma_{\mathrm{tot}} = \sqrt{\sigma^2_{\mathrm{min}} + \sigma^2_{\mathrm{int}}} \simeq 0.07$ (41%). This implies that the relative error made when using FWHM$_{\mathrm{min}}$ instead of FWHM$_{\mathrm{fit}}$ is approximately 41%, as opposed to the 35% estimated on synthetic LCs by Camisasca et al. (2023a). This comparison ensures the robustness of our MVT measurements by validating them against an established LC fitting method.

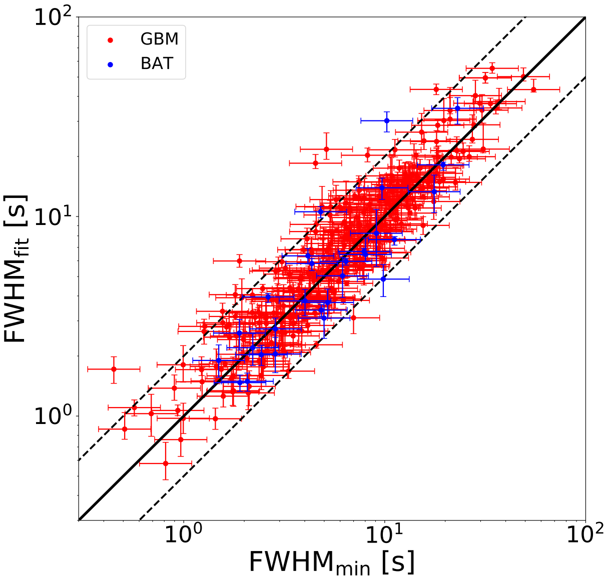

Fig. A.1. Plot presenting FWHM$_{\mathrm{min}}$ computed either by following the method described in C23, or by directly fitting the narrowest pulse by a Norris function (called here FWHM$_{\mathrm{fit}}$). Red (blue) points were obtained using GBM (resp. BAT) data. The black line indicates the equality line while the dashed lines show a factor 2 of discrepancy, illustrating that most measurements fall within this range.

Appendix B: Comparison between BAT and GBM

We compared the results obtained by C23 with BAT data with those obtained in this work with GBM data. The FWHM$_{\mathrm{min}}$ obtained with the GBM is in mean twice as small as those obtained with the BAT. This was expected due to the dependance of the MVT on the energy band. We also carried this analysis restricting the GBM energy range to the *Swift*/BAT one (15-150 keV). The results show a dispersion around the equality line but no general trend, indicating that our results are consistent with the ones of C23. The results of these two analyses are shown in Figure B.1.

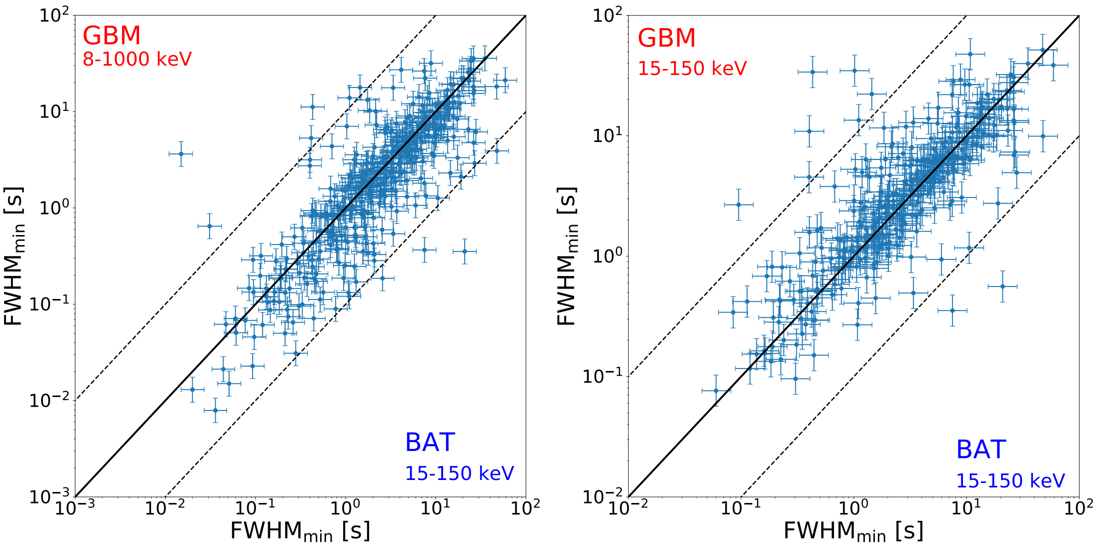

Fig. B.1. Left: $\mathrm{FWHM_{min}}$ computed by C23 with BAT data on 15-150 keV against the $\mathrm{FWHM_{min}}$ of the same bursts but computed in this work on GBM data on the 8-1000 keV range. **Right**: Same but the GBM energy range is restricted to 15-150 keV to be the same as BAT.

Appendix C: $\mathrm{FWHM_{min}}$ compared with Bayesian blocks

In this section, we compared our results with those obtained by segmenting the LC using Bayesian blocks[4] (BBs, Scargle et al. 2013). We applied BBs, using a false alarm threshold of $p_0 = 10^{-3}$ to a sample of 96 GRBs, chosen with $\mathrm{FWHM_{min}} < 50$ ms. This choice was made to obtain enough GRBs to make a sound statistical analysis and to include bright GRBs with evident sub-second structures with exquisite S/N. This sample includes, for instance, GRBs as 211211A, 230307A, 190114C, and others known for their rapid temporal variability and brightness, making them ideal test cases. We computed the MVT using BBs, defining it as the shortest block in the segmentation, $\Delta\mathrm{T_{BB}}$. Figure C.1 compares these values with those from the MEPSA-based approach. The points scatter around the equality line without a clear systematic bias in either direction. The distribution of the ratio $\Delta T_{BB}/\mathrm{FWHM_{min}}$ is shown in Fig. C.2 with a median of about 1.03–meaning that, on average, BBs yield MVT values $\sim$ 3% larger than those obtained with MEPSA. The 90 % confidence interval is [0.4-2.3], meaning that for most GRBs, the discrepancy between the MVTs obtained using BBs and those obtained using MEPSA is smaller than a factor of 2. We further estimated that in roughly 60% cases, the temporal structures identified by MEPSA and BBs coincide; in such cases the discrepancies in MVT values arise only from different ways of estimating the width. BBs, which approximate the pulse as a rectangle, tend to overestimate the width, whereas MEPSA uses a more realistic, though simplified, pulse shape.

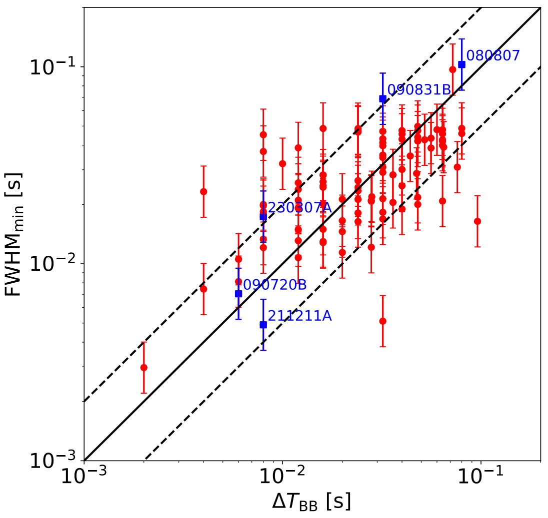

Fig. C.1. Plot of $\mathrm{FWHM_{min}}$ versus the shortest segment of the BBs segmentation, $\Delta\mathrm{T_{BB}}$. Blue points represents the GRBs shown in Fig. 5.

---

[4] We used the function *bayesian_blocks* from the *astropy.stats* python library.

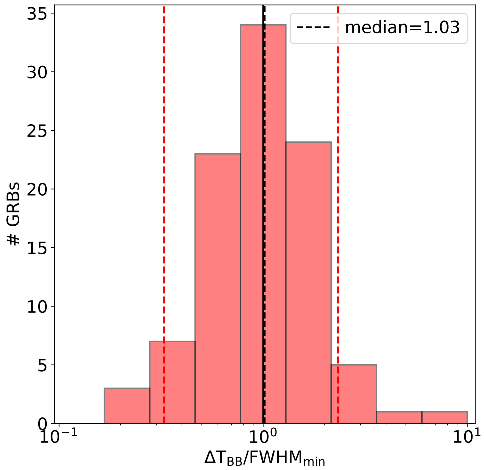

Fig. C.2. Distribution of the ratio ΔT_{BB} over FWHM_{min}. The solid black line represents the case $\mathrm{FWHM}_{min} = \Delta T_{BB}$, while the dashed one shows the median value. The two red dashed lines enclose the 90 % confidence interval [0.4-2.3].

Appendix D: Dependence of FWHM_{min} on energy

We computed FWHM_{min} as a function of the geometric mean of the energy range boundaries, for six different energy ranges: 8-30, 8-90, 30-90, 8-1000, 90-300, and 90-1000 keV. We carried out this analysis on 286 bursts, each having a measured FWHM_{min} with $S/N > 7$ across all six energy ranges. We found that $\mathrm{FWHM}_{min} \propto E^{-\alpha}$ with $\alpha_{mean} = 0.46 \pm 0.19$, with a standard dispersion of $\sigma = 0.7$, and $\alpha_{median} = 0.26 \pm 0.12$. Results are shown in Figure D.1. The results are consistent with those of C23 that obtained $\alpha_{mean} = 0.45 \pm 0.08$, $\alpha_{median} = 0.54 \pm 0.07$ and those of Fenimore et al. (1989): $\alpha \in [0.37; 0.46]$.

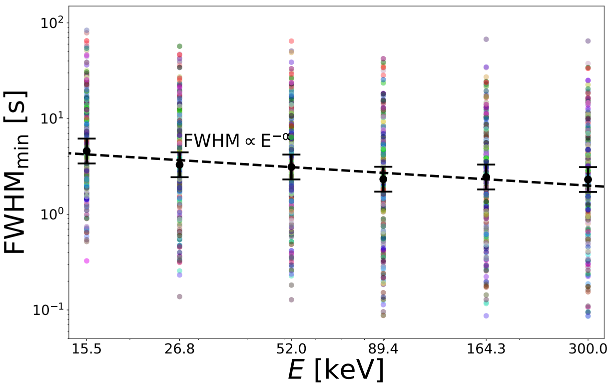

Fig. D.1. Plot showing FWHM_{min} as a function of the geometric mean of the energy range boundaries. The coloured dots are the FWHM_{min} of 286 bursts in four different energy ranges: 8-30, 8-90, 30-90, 8-1000, 90-300, and 90-1000 keV. The values on the x-axis are the geometric means of the corresponding energy boundaries. Black dots with error bars are the weighted averages of the FWHM_{min} for each energy range and the black dashed line is the power-law that best fit the black points.

A.10 PAPER IV: A SET OF DISTINCTIVE PROPERTIES RULING THE PROMPT EMISSION OF GRB 230307A AND OTHER LONG γ-RAY BURSTS FROM COMPACT OBJECT MERGERS

Journal of High Energy Astrophysics 49 (2026) 100456

Contents lists available at ScienceDirect

Journal of High Energy Astrophysics

journal homepage: www.elsevier.com/locate/jheap

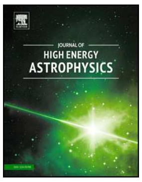

A set of distinctive properties ruling the prompt emission of GRB 230307A and other long γ-ray bursts from compact object mergers

R. Maccary [a,b,*], C. Guidorzi [a,b,c], M. Maistrello [a,b], S. Kobayashi [e], M. Bulla [a,c,d], R. Moradi [f], S.-X. Yi [f], C.W. Wang [f,g], W.L. Zhang [f,h], W.-J. Tan [f,g], S.-L. Xiong [f], S.-N. Zhang [f,g]

[a] *Department of Physics and Earth Science, University of Ferrara, via Saragat 1, I–44122, Ferrara, Italy*
[b] *INAF – Osservatorio di Astrofisica e Scienza dello Spazio di Bologna, Via Piero Gobetti 101, I-40129, Bologna, Italy*
[c] *INFN – Sezione di Ferrara, via Saragat 1, I–44122, Ferrara, Italy*
[d] *INAF, Osservatorio Astronomico d'Abruzzo, Via Mentore Maggini snc, 64100 Teramo, Italy*
[e] *Astrophysics Research Institute, Liverpool John Moores University, Liverpool Science Park IC2, 146 Brownlow Hill, Liverpool, L3 5RF, UK*
[f] *State Key Laboratory for Particle Astrophysics, Institute of High Energy Physics, Chinese Academy of Sciences, 19B Yuquan Road, Beijing 100049, China*
[g] *University of Chinese Academy of Sciences, Chinese Academy of Sciences, Beijing 100049, China*
[h] *School of Physics and Physical Engineering, Qufu Normal University, Qufu, Shandong 273165, China*

ARTICLE INFO

Keywords:
Gamma-ray bursts: individual
Gamma-ray bursts: general
Methods: statistical

ABSTRACT

Short gamma-ray bursts (SGRBs), occasionally followed by a long and spectrally soft extended emission, are associated with compact object mergers (COMs). Yet, a few recent long GRBs (LGRBs) show compelling evidence for a COM origin, in contrast with the massive-star core-collapse origin of most LGRBs. While possible COM indicators were found, such as the minimum variability timescale (MVT), a detailed and unique characterisation of their γ-ray prompt emission that may help identify and explain their deceptively long profile is yet to be found. Here we report the discovery of a set of distinctive properties that rule the temporal and spectral evolution of GRB 230307A, a LGRB with evidence for a COM origin. Specifically, the sequence of pulses that make up its profile is characterised by an exponential evolution of (i) flux intensities, (ii) waiting times between adjacent pulses, (iii) pulse durations, and (iv) spectral peak energy. Analogous patterns are observed in the prompt emission of other long COM candidates. The observed evolution of gamma-ray pulses would imply that a relativistic jet is colliding with more slowly expanding material. This contrasts with the standard internal shock model for typical LGRBs, in which dissipation occurs at random locations within the jet itself. We tentatively propose a few simple toy models that may explain these properties and are able to reproduce the overall time profile.

1. Introduction

At least two kinds of progenitors of gamma-ray bursts (GRBs) are known: (i) the core-collapse of some kind of massive stars (a collapsar; Woosley 1993; Paczyński 1998; MacFadyen and Woosley 1999); (ii) compact object mergers (COMs), in particular the coalescence of two neutron stars (NS; Eichler et al. 1989; Paczynski 1991; Narayan et al. 1992), or a NS with a black hole (BH). While the former class usually leads to a long ($\gtrsim 2$ s) GRB, the latter typically results in a short and hard GRB and, in the optical band, is expected to be associated with a kilonova (KN), radiation powered by the radioactive decay of r-process elements created in the aftermath of the merger (see Metzger 2020 for a review).

Although GRB duration was initially considered as an irrefutable property revealing the progenitor's nature, a number of baffling cases have recently been discovered: the apparently short GRB 200826A (Ahumada et al., 2021; Zhang et al., 2021; Rossi et al., 2022), which is instead associated with a core-collapse supernova (SN), or long GRBs (LGRBs) GRB 060614 (Della Valle et al., 2006; Fynbo et al., 2006; Jin et al., 2015), GRB 211211A (Rastinejad et al., 2022; Yang et al., 2022; Troja et al., 2022; Xiao et al., 2022), GRB 191019A (Levan et al., 2023; Stratta et al., 2025), for which a COM origin is strongly favoured. Furthermore, a subclass of events emerged —known as short GRBs with extended emission (SEE-GRBs)— which are characterised by an initial narrow, hard spike followed by a longer, softer tail (Norris and Bonnell, 2006). These events, possibly originating from mergers, further challenged the

---

* Corresponding author.
E-mail address: romain.maccary@edu.unife.it (R. Maccary).

https://doi.org/10.1016/j.jheap.2025.100456
Received 30 June 2025; Received in revised form 14 August 2025; Accepted 25 August 2025

reliability of GRB duration as a robust classification criterion. To avoid confusion, Zhang et al. (2009) referred to GRBs with a merger origin as Type I GRBs, and to collapsars as Type II GRBs.

Recent GRB 230307A was thrust into the spotlight thanks to its exceptional brightness along with its peculiar properties. On March 7, 2023, at 15:44:06.650 UTC, GRB 230307A triggered the Gravitational wave high-energy Electromagnetic Counterpart All-sky Monitor (GECAM; Li et al. 2020), which observed it without saturation effects (Xiong et al., 2023). Despite its long duration ($T_{90} \sim 30$ s), this burst shows several pieces of evidence for a COM origin. Indeed, its locations in the Amati (Amati et al., 2002; Amati, 2006) and Yonetoku planes (Yonetoku et al., 2004) fall outside the 90% confidence predictions for Type II GRBs (Svinkin et al., 2023), and a short minimum variability timescale (MVT) of around 30 ms—typical of Type I GRBs—is observed (Camisasca et al., 2023b). Moreover, the X-ray afterglow flux, rescaled by the early γ-ray emission fluence, is comparably faint to those of other long Type I GRBs. Most importantly, the optical transient associated with it and with a projected offset of 30 kpc from its host galaxy, showed photometric and spectroscopic evidence for the presence of a KN (Levan et al., 2024; Gillanders and Smartt, 2025), which tipped the balance towards a COM origin.

GRB 230307A exhibits a well-structured γ-ray light curve (LC), made of three distinct episodes: a short initial soft spike, identified as a precursor (Dichiara et al., 2023), shortly followed by a long and hard main emission preceding a softer extended emission, the main and the extended emission being separated by a dip-like feature. This three-phase structure has been claimed to be shared by some similar long Type I GRBs, possibly forming a sub-class of the Type I GRBs, referred to as Type IL GRBs (e.g. Wang et al. 2025; Tan et al. 2025). GRB 230307A shares many properties with GRB 211211A: both exploded at close distances ($z = 0.076$ for GRB 211211A and $z = 0.065$ for GRB 230307A), have short MVTs of a few ten ms, and are clear outliers of the Amati relation for Type II GRBs (Peng et al., 2024).

NS-NS and NS-BH mergers might struggle to produce GRBs as long as GRB 230307A, owing to their short accretion timescale. A white dwarf (WD) disrupted by a NS companion, producing a less compact remnant, might be able to last long enough to explain the GRB duration. Wang et al. (2024) argues that a WD-NS merger could lead to a magnetar that could power a long GRB and a KN. The soft X-ray light curve measured by the Lobster Eye Imager for Astronomy (LEIA; Zhang et al. 2022) presents a plateau followed by a steeper decay compatible with a magnetar spin-down model. Sun et al. (2025) shows that broad-band (soft X to γ-rays) observations of GRB 230307A revealed a distinct X-ray component, possibly due to a newly born magnetar. A magnetar as a GRB central engine would lead to a Poynting-flux dominated outflow, which is confirmed by the non-detection of a thermal component, implying a high magnetisation parameter ($\sigma > 7$ at radius $R_0 = 10^{10}$ cm) to suppress the expected photospheric emission (Du et al., 2024).

The emission mechanism powering GRB 230307A is uncertain. Moradi et al. (2024) carried out a systematic spectral and temporal analysis of *Fermi*/GBM and GECAM data and showed that the energy flux and the peak energy temporal evolution in the late prompt emission are not fully compatible with the predictions of the internal shock (IS) model (Rees and Meszaros, 1994; Kobayashi et al., 1997; Daigne and Mochkovitch, 1998), although uncertainties in the micro-physics of the shock region might be responsible for the observed discrepancies (Bošnjak and Daigne, 2014). Yi et al. (2025a) shows that the long broad pulse shaping the overall GRB 230307A time profile could be the result of many superimposed narrow pulses produced by local magnetic reconnection events, as foreseen by the Internal-Collision-Induced Magnetic Reconnection and Turbulence (ICMART; Zhang and Yan 2011) model. Yi et al. (2025b) proposed a model in which a brief energy injection from the central engine triggers turbulence in a small localised region. Turbulence then propagates radially as the jet expands forward, moving away from the central engine. This model predicts a single broad pulse that widens with decreasing energy ranges and progressively softens throughout the burst.

A progressive increase of the pulse width over time is a natural outcome of external shocks (ES). An intense debate emerged among the GRB community in the late 90s as to whether the dissipation mechanism into γ-rays was due to internal or external shocks (Fenimore et al., 1996; Dermer et al., 1999; Dermer, 2008). The absence of any timescale evolution along the profile of GRB 990123 (Fenimore et al., 1999) and of other long and multi-peaked GRBs tipped the balance towards ISs. In this respect, the temporal evolution of GRB 230307A, as well as of other similar events, might suggest a new distinctive hallmark of the elusive class of LGRBs that are COM candidates.

In this work, we focus on the GECAM LC in the 30-6000 keV passband: owing to the exquisite quality of the data, we could identify about one hundred peaks, thus enabling a statistical analysis, which is usually impossible for a single GRB. As a result, the prompt emission of GRB 230307A displays a set of distinctive properties, which suggest a different origin from the canonical LGRBs associated with the core-collapse of massive stars. Some of these properties are also observed in similar long-duration COM candidates mentioned above, as revealed by a preliminary analysis.

The identification and characterisation of this rare set of observed properties, which appear to distinguish COM candidates from most long GRBs, and particularly from collapsars, form the core of the present work. As a secondary objective, we tentatively propose a few possible toy models and interpretations that aim to account for these properties in a self-consistent way, discussing the advantages and limitations of each, without necessarily excluding alternative scenarios. Data analysis is reported in Section 2, results are presented in Section 3 and discussed in Section 4. Conclusions are drawn in Section 5. We adopted the cosmological parameter values from Planck Collaboration et al. (2020).

2. Data analysis

We obtained the GECAM background-subtracted LCs with 5 ms bin time in the following energy passbands: 30–70, 70–100, 100–150, 150–200, 200–300, 300–500, 500–1000, 1000–6000 keV, respectively. Background interpolation and subtraction were obtained as described in Zhang et al. (2025). In each of these profiles, peaks were identified by means of MEPSA, a flexible code that was specifically designed to identify peaks in GRB LCs across different timescales (Guidorzi, 2015). In this present study, we used both MEPSA and a faster version of it, which significantly reduces the computing time.[1]

Peaks were selected imposing a threshold of $S/N \geq 5$ on the signal-to-noise ratio calculated by MEPSA. Each peak is automatically characterised by the following pieces of information: peak time t_p and its uncertainty, which corresponds to the MEPSA detection timescale δt_p; peak amplitude A and its uncertainty; estimate of the full width at half maximum (FWHM) of the peak; S/N of the total net counts ascribed to the peak. The FWHM is estimated from the combination of MEPSA parameters as prescribed in eq. (A.3) of Camisasca et al. (2023a). We studied the evolution with time of peak times, FWHM, and of the waiting times (WT) Δt, defined as the time intervals between adjacent peaks. We also examined the evolution of $E_{\rm p}$, which is the peak of the νF_ν energy spectrum: its values were taken from Moradi et al. (2024).

Hereafter, we focus on the 100–150 keV band LC, which displays the largest number of peaks (103).

3. Results and interpretations

The analysis of the 100-150 keV profile revealed the following properties:

---

[1] It is ~ 100 times faster than classical MEPSA at the cost of losing $\sim 5\%$ of all the detected peaks. This is made possible by a sparser sampling of the rebinning factors and related phases. See Maistrello et al. (in prep.) for details.

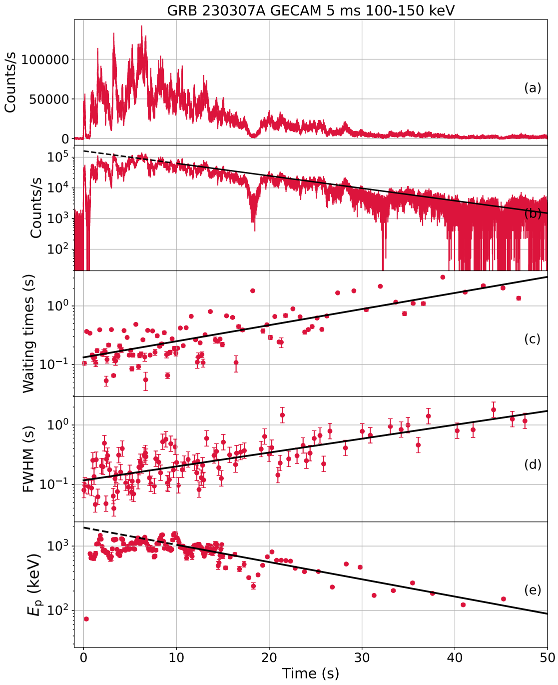

Fig. 1. Properties of GRB 230307A. (a) LC in the 100-150 keV band with 5-ms bin time. (b) same as (a), but in semi-logarithmic scale; (c) WTs of the peaks detected with MEPSA as a function of time; (d) FWHMs of the same peaks of (c) as a function of time; (e) time-resolved evolution of spectral peak energy. In panel (b), the solid line represents the exponential fit of the peak rates of the pulses. In panels (c), (d), and (e), solid lines show the exponential models obtained within the corresponding temporal window, whereas the dashed line, if present, shows the extrapolated fit to the time interval that was ignored by the fitting procedure.

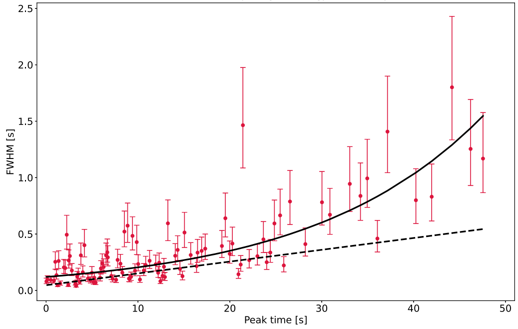

Fig. 2. FWHM evolution over time. Solid (dashed) line represents the exponential (linear) model.

1. the overall envelope of the LC looks like a so-called FRED. In particular, from $t > 10$ s the count rate decays exponentially, covering two decades, as shown in panels (a) and (b) of Fig. 1. Similarly, the peak rates of the pulses detected with MEPSA also evolve exponentially with time. Their evolution is described by Eq. (1):

   $$P(t) \simeq \; P_0\, e^{-t/\tau_p} \,, \tag{1}$$

   with $P_0 = (1.64 \pm 0.12) \times 10^5$ cts s^{-1} and $\tau_p = 10.7 \pm 0.4$ s. This model is shown in panel (b) of Fig. 1 along with the LC.
2. WTs evolve exponentially with time, spanning two decades, from ~ 0.1 to ~ 10 s, during the first 50 seconds, as described by Eq. (2),

   $$\Delta t \simeq \; \Delta t_0\, e^{t/\tau_{\Delta t}} \,, \tag{2}$$

   with $\Delta t_0 = 0.14 \pm 0.02$ s and $\tau_{\Delta t} \simeq 15.8$ s (panel (c) of Fig. 1).
3. The FWHM of the pulses detected by MEPSA also increases with time: it could be either exponential or linear, spanning more than one decade, from 0.1 s. If modelled with an exponential, this is described by Eq. (3),

   $$\mathrm{FWHM}(t) \simeq \; \mathrm{FWHM}_0\, e^{t/\tau_F} \,, \tag{3}$$

   with $\mathrm{FWHM}_0 = 0.12 \pm 0.01$ s and $\tau_F = 18.6 \pm 1.7$ s. Panel (d) of Fig. 1 shows the FWHM values as a function of time.
   We also performed a linear fit $\mathrm{FWHM} = \mathrm{FWHM}_0' + \alpha t$ (see Fig. 2) and obtained $\mathrm{FWHM}_0' = 0.05 \pm 0.01$ s and $\alpha = 0.010 \pm 0.001$, but the result appears to be worse than the exponential model. We fitted both linear and exponential models, $y = mx + q$, modelling the dispersion as a further parameter, by adopting the D'Agostini likelihood (D'Agostini, 2005). When we used $y = \mathrm{FWHM}$, the best-fit parameters are $m = 0.012 \pm 0.002$, $q = 0.077^{+0.026}_{-0.024}$ s, and $\sigma = 0.068^{+0.020}_{-0.017}$ s. Instead, when we use $y = \ln(\mathrm{FWHM/s})$, we find $m = 0.054 \pm 0.008$, $q = -2.14 \pm 0.14$, and $\sigma = 0.48^{+0.08}_{-0.07}$. The corresponding goodness of the fit was evaluated as $\chi^2 = \sum (y_i - y_{\mathrm{model},i})^2/\sigma^2_{\mathrm{tot},i}$, where $\sigma^2_{\mathrm{tot},i} = \sigma^2 + \sigma^2_{y,i} + m^2\sigma^2_{x,i}$, with $\sigma_{y,i}$ and $\sigma_{x,i}$ being the measurement uncertainties of the generic i-th point. We obtained $\chi^2_{\mathrm{lin}} = 134$ and $\chi^2_{\mathrm{exp}} = 99.6$ (100 degrees of freedom).
4. The evolution of the peak energy, E_p, from $t > 10$ s can also be described as a negative exponential,

   $$E_p(t) \simeq \; (1940 \pm 150 \text{ keV})\, e^{-t/\tau_E} \,, \tag{4}$$

   with $\tau_E = 16.2 \pm 0.9$ s (see panel (e) of Fig. 1).

Equations (1)–(4) were fitted using a nonlinear least squares algorithm (applied on the logarithmic quantities), accounting for y-axis errors. Parameter uncertainties were estimated as the square root of the covariance matrix diagonal.

3.1. A simple toy model

Typically, long and multi-peaked GRB LCs do not show any specific evolution of WTs: moreover, this lack of systematic evolution represents one of the pillars of the IS model as opposed to the ES model as a possible explanation of GRB prompt emission (Fenimore et al., 1999). In this respect, the exponential evolution of WTs exhibited by GRB 230307A is enough to make it stand out from the population of long and multi-peaked GRBs. Hence, inspired by the unusual WT evolution, we conceived a toy model that can naturally account for it, along with the other observed properties described in Section 3.

The sequence of peak times $t_{p,i}$ ($i = 1, \ldots, N_p$), where N_p is the total number of peaks, can be described in terms of a stochastic point process: each peak time marks the occurrence of an event. In this toy model, there are initially N_0 elementary bunches of energy, which share the same probability of "decaying" (= releasing their amount of energy within a single shot that manifests itself as a pulse) as well as the same amount of (bolometric) energy. They "decay" or release their energy independently of one another. From these simple assumptions, which are the same that rule the radioactive decay of a bunch of N_0 atoms of a given element, the exponential distribution of the peak (or release) times $\{t_{p,i}\}$ follows as a consequence. In particular, the mean number of energy bunches still available at time t, $N(t)$, is simply given by:

$$N(t) \; = \; N_0\; e^{-t/\tau} \,, \tag{5}$$

where τ is the mean lifetime of each bunch. This model predicts the temporal evolution of the expected (or mean) WT, as

$$\langle \Delta t \rangle \;=\; -\frac{1}{\dot{N}(t)} \;=\; \frac{\tau}{N_0}\, e^{t/\tau}\,, \tag{6}$$

which accounts for the observed property modelled in Eq. (2).

The toy model aims to reproduce a surrogate version of the LC to be compared with that of GRB 230307A. The key idea is that the LC is the result of the superposition of elementary pulses, whose properties are governed by a few assumptions, which are hereafter defined along with the corresponding model parameters:

- N_0 peak times are sampled from an exponential distribution with e-folding time τ, in agreement with Eq. (5);
- pulse FWHMs are calculated assuming Eq. (3), where FWHM_0 and τ_F are treated as free parameters;
- the counts of each pulse is constant and is parametrised by $N_{\rm cts}$;
- the peak rate P of a given pulse is calculated by dividing the counts by the corresponding FWHM: this choice is corroborated by the fact that τ_p of Eq. (1) is not wildly different from τ_F of Eq. (3). By doing so, we are implicitly assuming that the peak rate decay and the FWHM rise evolve on a common timescale, τ_F. This assumption is not driven by any specific theoretical interpretation but rather stems from the observation of the data and adopting Occam's razor. To model the fact that the overall LC shows a finite rise time, we added an extra term that accounts for the suppressed flux of the initial pulses over a timescale described by the parameter τ_r, which acts as the rise time. As a result, peak rates are calculated as a function of the corresponding peak times t_p as

  $$P(t_p) = \frac{N_{\rm cts}}{\mathrm{FWHM}_0}\; e^{-t_p/\tau_F}\; (1 - e^{-t_p/\tau_r})\,. \tag{7}$$

  The corresponding additional free parameter is τ_r.
- Concerning the pulse shape, with reference to the Norris et al. (1996) model, the peakedness is fixed to $\nu = 2$, while the decay-to-rise time ratio r to 3 for all pulses. Since the FWHM is calculated for each pulse, rise and decay times are consequently computed as $t_r = \mathrm{FWHM}/((1+r)(\ln 2)^{1/\nu}) \simeq \mathrm{FWHM}/3.33$ and $t_d = r t_r$, respectively.

3.2. Physical model 1: multiple shells emitted with equal Lorentz factors

In the toy model of Section 3.1, the FWHM is assumed to evolve exponentially. Here, we adopted another FWHM evolution, derived from shock kinematics. In this model, the central engine is working in the same way as in Section 3.1, but, in addition, the train of shells emitted by the central engine is colliding with a so-called target shell. The target shell is expanding, so successive shocks occur at increasing radii. The target shell could have been expelled some time before the train of shells or right at the beginning of the merger. Alternatively to the target shell, the various shells might be refreshing the external blast wave, as it was suggested in the refreshed shock scenario to explain long-lived afterglows (Rees and Meszaros, 1998). The origin of the target shell is further discussed in Section 4.

To be more quantitative, we let $t_{e,i}$ be the emission time (lab frame) of the i-th shell. All shells are emitted with the same velocity $\beta = v/c$, whereas the target shell is moving with $\beta_s = v_s/c < \beta$. We let R_0 be the initial radius of the target shell at $t = 0$, when the first shell is emitted. We define $t_{c,i}$ the collision time (lab frame) of the i-th shell, which takes place at radius $R_{c,i}$. Since different collisions take place at different radii, the WTs measured by the observer will appear shorter than the corresponding WTs in the lab frame: to avoid confusion, the observed collision times are denoted as $t_{c,i}^{\rm (obs)}$ and are measured by the observer since the arrival of the first pulse. The kinematic solution for these quantities is

$$t_{c,i} \;=\; \frac{R_0}{v - v_s} + \left(\frac{v}{v - v_s}\right) t_{e,i}\,, \tag{8}$$

$$t_{c,i}^{\rm (obs)} \;=\; \left(\frac{\beta}{\beta - \beta_s}\right)(1 - \beta_s)\, t_{e,i}\,, \tag{9}$$

$$R_{c,i} \;=\; \left(\frac{\beta}{\beta - \beta_s}\right)(R_0 + v_s\, t_{e,i})\,. \tag{10}$$

From Eq. (9) the observed WTs, $\Delta t_{c,i}^{\rm (obs)}$, inherit the same exponential temporal evolution of the lab-frame WTs, $\Delta t_{e,i}$. The duration of each pulse is given by the angular timescale: because of the progressive expansion of the target shell, durations are predicted to increase linearly with time,

$$\mathrm{FWHM}_i \;=\; \frac{R_{c,i}}{2c\Gamma^2} \;=\; \frac{1}{2c\Gamma^2}\left(\frac{\beta}{\beta - \beta_s}\right)(R_0 + v_s\, t_{e,i})\,. \tag{11}$$

That the velocity of the target shell would change only negligibly could be explained by its being more massive than the faster shells. If both fast and target shells are relativistic, the term $\beta/(\beta - \beta_s)$ is approximately $2\Gamma^2/((\Gamma/\Gamma_s)^2 - 1)$. In particular, Eqs. (9) and (11) would become,

$$t_{c,i}^{\rm (obs)} \;\simeq\; \frac{1}{1 - (\Gamma_s/\Gamma)^2}\; t_{e,i}\,, \tag{12}$$

$$\mathrm{FWHM}_i \;\simeq\; \frac{R_0/c + \beta_s\, t_{e,i}}{(\Gamma/\Gamma_s)^2 - 1}\,. \tag{13}$$

Within this interpretation, from Eq. (11), FWHM is expected to grow linearly with time, in possible agreement with observations. Hence, to simulate the model, we replaced Eq. (3) with Eq. (11), and modified Eq. (7) to take into account the linear evolution of the FWHM. Furthermore, the emission times $t_{e,i}$ are still generated from an exponential distribution, but need to be transformed into the observed collision times, using Eq. (9).

We initially assumed a non-relativistic target shell, $\beta_s < 1$. This led to an untenable physical solution, in particular because of the compactness problem[2] (see Sect. 3.5). We consequently adopted Γ_s instead of β_s as a more convenient parameter, implicitly assuming an ultra-relativistic motion for the target shell.

3.3. Physical model 2: multiple shells emitted with gradually decreasing Lorentz factors

This model is almost the same as the previous one described in Section 3.2, except for one assumption: the Lorentz factors of the different shells decrease with the emission times, so that later shells are slower. In this model, the previous equations Eqs. (8)–(11) are still valid, but since the Lorentz factor is changing from one emitted shell to another, Γ has to be replaced by $\Gamma_i \equiv \Gamma(t_{e,i})$. Prompted by the exponential evolution of FWHM and peak energy (Eqs. (3) and (4)), we parametrised the temporal evolution of $\Gamma(t)$ as

$$\Gamma(t) = \Gamma_0 e^{-t/\tau_\Gamma}\,. \tag{14}$$

Instead of Γ of the model of Sect. 3.2, this scenario requires a couple of new parameters, Γ_0 and τ_Γ, through which each Γ_i is calculated.

3.4. Genetic algorithm based parameter optimisation

We determined the free parameters of each model using a genetic algorithm (GA; see Bazzanini et al. 2024; Maistrello et al. 2025 for similar usages). The loss function to be minimised by the GA consists of four different contributions. Each term aims to ensure that the corresponding property of the real LC of GRB 230307A is correctly reproduced by the simulated LC. The four properties include:

1. similar envelopes (smoothed time profiles);

---

[2] In this case, we obtained $\beta_s \sim 0.4$, $R_0 = 3 \times 10^{10}$ cm, and $\Gamma \sim 6.5$, implying sub-photospheric shocks between 5×10^{10} and 10^{12} cm, with pair-production opacity $\tau_{\gamma\gamma}$ (computed in Sect. 3.5) remaining extremely high (from 10^9 initially to 10^7) throughout the burst.

Table 1
Parameters of the three GRB emission models used to reproduce the temporal evolution of GRB 230307A.

Parameter	Toy Model	Physical Model 1 (Constant Γ)	Physical Model 2 (Declining Γ)
N_0	862^{+1}_{-25}	1270^{+110}_{-90}	894^{+21}_{-101}
τ [s]	$10.9^{+0.1}_{-0.5}$	$10.9^{+1.0}_{-2.3}$	$10.1^{+1.4}_{-0.8}$
FWHM_0 [s]	$0.05^{+0.01}_{-0.01}$	—	—
τ_F [s]	$14.0^{+0.2}_{-0.4}$	—	—
τ_r [s]	$2.5^{+0.1}_{-0.7}$	$2.9^{+0.3}_{-0.5}$	$3.4^{+0.7}_{-0.9}$
N_{cts}	1449^{+26}_{-5}	920^{+30}_{-20}	1431^{+49}_{-20}
Γ or Γ_0	—	94^{+8}_{-1}	339^{+18}_{-20}
Γ_s	—	$8.6^{+0.1}_{-0.4}$	$26.2^{+0.5}_{-0.5}$
τ_Γ [s]	—	—	96^{+30}_{-17}
R_0 [cm]	—	$9.1^{+3.8}_{-1.5} \times 10^{10}$	$1.4^{+0.4}_{-0.3} \times 10^{11}$

2. compatible distributions of peak times;
3. comparable numbers of peaks detected with MEPSA;
4. compatible distributions of FWHM values.

A detailed description of the GA-based optimisation procedure is reported in Appendix A.

3.4.1. Results for the toy model

The best model parameters that we have come up with for the toy model of Sect. 3.1 are shown in Table 1. We converted the pulse counts N_{cts} to fluence N_F in erg cm^{-2}. This was done by multiplying N_{cts} by the fluence-to-counts ratio R computed using the values of the time-resolved spectral modelling of Moradi et al. (2024). For a constant N_{cts}, N_F decreases with time; thus, we adopted an average value of 1.8×10^{-7} erg cm^{-2} in the 100-150 keV energy range. After applying the k-correction, the fluence of a single shot over the full energy band (6-8000 keV) is 3.9×10^{-6} erg cm^{-2}, which, placed at a distance of 300 Mpc ($z = 0.065$), corresponds to an isotropic-equivalent energy of $\sim 4.1 \times 10^{49}$ erg. Given that the total time-integrated fluence is 4.8×10^{-3} erg cm^{-2}, the fluence of a single elementary pulse, multiplied by the number of pulses, roughly matches the total GRB fluence. The central engine is emitting numerous energy bunches with an average energy of 4.1×10^{49} erg. Earlier bunches are more energetic, ranging from 2.5×10^{50} all the way down to 1×10^{48} erg.

Noticeably, the intrinsic number of bunches of energy, N_0, which is also the number of intrinsic peaks that make up the overall profile, is about ten times higher than the number of MEPSA-detected peaks (1000 vs 100). This result suggests that the observed LC consists of a myriad of short overlapping peaks, which blend together and appear as fewer, broader peaks.

We generated a synthetic profile and compared it and its properties with the corresponding real ones: Fig. 3 shows the overall LC in both linear (a) and logarithmic scale (b). The temporal evolution of WTs and of FWHMs of the peaks detected with MEPSA are displayed in panels (c) and (d), respectively. All the temporal properties that are found in the real data are faithfully reproduced by the synthetic profile. A possible weakness of this model is that the broad dip observed at 20 s can hardly be reproduced in its depth.

3.4.2. Results for the physical models

The results for the constant-Γ scenario (Section 3.2) and for the declining-Γ factor scenario (Section 3.3) are shown in Table 1. Fig. 4 shows the corresponding results analogously to Fig. 3. In the last scenario considered, the results show that Γ decreases relatively slowly for the model to reproduce the observed GRB time profile. Assuming a constant fluid-comoving-frame peak energy—thus attributing all observed peak energy variation to a decreasing Γ—is ruled out. In fact, a decay timescale of $\tau_\Gamma \sim 100$ s is not short enough to explain the drop seen in Panel (e) of Fig. 1. The observed peak energy decline should be a consequence of the decreasing shock energy density resulting from the expansion of the emission radius.

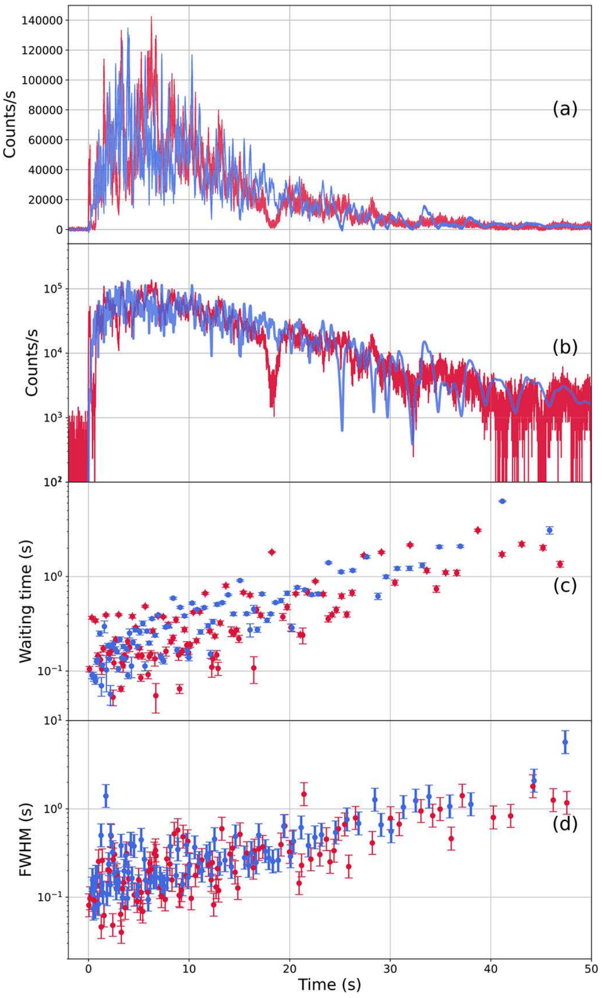

Fig. 3. Panels (a) and (b) illustrate the temporal evolution of count rates, (a) in linear and (b) in logarithmic scale. Panels (c) and (d) show the temporal evolution of the WTs and of the pulse FWHMs, respectively. Red points show real data, while blue points are simulated according to the toy model of Section 3.1.

Journal of High Energy Astrophysics 49 (2026) 100456

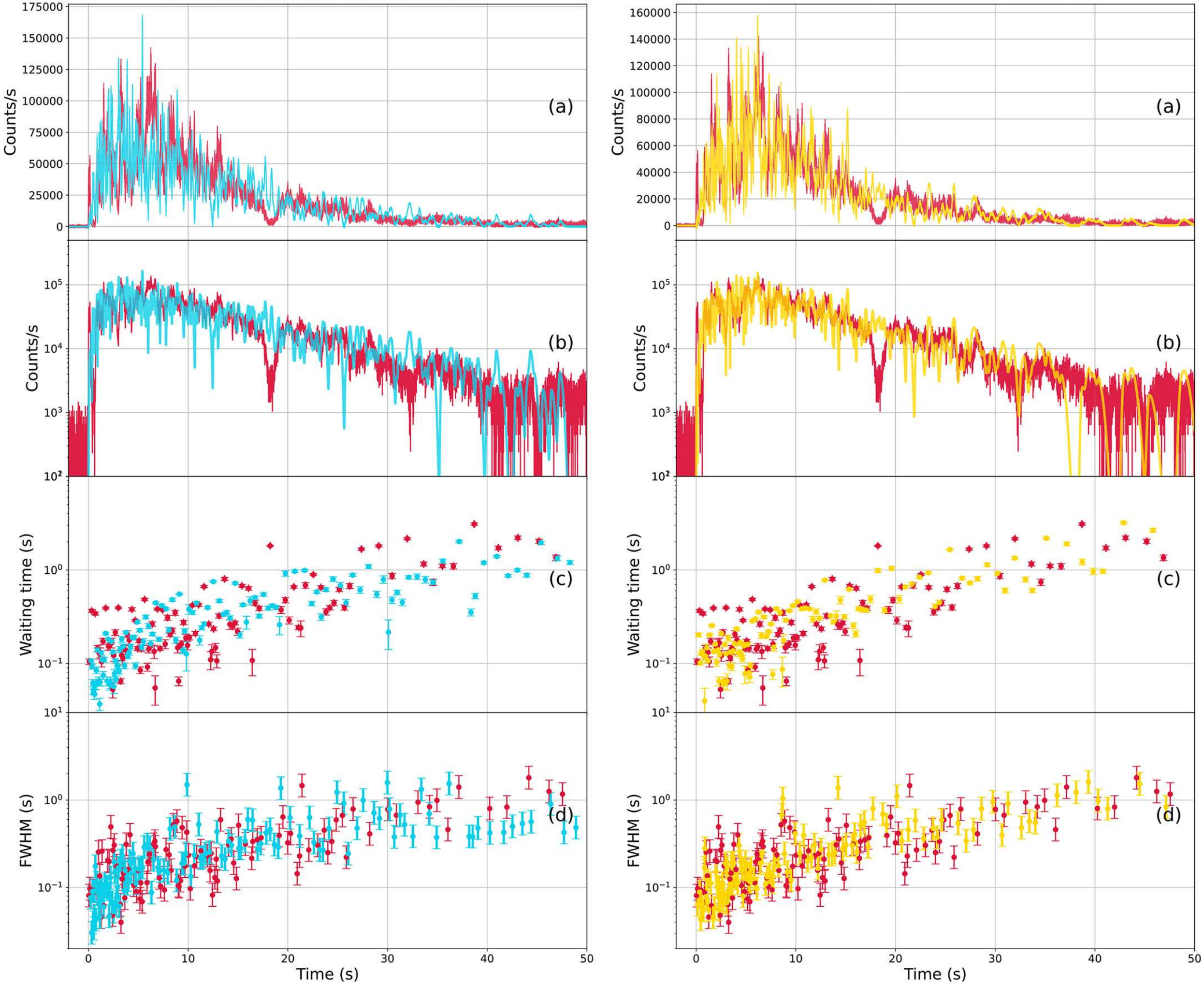

Fig. 4. Same as in Fig. 3, for the physical model with a wind of shells with constant Γ described in Section 3.2 (left panel) and the one with declining Γ's described in Section 3.3 (right panel). Real data are shown in red, while simulated data from constant and declining Γ model are shown in cyan and yellow, respectively.

3.5. Testing the physical constraints: compactness problem, photosphere, and internal shock radii

We verified that the compactness problem is not an issue for our model. To this aim, we have computed the optical depth to pair production

$$\tau_{\gamma\gamma} = \frac{f_p \sigma_T \phi D_L^2}{\Gamma^3 R_e^2 m_e c^2}, \tag{15}$$

with f_p the fraction of photons making pairs, σ_T the Thomson scattering cross section, ϕ the fluence, D_L the luminosity distance, R_e the emission radius, m_e the electron mass, and c the speed of light (Piran, 2004). We evaluated $\tau_{\gamma\gamma}$ at early and late times, taking for R_e the radius of the first and last shocks, respectively. Given that the first pulses produced by the model have a width of about 25 ms, from Eq. (11) the initial shock radius is about 1.3×10^{13} cm and $\tau_{\gamma\gamma} \simeq 19 \times f_p$, while for the last wider pulses of about 1 s, the opacity drops to $\tau_{\gamma\gamma} = 1.2 \times 10^{-2} \times f_p$. The high initial opacity may account for the early rise in the observed flux, which in our model is modelled by the rise time τ_r. Consequently, the rising phase could reflect the transition from an initially optically thick to an optically thin regime as the emitting region expands.

We also computed the photospheric radius, $R_{\rm ph}$, to evaluate whether any emission in our model could originate below the photosphere, which would typically give rise to a thermal spectral component not observed in the data

$$R_{\rm ph} = \frac{L \sigma_T}{8\pi m_p c^3 \Gamma^3}, \tag{16}$$

here L is the isotropic luminosity, m_p the proton mass (Daigne and Mochkovitch, 2002). Using $L = 7.6 \times 10^{51}$ erg s^{-1} (Svinkin et al., 2023), it is $R_{\rm ph} = 5.5 \times 10^{12}$ cm, which is lower than the radius of the first shocks (1.3×10^{13} cm). Hence, all shocks in our model occur above the photosphere, consistent with the absence of a detectable thermal component in the prompt emission spectrum.

Finally, we verified that internal shocks between two fast shells do not occur before the collision with the target shell. While some variability in the ejection velocities is expected and may lead to internal shocks among the fast shells themselves, we computed the corresponding internal shock radius using

$$R_{\rm IS} = \Gamma^2 c \Delta t, \tag{17}$$

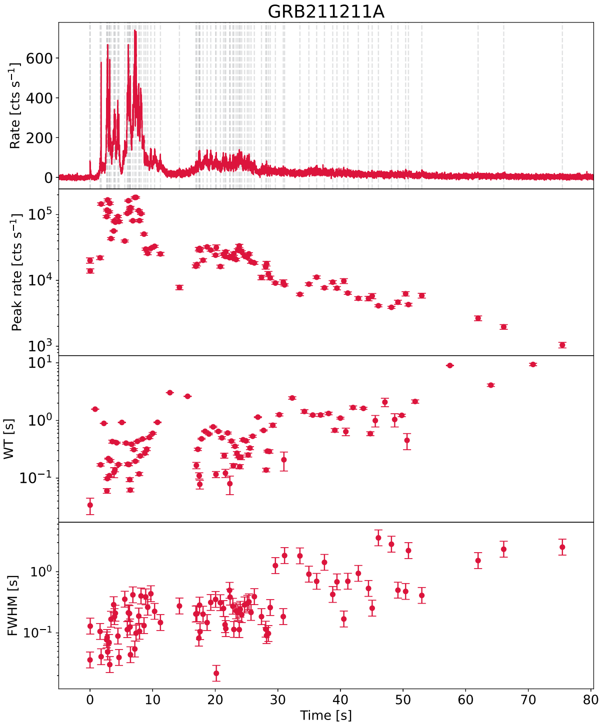

Fig. 5. GRB 211211A *Fermi*/GBM 8-1000 keV LC binned at 4 ms.

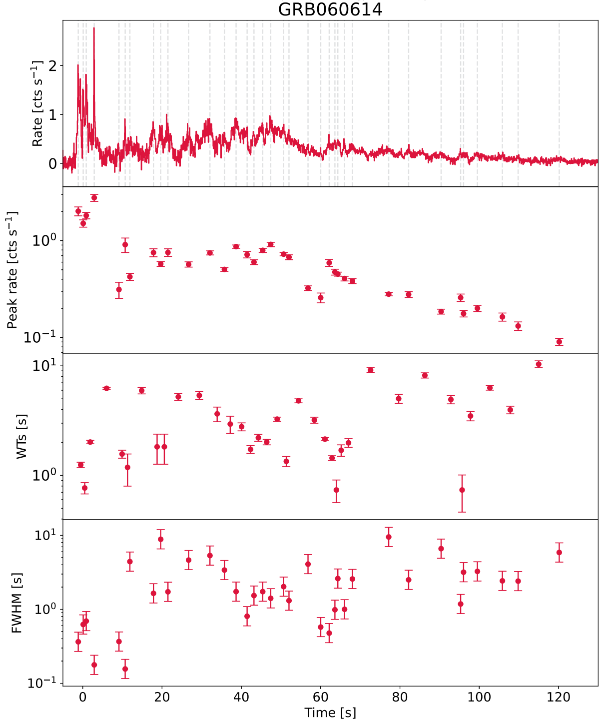

Fig. 6. GRB 060614 *Swift*/BAT 15-350 keV LC binned at 64 ms.

where Δt represents the time interval between the emission of two consecutive shells (Daigne and Mochkovitch, 1998). Assuming a typical value of $\Delta t = 0.1$ s for the early shells, we found $R_{IS} \simeq 2.6 \times 10^{13}$ cm, which lies beyond the radius of the first shock with the target shell. Since the WTs increase more rapidly than the pulse widths, $R_{\rm IS}$ continues to grow and remains larger than the radius of the shocks between the fast and target shells. This confirms that the shell collisions between the fast shells and the slow target shell always occur before any possible internal shocks between fast shells.

3.6. *Similar analysis of other known long COM candidates*

We carried out a similar and preliminary analysis to other known LGRBs that are COM candidates with enough peaks: GRB 211211A and GRB 060614. Figs. 5 and 6 illustrate that these events exhibit similar trends as those observed in GRB 230307A, suggesting that such properties might be characteristic of this subclass of GRBs. A more detailed analysis of their temporal evolution is reported in Appendix B. To test whether these properties can be taken as indicators of a COM origin, we applied the same analysis to a LGRB with enough peaks and that is associated with a Ic broad-lined supernova and for which, therefore, a merger origin is excluded with confidence.

To this aim, the well-known naked-eye burst GRB 080319B (Racusin et al., 2008) represents an ideal test-bed: the exceptional quality of its *Swift*/BAT 15–150 keV spiky LC offers an excellent opportunity to detect possible temporal trends in WTs and FWHMs. However, as shown in Fig. 7, no such evolution of WTs or of FWHMs with time emerges, in full agreement with an IS interpretation. We extended the same test to the other known SN-associated GRBs having a LC with a suitable number of detected peaks for the same analysis to be applied. To this aim, we could identify six SN-GRBs, in addition to the extraordinary case of GRB 221009A: their analysis is reported in Appendix C. As a result, none of them exhibits the systematic exponential evolution of WT and of FWHM seen in GRB 230307A (see Fig. C.11). Further analysis involving a larger sample of GRBs is planned for future work, but the current examples already suggest that such temporal characteristics can serve as valuable indicators to identify long COM candidates from their prompt emission profile.

4. Discussion

Contrary to the majority of multi-peaked LGRBs, GRB 230307A remarkably displays a number of properties that evolve with time exponentially. For other COM candidates, it was already found that both $E_{\rm p}$ and X-ray luminosity appear to decline exponentially with time (Gompertz et al., 2023): in this respect, our findings reinforce the role of an exponential evolution for the COM candidates and extend it to other properties, such as peak times, durations, WTs, and peak rates of the pulses that make up the GRB prompt emission.

The deterministic evolution of WTs and of FWHMs with time observed in GRB 230307A directly clashes with the key idea of the IS model, which was conceived at the time to explain the apparent lack of evolution of timescales within a number of BATSE bursts (Fenimore et al., 1999). Rather, the systematic increase of pulse durations with time, as pointed by the FWHM evolution, agrees with the expectations of a simple ES model: as the blast wave expands, the duration of pulses, supposedly caused by interactions with the medium inhomogeneities, increases with time (Fenimore et al., 1996; Dermer et al., 1999; Dermer, 2008).

4.1. *Emission from multiple shells emitted by the central engine*

Our model assumes that multiple shells (corresponding to the energy bunches described in Section 3.1) are emitted by the central engine and are colliding with either a previously emitted, more massive target shell that is expanding more slowly, or alternatively with the external blast wave as it was suggested to explain long-lived afterglows in the so-called refreshed shocks scenario (Rees and Meszaros, 1998). To ac-

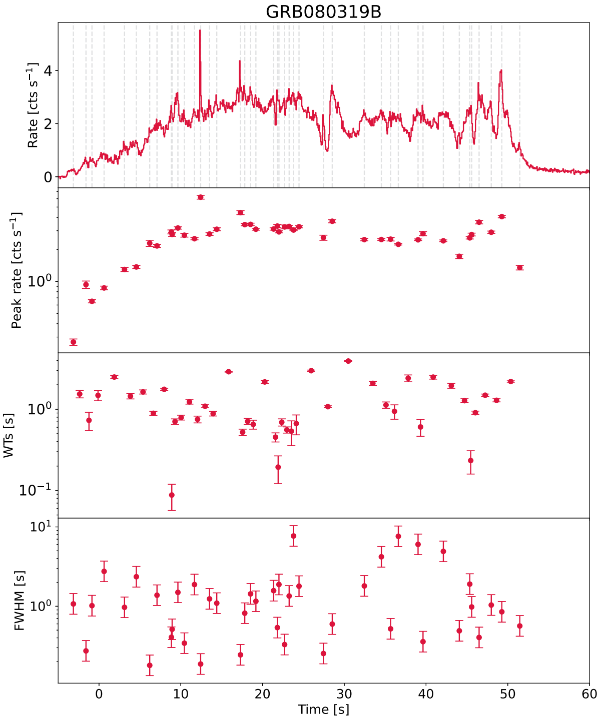

Fig. 7. Naked-eye burst GRB 080319B *Swift*/BAT 15-350 keV LC binned at 64 ms. Unlike COM candidates GRB 230307A, GRB 211211A, and GRB 060614, this collapsar event does not show the same monotonic evolution of the various observables.

count for the observed rapid variability and high-energy emission in the gamma-ray band – rather than in the optical – the collisions must occur at relatively small radii ($\sim 10^{13}$ cm), as discussed in Section 3.5. If the target shell corresponds to an external blast wave, the deceleration radius of the jet (or the radius at which a significant portion of jet begins to decelerate) must lie within the collision radius. This would imply that the merger occurred in an unusually high-density environment, and a bright afterglow would be expected. However, a low circumburst density of approximately 10^{-5}–10^{-4} cm^{-3} is required to explain both the non-detection of GeV emission and the multi-band afterglow data for this event (Dai et al., 2024). Therefore, the refreshed shock scenario – where the target shell is a blast wave – is disfavoured by these observations.

A plausible candidate for the slowly expanding target shell is the dynamical ejecta produced during the merger (e.g., neutron star–neutron star merger). Tidal interactions and shocks experienced by the neutron stars near the time of coalescence lead to the ejection of material on a dynamical timescale (e.g. Dietrich and Ujevic 2017; Radice et al. 2018; Shibata and Hotokezaka 2019; Rosswog et al. 2025). The tidal component of the dynamical ejecta is launched first, predominantly along the orbital plane, followed by a more isotropic, shock-driven ejecta component. Although the bulk of the merger ejecta is sub-relativistic, material along the rotational (jet) axis may be further accelerated by the leading edge or early-ejected component of the relativistic jet. Since the first interaction likely occurs well inside the photosphere, the associated shock radiation would be totally suppressed. Instead, the shock energy is efficiently converted into the bulk kinetic energy of the target shell (Kobayashi et al., 2002). Given the low baryon contamination along the jet axis, a significant boost in velocity may be achievable.

Another, more ad hoc possibility relates to the nature of the central engine. Since the jet acceleration process is still poorly understood, it is possible that the engine initially ejects a slower, more massive shell, followed by faster, less massive ejecta. In our model, the initial radius of the target shell is 9×10^{10} cm. Given its relativistic velocity, this suggests that the massive, slow shell was expelled approximately 3 seconds prior to the rest of the ejecta in this scenario.

The central engine may be powered by a black hole accretion disc, into which fragmented material accretes independently. The accretion of each fragment leads to the ejection of a shell, which subsequently collides with the slower target shell at progressively larger radii. This simple toy model predicts a sequence of pulses that can be described as a piecewise Poisson process, whose shot rate gradually decreases with time (for further details, see Guidorzi et al. 2015). This mechanism explains the exponential distribution of the peak times as well as the exponential evolution with time of their WTs expressed by Eq. (6). In the so-called toy model, the FWHM evolution is phenomenological: to match the observed trend, an exponential evolution seems at first sight the best solution. However, the evolution of the FWHM could be directly inferred from shock kinematics, using Eq. (11).

We considered possible evolutions of the Lorentz factor Γ of the various shells: (i) approximately constant (Sect. 3.2); (ii) gradually decreasing with time (Sect. 3.3). In scenario (i), the FWHM is increasing linearly with time. Alternately to (i), scenario (ii) assumes a gradually decreasing Lorentz factor: this naturally explains both the evolution of FWHM, which can also be stronger than linear, as well as a decreasing Doppler boosting. In scenario (ii), the pulses' broadening and the spectral softening share a common explanation. The decaying E_p could either indicate a gradually decreasing efficiency of the shocks in particle acceleration (i), or be due to a time decreasing Doppler boosting (ii). Fig. 8 illustrates both possibilities. The dip observed in the light curve is not neatly reproduced by our toy models. Yi et al. (2025a) interpreted the dip as a gap between two fast mini-jet pulses, implying that GRB 230307A's time profile consists solely of short pulses without a slow variability component. Our model builds on the same assumption and also produces dips, most of which are less pronounced than the observed one, though. Alternative explanations include a temporary shutdown of the central engine or absorption/geometrical blocking along the line of sight. Given the rarity of this feature (possibly unique), stochasticity cannot be ruled out as its cause.

An alternative scenario invokes a central engine emitting a single shell, that is then expanding. In this scenario, the GRB emission could be due to: (a) an external shock between the expanding shell and inhomogeneities (clumps) present in the circumburst medium (Fenimore et al., 1996; Dermer et al., 1999; Dermer, 2008), or (b) magnetic reconnection events happening within the expanding shell, as proposed by Yi et al. (2025b). In both cases, the late, soft, and broad emission could be due to high-latitude photons arriving from large angles with respect to the line of sight. A major drawback of (a) is that the rate of shocked clumps, under the simple assumption of a spatially homogeneous distribution of clumps, should increase with time, whereas a decreasing rate of pulses is observed. The only way out would be assuming that the clumps are spatially clustered around the jet axis, which should roughly coincide with the line of sight, — a rather contrived assumption.

In (b) the emission arises from magnetic reconnection within a single expanding shell. A brief energy injection from the central engine triggers turbulence near the jet axis, which then spreads across the shell, producing delayed emission in expanding rings. This process leads to a broad pulse and naturally explains the observed spectral softening and the softer-wider/softer-later behaviour seen in GRBs like GRB 230307A. Table 2 summarises the different theoretical interpretations of the temporal and spectral properties observed in GRB 230307A.

5. Summary and conclusions

We discovered new features in the GRB 230307A time profile using exquisite data from GECAM. In particular, the waiting times, peak rate, pulse FWHM, and peak energy follow a characteristic exponential evolution over time. We show that these properties are also present in other

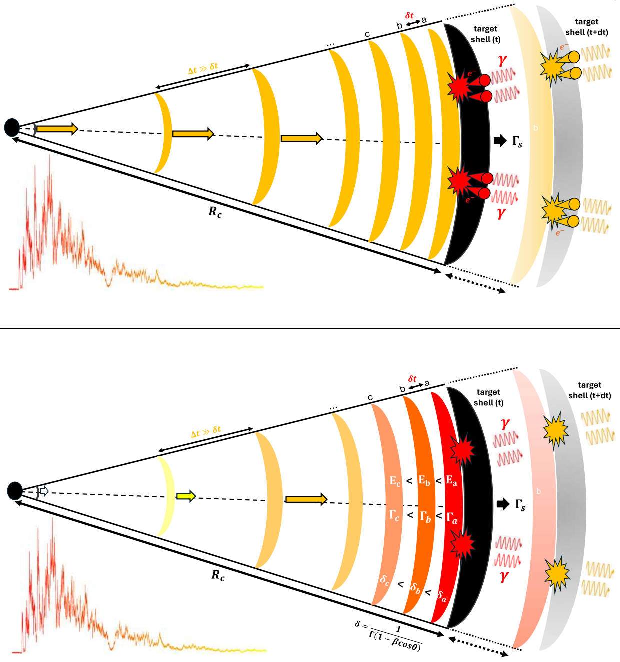

Fig. 8. Sketch of the emission from multiple shells in the (i) constant Lorentz factor (Sect. 3.2) model (top panel) and in the (ii) decreasing Lorentz factor (Sect. 3.3) model (bottom panel). Energy bunches emitted from the central engine collide with a slower target shell (shown in black) that was emitted earlier by the central engine. In (i), all shells nearly have the same Lorentz factor, while in (ii) the later-emitted shells (in yellow or light orange) are slower and carry less energy than the earlier ones (in deep orange and red). The first shocks correspond to the intense and narrow peaks observed in the early prompt emission of GRB 230307A, while the later shocks are associated with the dim and broad pulses seen in the extended emission phase.

Table 2
Summary of the different theoretical interpretations of the observed temporal and spectral properties of GRB 230307A.

Observed properties	Single shell model	Multiple shells model
Evolution of the peak rates	FRED shape expected	FRED envelope formed as a superposition of the shots
Evolution of the peak times/waiting times	constrained spatial distribution of the clumps	fading central engine activity
Evolution of the FWHM	high latitude emission and increasing emission radius	slower late emitted shells
Evolution of the peak energy	high latitude emission and increasing emission radius	slower late emitted shells

long GRBs, that are merger candidates, suggesting the existence of a new subclass of long GRBs—so-called type IL—as proposed in the literature (Wang et al., 2025; Tan et al., 2025). These would originate from compact object mergers rather than from collapsars, as is typical for classical long GRBs. We built a toy model that is able to accurately reproduce GRB 230307A light curve, which we optimised using a genetic algorithm. We proposed different theoretical scenarios to explain the observed trends, assuming either a central engine emitting multiple shells that collide with previously ejected material, or a single shell that expands and dissipates its energy progressively at larger radii. We also revisit the idea that external/refreshed shocks could explain prompt emission variability. While this scenario was previously disfavoured due to the apparent lack of timescale evolution within a sample of BATSE bursts, we show that the main criticisms that were historically used to support internal shocks as opposed to an external shocks interpretation of the GRB prompt emission, do not apply to GRB 230307A, whose FWHMs clearly increase over time.

In summary, while our toy and physical models are attempts to account for the unprecedented observed phenomenology within self-consistent pictures, alternative interpretations cannot be excluded in principle. Yet the fact remains that GRB 230307A, along with other long compact object mergers candidates, exhibits a set of properties that is rarely seen in any other long GRBs, especially in GRBs with associated SNe that are currently known. Such a potentially distinctive signature of this class of GRBs may help their identification and challenges our current understanding of how GRB central engines operate.

Identifying clear prompt γ-ray signatures of events coming from compact object mergers is particularly relevant in an era where new space missions such as the *Space-based multi-band astronomical Variable Objects Monitor* (SVOM; Atteia et al. 2022) and *Einstein Probe* (Yuan et al., 2022) are capable of performing prompt X-ray and optical follow-up of merger candidates, consequently enhancing the chances of coincident gravitational wave detection.

CRediT authorship contribution statement

R. Maccary: Writing – original draft, Visualization, Software, Methodology, Formal analysis, Data curation, Conceptualization. **C. Guidorzi:** Writing – review & editing, Validation, Supervision, Software, Methodology, Conceptualization. **M. Maistrello:** Writing – review & editing, Validation, Software. **S. Kobayashi:** Writing – review & editing, Validation. **M. Bulla:** Writing – review & editing, Validation. **R. Moradi:** Writing – review & editing, Resources. **S.-X. Yi:** Writing – review & editing, Resources. **C.W. Wang:** Writing – review & editing, Resources. **W.L. Zhang:** Writing – review & editing, Resources. **W.-J. Tan:** Writing – review & editing, Resources. **S.-L. Xiong:** Writing – review & editing, Resources. **S.-N. Zhang:** Writing – review & editing, Resources.

Table A.3
Loss function values from the genetic algorithm optimization for the three models.

Loss Component	Toy Model	Model 1 (Constant Γ)	Model 2 (Declining Γ)
$L_{\rm Np}$ (number of peaks)	0.091	0.370	0.181
$L_{\rm peak}$ (peak times)	0.000	0.000	0.000
$L_{\rm FWHM}$ (FWHM dist.)	1.160	0.047	0.012
$L_{\rm avgd}$ (smoothed profile)	0.860	0.935	0.770
Total loss $L_{\rm tot}$	**0.527**	**0.340**	**0.241**

Declaration of competing interest

The authors declare that they have no known competing financial interests or personal relationships that could have appeared to influence the work reported in this paper.

Acknowledgments

We are grateful to the anonymous reviewer for their valuable report, which helped us improve the quality of this work. R.M. and M.M. acknowledge the University of Ferrara for the financial support for their PhD scholarships. M.B. acknowledges the Department of Physics and Earth Science of the University of Ferrara for the financial support through the FIRD 2024 grant.

Appendix A. Optimisation of the model

To optimise our toy model, we employed a genetic algorithm (GA), whose principle is described in Bazzanini et al. (2024). We are using four losses to optimise the different models we considered:

- A loss $L_{\rm avgd}$ regarding the averaged time profile of GRB 230307A. To compute $L_{\rm avgd}$, we applied a 5 s window moving averaged to the simulated and observed time profile and have computed

$$L_{avgd} = \sum_{i=1}^{i=N_{\rm bins}} (y_{sim,i} - y_{obs,i})^2, \tag{A.1}$$

  where $y_{sim,i}$ and $y_{obs,i}$ are the averaged observed and simulated time, and $N_{\rm bins}$ is the number of bins of the 5 s binned time averaged profile.
- A loss $L_{\rm peak}$ regarding the peak times distribution. $L_{\rm peak}$ is computed by performing a two-population Kolmogorov-Smirnov (KS) test between the simulated and the observed peak time distributions. If p is the p-value of the KS test,

$$L_{\rm peak} = \begin{cases} 1 - \log(p) & \text{if } p \leq 0.05, \\ 0 & \text{otherwise.} \end{cases} \tag{A.2}$$

- A loss L_{N_p} regarding the number of peaks produced by the model.

$$L_{N_p} = 3\left|\log\left(\frac{N_{\rm obs}}{N_{\rm sim}}\right)\right|. \tag{A.3}$$

  The number of peaks in the observed and simulated profiles were obtained by applying MEPSA to these light curves. We defined L_{N_p} so to have $L_{N_p} = 0$ when $N_{\rm obs} = N_{\rm sim}$ and growing when the ratio deviates from 1, the absolute value is chosen to equally penalise the solution with too few or too many simulated peaks. The factor 3 is here to ensure that L_{N_p} weights equally as the other losses.
- A loss $L_{\rm FWHM}$ regarding the FWHM distribution. The FWHMs of the pulses contained in the simulated and observed profiles were computed using MEPSA, and the method described in Camisasca et al. (2023a). $L_{\rm FWHM}$ is computed by performing a two-population KS test between the simulated and the observed FWHM distributions, and computed similarly to $L_{\rm peak}$.

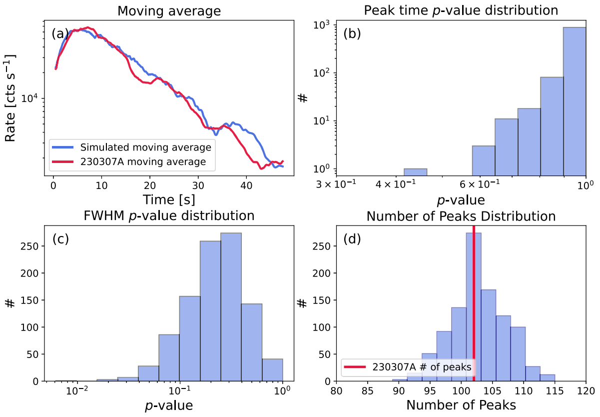

Fig. A.9. Four losses involved in the GA optimisation. Panel (a): Moving average time profile (5 s window) for the real (red) and simulated (blue) LCs. Panel (b): Distribution of p-values from the KS test comparing peak time distributions. Panel (c): Same as (b), but for FWHM distributions. Panel (d): Number of peaks detected in simulated LCs (blue histogram) compared with GRB 230307A (vertical red line).

We finally took the average of the four losses described above to compute the total loss $L_{\rm tot}$. Each individual's set of parameters was initially sampled randomly from a uniform distribution in the logarithmic space of each quantity, within the following ranges:

- $N_0 \in [100, 2000]$.
- $\tau \in [5, 25]$ s.
- $\mathrm{FWHM}_0 \in [0.01, 0.5]$ s.
- $\tau_F \in [10, 30]$ s.
- $\tau_{\rm rise} \in [0.1 - 100]$ s.
- $N_F \in [500, 2000]$.

In addition, for the two physical models, Γ, Γ_s, and Γ_0 were sampled in $1 - 10^4$, R_0 in $10^{10} - 10^{17}$ cm and τ_Γ in $1 - 10^3$ s. These ranges were chosen to constrain the parameter space in a way that ensures coverage and diversity among potential solutions. For each individual, the loss was computed using 100 light curves generated from the same parameter set. We ran the genetic algorithm on at least 60 generations, using a population of 2000 individuals. From the total population, 300 individuals were selected for mating in each generation. The probability for a random mutation of the parameters was set to 10%.

A.1. Results of the toy models

The final optimised parameters are given by the median values of the individual parameter distributions in the final generation. The uncertainties are defined by the 16th and 84th quantiles of these distributions. We generated 1000 light curves to test the best-fit parameters, reported in Table 1, for the three models considered in this study and computed the loss on these profiles. The values of the individual losses and the total losses for the toy model (Sect. 3.1) and the physical model 1 (Sect. 3.2) and 2 (Sect. 3.3) are reported in Table A.3.

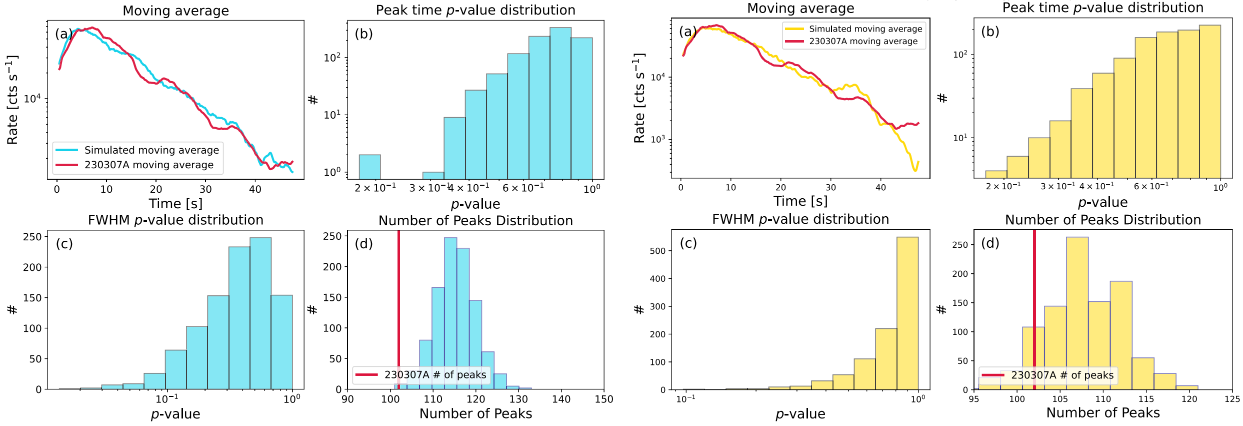

Fig. A.10. Same as in Fig. A.9, but for the constant (left panel) and decreasing (right panel) Γ-shell emission model.

Table B.4
Results and comparison of exponential temporal evolution modelling of WTs, FWHMs, and peak rates for GRB 211211A, GRB 230307A, and GRB 060614.

Property	GRB 211211A	GRB 230307A	GRB 060614
Waiting times	$\tau = 22.7^{+6.3}_{-4.0}$ s $N_0 = 136^{+23}_{-19}$ $\sigma = 0.85^{+0.12}_{-0.10}$ $\chi^2 = 86.5$ (dof = 86)	$\tau = 15.8^{+2.2}_{-1.8}$ s $N_0 = 124^{+12}_{-11}$ $\sigma = 0.54^{+0.07}_{-0.06}$ $\chi^2 = 100.1$ (dof = 99)	$\tau = 125^{+291}_{-56}$ s $N_0 = 68^{+106}_{-21}$ $\sigma = 0.66^{+0.17}_{-0.12}$ $\chi^2 = 32.4$ (dof = 32)
FWHM	$\tau_F = 21.6^{+4.4}_{-3.2}$ s $\mathrm{FWHM}_0 = 0.09^{+0.02}_{-0.02}$ s $\sigma = 0.70^{+0.11}_{-0.10}$ $\chi^2 = 86.6$ (dof = 87)	$\tau_F = 18.6^{+3.2}_{+2.5}$ s $\mathrm{FWHM}_0 = 0.12 \pm 0.02$ s $\sigma = 0.48^{+0.09}_{-0.07}$ $\chi^2 = 99.9$ (dof = 100)	$\tau_F = 74^{+97}_{-28}$ s $\mathrm{FWHM}_0 = 0.85^{+0.50}_{-0.32}$ s $\sigma = 0.90^{+0.24}_{-0.18}$ $\chi^2 = 32.4$ (dof = 33)
Peak rate	$\tau_p = 18.8^{+2.0}_{-1.6}$ s $P_0 = 6.5^{+1.2}_{-1.0} \times 10^4$ cts/s $\sigma = 0.32^{+0.06}_{-0.05}$ $\chi^2 = 56.1$ (dof = 56)	$\tau_p = 10.9 \pm 0.6$ s $P_0 = 1.56^{+0.21}_{-0.18} \times 10^5$ cts/s $\sigma = 0.22^{+0.05}_{-0.03}$ $\chi^2 = 48.7$ (dof = 49)	$\tau_p = 51.4^{+10.4}_{-7.4}$ s $P_0 = 1.33^{+0.30}_{-0.25}$ cts/s $\sigma = 0.39^{+0.10}_{-0.07}$ $\chi^2 = 33.5$ (dof = 33)

Figs. A.9 and A.10 illustrate the outcome of the GA optimisation, showing how the synthetic light curves reproduce the main temporal features of GRB 230307A, including the overall smoothed time profile, the distributions of peak times and FWHMs, and the total number of detected peaks.

Appendix B. Analysis of other long merger candidates

As anticipated in Section 3.6, adopting the procedure of Section 3, we analysed the temporal behaviour of other long merger candidates, namely GRB 211211A and GRB 060614. Results are reported in Table B.4.

Overall, we found that the exponential model provides an accurate description of the data (see χ^2 values reported in Table B.4). In this respect, GRB 211211A behaves very similarly to GRB 230307A, consistent with previous claims (e.g. Peng et al. 2024). The WTs, the FWHMs, and the peak rates evolve with time as exponentials with timescales close to 20 s. In the case of GRB 060614, the different timescales are longer than in the case of GRBs 211211A/230307A, and are less tightly constrained. In this case, both WT and FWHM increase, and the PR decay does not seem to share a common timescale; although, given the parameters' uncertainties, we cannot exclude the possibility that they are equal.

Appendix C. Analysis of SN-GRBs

We investigated whether some Type-II GRBs could display behaviour similar to GRB 230307A by focusing on bursts associated with Type Ic-BL supernovae, a clear indicator of a collapsar origin. Table C.5 reports a list of known SN-GRB associations, along with the corresponding number of detected peaks. We searched for SN-GRBs with sufficiently complex light curves ($N_p \geq 10$), as detected by MEPSA using either *Swift*/BAT or *Fermi*/GBM data (same dataset as Guidorzi et al. 2024). Only six GRBs met this criterion, namely GRB 080319B, GRB 111228A, GRB 130427A, GRB 171010A, GRB 211023A, and GRB 190114C (in addition to the exceptional GRB 221009A, which is analysed separately). The LCs of these bursts, the corresponding WT and pulse FWHM evolution are displayed in Fig. C.11. None of these GRBs exhibits a similar joint temporal evolution of the observables to that of GRB 230307A.

The case of GRB 221009A was also considered. Its exceptional brightness makes it hard to obtain a complete time profile, unaffected by strong dead time and electronics saturation effects. We carried out a detailed analysis using both HXMT/HE and GECAM data (Zhang et al., 2025). HXMT/HE data cover $T_0 - 141$ to $T_0 + 1800$ s, with three saturation intervals (187–194 s, 216–290 s, 500–535 s). Data are binned at 1 s, and background estimated via 8th-order polynomial interpolation. GECAM data (180–550 s) cover the main and the last emission episodes, are unaffected by saturation and binned at 50 ms. MEPSA was applied to both data sets, excluding the HXMT/HE saturated intervals.

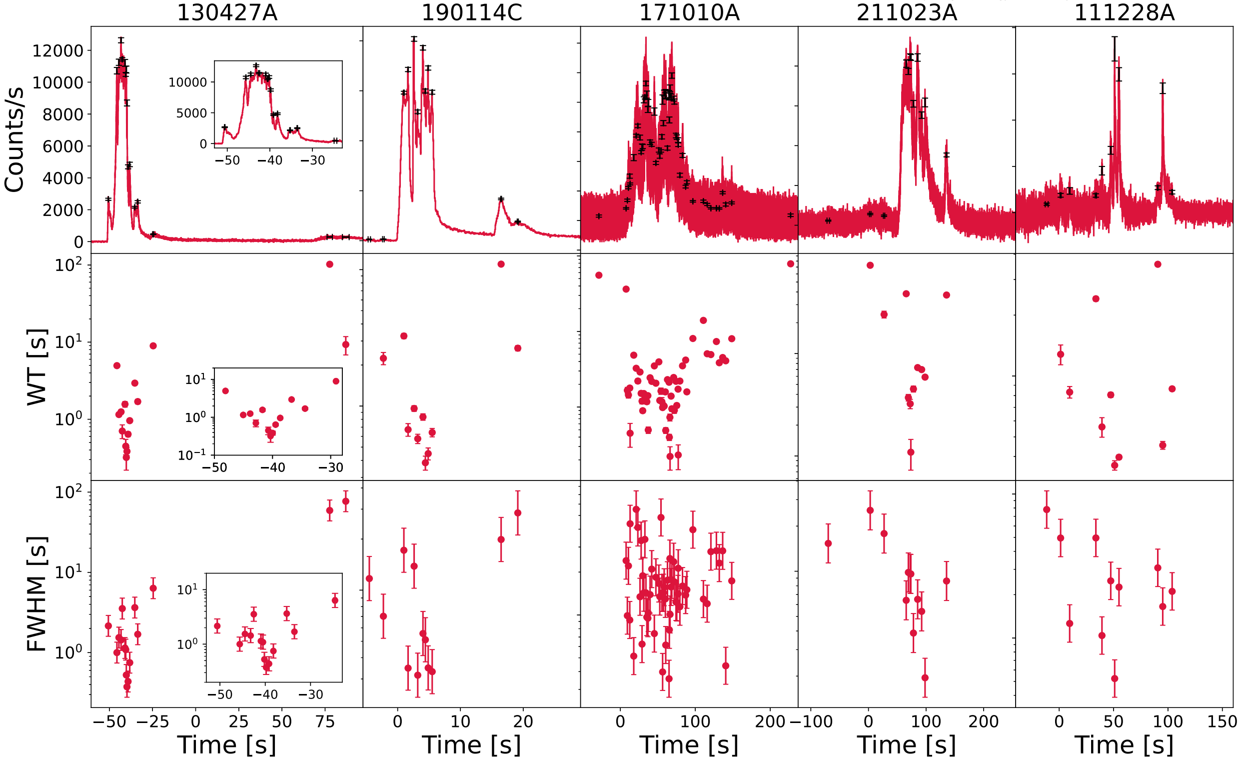

Fig. C.11. Five SN-GRBs having $N_p \geq 10$. Each top panel shows the γ-ray time profile (obtained with either *Fermi*/GBM or *Swift*/BAT). Black points represent the peaks detected by MEPSA. Middle and bottom panels respectively show the temporal evolution of WT and of FWHM throughout each burst. For GRB 130427A, two insets show a close-in view of the densely populated interval.

The combined HXMT/HE and GECAM light curves, along with the derived WTs, are shown in Fig. C.12. The complex profile consists of two long quiescent times: one between the precursor and the main emission, and the other between the main and late emission, separated by closely spaced pulses during each outburst. WTs in the main and late emission episodes were derived from GECAM data. Apart from noting that the WTs belonging to the late emission are somehow longer than those of the main episode, the overall evolution of WTs with time is very different from the monotonic WT rise seen in GRB 230307A.

Data availability

Data will be made available on request.

References

Ahumada, T., Singer, L.P., Anand, S., Coughlin, M.W., Kasliwal, M.M., Ryan, G., Andreoni, I., Cenko, S.B., Fremling, C., Kumar, H., Pang, P.T.H., Burns, E., Cunningham, V., Dichiara, S., Dietrich, T., Svinkin, D.S., Almualla, M., Castro-Tirado, A.J., De, K., Dunwoody, R., Gatkine, P., Hammerstein, E., Iyyani, S., Mangan, J., Perley, D., Purkayastha, S., Bellm, E., Bhalerao, V., Bolin, B., Bulla, M., Cannella, C., Chandra, P., Duev, D.A., Frederiks, D., Gal-Yam, A., Graham, M., Ho, A.Y.Q., Hurley, K., Karambelkar, V., Kool, E.C., Kulkarni, S.R., Mahabal, A., Masci, F., McBreen, S., Pandey, S.B., Reusch, S., Ridnaia, A., Rosnet, P., Rusholme, B., Carracedo, A.S., Smith, R., Soumagnac, M., Stein, R., Troja, E., Tsvetkova, A., Walters, R., Valeev, A.F., 2021. Discovery and confirmation of the shortest gamma-ray burst from a collapsar. Nat. Astron. 5, 917–927. https://doi.org/10.1038/s41550-021-01428-7.

Amati, L., 2006. The $E_{p,i}$-E_{iso} correlation in gamma-ray bursts: updated observational status, re-analysis and main implications. Mon. Not. R. Astron. Soc. 372, 233–245. https://doi.org/10.1111/j.1365-2966.2006.10840.x. arXiv:astro-ph/0601553.

Amati, L., Frontera, F., Tavani, M., in't Zand, J.J.M., Antonelli, A., Costa, E., Feroci, M., Guidorzi, C., Heise, J., Masetti, N., Montanari, E., Nicastro, L., Palazzi, E., Pian, E., Piro, L., Soffitta, P., 2002. Intrinsic spectra and energetics of BeppoSAX Gamma-Ray Bursts with known redshifts. Astron. Astrophys. 390, 81–89. https://doi.org/10.1051/0004-6361:20020722. arXiv:astro-ph/0205230.

Atteia, J.L., Cordier, B., Wei, J., 2022. The SVOM mission. Int. J. Mod. Phys. D 31, 2230008. https://doi.org/10.1142/S0218271822300087. arXiv:2203.10962.

Bazzanini, L., Ferro, L., Guidorzi, C., Angora, G., Amati, L., Brescia, M., Bulla, M., Frontera, F., Maccary, R., Maistrello, M., Rosati, P., Tsvetkova, A., 2024. Long gamma-ray burst light curves as the result of a common stochastic pulse–avalanche process. Astron. Astrophys. 689, A266. https://doi.org/10.1051/0004-6361/202450150. arXiv:2403.18754.

Bošnjak, Ž., Daigne, F., 2014. Spectral evolution in gamma-ray bursts: predictions of the internal shock model and comparison to observations. Astron. Astrophys. 568, A45. https://doi.org/10.1051/0004-6361/201322341. arXiv:1404.4577.

Camisasca, A.E., Guidorzi, C., Amati, L., Frontera, F., Song, X.Y., Xiao, S., Xiong, S.L., Zhang, S.N., Margutti, R., Kobayashi, S., Mundell, C.G., Ge, M.Y., Gomboc, A., Jia, S.M., Jordana-Mitjans, N., Li, C.K., Li, X.B., Maccary, R., Shrestha, M., Xue, W.C., Zhang, S., 2023a. GRB minimum variability timescale with Insight-HXMT and Swift. Implications for progenitor models, dissipation physics, and GRB classifications. Astron. Astrophys. 671, A112. https://doi.org/10.1051/0004-6361/202245657. arXiv:2301.01176.

Camisasca, A.E., Guidorzi, C., Bulla, M., Amati, L., Rossi, A., Stratta, G., Singh, P., 2023b. GRB 230307A: short minimum variability timescale compatible with a merger origin. GRB Coord. Netw. 33577, 1.

D'Agostini, G., 2005. Fits, and especially linear fits, with errors on both axes, extra variance of the data points and other complications. ArXiv Physics e-prints arXiv:physics/0511182.

Dai, C.Y., Guo, C.L., Zhang, H.M., Liu, R.Y., Wang, X.Y., 2024. Evidence for a compact stellar merger origin for GRB 230307A from Fermi-LAT and multiwavelength afterglow observations. Astrophys. J. Lett. 962, L37. https://doi.org/10.3847/2041-8213/ad2680. arXiv:2312.01074.

Daigne, F., Mochkovitch, R., 1998. Gamma-ray bursts from internal shocks in a relativistic wind: temporal and spectral properties. Mon. Not. R. Astron. Soc. 296, 275–286. https://doi.org/10.1046/j.1365-8711.1998.01305.x. arXiv:astro-ph/9801245.

Daigne, F., Mochkovitch, R., 2002. The expected thermal precursors of gamma-ray bursts in the internal shock model. Mon. Not. R. Astron. Soc. 336, 1271–1280. https://doi.org/10.1046/j.1365-8711.2002.05875.x. arXiv:astro-ph/0207456.

Della Valle, M., Chincarini, G., Panagia, N., Tagliaferri, G., Malesani, D., Testa, V., Fugazza, D., Campana, S., Covino, S., Mangano, V., Antonelli, L.A., D'Avanzo, P., Hurley, K., Mirabel, I.F., Pellizza, L.J., Piranomonte, S., Stella, L., 2006. An enigmatic long-lasting γ-ray burst not accompanied by a bright supernova. Nature 444, 1050–1052. https://doi.org/10.1038/nature05374. arXiv:astro-ph/0608322.

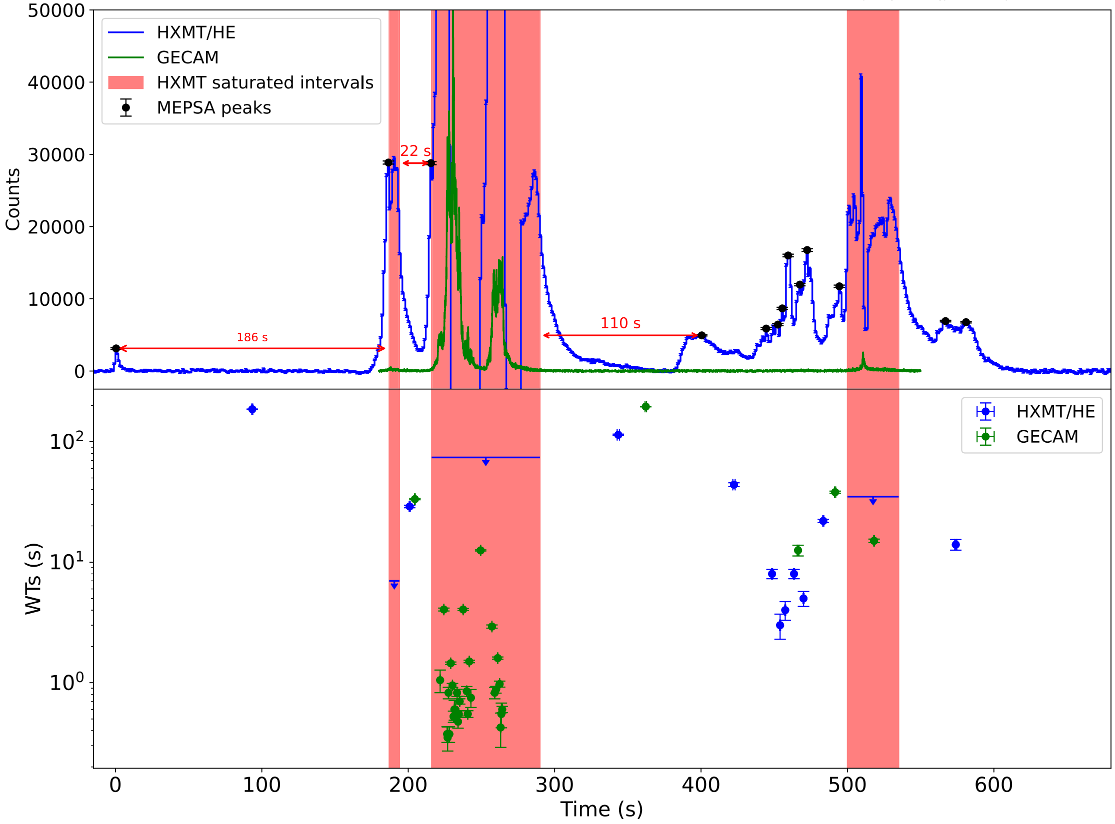

Fig. C.12. *Top panel*: Background-subtracted LCs of GRB 221009A from HXMT/HE (blue, 1 s binning) and GECAM (green, 50 ms binning). Red shaded areas mark intervals were HXMT/HE is affected by saturation. Peaks detected by MEPSA are shown as black markers. The two long quiescent intervals between the precursor and main emission (186 s) and between the main and late emission (110 s) are indicated. *Bottom panel:* WTs derived from MEPSA detections in HXMT/HE and GECAM data as a function of time. WTs inside HXMT/HE saturated intervals are computed from GECAM measurements.

Dermer, C.D., 2008. Nonthermal synchrotron radiation from gamma-ray burst external shocks and the X-ray flares observed with Swift. Astrophys. J. 684, 430–448. https://doi.org/10.1086/589730. arXiv:astro-ph/0703223.

Dermer, C.D., Böttcher, M., Chiang, J., 1999. The external shock model of gamma-ray bursts: three predictions and a paradox resolved. Astrophys. J. 515, L49–L52. https://doi.org/10.1086/311972. arXiv:astro-ph/9902306.

Dichiara, S., Tsang, D., Troja, E., Neill, D., Norris, J.P., Yang, Y.H., 2023. A luminous precursor in the extremely bright GRB 230307A. Astrophys. J. Lett. 954, L29. https://doi.org/10.3847/2041-8213/acf21d. arXiv:2307.02996.

Dietrich, T., Ujevic, M., 2017. Modeling dynamical ejecta from binary neutron star mergers and implications for electromagnetic counterparts. Class. Quantum Gravity 34, 105014. https://doi.org/10.1088/1361-6382/aa6bb0. arXiv:1612.03665.

Du, Z.W., Lü, H., Liu, X., Liang, E., 2024. The jet composition of GRB 230307A: Poynting-flux-dominated outflow? Mon. Not. R. Astron. Soc. 529, L67–L72. https://doi.org/10.1093/mnrasl/slad203. arXiv:2401.05002.

Eichler, D., Livio, M., Piran, T., Schramm, D.N., 1989. Nucleosynthesis, neutrino bursts and γ-rays from coalescing neutron stars. Nature 340, 126–128. https://doi.org/10.1038/340126a0.

Fenimore, E.E., Madras, C.D., Nayakshin, S., 1996. Expanding relativistic shells and gamma-ray burst temporal structure. Astrophys. J. 473, 998. https://doi.org/10.1086/178210. arXiv:astro-ph/9607163.

Fenimore, E.E., Ramirez-Ruiz, E., Wu, B., 1999. GRB 990123: evidence that the gamma rays come from a central engine. Astrophys. J. 518, L73–L76. https://doi.org/10.1086/312075. arXiv:astro-ph/9902007.

Fynbo, J.P.U., Watson, D., Thöne, C.C., Sollerman, J., Bloom, J.S., Davis, T.M., Hjorth, J., Jakobsson, P., Jørgensen, U.G., Graham, J.F., Fruchter, A.S., Bersier, D., Kewley, L., Cassan, A., Castro Cerón, J.M., Foley, S., Gorosabel, J., Hinse, T.C., Horne, K.D., Jensen, B.L., Klose, S., Kocevski, D., Marquette, J.B., Perley, D., Ramirez-Ruiz, E., Stritzinger, M.D., Vreeswijk, P.M., Wijers, R.A.M., Woller, K.G., Xu, D., Zub, M., 2006. No supernovae associated with two long-duration γ-ray bursts. Nature 444, 1047–1049. https://doi.org/10.1038/nature05375. arXiv:astro-ph/0608313.

Gillanders, J.H., Smartt, S.J., 2025. Analysis of the JWST spectra of the kilonova AT 2023vfi accompanying GRB 230307A. Mon. Not. R. Astron. Soc. 538, 1663–1689. https://doi.org/10.1093/mnras/staf287. arXiv:2408.11093.

Gompertz, B.P., Ravasio, M.E., Nicholl, M., Levan, A.J., Metzger, B.D., Oates, S.R., Lamb, G.P., Fong, W.f., Malesani, D.B., Rastinejad, J.C., Tanvir, N.R., Evans, P.A., Jonker, P.G., Page, K.L., Pe'er, A., 2023. The case for a minute-long merger-driven gamma-ray burst from fast-cooling synchrotron emission. Nat. Astron. 7, 67–79. https://doi.org/10.1038/s41550-022-01819-4. arXiv:2205.05008.

Guidorzi, C., 2015. MEPSA: a flexible peak search algorithm designed for uniformly spaced time series. Astron. Comput. 10, 54–60. https://doi.org/10.1016/j.ascom.2015.01.001. http://www.sciencedirect.com/science/article/pii/S2213133715000025.

Guidorzi, C., Dichiara, S., Frontera, F., Margutti, R., Baldeschi, A., Amati, L., 2015. A common stochastic process rules gamma-ray burst prompt emission and X-ray flares. Astrophys. J. 801, 57. https://doi.org/10.1088/0004-637X/801/1/57. arXiv:1501.02706.

Guidorzi, C., Sartori, M., Maccary, R., Tsvetkova, A., Amati, L., Bazzanini, L., Bulla, M., Camisasca, A.E., Ferro, L., Frontera, F., Li, C.K., Xiong, S.L., Zhang, S.N., 2024. Distribution of the number of peaks within a long gamma-ray burst. Astron. Astrophys. 685, A34. https://doi.org/10.1051/0004-6361/202449200. arXiv:2402.17282.

Jin, Z.P., Li, X., Cano, Z., Covino, S., Fan, Y.Z., Wei, D.M., 2015. The light curve of the macronova associated with the long–short burst GRB 060614. Astrophys. J. 811, L22. https://doi.org/10.1088/2041-8205/811/2/L22. arXiv:1507.07206.

Kobayashi, S., Piran, T., Sari, R., 1997. Can internal shocks produce the variability in gamma-ray bursts? Astrophys. J. 490, 92. https://doi.org/10.1086/512791. arXiv:astro-ph/9705013.

Kobayashi, S., Ryde, F., MacFadyen, A., 2002. Luminosity and variability of collimated gamma-ray bursts. Astrophys. J. 577, 302–310. https://doi.org/10.1086/342123. arXiv:astro-ph/0110080.

Levan, A.J., Gompertz, B.P., Salafia, O.S., Bulla, M., Burns, E., Hotokezaka, K., Izzo, L., Lamb, G.P., Malesani, D.B., Oates, S.R., Ravasio, M.E., Rouco Escorial, A., Schneider, B., Sarin, N., Schulze, S., Tanvir, N.R., Ackley, K., Anderson, G., Brammer, G.B., Christensen, L., Dhillon, V.S., Evans, P.A., Fausnaugh, M., Fong, f.W., Fruchter, A.S., Fryer, C., Fynbo, J.P.U., Gaspari, N., Heintz, K.E., Hjorth, J., Kennea, J.A., Kennedy, M.R., Laskar, T., Leloudas, G., Mandel, I., Martin-Carrillo, A., Metzger, B.D., Nicholl, M., Nugent, A., Palmerio, J.T., Pugliese, G., Rastinejad, J., Rhodes, L., Rossi, A., Saccardi, A., Smartt, S.J., Stevance, H.F., Tohuvavohu, A., van der Horst, A., Vergani, S.D.,

Table C.5

SN-GRBs with number of peaks N_p detected by MEPSA, using LCs binned at 64 ms. The SN Spec column indicates whether the evidence for the SN was both photometric and spectroscopic (1) or just photometric (0).

GRB	SN	SN Spec	z	N_p
221009A	2022xiw	1	0.1505	-
171010A	2017htp	1	0.3285	49
080319B	——	0	0.937	43
130427A	2013cq	1	0.3399	16
211023A	——-	1	0.39	12
111228A	——	0	0.71627	11
190114C	2019jrj	1	0.4245	11
090618	——	0	0.54	9
111228A	——	0	0.71627	6
140506A	——	0	0.889	5
091127	2009nz	1	0.49034	4
140506A	——	0	0.889	3
060729	——	0	0.54	3
091127	2009nz	1	0.49034	3
180728A	2018fip	1	0.117	2
190829A	2019oyw	1	0.0785	2
140606B	iPTF14bfu	1	0.384	2
130831A	2013fu	1	0.4791	2
100316D	2010bh	1	0.0592	1
101219B	2010ma	1	0.5519	1
130215A	2013ez	1	0.597	1
130702A	2013dx	1	0.145	1
101219B	2010ma	1	0.5519	1
120422A	2012bz	1	0.283	1
120714B	2012eb	1	0.3984	1
120729A	——	0	0.8	1
171205A	2017iuk	1	0.0368	1
141004A	——	0	0.573	1
161219B	2016jca	1	0.1475	1
200826A	——-	0	0.7481	1
201015A	——-	1	0.426	1
980425	1998bw	1	0.0085	1

Watson, D., Barclay, T., Bhirombhakdi, K., Breedt, E., Breeveld, A.A., Brown, A.J., Campana, S., Chrimes, A.A., D'Avanzo, P., D'Elia, V., De Pasquale, M., Dyer, M.J., Galloway, D.K., Garbutt, J.A., Green, M.J., Hartmann, D.H., Jakobsson, P., Kerry, P., Kouveliotou, C., Langeroodi, D., Le Floc'h, E., Leung, J.K., Littlefair, S.P., Munday, J., O'Brien, P., Parsons, S.G., Pelisoli, I., Sahman, D.I., Salvaterra, R., Sbarufatti, B., Steeghs, D., Tagliaferri, G., Thöne, C.C., de Ugarte Postigo, A., Kann, D.A., 2024. Heavy-element production in a compact object merger observed by JWST. Nature 626, 737–741. https://doi.org/10.1038/s41586-023-06759-1. arXiv:2307.02098.

Levan, A.J., Malesani, D.B., Gompertz, B.P., Nugent, A.E., Nicholl, M., Oates, S.R., Perley, D.A., Rastinejad, J., Metzger, B.D., Schulze, S., Stanway, E.R., Inkenhaag, A., Zafar, T., AgüíFernández, J.F., Chrimes, A.A., Bhirombhakdi, K., de Ugarte Postigo, A., Fong, f.W., Fruchter, A.S., Fragione, G., Fynbo, J.P.U., Gaspari, N., Heintz, K.E., Hjorth, J., Jakobsson, P., Jonker, P.G., Lamb, G.P., Mandel, I., Mandhai, S., Ravasio, M.E., Sollerman, J., Tanvir, N.R., 2023. A long-duration gamma-ray burst of dynamical origin from the nucleus of an ancient galaxy. Nat. Astron. 7, 976–985. https://doi.org/10.1038/s41550-023-01998-8. arXiv:2303.12912.

Li, L., Wang, X.G., Zheng, W., Pozanenko, A.S., Filippenko, A.V., Qin, S., Wang, S.Q., Jiang, L.Y., Li, J., Lin, D.B., Liang, E.W., Volnova, A.A., Elenin, L., Klunko, E., Inasaridze, R.Y., Kusakin, A., Lu, R.J., 2020. GRB 140423A: a case of stellar wind to interstellar medium transition in the afterglow. Astrophys. J. 900, 176. https://doi.org/10.3847/1538-4357/aba757. arXiv:2008.02445.

MacFadyen, A.I., Woosley, S.E., 1999. Collapsars: gamma-ray bursts and explosions in "failed supernovae". Astrophys. J. 524, 262–289. https://doi.org/10.1086/307790. arXiv:astro-ph/9810274.

Maistrello, M., Ferro, L., Bazzanini, L., Maccary, R., Guidorzi, C., 2025. An advanced pulse-avalanche stochastic model of long gamma-ray burst light curves. Astron. Astrophys. 697, A76. https://doi.org/10.1051/0004-6361/202553821.

Metzger, B.D., 2020. Kilonovae. Living Rev. Relativ. 23, 1. https://doi.org/10.1007/s41114-019-0024-0.

Moradi, R., Wang, C.W., Zhang, B., Wang, Y., Xiong, S.L., Yi, S.X., Tan, W.J., Karlica, M., Zhang, S.N., 2024. Temporal and spectral analysis of the unique and second-brightest gamma-ray burst GRB 230307A: insights from GECAM and Fermi/GBM observations. Astrophys. J. 977, 155. https://doi.org/10.3847/1538-4357/ad8a64. arXiv:2410.17189.

Narayan, R., Paczynski, B., Piran, T., 1992. Gamma-ray bursts as the death throes of massive binary stars. Astrophys. J. 395, L83–L86. https://doi.org/10.1086/186493. arXiv:astro-ph/9204001.

Norris, J.P., Bonnell, J.T., 2006. Short gamma-ray bursts with extended emission. Astrophys. J. 643, 266–275. https://doi.org/10.1086/502796. arXiv:astro-ph/0601190.

Norris, J.P., Nemiroff, R.J., Bonnell, J.T., Scargle, J.D., Kouveliotou, C., Paciesas, W.S., Meegan, C.A., Fishman, G.J., 1996. Attributes of pulses in long bright gamma-ray bursts. Astrophys. J. 459, 393. https://doi.org/10.1086/176902.

Paczynski, B., 1991. Cosmological gamma-ray bursts. Acta Astron. 41, 257–267.

Paczyński, B., 1998. Are gamma-ray bursts in star-forming regions? Astrophys. J. Lett. 494, L45–L48. https://doi.org/10.1086/311148. arXiv:astro-ph/9710086.

Peng, Z.Y., Chen, J.M., Mao, J., 2024. A comparative analysis of two peculiar gamma-ray bursts: GRB 230307A and GRB 211211A. Astrophys. J. 969, 26. https://doi.org/10.3847/1538-4357/ad45fc. arXiv:2404.17913.

Piran, T., 2004. The physics of gamma-ray bursts. Rev. Mod. Phys. 76, 1143–1210. https://doi.org/10.1103/RevModPhys.76.1143. arXiv:astro-ph/0405503.

Planck Collaboration, Aghanim, N., Akrami, Y., Ashdown, M., Aumont, J., Baccigalupi, C., Ballardini, M., Banday, A.J., Barreiro, R.B., Bartolo, N., Basak, S., Battye, R., Benabed, K., Bernard, J.P., Bersanelli, M., Bielewicz, P., Bock, J.J., Bond, J.R., Borrill, J., Bouchet, F.R., Boulanger, F., Bucher, M., Burigana, C., Butler, R.C., Calabrese, E., Cardoso, J.F., Carron, J., Challinor, A., Chiang, H.C., Chluba, J., Colombo, L.P.L., Combet, C., Contreras, D., Crill, B.P., Cuttaia, F., de Bernardis, P., de Zotti, G., Delabrouille, J., Delouis, J.M., Di Valentino, E., Diego, J.M., Doré, O., Douspis, M., Ducout, A., Dupac, X., Dusini, S., Efstathiou, G., Elsner, F., Enßlin, T.A., Eriksen, H.K., Fantaye, Y., Farhang, M., Fergusson, J., Fernandez-Cobos, R., Finelli, F., Forastieri, F., Frailis, M., Fraisse, A.A., Franceschi, E., Frolov, A., Galeotta, S., Galli, S., Ganga, K., Génova-Santos, R.T., Gerbino, M., Ghosh, T., González-Nuevo, J., Górski, K.M., Gratton, S., Gruppuso, A., Gudmundsson, J.E., Hamann, J., Handley, W., Hansen, F.K., Herranz, D., Hildebrandt, S.R., Hivon, E., Huang, Z., Jaffe, A.H., Jones, W.C., Karakci, A., Keihänen, E., Keskitalo, R., Kiiveri, K., Kim, J., Kisner, T.S., Knox, L., Krachmalnicoff, N., Kunz, M., Kurki-Suonio, H., Lagache, G., Lamarre, J.M., Lasenby, A., Lattanzi, M., Lawrence, C.R., Le Jeune, M., Lemos, P., Lesgourgues, J., Levrier, F., Lewis, A., Liguori, M., Lilje, P.B., Lilley, M., Lindholm, V., López-Caniego, M., Lubin, P.M., Ma, Y.Z., Macías-Pérez, J.F., Maggio, G., Maino, D., Mandolesi, N., Mangilli, A., Marcos-Caballero, A., Maris, M., Martin, P.G., Martinelli, M., Martínez-González, E., Matarrese, S., Mauri, N., McEwen, J.D., Meinhold, P.R., Melchiorri, A., Mennella, A., Migliaccio, M., Millea, M., Mitra, S., Miville-Deschênes, M.A., Molinari, D., Montier, L., Morgante, G., Moss, A., Natoli, P., Nørgaard-Nielsen, H.U., Pagano, L., Paoletti, D., Partridge, B., Patanchon, G., Peiris, H.V., Perrotta, F., Pettorino, V., Piacentini, F., Polastri, L., Polenta, G., Puget, J.L., Rachen, J.P., Reinecke, M., Remazeilles, M., Renzi, A., Rocha, G., Rosset, C., Roudier, G., Rubiño-Martín, J.A., Ruiz-Granados, B., Salvati, L., Sandri, M., Savelainen, M., Scott, D., Shellard, E.P.S., Sirignano, C., Sirri, G., Spencer, L.D., Sunyaev, R., Suur-Uski, A.S., Tauber, J.A., Tavagnacco, D., Tenti, M., Toffolatti, L., Tomasi, M., Trombetti, T., Valenziano, L., Valiviita, J., Van Tent, B., Vibert, L., Vielva, P., Villa, F., Vittorio, N., Wandelt, B.D., Wehus, I.K., White, M., White, S.D.M., Zacchei, A., Zonca, A., 2020. Planck 2018 results. VI. Cosmological parameters. Astron. Astrophys. 641, A6. https://doi.org/10.1051/0004-6361/201833910. arXiv:1807.06209.

Racusin, J.L., Karpov, S.V., Sokolowski, M., Granot, J., Wu, X.F., Pal'Shin, V., Covino, S., van der Horst, A.J., Oates, S.R., Schady, P., Smith, R.J., Cummings, J., Starling, R.L.C., Piotrowski, L.W., Zhang, B., Evans, P.A., Holland, S.T., Malek, K., Page, M.T., Vetere, L., Margutti, R., Guidorzi, C., Kamble, A.P., Curran, P.A., Beardmore, A., Kouveliotou, C., Mankiewicz, L., Melandri, A., O'Brien, P.T., Page, K.L., Piran, T., Tanvir, N.R., Wrochna, G., Aptekar, R.L., Barthelmy, S., Bartolini, C., Beskin, G.M., Bondar, S., Bremer, M., Campana, S., Castro-Tirado, A., Cucchiara, A., Cwiok, M., D'Avanzo, P., D'Elia, V., Della Valle, M., de Ugarte Postigo, A., Dominik, W., Falcone, A., Fiore, F., Fox, D.B., Frederiks, D.D., Fruchter, A.S., Fugazza, D., Garrett, M.A., Gehrels, N., Golenetskii, S., Gomboc, A., Gorosabel, J., Greco, G., Guarnieri, A., Immler, S., Jelinek, M., Kasprowicz, G., La Parola, V., Levan, A.J., Mangano, V., Mazets, E.P., Molinari, E., Moretti, A., Nawrocki, K., Oleynik, P.P., Osborne, J.P., Pagani, C., Pandey, S.B., Paragi, Z., Perri, M., Piccioni, A., Ramirez-Ruiz, E., Roming, P.W.A., Steele, I.A., Strom, R.G., Testa, V., Tosti, G., Ulanov, M.V., Wiersema, K., Wijers, R.A.M.J., Winters, J.M., Zarnecki, A.F., Zerbi, F., Mészáros, P., Chincarini, G., Burrows, D.N., 2008. Broadband observations of the naked-eye γ-ray burst GRB080319B. Nature 455, 183–188. https://doi.org/10.1038/nature07270. arXiv:0805.1557.

Radice, D., Perego, A., Hotokezaka, K., Fromm, S.A., Bernuzzi, S., Roberts, L.F., 2018. Binary neutron star mergers: mass ejection, electromagnetic counterparts, and nucleosynthesis. Astrophys. J. 869, 130. https://doi.org/10.3847/1538-4357/aaf054. arXiv:1809.11161.

Rastinejad, J.C., Gompertz, B.P., Levan, A.J., Fong, f.W., Nicholl, M., Lamb, G.P., Malesani, D.B., Nugent, A.E., Oates, S.R., Tanvir, N.R., de Ugarte Postigo, A., Kilpatrick, C.D., Moore, C.J., Metzger, B.D., Ravasio, M.E., Rossi, A., Schroeder, G., Jencson, J., Sand, D.J., Smith, N., AgüíFernández, J.F., Berger, E., Blanchard, P.K., Chornock, R., Cobb, B.E., De Pasquale, M., Fynbo, J.P.U., Izzo, L., Kann, D.A., Laskar, T., Marini, E., Paterson, K., Escorial, A.R., Sears, H.M., Thöne, C.C., 2022. A kilonova following a long-duration gamma-ray burst at 350 Mpc. Nature 612, 223–227. https://doi.org/10.1038/s41586-022-05390-w. arXiv:2204.10864.

Rees, M.J., Meszaros, P., 1994. Unsteady outflow models for cosmological gamma-ray bursts. Astrophys. J. 430, L93–L96. https://doi.org/10.1086/187446. arXiv:astro-ph/9404038.

Rees, M.J., Meszaros, P., 1998. Refreshed shocks and afterglow longevity in gamma-ray bursts. Astrophys. J. 496, L1. https://doi.org/10.1086/311244. arXiv:astro-ph/9712252.

Rossi, A., Rothberg, B., Palazzi, E., Kann, D.A., D'Avanzo, P., Amati, L., Klose, S., Perego, A., Pian, E., Guidorzi, C., Pozanenko, A.S., Savaglio, S., Stratta, G., Agapito, G., Covino, S., Cusano, F., D'Elia, V., Pasquale, M.D., Valle, M.D., Kuhn, O., Izzo, L., Loffredo, E., Masetti, N., Melandri, A., Minaev, P.Y., Guelbenzu, A.N., Paris, D., Paiano, S., Plantet, C., Rossi, F., Salvaterra, R., Schulze, S., Veillet, C., Volnova, A.A., 2022. The peculiar short-duration GRB 200826A and its supernova. Astrophys. J. 932, 1. https://doi.org/10.3847/1538-4357/ac60a2. arXiv:2105.03829.

Rosswog, S., Sarin, N., Nakar, E., Diener, P., 2025. Fast dynamic ejecta in neutron star mergers. Mon. Not. R. Astron. Soc. 538, 907–924. https://doi.org/10.1093/mnras/staf324. arXiv:2411.18813.

Shibata, M., Hotokezaka, K., 2019. Merger and mass ejection of neutron star binaries. Annu. Rev. Nucl. Part. Sci. 69, 41–64. https://doi.org/10.1146/annurev-nucl-101918-023625. arXiv:1908.02350.

Stratta, G., Nicuesa Guelbenzu, A.M., Klose, S., Rossi, A., Singh, P., Palazzi, E., Guidorzi, C., Camisasca, A., Bernuzzi, S., Rau, A., Bulla, M., Ragosta, F., Maiorano, E., Paris, D., 2025. The puzzling long GRB 191019A: evidence for kilonova light. Astrophys. J. 979, 159. https://doi.org/10.3847/1538-4357/ad9b7b. arXiv:2412.04059.

Sun, H., Wang, C.W., Yang, J., Zhang, B.B., Xiong, S.L., Yin, Y.H.I., Liu, Y., Li, Y., Xue, W.C., Yan, Z., Zhang, C., Tan, W.J., Pan, H.W., Liu, J.C., Cheng, H.Q., Zhang, Y.Q., Hu, J.W., Zheng, C., An, Z.H., Cai, C., Cai, Z.M., Hu, L., Jin, C., Li, D.Y., Li, X.Q., Liu, H.Y., Liu, M., Peng, W.X., Song, L.M., Sun, S.L., Sun, X.J., Wang, X.L., Wen, X.Y., Xiao, S., Yi, S.X., Zhang, F., Zhang, W.D., Zhang, X.F., Zhang, Y.H., Zhao, D.H., Zheng, S.J., Ling, Z.X., Zhang, S.N., Yuan, W., Zhang, B., 2025. Magnetar emergence in a peculiar gamma-ray burst from a compact star merger. Natl. Sci. Rev. 12, nwae401. https://doi.org/10.1093/nsr/nwae401.

Svinkin, D., Frederiks, D., Ridnaia, A., Tsvetkova, A., Lysenko, A., Konus-Wind Team, 2023. GRB 230307A: further analysis of the Konus-Wind detection and rest-frame energetics. GRB Coord. Netw. 33579, 1.

Tan, W.J., Wang, C.W., Zhang, P., Xiong, S.L., Wu, B.b., Liu, J.C., Wang, Y., Xie, S.L., Xue, W.C., Yu, Z.H., Zhang, J.P., Zhang, W.L., Zhang, Y.Q., Zheng, C., 2025. Search for Type IL Gamma-ray Bursts: Criterion, Results, Verification and Physical Implication. ArXiv e-prints arXiv:2504.06616. https://doi.org/10.48550/arXiv.2504.06616, 2025.

Troja, E., Fryer, C.L., O'Connor, B., Ryan, G., Dichiara, S., Kumar, A., Ito, N., Gupta, R., Wollaeger, R., Norris, J.P., Kawai, N., Butler, N., Aryan, A., Misra, K., Hosokawa, R., Murata, K.L., Niwano, M., Pandey, S.B., Kutyrev, A., van Eerten, H.J., Chase, E.A., Hu, Y.D., Caballero-Garcia, M.D., Castro-Tirado, A.J., 2022. A long gamma-ray burst from a merger of compact objects. Nature 612, 228–231. https://doi.org/10.1038/s41586-022-05327-3.

Wang, C.W., Tan, W.J., Xiong, S.L., Yi, S.X., Moradi, R., Li, B., Zhang, Z., Wang, Y., Meng, Y.Z., Wu, B.B., Liu, J.C., Wang, Y., Xie, S.L., Xue, W.C., Yu, Z.H., Zhang, P., Zhang, W.L., Zhang, Y.Q., Zheng, C., 2025. A subclass of gamma-ray burst originating from compact binary merger. Astrophys. J. 979, 73. https://doi.org/10.3847/1538-4357/ad98ec. arXiv:2407.02376.

Wang, X.I., Yu, Y.W., Ren, J., Yang, J., Zou, Z.C., Zhu, J.P., 2024. What powered the kilonova-like emission after GRB 230307A in the framework of a neutron star–white dwarf merger? Astrophys. J. Lett. 964, L9. https://doi.org/10.3847/2041-8213/ad2df6. arXiv:2402.11304.

Woosley, S.E., 1993. Gamma-ray bursts from stellar mass accretion disks around black holes. Astrophys. J. 405, 273–277. https://doi.org/10.1086/172359.

Xiao, S., Peng, W.X., Zhang, S.N., Xiong, S.L., Li, X.B., Tuo, Y.L., Gao, H., Wang, Y., Xue, W.C., Zheng, C., Zhang, Y.Q., Liu, J.C., Li, C.K., Yi, S.X., Wang, X.L., Zhang, Z., Cai, C., Dong, A.J., Xie, W., Feng, J.C., Ma, Q.B., Wang, D.H., Luo, X.H., Zhi, Q.J., Song, L.M., Li, T.P., 2022. Search for quasiperiodic oscillations in precursors of short and long gamma-ray bursts. Astrophys. J. 941, 166. https://doi.org/10.3847/1538-4357/aca018. arXiv:2210.08491.

Xiong, S., Wang, C., Huang, Y., Gecam Team, 2023. GRB 230307A: GECAM detection of an extremely bright burst. GRB Coord. Netw. 33406, 1.

Yang, J., Ai, S., Zhang, B.B., Zhang, B.K., Liu, Z.K., Wang, X.I., Yang, Y.H., Yin, Y.H., Li, Y., Lü, H.J., 2022. A long-duration gamma-ray burst with a peculiar origin. Nature 612, 232–235. https://doi.org/10.1038/s41586-022-05403-8.

Yi, S.X., Wang, C.W., Shao, X., Moradi, R., Gao, H., Zhang, B., Xiong, S.L., Zhang, S.N., Tan, W.J., Liu, J.C., Xue, W.C., Zhang, Y.Q., Zheng, C., Wang, Y., Zhang, P., An, Z.H., Cai, C., Feng, P.Y., Gong, K., Guo, D.Y., Huang, Y., Li, B., Li, X.B., Li, X.Q., Liu, X.J., Liu, Y.Q., Ma, X., Peng, W.X., Qiao, R., Song, L.M., Wang, J., Wang, P., Wen, X.Y., Xiao, S., Xu, Y.B., Yang, S., Yi, Q.B., Zhang, D.L., Zhang, F., Zhang, H.M., Zhang, J.P., Zhang, Z., Zhao, X.Y., Zhao, Y., Zheng, S.J., 2025a. Evidence of minijet emission in a large emission zone from a magnetically dominated gamma-ray burst jet. Astrophys. J. 985, 239. https://doi.org/10.3847/1538-4357/adcf98. arXiv:2310.07205.

Yi, S.X., Yorgancioglu, E.S., Xiong, S.L., Zhang, S.N., 2025b. Long pulse by short central engine: prompt emission from expanding dissipation rings in the jet front of gamma-ray bursts. J. High Energy Astrophys. 47, 100359. https://doi.org/10.1016/j.jheap.2025.100359.

Yonetoku, D., Murakami, T., Nakamura, T., Yamazaki, R., Inoue, A.K., Ioka, K., 2004. Gamma-ray burst formation rate inferred from the spectral peak energy-peak luminosity relation. Astrophys. J. 609, 935–951. https://doi.org/10.1086/421285. arXiv:astro-ph/0309217.

Yuan, W., Zhang, C., Chen, Y., Ling, Z., 2022. The Einstein probe mission. In: Bambi, C., Sangangelo, A. (Eds.), Handbook of X-ray and Gamma-ray Astrophysics, p. 86.

Zhang, B., Yan, H., 2011. The internal-collision-induced magnetic reconnection and turbulence (ICMART) model of gamma-ray bursts. Astrophys. J. 726, 90. https://doi.org/10.1088/0004-637X/726/2/90. arXiv:1011.1197.

Zhang, B., Zhang, B.B., Virgili, F.J., Liang, E.W., Kann, D.A., Wu, X.F., Proga, D., Lv, H.J., Toma, K., Mészáros, P., Burrows, D.N., Roming, P.W.A., Gehrels, N., 2009. Discerning the physical origins of cosmological gamma-ray bursts based on multiple observational criteria: the cases of $z = 6.7$ GRB 080913, $z = 8.2$ GRB 090423, and some short/hard GRBs. Astrophys. J. 703, 1696–1724. https://doi.org/10.1088/0004-637X/703/2/1696. arXiv:0902.2419.

Zhang, B.B., Liu, Z.K., Peng, Z.K., Li, Y., Lü, H.J., Yang, J., Yang, Y.S., Yang, Y.H., Meng, Y.Z., Zou, J.H., Ye, H.Y., Wang, X.G., Mao, J.R., Zhao, X.H., Bai, J.M., Castro-Tirado, A.J., Hu, Y.D., Dai, Z.G., Liang, E.W., Zhang, B., 2021. A peculiarly short-duration gamma-ray burst from massive star core collapse. Nat. Astron. 5, 911–916. https://doi.org/10.1038/s41550-021-01395-z. arXiv:2105.05021.

Zhang, C., Ling, Z.X., Sun, X.J., Sun, S.L., Liu, Y., Li, Z.D., Xue, Y.L., Chen, Y.F., Dai, Y.F., Jia, Z.Q., Liu, H.Y., Zhang, X.F., Zhang, Y.H., Zhang, S.N., Chen, F.S., Cheng, Z.W., Fu, W., Han, Y.X., Li, H., Li, J.F., Li, Y., Liu, P.R., Ma, X.H., Tang, Y.J., Wang, C.B., Xie, R.J., Yan, A.L., Zhang, Q., Jiang, B.W., Jin, G., Li, L.H., Qiu, X.B., Su, D.T., Sun, J.N., Xu, Z., Zhang, S.K., Zhang, Z., Zhang, N., Bi, X.Z., Cai, Z.M., He, J.W., Liu, H.Q., Zhu, X.C., Cheng, H.Q., Cui, C.Z., Fan, D.W., Hu, H.B., Huang, M.H., Jin, C.C., Li, D.Y., Pan, H.W., Wang, W.X., Xu, Y.F., Yang, X., Zhang, B., Zhang, M., Zhang, W.D., Zhao, D.H., Bai, M., Ji, Z., Liu, Y.R., Ma, F.L., Su, J., Tong, J.Z., Wang, Y.S., Zhao, Z.J., Feldman, C., O'Brien, P., Osborne, J.P., Willingale, R., Burwitz, V., Hartner, G., Langmeier, A., Müller, T., Rukdee, S., Schmidt, T., Kuulkers, E., Yuan, W., 2022. First wide field-of-view X-ray observations by a lobster-eye focusing telescope in orbit. Astrophys. J. Lett. 941, L2. https://doi.org/10.3847/2041-8213/aca32f. arXiv:2211.10007.

Zhang, W.L., Xue, W.C., Li, C.K., Xiong, S.L., Li, G., Chen, Y., Cui, W.W., Li, X.B., Liu, C.Z., Ge, M.Y., Tan, W.J., Liu, J.C., Wang, C.W., Zheng, C., Zhang, Y.Q., Wang, Y., Zhang, Z., Yi, S.X., Xiao, S., Cai, C., Yi, S.X., Song, L.M., Tao, L., Zhang, S., Zhang, S.N., 2025. Insight-HXMT observations of the extremely bright GRB 221009A. Astrophys. J. 986, 170. https://doi.org/10.3847/1538-4357/add14f. arXiv:2504.18952.

BIBLIOGRAPHY

Abbott, B. P. et al. (Oct. 2017). "Gravitational Waves and Gamma-Rays from a Binary Neutron Star Merger: GW170817 and GRB 170817A." In: *ApJL* 848, L13, p. L13. doi: `10.3847/2041-8213/aa920c`. arXiv: `1710.05834 [astro-ph.HE]`.

Abbott, B. P. et al. (Oct. 2017). "Multi-messenger Observations of a Binary Neutron Star Merger." In: *ApJL* 848, L12, p. L12. doi: `10.3847/2041-8213/aa91c9`. arXiv: `1710.05833 [astro-ph.HE]`.

Abdalla, H. et al. (2019). "A very-high-energy component deep in the Gamma-ray Burst afterglow." In: *Nature* 575, pp. 464–467. doi: `10.1038/s41586-019-1743-9`. eprint: `1911.08961` (astro-ph.HE).

Abdo, A. A. et al. (Nov. 2009a). "A limit on the variation of the speed of light arising from quantum gravity effects." In: *Nature* 462.7271, pp. 331–334. doi: `10.1038/nature08574`. arXiv: `0908.1832 [astro-ph.HE]`.

Abdo, A. A. et al. (Mar. 2009b). "Fermi Observations of High-Energy Gamma-Ray Emission from GRB 080916C." In: *Science* 323, pp. 1688–. doi: `10.1126/science.1169101`.

Abe, H. et al. (Jan. 2024). "MAGIC detection of GRB 201216C at z = 1.1." In: *MNRAS* 527.3, pp. 5856–5867. doi: `10.1093/mnras/stad2958`. arXiv: `2310.06473 [astro-ph.HE]`.

Abe, K. et al. (Aug. 2025). "GRB 221009A: Observations with LST-1 of CTAO and Implications for Structured Jets in Long Gamma-Ray Bursts." In: *ApJL* 988.2, L42, p. L42. doi: `10.3847/2041-8213/ade4cf`. arXiv: `2507.03077 [astro-ph.HE]`.

Ackermann, M. et al. (2010). "Fermi Observations of GRB 090510: A Short-Hard Gamma-ray Burst with an Additional, Hard Power-law Component from 10 keV TO GeV Energies." In: *ApJ* 716.2, pp. 1178–1190. doi: `10.1088/0004-637X/716/2/1178`. arXiv: `1005.2141 [astro-ph.HE]`.

Ackermann, M. et al. (Jan. 2014). "Fermi-LAT Observations of the Gamma-Ray Burst GRB 130427A." In: *Science* 343, pp. 42–47. doi: `10.1126/science.1242353`.

Ahumada, Tomás et al. (July 2021). "Discovery and confirmation of the shortest gamma-ray burst from a collapsar." In: *Nature Astronomy* 5, pp. 917–927. doi: `10.1038/s41550-021-01428-7`.

Ajello, M. et al. (June 2019). "A Decade of Gamma-Ray Bursts Observed by Fermi-LAT: The Second GRB Catalog." In: *ApJ* 878.1, 52, p. 52. doi: `10.3847/1538-4357/ab1d4e`. arXiv: `1906.11403 [astro-ph.HE]`.

Aldowma, T. K. M. et al. (Oct. 2025). "Implications of Joint Spectral Analysis of Gamma-Ray Bursts detected by Fermi Large Area Telescope and Gamma-ray Burst Monitor on Phenomenological Correlations." In: *arXiv e-prints*, arXiv:2510.16475, arXiv:2510.16475. doi: `10.48550/arXiv.2510.16475`. arXiv: `2510.16475 [astro-ph.HE]`.

Aleksić, J. et al. (Jan. 2016). "The major upgrade of the MAGIC telescopes, Part II: A performance study using observations of the Crab Nebula." In: *Astroparticle Physics* 72, pp. 76–94. doi: `10.1016/j.astropartphys.2015.02.005`. arXiv: `1409.5594 [astro-ph.IM]`.

Amati, L. et al. (July 2002). "Intrinsic spectra and energetics of BeppoSAX Gamma-Ray Bursts with known redshifts." In: *A&A* 390, pp. 81–89. doi: `10.1051/0004-6361:20020722`. eprint: `arXiv:astro-ph/0205230`.

Amati, L. et al. (Dec. 2021). “The THESEUS space mission: science goals, requirements and mission concept.” In: *Experimental Astronomy* 52.3, pp. 183–218. DOI: 10.1007/s10686-021-09807-8. arXiv: 2104.09531 [astro-ph.IM].

Amigó, J. M., S. Zambrano, and M. A. F. Sanjuán (Sept. 2007). “True and false forbidden patterns in deterministic and random dynamics.” In: *EPL (Europhysics Letters)* 79.5, p. 50001. DOI: 10.1209/0295-5075/79/50001.

Amigó, José M., Ljupco Kocarev, and Janusz Szczepanski (June 2006). “Order patterns and chaos.” In: *Physics Letters A* 355.1, pp. 27–31. DOI: 10.1016/j.physleta.2006.01.093.

Aptekar, R. L. et al. (Feb. 1995). “Konus-W Gamma-Ray Burst Experiment for the GGS Wind Spacecraft.” In: 71.1-4, pp. 265–272. DOI: 10.1007/BF00751332.

Arcavi, Iair et al. (Nov. 2017). “Optical emission from a kilonova following a gravitational-wave-detected neutron-star merger.” In: *Nature* 551.7678, pp. 64–66. DOI: 10.1038/nature24291. arXiv: 1710.05843 [astro-ph.HE].

Ascenzi, S. et al. (Sept. 2020). “High-latitude emission from the structured jet of γ-ray bursts observed off-axis.” In: *A&A* 641, A61, A61. DOI: 10.1051/0004-6361/202038265. arXiv: 2004.12215 [astro-ph.HE].

Aschwanden, M. J. (Mar. 2012a). “A statistical fractal-diffusive avalanche model of a slowly-driven self-organized criticality system.” In: *A&A* 539, A2, A2. DOI: 10.1051/0004-6361/201118237. arXiv: 1112.4859 [astro-ph.SR].

— (2013). *Self-Organized Criticality Systems*. DOI: https://doi.org/10.1007/978-3-642-15001-2.

Aschwanden, Markus J. (Dec. 2011). “The State of Self-organized Criticality of the Sun During the Last Three Solar Cycles. I. Observations.” In: 274.1-2, pp. 99–117. DOI: 10.1007/s11207-011-9755-0. arXiv: 1006.4861 [astro-ph.SR].

— (Sept. 2012b). “The Spatio-temporal Evolution of Solar Flares Observed with AIA/SDO: Fractal Diffusion, Sub-diffusion, or Logistic Growth?” In: *ApJ* 757.1, 94, p. 94. DOI: 10.1088/0004-637X/757/1/94. arXiv: 1208.1527 [astro-ph.SR].

— (Feb. 2014). “A Macroscopic Description of a Generalized Self-organized Criticality System: Astrophysical Applications.” In: *ApJ* 782.1, 54, p. 54. DOI: 10.1088/0004-637X/782/1/54. arXiv: 1310.4191 [astro-ph.SR].

Aschwanden, Markus J. and Clare E. Parnell (June 2002). “Nanoflare Statistics from First Principles: Fractal Geometry and Temperature Synthesis.” In: *ApJ* 572.2, pp. 1048–1071. DOI: 10.1086/340385.

Aschwanden, Markus J. and Carolus J. Schrijver (July 2025). “Self-organized Criticality across 13 Orders of Magnitude in the Solar–Stellar Connection.” In: *ApJ* 987.2, 140, p. 140. DOI: 10.3847/1538-4357/addc58. arXiv: 2503.18136 [astro-ph.SR].

Aschwanden, Markus J. et al. (Jan. 2016). “25 Years of Self-Organized Criticality: Solar and Astrophysics.” In: 198.1-4, pp. 47–166. DOI: 10.1007/s11214-014-0054-6. arXiv: 1403.6528 [astro-ph.IM].

Atwood, W. B. et al. (2009). “The Large Area Telescope on the Fermi Gamma-Ray Space Telescope Mission.” In: *ApJ* 697.2, pp. 1071–1102. DOI: 10.1088/0004-637X/697/2/1071. arXiv: 0902.1089 [astro-ph.IM].

Axelsson, M. et al. (Mar. 2025). “GRB 221009A: The B.O.A.T. Burst that Shines in Gamma Rays.” In: *ApJS* 277.1, 24, p. 24. DOI: 10.3847/1538-4365/ada272. arXiv: 2409.04580 [astro-ph.HE].

Bak, Per, Chao Tang, and Kurt Wiesenfeld (July 1987). "Self-organized criticality: An explanation of the 1/f noise." In: 59.4, pp. 381–384. DOI: `10.1103/PhysRevLett.59.381`.

— (July 1988). "Self-organized criticality." In: 38.1, pp. 364–374. DOI: `10.1103/PhysRevA.38.364`.

Band, D. et al. (Aug. 1993). "BATSE observations of gamma-ray burst spectra. I - Spectral diversity." In: *ApJ* 413, pp. 281–292. DOI: `10.1086/172995`.

Bandt, Christoph and Bernd Pompe (Apr. 2002). "Permutation Entropy: A Natural Complexity Measure for Time Series." In: 88.17, p. 174102. DOI: `10.1103/PhysRevLett.88.174102`.

Bazzanini, L. et al. (Sept. 2024). "Long gamma-ray burst light curves as the result of a common stochastic pulse–avalanche process." In: *A&A* 689, A266, A266. DOI: `10.1051/0004-6361/202450150`. arXiv: `2403.18754 [astro-ph.HE]`.

Beloborodov, A. M., R. Hascoët, and I. Vurm (June 2014). "On the Origin of GeV Emission in Gamma-Ray Bursts." In: *ApJ* 788, 36, p. 36. DOI: `10.1088/0004-637X/788/1/36`. arXiv: `1307.2663 [astro-ph.HE]`.

Beloborodov, A. M., B. E. Stern, and R. Svensson (May 2000). "Power Density Spectra of Gamma-Ray Bursts." In: *ApJ* 535, pp. 158–166. DOI: `10.1086/308836`.

Beniamini, Paz and Tsvi Piran (Aug. 2019). "The Gravitational waves merger time distribution of binary neutron star systems." In: *MNRAS* 487.4, pp. 4847–4854. DOI: `10.1093/mnras/stz1589`. arXiv: `1903.11614 [astro-ph.HE]`.

Beniamini, Paz et al. (Feb. 2020). "X-ray plateaus in gamma-ray bursts' light curves from jets viewed slightly off-axis." In: *MNRAS* 492.2, pp. 2847–2857. DOI: `10.1093/mnras/staa070`. arXiv: `1907.05899 [astro-ph.HE]`.

Berger, E., W. Fong, and R. Chornock (Sept. 2013). "An r-process Kilonova Associated with the Short-hard GRB 130603B." In: *ApJL* 774.2, L23, p. L23. DOI: `10.1088/2041-8205/774/2/L23`. arXiv: `1306.3960 [astro-ph.HE]`.

Berger, E., S. R. Kulkarni, and R. A. Chevalier (Sept. 2002). "The Radio Evolution of the Ordinary Type Ic Supernova SN 2002ap." In: *ApJL* 577, pp. L5–L8. DOI: `10.1086/344045`. eprint: `astro-ph/0206183`.

Bernardini, M. G. et al. (Jan. 2015). "Comparing the spectral lag of short and long gamma-ray bursts and its relation with the luminosity." In: *MNRAS* 446.2, pp. 1129–1138. DOI: `10.1093/mnras/stu2153`. arXiv: `1410.5216 [astro-ph.HE]`.

Bernardini, Maria Grazia (Sept. 2015). "Gamma-ray bursts and magnetars: Observational signatures and predictions." In: *Journal of High Energy Astrophysics* 7, pp. 64–72. DOI: `10.1016/j.jheap.2015.05.003`.

Blanchard, Peter K., Edo Berger, and Wen-fai Fong (Feb. 2016). "The Offset and Host Light Distributions of Long Gamma-Ray Bursts: A New View From HST Observations of Swift Bursts." In: *ApJ* 817.2, 144, p. 144. DOI: `10.3847/0004-637X/817/2/144`. arXiv: `1509.07866 [astro-ph.HE]`.

Blandford, R. D. and C. F. McKee (Aug. 1976). "Fluid dynamics of relativistic blast waves." In: *Physics of Fluids* 19, pp. 1130–1138. DOI: `10.1063/1.861619`.

Blandford, R. D. and R. L. Znajek (1977). "Electromagnetic extraction of energy from Kerr black holes." In: *MNRAS* 179, pp. 433–456. DOI: `10.1093/mnras/179.3.433`.

Bloom, J. S., S. R. Kulkarni, and S. G. Djorgovski (2002). "The Observed Offset Distribution of Gamma-Ray Bursts from Their Host Galaxies: A Robust Clue to the Nature of the

Progenitors." In: 123.3, pp. 1111–1148. DOI: 10.1086/338893. arXiv: astro-ph/0010176 [astro-ph].

Boella, G. et al. (1997a). "BeppoSAX, the wide band mission for X-ray astronomy." In: 122, pp. 299–307. DOI: 10.1051/aas:1997136.

Boella, G. et al. (Apr. 1997b). "The medium-energy concentrator spectrometer on board the BeppoSAX X-ray astronomy satellite." In: 122, pp. 327–340. DOI: 10.1051/aas:1997138.

Bohlin, J. David et al. (Feb. 1980). "Solar Maximum Mission." In: 65.1, pp. 5–14. DOI: 10.1007/BF00151380.

Borgonovo, L. et al. (Apr. 2007). "On the temporal variability classes found in long gamma-ray bursts with known redshift." In: *A&A* 465, pp. 765–775. DOI: 10.1051/0004-6361:20066613. eprint: arXiv:astro-ph/0701920.

Bouchaud, Jean-Philippe (July 2024). "The Self-Organized Criticality Paradigm in Economics & Finance." In: *arXiv e-prints*, arXiv:2407.10284, arXiv:2407.10284. DOI: 10.48550/arXiv.2407.10284. arXiv: 2407.10284 [q-fin.GN].

Bošnjak, Ž. and F. Daigne (Aug. 2014). "Spectral evolution in gamma-ray bursts: Predictions of the internal shock model and comparison to observations." In: *A&A* 568, A45, A45. DOI: 10.1051/0004-6361/201322341. arXiv: 1404.4577 [astro-ph.HE].

Båth, Markus (Jan. 1955). "The relation between magnitude and energy of earthquakes." In: *Transactions, American Geophysical Union* 36.5, pp. 861–865. DOI: 10.1029/TR036i005p00861.

Bromberg, O. et al. (Feb. 2013). "Short versus Long and Collapsars versus Non-collapsars: A Quantitative Classification of Gamma-Ray Bursts." In: *ApJ* 764, 179, p. 179. DOI: 10.1088/0004-637X/764/2/179. arXiv: 1210.0068 [astro-ph.HE].

Brown, Stephen R., Christopher H. Scholz, and John B. Rundle (Feb. 1991). "A simplified spring-block model of earthquakes." In: 18.2, pp. 215–218. DOI: 10.1029/91GL00210.

Burgess, J. M. et al. (Apr. 2014). "An Observed Correlation between Thermal and Non-thermal Emission in Gamma-Ray Bursts." In: *ApJ* 784, L43, p. L43. DOI: 10.1088/2041-8205/784/2/L43. arXiv: 1403.0374 [astro-ph.HE].

Burridge, R. and L. Knopoff (June 1967). "Model and theoretical seismicity." In: *Bulletin of the Seismological Society of America* 57.3, pp. 341–371. DOI: 10.1785/BSSA0570030341.

Burrows, D. N. et al. (Oct. 2005). "The Swift X-Ray Telescope." In: *Space Sci. Rev.* 120, pp. 165–195. DOI: 10.1007/s11214-005-5097-2. eprint: arXiv:astro-ph/0508071.

Camilloni, Filippo et al. (July 2022). "Blandford-Znajek monopole expansion revisited: novel non-analytic contributions to the power emission." In: 2022.7, 032, p. 032. DOI: 10.1088/1475-7516/2022/07/032. arXiv: 2201.11068 [gr-qc].

Camisasca, A. E. et al. (Apr. 2023a). "GRB 230307A: short mininum variability timescale compatible with a merger origin." In: *GRB Coordinates Network* 33577, p. 1.

Camisasca, A. E. et al. (Mar. 2023b). "GRB minimum variability timescale with Insight-HXMT and Swift. Implications for progenitor models, dissipation physics, and GRB classifications." In: *A&A* 671, A112, A112. DOI: 10.1051/0004-6361/202245657. arXiv: 2301.01176 [astro-ph.HE].

Carlson, J. M. and J. S. Langer (Dec. 1989a). "Mechanical model of an earthquake fault." In: 40.11, pp. 6470–6484. DOI: 10.1103/PhysRevA.40.6470.

— (May 1989b). "Properties of earthquakes generated by fault dynamics." In: 62.22, pp. 2632–2635. DOI: 10.1103/PhysRevLett.62.2632.

Castignani, G. et al. (May 2014). “Time delays between Fermi-LAT and GBM light curves of gamma-ray bursts.” In: *A&A* 565, A60, A60. DOI: `10.1051/0004-6361/201322636`. arXiv: `1403.1199 [astro-ph.HE]`.

Charbonneau, Paul et al. (Nov. 2001). “Avalanche models for solar flares (Invited Review).” In: 203.2, pp. 321–353. DOI: `10.1023/A:1013301521745`.

Cheng, Kang-Fa et al. (Aug. 2021). “The afterglow emission from a stratified jet in GRB 170817A.” In: *Research in Astronomy and Astrophysics* 21.7, 177, p. 177. DOI: `10.1088/1674-4527/21/7/177`. arXiv: `2103.08205 [astro-ph.HE]`.

Cheng, L. X. et al. (Aug. 1995). “The time delay of gamma-ray bursts in the soft energy band.” In: *A&A* 300, p. 746.

Cherenkov Telescope Array Consortium et al. (2019). *Science with the Cherenkov Telescope Array*. DOI: `10.1142/10986`.

Chincarini, G. et al. (Aug. 2010). “Unveiling the origin of X-ray flares in gamma-ray bursts.” In: *MNRAS* 406, pp. 2113–2148. DOI: `10.1111/j.1365-2966.2010.17037.x`. arXiv: `1004.0901 [astro-ph.HE]`.

Christe, S. et al. (Apr. 2008). “RHESSI Microflare Statistics. I. Flare-Finding and Frequency Distributions.” In: *ApJ* 677.2, pp. 1385–1394. DOI: `10.1086/529011`.

Ciprini, S. et al. (July 2003). “The Optical Variability of the Blazar GC 0109+224. Hints of Self-organized Criticality? (Poster).” In: *High Energy Blazar Astronomy*. Ed. by Leo O. Takalo and Esko Valtaoja. Vol. 299. Astronomical Society of the Pacific Conference Series, p. 265.

Colgate, Stirling A. and Hui Li (May 1998). “The galactic model of GRBs.” In: *Gamma-Ray Bursts, 4th Hunstville Symposium*. Ed. by Charles A. Meegan, Robert D. Preece, and Thomas M. Koshut. Vol. 428. American Institute of Physics Conference Series. AIP, pp. 820–824. DOI: `10.1063/1.55437`.

Cordier, B. et al. (July 2025). “SVOM GRB 250314A at $z \simeq 7.3$: an exploding star in the era of reionization.” In: *arXiv e-prints*, arXiv:2507.18783, arXiv:2507.18783. DOI: `10.48550/arXiv.2507.18783`. arXiv: `2507.18783 [astro-ph.HE]`.

Costa, E. et al. (June 1997a). “Discovery of an X-ray afterglow associated with the γ-ray burst of 28 February 1997.” In: *Nature* 387, pp. 783–785. DOI: `10.1038/42885`. eprint: `astro-ph/9706065`.

Costa, E. et al. (May 1997b). “GRB 970508.” In: 6649, p. 1.

Creutz, Michael (Nov. 1996). “Cellular automata and self-organized criticality.” In: *arXiv e-prints*, hep-lat/9611017, hep–lat/9611017. DOI: `10.48550/arXiv.hep-lat/9611017`. arXiv: `hep-lat/9611017 [hep-lat]`.

Crosby, N., M. Aschwanden, and B. Dennis (Sept. 1993). “Frequency distributions of solar X-ray flare parameters.” In: *Advances in Space Research* 13.9, pp. 179–182. DOI: `10.1016/0273-1177(93)90474-P`.

Dai, Z. G. and T. Lu (Feb. 2001). “Could the unusual optical afterglow of GRB 000301c arise from a non-relativistic shock with energy injection?” In: *A&A* 367, pp. 501–505. DOI: `10.1051/0004-6361:20010062`. arXiv: `astro-ph/0005417 [astro-ph]`.

Daigne, F. and R. Mochkovitch (May 1998). “Gamma-ray bursts from internal shocks in a relativistic wind: temporal and spectral properties.” In: *MNRAS* 296, pp. 275–286. DOI: `10.1046/j.1365-8711.1998.01305.x`. eprint: `astro-ph/9801245`.

Dall'Osso, S. et al. (Feb. 2011). "Gamma-ray bursts afterglows with energy injection from a spinning down neutron star." In: *A&A* 526, A121, A121. DOI: 10.1051/0004-6361/201014168. arXiv: 1004.2788 [astro-ph.HE].

Deesamer, Chitipat, Poemwai Chainakun, and Warintorn Sreethawong (Oct. 2024). "Neutrino Oscillation Effects on the Luminosity of Neutrino-dominated Accretion Flows around Black Holes." In: *ApJ* 973.2, 165, p. 165. DOI: 10.3847/1538-4357/ad68f5. arXiv: 2407.20507 [astro-ph.HE].

Dennis, B. R. (Oct. 1985). "Solar Hard X-Ray Bursts." In: 100, p. 465. DOI: 10.1007/BF00158441.

Denton, Peter B. and Irene Tamborra (Mar. 2018). "Exploring the Properties of Choked Gamma-ray Bursts with IceCube's High-energy Neutrinos." In: *ApJ* 855.1, 37, p. 37. DOI: 10.3847/1538-4357/aaab4a. arXiv: 1711.00470 [astro-ph.HE].

Dereli-Bégué, Hüsne et al. (Sept. 2022). "A wind environment and Lorentz factors of tens explain gamma-ray bursts X-ray plateau." In: *Nature Communications* 13, 5611, p. 5611. DOI: 10.1038/s41467-022-32881-1. arXiv: 2207.11066 [astro-ph.HE].

Dichiara, S. et al. (June 2013). "Average power density spectrum of long GRBs detected with BeppoSAX/GRBM and with Fermi/GBM." In: *MNRAS* 431, pp. 3608–3617. DOI: 10.1093/mnras/stt445. arXiv: 1303.2584 [astro-ph.HE].

Dichiara, S. et al. (Apr. 2016). "Correlation between peak energy and Fourier power density spectrum slope in gamma-ray bursts." In: *A&A* 589, A97, A97. DOI: 10.1051/0004-6361/201527635. arXiv: 1603.06889 [astro-ph.HE].

Dichiara, S. et al. (Sept. 2023). "A Luminous Precursor in the Extremely Bright GRB 230307A." In: *ApJL* 954.1, L29, p. L29. DOI: 10.3847/2041-8213/acf21d. arXiv: 2307.02996 [astro-ph.HE].

Dilillo, Giuseppe et al. (Feb. 2024). "Gamma-Ray Burst Detection with Poisson-FOCuS and Other Trigger Algorithms." In: *ApJ* 962.2, 137, p. 137. DOI: 10.3847/1538-4357/ad15ff. arXiv: 2312.08817 [astro-ph.IM].

Dong, YongWei et al. (Jan. 2010). "SVOM gamma ray monitor." In: *Science China Physics, Mechanics, and Astronomy* 53, pp. 40–42. DOI: 10.1007/s11433-010-0011-7. arXiv: 0907.2768 [astro-ph.IM].

Drenkhahn, G. and H. C. Spruit (Sept. 2002). "Efficient acceleration and radiation in Poynting flux powered GRB outflows." In: *A&A* 391, pp. 1141–1153. DOI: 10.1051/0004-6361:20020839. arXiv: astro-ph/0202387 [astro-ph].

Dănilă, B., T. Harko, and G. Mocanu (Nov. 2015). "Self-organized criticality in a two-dimensional cellular automaton model of a magnetic flux tube with background flow." In: *MNRAS* 453.3, pp. 2982–2991. DOI: 10.1093/mnras/stv1821. arXiv: 1508.02305 [astro-ph.HE].

Einstein, A. (Jan. 1905). "Über die von der molekularkinetischen Theorie der Wärme geforderte Bewegung von in ruhenden Flüssigkeiten suspendierten Teilchen." In: *Annalen der Physik* 322.8, pp. 549–560. DOI: 10.1002/andp.19053220806.

Estevez-Rams, Ernesto et al. (May 2019). "Complexity-entropy analysis at different levels of organisation in written language." In: *pone* 24.12, 1744, p. 1744. DOI: 10.1371/journal.pone.0214863. URL: https://doi.org/10.1371/journal.pone.0214863.

Fadlallah, Bilal et al. (Feb. 2013). "Weighted-permutation entropy: A complexity measure for time series incorporating amplitude information." In: 87.2, 022911, p. 022911. DOI: 10.1103/PhysRevE.87.022911.

Fan, Xuewu et al. (Dec. 2020). "The Visible Telescope onboard the Chinese-French SVOM satellite." In: *Space Telescopes and Instrumentation 2020: Optical, Infrared, and Millimeter Wave.*

Ed. by Makenzie Lystrup and Marshall D. Perrin. Vol. 11443. Society of Photo-Optical Instrumentation Engineers (SPIE) Conference Series, 114430Q, 114430Q. DOI: 10.1117/12.2561854.

Fan, Yizhong and Tsvi Piran (June 2006). “Gamma-ray burst efficiency and possible physical processes shaping the early afterglow.” In: *MNRAS* 369.1, pp. 197–206. DOI: 10.1111/j.1365-2966.2006.10280.x. arXiv: astro-ph/0601054 [astro-ph].

Fenimore, E. E., E. Ramirez-Ruiz, and B. Wu (June 1999). “GRB 990123: Evidence that the Gamma Rays Come from a Central Engine.” In: *ApJ* 518, pp. L73–L76. DOI: 10.1086/312075. eprint: astro-ph/9902007.

Fenimore, E. E. et al. (Aug. 1995). “Gamma-Ray Burst Peak Duration as a Function of Energy.” In: *ApJ* 448, p. L101. DOI: 10.1086/309603. eprint: arXiv:astro-ph/9504075.

Fishman, Gerald J. et al. (May 1994). “The First BATSE Gamma-Ray Burst Catalog.” In: *ApJS* 92, p. 229. DOI: 10.1086/191968.

Fletcher, L. et al. (Sept. 2011). “An Observational Overview of Solar Flares.” In: 159.1-4, pp. 19–106. DOI: 10.1007/s11214-010-9701-8. arXiv: 1109.5932 [astro-ph.SR].

Fong, W. et al. (2013). “Demographics of the Galaxies Hosting Short-duration Gamma-Ray Bursts.” In: *ApJ* 769.1, 56, p. 56. DOI: 10.1088/0004-637X/769/1/56. arXiv: 1302.3221 [astro-ph.HE].

Fong, Wen-fai et al. (Nov. 2022). “Short GRB Host Galaxies. I. Photometric and Spectroscopic Catalogs, Host Associations, and Galactocentric Offsets.” In: *ApJ* 940.1, 56, p. 56. DOI: 10.3847/1538-4357/ac91d0. arXiv: 2206.01763 [astro-ph.GA].

Frontera, F. et al. (1997). “The high energy instrument PDS on-board the BeppoSAX X–ray astronomy satellite.” In: 122, pp. 357–369. DOI: 10.1051/aas:1997140.

Frontera, Filippo (June 2024). “A Short History of the First 50 Years: From the GRB Prompt Emission and Afterglow Discoveries to the Multimessenger Era.” In: *Universe* 10.6, 260, p. 260. DOI: 10.3390/universe10060260. arXiv: 2407.20305 [astro-ph.HE].

Fruchter, A. S. et al. (2006). “Long γ-ray bursts and core-collapse supernovae have different environments.” In: *Nature* 441.7092, pp. 463–468. DOI: 10.1038/nature04787. arXiv: astro-ph/0603537 [astro-ph].

Fynbo, J. P. U., D. Malesani, and P. Jakobsson (Nov. 2012). “Long Gamma-Ray Burst Host Galaxies and their Environments.” In: *Gamma-Ray Bursts, Cambridge Astrophysics Series 51, p. 269-301*, pp. 269–301.

Galama, T. J. et al. (Oct. 1998). “An unusual supernova in the error box of the γ-ray burst of 25 April 1998.” In: *Nature* 395, pp. 670–672. DOI: 10.1038/27150. eprint: astro-ph/9806175.

Gao, H., B.-B. Zhang, and B. Zhang (Apr. 2012). “Stepwise Filter Correlation Method and Evidence of Superposed Variability Components in Gamma-Ray Burst Prompt Emission Light Curves.” In: *ApJ* 748, 134, p. 134. DOI: 10.1088/0004-637X/748/2/134. arXiv: 1103.0074 [astro-ph.HE].

Gehrels, N. et al. (Dec. 1993). “The Compton Gamma-Ray Observatory.” In: *Scientific American* 269, p. 68. DOI: 10.1038/scientificamerican1293-68.

Gehrels, N. et al. (Aug. 2004). “The Swift Gamma-Ray Burst Mission.” In: *ApJ* 611, pp. 1005–1020. DOI: 10.1086/422091.

Gehrels, N. et al. (Dec. 2006). “A new γ-ray burst classification scheme from GRB060614.” In: *Nature* 444, pp. 1044–1046. DOI: 10.1038/nature05376. eprint: arXiv:astro-ph/0610635.

Genet, F., F. Daigne, and R. Mochkovitch (Oct. 2007). "Can the early X-ray afterglow of gamma-ray bursts be explained by a contribution from the reverse shock?" In: *MNRAS* 381.2, pp. 732–740. DOI: 10.1111/j.1365-2966.2007.12243.x. arXiv: astro-ph/0701204 [astro-ph].

Geng, Jin-Jun et al. (June 2019). "Propagation of a Short GRB Jet in the Ejecta: Jet Launching Delay Time, Jet Structure, and GW170817/GRB 170817A." In: *ApJL* 877.2, L40, p. L40. DOI: 10.3847/2041-8213/ab224b. arXiv: 1904.02326 [astro-ph.HE].

Ghirlanda, G., A. Pescalli, and G. Ghisellini (July 2013). "Photospheric emission throughout GRB 100507 detected by Fermi." In: *MNRAS* 432.4, pp. 3237–3244. DOI: 10.1093/mnras/stt681. arXiv: 1305.3287 [astro-ph.HE].

Ghirlanda, G. et al. (Jan. 2018). "Bulk Lorentz factors of gamma-ray bursts." In: *A&A* 609, A112, A112. DOI: 10.1051/0004-6361/201731598. arXiv: 1711.06257 [astro-ph.HE].

Ghisellini, G. et al. (Apr. 2007). ""Late Prompt" Emission in Gamma-Ray Bursts?" In: *ApJL* 658.2, pp. L75–L78. DOI: 10.1086/515570. arXiv: astro-ph/0701430 [astro-ph].

Gill, Ramandeep and Jonathan Granot (Aug. 2018). "Afterglow imaging and polarization of misaligned structured GRB jets and cocoons: breaking the degeneracy in GRB 170817A." In: *MNRAS* 478.3, pp. 4128–4141. DOI: 10.1093/mnras/sty1214. arXiv: 1803.05892 [astro-ph.HE].

Gillanders, J. H. and S. J. Smartt (Apr. 2025). "Analysis of the JWST spectra of the kilonova AT 2023vfi accompanying GRB 230307A." In: *MNRAS* 538.3, pp. 1663–1689. DOI: 10.1093/mnras/staf287. arXiv: 2408.11093 [astro-ph.HE].

Godet, O. et al. (July 2014). "The x-/gamma-ray camera ECLAIRs for the gamma-ray burst mission SVOM." In: *Space Telescopes and Instrumentation 2014: Ultraviolet to Gamma Ray*. Ed. by Tadayuki Takahashi, Jan-Willem A. den Herder, and Mark Bautz. Vol. 9144. Society of Photo-Optical Instrumentation Engineers (SPIE) Conference Series, 914424, p. 914424. DOI: 10.1117/12.2055507. arXiv: 1406.7759 [physics.ins-det].

Golkhou, V. Z. and N. R. Butler (May 2014). "Uncovering the Intrinsic Variability of Gamma-Ray Bursts." In: *ApJ* 787, 90, p. 90. DOI: 10.1088/0004-637X/787/1/90. arXiv: 1403.4254 [astro-ph.HE].

Golkhou, V. Z., N. R. Butler, and O. M. Littlejohns (Oct. 2015). "The Energy Dependence of GRB Minimum Variability Timescales." In: *ApJ* 811, 93, p. 93. DOI: 10.1088/0004-637X/811/2/93. arXiv: 1501.05948 [astro-ph.HE].

Gottlieb, Ore, Amir Levinson, and Ehud Nakar (Sept. 2019). "High efficiency photospheric emission entailed by formation of a collimation shock in gamma-ray bursts." In: *MNRAS* 488.1, pp. 1416–1426. DOI: 10.1093/mnras/stz1828. arXiv: 1904.07244 [astro-ph.HE].

— (June 2020). "Intermittent hydrodynamic jets in collapsars do not produce GRBs." In: *MNRAS* 495.1, pp. 570–577. DOI: 10.1093/mnras/staa1216. arXiv: 2002.12384 [astro-ph.HE].

Gottlieb, Ore, Ehud Nakar, and Omer Bromberg (Jan. 2021). "The structure of hydrodynamic γ-ray burst jets." In: *MNRAS* 500.3, pp. 3511–3526. DOI: 10.1093/mnras/staa3501. arXiv: 2006.02466 [astro-ph.HE].

Gottlieb, Ore et al. (Nov. 2020). "The structure of weakly magnetized γ-ray burst jets." In: *MNRAS* 498.3, pp. 3320–3333. DOI: 10.1093/mnras/staa2567. arXiv: 2007.11590 [astro-ph.HE].

Gottlieb, Ore et al. (July 2021). "Intermittent mildly magnetized jets as the source of GRBs." In: *MNRAS* 504.3, pp. 3947–3955. DOI: 10.1093/mnras/stab1068. arXiv: 2102.00005 [astro-ph.HE].

Götz, D. et al. (May 2009). "SVOM: a new mission for Gamma-Ray Burst Studies." In: *Gamma-ray Burst: Sixth Huntsville Symposium*. Ed. by Charles Meegan, Chryssa Kouveliotou, and Neil Gehrels. Vol. 1133. American Institute of Physics Conference Series. AIP, pp. 25–30. DOI: `10.1063/1.3155898`. arXiv: `0906.4195 [astro-ph.IM]`.

Götz, D. et al. (Apr. 2023). "The scientific performance of the microchannel X-ray telescope on board the SVOM mission." In: *Experimental Astronomy* 55.2, pp. 487–519. DOI: `10.1007/s10686-022-09881-6`. arXiv: `2211.13489 [astro-ph.IM]`.

Götz, Diego et al. (Feb. 2021). "The Infra-Red Telescope (IRT) on board the THESEUS mission." In: *arXiv e-prints*, arXiv:2102.08696, arXiv:2102.08696. DOI: `10.48550/arXiv.2102.08696`. arXiv: `2102.08696 [astro-ph.IM]`.

Göğüş, E. et al. (Dec. 1999). "Statistical Properties of SGR 1900+14 Bursts." In: *ApJ* 526, pp. L93–L96. DOI: `10.1086/312380`. eprint: `astro-ph/9910062`.

Gowri, A et al. (Sept. 2024). "Gamma-ray burst pulse structures and emission mechanisms." In: *arXiv e-prints*, arXiv:2409.17860, arXiv:2409.17860. DOI: `10.48550/arXiv.2409.17860`. arXiv: `2409.17860 [astro-ph.HE]`.

Granot, Jonathan, Johann Cohen-Tanugi, and Eduardo do Couto e. Silva (Apr. 2008). "Opacity Buildup in Impulsive Relativistic Sources." In: *ApJ* 677.1, pp. 92–126. DOI: `10.1086/526414`. arXiv: `0708.4228 [astro-ph]`.

Granot, Jonathan and Pawan Kumar (2006). "Distribution of gamma-ray burst ejecta energy with Lorentz factor." In: *MNRAS* 366.1, pp. L13–L16. DOI: `10.1111/j.1745-3933.2005.00121.x`. arXiv: `astro-ph/0511049 [astro-ph]`.

Greco, G. et al. (Sept. 2011). "Evidence of Deterministic Components in the Apparent Randomness of GRBs: Clues of a Chaotic Dynamic." In: *NatSR* 1, 91. DOI: `10.1038/srep00091`.

Guidorzi, C. (Apr. 2015). "MEPSA: a flexible peak search algorithm designed for uniformly spaced time series." In: *Astronomy and Computing* 10, pp. 54–60. ISSN: 2213-1337. DOI: `10.1016/j.ascom.2015.01.001`. URL: `http://www.sciencedirect.com/science/article/pii/S2213133715000025`.

Guidorzi, C., S. Dichiara, and L. Amati (Apr. 2016). "Individual power density spectra of Swift gamma-ray bursts." In: *A&A* 589, A98, A98. DOI: `10.1051/0004-6361/201527642`. arXiv: `1603.06890 [astro-ph.HE]`.

Guidorzi, C. et al. (May 2012). "Average power density spectrum of Swift long gamma-ray bursts in the observer and in the source-rest frames." In: *MNRAS* 422, pp. 1785–1803. DOI: `10.1111/j.1365-2966.2012.20758.x`. arXiv: `1202.3443 [astro-ph.HE]`.

Guidorzi, C. et al. (Mar. 2015). "A Common Stochastic Process Rules Gamma-Ray Burst Prompt Emission and X-Ray Flares." In: *ApJ* 801, 57, p. 57. DOI: `10.1088/0004-637X/801/1/57`. arXiv: `1501.02706 [astro-ph.HE]`.

Guidorzi, C. et al. (May 2020). "A search for prompt γ-ray counterparts to fast radio bursts in the Insight-HXMT data." In: *A&A* 637, A69, A69. DOI: `10.1051/0004-6361/202037797`. arXiv: `2003.10889 [astro-ph.HE]`.

Guidorzi, C. et al. (May 2024). "Distribution of the number of peaks within a long gamma-ray burst." In: *A&A* 685, A34, A34. DOI: `10.1051/0004-6361/202449200`. arXiv: `2402.17282 [astro-ph.HE]`.

Guidorzi, C. et al. (Sept. 2025). "GRB X-ray plateaus as evidence that the afterglow begins before the prompt gamma-ray emission." In: *arXiv e-prints*, arXiv:2509.18996, arXiv:2509.18996. DOI: `10.48550/arXiv.2509.18996`. arXiv: `2509.18996 [astro-ph.HE]`.

Guiriec, S. et al. (Feb. 2011). "Detection of a Thermal Spectral Component in the Prompt Emission of GRB 100724B." In: *ApJ* 727, L33, p. L33. DOI: `10.1088/2041-8205/727/2/L33`. arXiv: `1010.4601 [astro-ph.HE]`.

Guiriec, S. et al. (2013). "Evidence for a Photospheric Component in the Prompt Emission of the Short GRB 120323A and Its Effects on the GRB Hardness-Luminosity Relation." In: *ApJ* 770.1, 32, p. 32. DOI: `10.1088/0004-637X/770/1/32`. arXiv: `1210.7252 [astro-ph.HE]`.

Gupta, Rahul et al. (Aug. 2021). "GRB 140102A: insight into prompt spectral evolution and early optical afterglow emission." In: *MNRAS* 505.3, pp. 4086–4105. DOI: `10.1093/mnras/stab1573`. arXiv: `2105.13145 [astro-ph.HE]`.

Gutenberg, B. and C. F. Richter (Oct. 1944). "Frequency of earthquakes in California*." In: *Bulletin of the Seismological Society of America* 34.4, pp. 185–188. DOI: `10.1785/BSSA0340040185`.

H. E. S. S. Collaboration et al. (June 2021). "Revealing x-ray and gamma ray temporal and spectral similarities in the GRB 190829A afterglow." In: *Science* 372.6546, pp. 1081–1085. DOI: `10.1126/science.abe8560`. arXiv: `2106.02510 [astro-ph.HE]`.

Hakkila, Jon and Robert D. Preece (Mar. 2014). "Gamma-Ray Burst Pulse Shapes: Evidence for Embedded Shock Signatures?" In: *ApJ* 783.2, 88, p. 88. DOI: `10.1088/0004-637X/783/2/88`. arXiv: `1401.4047 [astro-ph.HE]`.

Hakkila, Jon et al. (Apr. 2008). "Correlations between Lag, Luminosity, and Duration in Gamma-Ray Burst Pulses." In: *ApJL* 677.2, p. L81. DOI: `10.1086/588094`. arXiv: `0803.1655 [astro-ph]`.

Hascoët, R., F. Daigne, and R. Mochkovitch (Mar. 2013). "Prompt thermal emission in gamma-ray bursts." In: *A&A* 551, A124, A124. DOI: `10.1051/0004-6361/201220023`. arXiv: `1302.0235 [astro-ph.HE]`.

— (July 2014). "The prompt-early afterglow connection in gamma-ray bursts: implications for the early afterglow physics." In: *MNRAS* 442, pp. 20–27. DOI: `10.1093/mnras/stu750`. arXiv: `1401.0751 [astro-ph.HE]`.

Hascoët, R. et al. (Mar. 2012). "Do Fermi Large Area Telescope observations imply very large Lorentz factors in gamma-ray burst outflows?" In: *MNRAS* 421, pp. 525–545. DOI: `10.1111/j.1365-2966.2011.20332.x`. arXiv: `1107.5737 [astro-ph.HE]`.

Heise, J. et al. (May 1997). "GRB 970508." In: 6654, p. 2.

Howedi, Aadel, Ahmad Lotfi, and Amir Pourabdollah (July 2020). "An Entropy-Based Approach for Anomaly Detection in Activities of Daily Living in the Presence of a Visitor." In: *Entropy* 22.8, 845, p. 845. DOI: `10.3390/e22080845`.

Huang, Jie, Galina Narkounskaia, and Donald L. Turcotte (Nov. 1992). "A cellular-automata, slider-block model for earthquakes II. Demonstration of self-organized criticality for a 2-D system." In: *Geophysical Journal International* 111.2, pp. 259–269. DOI: `10.1111/j.1365-246X.1992.tb00575.x`.

Ioka, K. et al. (Oct. 2006). "Efficiency crisis of swift gamma-ray bursts with shallow X-ray afterglows: prior activity or time-dependent microphysics?" In: *A&A* 458.1, pp. 7–12. DOI: `10.1051/0004-6361:20064939`. arXiv: `astro-ph/0511749 [astro-ph]`.

Jager, R. et al. (Nov. 1997). "The Wide Field Cameras onboard the BeppoSAX X-ray Astronomy Satellite." In: 125, pp. 557–572. DOI: `10.1051/aas:1997243`.

Janiuk, Agnieszka, Bestin James, and Ishika Palit (Aug. 2021). "Variability of Magnetically Dominated Jets from Accreting Black Holes." In: *ApJ* 917.2, 102, p. 102. DOI: `10.3847/1538-4357/ac0624`. arXiv: `2105.13624 [astro-ph.HE]`.

Jin, Z.-P. et al. (Oct. 2015). “The Light Curve of the Macronova Associated with the Long–Short Burst GRB 060614.” In: *ApJ* 811, L22, p. L22. DOI: 10.1088/2041-8205/811/2/L22. arXiv: 1507.07206 [astro-ph.HE].

Jin, Zhi-Ping et al. (Jan. 2020). “A kilonova associated with GRB 070809.” In: *Nature Astronomy* 4, pp. 77–82. DOI: 10.1038/s41550-019-0892-y. arXiv: 1901.06269 [astro-ph.HE].

Kaneko, Y. et al. (Sept. 2015). “Short gamma-ray bursts with extended emission observed with Swift/BAT and Fermi/GBM.” In: *MNRAS* 452.1, pp. 824–837. DOI: 10.1093/mnras/stv1286. arXiv: 1506.05899 [astro-ph.HE].

Kasen, Daniel et al. (Nov. 2017). “Origin of the heavy elements in binary neutron-star mergers from a gravitational-wave event.” In: *Nature* 551.7678, pp. 80–84. DOI: 10.1038/nature24453. arXiv: 1710.05463 [astro-ph.HE].

Kelly, B. C., J. Bechtold, and A. Siemiginowska (June 2009). “Are the Variations in Quasar Optical Flux Driven by Thermal Fluctuations?” In: *ApJ* 698, 895-910, pp. 895–910. DOI: 10.1088/0004-637X/698/1/895. arXiv: 0903.5315 [astro-ph.CO].

Kelly, P. L., R. P. Kirshner, and M. Pahre (Nov. 2008). “Long γ-Ray Bursts and Type Ic Core-Collapse Supernovae Have Similar Locations in Hosts.” In: *ApJ* 687, pp. 1201–1207. DOI: 10.1086/591925. arXiv: 0712.0430.

Kennedy, M. R. et al. (June 2018). “Kepler K2 observations of the transitional millisecond pulsar PSR J1023+0038.” In: *MNRAS* 477.1, pp. 1120–1132. DOI: 10.1093/mnras/sty731. arXiv: 1801.10609 [astro-ph.HE].

Klebesadel, R. W., I. B. Strong, and R. A. Olson (June 1973). “Observations of Gamma-Ray Bursts of Cosmic Origin.” In: *ApJL* 182, p. L85. DOI: 10.1086/181225.

Kobayashi, S., T. Piran, and R. Sari (Nov. 1997). “Can Internal Shocks Produce the Variability in Gamma-Ray Bursts?” In: *ApJ* 490, p. 92. DOI: 10.1086/512791. eprint: arXiv:astro-ph/9705013.

Kocevski, D., F. Ryde, and E. Liang (Oct. 2003). “Search for Relativistic Curvature Effects in Gamma-Ray Burst Pulses.” In: *ApJ* 596, pp. 389–400. DOI: 10.1086/377707. eprint: astro-ph/0303556.

Kouveliotou, C. et al. (Aug. 1993). “Identification of two classes of gamma-ray bursts.” In: *ApJ* 413, pp. L101–L104. DOI: 10.1086/186969.

Krucker, Säm and Arnold O. Benz (July 1998). “Energy Distribution of Heating Processes in the Quiet Solar Corona.” In: *ApJL* 501.2, pp. L213–L216. DOI: 10.1086/311474.

Kumar, P. and B. Zhang (2015). “The Physics of Gamma-Ray Bursts and Relativistic Jets.” In: *Phys. Rep.* 561, pp. 1–109. ISSN: 0370-1573. DOI: 10.1016/j.physrep.2014.09.008. URL: http://www.sciencedirect.com/science/article/pii/S0370157314003846.

Kunjaya, C. et al. (Dec. 2011). “Can self-organized critical accretion disks generate a log-normal emission variability in AGN?” In: 336.2, pp. 455–460. DOI: 10.1007/s10509-011-0790-y. arXiv: 1107.1552 [astro-ph.CO].

LHAASO Collaboration et al. (June 2023). “A tera-electron volt afterglow from a narrow jet in an extremely bright gamma-ray burst.” In: *Science* 380.6652, pp. 1390–1396. DOI: 10.1126/science.adg9328. arXiv: 2306.06372 [astro-ph.HE].

Labanti, Claudio et al. (Feb. 2021). “The X/Gamma-ray Imaging Spectrometer (XGIS) on-board THESEUS: design, main characteristics, and concept of operation.” In: *arXiv e-prints*, arXiv:2102.08701, arXiv:2102.08701. DOI: 10.48550/arXiv.2102.08701. arXiv: 2102.08701 [astro-ph.IM].

Lamb, D. Q. (Dec. 1995). “The Distance Scale to Gamma-Ray Bursts.” In: 107, p. 1152. DOI: 10.1086/133673.

Lamb, G. P. et al. (Sept. 2019). “Short GRB 160821B: A Reverse Shock, a Refreshed Shock, and a Well-sampled Kilonova.” In: *ApJ* 883.1, 48, p. 48. DOI: 10.3847/1538-4357/ab38bb. arXiv: 1905.02159 [astro-ph.HE].

Lamb, Gavin P. and Shiho Kobayashi (July 2018). “GRB 170817A as a jet counterpart to gravitational wave triggerGW 170817.” In: *MNRAS* 478.1, pp. 733–740. DOI: 10.1093/mnras/sty1108. arXiv: 1710.05857 [astro-ph.HE].

Lan, Lin et al. (Mar. 2020). “The properties of prompt emission in short gamma-ray bursts with extended emission observed by Fermi/GBM.” In: *MNRAS* 492.3, pp. 3622–3630. DOI: 10.1093/mnras/staa044. arXiv: 2001.01150 [astro-ph.HE].

Langevin, Paul (1908). “Sur la théorie du mouvement brownien.” French. In: *Comptes Rendus de l’Académie des Sciences* 146, pp. 530–533.

Larsson, J., J. L. Racusin, and J. M. Burgess (Feb. 2015). “Evidence for Jet Launching Close to the Black Hole in GRB 101219b—A Fermi GRB Dominated by Thermal Emission.” In: *ApJL* 800.2, L34, p. L34. DOI: 10.1088/2041-8205/800/2/L34. arXiv: 1502.00645 [astro-ph.HE].

Lawrence, A. and I. Papadakis (Sept. 1993). “X-Ray Variability of Active Galactic Nuclei: A Universal Power Spectrum with Luminosity-dependent Amplitude.” In: *ApJL* 414, p. L85. DOI: 10.1086/187002.

Lazzati, D. and R. Perna (Feb. 2007). “X-ray flares and the duration of engine activity in gamma-ray bursts.” In: *MNRAS* 375, pp. L46–L50. DOI: 10.1111/j.1745-3933.2006.00273.x. eprint: astro-ph/0610730.

Leighly, Karen M. et al. (July 1997). “X-Ray Observations of the Broad-Line Radio Galaxy 3C 390.3.” In: *ApJ* 483.2, pp. 767–773. DOI: 10.1086/304276. arXiv: astro-ph/9703013 [astro-ph].

Lempel, Abraham and Jacob Ziv (1978). “Compression of Individual Sequences via Variable-Rate Coding.” In: *IEEE Transactions on Information Theory* 24.5, pp. 530–536. DOI: 10.1109/TIT.1978.1055934.

Levan, Andrew J. et al. (Feb. 2024). “Heavy-element production in a compact object merger observed by JWST.” In: *Nature* 626.8000, pp. 737–741. DOI: 10.1038/s41586-023-06759-1. arXiv: 2307.02098 [astro-ph.HE].

Li, Liande and Jirong Mao (Apr. 2022). “Temporal Analysis of GRB Precursors in the Third Swift-BAT Catalog.” In: *ApJ* 928.2, 152, p. 152. DOI: 10.3847/1538-4357/ac4af2. arXiv: 2201.12485 [astro-ph.HE].

Li, Ti-Pei (Aug. 2001). “Timing in the Time Domain: Cygnus X-1.” In: 1, pp. 313–332. DOI: 10.1088/1009-9271/1/4/313. arXiv: astro-ph/0109468 [astro-ph].

Li, Xiu-Juan and Yu-Peng Yang (Oct. 2023). “Signatures of the Self-organized Criticality Phenomenon in Precursors of Gamma-Ray Bursts.” In: *ApJL* 955.2, L34, p. L34. DOI: 10.3847/2041-8213/acf12c. arXiv: 2308.14281 [astro-ph.GA].

Li, Xiu-Juan et al. (Apr. 2023). “Evidence for the Self-organized Criticality Phenomenon in the Prompt Phase of Short Gamma-Ray Bursts.” In: *ApJS* 265.2, 56, p. 56. DOI: 10.3847/1538-4365/acc398. arXiv: 2303.06667 [astro-ph.HE].

Li, Ya-Ping et al. (Sept. 2015). "Statistics of X-Ray Flares of Sagittarius A*: Evidence for Solar-like Self-organized Criticality Phenomena." In: *ApJ* 810.1, 19, p. 19. DOI: 10.1088/0004-637X/810/1/19. arXiv: 1506.02946 [astro-ph.HE].

Li, Ye et al. (2019). "The FRB 121102 Host Is Atypical among Nearby Fast Radio Bursts." In: *ApJL* 884.1, L26, p. L26. DOI: 10.3847/2041-8213/ab3e41. arXiv: 1906.08749 [astro-ph.HE].

Lien, A. et al. (Sept. 2016). "The Third Swift Burst Alert Telescope Gamma-Ray Burst Catalog." In: *ApJ* 829, 7, p. 7. DOI: 10.3847/0004-637X/829/1/7. arXiv: 1606.01956 [astro-ph.HE].

Lin, Da-Bin et al. (Nov. 2016). "Variabilities of gamma-ray bursts from black hole hyper-accretion discs." In: *MNRAS* 463.1, pp. 245–250. DOI: 10.1093/mnras/stw1985. arXiv: 1608.01923 [astro-ph.HE].

Lin, R. P., P. T. Feffer, and R. A. Schwartz (Aug. 2001). "Solar Hard X-Ray Bursts and Electron Acceleration Down to 8 keV." In: *ApJL* 557.2, pp. L125–L128. DOI: 10.1086/323270.

Lin, R. P. et al. (Nov. 2002). "The Reuven Ramaty High-Energy Solar Spectroscopic Imager (RHESSI)." In: 210.1, pp. 3–32. DOI: 10.1023/A:1022428818870.

López-Ruiz, R., H. L. Mancini, and X. Calbet (Feb. 1995). "A statistical measure of complexity." In: *Physics Letters A* 209.5, pp. 321–326. DOI: 10.1016/0375-9601(95)00867-5. arXiv: nlin/0205033 [nlin.CD].

Lu, Edward T. and Russell J. Hamilton (Oct. 1991). "Avalanches and the Distribution of Solar Flares." In: *ApJL* 380, p. L89. DOI: 10.1086/186180.

Lü, Jing et al. (May 2012). "Lorentz-factor-Isotropic-luminosity/Energy Correlations of Gamma-Ray Bursts and Their Interpretation." In: *ApJ* 751.1, 49, p. 49. DOI: 10.1088/0004-637X/751/1/49. arXiv: 1109.3757 [astro-ph.HE].

Lu, R.-J. et al. (Feb. 2012). "Selection Effects on the Observed Redshift Dependence of Gamma-Ray Burst Jet Opening Angles." In: *ApJ* 745, 168, p. 168. DOI: 10.1088/0004-637X/745/2/168. arXiv: 1110.4943 [astro-ph.HE].

Lyu, Fen et al. (Oct. 2020). "Self-organized criticality in multi-pulse gamma-ray bursts." In: *Frontiers of Physics* 16.1, 14501, p. 14501. DOI: 10.1007/s11467-020-0989-x. arXiv: 2009.06180 [astro-ph.HE].

Lyutikov, M. (June 2006). "Did Swift measure gamma-ray burst prompt emission radii?" In: *MNRAS* 369, pp. L5–L8. DOI: 10.1111/j.1745-3933.2006.00161.x. eprint: astro-ph/0601557.

MAGIC Collaboration et al. (2019a). "Observation of inverse Compton emission from a long γ-ray burst." In: *Nature* 575.7783, pp. 459–463. DOI: 10.1038/s41586-019-1754-6.

MAGIC Collaboration et al. (2019b). "Teraelectronvolt emission from the γ-ray burst GRB 190114C." In: *Nature* 575.7783, pp. 455–458. DOI: 10.1038/s41586-019-1750-x.

MacFadyen, A. I., S. E. Woosley, and A. Heger (Mar. 2001). "Supernovae, Jets, and Collapsars." In: *ApJ* 550.1, pp. 410–425. DOI: 10.1086/319698. arXiv: astro-ph/9910034 [astro-ph].

MacLachlan, G. A. et al. (June 2013). "Minimum variability time-scales of long and short GRBs." In: *MNRAS* 432.2, pp. 857–865. DOI: 10.1093/mnras/stt241. arXiv: 1201.4431 [astro-ph.HE].

Maccary, R. et al. (Aug. 2024a). "Distribution of the number of peaks within a long gamma-ray burst: The full Fermi/GBM catalogue." In: *A&A* 688, L8, p. L8. DOI: 10.1051/0004-6361/202450666. arXiv: 2407.06002 [astro-ph.HE].

Maccary, R. et al. (Apr. 2024b). “Distributions of Energy, Luminosity, Duration, and Waiting Times of Gamma-Ray Burst Pulses with Known Redshift Detected by Fermi/GBM.” In: *ApJ* 965.1, 72, p. 72. DOI: `10.3847/1538-4357/ad26f4`. arXiv: `2401.14063 [astro-ph.HE]`.

Maccary, R. et al. (Oct. 2025). “Gamma-ray burst minimum variability timescales with Fermi/GBM.” In: *A&A* 702, A95, A95. DOI: `10.1051/0004-6361/202555418`. arXiv: `2508.08995 [astro-ph.HE]`.

Maccary, R. et al. (Jan. 2026). “A set of distinctive properties ruling the prompt emission of GRB 230307A and other long γ-ray bursts from compact object mergers.” In: *Journal of High Energy Astrophysics* 49, 100456, p. 100456. DOI: `10.1016/j.jheap.2025.100456`. arXiv: `2509.05628 [astro-ph.HE]`.

Maistrello, M. et al. (Apr. 2024). “The dispersion of the $E_{p,i}$-L_{iso} correlation of long gamma-ray bursts is partially due to assembling different sources.” In: *A&A* 684, L10, p. L10. DOI: `10.1051/0004-6361/202449165`. arXiv: `2403.11923 [astro-ph.HE]`.

Maistrello, M. et al. (May 2025). “An advanced pulse-avalanche stochastic model of long gamma-ray burst light curves.” In: *A&A* 697, A76, A76. DOI: `10.1051/0004-6361/202553821`.

Mangano, V. et al. (July 2007). “Swift observations of GRB 060614: an anomalous burst with a well behaved afterglow.” In: *A&A* 470.1, pp. 105–118. DOI: `10.1051/0004-6361:20077232`. arXiv: `0704.2235 [astro-ph]`.

Manzo, G. et al. (Apr. 1997). “The high pressure gas scintillation proportional counter onboard the BeppoSAX X-ray astronomy satellite.” In: 122, pp. 341–356. DOI: `10.1051/aas:1997139`.

Mao, Shude and Bohdan Paczynski (Apr. 1992). “On the Galactic Disk and Halo Models of Gamma-Ray Bursts.” In: *ApJL* 389, p. L13. DOI: `10.1086/186337`.

Maraventano, C. et al. (May 2025). “High energy time lags of gamma-ray bursts.” In: *A&A* 697, A161, A161. DOI: `10.1051/0004-6361/202554053`. arXiv: `2503.17216 [astro-ph.HE]`.

Margutti, R. et al. (Oct. 2008). “Temporal variability of GRB early X-ray afterglows and GRB080319B prompt emission.” In: *2008 Nanjing Gamma-ray Burst Conference*. Ed. by Yong-Feng Huang, Zi-Gao Dai, and Bing Zhang. Vol. 1065. American Institute of Physics Conference Series, pp. 259–262. DOI: `10.1063/1.3027924`. arXiv: `0809.0189 [astro-ph]`.

Margutti, R. et al. (Feb. 2010a). “GRB081028 and its late-time afterglow re-brightening.” In: *MNRAS* 402, pp. 46–64. DOI: `10.1111/j.1365-2966.2009.15882.x`. arXiv: `0910.3166 [astro-ph.HE]`.

Margutti, R. et al. (Aug. 2010b). “Lag-luminosity relation in γ-ray burst X-ray flares: a direct link to the prompt emission.” In: *MNRAS* 406, pp. 2149–2167. DOI: `10.1111/j.1365-2966.2010.16824.x`. arXiv: `1004.1568 [astro-ph.HE]`.

Margutti, Raffaella and Ryan Chornock (Sept. 2021). “First Multimessenger Observations of a Neutron Star Merger.” In: *ARA&A* 59, pp. 155–202. DOI: `10.1146/annurev-astro-112420-030742`. arXiv: `2012.04810 [astro-ph.HE]`.

Martin, M. T., A. Plastino, and O. A. Rosso (Sept. 2006). “Generalized statistical complexity measures: Geometrical and analytical properties.” In: *Physica A Statistical Mechanics and its Applications* 369.2, pp. 439–462. DOI: `10.1016/j.physa.2005.11.053`.

Mazets, E. P. et al. (1979). “Observations of a flaring X-ray pulsar in Dorado.” In: *Nature* 282.5739, pp. 587–589. DOI: `10.1038/282587a0`.

Meegan, C. A. et al. (1992). “Spatial distribution of γ-ray bursts observed by BATSE.” In: *Nature* 355.6356, pp. 143–145. doi: 10.1038/355143a0.

Meegan, C. et al. (Sept. 2009). “THE fermi gamma-ray burst monitor.” In: *ApJ* 702, 791, pp. 791–804. doi: 10.1088/0004-637X/702/1/791. arXiv: 0908.0450 [astro-ph.IM].

Meegan, Charles A. et al. (May 1998). “The 4B BATSE gamma-ray burst catalog.” In: *Gamma-Ray Bursts, 4th Hunstville Symposium*. Ed. by Charles A. Meegan, Robert D. Preece, and Thomas M. Koshut. Vol. 428. American Institute of Physics Conference Series. AIP, pp. 3–9. doi: 10.1063/1.55355.

Mesa-Rodríguez, Ania et al. (Nov. 2022). “Cancer Segmentation by Entropic Analysis of Ordered Gene Expression Profiles.” In: *Entropy* 24.12, 1744, p. 1744. doi: 10.3390/e24121744.

Metzger, B. D. et al. (May 2011). “The protomagnetar model for gamma-ray bursts.” In: *MNRAS* 413, pp. 2031–2056. doi: 10.1111/j.1365-2966.2011.18280.x. arXiv: 1012.0001 [astro-ph.HE].

Metzger, Brian D. (Dec. 2020). “Kilonovae.” In: *Living Reviews in Relativity* 23.1, 1, p. 1. doi: 10.1007/s41114-019-0024-0.

Metzger, M. R. et al. (1997). “Spectral constraints on the redshift of the optical counterpart to the γ-ray burst of 8 May 1997.” In: *Nature* 387.6636, pp. 878–880. doi: 10.1038/43132.

Milisavljevic, D. et al. (Jan. 2015). “The Broad-lined Type Ic SN 2012ap and the Nature of Relativistic Supernovae Lacking a Gamma-Ray Burst Detection.” In: *ApJ* 799, 51, p. 51. doi: 10.1088/0004-637X/799/1/51. arXiv: 1408.1606 [astro-ph.HE].

Minaev, P. Y. and A. S. Pozanenko (Feb. 2020). “The $E_{\mathrm{p,I}}$-E_{iso} correlation: type I gamma-ray bursts and the new classification method.” In: *MNRAS* 492.2, pp. 1919–1936. doi: 10.1093/mnras/stz3611. arXiv: 1912.09810 [astro-ph.HE].

Mineshige, S., N. B. Ouchi, and H. Nishimori (Feb. 1994). “On the generation of 1/f fluctuations in X-rays from black-hole objects.” In: *PASJ* 46, pp. 97–105.

Moresco, Michele et al. (Dec. 2022). “Unveiling the Universe with emerging cosmological probes.” In: *Living Reviews in Relativity* 25.1, 6, p. 6. doi: 10.1007/s41114-022-00040-z. arXiv: 2201.07241 [astro-ph.CO].

Nakanishi, Hiizu (June 1990). “Cellular-automaton model of earthquakes with deterministic dynamics.” In: 41.12, pp. 7086–7089. doi: 10.1103/PhysRevA.41.7086.

— (June 1991). “Statistical properties of the cellular-automaton model for earthquakes.” In: 43.12, pp. 6613–6621. doi: 10.1103/PhysRevA.43.6613.

Neill, Duncan et al. (Aug. 2022). “Resonant shattering flares in black hole-neutron star and binary neutron star mergers.” In: *MNRAS* 514.4, pp. 5385–5402. doi: 10.1093/mnras/stac1645. arXiv: 2111.03686 [astro-ph.HE].

Norris, J. P. (Nov. 2002). “Implications of the Lag-Luminosity Relationship for Unified Gamma-Ray Burst Paradigms.” In: *ApJ* 579.1, pp. 386–403. doi: 10.1086/342747. arXiv: astro-ph/0201503 [astro-ph].

Norris, J. P. and J. T. Bonnell (May 2006). “Short Gamma-Ray Bursts with Extended Emission.” In: *ApJ* 643, pp. 266–275. doi: 10.1086/502796. eprint: arXiv:astro-ph/0601190.

Norris, J. P., G. F. Marani, and J. T. Bonnell (2000). “Connection between Energy-dependent Lags and Peak Luminosity in Gamma-Ray Bursts.” In: *ApJ* 534.1, pp. 248–257. doi: 10.1086/308725. arXiv: astro-ph/9903233 [astro-ph].

Norris, J. P. et al. (Mar. 1996). “Attributes of Pulses in Long Bright Gamma-Ray Bursts.” In: *ApJ* 459, p. 393. doi: 10.1086/176902.

Norris, J. P. et al. (July 2005). “Long-Lag, Wide-Pulse Gamma-Ray Bursts.” In: *ApJ* 627, pp. 324–345. DOI: `10.1086/430294`. eprint: `arXiv:astro-ph/0503383`.

O’Brien, Paul et al. (Jan. 2021). “The soft x-ray imager on THESEUS: the transient high energy survey and early universe surveyor.” In: *Society of Photo-Optical Instrumentation Engineers (SPIE) Conference Series*. Ed. by Jan-Willem A. den Herder, Shouleh Nikzad, and Kazuhiro Nakazawa. Vol. 11444. Society of Photo-Optical Instrumentation Engineers (SPIE) Conference Series, 114442L, p. 114442L. DOI: `10.1117/12.2561301`.

Oganesyan, Gor et al. (Apr. 2020). “Structured Jets and X-Ray Plateaus in Gamma-Ray Burst Phenomena.” In: *ApJ* 893.2, 88, p. 88. DOI: `10.3847/1538-4357/ab8221`. arXiv: `1904.08786 [astro-ph.HE]`.

Orwig, L. E., K. J. Frost, and B. R. Dennis (Feb. 1980). “The hard X-ray burst spectrometer on the Solar Maximum Mission.” In: 65.1, pp. 25–37. DOI: `10.1007/BF00151382`.

Otsuka, Michio (Jan. 1972). “A simulation of earthquake occurrence.” In: *Physics of the Earth and Planetary Interiors* 6.4, pp. 311–315. DOI: `10.1016/0031-9201(72)90015-5`.

Paczynski, B. (1986). “Gamma-ray bursters at cosmological distances.” In: *ApJL* 308, pp. L43–L46. DOI: `10.1086/184740`.

Paczynski, Bohdan (Jan. 1991). “Cosmological gamma-ray bursts.” In: 41, pp. 257–267.

Pais, Matteo, Tsvi Piran, and Ehud Nakar (Aug. 2022). “The velocity distribution of outflows driven by choked jets in stellar envelopes.” In: *arXiv e-prints*, arXiv:2208.14459, arXiv:2208.14459. arXiv: `2208.14459 [astro-ph.HE]`.

Palmerio, J. T. et al. (2019). “Are long gamma-ray bursts biased tracers of star formation? Clues from the host galaxies of the Swift/BAT6 complete sample of bright LGRBs. III. Stellar masses, star formation rates, and metallicities at z > 1.” In: *A&A* 623, A26, A26. DOI: `10.1051/0004-6361/201834179`. arXiv: `1901.02457 [astro-ph.HE]`.

Panaitescu, A., M. Spada, and P. Mészáros (Sept. 1999). “Power Density Spectra of Gamma-Ray Bursts in the Internal Shock Model.” In: *ApJL* 522.2, pp. L105–L108. DOI: `10.1086/312230`. arXiv: `astro-ph/9905026 [astro-ph]`.

Parker, E. N. (July 1988). “Nanoflares and the Solar X-Ray Corona.” In: *ApJ* 330, p. 474. DOI: `10.1086/166485`.

Parmar, A. N. et al. (Apr. 1997). “The low-energy concentrator spectrometer on-board the BeppoSAX X-ray astronomy satellite.” In: 122, pp. 309–326. DOI: `10.1051/aas:1997137`.

Pelassa, V. et al. (Feb. 2010). “The LAT Low-Energy technique for Fermi Gamma-Ray Bursts spectral analysis.” In: *arXiv e-prints*, arXiv:1002.2617, arXiv:1002.2617. DOI: `10.48550/arXiv.1002.2617`. arXiv: `1002.2617 [astro-ph.HE]`.

Pellouin, Clément and Frédéric Daigne (Oct. 2024). “Very high energy afterglow of structured jets: GW 170817 and prospects for future detections.” In: *A&A* 690, A281, A281. DOI: `10.1051/0004-6361/202347516`. arXiv: `2406.08254 [astro-ph.HE]`.

Peng, Zhao-Yang, Jia-Ming Chen, and Jirong Mao (July 2024). “A Comparative Analysis of Two Peculiar Gamma-Ray Bursts: GRB 230307A and GRB 211211A.” In: *ApJ* 969.1, 26, p. 26. DOI: `10.3847/1538-4357/ad45fc`. arXiv: `2404.17913 [astro-ph.HE]`.

Perley, D. A. et al. (Jan. 2016). “The Swift GRB Host Galaxy Legacy Survey. II. Rest-frame Near-IR Luminosity Distribution and Evidence for a Near-solar Metallicity Threshold.” In: *ApJ* 817.1, 8, p. 8. DOI: `10.3847/0004-637X/817/1/8`. arXiv: `1504.02479 [astro-ph.GA]`.

Pessa, Arthur A. B. and Haroldo V. Ribeiro (June 2021). “ordpy: A Python package for data analysis with permutation entropy and ordinal network methods.” In: *Chaos* 31.6, 063110, p. 063110. DOI: `10.1063/5.0049901`. arXiv: `2102.06786 [physics.data-an]`.

Plenz, Dietmar et al. (July 2021). “Self-Organized Criticality in the Brain.” In: *Frontiers in Physics* 9, 639389, p. 639389. DOI: `10.3389/fphy.2021.639389`. arXiv: `2102.09124 [q-bio.NC]`.

Popham, R., S. E. Woosley, and C. Fryer (June 1999). “Hyperaccreting Black Holes and Gamma-Ray Bursts.” In: *ApJ* 518, pp. 356–374. DOI: `10.1086/307259`. eprint: `astro-ph/9807028`.

Pühlhofer, Gerd, Fabian Leuschner, and Heiko Salzmann (2023). “H.E.S.S.: The High Energy Stereoscopic System.” In: *Handbook of X-ray and Gamma-ray Astrophysics*, 142, p. 142. DOI: `10.1007/978-981-16-4544-0_69-1`.

Ramirez-Ruiz, E. and E. E. Fenimore (Sept. 1999). “Temporal evolution of the pulse width in GRBs.” In: 138, pp. 521–522. DOI: `10.1051/aas:1999336`. arXiv: `astro-ph/9812426 [astro-ph]`.

Ramirez-Ruiz, E. and N. M. Lloyd-Ronning (July 2002). “Beam models for gamma-ray bursts sources: outflow structure, kinematics and emission mechanisms.” In: 7, pp. 197–210. DOI: `10.1016/S1384-1076(02)00106-9`. eprint: `astro-ph/0203447`.

Rastinejad, Jillian C. et al. (Dec. 2022). “A kilonova following a long-duration gamma-ray burst at 350 Mpc.” In: *Nature* 612.7939, pp. 223–227. DOI: `10.1038/s41586-022-05390-w`. arXiv: `2204.10864 [astro-ph.HE]`.

Rees, M. J. and P. Meszaros (Aug. 1994). “Unsteady outflow models for cosmological gamma-ray bursts.” In: *ApJ* 430, pp. L93–L96. DOI: `10.1086/187446`. eprint: `arXiv:astro-ph/9404038`.

Rhodes, Lauren et al. (May 2021). “An early peak in the radio light curve of short-duration gamma-ray burst 200826A.” In: *MNRAS* 503.2, pp. 2966–2972. DOI: `10.1093/mnras/stab640`. arXiv: `2103.01881 [astro-ph.HE]`.

Roming, P. W. A. et al. (Oct. 2005). “The Swift Ultra-Violet/Optical Telescope.” In: *Space Sci. Rev.* 120, pp. 95–142. DOI: `10.1007/s11214-005-5095-4`. eprint: `arXiv:astro-ph/0507413`.

Rossi, A. et al. (June 2022). “The Peculiar Short-duration GRB 200826A and Its Supernova.” In: *ApJ* 932.1, 1, p. 1. DOI: `10.3847/1538-4357/ac60a2`. arXiv: `2105.03829 [astro-ph.HE]`.

Ryde, F. et al. (Nov. 2003). “Gamma-ray bursts observed by the INTEGRAL-SPI anticoincidence shield: A study of individual pulses and temporal variability.” In: *A&A* 411, pp. L331–L342. DOI: `10.1051/0004-6361:20031440`.

Ryde, F. et al. (Feb. 2010). “Identification and Properties of the Photospheric Emission in GRB090902B.” In: *ApJ* 709, pp. L172–L177. DOI: `10.1088/2041-8205/709/2/L172`. arXiv: `0911.2025 [astro-ph.HE]`.

Salafia, Om Sharan and Giancarlo Ghirlanda (2022). “The Structure of Gamma Ray Burst Jets.” In: *Galaxies* 10.5. ISSN: 2075-4434. DOI: `10.3390/galaxies10050093`. URL: `https://www.mdpi.com/2075-4434/10/5/93`.

Sari, R., T. Piran, and R. Narayan (Apr. 1998). “Spectra and Light Curves of Gamma-Ray Burst Afterglows.” In: *ApJ* 497, p. L17. DOI: `10.1086/311269`. eprint: `arXiv:astro-ph/9712005`.

Särkkä, Simo and Arno Solin (2019). *Applied Stochastic Differential Equations*. Vol. 10. Institute of Mathematical Statistics Textbooks. Cambridge University Press. DOI: `10.1017/9781108684163`.

Savaglio, S., K. Glazebrook, and D. Le Borgne (Jan. 2009). "The Galaxy Population Hosting Gamma-Ray Bursts." In: *ApJ* 691.1, pp. 182–211. DOI: 10.1088/0004-637X/691/1/182. arXiv: 0803.2718 [astro-ph].

Schaefer, Bradley E. and Andrew C. Collazzi (Feb. 2007). "Generalized Tests for Eight GRB Luminosity Relations." In: *ApJL* 656.2, pp. L53–L56. DOI: 10.1086/512855. arXiv: astro-ph/0701548 [astro-ph].

Schneider, B. et al. (Oct. 2022). "Are the host galaxies of long gamma-ray bursts more compact than star-forming galaxies of the field?" In: *A&A* 666, A14, A14. DOI: 10.1051/0004-6361/202243367. arXiv: 2206.14873 [astro-ph.GA].

Shannon, C. E. (July 1948). "A mathematical theory of communication." In: *Bell Labs Technical Journal* 27.3, pp. 379–423. DOI: 10.1002/j.1538-7305.1948.tb01338.x.

Shao, L., Z. G. Dai, and N. Mirabal (Mar. 2008). "Echo Emission from Dust Scattering and X-Ray Afterglows of Gamma-Ray Bursts." In: *ApJ* 675.1, pp. 507–518. DOI: 10.1086/527047. arXiv: 0711.3800 [astro-ph].

Shao, Lang et al. (Aug. 2017). "A New Measurement of the Spectral Lag of Gamma-Ray Bursts and its Implications for Spectral Evolution Behaviors." In: *ApJ* 844.2, 126, p. 126. DOI: 10.3847/1538-4357/aa7d01. arXiv: 1610.07191 [astro-ph.HE].

Shen, Rongfeng and Christopher D. Matzner (Jan. 2012). "Coasting External Shock in Wind Medium: An Origin for the X-Ray Plateau Decay Component in Swift Gamma-Ray Burst Afterglows." In: *ApJ* 744.1, 36, p. 36. DOI: 10.1088/0004-637X/744/1/36. arXiv: 1109.3453 [astro-ph.HE].

Smartt, S. J. et al. (2017). "A kilonova as the electromagnetic counterpart to a gravitational-wave source." In: *Nature* 551.7678, pp. 75–79. DOI: 10.1038/nature24303. arXiv: 1710.05841 [astro-ph.HE].

Soderberg, A. M. et al. (Jan. 2010). "A relativistic type Ibc supernova without a detected γ-ray burst." In: *Nature* 463, pp. 513–515. DOI: 10.1038/nature08714. arXiv: 0908.2817 [astro-ph.HE].

Spada, M., A. Panaitescu, and P. Mészáros (July 2000). "Analysis of Temporal Features of Gamma-Ray Bursts in the Internal Shock Model." In: *ApJ* 537, pp. 824–832. DOI: 10.1086/309048. eprint: arXiv:astro-ph/9908097.

Stanek, K. Z. et al. (July 2003). "Spectroscopic Discovery of the Supernova 2003dh Associated with GRB 030329." In: *ApJL* 591.1, pp. L17–L20. DOI: 10.1086/376976. arXiv: astro-ph/0304173 [astro-ph].

Stern, Boris E. (June 1996). "A Stretched Exponential Law for the Average Time History of Gamma-Ray Bursts and Their Time Dilations." In: *ApJL* 464, p. L111. DOI: 10.1086/310113. arXiv: astro-ph/9509150 [astro-ph].

Stern, Boris E. and Roland Svensson (Oct. 1996). "Evidence for "Chain Reaction" in the Time Profiles of Gamma-Ray Bursts." In: *ApJL* 469, p. L109. DOI: 10.1086/310267. arXiv: astro-ph/9607070 [astro-ph].

Stratta, Giulia et al. (2018). "On the Magnetar Origin of the GRBs Presenting X-Ray Afterglow Plateaus." In: *ApJ* 869.2, 155, p. 155. DOI: 10.3847/1538-4357/aadd8f. arXiv: 1804.08652 [astro-ph.HE].

Takahashi, Kazuya and Kunihito Ioka (Mar. 2021). "Diverse jet structures consistent with the off-axis afterglow of GRB 170817A." In: *MNRAS* 501.4, pp. 5746–5756. DOI: 10.1093/mnras/stab032. arXiv: 2007.13116 [astro-ph.HE].

Tan, Wen-Jun et al. (Apr. 2025). “Search for Type IL Gamma-ray Bursts: Criterion, Results, Verification and Physical Implication.” In: *arXiv e-prints*, arXiv:2504.06616, arXiv:2504.06616. DOI: `10.48550/arXiv.2504.06616`. arXiv: `2504.06616 [astro-ph.HE]`.

Tanvir, N. R. et al. (Aug. 2013). “A ‘kilonova’ associated with the short-duration γ-ray burst GRB 130603B.” In: *Nature* 500.7464, pp. 547–549. DOI: `10.1038/nature12505`. arXiv: `1306.4971 [astro-ph.HE]`.

Tanvir, N. R. et al. (Oct. 2017). “The Emergence of a Lanthanide-rich Kilonova Following the Merger of Two Neutron Stars.” In: *ApJL* 848.2, L27, p. L27. DOI: `10.3847/2041-8213/aa90b6`. arXiv: `1710.05455 [astro-ph.HE]`.

Tchekhovskoy, Alexander, Ramesh Narayan, and Jonathan C. McKinney (Mar. 2010). “Black Hole Spin and The Radio Loud/Quiet Dichotomy of Active Galactic Nuclei.” In: *ApJ* 711.1, pp. 50–63. DOI: `10.1088/0004-637X/711/1/50`. arXiv: `0911.2228 [astro-ph.HE]`.

Thorne, Kip S. (1994). *Black Holes and Time Warps: Einstein's Outrageous Legacy*. New York: W. W. Norton.

Toma, Kenji et al. (Apr. 2006). “Shallow Decay of Early X-Ray Afterglows from Inhomogeneous Gamma-Ray Burst Jets.” In: *ApJL* 640.2, pp. L139–L142. DOI: `10.1086/503384`. arXiv: `astro-ph/0511718 [astro-ph]`.

Troja, E. et al. (July 2017). “Significant and variable linear polarization during the prompt optical flash of GRB 160625B.” In: *Nature* 547, pp. 425–427. DOI: `10.1038/nature23289`.

Troja, E. et al. (Dec. 2022). “A long gamma-ray burst from a merger of compact objects.” In: *Nature* 612, pp. 228–231. DOI: `10.1038/s41586-022-05327-3`.

Tsang, David et al. (Jan. 2012). “Resonant Shattering of Neutron Star Crusts.” In: 108.1, 011102, p. 011102. DOI: `10.1103/PhysRevLett.108.011102`. arXiv: `1110.0467 [astro-ph.HE]`.

Tsvetkova, A. et al. (Dec. 2017). “The Konus-Wind Catalog of Gamma-Ray Bursts with Known Redshifts. I. Bursts Detected in the Triggered Mode.” In: *ApJ* 850.2, 161, p. 161. DOI: `10.3847/1538-4357/aa96af`. arXiv: `1710.08746 [astro-ph.HE]`.

Turcotte, Donald L. (Oct. 1999). “Self-organized criticality.” In: *Reports on Progress in Physics* 62.10, pp. 1377–1429. DOI: `10.1088/0034-4885/62/10/201`.

Uhm, Z. Lucas and Andrei M. Beloborodov (Aug. 2007). “On the Mechanism of Gamma-Ray Burst Afterglows.” In: *ApJL* 665.2, pp. L93–L96. DOI: `10.1086/519837`. arXiv: `astro-ph/0701205 [astro-ph]`.

Ukwatta, T. N. et al. (Mar. 2010). “Spectral Lags and the Lag-Luminosity Relation: An Investigation with Swift BAT Gamma-ray Bursts.” In: *ApJ* 711.2, pp. 1073–1086. DOI: `10.1088/0004-637X/711/2/1073`. arXiv: `0908.2370 [astro-ph.HE]`.

Ukwatta, T. N. et al. (Jan. 2012). “The lag-luminosity relation in the GRB source frame: an investigation with Swift BAT bursts.” In: *MNRAS* 419.1, pp. 614–623. DOI: `10.1111/j.1365-2966.2011.19723.x`. arXiv: `1109.0666 [astro-ph.HE]`.

Uttley, Philip and Ian M. McHardy (Oct. 2005). “X-ray variability of NGC 3227 and 5506 and the nature of active galactic nucleus ‘states’.” In: *MNRAS* 363.2, pp. 586–596. DOI: `10.1111/j.1365-2966.2005.09475.x`.

Valenti, Stefano et al. (Oct. 2017). “The Discovery of the Electromagnetic Counterpart of GW170817: Kilonova AT 2017gfo/DLT17ck.” In: *ApJL* 848.2, L24, p. L24. DOI: `10.3847/2041-8213/aa8edf`. arXiv: `1710.05854 [astro-ph.HE]`.

Vergani, S. D. et al. (Sept. 2015). “Are long gamma-ray bursts biased tracers of star formation? Clues from the host galaxies of the Swift/BAT6 complete sample of LGRBs . I. Stellar mass at z < 1." In: *A&A* 581, A102, A102. DOI: 10.1051/0004-6361/201425013. arXiv: 1409.7064 [astro-ph.HE].

Vernani, Dervis et al. (Aug. 2022). "Follow-up x-ray telescope (FXT) mirror module for the Einstein probe mission." In: *Space Telescopes and Instrumentation 2022: Ultraviolet to Gamma Ray*. Ed. by Jan-Willem A. den Herder, Shouleh Nikzad, and Kazuhiro Nakazawa. Vol. 12181. Society of Photo-Optical Instrumentation Engineers (SPIE) Conference Series, 121811R, 121811R. DOI: 10.1117/12.2630147.

Vetere, L. et al. (Feb. 2006). "Slow and fast components in the X-ray light curves of gamma-ray bursts." In: *A&A* 447, pp. 499–513. DOI: 10.1051/0004-6361:20053800.

Vianello, Giacomo et al. (July 2015). "The Multi-Mission Maximum Likelihood framework (3ML)." In: *arXiv e-prints*, arXiv:1507.08343, arXiv:1507.08343. DOI: 10.48550/arXiv.1507.08343. arXiv: 1507.08343 [astro-ph.HE].

Vidiella, B., A. Guillamon, and J. et al Sardanyès (2021). "Engineering self-organized criticality in living cells." In: *Nature communications*. DOI: 10.1038/s41467-021-24695-4.

Wang, Chen-Wei et al. (Jan. 2025). "A Subclass of Gamma-Ray Burst Originating from Compact Binary Merger." In: *ApJ* 979.1, 73, p. 73. DOI: 10.3847/1538-4357/ad98ec. arXiv: 2407.02376 [astro-ph.HE].

Wang, F. Y. and Z. G. Dai (Aug. 2013). "Self-organized criticality in X-ray flares of gamma-ray-burst afterglows." In: *Nature Physics* 9, pp. 465–467. DOI: 10.1038/nphys2670. arXiv: 1308.1253 [astro-ph.HE].

Wang, F. Y. et al. (Jan. 2015). "Universal Behavior of X-Ray Flares from Black Hole Systems." In: *ApJS* 216, 8, p. 8. DOI: 10.1088/0067-0049/216/1/8. arXiv: 1411.4209 [astro-ph.HE].

Wang, L. J. et al. (Mar. 2017). "Evidence for Magnetar Formation in Broad-lined Type Ic Supernovae 1998bw and 2002ap." In: *ApJ* 837, 128, p. 128. DOI: 10.3847/1538-4357/aa5ff5. arXiv: 1610.09061 [astro-ph.HE].

Wang, Xiangyu Ivy, Bin-Bin Zhang, and Wei-Hua Lei (May 2022). "GRB 200826A: A Precursor of a Long Gamma-Ray Burst with Missing Main Emission." In: *ApJL* 931.1, L2, p. L2. DOI: 10.3847/2041-8213/ac6c7e. arXiv: 2202.12460 [astro-ph.HE].

Watkins, Nicholas W. et al. (Jan. 2016). "25 Years of Self-organized Criticality: Concepts and Controversies." In: 198.1-4, pp. 3–44. DOI: 10.1007/s11214-015-0155-x. arXiv: 1504.04991 [cond-mat.stat-mech].

Weekes, T. C. et al. (May 2002). "VERITAS: the Very Energetic Radiation Imaging Telescope Array System." In: *Astroparticle Physics* 17.2, pp. 221–243. DOI: 10.1016/S0927-6505(01)00152-9. arXiv: astro-ph/0108478 [astro-ph].

Wei, Fang et al. (Dec. 2022). "The two-Gaussian jet structure and its formation process: Constraints from the afterglows of GRB 170817A." In: *Scientia Sinica Physica, Mechanica & Astronomica* 52.12, p. 129511. DOI: 10.1360/SSPMA-2022-0120.

Wei, Jun-Jie (Jan. 2023). "Scale invariance in x-ray flares of gamma-ray bursts." In: *Physical Review Research* 5.1, 013019, p. 013019. DOI: 10.1103/PhysRevResearch.5.013019. arXiv: 2212.08813 [astro-ph.HE].

Wu, Bobing and Edward Fenimore (May 2000). "Spectral Lags of Gamma-Ray Bursts From Ginga and BATSE." In: *ApJL* 535.1, pp. L29–L32. DOI: 10.1086/312700. arXiv: astro-ph/9908281 [astro-ph].

Xia, Zi-Qing et al. (May 2024). “A delayed 400 GeV photon from GRB 221009A and implication on the intergalactic magnetic field.” In: *Nature Communications* 15, 4280, p. 4280. DOI: `10.1038/s41467-024-48668-5`. arXiv: `2210.13052 [astro-ph.HE]`.

Xin, Li-Ping et al. (Feb. 2016). “Multi-wavelength Observations of GRB 111228A and Implications for the Fireball and its Environment.” In: *ApJ* 817.2, 152, p. 152. DOI: `10.3847/0004-637X/817/2/152`. arXiv: `1512.07697 [astro-ph.HE]`.

Xue, Liang, Fu-Wen Zhang, and Si-Yuan Zhu (May 2019). “Characteristics of Long Gamma-Ray Bursts in the Comoving Frame.” In: *ApJ* 876.1, 77, p. 77. DOI: `10.3847/1538-4357/ab16f3`. arXiv: `1904.07767 [astro-ph.HE]`.

Yamazaki, Ryo (Jan. 2009). “Prior Emission Model for X-ray Plateau Phase of Gamma-Ray Burst Afterglows.” In: *ApJL* 690.2, pp. L118–L121. DOI: `10.1088/0004-637X/690/2/L118`. arXiv: `0810.1089 [astro-ph]`.

Yang, B. et al. (Apr. 2015). “A possible macronova in the late afterglow of the long-short burst GRB 060614.” In: *NatCo* 6, 7323. DOI: `10.1038/ncomms8323`.

Yonetoku, D. et al. (July 2004). “Gamma-Ray Burst Formation Rate Inferred from the Spectral Peak Energy-Peak Luminosity Relation.” In: *ApJ* 609, pp. 935–951. DOI: `10.1086/421285`. eprint: `astro-ph/0309217`.

Yuan, Qiang et al. (Jan. 2018). “A systematic Chandra study of Sgr A*: II. X-ray flare statistics.” In: *MNRAS* 473.1, pp. 306–316. DOI: `10.1093/mnras/stx2408`. arXiv: `1709.03709 [astro-ph.HE]`.

Yuan, Weimin et al. (2022). “The Einstein Probe Mission.” In: *Handbook of X-ray and Gamma-ray Astrophysics*. Ed. by Cosimo Bambi and Andrea Sangangelo, 86, p. 86. DOI: `10.1007/978-981-16-4544-0_151-1`.

Zanin, Massimiliano and Felipe Olivares (Dec. 2021). “Ordinal patterns-based methodologies for distinguishing chaos from noise in discrete time series.” In: *Communications Physics* 4.1, 190, p. 190. DOI: `10.1038/s42005-021-00696-z`.

Zhang, B. and H. Yan (Jan. 2011). “The Internal-collision-induced Magnetic Reconnection and Turbulence (ICMART) Model of Gamma-ray Bursts.” In: *ApJ* 726, 90, p. 90. DOI: `10.1088/0004-637X/726/2/90`. arXiv: `1011.1197 [astro-ph.HE]`.

Zhang, B. and B. Zhang (Feb. 2014). “Gamma-Ray Burst Prompt Emission Light Curves and Power Density Spectra in the ICMART Model.” In: *ApJ* 782, 92, p. 92. DOI: `10.1088/0004-637X/782/2/92`. arXiv: `1312.7701 [astro-ph.HE]`.

Zhang, B. et al. (May 2006). “Physical Processes Shaping Gamma-Ray Burst X-Ray Afterglow Light Curves: Theoretical Implications from the Swift X-Ray Telescope Observations.” In: *ApJ* 642, pp. 354–370. DOI: `10.1086/500723`. eprint: `arXiv:astro-ph/0508321`.

Zhang, Bing (Dec. 2006). “Astrophysics: A burst of new ideas.” In: *Nature* 444.7122, pp. 1010–1011. DOI: `10.1038/4441010a`. arXiv: `astro-ph/0612614 [astro-ph]`.

— (Feb. 2020). “Synchrotron radiation in γ-ray bursts prompt emission.” In: *Nature Astronomy* 4, pp. 210–211. DOI: `10.1038/s41550-020-1041-3`. arXiv: `2002.09638 [astro-ph.HE]`.

Zhang, Bing and Peter Mészáros (2001). “Gamma-Ray Burst Afterglow with Continuous Energy Injection: Signature of a Highly Magnetized Millisecond Pulsar.” In: *ApJL* 552.1, pp. L35–L38. DOI: `10.1086/320255`. arXiv: `astro-ph/0011133 [astro-ph]`.

Zhang, Bing and Asaf Pe’er (Aug. 2009). “Evidence of an Initially Magnetically Dominated Outflow in GRB 080916C.” In: *ApJL* 700.2, pp. L65–L68. DOI: `10.1088/0004-637X/700/2/L65`. arXiv: `0904.2943 [astro-ph.HE]`.

Zhang, C. et al. (Dec. 2022a). “First Wide Field-of-view X-Ray Observations by a Lobster-eye Focusing Telescope in Orbit.” In: *ApJL* 941.1, L2, p. L2. DOI: `10.3847/2041-8213/aca32f`. arXiv: `2211.10007 [astro-ph.HE]`.

Zhang, Shuang-Nan et al. (Feb. 2020). “Overview to the Hard X-ray Modulation Telescope (Insight-HXMT) Satellite.” In: *Science China Physics, Mechanics, and Astronomy* 63.4, 249502, p. 249502. DOI: `10.1007/s11433-019-1432-6`. arXiv: `1910.09613 [astro-ph.IM]`.

Zhang, Wen-Long et al. (June 2022b). “Statistical Properties of X-Ray Flares from the Supergiant Fast X-Ray Transients.” In: *Research in Astronomy and Astrophysics* 22.6, 065012, p. 065012. DOI: `10.1088/1674-4527/ac6aac`.

Zhang, Wen-Long et al. (June 2025a). “Insight-HXMT Observations of the Extremely Bright GRB 221009A.” In: *ApJ* 986.2, 170, p. 170. DOI: `10.3847/1538-4357/add14f`. arXiv: `2504.18952 [astro-ph.HE]`.

Zhang, Wen-Long et al. (Jan. 2025b). “Self-organized critical characteristics of teraelectronvolt photons from GRB 221009A.” In: *A&A* 693, A290, A290. DOI: `10.1051/0004-6361/202453174`. arXiv: `2412.16052 [astro-ph.HE]`.

Zitouni, Hannachi, Nidhal Guessoum, and Walid Azzam (Aug. 2022). “Testing the Amati and Yonetoku correlations for short gamma-ray bursts.” In: 367.8, 74, p. 74. DOI: `10.1007/s10509-022-04100-2`.

di Sciascio, G. and Lhaaso Collaboration (Oct. 2016). “The LHAASO experiment: From Gamma-Ray Astronomy to Cosmic Rays.” In: *Nuclear and Particle Physics Proceedings* 279-281, pp. 166–173. DOI: `10.1016/j.nuclphysbps.2016.10.024`. arXiv: `1602.07600 [astro-ph.HE]`.

van Paradijs, J. et al. (Apr. 1997). “Transient optical emission from the error box of the γ-ray burst of 28 February 1997.” In: *Nature* 386, pp. 686–689. DOI: `10.1038/386686a0`.

von Kienlin, A. et al. (Mar. 2014). “The Second Fermi GBM Gamma-Ray Burst Catalog: The First Four Years.” In: *ApJS* 211, 13, p. 13. DOI: `10.1088/0067-0049/211/1/13`. arXiv: `1401.5080 [astro-ph.HE]`.

von Kienlin, A. et al. (Apr. 2020). “The Fourth Fermi-GBM Gamma-Ray Burst Catalog: A Decade of Data.” In: *ApJ* 893.1, 46, p. 46. DOI: `10.3847/1538-4357/ab7a18`. arXiv: `2002.11460 [astro-ph.HE]`.

DECLARATION

I declare that this thesis is officially over.

Ferrara, October 2025

Romain Maccary

COLOPHON

This document was typeset using the typographical look-and-feel `classicthesis` developed by André Miede. The style was inspired by Robert Bringhurst's seminal book on typography "*The Elements of Typographic Style*". `classicthesis` is available for both LaTeX and LyX:

`https://bitbucket.org/amiede/classicthesis/`

Happy users of `classicthesis` usually send a real postcard to the author, a collection of postcards received so far is featured here:

`http://postcards.miede.de/`